

**THE IMPACT OF PROCESS VARIABLES ON
THE CHEMICAL VAPOUR DEPOSITION
OF
SILICON CARBIDE**

By

Robert Douglas Cromarty

Submitted in partial fulfilment of the requirements
for the degree:

Philosophiae Doctor

In the Department of Materials Science and Metallurgical
Engineering,
Faculty of Engineering, the Built Environment and Information
Technology, University of Pretoria, Pretoria, South Africa.

November, 2012

THE IMPACT OF PROCESS VARIABLES ON THE CHEMICAL VAPOUR DEPOSITION OF SILICON CARBIDE

Candidate : Robert Douglas Cromarty
Supervisor : Professor J. P. R de Villiers
Department : Materials Science and Metallurgical Engineering
Degree : Philosophiae Doctor

Abstract

High temperature gas cooled nuclear reactors often make use of Tristructural Isotropic (TRISO) coated fuel particles. In these particles, a layer of silicon carbide plays the key role of providing mechanical strength and acting as a diffusion barrier so preventing the release of fission products. TRISO particles are produced by a chemical vapor deposition (CVD) process in a spouted bed coater.

Operating conditions of chemical vapor deposition processes are known to influence the properties of the deposited material. In the case of silicon carbide deposited by pyrolysis of methyltrichlorosilane (MTS) in a hydrogen atmosphere, process parameters that may influence the properties of the silicon carbide deposited include deposition temperature, MTS concentration and hydrogen flow rates.

In this study the coating process was investigated using a laboratory scale spouted bed CVD coater. In all the test work conducted, carbon coated zirconia particles were used as a starting material. Only silicon carbide was deposited during these trials. Process parameters investigated were temperature, MTS concentration and hydrogen flow rate. The range investigated was 1250 °C to 1550 °C for temperature, 0.5 % to 2.5 % for MTS concentration and 10.0 l.minute⁻¹ to 15.0 l.minute⁻¹ for hydrogen flow. This covered the range that is typically used for small-scale production coatiers. Two different gas inlet configurations, a conventional water cooled inlet and an inlet without any cooling, were used in the investigation.

Properties of the coating process, such as the deposition rate and coating efficiency, as well as material properties were measured. Material properties investigated included: density, crush strength, micro-hardness, fracture toughness, nano-hardness, Young's modulus, elemental composition, phase composition and microstructure.

It was found that, of the variables investigated, temperature had the strongest effect while hydrogen flow rate had the least effect on material properties. There was considerable variability in all measured parameters; this introduced considerable uncertainty into the predicted effects of process conditions on material properties.

Keywords: TRISO, spouted bed, chemical vapor deposition, silicon carbide, methyltrichlorosilane, deposition rate, deposition efficiency, free silicon mechanical properties, morphology

ACKNOWLEDGEMENTS

I would like to express my gratitude and appreciation to the following people for their assistance during the course of this project:

- Professor Johan de Villiers for creating the opportunity for me to undertake this project and for many valuable discussions, support and trust during the course of this project. Without your support this project could not have succeeded.
- Wiebke Grote, Peter Gräser and Lucas Mabena of the Department of Geology for XRD analyses, electron microprobe analyses and sample preparation.
- Antoinette Buys and Andre Botha of the Laboratory for Microscopy and Microanalysis, University of Pretoria, for assistance with SEM microscopy and advice.
- Carel Coetzee of IMMRI, University of Pretoria, for much time, and patience, spent assisting me with SEM imaging.
- Linda Prinsloo of the Department of Physics, University of Pretoria, for assistance with Raman spectroscopy.
- Professor Francois Steffens and Dr Lizelle Fletcher of the Department of Statistics for valuable advice.
- Dr Jaco Olivier of the Centre for HRTEM, Nelson Mandela Metropolitan University, for nano-indentation measurements.
- PBMR (Pty) Ltd. For support, valuable information and samples. A special word of thanks to John Barry, Kobus Hancke and Robert Peters for their assistance.
- All my colleagues in the Department of Materials Science and Metallurgical Engineering their assistance, support, encouragement and friendship. You made it fun.
- Financial support received from the Department of Materials Science and Metallurgical Engineering is gratefully acknowledged. Without the financial support received, as both bursary payments and employment, I would never have been able to undertake this endeavour.
- Sanet, thank you for all your support, patience and love. I can't fully express my appreciation for your love and friendship.

DECLARATION

Unless otherwise indicated all experimental work, data analysis and interpretation reported on in this thesis is my own work.

This thesis has not been submitted in part, or in whole, for another degree at any other institution.

Robert Douglas Cromarty
November 2012

TABLE OF CONTENTS

1	INTRODUCTION	1
1.1	BACKGROUND	1
1.2	MOTIVATION	1
1.3	AIMS.....	2
1.4	APPROACH	2
1.5	CONTRIBUTION.....	2
2	HIGH TEMPERATURE GAS REACTORS.....	3
2.1	BACKGROUND	3
2.2	HISTORICAL BACKGROUND	5
3	TRISO FUEL PARTICLE	9
3.1	STRUCTURE OF TRISO COATED PARTICLE	9
3.2	TRISO COATING FAILURE MECHANISMS	11
3.3	OXYGEN RELEASE	18
3.4	PYROCARBON INTERACTION	19
3.5	ADVANCED COATING OPTIONS	20
4	SILICON CARBIDE	21
4.1	BACKGROUND	21
4.2	PROCESSING OF SILICON CARBIDE.....	24
5	CHEMICAL VAPOUR DEPOSITION.....	28
5.1	BACKGROUND	28
5.2	CVD MECHANISMS	30
5.3	DEPOSITION RATE CONTROL.....	32
5.4	DEPOSIT MORPHOLOGY	37
6	SILICON CARBIDE CVD.....	49
6.1	SILICON CARBIDE CVD APPLICATIONS	49
6.2	SILICON CARBIDE CVD CHEMISTRY.....	50
6.3	DEPOSIT COMPOSITION.....	55
6.4	DEPOSITION RATE.....	56
6.5	DEPOSITION EFFICIENCY	59
6.6	DEPOSIT DENSITY	60
6.7	CRYSTAL STRUCTURE AND MORPHOLOGY	61
6.8	MECHANICAL PROPERTIES	64
7	FLUIDIZATION AND SPOUTED BEDS.....	67
7.1	INTRODUCTION	67
7.2	DIMENSIONLESS NUMBERS	68
7.3	HAGEN-POISEUILLE EQUATION.....	69
7.4	DARCY-WEISBACH EQUATION.....	70
7.5	FRICTION FACTOR	70
7.6	TERMINAL VELOCITY	71
7.7	FLOW THROUGH A BED OF PARTICLES	73
7.8	FLUIDIZATION.....	75
7.9	SPOUTING.....	83
8	TEST METHODS.....	88
8.1	DENSITY	88
8.2	LAYER THICKNESS	91
8.3	CHEMICAL AND PHASE COMPOSITION	92
8.4	PHASE COMPOSITION.....	94
8.5	MECHANICAL PROPERTIES	99

8.6	MICROSCOPY	116
9	COATER DESIGN AND SETUP	122
9.1	SYSTEM DESIGN	123
9.2	INSTRUMENTATION AND CONTROL SYSTEM	124
9.3	HEATING SYSTEM	128
9.4	GAS SUPPLY	128
9.5	COATING CHAMBER	130
9.6	EXHAUST SYSTEM	134
9.7	SYSTEM SETUP	134
10	EXPERIMENTAL PLAN AND PROCEDURES	140
10.1	INTRODUCTION	140
10.2	EXPERIMENTAL PARAMETERS	141
10.3	EXPERIMENTAL PLAN	142
10.4	TEST RUN PROCEDURE	147
11	SAMPLE PREPARATION AND ANALYSIS	149
11.1	SAMPLE PREPARATION	149
11.2	MICROSCOPY	152
11.3	DENSITY	153
11.4	HARDNESS AND FRACTURE TOUGHNESS	156
11.5	NANO-INDENTATION	159
11.6	CRUSH STRENGTH	160
11.7	GRAIN SIZE	165
11.8	THICKNESS	166
11.9	PHASE COMPOSITION	173
11.10	ELEMENTAL COMPOSITION	174
11.11	DATA ANALYSIS	175
12	RESULTS	176
12.1	DEPOSITION CHARACTERISTICS	176
12.2	DENSITY	186
12.3	SEM GRAIN SIZE	188
12.4	MECHANICAL PROPERTIES	196
12.5	X-RAY DIFFRACTION ANALYSIS	224
12.6	RAMAN SPECTROSCOPY	233
12.7	MICROPROBE ANALYSIS	240
12.8	SEM MICROSCOPY	244
12.9	POLISHED AND ETCHED SAMPLES	252
13	DISCUSSION	257
13.1	DEPOSITION CHARACTERISTICS	257
13.2	PHYSICAL PROPERTIES	259
13.3	ELEMENTAL COMPOSITION	263
13.4	MECHANICAL PROPERTIES	264
13.5	IMPACT OF INLET TYPE	269
14	CONCLUSIONS	271
15	REFERENCES	277

APPENDIX A: DATA TABLES

1	EXPERIMENTAL CONDITIONS	302
2	DEPOSIT MASS AND DEPOSITION EFFICIENCY	304
3	DEPOSIT THICKNESS	306
4	DEPOSITION RATE	308
5	DENSITY	310
6	SEM GRAIN SIZE	312
6.1	SURFACE STRUCTURE	312
6.2	CROSS SECTION	313
7	CRUSH STRENGTH	314
8	MICROINDENTATION	317
8.1	HARDNESS	317
8.2	FRACTURE TOUGHNESS	319
9	NANO-INDENTATION	323
9.1	HARDNESS	323
9.2	YOUNG'S MODULUS	325
10	X-RAY DIFFRACTION	327
11	RAMAN SPECTROSCOPY	328
12	ELECTRON MICROPROBE ANALYSIS	329

APPENDIX B: X-RAY DIFFRACTION PATTERNS AND RAMAN SPECTRA

1	X-RAY DIFFRACTION PATTERNS	332
1.1	X-RAY DIFFRACTION PATTERNS: HOT INLET	332
1.2	X-RAY DIFFRACTION PATTERNS: COLD INLET	337
2	RAMAN SPECTROSCOPY	343
2.1	RAMAN SPECTRA: HOT INLET	343
2.2	RAMAN SPECTRA: COLD INLET	349

APPENDIX C: ELECTRON MICROSCOPY IMAGES

1	POLISHED SAMPLE: BACKSCATTER ELECTRON	356
1.1	COLD INLET	356
1.2	HOT INLET	367
2	ETCHED SAMPLE SECONDARY ELECTRON IMAGES	374
2.1	COLD INLET	374
2.2	HOT INLET	384
3	SURFACE STRUCTURE SECONDARY ELECTRON IMAGE	393
3.1	COLD INLET	393
3.2	HOT INLET	401

ABBREVIATIONS

au	: Arbitrary units (Used for Raman spectroscopy peak intensity)
AGR	: Advanced Gas Reactor
a-Si	: Amorphous silicon
a-SiC	: Amorphous silicon carbide
α -SiC	: Alpha phase silicon carbide
β -SiC	: Cubic silicon carbide
AVR	: Arbeitsgemeinschaft Versuchsreaktor (German research reactor)
BCF	: Burton-Cabrerra-Frank model
CI	: Confidence Interval
CVD	: Chemical Vapor Deposition
CVI	: Chemical Vapor Infiltration
EBSD	: Electron Backscatter Diffraction
GIF	: Generation 4 International Forum
GFR	: Gas Fast Reactor
HRTEM	: High Resolution Transmission Electron Microscope
HTGR	: High Temperature Gas Reactor
HTR-10	: Chinese 10 MW research reactor
HTTR	: High Temperature Test Reactor (Japanese research reactor)
HVN	: Vickers Hardness Number
IPyc	: Inner Pyrocarbon
ISE	: Indentation Size Effect
KS test	: Kalmogorov-Smirnov goodness of fit test
LFR	: Liquid Metal Cooled Fast Reactor
LO	: Longitudinal Optic
LPCVD	: Low Pressure Chemical Vapor Deposition
MFC	: Mass Flow Controller
MSR	: Molten Salt Reactor
MTS	: Methyl Trichlorosilane
MAGNOX	: Magnesium Non-Oxidising
MOX	: Mixed Oxide fuel
PID	: Proportional Integral Differential control
P-P plot	: Probability – Probability plot
PVD	: Physical Vapor Deposition
PVT	: Physical Vapour Transport
SAED	: Selected Area Electron Diffraction
SCWR	: Supercritical Water Cooled Reactor
SEM	: Scanning Electron Microscope
SFR	: Sodium-cooled Fast Reactor
SLM	: Standard Litre per Minute
SSM	: Sublimation Sandwich Method
TEM	: Transmission Electron Microscope
TO	: Transverse Optic
TPRE	: Twin Plane Reentrant Edge model
TRISO	: Tri Isotropic
VHTR	: Very High Temperature Reactor
XRD	: X-Ray Diffraction

1 INTRODUCTION

1.1 BACKGROUND

Chemical vapour deposition of silicon carbide is currently used in the manufacture of Tri-Isotropic (TRISO) coated fuel particles employed in high temperature gas cooled nuclear reactor fuel. These reactors offer many advantages over conventional water cooled and low temperature gas cooled reactors including improved safety and economics. These advantages have resulted in a considerable level of interest in their application with operating research reactors in Japan and China as well as research projects in several other countries.

Coated fuel particles consist of a kernel of fissile material coated with layers of pyrocarbon and silicon carbide. Fission in the kernel generates heat and, as a by product, radioactive fission products. These fission products present a serious safety and environmental risk and must be retained. In the modern coated fuel particle concept it is intended to retain all the fission products within the coated particle, this is primarily achieved by the silicon carbide coating. To fulfil this role the silicon carbide must possess sufficient strength to constrain the internal pressure generated within the coated particle as well as act as a diffusion barrier to prevent the release of fission products by diffusion at high temperatures.

Fuel particles are coated in a spouted bed chemical vapour deposition coater. In this system a jet of gas containing a precursor is blown upward through a bed of particles. The gas stream carries particles from the bottom of the particle bed upwards to form a fountain of particles above the bed. The particles then return towards the gas inlet in the descending bed of particles. In this way the particles are continuously circulated. For a silicon carbide coating, hydrogen is used as a carrier gas and methyltrichlorosilane as the precursor. Pyrolysis of the methyltrichlorosilane produces silicon carbide and hydrogen chloride as a by product. Typically the process is carried out at approximately 1500 °C. It is known that the operating conditions, such as deposition temperature, precursor concentration and gas flow rate, determine the properties of the deposits formed.

This study aims to investigate the relationship between process conditions and the properties of the deposited silicon carbide.

1.2 MOTIVATION

Enhanced understanding of the silicon carbide deposition process will result in an improved ability to manufacture TRISO coated fuel particles that will have the correct combination of properties required to retain fission products within coated fuel particles. Understanding of the silicon carbide properties will allow for specification of the silicon carbide deposit in terms of measurable deposit properties rather than in terms of deposition process parameters that may not be transferable between different coater designs.

1.3 AIMS

Improve understanding of TRISO particle silicon carbide coating process in terms of:

1. The design and operation of a laboratory scale spouted bed CVD coater specifically with the aim of producing coated fuel particles with various characteristics.
2. Impact of CVD coating parameters on the properties of the deposited silicon carbide.
3. Establish the relationships between material properties that will allow for the specification of silicon carbide layers in terms of material properties rather than process conditions.

1.4 APPROACH

In this study an experimental approach was followed. A laboratory scale spouted bed CVD coater was designed and built and the impact of deposition temperature, precursor concentration and hydrogen flow rate was investigated. As it was intended that the research be applicable to the current production processes parameter values close to existing processes were selected.

This study focussed on the understanding of the room temperature properties of the CVD deposited silicon carbide. Material performance in terms of high temperature properties, diffusion rates and radiation resistance were not investigated. Process outputs that were measured were deposition rate and deposition efficiency. Material properties measured were: density; crush strength; micro-hardness; nano-hardness; Young's modulus (by means of nano-indentation); Vickers indentation fracture toughness; grain size (surface and cross section); X-ray diffraction phase composition, crystallite size and lattice parameters; Raman spectroscopy phase composition; Microprobe chemical analysis.

1.5 CONTRIBUTION

This study built on a considerable existing body of knowledge. Although all the measurement techniques used in this study have been used previously several aspects of this study may be regarded as unique, amongst these are:

1. Fracture toughness of the silicon carbide deposit was measured for a wide range of process conditions
2. A recently developed crush test technique, using soft anvils, was used to investigate the crush load of silicon carbide produced under a variety of processing conditions.
3. Nano-indentation hardness and Young's modulus measurements performed over a range of process conditions.
4. Although many previous studies had commented on the details of the gas inlet system, no previous studies had systematically investigated the impact of gas inlet design on the properties of the deposits.

2 HIGH TEMPERATURE GAS REACTORS

2.1 BACKGROUND

In recent years there has been a renewed interest in nuclear energy as a viable energy source. This is based on both economic factors as well as concerns about the environmental effects of carbon dioxide emissions. Interest in nuclear energy is not restricted to electricity generation, serious proposals have been put forward to utilize nuclear energy for process heat applications such as thermo-chemical hydrogen production, metallurgical process heat, coal gasification, tar sand processing, desalination and district heating (for example [1][2][3]). Of particular interest is the use of nuclear energy for thermo-chemical hydrogen production as part of proposals for a future “hydrogen-economy”. Although some of these applications can utilise heat from any reactor many proposed applications require significantly higher temperatures than can be supplied by water cooled reactors. High Temperature Gas-cooled Reactors (HTGR) are receiving considerable attention as a viable source of electric power and high grade process heat. In an advanced form, as the Very High Temperature Reactor (VHTR), this concept has been selected as one of the candidate Generation IV reactors by the Generation IV International Forum (GIF). Interest in high temperature gas cooled reactors is based, amongst other factors, on inherent safety and high gas outlet temperatures. High operating temperatures allows for increased thermal efficiency and the possibility of high temperature process heat applications. If operating temperatures can be increased sufficiently Brayton cycle gas turbines can replace currently used Rankine cycle steam turbines. This has the potential for further increasing fuel efficiency and reducing capital costs.

Generation IV International Forum (GIF) was chartered in July 2001 as an international collaborative effort to develop next generation nuclear reactor technologies. Goals that have been set for Generation IV reactors include [4]:

1. Provide sustainable energy generation that meets clean air objectives and provides long-term availability of systems and effective fuel utilization for worldwide energy production.
2. Minimize and manage their nuclear waste production to reduce the long-term stewardship burden, thereby improving protection for the public health and the environment.
3. Have a clear life-cycle cost advantage over other energy sources.
4. Have a level of financial risk comparable to other energy projects.
5. Excel in safety and reliability.
6. Will have a very low likelihood and degree of reactor core damage.
7. Eliminate the need for offsite emergency response.
8. Increase the assurance that they are very unattractive, and the least desirable route, for diversion or theft of weapons-usable materials, and provide increased physical protection against acts of terrorism.

Six reactor concepts have been identified as meeting the above criteria, namely:

1. Very-High Temperature Reactor (VHTR) is a next step in the evolutionary development of high-temperature reactors. The VHTR is a helium gas-cooled, graphite-moderated, thermal neutron spectrum reactor with a core outlet temperature greater than 900°C, and a goal of 1000°C.
2. Sodium-cooled Fast Reactor (SFR) a liquid sodium cooled reactor with a fast neutron spectrum.
3. Supercritical-water-cooled reactors (SCWR) a class of high-temperature, high-pressure water-cooled reactors operating above the critical point of water. Both thermal neutron and fast neutron spectra are envisaged.
4. Gas-cooled Fast Reactor (GFR) a gas cooled reactor with a fast neutron spectrum.
5. Lead-cooled Fast Reactor (LFR) system is characterized by a fast-neutron spectrum and either lead or lead/bismuth eutectic coolant.
6. Molten-Salt Reactor (MSR) uses fuel and coolant in the form of a molten salt. Neutron spectrum may be either fast or thermal.

Currently there are several development projects actively investigating high temperature gas cooled reactors. Amongst these are the operational High Temperature Test Reactor (HTTR) in Japan and the HTR-10 test reactor in China. The Chinese design uses fuel elements similar to those used in the German Arbeitsgemeinschaft Versuchsreaktor (AVR) experimental reactor [5][6]. These systems utilise fuel elements in the form of spherical balls, or pebbles. The Japanese design utilises fuel elements in the form of tubular fuel compacts inserted into fuel rods which are in turn load into graphite blocks [7]. Other high temperature gas cooled reactor programs are in progress in USA, Russian Federation, European Union and Korea [8][9]. A feature common to all these systems is the use of coated fuel particles that are distributed in larger fuel elements, either pebbles or compacts in the shape of rods or tubes.

Coated fuel particles consist of a fuel kernel, containing fissile isotopes, coated to prevent the escape of fission products. Currently the most common coating scheme is the Tri Isotropic (TRISO) coating consisting of layers of pyrocarbon and silicon carbide deposited onto the fuel kernel. The complete TRISO coating consists of a buffer layer of low density pyrocarbon, a layer of high density pyrocarbon, a layer of silicon carbide and a final layer of high density pyrocarbon. Dimensions of the fuel kernel vary but are typically in the region of 300 - 500µm diameter. Complete TRISO particles are typically up to 900µm in diameter. Within the TRISO coating the layer of silicon carbide has two functions. Firstly, it provides mechanical strength required to resist internal pressure. Secondly, SiC prevents the escape of fission products, especially metallic elements.

To meet the goals set by the GIF the TRISO coating needs to contain all the fission products within the coated particle with a high reliability under normal operating conditions as well as under accident conditions. Additionally, TRISO coated fuel must be produced at a cost low enough to ensure that the economic goals are attained.

2.2 HISTORICAL BACKGROUND

Gas cooled, graphite moderated, nuclear reactors have been in existence since the beginning of nuclear technology. Many of the initial military reactors, used to produce weapons grade plutonium, were graphite moderated, air-cooled reactors. A series of proposals for high temperature gas cooled reactors were made by F. Daniels between 1944 and 1956. Many of the concepts included in modern high temperature gas cooled reactors were contained in these proposals including pebble beds reactors, fuel in block reactors, helium coolant and direct cycle gas turbine power generation [10]. Further proposals for high temperature gas cooled reactors were made in the late 1950's [11], these ideas culminated in the Ultra High Temperature Reactor Experiment (UHREX) reactor that operated between 1966 and 1970. This helium cooled, graphite moderated reactor was operated with gas outlet temperatures of up to 1300 °C.

In the United Kingdom commercial reactors using graphite as a moderator and carbon dioxide gas as a coolant were developed starting in the 1950's. Calder Hall, a graphite moderated, carbon dioxide cooled, reactor became one of the first reactors to produce electricity commercially when connected to the grid in 1959. These reactors, known as MAGNOX reactors, used a magnesium alloy fuel cladding. This allowed for the use of natural uranium fuel but restricted gas outlet temperature to approximately 350°C. As a result, thermal efficiency was limited to approximately 30%. In total 26 MAGNOX type reactors were built in the UK, 1 in Japan and 1 in Italy. France developed a similar reactor, the UNGG (Uranium Naturel Graphite Gaz), 9 of which were built in France and 1 in Spain. Power output of MAGNOX type reactors ranged from 50MWe for Calder Hall to 540MWe for the UNGG reactor at Bugey in France. North Korea built a 5MWe MAGNOX reactor for plutonium production as part of their nuclear weapons program.

A development of the MAGNOX reactors, the Advanced Gas-cooled Reactor (AGR), used stainless steel fuel cladding allowing gas outlet temperature to be increased to approximately 640°C. In the case of AGR, operating temperatures were limited by interaction between the CO₂ coolant and the graphite moderator. Stainless steel cladding allowed higher coolant temperatures, however due to the higher neutron capture of the stainless steel it was necessary to use uranium enriched to 2.5 % – 3.5 % ²³⁵U. AGR reactors used UO₂ fuel in place of the metallic fuel used for the MAGNOX reactors. Both the MAGNOX and AGR design used an indirect cycle; reactor coolant gas was passed through boilers, the steam then being used to generate power via a Rankin cycle steam turbines.

To improve thermal efficiency further gas outlet temperatures needed to be increased above the levels possible with either the MAGNOX or AGR type designs. One high temperature gas cooled reactor concept that has achieved significantly higher temperatures is that of the coated fuel particle imbedded in a graphite matrix. Much development work on coated fuel particles was conducted during the Dragon project that was active between 1964 and 1975. The Dragon reactor, itself a high temperature gas cooled reactor, was intended as a materials test reactor for high temperature gas reactor development. Dragon made use of graphite fuel elements

that contained tubular compacts made up of coated fuel particles and graphite [12]. Another test reactor using tubular compacts of coated fuel particles was the Peach Bottom reactor [13]. This 40MWe research reactor operated between 1967 and 1974. In Germany, the 15MWe Arbeitsgemeinschaft Versuchsreaktor (AVR) was used to test a range of coated particle fuel types. This reactor, which was operated between 1967 and 1988, also demonstrated the pebble bed concept where fuel elements consisted of spherical graphite balls that contained the coated fuel particles.

Peach Bottom initially operated with fuel particles coated by a single layer of pyrolytic carbon. This scheme experienced problems due to dimensional changes in the carbon resulting from fast neutron irradiation and fission product recoil damage. This resulted in dimensional changes in the fuel compacts leading to cracking of the fuel elements. An improved coating consisting of a porous inner layer and a dense outer layer of pyrocarbon performed satisfactorily [13]. This arrangement of a fissile particle coated with a dual pyrolytic carbon layer is referred to as Bistructural Isotropic (BISO) fuel. Fission products generated during operation were to be retained by the dense outer pyrolytic carbon layer while the inner porous layer absorbed gaseous fission products, absorbed fission recoil energy and accommodated kernel swelling.

It was found that when operating temperatures were increased BISO particles no longer retained all fission products, especially metallic elements. In the case of operation of the German AVR reactor it was found that when the reactor gas outlet temperature was increased above 900°C BISO coated (UTh)₂C₂ fuel released fission products [14]. Dragon had successfully operated with particles coated with a Tri-Isotropic, or TRISO, coating scheme. This consisted of a porous inner pyrocarbon, dense pyrocarbon, silicon carbide and a final layer of dense pyrocarbon. TRISO coated fuel particles have been used at temperature of up to 950 °C with very low fission product release rates. Even after the development of TRISO particles some reactors, for example THTR-300, were still operated with BISO coated fuel. THTR-300 utilised an indirect steam cycle so fuel temperature could be kept at a level where fission product release was not serious. Also, any fission products released were retained within the cooling gas circuit and so did not present a hazard during turbine maintenance operations.

Two main uses of the coated fuel particles have developed. One scheme forms the coated fuel particles into cylindrical or tubular fuel compacts. These compacts are then loaded into fuel elements. Rod shaped fuel elements were used for the Dragon and Peach Bottom reactor. Another style of fuel element, first used in the 300 MWe Fort St Vrain commercial power reactor, makes use of hexagonal graphite blocks. Fuel compacts are inserted into holes within the graphite block that also contained channels for coolant flow and control rods. In this case, the reactor core was formed from fixed stacks of the hexagonal blocks. This concept forms the basis of new reactors being developed in USA, Russian Federation and France. The HTTR test reactor in Japan uses a combined system where tubular fuel compacts are loaded into graphite fuel rods that are then inserted into hexagonal graphite blocks.

An alternative approach, developed in Germany, makes use of spherical fuel elements made up of coated fuel particles and graphite. These fuel elements are circulated through the reactor core by continuously extracting fuel spheres from the

bottom, and adding spheres to the top of the reactor. Various operating modes have been proposed. In the multi-pass system fuel elements extracted from the reactor are measured to check the level of burn up. Those that have reached their maximum level of burn up are removed while fuel elements still containing sufficient fissile material are cycled back through the reactor. Fresh fuel elements are added together with the recycled elements to make up for those removed. This allows for a mixture of fuel elements of varying burn up to be distributed throughout the reactor core. Another system is that of the Once-Through-Then-Out (OTTO) where the fuel elements are not cycled back through the reactor but are discarded after passing through the reactor once. Fresh fuel is added to the top of the reactor while used fuel elements are extracted from the bottom. In both the multi-pass and the once through cycle fuel elements are continuously added and extracted from the reactor during operation. Continuous on load refuelling is a major advantage of these refuelling schemes. In the peu-a-peu scheme fresh fuel is added to the reactor on a continuous basis; however, no fuel elements are extracted. Once the reactor vessel is fully loaded, and the fuel has been consumed, the reactor is shut down and the used fuel elements removed. This scheme has the advantage of having a very simple fuel handling system but suffers from the drawback of requiring shut downs to unload the used fuel elements.

A summary of high temperature gas cooled reactors is presented in Table 1.

It should be noted that the reactor concepts described in Table 1 are only examples of HTGR reactor using coated fuel particles that have been operated or are currently receiving considerable attention. Other reactors that make use of coated fuel particles have been proposed. For example using coated fuel particles in water or molten salt cooled reactors [15][13] or using a fluidized bed of coated particles [15]. Alternatives to using coated fuel particles for very high temperature reactors have also been operated and still receive attention; the molten salt reactor is one example. Extremely high output temperatures have been achieved while accepting that the coolant gas will be contaminated. For example, the Ultra High Temperature Reactor Experiment reactor achieved a gas outlet temperature of over 1300 °C. Temperatures of up to 2100 °C, at power output of up to 4 GW, were achieved by gas cooled reactors operated to investigate nuclear rocket propulsion [16]. A feature of modern coated fuel particles is the concept of retaining all the fission products within the coated fuel particles. Some of the original high temperature gas cooled reactor concepts, including the Dragon, allowed for fission product release into the coolant. This required a gas purification system to be added to the cooling circuit. Currently the strategy is to retain all fission products within the coated particles; this is especially important where direct cycle systems are being envisaged.

Table 1. Characteristics of some High Temperature Gas Cooled reactors. [12][13][14][17][18][7]

	Dragon	Peach Bottom	AVR	THTR-300	Fort St Vrain	HTTR	HTR-10
Operation	1964 - 1975	1967-1974	1967 - 1988	1986 - 1989	1976 - 1989	1998 -	2000 -
Power (MWt / MWe)	21.5	115 / 40	46 / 15	750 / 300	842 / 300	30	10
Power Density (MWt.m⁻³)	14	8.3	2.6	6	6.3		
Outlet temperature (°C)	750	750	Up to 950	750	784	850	
Inlet Temperature (°C)	350	377	270	270	405	395	
Coolant Pressure (MPa)	20	2.5	1.0	3.9	4.5	4	
Fuel¹	HEU UO ₂	(Th, U)C ₂	Various ²	(Th, U)O ₂	(Th, U)C ₂ ThC ₂	6% UO ₂	UO ₂
Particle Coating	TRISO	Pyrocarbon BISO	BISO TRISO	BISO	TRISO	TRISO	TRISO
Fuel element type	Tubular Compact	Tubular Compact	60 mm Pebbles	60 mm Pebbles	Cylindrical compact	Tubular Compact (OD:26 mm ID:10 mm L: 39 mm) in graphite tube (OD:34 mm,L:577mm)	60 mm Pebbles
Core Construction	37 hexagonal assemblies of 6 fuel rods	804 Rods 89 X 3658 mm (3.5" X 144")			Hexagonal Block	Hexagonal Block (360 mm across flats, 580 mm long)	

1. HEU: Highly Enriched Uranium (>20 % ²³⁵U), LEU: Low Enriched Uranium (< 20% ²³⁵U).

2. A variety of fuel and coating systems were tested including HEU (Th,U)C₂, (Th,U)O₂, UO₂, UC₂, LEU UO₂, ThO₂ with coatings of BISO and TRISO.

3 TRISO FUEL PARTICLE

3.1 STRUCTURE OF TRISO COATED PARTICLE

TRISO particles consist of a kernel coated with layers of pyrocarbon and silicon carbide. A typical example of a TRISO coated particle is shown in Figure 1. The complete coated fuel particle consists of:

- Fuel particle containing fissile material
- Buffer layer of porous carbon
- Inner pyrolytic carbon layer (IPyC)
- Silicon carbide layer
- Outer pyrolytic carbon layer (OPyC)

Exact detail of the particle dimensions and material specifications depend on the intended application. A comparison of typical TRISO fuel particles is shown in Table 2. Most TRISO coated fuel particles have similar specifications for thickness and properties of the various coating layer, the major differences being in the size and composition of the kernel. Kernel sizes between approximately 300 μm and 600 μm have been tested. Various kernel compositions have been used. Uranium dioxide (UO_2) is commonly used, however uranium carbide (UC_2) and uranium oxide/carbide (UCO), as well as uranium oxide mixed with thorium oxide or plutonium oxide (MOX) and plutonium oxide together with other transuranium elements oxides have been investigated [19] [20]. Enrichment levels have ranged from approximately 7 % up to 93 % ^{235}U [14]. Modern fuels avoid the use of HEU, limiting enrichment to below 20 % ^{235}U .

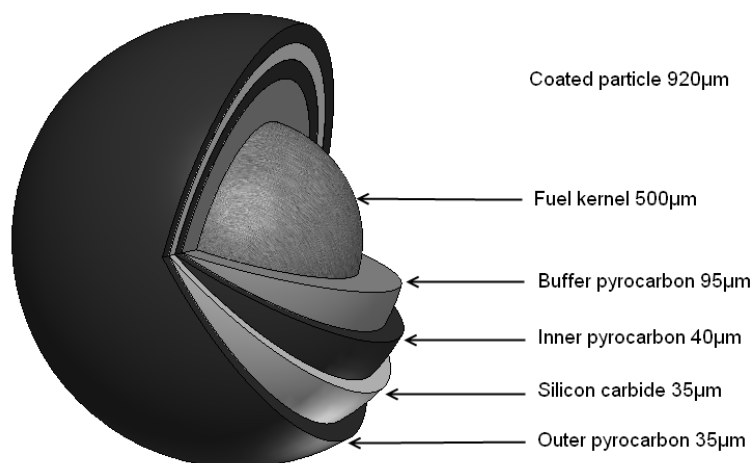


Figure 1. Schematic TRISO coated fuel particle.

Table 2. Specification of typical TRISO fuel particles.

	AVR	HTRR [1]	HTR-10 [3]	V/HTR [2]
FUEL KERNEL				
Composition	UO ₂	UO ₂	UO ₂	UO ₂
Diameter (μm)	500	600 ±55	500	500 ±40
Density (g.cm ³)		10.63 ±0.26	≥ 10.4	≥10.4
COATING LAYERS				
Buffer Thickness	95	60 ± 12	95	95 ±20
Buffer Density		1.10 ± 0.10	≤ 1.10	≤ 1.05
IPyC Thickness	40	30 ±6	40	40 ±10
IPyC Density		1.80 to 1.95	1.9 ±0.1	1.85 to 2.0
SiC Thickness	35	25 to 37	35	35 ±7
SiC Density		≥3.20	≥ 3.18	≥3.18
OPyC Thickness	40	45 ±6	40	40 ±10
OPyC Density		1.80 to 1.95	1.9 ±0.1	1.85 to 2.0

Each of the coating layers in the TRISO coating performs a particular function. Briefly these are [5]:

Buffer layer

- Absorbs gaseous fission products
- Protects the overlying layers against fission product recoil damage
- Accommodates swelling of the fuel kernel during irradiation.

Inner pyrolytic carbon (IPyC)

- Acts as a diffusion barrier protecting the silicon carbide from damage due to interaction with fission products and CO
- Provides some of the mechanical strength required to restrain internal gas pressure generated by gaseous fission products and CO/CO₂
- Sealing of the buffer layer to prevent ingress of chlorine containing gas during deposition of the silicon carbide layer

Silicon carbide

- Diffusion barrier to fission products, especially metallic fission products that rapidly diffuse through the IPyC, especially at high temperatures
- Serves as the main structural element in the TRISO coating restraining internal pressure

Outer pyrolytic carbon (OPyC)

- Diffusion barriers to fission products
- Provides some of the mechanical strength required to restrain internal gas pressure generated during use
- Prevents damage to the silicon carbide layer during further processing
- Maintains a compressive stress on the silicon carbide layer thus reducing the tensile stress during use

3.2 TRISO COATING FAILURE MECHANISMS

Considering the function of the TRISO coating a failure can be regarded as any condition that leads to the release of fission products. Under normal operating conditions German manufactured fuel pebbles were shown to have a negligible release of the important fission products Cs, Sr, Ag, I, Xe and Kr [17]. Several mechanisms have been identified that can result in particle failure [21][22][23][24]. These are discussed in the following sections.

3.2.1 PRESSURE VESSEL FAILURE

During operation considerable pressure is generated within the coated fuel particle by gaseous fission products, such as xenon and krypton, volatile fission products and oxygen released from the fuel. Any oxygen released by the fuel will react with carbon in the buffer and IPyC coating to form a CO/CO₂ gas mixture. Fission product gas pressure will be dependent on fuel type (i.e. the fissile component of the fuel) and level of burnup. Pressure due to the build up of CO/CO₂ will be a function of the kernel chemical composition (both fuel type and chemical form), burnup and temperature history of the fuel. Estimates of internal gas pressure are in the 10 MPa to 100 MPa range each for gaseous fission products and CO [25][26].

Stresses due to internal gas pressure may exceed the tensile strength of the silicon carbide layer leading to fracture of the silicon carbide layer as seen in Figure 2. Although analytical solutions to the stress in the silicon carbide layer have been developed, for example [27][28], finite element methods are commonly used to assess failure probabilities due to internal pressure. Silicon carbide exhibits brittle behaviour making it necessary to evaluate failure probabilities statistically. It is common to calculate failure probability based on the Weibull distribution when analysing brittle material, however for silicon carbide the normal distribution may be more applicable [29].

Stress within the silicon carbide layer of a TRISO coated particle cannot be determined easily. Not only is the pressure within the particle dependent on the initial fuel type, composition and operational history but there are interactions between the pyrocarbon layers and the silicon carbide. Behaviour of the pyrocarbon is itself complex depending on both the material properties, as determined by the deposition process, and on the operational history. Pyrocarbon will exhibit shrinkage, swelling and creep behaviour dependent on temperature and neutron fluence. Stresses within the pyrocarbon layers impacts on the total stress experienced by the silicon carbide layer. Finite element models have been used to simulate these effects and the impact of various defects on the failure probability of the TRISO shell. Defects considered include localised thinning (due to for example palladium attack) and uniform thinning (attack by CO or sublimation of SiC), and particle asphericity as well as defects such as delamination and cracking of the pyrocarbon layers [7][30][31][32].

The probability of pressure vessel failure is small compared to other failure mechanisms when coatings are properly specified and manufactured. Failure probabilities do however increase dramatically if pyrocarbon or buffer layers are defective [22][33].

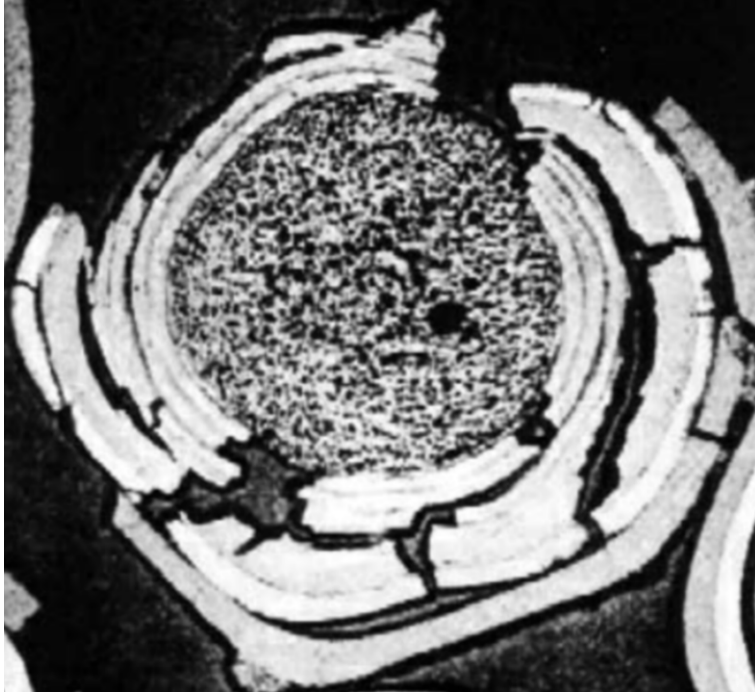


Figure 2. Pressure vessel failure of TRISO coated particle [24].

3.2.2 KERNEL MIGRATION

When coated fuel particles are exposed to a temperature gradient the particle kernel may tend to migrate towards the hot side of the coated particle. In severe cases, the kernel may penetrate the inner carbon layers leading to failure of the silicon carbide due to interaction with the kernel. This effect, often referred to as the “amoeba effect”, is caused by the transport of carbon, in the form of CO, from the hot side to the cold side of the particle. An example of kernel migration is shown in Figure 3. Without a temperature gradient across the particle and free oxygen being present no migration takes place.

In the case of pebble bed type reactors the thermal gradient is sufficiently low for kernel migration to be of little concern [23]. However, thermal gradients in fixed block type reactors are severe enough for this failure mode to potentially be a problem [24]. Use of UCO kernels eliminates oxygen release from the fuel and so prevents the transport of carbon in the particle, this effectively eliminates kernel migration [24][33]. An alternative approach is to make use of an oxygen getter since this has been shown to effectively suppress kernel migration [25].

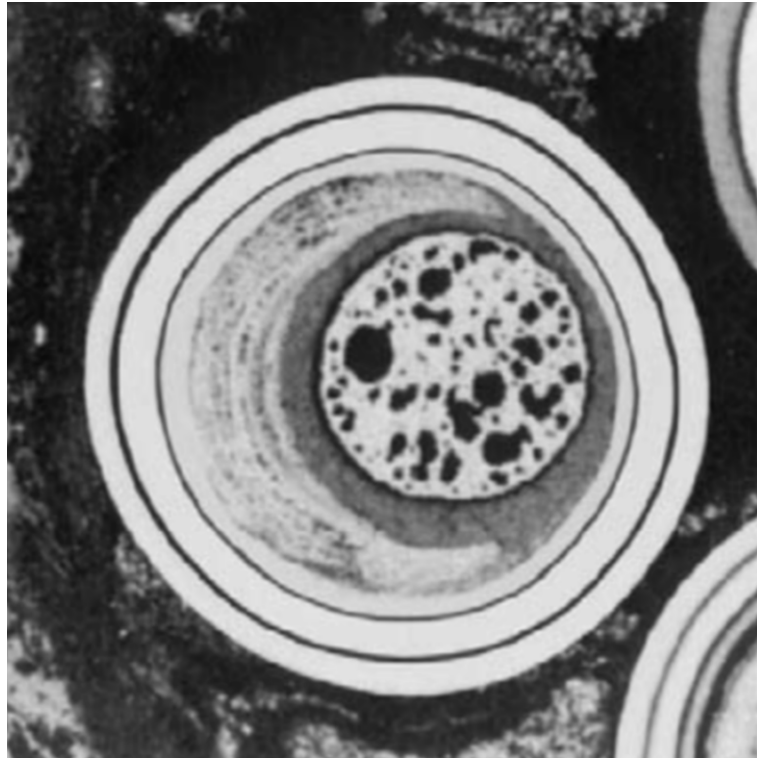


Figure 3. Kernel migration in irradiated TRISO coated fuel particle [24].

3.2.3 SILICON CARBIDE FISSION PRODUCT INTERACTION

Reaction between metallic fission products and silicon carbide can lead to penetration of the SiC or reduce the layer thickness. Palladium is one of the most important fission product that reacts with silicon carbide [24] and is one of the main causes of coating failure [34]. Although palladium release is not a serious concern, damage to the silicon carbide layer by palladium may allow for the release of other harmful elements. Palladium reacts with silicon carbide to form palladium silicide and free carbon as shown in the following reaction:



Attack of the SiC by palladium has been observed in a wide variety of fuel types, including UO₂, UC₂, UCO as well as plutonium and thorium containing oxide and carbide fuels [35] [36][34]. Plutonium fission has a much higher palladium yield than uranium fission. Fuels in which plutonium fission is significant, such PuO₂; mixed oxide; LEU, will therefore have a higher palladium inventory. This will in turn result in a more significant palladium attack. For LEU based fuels the contribution of plutonium fission increases with increasing burnup, it can be expected that palladium attack will be burnup dependent in these fuels.

Palladium attack of the silicon carbide does not take place uniformly across the surface of the silicon carbide but tends to be localised. This may be seen in Figure 4

as the localised penetration of the silicon carbide. It has also been found that there is no minimum amount of palladium required before attack is initiated. Even at low concentrations, palladium accumulates in nodules on the surface of the silicon carbide and initiates localised attack. Attack rates increase with temperature, exhibiting Arrhenius behaviour increasing rapidly with temperature. Below a fuel temperature of 1100 °C palladium attack is however of little concern [35].

Carbide fuel kernels are less likely than oxide and oxycarbide kernels to retain fission products in the kernel. Use of carbide containing kernels has been proposed as a solution to CO generation and kernel migration. However, the increased release rate of fission products from the kernel may result in increased attack of the silicon carbide. Lanthanide attack of SiC has been observed in carbide fuels [36][34].

Properties of the silicon carbide layer appear to influence the rate of attack by palladium. Silicon carbide deposited at lower temperatures has a lower rate of attack than material deposited at high temperature [35]. It has been shown that silicon carbide grain size has little effect on susceptibility to palladium attack however, grain orientation is important. Porosity and excess silicon increase the rate of attack [37].

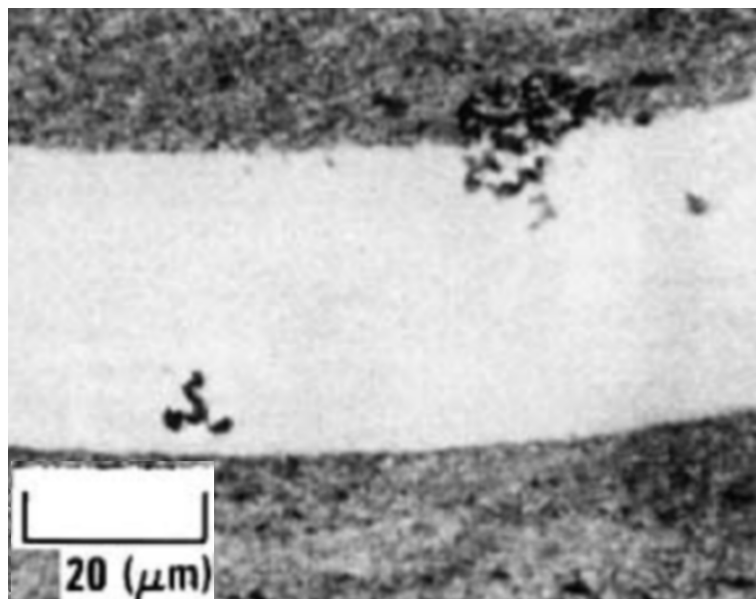


Figure 4. Fission product attack of silicon carbide [24].

3.2.4 ATTACK BY CARBON MONOXIDE

Cracking of the inner pyrocarbon layer will allow CO gas to come into contact with the silicon carbide layer. At temperatures above 1400 °C the CO can react with the silicon carbide resulting in damage to the silicon carbide layer [22]. Normally the reaction would be described by reaction 2 and 3. It has been observed that where attack has taken place that (Pd, Rh, Ru, Tc, Mo) silicides form in the kernel and that (Si, Ce, Ba) oxide form on the buffer/IPyC interface. This may be explained by the

formation of SiO vapour (reaction 3) which then reacts with noble metals in the kernel to form silicides or combines with cerium and barium oxides that have escaped the kernel [38].



An example of CO attack on silicon carbide is shown in Figure 5.

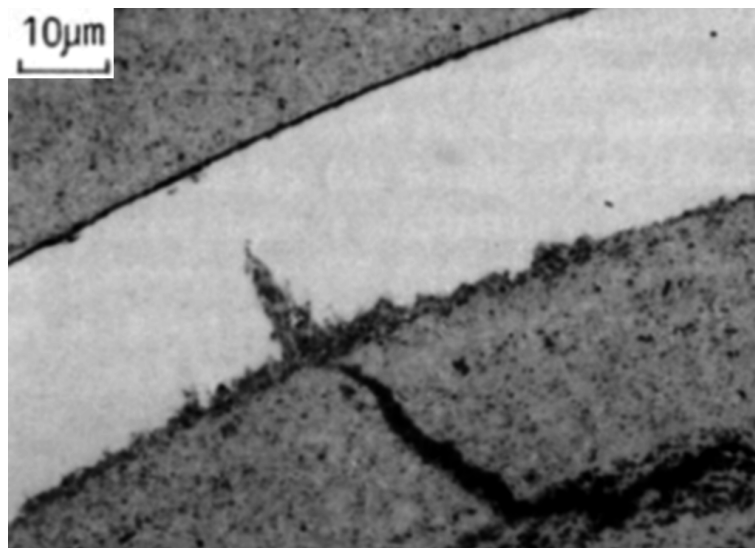


Figure 5. Carbon monoxide attack of silicon carbide [38].

An indication of the interaction between CO and silicon carbide can be obtained from studies of oxygen gettering. It was found that silicon carbide acted as an efficient oxygen getter, even in cases where it was unintentionally exposed to CO in particles where the inner pyrocarbon layers had been damaged [39]. In these cases, any reduction in CO content of the particles would indicate a loss of silicon carbide.

3.2.5 DIFFUSION THROUGH TRISO COATING

Of all the fission products the most important, due to their high fission yield and radiological risk, are caesium, strontium, silver, iodine, xenon and krypton [14]. Other elements that have been shown to be released include europium [40][41][42] and palladium (for example[34]). The main sources of release from coated particle fuel have been identified as heavy metal contamination (i.e. heavy metal outside of the coated particle) and damaged particles where the coating provides no barrier to release [22]. However, for some elements significant amounts can penetrate an intact silicon carbide layer when the operating temperature is increased sufficiently.

Metallic fission product release rates exhibit Arrhenius type behaviour. Release rates increase rapidly at temperatures in excess of 1250 °C [19]. Silver release becomes significant at temperatures exceeding 1000 - 1100 °C [23] [21]. Caesium release

only starts becoming significant at temperatures exceeding 1300 °C [23]. Under simulated accident conditions particle failure and metallic fission product release starts at approximately 1800 °C. Intact TRISO particles have been shown to retain all fission gases up to temperatures of 2000 °C. At temperature exceeding 2100 °C decomposition of the silicon carbide led to an increase in fission product release [23].

Various mechanisms have been proposed to explain the high diffusion rate of silver through silicon carbide. Studies of the difference between coated fuel particles produced in Germany and USA have suggested that the microstructure of the silicon carbide layer plays a role in the retention of silver. American produced particles contained large columnar grains extending through the layer. Particles produced in Germany had smaller grains. It has been argued that the larger grains provided a more direct diffusion path and so was less effective as a diffusion barrier [24]. Other researchers have also recognised that grain boundary diffusion is the most likely path for silver release. Although it was recognised that the silicon carbide deposition process played a role in determining the silver diffusion rates the exact link between silver diffusion and deposition process was not identified [43]. Förthmann [44] found that large columnar grains and striated deposits had a higher silver release rate than imperfectly crystallised deposits formed in hydrogen/argon mixtures. McClean and Ballinger [45] and Friedland et al [46] studied the diffusion rate of silver in silicon carbide and concluded that diffusion rates through the silicon carbide matrix was negligibly small. From this it was concluded that the only explanation for observed high rates of silver release are due to grain boundary diffusion or transport through nano-scale defects. A recent study by López-Honorato et al [47] has shown that silver diffuses along silicon grain boundaries and through nano-porosity. The nature of the grain boundaries was found to be important. Previous suggestions that silver diffuses through nano-cracks or is enhanced by free silicon were not supported by these studies.

As with oxygen and palladium, the amount of silver generated by fission is dependent on the fuel. Fission of plutonium releases significantly more silver than uranium fission. In the case of LEU fuels the contribution of plutonium will increase with increasing burnup [21][24].

3.2.6 THERMAL DEGRADATION OF SILICON CARBIDE

Under normal operating conditions decomposition of silicon carbide is not a serious concern. However, under accident conditions it may become important. Maximum fuel temperature during normal operations depends on the design of the reactor core but will always be higher than the maximum gas outlet temperature. In power plants using steam cycles reactor coolant outlet temperatures are in the region of 700 °C to 800 °C. Fuel temperatures under these conditions are well within the capabilities of conventional TRISO coated particles. Direct cycle power generation and process heat applications will require coolant outlet temperatures of up to 1000 °C requiring higher fuel temperatures. This is more serious in prismatic block type reactors that tend to have higher maximum fuel temperatures than pebble bed type. Tests on the Japanese HTTR reactor indicated that when gas outlet temperature was 950 °C

maximum fuel temperature was 1478 °C [48]. Under accident conditions fuel temperature is restricted to a maximum of 1600 °C. Damage to the silicon carbide layer only takes place at temperatures significantly greater than 1600 °C [23]

Sublimation of silicon carbide starts at approximately 1800 °C [19]. In TRISO particles the surrounding carbon layers will reduce the sublimation rate [49]. Thermal decomposition of silicon carbide takes place above 2545 °C. Species present in the vapour phase include Si, SiC₂ and Si₂C. Silicon carbide can also decompose into constituent elements at high temperatures. Silicon tends to vaporise leaving a porous carbon layer. This allows fission products to escape from the coated particle. Failure rates increase as the temperature increases above 1700 °C to 1800 °C for extended periods. Above 2000 °C silicon carbide will decompose rapidly and become ineffective [22]. Simulated accident testing has shown that above 2000 °C thermal decomposition of the silicon carbide is the major failure mode [14].

During manufacture of fuel elements, particles are heated to temperatures in the 1800 °C to 2000 °C range without damage to high quality silicon carbide. Poor quality silicon carbide has however been shown to be severely impacted by heat treatments [50].

3.2.7 DAMAGE DURING MANUFACTURE

Under normal operating conditions, the two major sources of fission product release are contamination and defective particles. Several studies have attributed radiation release during testing to heavy metal contamination of fuel pebble and block graphite, for example [14] [48]. Other studies have however concluded that uranium contamination of the graphite is negligible and that the major source of release is damaged or missing coating layers [23].

Coating layer damage can occur during both the actual coating process or during fuel element manufacture. Coating of the TRISO fuel particle with a layer of graphite and binder prior to the formation of fuel compacts or pebbles has reduced particle-to-particle contact and consequential cracking of the TRISO layers. Removal of non-spherical particles has also resulted in a significant reduction in defect rates. For German manufactured fuel pebbles burn leach tests have indicated that defect rates are as low as 3×10^{-5} . The burn leach test will detect particle with missing or defective coatings [23].

Fluidization conditions within the spouted bed coater have been shown to have a significant effect on coating layer defect rate. Optimisation of the fluidization conditions has been shown to reduce the defect rate

Mechanical handling of particles after coating may also result in particle damage. Damage can occur at both the pyrocarbon and silicon carbide coating steps. Cracks in the silicon carbide layer have been shown to penetrate through the IPyC to the buffer layer. The incidence of cracking was markedly reduced by making changes to the coating process. Coating of all layers in a continuous process reduced the amount

of handling of the particle, so reducing the damage due to handling. Optimisation of the coater gas inlet shape and diameter as well as the gas flow rates reduced the cracking of the layers due to energetic impacts between particles and between particles and the coater side walls [51].

Besides cracking of the deposited layers a second type of flaw has been identified. These are internal flaws within the silicon carbide layer. Unlike cracks that form in a radial direction these flaws form in a tangential direction. When the particles are viewed in cross section the defects appear as delamination within the silicon carbide layer. When the surface of the particle is viewed these defects appear as discoloured patches on the particles. Under high magnification the defects appear to be layers of porosity within the silicon carbide layer. These defects are not detected by the burn leach test as they do not penetrate through the silicon carbide layer. Control of fluidization conditions appears to reduce the incidence of internal defects. Under condition of mild spouting few defects are formed while under conditions of violent spouting (i.e. high gas flow rate) internal defects form. It has been suggested that the defects form due to temperature cycling as the particles circulate through the bed of particles [52].

3.3 OXYGEN RELEASE

In the preceding section it was seen that the release of oxygen from oxide fuels during irradiation is detrimental, leading to high internal pressure, kernel migration and possibly CO attack of the silicon carbide. Oxygen is released by oxide fuels because fission products cannot take up all of the oxygen originally bound to the fissile element. As the atomic mass distribution of fission products is dependent on the fissile isotope the amount of oxygen released depends on the fuel. As can be seen from Table 3 the amount of oxygen released per fission depends on the oxidation state of the products formed and the fissile element. Highly enriched uranium and uranium/thorium fuels will release less oxygen than fuels, such as LEU, mixed uranium/plutonium oxide (MOX) and PuO₂, in which plutonium fission contribute significantly to the fission product composition.

Table 3. Oxygen atoms released per fission from oxide fuels [25][40].

Fission Product Oxidation State	Fissile Element			
	²³³ U	²³⁵ U	²³⁹ Pu	²⁴¹ Pu
Mo, Tc, Cs, noble metal: Free metal Alkaline earths: Divalent oxides Lanthanide, Zr, Y: Tetravalent oxides	0.08	0.13	0.63	0.67
Mo, Tc, Cs, noble metal: Free metal Alkaline earths: Divalent oxides Lanthanide, Y: Trivalent oxides Zr: Tetravalent oxides	0.35	0.40	0.86	0.91
Alkaline earths: Divalent oxides Lanthanides, Y: Sesquioxides	0.36	0.40	0.85	0.85

For pure oxide kernels excess oxygen is generated from the start of irradiation. However at low burnup and irradiation temperature oxygen may remain trapped within the kernel. As a result pressure in the coated particles may be lower than expected at low burnup. Increased operating temperature and porosity developed at high burnup will enhance oxygen release [25] [53].

A potential solution the problem of oxygen release is the use of UC_2 kernels. However oxide fuels are advantageous in that they retain fission products better than carbide fuels [22]. Mixed uranium oxide/uranium carbide fuel, referred to as UCO, have successfully been used to suppress oxygen release [40]. For UCO fuels the carbon content must be limited to ensure $O/U > 1.1$. Higher carbide fractions result in the release of lanthanides that may attack SiC [35][36].

Addition of oxygen getters to the fuel kernel may reduce the oxygen potential and so reduce the impact of CO. Various getters have been proposed, including UC_2 (in UCO fuel), SiC, ZrC, Ce_2O_3 and La_2O_3 [22][40]. Of these UC_2 , SiC and ZrC are the most effective. An alternative to including the getter into the fuel kernel is to use a getter on the outer surface of the kernel or dispersed in the pyrocarbon layer. ZrC layers have been tested in this role with positive results [19].

3.4 PYROCARBON INTERACTION

Although the silicon carbide component of the TRISO coating is regarded as being the most important in terms of structural integrity and acting as a diffusion barrier the pyrocarbon layers play an important role. Failure of the pyrocarbon layers can lead to failure of the silicon carbide layer. The behaviour of the pyrocarbon during use has an important impact on the coated particle integrity.

In use, at high temperature and neutron irradiation, pyrocarbon will exhibit dimensional changes. Initial shrinkage of the outer pyrocarbon ensures that the silicon carbide is under compression. With time the compressive stresses are reduced as creep relieves tensile stresses in the carbon layers. Pyrocarbon shrinkage strain depends on four variables: neutron fluence, irradiation temperature, carbon density, carbon anisotropy. Creep of the pyrocarbon is dependent on pyrocarbon density and operating temperature. Finite element analysis of the behaviour of the pyrocarbon layers has highlighted the importance of the shrinkage behaviour of the pyrocarbon layers. Delamination and cracking of the pyrocarbon has been shown to increase the failure probability of the silicon carbide layer [54][32].

Asphericity of particles can originate from kernel manufacturing defects or non-uniform coating, especially the buffer and IPyC coatings. Asphericity of coated particles can increase the failure probability significantly [32]. Kernel and coated particle quality control procedures call for the removal of non-spherical kernels and particles [41][24]. Metrology systems have also been developed for assessing the degree of asphericity of the particles (for example [55][56]).

Cracking of the IPyC layer due to shrinkage has the additional risk of exposing the silicon carbide layer to direct exposure to fission products and CO. This may lead to

failure of the silicon carbide layer due to the mechanisms previously mentioned in sections 3.2.3 and 3.2.4.

3.5 ADVANCED COATING OPTIONS

Several attempts have been made to improve the performance of TRISO particles. These have focused on improving the resistance to attack by fission products and improved high temperature performance. High temperature performance is limited by the properties of silicon carbide, attempts at improving TRISO particles in this regard have focused on replacing the silicon carbide layer with alternative materials. Zirconium carbide has been identified as the most viable alternative to silicon carbide. Direct replacement of silicon carbide with zirconium carbide results in the so-called TRIZO particles. These have resulted in improved high temperature performance and resistance to palladium attack. Despite their improved performance TRIZO particles are not without problems. Zirconium carbide may also be susceptible to attack by CO [57] and possible enhanced release of ruthenium isotopes [19].

An alternative scheme that also uses zirconium carbide without replacing the silicon carbide is to use a conventional TRISO coating on a modified kernel. These kernels, referred to as UO_2^* , consist of a conventional UO_2 kernel that has been over coated with 9 μm dense pyrocarbon and 9 μm ZrC layer. TRISO coated UO_2^* kernels exhibited very good performance during irradiation testing. Testing of these particles indicated that all fission products, including silver and europium, were retained. Although it was anticipated that the ZrC layer would only act as an oxygen getter reducing the formation of CO in the particle other effects must have come into play as the performance of these particles was significantly better than particles in which ZrC getter was dispersed in the pyrocarbon layer. It has been proposed that the ZrC coating, which remained intact, prevented the release of fission products released by other particle/coating configurations [42].

Silicon carbide has also been investigated as a getter. Tests have been carried out with silicon carbide dispersed in the kernel [39] as well as added to the coating layers [36]. Adding silicon carbide to the kernel was intended to react with oxygen and so prevent the formation of CO. Extra silicon carbide added to the coating layers was intended to react with palladium and so prevent the palladium from attacking the main silicon carbide layer. Additional silicon carbide was added as either a separate thin layer of silicon carbide or a mixed silicon carbide/pyrocarbon layer within the IPyC layer of TRISO coated particles. The additional silicon carbide proved to be effective at preventing palladium attack of the main silicon carbide layer [36].

4 SILICON CARBIDE

4.1 BACKGROUND

Natural silicon carbide only occurs in very small quantities on earth, it has however been detected in large quantities in space. On earth, the first natural silicon carbide was found by Henri Moissan in fragments of the Canyon Diablo meteorite from the Barringer impact crater. Silicon carbide is sometimes referred to as Moissanite in Moissan's honour. Berzelius is credited with first synthesising silicon carbide in 1824. Large scale production of silicon carbide was developed by Acheson who patented a production process in 1893 [58]. Although the purity varies significantly most of the silicon carbide produced by the Acheson process is of low purity and only suitable for metallurgical use, use as a refractory or use as an abrasive. As an abrasive, silicon carbide is often referred to as carborundum. Production of high quality silicon carbide crystals was first achieved by Lely in 1955 by means of a high temperature sublimation process. This method was further developed by Tairov and Tsvetkov [59]. A variety of methods for producing pure high quality single crystal silicon carbide for electronic applications have been developed in recent years, amongst these methods are vapour phase epitaxy, liquid phase epitaxy and high temperature chemical vapour deposition [60][61].

Initially silicon carbide was used as an abrasive material due to its high hardness. Other long-standing uses of silicon carbide include deoxidisation of steel, as refractory material, electric heating elements and furnace furniture. However, silicon carbide possesses a number of properties that makes it useful for a wide variety of applications. Some of these properties are listed in Table 4. Although silicon carbide possesses many desirable properties it can be difficult to process limiting its use to niche applications where performance considerations override cost considerations. Some actual, and proposed, applications of silicon carbide are listed below:

Silicon carbide's semiconducting properties were utilised in very early point contact diodes used as radio detectors. In 1907 H.J. Round observed the first emission of light from a silicon carbide/metal contact diode; this was the first recorded light emitting diode (LED). Silicon carbide LEDs have been produced commercially but it is now more commonly used as a substrate for direct band gap semiconductors. In this application silicon carbide's high thermal and electrical conductivity make it useful. Silicon carbide has received much attention for high power, high temperature electronic applications due to its high thermal conductivity, high electron mobility and wide band gap [62][63][64].

Silicon carbide's high hardness has resulted in several applications where wear resistance is important. Examples of this include wear linings applied to equipment used to handle abrasive fluids, mechanical seals and valve components. Another use that relies on high hardness and high strength is as an armour material. Silicon carbide has been included in vehicle armour as well as armoured jackets.

Table 4. Typical properties of silicon carbide.

Physical Properties		
Density	g.cm^{-3}	3C: 3.166 – 3.214 [65] 2H: 3.214 [65] 6H: 3.211 – 3.249 [65]
Lattice Parameter	Å	3C: 4.3596 @ 297 K [65] 2H: a = 3.0763, c = 5.0480 @ 300 K [65] 4H: a = 3.0760, c = 10.053 @ 300 K [65] 6H: a = 3.0806, c = 15.1173 @ 297 K [65] 15R: a = 12.691 @ 300 K [65]
Thermal conductivity	$\text{Wm}^{-1}.\text{K}^{-1}$	360 [23] 3C: 255 [66] 6H: 410 [66]
Thermal expansion	K^{-1}	3.8×10^{-6} [23] 3C: 3.8×10^{-6} [66] α -SiC: 5.12×10^{-6}
Melting Point	$^{\circ}\text{C}$	Decomposes at 2545 ± 40 $^{\circ}\text{C}$ [66]
Hardness	Knoop (GPa)	3C: 29 – 31 [23] 6H: 19 [67]
	Vickers (GPa)	6H: 22 [67]
	Mohs	3C: 9.2 – 9.3 [23]
Young's Modulus	GPa	3C: 460 [49] 3C: 392 – 448 [65]
Bulk Modulus	GPa	192 [66]
Shear Modulus	GPa	96 [66]
Poisson Ratio		0.142 [66]
Fracture Toughness	$\text{MPa.m}^{1/2}$	6H: 1.8 [67]
Electrical Properties		
Band Gap E_g	eV	3C: 2.2 [62] 6H: 2.86 [62]
Breakdown Voltage	V.cm^{-1}	3C: 3×10^6 [62] 6H: 4×10^6 [62]
Carrier Mobility μ_n	$\text{cm}^2.\text{V}^{-1}.\text{s}^{-1}$	3C: 1000 [62] 6H: 500 [62]
Dielectric constant ϵ		9.72 (DC) [23] 6.52 (High frequency) [23]
Saturation Velocity V_{Sat}	cm.s^{-1}	3C: 2.5×10^7 [62] 6H: 2×10^7 [62]
Resistivity	$\Omega.\text{cm}$	3C: $0.001 - 10^6$ [66] α -SiC: $0.0015 - 10^3$ [66] Strongly dependent on purity and temperature

Optical Properties		
Refractive index		3C: $2.55378 + 3.417 \times 10^4 \cdot \lambda^{-2}$ (467nm - 691nm) [23] 3C: 2.652 (589nm) [68] 2H: $n_o = 2.633$ $n_e = 2.707$ (589 nm) [68] 4H: $n_o = 2.6359$ $n_e = 2.712$ (589 nm) [68] 6H: $n_o = 2.648$ $n_e = 2.691$ (589 nm) [68] 15R: $n_o = 2.650$ $n_e = 2.797$ (589 nm) [68]
Birefringence ($n_e - n_o$) (589 nm)		2H: 0.074 [68] 4H: 0.053 [68] 6H: 0.043 [68] 15R: 0.047 [68]
Dispersion $n_o(431\text{nm}) - n_o(687\text{ nm})$		3C: 0.112 [68] 2H: 0.106 [68] 4H: 0.122 [68] 6H: 0.104 [68] 15R: 0.108 [68]

Considerable interest has been shown in using SiC as a structural ceramic, mainly due to its high strength at elevated temperatures. Silicon carbide is often used in low stress situations where its high temperature properties are crucial, such as in furnace furniture. For highly stressed application, for example gas turbine rotors, application has been limited by its low fracture strength. Considerable effort was put into trying to develop silicon carbide based materials for high temperature, high stress applications, however very few commercial applications have resulted. A development in this area is that of ceramic matrix composites. In the case of silicon carbide one option is the use of carbon fibre reinforced silicon carbide. Potential uses for this material include disc brake discs, turbine components and rockets combustion chambers and nozzles. Silicon carbide composites have also been proposed as a construction material for fusion research reactors. For lower temperature applications silicon carbide has also been used as reinforcement in metal matrix composites. In this application silicon carbide powders, whiskers or fibres are used to reinforce metals such as aluminium, magnesium and titanium. These composites have been utilised in automotive, aeronautical and space applications.

A combination of high stiffness, low density, low thermal expansion coefficient and high strength makes silicon carbide an ideal material for optical components such as mirrors [69]. An example of this is the main mirror of the Herschel Space Observatory that was launched in May 2009. With a main mirror 3.5 m diameter it is currently the largest space based telescope.

Silicon carbide's ability to retain strength at high temperatures has led to proposals for its use in high temperature gas treatment system. For example filters for diesel engine exhaust systems and catalyst support structures.

A niche application that makes use of high purity transparent silicon carbide is as a replacement for diamond in high-pressure research. Anvils for high-pressure research equipment can be made from silicon carbide. In this application it has the

advantage of lower cost, larger size, high temperature capability and optical transparency at wavelengths where diamond is opaque. In this application the anvils for the test cell are made from single crystal silicon carbide. [70][71]

Single crystal silicon carbide is used as an artificial gemstone where it is referred to as moissanite. With many of its properties relatively close to those of diamond moissanite is a credible imitation diamond. One major difference between moissanite and diamond is that the α -SiC used exhibits birefringence that is not seen in the cubic structure of diamond.

Because of silicon carbides chemical inertness, oxidation resistance at high temperatures and impermeability, it is used as a coating for graphite to prevent oxidation, seal in impurities or prevent impurities from entering the graphite. A common use of this is in high temperature semiconductor processing equipment. Silicon carbide coatings have also been proposed for pebble bed power reactor pebbles to prevent oxidation of the pebbles in case of accidental air or moisture ingress into the reactor.

4.2 PROCESSING OF SILICON CARBIDE

Since being developed in the 1890s the Acheson process has remained the most important process for producing silicon carbide. This process is essentially the carbothermic reduction of silica:



In the Acheson process a mixture of silica and carbon is reacted in an electric furnace. Sawdust and salt are added to the mixture; saw dust to improve the porosity of the charge and salt as a source of chlorine that acts to purify the charge. Within the furnace the charge is packed around a carbon electrode which is electrically heated to between 2400 °C and 2700 °C [72][73]. Due to the temperature gradient from the carbon electrode to the outermost region of the charge zones of differing products form within the charge. In the region adjacent to the electrode silicon carbide is initially formed but this subsequently decomposes to form graphite and silicon vapour. The graphite is deposited near the electrode while the silicon vapour reacts with carbon to form silicon carbide in the cooler zones away from the electrode. In areas where the temperature is below the decomposition temperature, but above about 1400 °C to 1800 °C, silicon carbide crystals form. In cooler areas the silicon carbide tends to be amorphous. On the outer areas the charge does not get hot enough for any reaction to occur leaving a zone of unreacted charge. The purity of the silicon carbide formed in the Acheson process varies from about 90% up to 99.8% purity. Three grades of silicon carbide are produced by the Acheson process – metallurgical grade with the lowest purity, black and green that has the highest purity ($\pm 99\%$). Most of the silicon carbide formed is of the 6H polytype. Crystal size varies with distance from the central electrode. In the hotter areas crystals of up to 3 cm can be formed in cavities. Silicon carbide produced by the Acheson process is suitable for use in the metallurgical industries, as an abrasive material and as a refractory.

Worldwide capacity of Acheson silicon carbide is in the region of 1.25 million tons per annum. Of this approximately 45% is used in metallurgical industries, 30% as abrasives and 25% in refractory materials [72]. For many other uses Acheson SiC is of insufficient chemical purity or crystallographic perfection to be of value.

An important development in producing high quality silicon carbide crystals was the Physical Vapour Transport (PVT) process developed by Lely. In this process polycrystalline silicon carbide is packed into a graphite tube to form a layer on the inside of the tube. The closed tube is then heated to 2500 °C to 2700 °C in argon at atmospheric pressure. Silicon carbide on the outer side of the charge sublimates and then deposits on platelets growing in the central space. Nucleation takes place on the surface of existing silicon carbide pieces. An improvement in the Lely process uses a porous carbon tube to separate the silicon carbide charge from the central core where crystal growth takes place. This offers some control over the nucleation of new crystals; however growth rate is very slow, very inefficient and there is little control of nucleation and growth.

Tairov and Tsvetkov succeeded in controlling nucleation and maintaining high growth rates by a modification of the Lely process. Significant changes from the Lely process include the use of a seed crystal and operation at low pressure. Two versions of the modified Lely process have developed. In the first, an arrangement very similar to the improved Lely process is used with the source material packed into the annular space between a graphite crucible and a concentric porous graphite tube. A seed crystal is placed at the bottom of the central cavity. In the second method no porous graphite tube is used, instead the source material is packed into the bottom of the crucible and the seed crystal is mounted at the top. Argon at pressures ranging from 1 Torr to 40 Torr is used as an atmosphere during growth. Crystal growth takes place at a temperature of between 1800 °C to 2400 °C. A temperature gradient is maintained, with the growing boule at a lower temperature than the source material. This process has been developed to the point where it is possible to grow large high purity boules of a specific polytype. By using high purity source material, making use of degassing steps and accurate control of process parameter high purity, low defect density, boules suitable for electronic applications can be grown.

Another physical vapour transport method is the Sublimation Sandwich Method (SSM). In this technique a polycrystalline, or single crystal, source is separated from a substrate by a small distance – 0.02 mm to 3 mm. At high temperatures the source sublimates and forms an epitaxial deposit on the substrate. This technique is capable of high growth rates of epitaxial layers but is not easily adapted for growing large boules [73].

Details of PVT and SSM growth techniques for silicon carbide can be found in references [59][61][73][74][75][76].

Silicon carbide is not amenable to growth from a melt due to the high temperatures and pressures involved. However, it is possible to grow silicon carbide crystals from high temperature solutions of carbon in silicon. From the silicon/carbon phase diagram it can be seen that significant amounts of carbon can be dissolved into liquid silicon at high temperatures (There are discrepancies in the phase diagrams reported

in the literature. Glass [77] claims 0.01% to 19% dissolved carbon as the temperature is increased from 1412 °C to 2830 °C). This makes it possible to grow silicon carbide from a silicon/carbon melt. Due to the very high temperatures (1665 °C to 2400 °C) and pressures (10 MPa to 12 MPa) required this process is not considered an economically viable option for bulk growth. This technique has however achieved some success for growing epitaxial layers [73].

For mechanical applications high purity single crystals are not required, for these applications various methods of processing silicon carbide powders are used. Forming methods typically used for fine ceramics are used to produce green parts. Examples include slip casting and powder pressing, extrusion and injection moulding. In some of these processes a binder may be added to the powder to ensure sufficient green strength. Formed parts then need to be sintered to obtain final properties. Recrystallised silicon carbide is fired at temperatures exceeding 1750 °C without any sintering aids. This process is used to manufacture silicon carbide heating elements [72]. Sintering aids, such as boron carbide or alumina and aluminium, may be added to the powder to enhance the sintering process. Hot pressing techniques have also been developed whereby silicon carbide powder, together with sintering aids, is sintered at high temperature (>2000 °C) and pressure in inductively heated graphite dies [78].

Reaction sintering techniques have also been applied to silicon carbide. This sintering method involves the use of additives that react to form a bonding phase. In the case of silicon nitride bonding, silicon carbide powder is pressed together with silicon powder. The green parts are then sintered in a nitrogen atmosphere. Bonding takes place due to the formation of silicon nitride [72]. Similar techniques utilise silicon carbide together with carbon and silicon as a bonding agent. On heating the silicon and carbon react to form silicon carbide that bonds the silicon carbide powder. It is also possible to infiltrate silicon into a porous compact made of silicon carbide mixed with carbon powder. The infiltrated silicon then reacts with the free carbon to form silicon carbide. An advantage of this method is that pores can be filled with silicon resulting in a very low porosity; however this does limit the maximum use temperature. This technique is used to produce the cold end of heating elements [72]. Another bonding mechanism that has been investigated is the reaction between an oxide layer formed on the silicon carbide particles and alumina. Bonding is achieved by the formation of mullite ($3\text{Al}_2\text{O}_3 \cdot 2\text{SiO}_2$) [79].

A number of techniques for producing fine silicon carbide particles have been reported, some of these are:

- Reacting silicon and carbon containing gases in a plasma arc
- Reaction of high purity silica and carbon powder in an arc
- Direct reaction of silica and carbon powder
- Decomposition of polycarbosilanes
- High temperature treatment of spray dried powders made of silica gel and carbon powder
- Reaction of carbon with silica gel produced via a sol gel process

Many processes have been investigated where a carbon containing material is reacted with SiO_2 or SiO . Various carbon sources have been investigated including graphite, carbon black, carbonised polymers, charcoal and rice husks. Rice husks are

an interesting source material as they contain sufficient silica to form silicon carbide without the addition of silica [80][81]. In the case of carbonised polymer foams and charcoal the shape of the carbon starting material is maintained during processing. This allows for the manufacture of silicon carbide with the foam or wood structure[82][83][84][85].

Processes for producing near net shape silicon carbide components have also been developed. Examples of these include the reaction of SiO vapour with machined graphite component to produce a finished silicon carbide part. This technique is widely used to produce silicon carbide components for semiconductor processing equipment and is being investigated for the manufacture of precision mirrors [86].

Chemical vapour deposition (CVD) is another method used to form silicon carbide. In this method gaseous precursors are reacted to form silicon carbide on a surface. A wide variety of precursors and operating temperatures and pressures have been utilised for this process. CVD processes have been used for a wide variety of processes ranging from epitaxial films used for electronic application to bulk deposition. A variation of CVD processing is the deposition of the matrix for fibre reinforced composites – in this application it is referred to chemical vapour infiltration (CVI). A detailed discussion of chemical vapour deposition is presented in chapter 5.

5 CHEMICAL VAPOUR DEPOSITION

5.1 BACKGROUND

Chemical vapour deposition (CVD) is a process whereby gaseous precursors are reacted to directly to form solid materials. Reaction conditions and the choice of precursor will determine whether the solids form homogeneously, that is directly in the gas phase, or heterogeneously on a pre-existing surface. Whilst for some applications it is desirable for homogeneous reactions to take place it is more common for conditions to be chosen to favour heterogeneous reactions.

CVD processes have been utilised for many years. One of the first applications was a process, patented in 1893, for the deposition of tungsten onto carbon filaments for use in incandescent lamps [87]. At about the same time the carbonyl (Mond) nickel refining process was developed, this uses CVD type reaction to deposit pure nickel onto nickel powder. Another well known CVD process is the van Arkel – de Boer process for producing pure metals such as titanium, zirconium, hafnium and thorium. More recently, use of CVD has developed rapidly with significant use in the microelectronics industry. Examples of CVD applications include [87]:

1. Semiconductors such as Si, Ge, III-V and II-VI for use in microelectronics, optoelectronic and photovoltaic devices
2. Dielectrics such as SiO₂, Si₃N₄, AlN used in microelectronics and fibre optics
3. Metals e.g. W, Mo, Cu, Al used in electronics
4. Ceramics e.g. SiC, TiN, TiB₂, B₄C, BN used as hard coatings and protection against wear, corrosion, thermal shock and as a diffusion barrier
5. Ceramic fibres and matrix materials for ceramic matrix composites

Choy [87] lists the following strengths and weaknesses of CVD processing:

Strengths

1. Ability to produce pure, high density material
2. Good uniformity, deposition rates, adhesion and repeatability
3. Conformal coverage allows for uniform coating of complex shapes
4. Ability to control crystal structure and surface morphology of the deposit
5. Control over deposition rates
6. Relatively low process temperatures
7. Wide choice of precursors
8. Reasonable processing cost

Weaknesses

1. Use of hazardous chemical and hazardous by products
2. Difficult to deposit multi-component layers
3. In some situations where specialised processing conditions are required, (e.g. low pressure and low temperatures requiring plasma enhancement) cost may be high

In terms of depositing silicon carbide on TRISO fuel particles CVD allows for the rapid deposition of a uniform layer of dense, high purity silicon carbide at reasonably achievable processing temperatures. Processing equipment is relatively simple, not requiring any pressure control or additional energy inputs beside temperature control. The precursor, methyltrichlorosilane, does require careful handling but is not extremely hazardous while the waste gas, a mixture of HCl and hydrogen can be treated and disposed of quite easily.

CVD process equipment essentially consists of three major components:

1. Precursor feed system
2. CVD coater
3. Effluent handling systems

Gaseous, liquid and solid precursors have all been used in CVD system. Gaseous precursors are possibly the easiest to accurately control. Feed rate can be controlled with suitable pressure regulation and a flow control device such as a rotameter or mass flow controller (MFC). Rotameters can control gas flows to an accuracy of approximately 2% full scale however rotameters are pressure and temperature sensitive. Where more accurate control is required mass flow controllers can provide an accuracy of 0.2% full scale and are less sensitive to pressure variations. Mass flow controllers also have the advantage of being easily controllable allowing for changes in gas flow rates during a deposition run. In addition to flow control, gas feed systems often include filtration and some form of gas purification.

Various techniques are used for introducing vaporised liquids into CVD chambers. One commonly used method is to evaporate the liquid into a carrier gas stream using a bubbler. A bubbler is essentially a vessel containing the volatile liquid precursor. A carrier gas is bubbled through the liquid that evaporates into the gas stream. Vapour flow rates are governed by the liquid temperature, carrier gas flow rate and total pressure in the bubbler. All these parameters need to be well controlled for accurate control of the vapour flow rate. However even with these controls in place evaporation rates may still be variable, especially at high flow rates where lack of equilibrium and liquid carry over may be a problem. Various design details of the bubbler gas distribution system have been tried to improve control of the vapour flow rates by ensuring saturation of the carrier gas and minimizing liquid carry over. Where high accuracy is required various alternatives have been used. These include direct injection of liquid into the carrier gas stream using a pump, use of liquid mass flow controllers and vapour flow controllers.

Some precursor materials are volatile solids at normal temperatures and pressures. Evaporators, where a stream of carrier gas passes through a heated bed of solid precursor may be used provided the vapour pressure is sufficient. Alternatively, powder may be added directly to a stream of heated gas.

The purpose of the CVD coater is to provide the appropriate conditions for coating. This includes control of operating pressure, gas flow patterns, process temperature and activation energy. Operating conditions are mostly chosen so that a heterogeneous reaction occurs on an existing surface, however in some cases homogenous gas phase reactions are desired. Process parameters impact the nature of the deposited film. For example, in the case of silicon deposition, operating

temperature will determine if the deposit is amorphous, poly-crystalline or epitaxial. A wide range of operating temperatures, pressures and gas flows are used in practice. In some situations additional activation is required to enhance deposition rates, especially in the case of low temperature processes. Energy sources that have been used include plasma (Plasma Enhanced Chemical Vapour Deposition - PECVD), electric arc, ultra violet and laser light.

Many of the by products of the CVD process are hazardous and require some means of treatment. In the case of low pressure CVD this is a particular problem as any corrosive gasses or particulates are problematic for downstream vacuum equipment. It is common practice for carrier gasses to be used on a once through basis, especially for relatively small-scale systems. However, for some processes gasses may be recycled. The van Arkel – de Boer process operates as a closed system with iodine vapour released during deposition being used to generate new metal iodide vapour. Carbon monoxide used in the carbonyl process is recycled in a similar manner. In some large systems it becomes economically viable to purify and recycle carrier gasses [88].

Silicon carbide coating of TRISO particles is carried out in a spouted bed coater operating at atmospheric pressure and high temperature using methyltrichlorosilane (MTS) as a precursor. Important parameters in this process include deposition temperature, carrier gas flow and MTS concentration. Flow conditions within the coater have also been found to have a strong influence on coating uniformity and defect density. Hydrogen chloride gas is released as a by-product of the deposition process; this needs to be neutralised before the carrier gas can be released. Details of this process will be presented in the following sections.

5.2 CVD MECHANISMS

Although homogeneous gas phase reactions are feasible, and are utilised, it is the heterogeneous deposition onto a surface that is the main interest in this study. In the following discussion of CVD mechanisms, only heterogeneous mechanisms will be considered.

A general description of a CVD deposition process may involve the following [87] [89]:

1. Gas phase reactions resulting in intermediate species
2. Transport of species to the surface
3. Net adsorption of reactants onto the substrate
4. Migration of species on the substrate surface
5. Reaction of adsorbed species to form a solid deposit and by-products
6. Desorption of by-products from the substrate
7. Transport of by-products into the bulk gas
8. Gas phase reactions producing powders
9. Loss of unreacted precursor or intermediates

These are depicted in Figure 6.

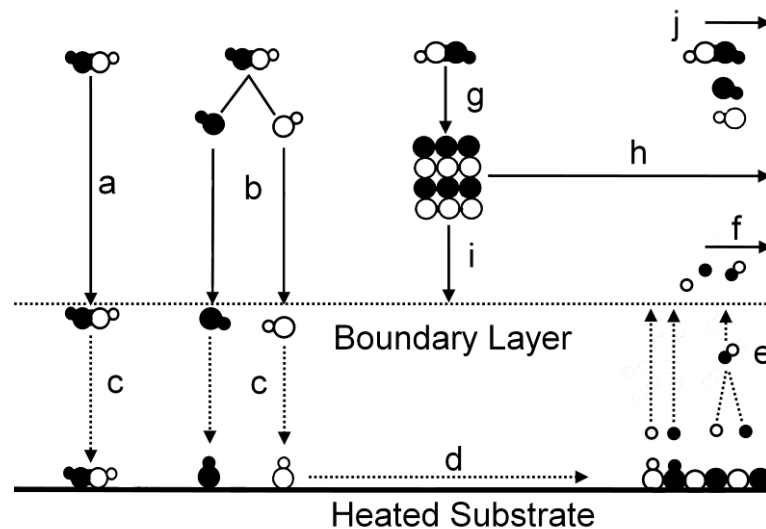


Figure 6. Processes taking place in CVD deposition. (a) transport of precursor to substrate or boundary layer (b) gas phase reactions and transport of intermediate compounds to substrate (c) diffusion of precursor or intermediates through a diffusion boundary layer (d) surface diffusion of precursor to reaction site and inclusion into the solid substrate (e) formation of byproducts and removal from the solid substrate (f) removal of by products from the reactor (g) homogenous gas phase reaction form powder (h) loss of powder with gas phase (i) inclusion of powder into substrate (j) loss of precursor and intermediates. Based on figures from [87][89].

Depending on the process and exact operating conditions, it is possible that not all of these steps are involved. Each of these steps may also be more complex than indicated by the above simplistic model. For example, deposition may involve several chemical pathways each of which may result in different deposit morphology [90][91].

These steps play an important part in determining the deposition rate and morphology of the deposit. Deposition rate will be governed by the slowest of the steps while deposit morphology is governed by the adsorption and migration of species on the substrate surface. A simplified view of deposition rate is that the rate determining step is either mass transport controlled or activation controlled. In reality, there are transition conditions under which both mechanisms will play a role.

5.3 DEPOSITION RATE CONTROL

As indicated in the previous section deposition rate is controlled by either mass transport or activation mechanisms. Which of these mechanisms predominates is dependent on the deposition temperature, nature of the species present, partial pressure of the various species in the gas mixture and fluid dynamics in the coater.

5.3.1 MASS TRANSPORT CONTROL

Mass transport control becomes significant under conditions where the reaction rate exceeds the rate of supply of reactants. Typically, this would occur at high temperatures or at low precursor concentrations. Under these conditions, the surface concentration of the precursor will be low, being restricted by diffusion across a boundary layer. The thickness of the boundary layer will be dependent on the configuration of the coater and the operating conditions.

Diffusion across a boundary layer can be described by Fick's first law:

$$J = -D \frac{\partial C}{\partial X} \quad (5)$$

Where:

- J : Diffusion flux (mol.s^{-1})
- D : Diffusion coefficient ($\text{m}^2.\text{s}^{-1}$)
- C : Reactant concentration (mol.m^{-3})
- X : Diffusion distance (m)

Boundary layer thickness is a function of the Reynolds number. A commonly used correlation for estimating the thickness of a boundary layer is:

$$l = \sqrt{\frac{1}{R_e}} = \sqrt{\frac{LV\rho}{\mu}} \quad (6)$$

Where

- l : Boundary layer thickness (m)
- R_e : Reynolds number (dimensionless)
- L : Characteristic length (m)
- V : Fluid velocity (m.s^{-1})
- ρ : Fluid density (kg.m^{-3})
- μ : Fluid dynamic viscosity (Pa.s)

5.3.2 ACTIVATION CONTROL

It is common to make use of the Arrhenius relationship when evaluating reactions under activation control. Arrhenius type plots of log reaction rate versus reciprocal temperature are often used to determine whether deposition rates are mass transport controlled or activation controlled. Strictly speaking Arrhenius's rate law applies only to elementary gas phase reactions [92]. For more complex reaction mechanism, the individual rate constants will also show Arrhenius type behaviour, however this does not necessarily mean that the overall reaction will exhibit Arrhenius behaviour.

In the following sections various models describing activation controlled homogenous gas phase reactions and heterogeneous surface reactions are reviewed.

5.3.2.1 GAS PHASE REACTION

In many CVD systems homogenous gas phase reactions play an important part of the system chemistry. This typically involves the formation of reactive species that subsequently react on a solid surface to form the final product. Examples of some typical reactions are listed in references [91].

At a fixed temperature the rate equation for a reaction of the form $A \rightarrow B + C$ may be given by:

$$r_A = -kC_A^n \quad (7)$$

Where:

- r_A : Reaction rate
- k : Reaction rate constant
- C_A : Concentration of A
- n : Order of the reaction

The reaction rate constant is often temperature dependent and will typically follow an Arrhenius relationship:

$$k = k^0 e^{-\frac{E_a}{RT}} \quad (8)$$

Where:

- k : Rate constant
- k^0 : Pre-exponential term
- E_a : Activation energy ($\text{kJ}\cdot\text{mol}^{-1}$)
- R : Gas constant ($8.314 \text{ kJ}\cdot\text{mol}^{-1}$)
- T : Temperature (K)

In some circumstances the Arrhenius model does not provide a very good fit to the experimental data. In these cases a modified Arrhenius equation, such as equation 9, may be used.

$$k = k^0 T^n e^{-\frac{E_a}{RT}} \quad (9)$$

Where:

- k : Rate constant
- k^0 : Pre-exponential term
- E_a : Activation energy ($\text{kJ}\cdot\text{mol}^{-1}$)
- R : Gas constant ($8.314 \text{ kJ}\cdot\text{mol}^{-1}$)
- T : Temperature (K)
- n : Temperature exponent

More complex gas phase reactions may proceed via an initiation-propagation series of reaction. In this case a complex reaction mechanism can be broken down into a series of elementary reactions that may be viewed as being initiation, propagation or termination reactions. Several reactions of each type may be taking place at the same time. Reaction rates for each of these elementary reactions may be expressed in terms of equation 7. Initiation-propagation mechanisms offer a valid explanation as to the large number of species that may be found in some reactions. Where the initiation-propagation process consists of a large number of elementary reactions the overall reaction rate may be difficult to determine. In these cases simplifying assumptions, such as the pseudo-steady state assumption, may be used to facilitate the calculation. The pseudo-steady state assumption assumes that the concentration of intermediate species remains constant [93].

5.3.2.2 SURFACE REACTIONS

Several mechanisms have been proposed for reactions taking place on a surface; amongst these are the unimolecular surface reaction, the Langmuir-Hinshelwood mechanism and the Eley-Riddeal mechanism. Each of these reaction mechanisms are based on the adsorption of species onto a surface. Unimolecular reactions involve the adsorption of a single species onto the surface sites, the reaction of the species and finally desorption of gaseous reaction products from the surface. For a first order unimolecular deposition reaction the deposition rate is given by equation 10 [94].

$$Rate = k\theta \quad (10)$$

Where:

- k : reaction rate constant
- θ : fraction of adsorption sites occupied by reactive species

For adsorption without dissociation, coverage of the adsorption sites can be calculated from the Langmuir isotherm. Other isotherms exist, however the Langmuir isotherm has been found to describe chemisorption well. Using Langmuir's theory the surface coverage can be calculated from equation 11 [95]:

$$\theta = \frac{Kp}{1 + Kp} \quad (11)$$

Where:

- θ : Fraction of adsorption sites occupied by reactive species
- K : Langmuir adsorption constant
- p : Pressure of adsorbing species

In equation 11, K is constant for a given temperature. When it is assumed that the adsorption rate is proportional to the fraction of sites available, $(1-\theta)$, and the desorption rate is proportional to the fraction of sites occupied, θ , then the Langmuir adsorption constant, K , may be calculated using the following relationship [96]:

$$K = \frac{s}{\nu} \frac{1}{\sqrt{2\pi mkT}} e^{\frac{\Delta H}{RT}} \quad (12)$$

Where:

- K : Langmuir adsorption constant
- s : Condensation coefficient
- ν : Pre exponential factor of the desorption rate coefficient
- m : Molecular mass of gaseous species ($\text{g}\cdot\text{mol}^{-1}$)
- k : Boltzmann coefficient
- T : Temperature (K)
- ΔH : Heat of adsorption ($\text{kJ}\cdot\text{mol}^{-1}$)
- R : Gas constant ($8.314 \text{ kJ}\cdot\text{mol}^{-1}\cdot\text{K}^{-1}$)

Two modifications of the Langmuir isotherm are of special interest; dissociative adsorption and competitive adsorption. In the case of dissociative adsorption the fraction of surface sites occupied will be given by [96]:

$$\theta = \frac{K^{1/2} p^{1/2}}{1 + K^{1/2} p^{1/2}} \quad (13)$$

In situations where an inactive species, C, competes with active species, A, by occupying adsorption sites, the fractions of sites occupied by A will be given by equation 14. Similar equation can be developed for situations where a second active species, B, contributes to the deposition reactions by adsorbing onto specific surface sites [96].

$$\theta_A = \frac{K_A p_A}{1 + K_A p_A + K_C p_C} \quad (14)$$

In situations where two gas phase species take part in the reaction, and each adsorb onto specific surface sites, the reaction rate will depend on the adsorption coverage of both sites. In this case the reaction rate will be given by equation 15 [97].

$$Rate = k\theta_A\theta_B \quad (15)$$

Where k is the reaction rate constant and θ_A and θ_B are the coverage of sites A and B respectively. Depending on the nature of the surfaces and species present the coverage for each of the adsorption sites (θ_A and θ_B) may be non competitive (i.e. equation 11), competitive (i.e. equation 14) or dissociative adsorption (i.e. equation 13).

In the above discussion the deposition rates were calculated from the surface coverage, θ , and a rate constant k . An alternative argument is to calculate the deposition rate from the impingement rate and a sticking coefficient. In this case, the deposition rate is proportional to the adsorption rate that may be calculated from [98]:

$$Rate = F \times S \quad (16)$$

Where:

F : Impingement rate
 S : Sticking coefficient

The impingement rate may be calculated from the Hertz-Knudsen equation:

$$F = \frac{p}{\sqrt{2\pi mkT}} \quad (17)$$

Where

p : Pressure (Pa)
 m : Molecular mass of gaseous species (kg.molecule^{-1})
 k : Boltzman constant ($1.380\ 6504 \times 10^{-23} \text{ J.K}^{-1}$)
 T : Temperature (K)

The sticking coefficient, S , is the probability that an impinging molecule adheres to the surface and remains on the surface until it reacts. This will depend on the gaseous species, the surface properties and the availability of free surface sites. In addition to influencing the deposition rate the sticking coefficient has significant influence on the morphology of the deposit and is often used in modelling of CVD deposition processes (for example [91][99][100]).

In practice it is likely that the situation will be more complex than one or two active species and a single blocking species. As will be seen in chapter 5, pyrolysis of MTS results in a large number of species. These may contribute to deposition, or retard deposition by preferentially adsorbing onto surface sites and so preventing the adsorption of active species.

5.4 DEPOSIT MORPHOLOGY

It is a well established that microscopic structure of a material plays a significant role in its physical properties. As a result there is considerable interest in understanding the mechanisms that govern the microstructure of vapour deposited materials. For sputter coated and evaporated deposits the Structure Zone Model has been used to describe the structure of the deposits as a function of homologous temperature and other process conditions [101]. Although the structure zone model has been used to describe CVD deposits it is doubtful if the model applies to CVD conditions [102]. Alternative models describing the structure of CVD deposits as a function of deposition conditions have been proposed by Stinton et al [103]. Two factors key to the final morphology of any deposit, are the growth rate of existing surfaces and the nucleation of new growth surfaces.

The driving force for both nucleation and growth of existing surfaces is the difference in chemical potential, $\Delta\mu$, between the vapour and crystalline phase. In the case of an ideal gas this may be expressed as:

$$\Delta\mu = kT \ln\left(\frac{p}{p_e}\right) \quad (18)$$

Where

- $\Delta\mu$: Difference in chemical potential
- k : Boltzmann constant
- T : Absolute temperature (K)
- p : Vapour pressure (Pa)
- p_e : Equilibrium vapour pressure (Pa)

In the case of deposition from a gas containing a single species, and no chemical reactions taking place, it is straightforward to understand which species need to be taken into account. For CVD reactions the situation is more complex. Hwang and Yoon [104] distinguish between chemical reactions and deposition processes and argue that the saturation ratio should be calculated using the actual and equilibrium vapour pressure of the deposited species. In contrast Lespiaux et al [105] used the

vapour pressure of the gaseous species involved in the reaction to calculate the saturation ratio, in effect calculating the driving force for the chemical reaction.

Lespiaux et al [105] highlighted the impact of reaction control mechanisms on the saturation ratio. In cases of activation control the concentration of reactant species close to the surface is the same as in the bulk while under diffusion controlled processes the reactant concentration at the surface would be very low. As a result nucleation and growth behaviour, which depend on saturation, are dependent on the deposition process control mechanism. The saturation model proposed by Hwang and Yoon [104] would however imply that the controlling mechanism would not impact the nucleation and growth process.

Extensive research has been carried out in trying to understand CVD deposit morphology by modelling the processes involved in deposit formation. In modelling CVD deposits two general methods appear to have been followed. Firstly, deposit formation has been treated as a process of growth of discrete nuclei to form a film consisting of a collection of crystallites. Orientation dependent growth rates are taken into account so as to allow for texture formation to be studied. Examples of this approach may be found in references [106][107][108][109][110]. A second approach has been to treat the deposit process as a continuous build up of a layer without consideration of the crystallite size and orientation. Examples of this methodology may be found in references [102][111][99][100].

5.4.1 EQUILIBRIUM CRYSTAL FORM

Gibbs explained crystal habit in terms of surface energy minimisation, although he also recognised that kinetics effects may play an important role. Wulff developed these ideas further and proposed a method of graphically determining the equilibrium structure of based on surface energy of the various crystal planes. This procedure is explained in Figure 7. Dynamic Wulff plots are an equivalent construction that uses the growth rate in a particular crystallographic direction instead of the facet surface energy, this yields the same result. For the cubic system the ratio of growth rates in the [100] and [111] direction, V_{100}/V_{111} , is useful in determining crystal habit. A growth parameter α , defined as $\sqrt{3}V_{100}/V_{111}$ has also commonly been used in the study of diamond film morphology (for example [112], [109]). Typical examples of crystal habit as a function of the growth parameter for diamond is shown in Figure 8. Alternative theories relating the growth rate in a particular crystallographic direction to lattice spacing and surface energy have also been proposed by Bravais, Hartman and Perdoc and van der Sluis and Kroon[113]. Some of these models have achieved success in predicting the habit of free standing crystals but are limited in that they do not take the growth environment into account.

From the Wulff construction it can easily be seen that planes that have the highest growth rates will not form facets in the equilibrium form. This would be true for the case of free standing crystals. However the situation is more complex in a polycrystalline film due to interaction between crystallites in the film. Van der Drift proposed a model whereby the rapidly growing facets of crystallites within a film outcompete slower growing facets resulting in textured films. In this case the rapidly

growing planes will tend to be orientated parallel to the substrate. Nucleation of new crystallites is not taken into account in the van der Drift model, however it has successfully been used in simulations of film growth (for example [109]). For some deposition processes this may be a realistic simplification, however for many cases this does not accurately reflect actual process conditions.

When process conditions suit the formation of faceted crystallites the free surface of the film reflects the morphology that would be expected from a collection of orientated, intertwined crystallites of the form predicted by a Wulff construction. Manipulation of growth conditions to alter the relative growth rate in particular crystallographic directions will result in a change in any preferred orientation as well as the surface morphology of the deposit.

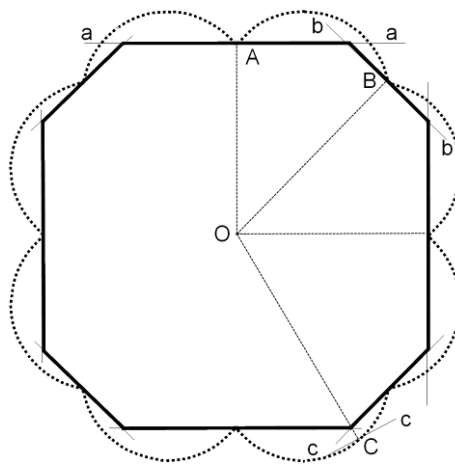


Figure 7. Two dimensional Wulff construction. Procedure for creating plot: Create a polar plot of surface energy versus direction (heavy dotted line). Draw lines from the centre to the surface energy plot for each crystallographic direction (e.g. lines OA, OB, OC). At the intersection between the direction line and the surface energy plot draw a perpendicular (e.g. line a-a, b-b, c-c). Lines forming the inner envelope (e.g. a-a, b-b) will define the facets that will form. Facets will not form for directions with perpendiculars outside of the inner envelope (e.g. line c-c).

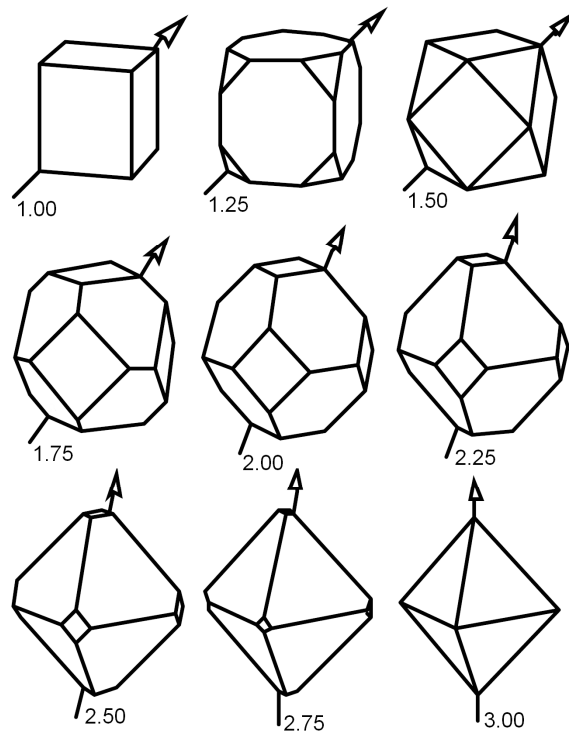


Figure 8. Variation in crystal habit of cubic crystals for values of growth parameter α ($\sqrt{3} V_{100}/V_{111}$) varying between 1.00 and 3.00. Arrows indicate the direction of fastest growth which is equivalent to largest crystal dimension. Modified from Wild et al [112].

Texturing of CVD deposits has been seen for a number of materials including silicon carbide [89]. Differences in orientation have also experimentally been shown to depend on growth conditions and deposition rate controlling mechanisms. Kajikawa et al [89] developed a model based on differences in adsorption site density and sticking coefficient for various crystallographic planes to explain preferred orientation of silicon carbide films deposited under conditions of activation and diffusion control respectively. Although the model was developed to explain deposition using dimethyldichlorosilane it should apply to MTS deposition processes as well.

5.4.2 IMPACT OF DEPOSITION MECHANISM

Deposition processes operating under diffusion control may exhibit unstable growth. Any convex perturbations projecting above the surface will have a higher growth rate due to local thinning of the boundary layer. By the same argument concave perturbations projecting into the surface will have a lower growth rate. This combination of regions of high and low growth rates can result in highly uneven morphology. Surface diffusion will tend to stabilise the surface by evening out the local differences in diffusion flux. Differences in precursor vapour pressure on convex and concave surfaces will also tend to reduce the destabilising effect of diffusion control. In processes where kinetic control predominates surfaces will tend

to be more stable. A useful measure of the relative importance of diffusion and kinetic control is the Damköhler number as given by equation 19 [102]:

$$D_a = \frac{Ak_{AD}\delta}{D_f} \quad (19)$$

Where:

- D_a : Damköhler number (dimensionless)
- A : Reaction rate constant ($\text{m}\cdot\text{s}^{-1}$)
- k_{AD} : Adsorption/desorption equilibrium constant (dimensionless)
- δ : Boundary layer thickness (m)
- D_f : Gas diffusivity ($\text{m}^2\cdot\text{s}^{-1}$)

When $D_a \ll 1$ kinetic control predominates while if $D_a \gg 1$ diffusion control predominates. Simulated surface profiles, as a function of Damköhler number, are shown in Figure 9 [102].

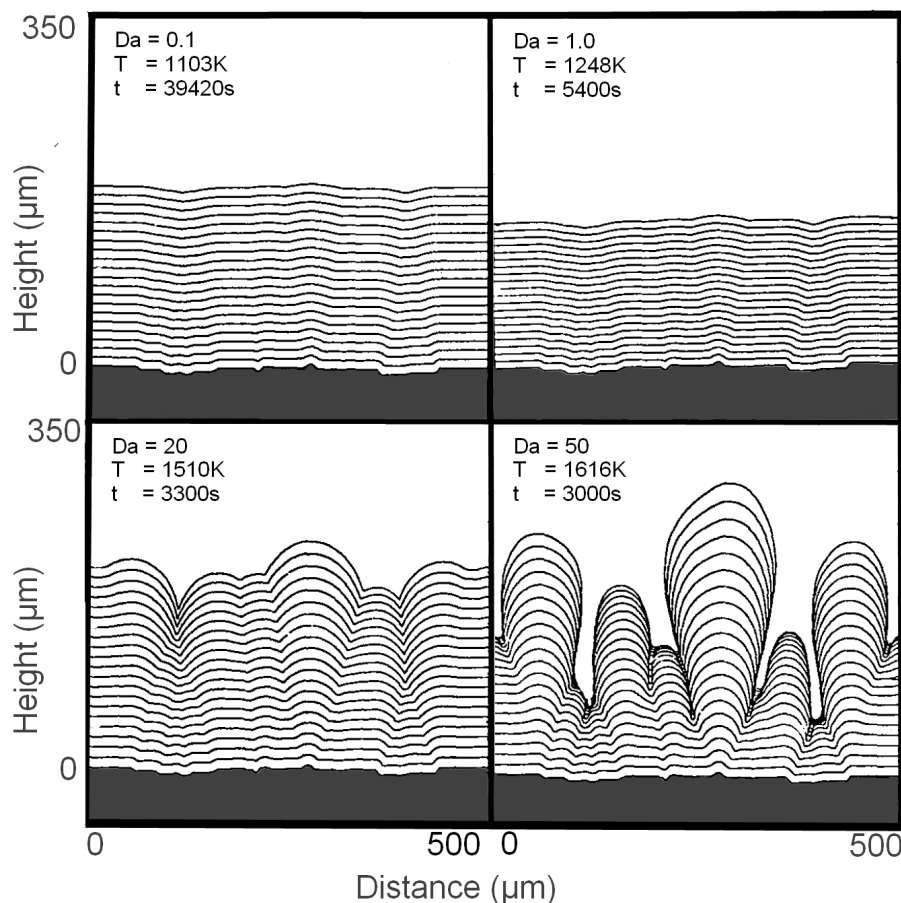


Figure 9. Surface morphology as a function of Damköhler number. Simulation results for atmospheric pressure CVD deposition at various temperatures. Damköhler number increases with increasing deposition temperature. Simulated deposition time varied to give approximately similar thickness for each condition. Modified from Hlavacek et al [102].

Several factors will impact the surface stability. Zero order reaction kinetics will not be sensitive to precursor concentration resulting in a stable surface [114]. As the reaction order increases the growth rate will become more sensitive to precursor concentration and stability of the surface will decrease. Higher vapour pressure on the convex surfaces will reduce the diffusion flux in these regions while reduced vapour pressure in the concave regions will result in an increased flux. The effect of vapour pressure will be more pronounced at smaller dimensions where the radius of curvature is small and the effect on vapour pressure more significant. Surface diffusion of species away from regions of high concentration of active species, i.e. regions of high incident flux, towards regions of low concentration will also tend to reduce any differences in deposition rate. As with the influence of vapour pressure this is a relatively short ranged effect and will have a marginal influence on the deposit morphology [102]. It has been shown that a low sticking coefficient results in deposits that are better able to cover irregular surfaces uniformly [114]. Good “step coverage”, the ability of a deposition process to uniformly cover surface irregularities, such as steps, holes and trenches, is of vital importance in the semiconductor industry and has been extensively studied for this application. It also has importance to the production of TRISO coated particles in that gaps and holes between grains need to be filled without the formation of porosity. Another important consideration is the ability of the process to deposit silicon carbide into the porosity in the inner pyrolytic carbon layer. Penetration of silicon carbide into the pyrocarbon results in a stronger bond between the layers.

It is interesting to note that the morphology, particularly step coverage, of the deposit has been used in a number of studies to determine the reaction mechanisms and sticking coefficients of active species for a number of deposits. A general procedure is to experimentally determine step coverage by depositing a film onto a substrate with features etched into the surface. The deposition process is then repetitively simulated with differing process parameters until a good match between the experimental results and simulated results is obtained. Details of the method may be found in, for example, [90], [91], [114] and [99].

5.4.3 NUCLEATION

Growth models as discussed in the preceding section rely on an existing surface for growth to proceed. New growth surfaces can be created by a process of nucleation. Nucleation can take place homogeneously in the gas phase, heterogeneously on a dissimilar surface (e.g. silicon carbide on carbon) or as secondary nucleation where nuclei form on similar existing surfaces (e.g. silicon carbide nucleation on an existing silicon carbide surface). For most CVD deposition processes homogeneous nucleation is undesirable as it can give rise to the formation of porous, poorly adherent, films formed from particles adhering to the surface instead of a solid film deposited onto the surface.

Heterogeneous nuclei may have a 3 dimensional or 2 dimensional form. In the 3 dimensional case nuclei are in the form of a spherical cap. The exact shape of the cap depends on the contact angle between the nucleus and substrate, ranging from spherical for a contact angle of 180° to a flat disc for contact angles close to 0° . In

the 2 dimensional case the nuclei are in the form of flat discs. For analysis it is assumed that the 2 dimensional nuclei are in the form of a circular disc.

The rate of formation of heterogeneous 3 dimensional nuclei (i.e. spherical cap) and heterogeneous 2 dimensional (i.e. circular disc) nuclei can be calculated from equations 20 and 21 respectively (for example [115]).

$$Rate = Ae^{\left(\frac{-16\pi\gamma^3\nu^2 f(\theta)}{3k^3T^3(\ln S)^2}\right)} \quad (20)$$

$$Rate = Ae^{\left(\frac{-\pi h\gamma^2\nu}{k^2T^2(\ln S)}\right)} \quad (21)$$

Where:

- A : Rate constant ($m^{-2}s^{-1}$)
- γ : Surface energy (Jm^{-2})
- ν : Molecular volume (m^3)
- $f(\theta)$: Contact angle function ($\frac{1}{4}(2+\cos\theta)(1-\cos\theta)^2$)
- θ : Contact angle between nucleus and surface
- h : 2D nucleus edge height (m)
- k : Boltzmann constant ($J.K^{-1}$)
- T : Temperature (K)
- S : Saturation ratio (Pressure/Equilibrium Pressure)

In equation 20, the function $f(\theta)$ ranges between 0 and 1 depending on the contact angle between the nucleus and the substrate surface. The case of $f(\theta)$ having a value of 1 yields the same result as for homogenous nucleation i.e. the nucleation rate for homogenous nucleation and nucleation on a surface with a contact angle of 180° (i.e. a non-wetting surface) are identical.

At low saturation ratios the rate of nucleation will be negligibly small. Increasing saturation above a critical value will result in an exponential increase in the nucleation rate. Under similar conditions homogenous nucleation will be slower than heterogeneous nucleation. For most CVD processes conditions are chosen to avoid homogenous nucleation while allowing for heterogeneous nucleation. This allows for reasonable growth rates without the formation of free particles in the gas phase.

5.4.4 SURFACE GROWTH MODELS

When considering crystal growth mechanisms it is common to make use of a hypothetical crystal structure consisting of cubes arranged in a cubic lattice. This is commonly referred to as a Kossel crystal. Early growth models considered features on the (100) plane, later models included features of higher index planes and crystallographic defects. In a Kossel crystal the binding energy of a building block is dependent on the number of surfaces in contact with the bulk. Important sites considered were the sites on a flat face or terrace, step and a kink. These positions are marked as T, S and K respectively in Figure 10.

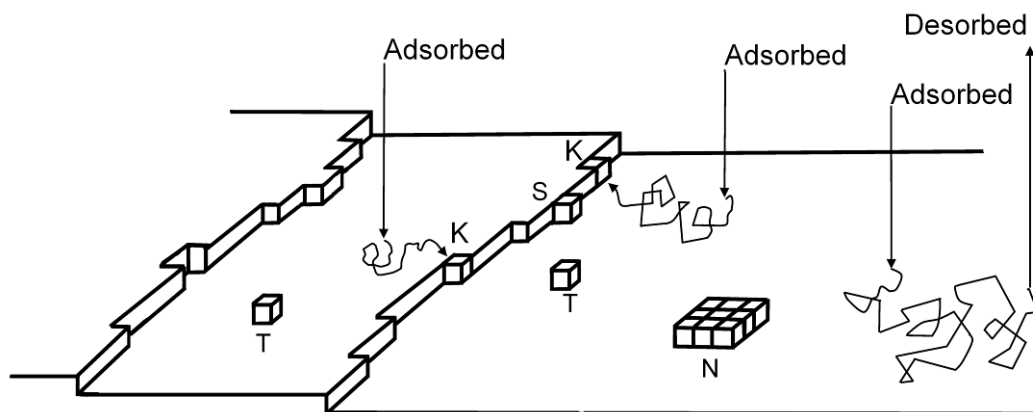


Figure 10. Crystal growth mechanism. Molecules adsorb onto the surface from the gas phase, a fraction of these subsequently desorb. Adsorbed molecules can diffuse on the surface of the crystal prior to desorption or incorporation into the lattice. Molecules are incorporated into the lattice at terrace (T), step (S) or kink (K) sites. Nuclei (N) may form to create new step and kink sites. Adapted from [116].

Kossel and Stranski independently proposed a model for growth of flat crystal surfaces whereby new molecules are added to the surface from the gas phase. Molecules attaching to kink sites have a higher binding energy than those attaching on the surface, or step, sites and are so more likely to be incorporated in the crystal. Those molecules adsorbing onto surface sites will have a low binding energy and so are likely to desorb back to the gas phase. In the Kossel-Stranski model kinks are repeatable, addition of a molecule to the kink serves to move the kink along the step. The process of adding molecules to kinks continues until the kink reaches the edge of the crystal. At this point a new kink needs to form by the addition of a molecule to a step. In this way the steps will also be advanced until the step reaches the edge of the crystal. Once all kinks and steps have grown to an edge new steps need to form by nucleation. Facet growth rate will be limited by the nucleation rate on the surface as there is a very low probability of enough molecules being adsorbed onto the surface to allow for rapid nucleation. Becker and Döring developed a quantitative model based on the Kossel-Stranski model, this was however incapable of explaining measured crystal growth rates.

Volmer modified the Kossel-Stranski model by allowing for surface diffusion of molecules that had been adsorbed onto the crystal surface. In this way a region either side of the step can feed the growth taking place as the kinks and steps advance across the flat crystal facet. As with the Kossel-Stranski model nucleation is required to generate new steps so that the growth process can proceed. Features of the Volmer model are shown in Figure 10. Although an improvement of the previous models the Volmer model could still not correctly explain measured growth rates.

Burton, Cabrera and Frank [117] proposed a model (BCF model) that included several significant improvements to the Volmer model. Based on earlier work Burton, Cabrera and Frank were able to show that the number of kinks in a step followed an Arrhenius type relationship. At temperatures above 0 K all steps would contain kinks. They estimated that for typical (“typical” was not clearly defined) conditions the average distance between kinks was 4 times the molecular spacing. It was also shown that at low values of supersaturation the probability of nucleation of new steps on a perfect crystal plane is very low. In the BCF model the growth rate is determined by the presence of screw defects. In this case steps are continuously generated, without the need for nucleation, as growth proceeds. Growth proceeds by the spreading of existing steps and the continuous extension of the defect to form a spiral. The formation and growth of a spiral from a screw dislocation is shown in Figure 11. Growth spirals of this sort have been observed in a number of materials including silicon carbide. A single screw dislocation will result in the formation of a single spiral while multiple spirals of the same sign will result in complex patterns of interlocking spiral. Adjacent dislocations of opposite sign will result in a series of concentric loops [117] appearing as stack of discs of decreasing size. Examples of growth spiral found in silicon carbide are shown in Figure 12.

Although the BCF model has been successful in describing crystal growth at low supersaturation it cannot explain all observed phenomena. For example it has been pointed out that growth spirals observed on the faces of platelets and tabular crystal cannot explain the high growth rate on the edges of these forms. In the Twin Plane Re-entrant Edge (TPRE) model, originally proposed by Wagner, and Hamilton and Seidensticker (referenced by [118]), high growth rates were attributed to re-entrant edges on twin planes. It was proposed that a re-entrant edge would act as a site for 2 dimensional nuclei to form. In the case of a single twin plane the re-entrant edge would disappear as growth proceeds. In the case of 2 parallel twin planes, forming a re-entrant edge and a ridge, self perpetuating growth mechanisms are possible [119][120][121]. The growth mechanism proposed by Lee [121] is briefly described in Figure 13.

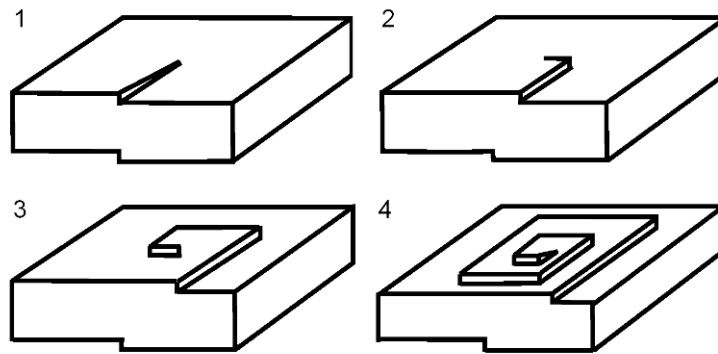


Figure 11. Formation of growth spirals. (1) Initial crystal containing a screw dislocation. (2) The step formed by the dislocation advances as growth proceeds forming a new step. (3) Each new step grows while new steps are formed in the centre of the spiral. (4) Growth proceeds by the advance of the steps and the generation of new steps from the centre of the spiral. Adapted from [122].

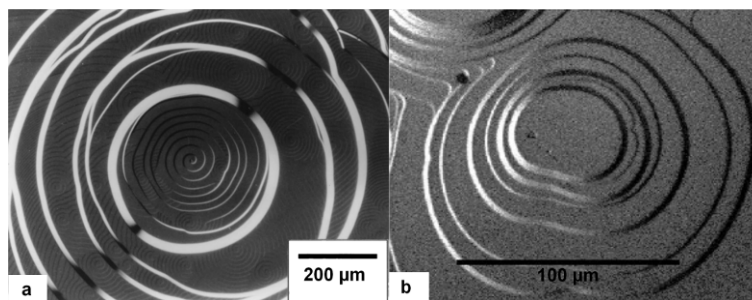


Figure 12. Silicon carbide growth spirals. (a) Multiple spiral on 6H-SiC with micro spirals growing on the terraces formed by a macro spiral. Micro spiral step height equivalent to c spacing, macro step height equivalent to $8c$. Image from reference [123]. (b) Concentric loops formed by two adjacent screw dislocations with equal but opposite Burgers vectors. Images from [73].

The TPRES growth model has not been universally accepted. For example Kitamura et al [124] argued that the TPRES mechanism can only be important for perfect crystals at low supersaturation. They claim that the high growth rate seen on the edges of tabular crystals is due to bundles of screw dislocations.

In addition to the growth sites provided by dislocation, re-entrant edges and nucleation sites certain crystallographic orientations may provide kinks and steps where growth can take place. This may easily be seen by considering a simple Kossel crystal as shown in Figure 14. In this case (110) planes will inherently be stepped while (111) planes will be kinked. In this case growth will be rapid on the kinked and stepped planes leading to the disappearance of these planes. Similar effects will be seen on higher order planes or off-axis surfaces.

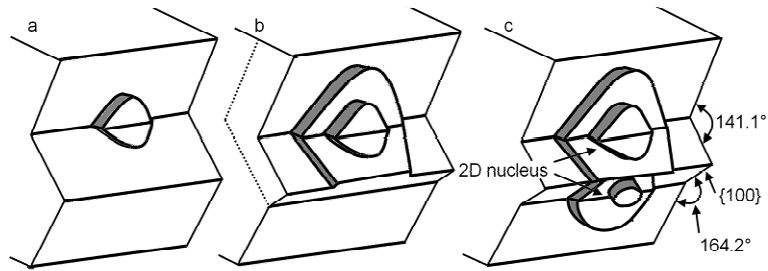


Figure 13. Twin Plane Re-entrant Edge (TPRE) growth mechanism as proposed by Lee et al [121].

(a) 2D nuclei preferentially form on the 141.1° re-entrant edge formed on the twin plane. (b) Growth of the (111) planes adjacent to the re-entrant edge cannot extend across the ridge resulting in the formation of a (100) plane and a 164.2° re-entrant edge. (c) Growth proceeds by 2D nucleation and growth on the 141.1° and 164.2° re-entrant edges. Figure adapted from [121].

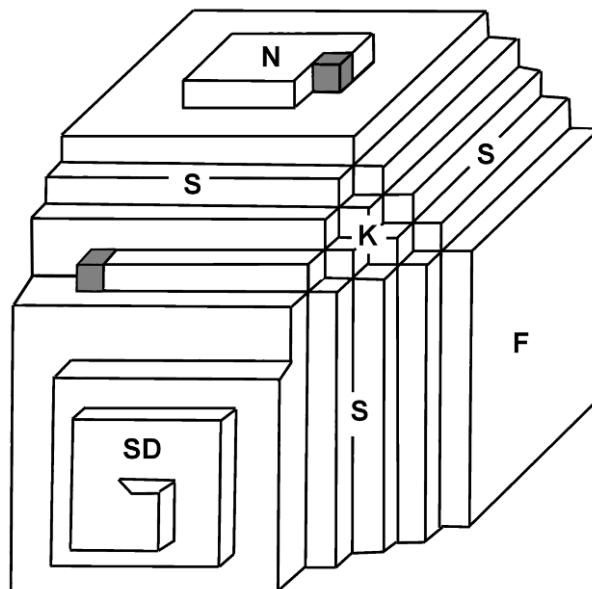


Figure 14. Kossel crystal showing flat (F), stepped (S) and kinked (K) planes. In addition to the stepped and kinked planes growth will also take place at nucleation sites (N) and dislocations (SD). Adapted from [125].

At sufficiently high values of supersaturation growth takes place by an adhesive growth mechanism whereby impinging molecules attach directly to the growth surface. Variation in the growth rate and deposit morphology as a function of supersaturation is shown in Figure 15.

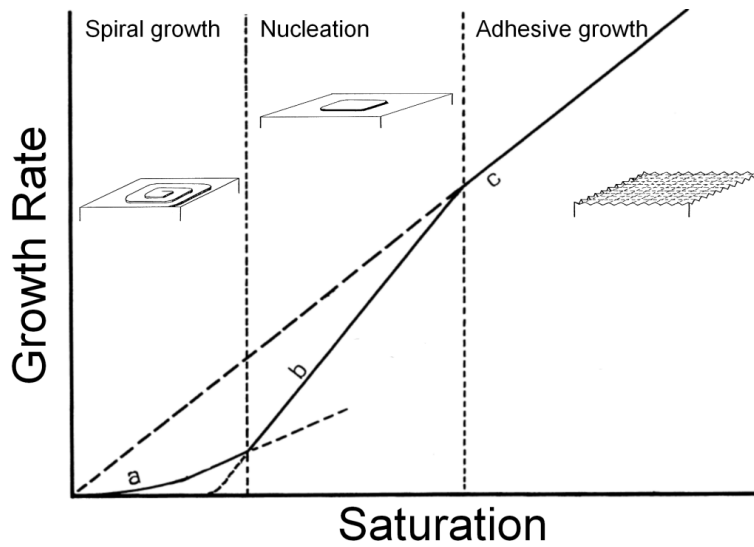


Figure 15. Growth rate as a function of supersaturation. Growth rate is controlled by: (a) dislocation density at low levels of saturation (b) nucleation rate or (c) impingement rate during adhesive growth at high levels of supersaturation. Adapted from [122] and [126].

6 SILICON CARBIDE CVD

6.1 SILICON CARBIDE CVD APPLICATIONS

Extensive research has been carried out on CVD of silicon carbide. A large portion of this is due to interest in silicon carbide as a semiconductor material and has focused on growth of high purity single crystal epitaxial layers of a specific polytype and crystallographic orientation. A review of CVD, together with several other, techniques used for producing electronic grade SiC substrates is given by Dhanaraj et al [116]. CVD techniques have been investigated for the production of polycrystalline SiC substrates as a means of reducing the cost of SiC wafers for electronic applications [127]. For non-electronic applications CVD SiC is commercially available as bulk material or as a protective coating on materials such as graphite. Due to the high cost of these materials they are typically only used in demanding applications where silicon carbide's properties or the high purity of CVD materials are demanded. Silicon carbide and carbon fibre reinforced SiC ceramic matrix composites (CMC) may be produced using chemical vapour infiltration (CVI), a process in which CVD is used to build up a matrix around fibre reinforcing [128][129][130][131]. Deposits of silicon carbide are also used as a protective coating for other materials [for example [87][88][132][133]]. Monolithic silicon carbide, ceramic matrix composites and silicon carbide coated material have found use in a number of demanding applications in ballistic protection, space craft heat shields, rocket combustion chambers and nozzles, gas turbine components, furnace components such as burners and support structures, engine components such as pistons, turbocharger rotors, valve guides [128]. In these applications silicon carbide is a material of choice due to its high strength, especially at high temperature, high hardness, resistance to oxidation and corrosion, low density, high resistance to thermal shock resulting from low thermal expansion and high thermal conductivity. For TRISO coated fuel particles the focus is on depositing uniform films that have good mechanical properties and act as effective diffusion barriers for fission products. The following section reviews some of the published silicon carbide CVD research.

6.2 SILICON CARBIDE CVD CHEMISTRY

In 1909, Pring and Fielding [134] reported a method of depositing silicon carbide onto a heated carbon rod using silicon tetrachloride (SiCl_4), benzene (C_6H_6) and hydrogen. Since then many other precursors have been reported, including:

1. SiH_4/CH_4 in nitrogen or hydrogen carrier [135]
2. $\text{SiH}_4/\text{C}_3\text{H}_8$ [90][136]
3. $\text{Si}_2\text{H}_6/\text{C}_2\text{H}_2$ [90]
4. $\text{SiCl}_4/\text{CH}_4$ [90][135]
5. $\text{SiHCl}_3/\text{C}_3\text{H}_8$ [90]
6. $\text{SiHCl}_3/\text{CH}_4$ [136]
7. $\text{SiCl}_4/\text{C}_2\text{H}_4$ in hydrogen carrier [137]
8. $\text{SiH}_2\text{Cl}_2/\text{C}_2\text{H}_2$ [138]
9. $\text{Si}_2(\text{CH}_3)_6$ (Hexamethyldisilane) [136] [137][139]
10. $(\text{CH}_3)_2\text{SiCl}_2$ in hydrogen [140][141] or helium [89]
11. $(\text{CH}_3)_3\text{SiCl}$ in hydrogen [142][140]
12. $(\text{CH}_3)_4\text{Si}$ in hydrogen [136][140]
13. $\text{H}_3\text{SiCH}_2\text{SiH}_2\text{CH}_3$ (1,3-Disilabutane; 1,3-DSB) [143]
14. $(\text{CH}_3\text{CH}_2)_2\text{SiH}_2$ (Diethylsilane) [142]
15. $(\text{C}_3\text{H}_7)_3\text{SiH}_2$ (Tripropylsilane) [142]
16. $\text{CH}_2\text{CHSiC}(\text{CH}_3)\text{Cl}_2$ (Dichloromethylvinylsilane) [144]
17. CH_3SiCl_3 (Methyltrichlorosilane) in He, H_2 , Ar, H_2/Ar mixture, H_2/N_2 mixture [Many references. See following sections for specific reference]

Methyltrichlorosilane (MTS), CH_3SiCl_3 , is one of the most widely used precursors for SiC deposition, and is virtually the only precursor used for TRISO coating. Overall the pyrolysis reaction for MTS can be expressed as:



MTS has the advantage of having a 1:1 silicon carbon ratio, so it would be expected that stoichiometric silicon carbide should be deposited. In practice it has been found that, depending on deposition conditions, either a silicon rich or carbon rich deposit may be formed. For TRISO applications co-deposition of silicon is regarded as more detrimental than co-deposition of carbon so process conditions are normally selected to ensure no free silicon is deposited. This restricts the allowable deposition conditions.

Several researchers have investigated the chemistry of SiC deposition from MTS. Attempts have been made to understand the exact pathways of the reactions involved. A useful tool in this regard uses thermodynamic considerations to calculate the equilibrium composition of the phases formed. Thermodynamics can explain a system under equilibrium conditions. However, CVD processes seldom reach equilibrium. Full understanding of the CVD process requires an understanding of the thermodynamics, chemical kinetics and mass transport phenomena involved.

It is generally accepted that pyrolysis of MTS starts with the breaking of the C-Si bond to form a methyl and chlorosilyl radical. This can be understood by considering the various bond strengths in the MTS molecule. At 290 kJ.mol⁻¹ the C-Si bond is weaker than the Si-Cl (359 kJ.mol⁻¹) and C-H bond (338 kJ.mol⁻¹) and is most likely to be the first bond to break [145]. Silicon carbide is subsequently formed from silicon and carbon derived from the chlorosilane and hydrocarbon radicals. The carbon and silicon containing radicals can also undergo further reactions to form a variety of silicon and carbon containing species. A separate reaction pathway for deposition of silicon and carbon makes it possible for non stoichiometric deposits to form. Addition of hydrogen to the deposition system is thought to increase the rate of dechlorination of the chlorosilane and decrease the rate of dehydrogenation of the hydrocarbon radical, resulting in a decreased C/Si ratio. Experiments using Ar/H₂ mixtures as carrier gas have confirmed increasing amounts of carbon in the deposits as Ar/H₂ ratio is increased [146].

Kostjuhina and Sotirchos [147] proposed a mechanism where most of the CH₃ and SiCl₃ radicals formed by decomposition of MTS react further to form CH₄ and SiCl₄. Other radicals and stable species such as SiCl₂, SiCl₃, C₂H₄, C₂H₂ are also present in significant concentrations. It is thought that C₂H₄ and C₂H₂ form the main precursors for carbon incorporation into the SiC deposits. These are formed from CH₄ formed from the reaction of hydrogen with CH₃ derived from MTS decomposition. The formation of C₂H₄ and C₂H₂ from CH₄ is the rate-controlling step in this sequence. Evidence for this is found in the fact that addition of CH₄ to the feed gas has little effect on the deposition rate while addition of C₂H₄ results in a significant increase in the deposition rate.

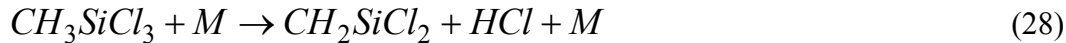
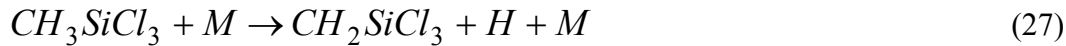
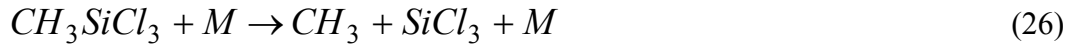
Carbon and silicon containing species adsorb onto the substrate surface and subsequently form silicon carbide and under the right conditions free silicon or free carbon. Reactions 23, 24 and 25 have been suggested:



Subscript “s” implies species adsorbed onto a surface. It is likely that CH₂ and SiCl₂ radicals are the main carbon and silicon containing species in the above reactions. CH₂ is thought to form from CH that is itself formed from the dissociative adsorption of C₂H₂.

That silicon carbide is formed by the reaction of separate silicon and carbon containing species is supported by experimental work carried out by Yagi and Nagasawa [138] and Nagasawa and Yamaguchi [148] who deposited silicon carbide by alternating a supply of SiH₂Cl₂ and C₂H₂. Silicon carbide formed from the reaction of adsorbed SiCl₂ and carbon containing species. It was shown that C₂H₂ adsorbed onto the surface and could take several seconds after interruption of the C₂H₂ flow before all C₂H₂ had reacted or desorbed from the surface. SiH₂Cl₂ cycles lead to the formation of a SiCl₂ layer on the surface. This then reacts with carbon containing species to form a silicon carbide layer.

Allendorf et al [149] used mass spectroscopy to determine the breakdown products of MTS decomposition in helium and hydrogen carrier gas. From a theoretical analysis they predicted that under typical CVD conditions the most likely unimolecular decomposition mechanisms would be:

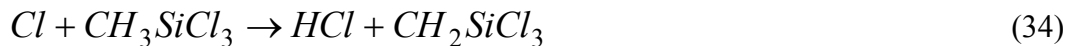
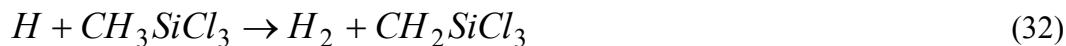


Where M represents a collision partner, such as other MTS or carrier gas molecules, required for the elementary reactions. Reaction 26 was predicted to be faster than reactions (27 and 28 under all conditions. Experimental results led to the conclusion that MTS decomposition proceeds by the initiation-propagation reaction sequence given by reactions 29 to 41.

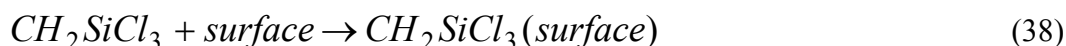
Initiation reaction:



Propagation reactions:



Termination reactions:



Initiation-propagation reactions require lower activation energies than the unimolecular decomposition reaction allowing for reactions to take place at lower temperatures. Rapid adsorption of silicon containing species is consistent with the observation of silicon rich deposits forming at low deposition temperatures. If methane is the principal species involved in depositing carbon it can be expected that carbon deposition will be slow as methane appears to have a low reactivity with silicon carbide surfaces.

Allendorf et al [149] only studied the decomposition of MTS and did not discuss the mechanisms involved in the formation of silicon carbide from the reaction products.

It was however shown that the decomposition of MTS into separate carbon and silicon containing species that can later react to form silicon carbide is feasible and takes place at relatively low temperatures.

Zhang and Hüttinger [150][151] investigated deposition rate as a function of temperature, residence time, and area to volume ratio (A/V) of the reactor. Thermodynamic analysis of the gas phase and condensed phases were carried out using HSC software. It was predicted that significant amounts of free carbon and small amounts of free silicon should be deposited together with the silicon carbide. Analysis of the deposits found only small amounts of free silicon. From this they concluded that deposition of carbon was inhibited while the deposition of free silicon was enhanced. Gas chromatograph analysis of the gas phase showed that CH₄ is the major carbon containing species while silicon is mainly in the form of HSiCl₃ and SiCl₄. Gas chromatograph measurements indicated that MTS concentration drops rapidly with increasing temperature. Above approximately 1000 °C virtually all MTS is decomposed within 0.3 s. Corresponding to the decreasing MTS concentration there is an initial increase in CH₄, SiCl₄ and HSiCl₃ concentration. With increasing temperature the concentration of these species declines. The concentration of HCl increases throughout the temperature range. In these studies it was found that the A/V ratio had minimal impact. Analysis of the deposits revealed that at 1100 °C pure SiC was deposited. This was not influenced by A/V ratio or position within the reactor. At lower temperatures silicon rich deposits were formed with the composition of the deposit being dependent on A/V ratio and position within the reactor. It appears that silicon deposition is strongly favoured at temperatures below 1000 °C, pure silicon carbide being deposited only after the removal by deposition of a portion of the silicon containing species.

Kington et al [152] studied a number of silicon carbide deposition chemistries, including CH₃SiCl₃-H₂, in the Si-C-H₂ and Si-C-Cl₂-H₂ systems, using SOLGASMIX-PV software to calculate the composition of gas and condensed phases. SOLGASMIX-PV calculates the equilibrium composition by calculating the system composition that minimises system free energy. From calculated data they were able to develop phase diagrams for the various chemistries investigated. For the MTS/Hydrogen system at atmospheric pressure it was predicted that pure β-SiC should form under a wide variety of conditions. Pressure was predicted to have only a weak influence – it was found that reducing pressure increased the size of the field in which free carbon was predicted to be deposited. Free carbon was predicted to form only at low hydrogen concentrations. The formation of free silicon was not predicted at all. These researchers were of the opinion that equilibrium calculations should be valid for CVD conditions but do acknowledge that for some processes equilibrium may not be achieved.

Fischman and Petusky [145] used SOLGASMIX-PV to study the Si-C-Cl₂-H₂ system. Calculated condensed phase compositions were plotted as a function of C/Si and H₂/Si ratios at various temperatures. These diagrams predicted the formation of β-SiC with free silicon, pure β-SiC and β-SiC with free carbon under various conditions. Their thermodynamic studies predicted that Si would preferentially form chlorine containing species while carbon would preferentially bond with hydrogen. The most common silicon containing species, SiCl₂, SiH₃Cl, SiCl₃, SiH₂Cl₂ and SiHCl₃, are all polar molecules that would have a sticking coefficient higher than the

non-polar hydrocarbon species such as CH_4 , C_2H_2 . As a result of this, reaction kinetics favours the deposition of silicon rather than carbon at low temperatures. Fischman and Petusky [145] highlighted the importance of reaction kinetics in determining the deposit composition.

Minato and Fukuda [153] performed similar calculations to Kingon but focussed on MTS in either hydrogen, argon or argon/hydrogen mixtures. In their analysis β -SiC could be deposited together with either free carbon or free silicon. In close agreement with Kingon, free carbon was predicted to be formed only at low Hydrogen/MTS ratios but for temperatures ranging from 1000 K to 2200 K. Unlike Kingon they predicted conditions where silicon could be deposited, either together with silicon carbide or alone. Experimental work reported by Minato and Fukuda again highlighted the discrepancy between thermodynamic calculations and experimental results in that mixed SiC/Si and SiC/C deposits are formed under conditions where thermodynamics calculations predict pure SiC.

Hydrogen Chloride formed as a by product has a significant impact on the deposition reactions. Besmann et al [154] investigated the effect of MTS depletion and HCl generated during deposition. Test work was conducted at pressures ranging from atmospheric down to 10 kPa and varying MTS and HCl concentrations in the feed gas. Deposition temperatures were varied between 1310 K and 1497 K. It was found that deposition rates decreased with decreasing pressure down to approximately 10 kPa after which the deposition rate increased rapidly with decreasing pressure. It is thought that this behaviour is due to two deposition mechanisms – direct deposition from MTS and an indirect route. Indirect deposition involves an initial splitting of MTS into silicon and carbon containing species that undergo further reactions to finally form silicon carbide; this appears to be the most important reaction mechanism. At atmospheric pressure (98 kPa) a linear relationship between deposition rate and total gas flow, with constant MTS, ratio was found. Addition of HCl gas to the feed was found to suppress deposition. This effect is much stronger than can be explained by a first order reaction. Possible explanations include an HCl etching effect and a blocking mechanism whereby HCl adsorbs onto the surface and prevents other species from adsorbing onto the surface where they can react.

The effect of HCl was also investigated by Papasouliotis and Sotirchos [92]. Without the addition of HCl they found silicon deposited rapidly at the low temperature regions at the coater inlet. This resulted in deposits containing up to 80% free silicon. With the addition of HCl to the feed gas free silicon deposition was completely suppressed while the deposition rate of SiC was reduced. This resulted in the deposition of pure SiC.

MTS has been used with hydrogen, argon, hydrogen/argon mixtures as well as hydrogen/nitrogen mixtures as the carrier gas. From reaction 22 it would seem that the carrier gas plays no role in the deposition process. Several studies have however shown that the composition of the carrier gas impacts the stoichiometry and morphology of the deposit. For example Minato and Fukuda [153] deposited layers containing pure β -SiC, β -SiC with free silicon and β -SiC with free carbon by changing deposition temperature and carrier gas composition from pure hydrogen to hydrogen/argon mixtures and pure argon. Addition of argon to the carrier gas tended to increase the carbon content of the deposit. This allowed for the deposition of pure

β -SiC at low temperatures when using hydrogen/argon mixtures or for the deposition of carbon rich layers when using pure argon as a carrier gas. This effect was utilized in modified TRISO coatings to deposit sacrificial layers of β -SiC containing 40 % free carbon to prevent palladium attack of the pure silicon carbide [36]. Addition of argon to the carrier gas has also been shown to influence the morphology of the deposit. For example Förthmann et al [44] found that addition of 50 % argon to the fluidizing gas resulting in smaller crystallites. Argon has a significantly higher viscosity than hydrogen; argon additions will therefore impact on the fluidization behaviour of the particles [155].

Addition of hydrocarbons to the feed gas can also be used to increase the C:Si ratio and so prevent the deposition of silicon under conditions that would normally result in the deposition of free silicon. López-Honorato et al [156] investigated the impact of ethyne and propene additions on TRISO coating. They found that with the addition of propene more carbon was deposited whereas addition of ethyne did not have a similar effect. This was attributed to the difference in sticking coefficient of the reaction products of ethyne and propene. Pyrolysis of propene produces ethane, ethyne and methane while pyrolysis of ethyne produces benzene.

6.3 DEPOSIT COMPOSITION

From thermodynamic calculations it would be expected that pure SiC would be formed under conditions typically used for TRISO coating. In practice it is found that either free silicon or free carbon may be deposited with SiC. Researchers using various reactor configurations and substrate types have reported this effect.

Van Kemenade and Stemfoort [157] deposited SiC onto graphite rods at temperatures between 1200 °C to 2000 °C using mixtures of MTS and hydrogen at atmospheric pressure. They found that free silicon was deposited only in small amounts at the lowest temperatures studied. In contrast to this Yeheskel and Dariel [158], using graphite substrates, deposited films with up to 90 % free silicon at 1383 K. At a fixed temperature they also found that the free silicon content of the deposit increased with increasing H/Si ratio of the gas. Papasouliotis and Sotirchos [92] used a thin molybdenum wire mounted parallel to the gas flow to investigate the deposition rate and composition of the deposits as a function of temperature, gas composition and position in the furnace. Their results matched those of Yeheskel and Dariel in that lower temperatures and higher H/Si ratios resulted in increasing silicon content of the deposit. The silicon content of the deposit was highly position dependent with free silicon being deposited preferentially at the cooler regions prior to the furnace isothermal zone. While investigating CVI, Besmann et al [159] deposited SiC onto carbon coated Nicalon (a polycarbosilane derived Si-C-O ceramic) fibres. They found that for an H:MTS ratio of 10:1 free silicon was deposited at temperatures of 913 °C and 957 °C. At higher temperatures, up to 1224 °C, no free silicon was reported.

Using a spouted bed coater Federer [160] found that free silicon was deposited at temperatures below about 1400 °C resulting in a decrease in the density of the

deposit. Gulden [161] reported deposition of free silicon together with SiC at temperatures of 1200 °C. Free silicon resulted in a reduced density of the deposit.

López-Honorato et al [156] used Raman spectroscopy to investigate the composition of the deposit at various temperatures and feed gas compositions. They found that for MTS hydrogen mixtures the deposit was silicon rich when the deposition temperature was below 1500 °C and carbon rich when the deposition temperature was above 1500 °C. Using Raman spectroscopy it was found that amorphous silicon was deposited under a variety of conditions. Crystalline silicon was detected only in samples prepared at 1300 °C with 1.27 % MTS in hydrogen. As can be expected this was also the only sample where any free silicon was detected with XRD analysis. Addition of propene resulted in the elimination of free silicon but when more than 0.5 % was added free carbon was deposited.

6.4 DEPOSITION RATE

Gulden [161] found that for coating TRISO particles in a spouted bed coater the deposition rate, expressed as $\mu\text{m}\cdot\text{minute}^{-1}$, was directly proportional to the MTS flux, expressed as $\text{mol}\cdot\text{cm}^{-2}\cdot\text{minute}^{-1}$. Deposition temperatures between 1400 °C and 1800 °C and carrier gas flow rate was found to have negligible influence on the deposition rate. Also using a spouted bed coating system Federer [160] found a linear relationship between coating rate and MTS flux (in $\text{cm}^3\cdot\text{cm}^{-2}\cdot\text{minute}^{-1}$). It was however noted that where tests were run over a range of temperature there was considerable spread in the measured deposition rate indicating that deposition temperature must play a role in the deposition rate. No relationship between deposition temperature and deposition rate was reported.

For TRISO particle coating Kim et al [162] found a linear relationship between deposition rate and deposition temperature for temperatures between 1400 °C and 1600 °C. Activation energy for this process was found to be 49.8 $\text{kJ}\cdot\text{mol}^{-1}$; this low value indicated that the process was probably under diffusion control.

Minato and Fukuda [153][155] analysed silicon carbide deposition from MTS in a spouted bed coating systems and developed the following relationship to calculate the deposition rate:

$$r = KT^{0.43} {}_bP_{MTS} \sqrt{Q} \quad (42)$$

Where:

- r : Deposition rate
- K : Rate constant
- T : Deposition temperature (K)
- ${}_bP_{MTS}$: Partial pressure of MTS in bulk gas phase (Pa)
- Q : Gas volumetric flow rate ($\text{l}\cdot\text{minute}^{-1}$)

Deposition rate may be expressed in a number of different ways, the units chosen impact the value and units of the rate constant K . The value of the rate constant is a function of the properties of the gas mixture and the particle dimensions. In the case of dilute gas mixture and depositing of thin films these may be considered to be constant.

From equation 42 it can be seen that under conditions of mass transport control the deposition rate is only weakly dependent on temperature and directly proportional to precursor partial pressure.

Kenemade and Stemfoort [157] investigated the deposition of silicon carbide onto resistance heated graphite rods. Up to a maximum temperature (approximately 1600 °C for low MTS flow rates, increasing to 1800 °C for high MTS flow rates), the deposition rate was found to follow Arrhenius behaviour with activation energy of 68 kJ.mol⁻¹. Above the critical temperature deposition rate was found to decrease with increasing temperature. This effect was attributed to etching of silicon in the deposit. This effect may also be due to increasing loss of precursor due to homogeneous formation of solids from the gas phase, these are removed from the system and do not contribute to deposition. Deposition rate was found to increase with increasing MTS flow for all temperatures investigated. Cheng et al [163] found a similar decrease in deposition rate when deposition temperature was increased above 1400 °C. They attributed the decrease in deposition rate to etching of the SiC surface.

The complex relationship between the various processes taking place during deposition were highlighted by a study conducted by Papasouliotis and Sotirchos [92] who studied the deposition of silicon carbide from MTS. Deposition at various positions within an atmospheric pressure coating system was investigated. Deposition rate varied significantly with position in the coater, showing a peak close to the entrance and then a second peak deeper into the furnace. It was also found that under some conditions deposition rate decreased with increasing temperature. This is similar to the findings Kenemade and Stemfoort [157] and Cheng et al [163]. This effect was thought to be due to depletion of reactants and the build up of by products, especially HCl. Addition of HCl to the gas feed was found to reduce the deposition rate and suppress the deposition of free silicon.

Choi and Kim [164] deposited silicon carbide onto graphite substrates using a cold wall coating system. As with Federer [160] and Gulden [161] a linear relationship between deposition rate ($\mu\text{m}\cdot\text{minute}^{-1}$) and MTS flux was found. In this case the gas flow rate was constant and the MTS concentration in the gas flow was varied. Deposition rate was also found to be dependent on temperature. Arrhenius plots indicated a decreasing slope at higher temperature indicating that for this system deposition rate control was changing from activation to diffusion control as the temperature increase from 1100 °C to 1500 °C. Increasing gas flow rates while maintaining a constant MTS concentration in the gas stream also increased deposition rate – this is consistent with the deposition rate being a function of MTS flux.

Using a low pressure CVD coating system Kostjuhin and Sotirchos [147] found a linear relationship between MTS flux and deposition rate. Hydrogen flow rate, and

concentration in hydrogen/helium mixtures, was found to have little influence on deposition rate. Addition of 5% C₂H₄ was found to increase the deposition rate by a factor of 3 without influencing the composition of the deposit. Larger additions of C₂H₄ showed complex behaviour with the deposition rate reaching a maximum before decreasing and then increasing again. With increasing concentration of C₂H₄ the carbon content of the deposit increased.

Kim and Choi [137] determined the activation energy for deposition in a low pressure (1.3 kPa) system using hydrogen and argon as carrier gas. Between 1000 °C and 1300 °C it was found that deposition was activation controlled with activation energy of 121 kJ.mol⁻¹ and 155 kJ.mol⁻¹ for hydrogen and argon respectively.

Besmann et al [159] investigated silicon carbide deposition from MTS for atmospheric pressure CVI application. From Arrhenius plots and the deposit morphology it was concluded that the process was activation controlled with activation energy of 66 kJ.mol⁻¹. It was also found that deposition rate had a first order dependence on MTS concentration.

Using a low pressure deposition system So and Chun [165] found the deposition rate to be dependent on temperature, system pressure and MTS concentration. It was claimed that the process was activation controlled, however activation energy was found to be dependent on deposition pressure and MTS concentration. For a fixed deposition temperature and pressure it was found that deposition rate depended on MTS concentration but not total gas flow rate. Clearly the deposition rate control mechanism of this system is more complex than a simple thermally activated or diffusion limited process.

Sone et al [97] measured deposition rates in a LPCVD system gravimetrically. Their results indicate that a simple stagnant layer model does not adequately describe the deposition rate. A two-site competitive adsorption model (equation 43 to 46) was found to adequately describe the measured deposition rates. In this model it was assumed that carbon containing species adsorb onto silicon sites on the substrate while silicon containing species adsorb onto carbon sites. These species compete with Cl and H for adsorption sites. It was assumed that CH₃ and SiCl₃ were the active carbon and silicon containing species.

Adsorption coverage of the carbon and silicon sites is given by the following equations:

$$\theta_C = \frac{AP_{SiCl_3}}{1 + AP_{SiCl_3} + C\sqrt{P_{HCl}}} \quad (43)$$

$$\theta_{Si} = \frac{BP_{CH_3}}{1 + BP_{CH_3} + C\sqrt{P_{HCl}}} \quad (44)$$

Where:

- θ_C, θ_{Si} : Coverage of carbon and silicon sites
 A, C, D : Temperature dependent constants
 $P_{SiCl_3}, P_{CH_3}, P_{HCl}$: Partial pressure of SiCl₃

Parameters A , B , C and D are temperature dependent exhibiting Arrhenius type behaviour.

The two-site competitive adsorption model describes the reaction rate in terms of a reaction coefficient and the absorption coverage, in this case the coverage of silicon and carbon sites. Using this model the deposition rate can be given by:

$$Rate = A_o e^{(-Q_0/RT)} \theta_C \theta_{Si} \quad (45)$$

Where:

- A_o : Rate constant
- Q_0 : Activation energy (kJ.mol^{-1})
- θ_C : Coverage of carbon site
- θ_{Si} : Coverage of silicon sites

Substituting equations 43 and 44 into equation 45 results in the following equation for growth rate:

$$Rate = A_o \exp(-Q_0/RT) \frac{ABP_{SiCl_3} P_{CH_3}}{(1 + AP_{SiCl_3} + CP_{HCl}^{1/2})(1 + AP_{CH_3} + CP_{HCl}^{1/2})} \quad (46)$$

Using equation 46 and experimentally determined deposition rates Sone et al [97] calculated adsorption coverage for carbon and silicon sites. This indicated that carbon sites have a significantly higher coverage than silicon sites for the temperature and pressure range considered. Increasing temperature resulted in a reduction in coverage while increasing MTS partial pressure increased coverage of carbon sites. In the case of silicon sites temperature and pressure had the opposite effects. From this it is concluded that adsorption of carbon containing species onto silicon sites is the rate limiting step in the deposition of silicon carbide from MTS at high temperatures. This model also explains the reduction in deposition rates with increasing HCl partial pressure.

6.5 DEPOSITION EFFICIENCY

Deposition efficiency may be defined as the ratio of silicon carbide formed on the particles to the amount that could have formed if all the MTS had formed silicon carbide deposited onto the particles. Thermodynamic calculations performed by Fukuda and Minato [153] predicted that under suitable processing conditions SiC deposition efficiencies of at least 95 % are possible. Theoretical efficiency is limited by losses due to the formation of free silicon or carbon as well as losses due to the formation of gaseous silicon and carbon containing species. In practice, losses such as the deposition of silicon carbide onto the coater walls and non-equilibrium conditions will limit the actual deposition efficiency to below theoretical efficiency.

Typical deposition efficiencies obtained using spouted bed coaters are discussed in the following paragraphs.

Gulden [161] found that deposition efficiency was strongly influenced by the mass of particles coated. Using a 1 ½ inch (38.1 mm) diameter coater he found that, at 1400 °C, 10 l.min⁻¹ hydrogen and 2.4 % MTS, deposition efficiency changed from 41 % to 97 % as the load was changed from 10 g to 200 g. For a constant load he found that the deposition efficiency remained constant at about 80 % for temperatures between 1400 °C and 1800 °C and for various hydrogen flow rates and MTS concentrations. This later finding is inconsistent with results reported by other researchers.

Voice and Lamb [50] presented contour plots of deposition efficiency as a function of deposition temperature and MTS concentration without providing actual experimental results. From these plots it can be seen that deposition efficiency increased with increasing temperature and decreasing MTS concentration. The effects of MTS concentration was found to be more pronounced at higher temperatures. From their plots deposition efficiency ranged between approximately 30 % and 75 % for temperatures between 1250 °C and 1550 °C and MTS concentrations up to 2.5 %.

Stinton and Lackey [166] reported deposition efficiencies between 70 % and 86 %. They found that temperature, MTS flux and H₂:MTS ratio all impacted deposition efficiency. Temperatures above 1475 °C resulted in a reduction in efficiency while a single data point at 1405 °C also showed reduced deposition efficiency. Increasing MTS flux and H₂:MTS ratio resulted in an increase in deposition efficiency, however the effect was not as strong as for temperature. Based on a single run using a 240 mm diameter coater they also concluded that efficiency would increase with increasing coater diameter.

Charollais et al [167] reported deposition efficiencies close to thermodynamic predictions using a laboratory scale coater. For a deposition temperatures of 1600 °C they reported deposition efficiencies of 93 %.

6.6 DEPOSIT DENSITY

Several researchers have noted the dependence of deposit density on deposition temperature. At low deposition temperatures density decreases, apparently due to the deposition of free silicon (Density of silicon is 2.32 g.cm⁻³ versus 3.21 g.cm⁻³ for SiC). Deposition temperatures above approximately 1600 °C lead to porosity and so a reduction in density. This effect of density increasing to a maximum and then decreasing as deposition temperature increases has been noted by several researchers including Voice and Lamb [50], Federer [160] and Stinton and Lackey [166]. For temperatures between 1150 °C and 1700 °C Minato and Fukuda [155] noted an initial increase in density up to 1400 °C after which the density remained constant. They also noted the correlation between density and silicon content. When the free silicon content exceeded 40 % they found that the density was lower than predicted,

from this it was assumed that at high free silicon content the deposit also became more porous [168].

As discussed in section 6.3 the composition of the deposit is influenced by deposition parameters such as temperature and MTS concentration. Deposition of any free silicon or carbon as well as the formation of any porosity will result in a reduction in density of the deposit. Deposit density has been identified as one of the key silicon carbide quality parameters. Opinions as the minimum acceptable density vary, Voice and Lamb [50] claimed a minimum density of 3.20 g.cm^{-3} is required. This corresponds to the specification limit for fuel for the HTTR reactor. In the case of the HTR-10 reactor the minimum silicon carbide density is specified as 3.18 g.cm^{-3} .

Voice and Lamb [50] present contour plots of density as a function of deposition temperature and MTS concentration in hydrogen carrier gas. These plots are based on experimental data but the actual results are not presented. Density increased with increasing MTS concentration. In the case of temperature, density initially increased, reached a maximum and then decreased with increasing temperature. The temperature of maximum density was about $1650 \text{ }^\circ\text{C}$ for MTS concentrations below 1 % and decreased with increasing MTS concentration.

Federer [160] found similar correlations between density, MTS concentration and deposition temperature. Acceptable density could only be achieved with H_2 :MTS ratios of greater than 20 (i.e. less than 4.8 % MTS). Density was found to reach a maximum at $1575 \text{ }^\circ\text{C}$. At a temperature of $1575 \text{ }^\circ\text{C}$ and H_2 :MTS ratio of 14 (6.7 % MTS) the density was found to be 3.15 g.cm^{-3} . At H_2 :MTS ratio of 5 (16.7 % MTS) the deposits were found to contain porosity. At lower temperatures density decreased due to the deposition of free silicon while at higher temperatures the deposits became porous. No link between density and deposition rate could be found as long as the temperature and H_2 :MTS ratio was high enough.

6.7 CRYSTAL STRUCTURE AND MORPHOLOGY

TRISO silicon carbide consists predominantly of β -SiC, this has been confirmed by a number of researchers using analytical techniques such as XRD, Raman spectroscopy and electron diffraction techniques. The presence of minor amounts of α -SiC phases have also been reported, however there seems to be uncertainty as to the amounts of α -SiC present. Both Helary et al [169] and De Villiers et al [170] have detected α -SiC in TRISO coating using SAED techniques leaving no doubt as to the presence of α -SiC. However, Helary pointed out this phase was not present in significant quantities. Other researchers claimed to have detected α -SiC using XRD; this would imply significantly more of the phase than the traces claimed by Helary. Some of the XRD diffraction features that have been used as an indication of the presence of α -SiC may be due to the stacking faults within the β -SiC structure [171][172]. Many β -SiC deposits have been shown to have a high density of stacking faults and microtwins (for example see [170] [173]) which may result in an apparent α -SiC content. However, some of the striations commonly seen in β -SiC, and

thought to be microtwins, may in fact be layers of α -SiC as they were resistant to chemical etching that selectively removed adjacent layers of β -SiC [174].

Voice [50] [175] found that the structure of the deposit depended on the deposition temperature and hydrogen:MTS ratio. The outer surface of the deposits had a botryoidal morphology when the deposition temperature was low but became increasingly faceted as the deposition temperature increased above 1600 °C. At high deposition temperature and low hydrogen:MTS ratio the deposit consisted of a mass of small features with many deep grooves and holes. A notable feature of the polished and etched samples was the presence of striations in the deposit, especially in the deposits formed at low temperatures and low hydrogen:MTS ratios. At the highest deposition temperatures and hydrogen:MTS ratios no striations formed and it was found that the deposits were more etch resistant. Stinton and Lackey [166] reported very similar correlations between process conditions and the formation of striations in the deposit.

Reported crystallite size of CVD silicon carbide deposits vary significantly depending on the measurement method used. Using XRD Voice [175] measured crystallite sizes ranging between 25 nm and 1000 nm with the smallest grains forming at the lowest deposition temperatures. Gulden [161] measured grain sizes microscopically. Reported grain sizes were in the range of 1 μm to 15 μm . These grains were found to be elongated, for example 1 μm wide and 5 μm long for a deposition temperature of 1400 °C. Grain size increased with increasing deposition temperature; at 1800 °C grains were found to extend through a 100 μm thick layer. Helary et al [169] measured grain sizes of approximately 1 μm wide and 4 μm to 5 μm long on polished and etched samples. Grains closer to the inner surface tended to be smaller; this was confirmed by EBSD analysis. For different deposition conditions distinct differences in the aspect ratio and grain size were found. Grains closest to the IPyc layer were small and more equiaxed than grains further away from the IPyc. Mokoduwe et al [176] measured grain sizes of approximately 1.2 μm using EBSD and 3.1 μm using a line intercept method. It was noted that the highly faulted structure made use of the line intercept method difficult and that a significant number of grains were in the same size range as the EBSD step size which invalidated a significant number of measurements.

Federer [160] found that deposition at 1375 °C resulted in a striated deposit with no visible grain structure. Grains became discernable at 1475 °C and increased in size as the deposition temperature was increased. It was noted that at deposition temperatures of 1775 °C the deposit was porous. Across the temperature range of 1225 °C to 1775 °C the deposit surface changed from rounded domes to faceted and finally well developed crystals at the highest deposition temperatures. The impact of hydrogen:MTS ratio was investigated by varying the ratio between 5:1 and 45:1 at a fixed deposition temperature of 1575 °C. At low hydrogen:MTS ratios the deposit was porous and had a striated structure as revealed by etching. As the hydrogen:MTS ratio was increased the porosity decreased and the striations gave way to a granular structure. At the same time the surface morphology changed from a rounded, globular, structure to a dense crystalline structure.

Xu et al [177] investigated the effect of deposition temperature on TRISO silicon carbide while using a 1:1 hydrogen:argon mixture as a carrier gas. Below 1550 °C

the deposits had a botryoidal form while at higher temperatures faceted crystals formed. Deposits became rougher as the temperature decreased or increased above 1550 °C. SEM imaging of fracture surfaces revealed that at low deposition temperatures (1450 °C) the deposits contain micro and macro-pores. At a deposition temperature of 1550 °C no porosity was found. Increasing the temperature further resulted in an increasing amount of porosity appearing; by 1650 °C the deposit contained a large number of macro-pores. Grain size tended to increase with increasing deposition temperature. It was also noted that as the deposition temperature was increased the fracture mode changed from predominantly intergranular to predominantly transgranular.

On polished and etched samples Helary et al [169] found a high fault density within the grains. This was consistent with TEM observations. EBSD texture analysis revealed that the grains had a [111] preferred orientation. HRTEM and SAED analysis showed that the deposits were β -SiC with very little α -SiC, a result confirmed by XRD and Raman spectroscopy. In a separate study Helary [178] used EBSD to investigate differences in morphology between silicon carbide coatings deposited under different conditions.. For one of the samples there was a weak [111] orientation whereas for the second sample no preferred orientation was detected. For the sample showing a preferred orientation the orientation effect grew stronger with increasing deposit thickness.

EBSD analysis of TRISO silicon carbide deposited from MTS at 1410 °C in a 1:1 hydrogen:argon mixture indicated that the deposit had a weak [111] preferred orientation. Average grain size for this deposit was 0.8 μm . The grain size distribution was highly skewed with a mode of approximately 0.6 μm and a maximum grain size of approximately 2.6 μm . In agreement with other studies, the grain size increased with deposit thickness. SEM images of the deposit revealed the presence of porosity within the layer as well as penetration of the silicon carbide into the IPyc [179].

Choi and Kim [164] deposited silicon carbide onto graphite using a MTS/hydrogen mixture. At 1500 °C the deposit consisted of large, faceted columnar grains with pyramidal caps. At lower deposition temperatures fine-grained deposits with a smooth surface formed. It was speculated that silicon, codeposited with the silicon carbide at 1400 °C and below, inhibited the growth of silicon carbide crystals resulting in a fine grain structure.

Several researchers have investigated the morphology of SiC deposited using low pressure CVD techniques. For example Chin et al [180] and Chichignoud et al [127] reported on the morphology of SiC deposited from MTS. It was found that deposition temperature, H_2 :MTS ratio and deposition pressure influenced the deposit morphology. Chichignoud et al [127] reported that for high supersaturation the process was under activation control resulting in a smooth [111] textured deposit with low crystalline perfection. Low supersaturation resulted in a highly crystalline faceted deposit with a [220] texture due to the process being diffusion controlled. In contrast Liu et al [181] reported [111] orientated deposits with a rough angular surface. High resolution TEM imaging revealed that initially the SiC deposit was orientated in the [200] direction, being controlled by the orientation of the graphite

substrate. As growth proceeded the orientation changed to [111] direction detected by XRD analysis.

Oh and Choi [182] were able to manipulate the grain structure of silicon carbide deposited at 1250 °C at 1.3 kPa by switching the hydrogen:MTS ratio between 1:1 and 4:1. At low MTS concentrations faceted grains formed while at high concentrations columnar grains formed. By switching between high and low MTS concentrations during a deposition cycle it was possible to create a deposit with alternating layers of columnar and faceted grains. It was also found that the initial deposit consisted of spherical grains. These spherical grains did not appear at the lower part of subsequent layers of columnar grains. This may indicate that they were related to an interaction between the reaction bonded silicon carbide substrate and the deposit.

Kim et al [183] investigated the effects of temperature and MTS depletion in a low pressure (1.3 kPa) horizontal tube coater. Depletion effects were investigated by measuring the deposition rate and deposit characteristics at various positions down the length of the tube, depletion effects increasing down the length of the tube. Mass transport control of the deposition process could be due to either a high deposition temperature or a high level of MTS depletion. Under conditions of activation control the preferred orientation was found to be [111] while for mass transport control the preferred orientation was [220]. It was found that for positions close to the coater inlet (i.e. with little MTS depletion) the preferred orientation changed from [111] to [220] with increasing temperature. In contrast, positions away from the gas inlet, (i.e. with significant MTS depletion) where mass transport control predominated for all temperatures, showed a [111] preferred orientation for all temperatures.

Zhu et al [135] deposited silicon carbide onto graphite disks at 1300 °C at 13 kPa using hydrogen:MTS ratios of 2:1 and 10:1. Deposits formed at low MTS concentrations formed domed deposits. At high MTS concentration the deposit was in the form of a mass of fibres. These fibres tended to have a round cross section without any facets, they were roughly of constant diameter and curved – resembling “soft noodles, bent and curved”. Interestingly where two fibres intersected they tended to continue growing in their original direction.

6.8 MECHANICAL PROPERTIES

Bongartz et al [184], [185] used the brittle ring test to study the effect of process conditions on the strength and Young’s modulus of TRISO deposits. They found that decreasing the deposition temperature from 1700 °C to 1400 °C increased the strength of the silicon carbide by 50 % when hydrogen was used as a carrier gas. A deposition temperature of 1200 °C resulted in silicon carbide strength similar to that deposited at higher temperatures; however the Weibull parameter was low implying a higher probability of failures at low stress. Silicon carbide deposited using pure argon as the carrier gas had low Young’s modulus and strength as well as a low Weibull parameters. This is probably due to the deposit consisting of a mixture of silicon carbide and free carbon. Table 5 contains a summary of their results for tests conducted on full rings; similar results were obtained for semicircular segments.

Table 5. Impact of temperature, carrier gas composition and MTS concentration on the mechanical properties of CVD silicon carbide [185].

DEP. TEMP. (°C)	H ₂ /Ar	MTS (vol %)	YOUNG'S MODULUS (GPa)	MEDIAN STRENGTH (GPa)	WEIBULL MODULUS
1200	1/0	2	326	930	4.7
1400	1/0	2	350	1390	9.4
1500	1/0	1	609	1400	5.4
1500	1/0	2	352	1540	6.8
1500	1/0	4	196	1390	8.1
1600	1/0	2	359	1310	6.7
1650	1/0	1	401	1330	5.9
1650	1/0	2	366	1120	6.0
1700	1/0	2	346	1290	7.8
1400	1/1	2	467	1890	8.1
1500	1/1	2	370	1080	6.3
1600	1/1	2	368	1190	5.2
1700	1/1	2	425	1050	4.8
1400	0/1	2	14	67	3.8
1500	0/1	2	13	130	4.0
1600	0/1	2	1.2	25	4.0
1700	0/1	2	1.9	47	1.6

Xu et al [177] used the brittle ring test to evaluate the impact of deposition temperature on the fracture strength and Young's modulus of TRISO silicon carbide. Maximum fracture strength of 1447 MPa was for material deposited at 1550 °C while maximum Young's modulus of 455 GPa was for material deposited at 1500 °C. Both fracture strength and Young's modulus showed considerable variation. A summary of their results is presented in Table 6.

Table 6. Effect of deposition temperature on strength and Young's modulus of CVD silicon carbide as measured by the brittle ring test. Deposits formed from 1 % MTS in a 1:1 hydrogen/argon mixture in a spouted bed coater. Data from Xu et al [177].

DEPOSITION TEMPERATURE (°C)	STRENGTH		YOUNG'S MODULUS	
	AVERAGE (MPa)	STANDARD DEVIATION (MPa)	AVERAGE (GPa)	STANDARD DEVIATION (GPa)
1450	670	146	392	188
1500	1285	223	455	107
1550	1447	269	422	111
1600	783	153	330	172
1650	693	214	330	118

López-Honorato et al [156] used nano-indentation to measure the hardness and Young's modulus of the deposit as a function of deposition temperature, MTS concentration and concentration of additional propene and ethyne. Their results are given in Table 7.

Table 7. Influence of deposition temperature and gas composition on nano-indentation properties of CVD silicon carbide. Data from López-Honorato et al [156].

TEMPERATURE (°C)	PRECURSOR CONCENTRATION (vol %)			YOUNG'S MODULUS (GPa)	HARDNESS (GPa)
	MTS	C ₃ H ₈	C ₂ H ₂		
1500	0.58	0	0	362	37
1500	0.72	0	0	372	35
1500	1.27	0	0	399	36
1500	9.1	0	0	382	37
1300	1.27	0	0	407	37
1300	9.1	0	0	442	36
1300	9.1	0.1	0	446	42
1300	9.1	0.5	0	448	42
1300	9.1	1	0	406	41
1300	9.1	5	0	155	17
1300	9.1	0	0.5	412	36
1300	9.1	0	1	411	37

A number of researchers have reported crush strength of TRISO particles. In most of these reports particles were crushed between hard anvils, this resulted in fracture being initiated at the contact between the particle and anvil.

7 FLUIDIZATION AND SPOUTED BEDS

7.1 INTRODUCTION

An important aspect of coating TRISO particles is to ensure that the various coating layers are of a consistent and uniform thickness. Various methods may be used to coat powders and particles, amongst these are flat hearths, rotating tubes, fixed beds, moving beds and fluidized beds [186]. Of these, only fluidized beds can provide sufficient uniformity to be suitable. However, fluidization of the relatively coarse (in terms of powders), high density TRISO particles is not an easy task. Geldart developed a scheme for classifying powders according to their fluidization properties. Within Geldart's classification TRISO particles would be classified as a type D powder [187]. For type D powders spouting is difficult, however Geldart notes "it does appear that if gas is admitted only through a centrally positioned hole, group D powders can be made to spout" [187]. Spouting refers to a particular form of gas flow through a bed of particles where a jet of fluid penetrates into the bed of particles. This causes a column, or spout, of particles to rise up with the fluid jet. After being carried up the spout particles move back down towards the base of the spout in the region of the bed surrounding the spout. In this way particles are circulated to the top of the bed in the spout and then back down to the bottom of the bed.

At low fluid velocity the spout will not develop and all the fluid will pass through the fixed bed. At intermediate fluid velocities the spout will be contained within the bed of particles forming a cavity within the bed. Above the cavity the particles will remain essentially static with the fluid flow upwards between the particles. Once the spout is fully developed a jet of fluid will penetrate through the bed and carry particles above the bed to form a fountain. However there will be a portion of the fluid that will flow out of the spout and proceed through the bed.

In the context of coating of TRISO fuel particles the coater is invariably a cylindrical tube with a base tapering towards a central gas injector. Simplistically the base of the tube will be in the form of a cone with an injector at the apex. In practice the tapering section is often not truly conical and the injector arrangements may be considerably more complex than a single injector hole. These spouted beds are operated in the region where spouting results in a fountain of material being lifted above the bed. Material is then circulated back to the injector in an annular descending bed.

Spouted beds are often closely associated with fluidized beds. As such they are often regarded as a special case of fluidized beds. However spouted beds have characteristics that allow them to perform tasks not possible in fluidized beds [188]. Of particular importance in this regard is the cyclical movement of the particles in a spouted bed as opposed to the random movement in a fluidized bed.

Initial development of spouted beds was carried out in Canada starting in 1954. Early work focused on drying operations, particularly of grain and foodstuff. In Canada the

first commercial units were used for drying operations [188]. Later developments extended the use of spouted beds to a wide variety of operations including coal carbonization [188], pyrolysis [188], petroleum processing [188], blending [188], tablet coating [188], CVD coating of TRISO particles with silicon carbide [many] and zirconium carbide [many] and silicon [189]. Spouted beds have also been used with liquid/solid systems.

It should be realised that the way in which a spouted bed is operated impacts on the coating characteristics. For example, Sathiyamoorthy et al [190] showed that for TRISO pyrocarbon coating the deposition rate and deposit density were dependant on bed depth and gas flow rate. Coating uniformity is also influenced by the gas flow conditions.

7.2 DIMENSIONLESS NUMBERS

Dimensionless numbers are often used in the study of fluid flow, fluidization and spouting. Some of these dimensionless numbers are discussed below. In all of these, the number will remain dimensionless so long as a consistent set of units is used.

7.2.1 REYNOLDS NUMBER

The Reynolds number gives the ratio of inertia forces to viscous forces in the flowing fluid:

$$R_e = \frac{LV\rho}{\mu} = \frac{LV}{\nu} \quad (47)$$

Where:

- R_e : Reynolds number (dimensionless)
- L : Characteristic length (m)
- V : Fluid velocity ($\text{m}\cdot\text{s}^{-1}$)
- ρ : Fluid density ($\text{kg}\cdot\text{m}^{-3}$)
- μ : Fluid dynamic viscosity (Pa.s)
- ν : Fluid kinematic viscosity ($\text{m}^2\cdot\text{s}$)

The characteristic length is dependent on the system under analysis, in the case of gas in pipes it is the diameter of the pipe while for spheres it is taken as the sphere's diameter. The choice of characteristic dimension is more convention than an underlying physical reasoning. Sometimes alternative dimensions are used; this will impact the numerical value of Reynolds number.

Fluid flow may be classified as being turbulent or laminar depending on the velocity, fluid properties and dimensions of the channel or object. At a sufficiently low velocity the flow will initially be laminar but will then transition to turbulent flow as the velocity increases. In reality the transition from laminar to turbulent flow is not

sudden, there being a transition region between laminar and turbulent flow. Critical Reynolds numbers for the laminar/turbulent transition have been identified for a number of situations.

It is common to define a critical Reynolds number below which flow will be laminar. This is more accurate than defining a number above which flow will become turbulent as laminar flow may be maintained at relatively high Reynolds numbers under controlled conditions. In the case of gas flowing in pipes the critical Reynolds number is 2000 [191].

7.2.2 ARCHIMEDES NUMBER

The ratio of gravitational forces to viscous forces gives the Archimedes number:

$$Ar = \frac{\rho_f (\rho_s - \rho_f) D^3 g}{\mu^2} \quad (48)$$

Where:

- ρ_f : fluid density ($\text{kg}\cdot\text{m}^{-3}$)
- ρ_s : particle density ($\text{kg}\cdot\text{m}^{-3}$)
- μ : fluid viscosity (Pa.s)
- D : particle diameter (m)
- g : gravitational acceleration ($\text{m}\cdot\text{s}^{-2}$)
- μ : dynamic viscosity (Pa.s)

7.3 HAGEN-POISEUILLE EQUATION

Pressure loss in pipes, under conditions of laminar flow, may be calculated using the Hagen–Poiseuille equation:

$$\Delta P = \frac{128\mu L Q}{\pi D^4} \quad (49)$$

Where:

- ΔP : pressure loss (Pa)
- μ : dynamic viscosity (Pa.s)
- L : length of pipe (m)
- Q : volume flow rate ($\text{m}^3\cdot\text{s}^{-1}$)
- D : pipe diameter (m)

This equation is valid for Reynolds numbers up to approximately 2000 [192]. Above this value the flow will start to become more turbulent.

7.4 DARCY-WEISBACH EQUATION

For situations where the flow is turbulent, i.e. $Re > 2000$, the pressure drop in a pipe can be calculated using the Darcy-Weisbach equation:

$$\Delta P = \frac{f\rho LV^2}{2D} \quad (50)$$

Where:

- ΔP : pressure loss (Pa)
- f : friction factor (Dimensionless)
- ρ : fluid density ($\text{kg}\cdot\text{m}^{-3}$)
- L : length of pipe (m)
- V : fluid velocity ($\text{m}\cdot\text{s}^{-1}$)
- D : pipe diameter (m)

7.5 FRICTION FACTOR

It has been found that the friction factor is a function of Reynolds number and the relative roughness of the pipe:

$$f = f(Re, \varepsilon / D) \quad (51)$$

Where:

- f : friction factor (Dimensionless)
- Re : Reynolds number (Dimensionless)
- ε : pipe roughness (same units as D)
- D : pipe diameter (same units as ε)

Researchers have developed equations for calculating values for friction factors for various flow conditions. Friction factor values, as a function of Reynolds number and relative roughness, have been compiled into the so called Moody diagrams.

For laminar flow, with Reynolds numbers below 2000, the friction factor may be calculated as:

$$f = \frac{64}{Re} \quad (52)$$

Where:

- f : friction factor (Dimensionless)
- Re : Reynolds number (Dimensionless) (<2000)

Substituting equation 52 into the Darcy–Weisbach equation, equation 50, results in the Hagen-Poiseuille equation, 49.

7.6 TERMINAL VELOCITY

Objects falling through a fluid will experience three forces: gravitational acceleration, buoyancy and drag. Both the gravitational acceleration and buoyancy forces are independent of the objects velocity. Drag forces are velocity dependent tending to increase as velocity increases. As a result of this, free falling objects will initially increase in speed and then asymptotically approach a maximum velocity where the gravitational forces are balanced by the buoyancy and drag forces. This is the objects terminal velocity.

In situations where the fluid is flowing upwards three situations may arise:

1. Fluid velocity < terminal velocity: in this situation the object will still fall downwards but at a reduced velocity. The maximum relative velocity between the gas flow and the particle will remain the terminal velocity of the particle.
2. Fluid velocity = terminal velocity: the object will remain stationary in the fluid stream
3. Fluid velocity > terminal velocity: the object will be accelerated upwards. The maximum relative velocity between the gas flow and the particle will remain the terminal velocity of the particle.

Drag forces acting on a body in a fluid stream may be calculated from:

$$F_D = C_D \rho A \frac{V^2}{2} \quad (53)$$

Where:

F_D : Drag force (N)

C_D : Drag coefficient (Dimensionless)

ρ : Fluid density (kg.m^{-3})

A : Bodies cross sectional area perpendicular to fluid flow (m^2)

V : Object velocity (m.s^{-1})

Drag coefficient is dependent on the shape and surface characteristics of the object as well as the Reynolds number. Depending on the Reynolds number various approximations may be used to estimate the drag coefficient [193]:

$$R_e < 1 \quad C_D = \frac{24}{R_e} \quad (54)$$

$$2 < R_e < 500 \quad C_D = 18.5 R_e^{-0.6} \quad (55)$$

$$500 < R_e < 250\,000 \quad C_D = 0.44 \quad (56)$$

Various maximum values of Reynolds number for equation 54 to valid have been reported in the literature. These range between 0.1 and 2 [193] [194]. Using

equation 54 to calculate the drag force, equation 53 simplifies to Stokes law, equation 57.

$$F_D = 3\pi\mu VD \quad (57)$$

Where:

- F_D : Drag force (N)
 μ : Dynamic viscosity (Pa.s)
 V : Object velocity through fluid (m.s⁻¹)
 D : Particle diameter (m)

Equations 54 to 56 are simplifications. Many more accurate models have been developed for calculating the value of C_D . These however tend to be more complex than the relationships given above. A common problem with many of these relationships is that they do not allow for a direct calculation of terminal velocity as the drag coefficient is expressed as a complex function of Reynolds number, itself a function of velocity. Turton and Clark [195] developed an explicit relationship for the terminal velocity of spherical particles in terms of dimensionless velocity, V_* , and dimensionless particle diameter, D_* :

$$V_* = \left[\left(\frac{18}{D_*^2} \right)^{0.824} + \left(\frac{0.321}{D_*} \right)^{0.412} \right]^{-1.214} \quad (58)$$

With:

$$V_* = V_t \left[\frac{\rho_f^2}{g\mu(\rho_s - \rho_f)} \right]^{1/3} \quad (59)$$

$$D_* = d \left[\frac{g\rho_f(\rho_s - \rho_f)}{\mu^2} \right]^{1/3} \quad (60)$$

Where:

- V_* : Dimensionless velocity
 D_* : Dimensionless diameter
 V_t : Terminal velocity (m.s⁻¹)
 ρ_f : Fluid density (kg.m⁻³)
 ρ_s : Particle density (kg.m⁻³)
 μ : Fluid viscosity (Pa.s)
 d : Particle diameter (m)
 g : Gravitational acceleration (m.s⁻²)

It should be noted that the above models are for a single particle uninfluenced by flow disturbances such as pipe walls and other particles. Richardson and Zaki (referenced in [196]) developed a model to describe the terminal velocity of a “cloud” of particles as would be found in sedimentation and fluidization. Actual terminal velocity may be calculated from equation 61.

$$V = V_t \varepsilon^n \quad (61)$$

Where:

V : Terminal velocity of constrained particles (ms^{-1})

V_t : Terminal velocity of free particles (ms^{-1})

ε : Voidage in cloud of particles

n : Richardson-Zaki exponent

The Richardson-Zaki exponent is dependent on Reynolds number. For a low Reynolds number ($R_e < 0.2$) n has a constant value of approximately 4.65, decreasing to about 2.3 as the Reynolds number exceeds 500.

Rowe [196] developed the following empirical equation for calculating the Richardson-Zaki exponent as a function of Reynolds number:

$$n = \frac{2.35(2 + 0.175R_e^{0.75})}{(1 + 0.175R_e^{0.75})} \quad (62)$$

7.7 FLOW THROUGH A BED OF PARTICLES

Fluidization of a bed of particles will take place once the fluid velocity reaches a critical value, V_{mf} . At lower velocities the bed will behave as a packed bed with gas flowing through the voids between the static particles. Fluid flowing through the bed will experience a pressure drop, the magnitude of which depends on the properties of the fluid, the particles and the flow rate of the fluid through the bed. Ergun (referenced in [192],[193]) developed a commonly used model for the pressure drop across a packed bed:

$$\frac{\Delta P}{L} = 150 \frac{(1 - \varepsilon)^2}{\varepsilon^3} \frac{\mu}{\varphi_p^2 d_p^2} V + 1.75 \frac{\rho_f}{\varphi_p d_p} \frac{(1 - \varepsilon)}{\varepsilon^3} V^2 \quad (63)$$

Where:

- ε : Voidage fraction (Dimensionless)
- μ : Fluid dynamic viscosity (Pa.s)
- φ_p : Particle sphericity, or shape factor
- d_p : Particle equivalent diameter (m)
- V : Superficial gas velocity (m.s⁻¹)
- ρ_f : Fluid density (kg.m⁻³)

Particle sphericity is defined as the ratio of the surface area of the particle to the surface area of a sphere with the same volume. Particle equivalent diameter is defined as 6× volume/area ratio of the particle. For spherical particles the sphericity, φ_p , is 1 while the equivalent diameter equals the particle diameter, D.

Various values of the numeric constants in equation 63 have been used; ranging between 150 and 200 for the left term and 1.75 and 4.0 for the right term [192].

Using values for spherical particles and rearranging equation 63 gives the following relationship:

$$\frac{\Delta P}{\rho_f V^2} \frac{D}{L} \frac{\varepsilon^3}{(1 - \varepsilon)} = \frac{150}{\text{Re}_p} + 1.75 \quad (64)$$

Where:

- ΔP : Pressure loss (Pa)
- ρ_f : Fluid density (kg.m⁻³)
- V : Superficial gas velocity (m.s⁻¹)
- D : Particle diameter (m)
- L : Bed length (m)
- ε : Voidage fraction (Dimensionless)
- Re_p : modified Reynolds number $\left(\frac{1}{(1 - \varepsilon)} \frac{DV\rho}{\mu} \right)$ (Dimensionless)

Equation 63 is applicable to a wide range of Reynolds numbers. For limited ranges of Reynolds number simplifications, such as the Kozeny-Carman and Burke-Plummer equations, may be used.

7.8 FLUIDIZATION

7.8.1 TYPES OF FLUIDIZATION

1. Particulate fluidization: particles are suspended in the fluid flow as discrete particles separated from each other. This situation often arises when liquids are used as the fluidizing medium. It may also be found in gas/solid systems with suitable particle properties and low fluidization velocities.
2. Aggregative fluidization: low density bubbles form in the bed of particles. These bubbles then rise to the surface of the fluidized bed. Depending on the properties of the particle being fluidized the bubbles may reach a maximum size or keep growing and coalescing as they rise through the bed.
3. Slugging: bubble size approaches the size of the area of the bed, this results in a layer of particles being lifted. This phenomenon tends to occur in beds with small cross sectional areas.
4. Channelling: gas flows through specific channels in the bed with little gas flowing through the rest of the bed. This results in a highly non uniform fluid flow through the bed.
5. Spouting: large, high density particles will not fluidize easily. These particles tend to form a spout above the gas injector where a stream, or spout, of particles is lifted up by the gas flow. After being carried upwards by the gas stream the particles flow downwards in the bed surrounding the spout. When the gas velocity is high enough the spout may reach the surface of the particle bed to form a fountain of particles above the bed.
6. Jet spouting: increasing the gas velocity during spouting will eventually lead to instability of the spouted bed. At sufficiently high gas velocities the distinction between the spout and annular zones disappears. This marks the onset of jet spouting. Characteristics of jet spouting include high gas velocity, high bed voidage of over 0.75 and cyclic movement of particles [197].
7. Pneumatic transport: gas velocity exceeds the terminal velocity of the particles resulting in the particles being carried away by the gas stream. In a circulating fluidized bed these particles are separated from the gas stream and returned to the bed.

In the context of TRISO particle coating, the main fluidization regime of interest is spouting. The combination of particle size and density of the TRISO particle results in this being the only form of fluidization that is applicable.

7.8.2 GELDART'S PARTICLE CLASSIFICATION

Geldart [187] developed a classification scheme in which powders were divided into 4 groups depending on their fluidization properties. Characteristics of these groups are described in Table 8.

Table 8. Geldart's classification of the fluidization characteristics of particles [187].

TYPE	SIZE (μm)	RELATIVE DENSITY	FLUIDIZATION PROPERTIES
A	Small	Low ≤ 1.4	1. Bed expands considerably before bubbling starts 2. Bed collapses slowly when gas supply is cut 3. Gross circulation of powders occurs 4. Bubbles rise faster than interstitial gas velocity 5. A maximum bubble size exists 6. Considerable back mixing of the gas occurs 7. Fast gas exchange between dens phase and bubbles
B	40 to 500	1.4 to 4.0	1. Bubble form at gas velocity close to minimum fluidization velocity 2. Bed expansion is low 3. Bed collapses rapidly 4. Little powder circulation in the absence of bubbles
C			1. Cohesive particles 2. Fluidization difficult. Slugging, channelling common 3. Poor particle mixing
D	Large	High	1. Bubbles rise more slowly than interstitial velocity 2. Gas velocity in the dens phase is high 3. Poor solids mixing 4. Little back mixing of gas in the dens phase 5. Flow past particle may be turbulent 6. Can be made to spout

Geldart proposed the following boundaries between groups:

$$\text{Group A – Group B boundary: } (\rho_s - \rho_f)D \leq 225 \quad (65)$$

$$\text{Group B – Group D boundary: } (\rho_s - \rho_f)D^2 \geq 10^6 \quad (66)$$

Where:

ρ_s : density of particle (g.cm^{-3})

ρ_f : density of fluid (g.cm^{-3})

D : particle diameter (μm)

Note that the units in the above correlations are inconsistent. The criteria listed in equations 65 and 66 are specifically for air at room temperature and atmospheric pressure.

Geldart did not propose any numerical criteria for separating group A and C powders but did indicate the boundary, together with the A-B and B-D boundaries on a plot of particle fluidization characteristics as a function of particle size (μm) and density difference (g.cm^{-3}). Geldart's classification of particles is shown in Figure 16. The position of TRISO particles during coating are also shown, changes in position on the plot are purely as a result of changes in particle diameter and density.

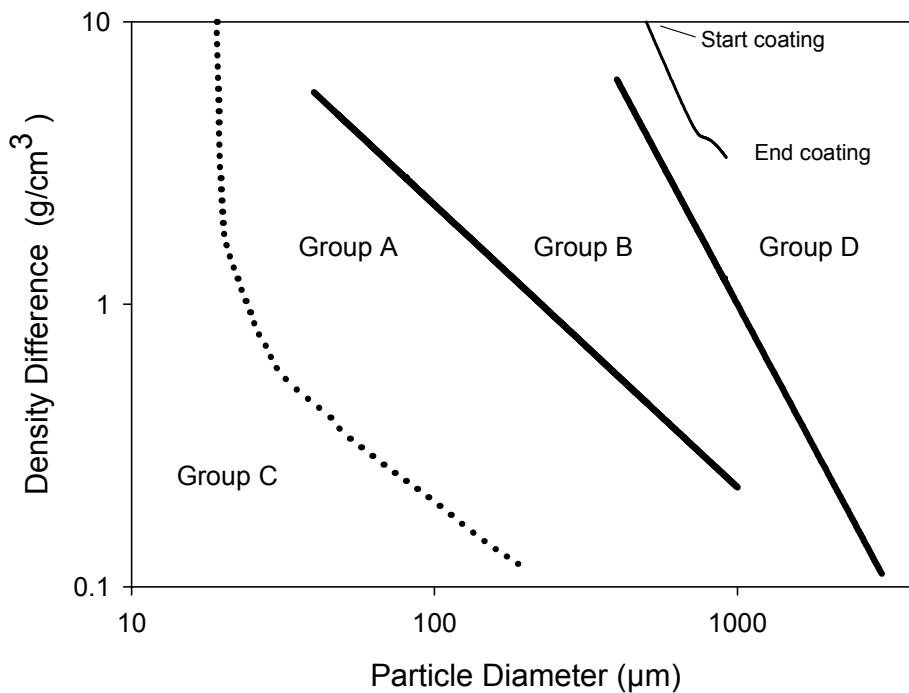


Figure 16. Geldart's classification of particles. Coating of TRISO particles results in a change in density and diameter causing a shift in position as coating progresses. On a Geldart plot TRISO particles would follow the line marked "Start coating" to "End coating". Modified from [187].

Goossens [198] proposed criteria based on Archimedes number for distinguishing between the various Geldart groups. In this scheme group D powders are defined as having an Archimedes number of greater than 176900. Other B-D boundaries defined in terms of Archimedes number alone are those of Chen and Pei ($Ar = 20\,000$); Baeyens and Geldart ($Ar = 100\,000$) (referenced in [199]). These boundaries all suffer from the drawback of being limited in terms of temperature and pressure range [200].

Grace [199] proposed boundaries between groups A/B and B/D that allowed for particles to be classified for gases other than atmospheric pressure air at room temperature. These boundaries are given by equations 67 and 68:

$$Ar_{AB} = 1.03 \times 10^{-6} \left(\frac{\Delta\rho}{\rho} \right)^{-1.275} \quad (67)$$

$$Ar_{BD} = 1.45 \times 10^5 \quad (68)$$

Where:

- Ar_{AB}, Ar_{BD} : Archimedes number for the A/B and B/D boundary
- $\Delta\rho$: Density difference between gas and solid phase (kg.m^{-3})
- ρ : Gas phase density (kg.m^{-3})

Conditions typically found in a number of industrial fluidized bed types are shown in Figure 17. Reactor bed type and particle behaviour are plotted against dimensionless superficial gas velocity and dimensionless particle diameter. These dimensionless numbers are defined as:

$$V^* = V \left(\frac{\rho^2}{\mu g \Delta \rho} \right)^{\frac{1}{3}} \quad (69)$$

$$D^* = D \left(\frac{\rho g \Delta \rho}{\mu^2} \right)^{\frac{1}{3}} \quad (70)$$

Where:

- V^* : Dimensionless velocity
- V : Superficial velocity (ms^{-1})
- ρ : Gas phase density (kg.m^{-3})
- $\Delta \rho$: Density difference between gas and solid phase (kg.m^{-3})
- μ : Gas viscosity (Pa.s)

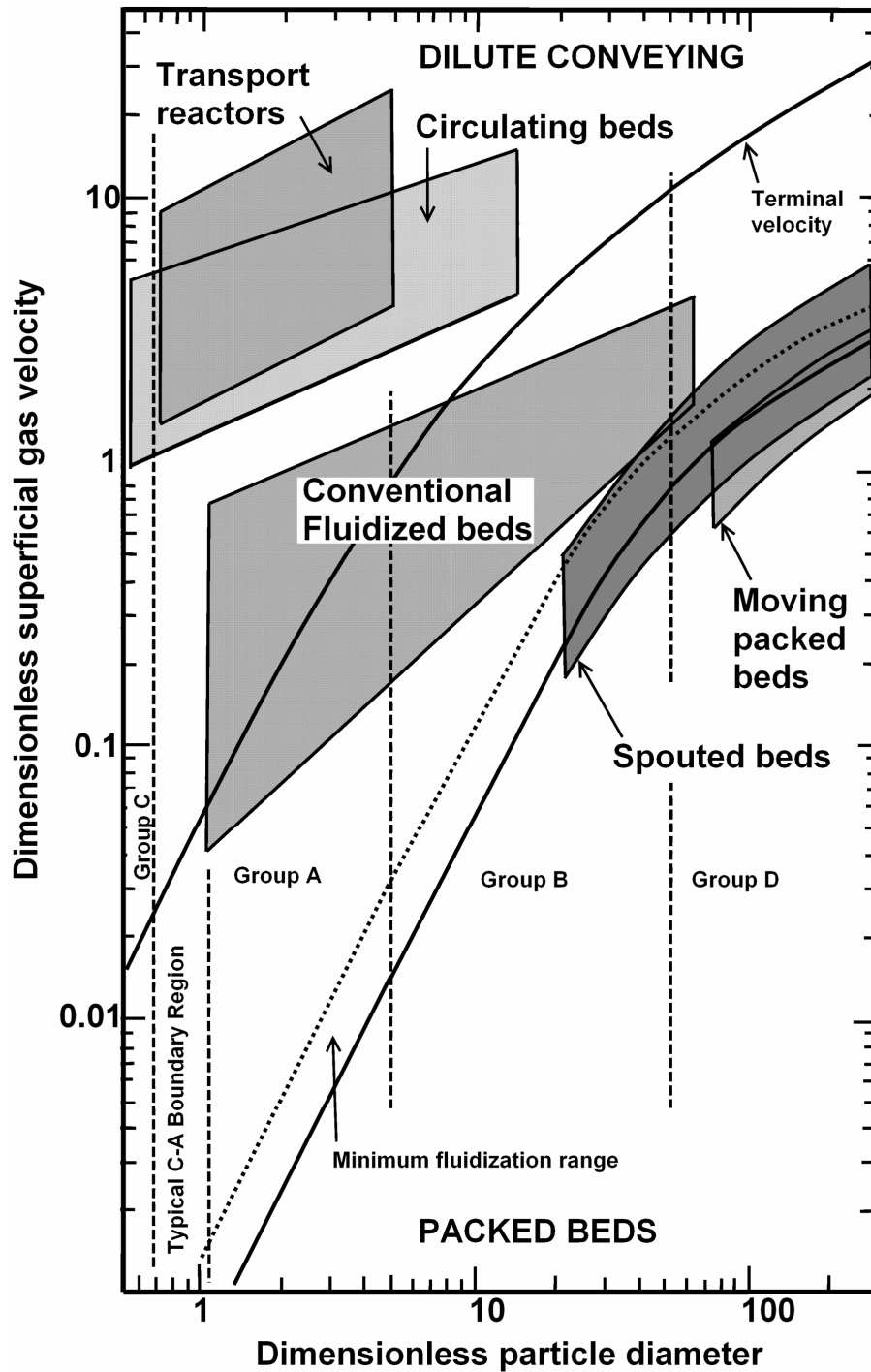


Figure 17. Typical operating conditions for industrial fluidized beds. Modified from Grace [199].

From Figure 17 it can be seen that there is considerable overlap between the various operating modes of fluidized beds. Of particular interest is the operating region of spouted beds which operate predominantly with type D particle but also with larger diameter type B particles. Similarly, operation of conventional fluidized beds can be extended into the lower end of the type D classification.

Yang [200] analyzed fluidization results in terms of a dimensionless density $((\rho_p - \rho_f)/\rho_f)$ and Archimedes number. He proposed a correlation for the type A/B boundary but not for the B/D boundary. Yang did however comment that by plotting Geldart's data on the dimensionless density/Archimedes number plots it is possible to extrapolate Geldart's original B/D boundary. Analysis in terms of dimensionless density/Archimedes number allows for the explanation of shifts in powder behaviour at high pressures and temperatures. When analyzed in terms of dimensionless density and Archimedes number TRISO particles are found to fall within the group B region under conditions typically encountered during coating. This would mean that bubbling fluidization is possible during coating.

TRISO particles with a urania kernel will always fall within the Group D region of a Geldart plot. When plotted using Yang's classification the TRISO particles are classified as type B for all steps except during silicon carbide deposition. Unlike the Geldart plot, which only shows differences in diameter and density, the Yang plot shows the effect of changing gas properties as well as particle properties.

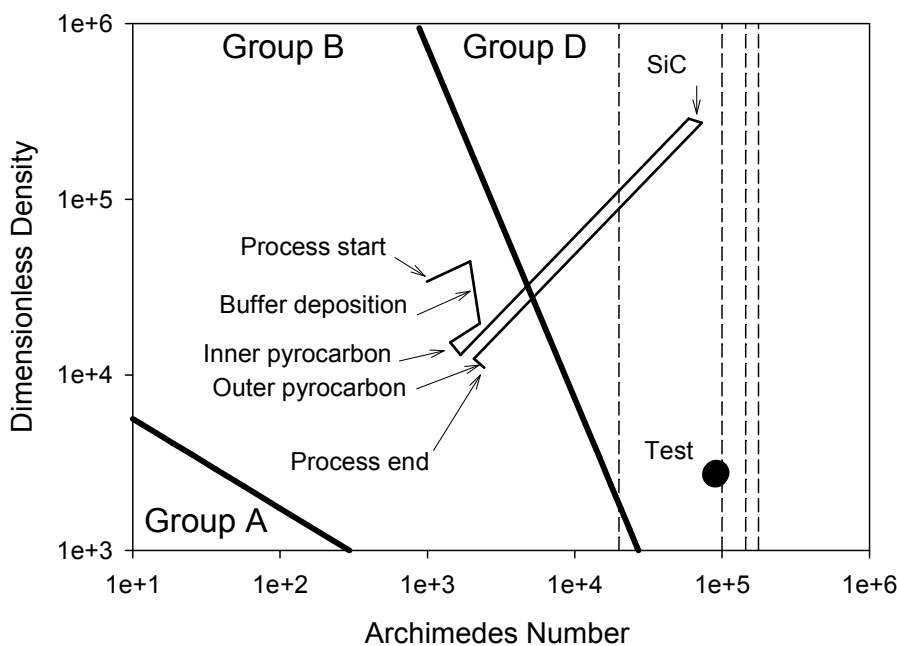


Figure 18. Geldart plot as modified by Yang. The position of TRISO particles during the coating process follows the line “Process start” to “Process end”. Room temperature fluidization of carbon coated zirconia particles in argon is marked by the point marked “Test”. Vertical dashed lines indicate alternative B-D boundaries as proposed by Chen ($Ar = 20\ 000$), Baeyens ($Ar = 100\ 000$), Grace ($Ar = 145\ 000$) and Goosens ($Ar = 176\ 900$).

7.8.3 MINIMUM FLUIDIZATION VELOCITY

Low flow rates of fluid through a bed of particles will not result in fluidization. At the onset of fluidization the net weight of the bed of particles must be balanced by the pressure drop across the bed. Assuming a bed of particles with a constant cross sectional area, A , the net weight of the bed is:

$$\frac{\Delta P}{L} = (1 - \varepsilon_{mf})(\rho_p - \rho_f)g \quad (71)$$

Where:

- ε_{mf} : bed voidage at minimum fluidization
- ρ_p : particle density (kg.m^{-3})
- ρ_f : fluid density (kg.m^{-3})
- L : bed length (m)
- G : gravitational acceleration (m.s^{-2})

From equations 63 and 71 the minimum velocity required for fluidization can be calculated. Wen and Yu (referenced in [192]) expressed the minimum fluidization equation in the form:

$$\text{Re}_{mf} = \sqrt{\left(\frac{k_2}{2k_1}\right)^2 + \frac{Ar}{k_1}} + \left(\frac{k_2}{2k_1}\right) \quad (72)$$

Where:

- Re_{mf} : Reynolds number for minimum fluidization
- Ar : Archimedes number

$$k_1 = \frac{1.75}{\varepsilon_{mf}^3 \varphi}$$

$$k_2 = \frac{150(1 - \varepsilon_{mf})}{\varepsilon_{mf}^3 \varphi^2}$$

Values for k_1 and k_2 in equation 72 have been determined empirically by a number of authors. Typical values for $1/k_1$ range between 0.0365 and 0.0651. For $k_2/2k_1$ values of between 27.2 and 36.8 have been reported [201]. Wen and Yu (referenced in [192]) used values of 0.0408 and 33.7 respectively to give:

$$Re_{mf} = \sqrt{33.7^2 + 0.0408Ar} - 33.7 \quad (73)$$

Where:

Re_{mf} : Reynolds number at minimum spouting velocity

Ar : Archimedes number

Several researchers besides Wen and Yu have also developed correlations for predicting minimum fluidization velocity. Sangeetha et al [202] proposed the correlations in equations 74, 75 and 76 for Geldart A, B and D type powders using high temperature (approximately 300 °C to 950 °C) air as the fluidizing gas.

Type A:
$$Re_{mf} = \sqrt{60.407^2 + 0.1536Ar} - 60.407 \quad (74)$$

Type B:
$$Re_{mf} = \sqrt{15.898^2 + 0.0201Ar} - 15.858 \quad (75)$$

Type D:
$$Re_{mf} = \sqrt{17.612^2 + 0.02613Ar} - 17.612 \quad (76)$$

Correlations 74, 75 and 76 have lower errors than the Wen and Yu and other correlations evaluated under the test conditions used by Sangeetha et al [202].

7.9 SPOUTING

7.9.1 MINIMUM SPOUTING VELOCITY

Many correlations between the minimum spouting velocity and particle and reactor have been developed. Mathur and Epstein [188] tabulated a number of these. Most of these empirical models are however applicable to large, low density particles (for example grain and seeds). Also, most of these empirical models are applicable to relatively deep particle beds. Zhou et al [203] developed the following correlation specifically for TRISO type particles in typical coating reactors:

$$Re_{ms} = 0.0015 Ar^{0.86} \left(\frac{H_0}{D_c}\right)^{1.59} \tan\left(\frac{\gamma}{2}\right)^{0.87} \quad (77)$$

Where:

- Re_{ms} : Reynolds number at minimum spouting velocity
- Ar : Archimedes number
- H_0 : Static bed depth (m)
- D_c : Tube diameter (m)
- γ : cone angle (radian)

This correlation was found to have a significantly better fit to typical TRISO data than correlations developed for other types of particles. Errors were estimated to be between 8 % and 13 % while errors for the best of the published correlations ranged between 12 % and 60 %.

7.9.2 Pressure drop

Prior to the onset of fluidization the pressure drop across a bed of particles will increase linearly with increasing flow as given by the Ergun, Kezény-Carman or Burke-Plummer equations. As flow through the packed bed increases there will be a decrease in pressure at the onset of spouting, at this flow the pressure drop across the bed will be at a maximum. Further increases in flow rate will result in a constant pressure drop or a pressure drop largely governed by the flow resistance of the gas distribution system as given by the Hagen–Poiseuille and Darcy-Weisbach equations. When flow through a spouting bed is reduced the pressure drop will decrease linearly, until the flow drops to the minimum spouting velocity. The minimum flow rate required to maintain spouting will be lower than the flow rate required to initiate spouting as flow rate was increased. As the flow rate is reduced below the minimum required for spouting, the pressure drop across the bed will suddenly increase to that expected of a loosely packed bed. A further reduction in the flow rate will result in a decreasing pressure drop as calculated by the Ergun equation 63.

Zhou et al [203] suggest the following empirical relationship for the pressure drop across a 50 mm diameter bed of 500 μm zirconia particles while spouting:

$$\frac{\Delta P}{\rho_b H_0 g} = \left[56.38 \left(\frac{V}{V_{ms}} \right)^3 - 179.6 \left(\frac{V}{V_{ms}} \right) + 110.01 \left(\frac{V}{V_{ms}} \right) - 74.35 \right] \times \left[\left(\tan \frac{\gamma}{2} \right)^{-0.235 + 0.454 \left(\frac{V}{V_{ms}} \right)} \left(\frac{H_0}{D_c} \right)^{-0.081 + 0.378 \left(\frac{V}{V_{ms}} \right)} \left(\frac{D_p}{D_c} \right)^{-0.304 - 0.516 \left(\frac{V}{V_{ms}} \right)} \right] \quad (78)$$

Where:

- ΔP : Pressure drop across bed (Pa)
- ρ_b : Particle bed bulk density (kg.m^{-3})
- H_0 : Static bed depth (m)
- g : Gravitational acceleration (m.s^{-2})
- V : Gas velocity (m.s^{-1})
- V_{ms} : Minimum spouting velocity (m.s^{-1})
- γ : Cone angle of tube base (Degrees)
- D_c : Tube diameter (m)
- D_p : Particle diameter (mm)

This correlation, together with that given in equation 77, was established in a set up used to investigate spouting properties of surrogate TRISO particles.

7.9.3 Gas and particle flow patterns

During spouting most gas flows up through the spout. However, some of the gas flows outward from the spout into the bed of descending particles surrounding the spout. With increasing distance from the gas injector a greater portion of the gas has left the spout and flows through the particle bed. As a result, gas velocity in the spout reduces while the gas velocity in the descending bed increases with increasing height above the injector.

Gas flowing through the bed of descending particles surrounding the spout may reach a velocity high enough to cause the fluidization of the top of the bed; this limits the maximum bed depth for spouting. San Jose et al [204] modelled gas flow and measured gas velocities in conical spouted beds. Their model assumed plug flow in the spout and concentric zones of constant descending particle flow in the annulus. Measured gas velocity across the spout was constant indicating plug flow within the spout. Velocity within the spout decreased with increasing height above the gas inlet. Typical measured gas flow patterns for a conical spouted bed are shown in Figure 19. A major portion of the gas will flow through the spout; however, significant volumes of gas will flow upwards through the descending annulus.

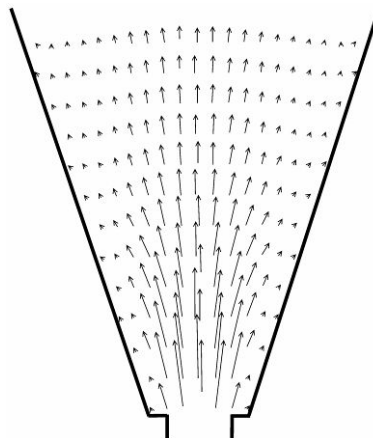


Figure 19. Typical gas flow patterns measured in a conical spouted bed. Diagram from San José et al [204].

Particle velocity patterns typically found in the annulus, spout and fountain of a spouted bed are presented in Figure 20 [205]. Particles enter the spout along the length of the spout; however, the majority of particles will enter the spout at the lower portion of the particle bed. Simulation and measurement of particle movements have shown that particles will tend to follow flow lines and circulate within zones as shown in Figure 21 [206]. Particles following the shorter routes on the inner portion of the bed will circulate faster than particles circulating around the outside of the bed. This will result in a non-uniform residence time for the particles in various parts of the bed. To ensure uniform circulation of the particles it is important that the fountain spread particles randomly across the whole surface of the annulus. The form of the fountain and spout depend on the geometry and operating conditions of the spouted bed [207], [208].

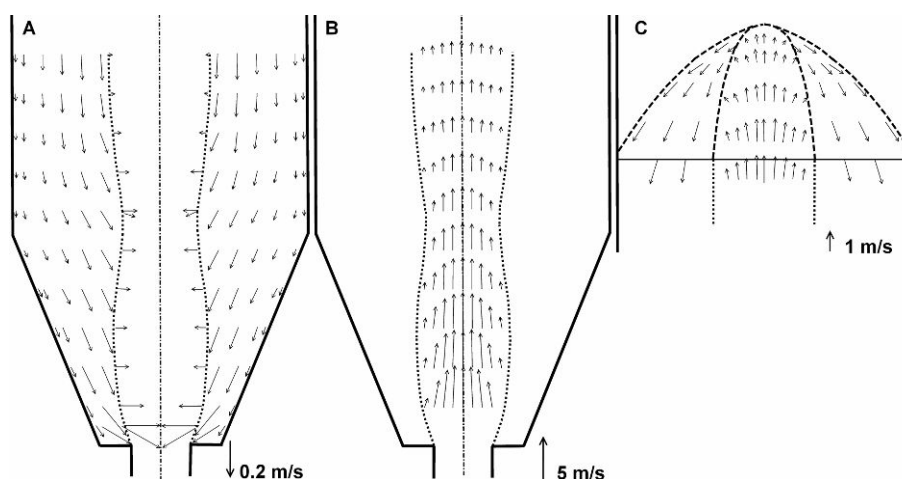


Figure 20. Typical measured particle velocity in a spouted bed. Velocity measured in (A) annulus, (B) spout and (C) fountain. Note the differences in velocity scale between the diagrams. Olazar et al [205].

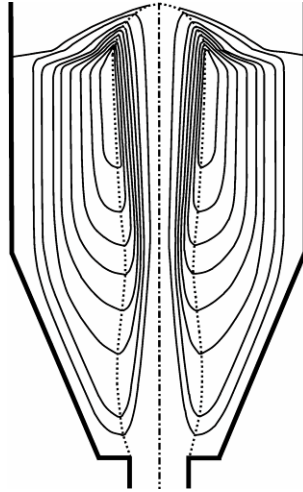


Figure 21. Particle flow patterns within a spouted bed. Particles tend to circulate along flow lines within the bed resulting in a wide range of cycle times. Olazar et al [205].

Data presented in Figure 20 and Figure 21 was measured on beds 0.152 m diameter, particle diameter of 0.004 m and a cone angle of 45 °. Very similar results were obtained by Voice and Lamb [50] using a thin rectangular model design to investigate fluidization of TRISO particles in a spouted bed coater.

San José et al [206] derived the following relationship for estimating cycle times of spouted beds with an included angle of greater than 45 ° :

$$t_c = 1.51 \left(\frac{D_p}{D_c} \right)^{-0.68} \left(\frac{D_o}{D_c} \right)^{1.07} \left(\frac{V}{V_{ms}} \right)^{-1.14} \left(\frac{H}{D_c} \right)^{0.56} \gamma^{0.91} \quad (79)$$

Where:

- t_c : Average cycle time (s)
- D_p : Diameter of particles (m)
- D_c : Diameter of the column (m)
- D_o : Diameter of the gas inlet (m)
- V : Gas velocity (ms^{-1})
- V_{ms} : Minimum spouting velocity (ms^{-1})
- H : Static bed height (m)
- γ : Included angle of the conical section (°)

Note: the exponents 1.07 and 0.56 in equation 79 are corrected values of the exponents listed in the original paper. The error in the published values was confirmed by Prof. San José [Private communication: 3 May 2012].

Cycle time and cycle time distribution is important from the point of view of ensuring uniform coating on all particles in a spouted bed coater. From equation 79 it is seen that, for a given coater and particle load, cycle time will be reduced by increasing the gas flow rate. From data presented by San Jose [206] it can be seen that an increase in gas flow rate has the effect of reducing the variability in average cycle time. Smaller cone angles also have the effect of decreasing the cycle time distribution. A typical distribution of cycle times is shown in Figure 22.

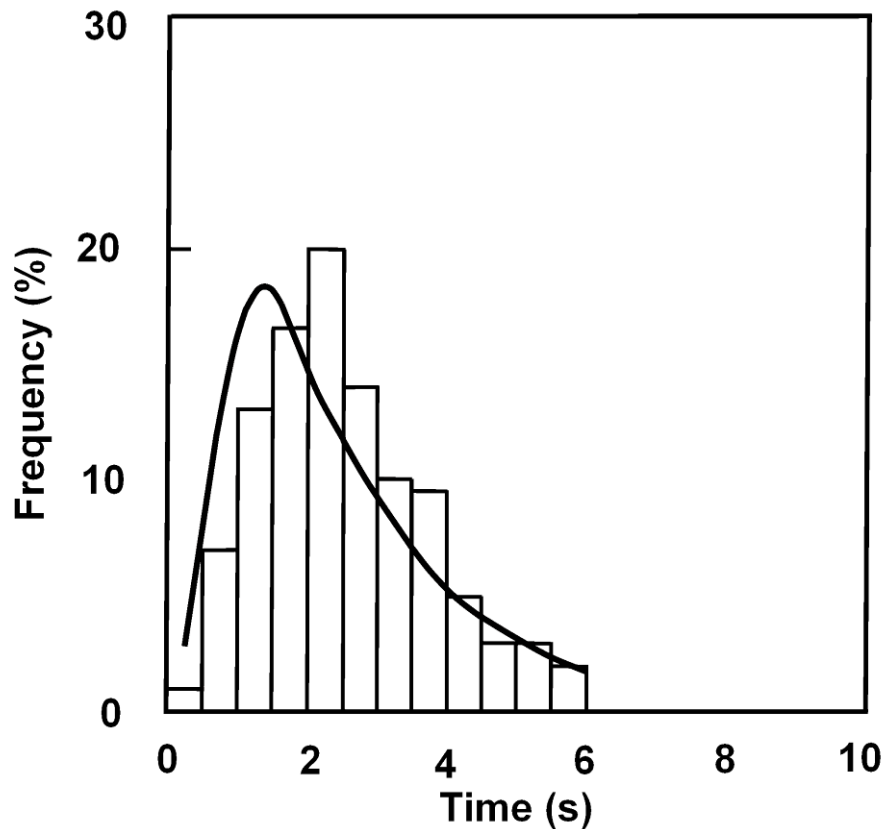


Figure 22. Typical cycle time distribution for a spouted bed. Solid line is for calculated values, histogram for measured data. $D_c = 0.152$ m, $D_o = 0.03$ m, $H = 0.2$ m, $\gamma = 45^\circ$, $D_p = 0.004$ m, $(V/V_{ms}) = 1.3$. San Jose [206].

8 TEST METHODS

8.1 DENSITY

Density of the silicon carbide deposit has been identified as one of the key quality parameters in the manufacture of TRISO coated particles. Typical density specifications require the silicon carbide to have a density greater than 3.18 g.cm^{-3} , that is at least 99 % theoretical density [167][5][166]. Porosity and low density second phases, such as free silicon or carbon, will reduce the density of the deposit. Both porosity and second phases are detrimental to the properties of the silicon carbide so density is a key measure of the quality of the deposit.

The combination of small samples size and required accuracy of the measurement limits the number of suitable methods. Some of these are discussed below. Sample density can be obtained directly from a density gradient column or titration by comparing the density of a sample to that of a liquid with a known density. Pycnometry may be used to measure sample volume, density can then be calculated using a separately measured sample mass.

8.1.1 DENSITY GRADIENT COLUMN

Density gradient columns are set up using a vertical column of liquid in which the density is varied from highest density at the bottom to lowest density at the top. Density ranges across the column depend on the solutions used to set up the column, for determining the density of silicon carbide methylene diiodide (CH_2I_2) is typically used as the dense liquid. Samples will sink into the column until a point is reached where the sample density matches the local density within the column. By calibrating the column with markers of known density it is possible to accurately determine the density of the sample by measuring the samples position within the column.

Density gradient columns are regarded as the most accurate means of comparing the density of solids, when suitably accurate calibration standards are available for measuring absolute density. With accurate temperature control, a long column and a narrow density range the accuracy of a density gradient column can far exceed the accuracy of gas pycnometers and pycnometer bottles [209]. It has been claimed that density gradient columns are the most accurate means of determining density [210] however for very small samples other methods may be more accurate. These do however require sophisticated equipment and very precise environmental control [211]. A major advantage of density gradient columns is the ability to accurately measure the density of very small samples. With suitable density markers for calibrating the column accurate temperature control is not required

Various methods have been developed to set up a density gradient column [212], [213]. It is important that the density gradient along the length of the column is linear, this may be achieved using the methods described by Brown [212]. Systems

using accurate pumping of the liquids rather than gravity feed have also been developed, these allow for rapid and accurate setting up of columns [55].

For small samples, such as silicon carbide fragments, Voice [175] made use of either a density gradient column or titration method. For the gradient column the density was varied between 3.10 g.cm^{-3} and 3.24 g.cm^{-3} over a length of 80 cm. Methylene diiodide (density 3.319 g.cm^{-3}) diluted with triethyl phosphate ($(\text{C}_2\text{H}_5)_3\text{PO}_4$, density 1.068 g.cm^{-3}) were used to set up the column. Triethyl phosphate had the advantage of allowing the recovery of the methylene diiodide by simply washing the mixture with water. The column was calibrated using glass marker floats whose density had been determined by titration. Theoretically this column would allow density determination to within $0.00035 \text{ g.cm}^{-3}$, however in practice an accuracy of 0.0005 g.cm^{-3} was more realistic due to the spread of particles within a batch. Fragments for testing were prepared by crushing the coated particles and cleaning by burning away the carbon in oxygen at $800 \text{ }^\circ\text{C}$ for 1 hour. No detrimental effect of the oxidation procedure was noticed. No details of the method used to set up the column were provided.

Keeley [214] used density gradient columns made up of bromoform (CHBr_3)/tetrachloroethylene (C_2Cl_4) and methylene iodide/bromoform mixtures for measuring the density of pyrocarbon and silicon carbide respectively. Stinton [166] reported a measurement standard deviation of 0.006 g.cm^{-3} but gave no details of the column or set up procedure. Federer [160] reported using a density gradient column but also gave no details of the set up or method used. Förthmann [44] and Osborne [215] used gradient columns made up using methylene iodide and bromoform.

Gulden [161] and Minato [168] used a “sink float” technique using mixtures of methylene diiodide and benzene (C_6H_6). No details of the method are provided. Density was reported to the 3rd decimal. It is assumed that what is referred to as a “sink float” method is a density gradient column.

8.1.2 DENSITY TITRATION

Accurate density determinations may be made using a technique similar to titration. Starting with a liquid with a known density, stepwise additions of a second liquid were made until the sample sinks or floats depending on the relative density of the two liquids. From the density of the two liquids and the volumes, or mass, of the liquids used the density of the mixture can be calculated.

A procedure for performing accurate density titrations is given by Gal [216] who used this technique to measure density changes in plastic due to radiation. Xu [177] and Voice [175] used density titration to accurately measure the density of silicon carbide deposits. Voice [175] also used this method to measure the density of glass markers used to calibrate density gradient columns. None of these authors reported estimated accuracy of the method used.

8.1.3 MERCURY DISPLACEMENT

Voice [175] used a mercury displacement method to determine the density of whole particles before and after silicon carbide coating. The mercury displacement method is similar to standard liquid pycnometry except that mercury is used as the fluid. Sample volume is calculated by measuring the mass of mercury displaced by the sample. To ensure that no air bubbles are trapped in the sample the pycnometer is evacuated before the mercury is introduced into the sample chamber. As the mercury does not wet the sample, and the mercury is not pressurised, the sample envelope volume is measured (pressurisation of the mercury allows the mercury to penetrate the pores allowing an estimate of the sample porosity). Voice [175] quoted sample sizes of “several thousand particles”. From the particle mass and density measured before and after silicon carbide coating the density of the deposited silicon carbide could be calculated using equation 80:

$$\rho = \frac{m_{After} - m_{Before}}{\left(\frac{m_{After}}{\rho_{After}} - \frac{m_{Before}}{\rho_{Before}} \right)} \quad (80)$$

Where

- ρ : Density of the deposit ($\text{g}\cdot\text{cm}^{-3}$)
 m_{Before}, m_{After} : Particle mass before and after deposition (g)
 $\rho_{Before}, \rho_{After}$: Particle density before and after deposition ($\text{g}\cdot\text{cm}^{-3}$)

According to Voice [175] this method could be used to calculate density to the 3rd decimal.

8.1.4 GAS PYCNOMETER

Gas pycnometry has the advantage of having no restriction in sample density and no liquid/sample compatibility concerns. Compared to liquid pycnometry this method also has the advantage of not having to ensure that the sample is completely air free as the gas used will penetrate into all open porosity.

Accuracy of gas pycnometry is reported to be 0.02 % under ideal conditions and 0.1 % or less when conditions are not as well controlled [217]. Accuracy may be influenced by several factors, one of the most important from an operational point of view is the volume fraction taken up by the sample in the sample chamber and the ratio of sample chamber volume to reference chamber volume [218]. The practical result of this is that a particular instrument can accurately measure a restricted range of sample volumes. Sample chamber volume can be adjusted to suit various sample sizes by making use of sample chamber inserts. However limitations on sample chamber volume to reference chamber volume restrict the range over which sample cup may be varied. As a result, separate instruments are required when the sample size varies significantly.

8.1.5 PYCNOMETER BOTTLE

In this method the volume of a sample is determined from the weight differences between a known volume of a reference liquid and a known volume of liquid plus sample. This is achieved using a pycnometer bottle with an accurately known volume. Three mass measurements are made – the empty pycnometer, the pycnometer with the dry sample and finally the pycnometer, containing the sample, which has been filled with liquid. If the density of the liquid is not accurately known the mass of the bottle filled with liquid, without any sample, can also be measured so as to determine the density of the liquid. Pycnometer bottles can be used to accurately determine the density of liquids, however when determining the density of solids additional factors come into play. It is important that the liquid used does not interact with the solids at all, for measuring the density of zirconia, pyrocarbons and silicon carbide this is not a problem when using water as the reference fluid. A more serious problem is encountered in that it must be ensured that no air is trapped in or between the solids being measured, in practice this can be difficult to achieve. Due to the limited penetration of liquids into open porosity this method will calculate envelope volume.

For small samples the precision of pycnometry is poor, Pratten [211] quotes precision 0.7% for a 40 mg sample. This is similar to the figure quoted by Davidson [209] for powder using a 100 ml pycnometer bottle. With large liquid samples (approximately 154 ml) and accurate temperature control Park [219] achieved a precision of 0.008 %.

8.2 LAYER THICKNESS

Several techniques have been developed for measuring the thickness of the silicon carbide deposits. Two methods are recommended by the International Atomic Energy Agency: microradiography and automated image analysis [21]. X-ray methods have the advantage of requiring no sample preparation and are non destructive. Automated microscopy and image analysis allows for many more particles to be analysed than is feasible with manual methods. It has been estimated that automated methods can make use of samples 100 times larger than manual methods [55]. Automatic image analysis is also more accurate, not suffering from operator bias, and more consistent than manual methods. Automated image analysis techniques have been applied to both microradiograph images as well as optical microscopy of silhouettes and polished sections.

In the case of microradiography a single layer of particles is placed directly onto the emulsion of high resolution X-ray film. After exposure and developing the thickness of the silicon carbide layer can be measured from the image of each particle [21]. Federer [160], Voice [175] and Gulden [161] used this method. Techniques using area detectors instead of film and automated image analysis have recently been

developed and shown to give results similar to those obtained from optical microscopy of polished sections [220].

Automated optical image analysis of whole particles and polished sections have been reported by Kercher [55] and Charolais [167] and IAEA publications [21]. Hunn [56] used optical microscopy and automated image analysis for measuring the thickness of TRISO layers of German reference fuel particles.

Besman used SEM or optical microscopy to determine the thickness of silicon carbide deposited onto silicon carbide fibres [159]. Takeuchi [90] studied the deposition of silicon carbide using dichlorodimethylsilane (DDS). He used SEM imaging to measure the thickness of deposits on silicon substrates with trenches etched into them. Variation in the silicon carbide thickness within the trenches etched into the silicon gave an indication of the sticking coefficient of the precursor. This gave insight into the deposition mechanisms involved. No details of the methods used were given by these researchers.

8.3 CHEMICAL AND PHASE COMPOSITION

Ideally only stoichiometrically pure silicon carbide should be deposited. Under non ideal conditions it is however possible to form non-stoichiometric deposits that are either silicon or carbon rich. When present in sufficient concentrations and in a crystalline form both the silicon and carbon may be detected using X-ray diffraction techniques. Unfortunately the detection limit for using this method is not sufficiently low to be of real practical use. Also if any second phase, free silicon or carbon, is in an amorphous form it will not be detected by X-ray diffraction.

Other methods that have been used to analyse the composition of the deposits include wet chemical analysis, electron beam microprobe analysis and Raman spectroscopy. Each of these methods has severe limitations.

8.3.1 WET CHEMICAL ANALYSIS

Voice [175] used two wet chemical methods to determine the silicon content of deposits. In the first method powdered samples were extracted using a HF/HNO₃ mixture. The silicon content of the resulting solution was then measured spectrophotometrically using ammonium molybdate. The sensitivity of this method was poor and it was only capable of detecting free silicon in very impure deposits.

The second method involved dissolving the free silicon in a mixture of AgF and HF. This resulted in silver being precipitated while the silicon went into solution. The silver precipitate was then dissolved in nitric acid and titrated. A problem with this method was that silicon tended to be occluded in the silicon carbide necessitating very fine grinding to liberate all the free silicon. It was found that the finer the grinding the higher the free silicon content.

Voice [175] concluded that no wet chemical analysis was suitably accurate for analysing free silicon in TRISO silicon carbide deposits.

8.3.2 ELECTRON BEAM ANALYSIS

Electron beam analysis has been a popular tool for analysing silicon carbide deposits. Unfortunately many of the researchers have not been thorough in reporting the exact techniques used, generally referring to “microprobe” analysis without giving any details.

Researchers who have reported using microprobe analysis include Federer [160], Voice and Lamb [50], [175] and Yeheskel [158].

Hélary [169] used microprobe analysis to confirm TRISO silicon carbide deposits were stoichiometric with a measured Si:C ratio of 1.02.

As part of a study aimed at improving the standard TRISO coatings Minato et al [36] deposited mixtures of silicon carbide and carbon. Microprobe analysis was used to determine the composition of the deposits which contained up to 40% carbon. In a separate study Minato et al [153] used microprobe analysis to determine the composition of layers deposited using MTS in hydrogen/argon mixtures. It seems that only deposits that potentially could contain carbon were analysed using microprobe analysis.

Papasouliotos [92] used only energy-dispersive x-ray (EDX) analysis to analyse the composition of deposits derived from MTS. In many of the samples investigated significant quantities of elemental silicon were deposited together with silicon carbide; silicon carbide content in the deposits being less than 10 percent in many cases. Kostjuhin [147] also used energy-dispersive x-ray analysis to examine deposits of silicon carbide mixed with free carbon, formed from a mixture of MTS and ethylene (C₂H₂). These analyses were supported by x-ray diffraction analysis of the deposits in which the presence of amorphous carbon was indicated.

Chin [180] studied the deposition of silicon carbide in a low pressure CVD system. Although the exact nature of the substrates was not specified it is assumed that they were flat plates as they were analysed using X-ray diffraction in addition to microprobe analysis. Chin does not give any details of the microprobe system used. Comparison of results obtained using x-ray diffraction and microprobe analysis do not match exactly although they do show similar trends.

Despite the difficulties in analysing low atomic mass elements with electron microprobe analysis none of the studies listed above make any commentary on any special precautions or procedures to ensure accuracy of the analyses. Results presented should therefore be treated with some caution.

Electron microprobe analysis has also been used to investigate the interaction between fission products and silicon carbide in TRISO coated particles. For example Minato [34] used wavelength dispersive microprobe analysis to investigate the interaction between silicon carbide and Palladium, Rhodium and Ruthenium. In a

separate study Minato used both energy (EDX) and wavelength dispersive (WDX) to study fission products in irradiated TRISO particles. MacLean [45] and López-Honorato [47] both used microprobe analysis in their investigation of silver diffusion in silicon carbide.

8.3.3 ALTERNATIVE ANALYTICAL TECHNIQUES

Several analytical techniques not discussed above have been used to analyse silicon carbide deposits. These are listed in Table 9.

Table 9. Additional chemical analysis techniques used to analyse silicon carbide

METHOD	USE	REF
Auger Electron Spectroscopy (AES)	Silicon/Carbon ratio and impurity content	[183][139][221] [162][140][141]
X-ray Photoelectron Spectroscopy (XPS)	Elemental composition and bonding	[169][45][137] [183][139][136]
Mass spectroscopy: various techniques	Elemental and isotope composition	[169][170]
Neutron Activation	Chlorine analysis	[222]

8.4 PHASE COMPOSITION

8.4.1 X-RAY DIFFRACTION

Powder X-ray diffraction techniques have been extensively used to determine the phases present in silicon carbide deposits. Voice and Lamb [50], [175], Minato [153], [168] and López-Honorato [156] used XRD analysis to determine the phases present in silicon carbide in TRISO deposits. In cases where the presence of free silicon or carbon was present the XRD analyses were often combined with other techniques such as microprobe [50], [175], [153] analysis or Raman spectroscopy [156].

Minato [168] used XRD to determine composition (SiC and free silicon), crystallite size and stress in TRISO silicon carbide on powdered samples. Despite the potential problems with using XRD analysis to determine the silicon content a good correlation was found between measured silicon content and density and the theoretical silicon content/density relationship.

In a separate study Minato [153] used X-ray diffraction to analyse deposits, prepared under varying process conditions, for free silicon and carbon. For deposits formed using hydrogen, or hydrogen/argon mixtures, as a carrier gas no free carbon was expected to form. For these deposits the coated particles were crushed and the carbon burnt off at 800 °C in air. Measured free silicon content of these deposits ranged between 0 % and 66 %. This procedure could not be used for deposits formed using pure argon as a carrier gas as it would have removed any exposed free carbon

deposited. In this case X-ray diffraction was performed on complete particles. Electron probe microanalysis was also performed on polished sections of these samples. No free carbon was detected by the X-ray diffraction analysis, microprobe analysis detected free carbon contents ranging between 39 % and 56 %.

X-ray diffraction has also been used to study non-TRISO applications of CVD silicon carbide. For example Liu et al [181], Kim [137] and Kim [183] used flat graphite substrates. This allowed for preferred orientation of the deposit to be investigated. Chin [180] used x-ray diffraction to study the phase composition, preferred orientation and chemical composition of silicon carbide deposited at low pressures. He was able to detect significant amounts (up to 40 %) free silicon in some of the deposits but the composition did not exactly match microprobe analysis results. Takeuchi [90] analysed deposits formed from dichlorodimethylsilane (DDS) using XRD. No free silicon or carbon was detected leading to the conclusion that the process deposited pure silicon carbide at deposition temperatures of 950 °C to 1150 °C. Other researchers who have used XRD to analyse silicon carbide deposit include Cheng [163], Oh [182], Zhu [135] and Zhang [150].

As the technique only detects crystalline phases XRD results need to be interpreted carefully when there is any possibility of amorphous components in the deposit. This is a particular problem in analysing TRISO silicon carbide deposits where free silicon or carbon may be in an amorphous form. Raman spectroscopy has clearly shown that amorphous silicon may be present in TRISO silicon carbide deposits Krautwasser [223].

Förthmann [44] used X-ray diffraction to determine the structure of TRISO deposits formed using hydrogen and hydrogen/argon mixtures as carrier gas. Use of pure hydrogen carrier gas resulted in sharp diffraction lines whereas use of a mixed carrier gas resulted in more diffuse lines. At 1300 °C trace amounts of α -SiC were detected, at higher temperatures pure β -SiC was deposited. Lattice parameter for β -SiC was reported to be 0.4359 ± 0.0001 nm.

Stacking faults readily form in silicon carbide. This has been shown to impact the X-ray diffraction patterns with additional peaks, peak broadening, peak shifting, enhanced background and changes to the relative intensity of the peaks [171], [172]. Diffraction results presented by many researchers, for example [181], [89], have shown these effects. Few authors have commented on these features of measured diffraction patterns. In some cases these effects have been attributed to the presence of α -SiC [137][151].

Stacking fault probability may be quantified from changes in the separation between peaks. Lu [224] used the change in the relative position of [111] and [200] β -SiC peaks to study the impact of deposition temperature, carrier gas (hydrogen) flow rate and MTS concentration on the stacking fault probability.

8.4.2 RAMAN SPECTROSCOPY

Raman spectroscopy provides a powerful tool for assessing the phase composition, crystallographic state and stress within a sample. In crystalline material Raman scattering is dependent on the interaction of incident light and vibrational modes of the crystal. Two specifically named vibrational modes are the longitudinal optic (LO) and transverse optic (TO) modes, both of these are present in the silicon carbide Raman spectrum. For silicon carbide each polytype has a characteristic Raman spectrum allowing for polytypes present in a sample to be detected. Carbon and silicon are also Raman active having their own characteristic peaks. A list of wave numbers for phases detected in the Si–SiC–C system is presented in Table 10.

As the exact characteristics of the peaks depend on crystallite size and orientation as well as crystallographic disorder it is possible to use Raman spectroscopy to assess polytypic composition, crystallite size and crystal quality [225]. Raman bands are also known to be sensitive to deformation of the crystal structure [226], this allows for the measurement of residual and applied stresses. Tensile stresses shift wave numbers upwards while compressive stresses result in lower wave numbers. Raman spectroscopy can be very sensitive, however it is difficult to quantify the phases within a sample [227].

Raman spectroscopy has been used by several researchers to investigate the properties of CVD silicon carbide. López-Honorato et al [156][228] used Raman spectroscopy to determine the composition of SiC deposited onto surrogate TRISO particles using conventional MTS/H₂ as well as MTS/C₃H₆ and MTS/Ar mixtures. It is interesting to note that it was possible to detect differences between surrogate particles and graphite plates mixed into the particle bed [228]. These differences may explain why previous research has found poor correlation between the properties of coated particles and test plates coated together with particles [229]. This effect had previously been thought to be due to different grain sizes resulting from different deposition rates. Krautwasser [223] investigated the impact of process conditions (deposition temperature, deposition rate, carrier gas composition), heat treatment and radiation damage using Raman spectroscopy. Hélyary [169] used Raman spectroscopy to investigate silicon carbide deposited onto TRISO surrogate particles. The only phase detected was β -SiC, a result confirmed by X-ray diffraction and TEM investigation. Ward [225], [230], Jin [231], and Gouadec [232] have used Raman spectroscopy to investigate the properties of CVD silicon carbide fibres.

Ward [225] found a correlation between crystal size and Raman spectrum for SiC fibres. As the grain size decreased from 400 nm to 10 nm the LO and TO peaks broadened, decreased in intensity and shifted to lower wave numbers. At the lowest crystallite sizes the SiC TO and LO bands merged into a single broad, low intensity band.

Stress will also cause the position of the peaks to shift. Tensile stresses cause a shift towards higher wave numbers while compressive stresses result in a reduction in wave number. Several researchers have measured stress, both qualitatively and quantitatively, in silicon carbide using Raman spectroscopy. Jin [231] observed the shifting of silicon peaks measured on SiC fibres and ascribed this to the silicon being under compressive stress. Lu [233] used the SiC LO band to qualitatively study

residual stress in SiC deposited onto flat graphite substrates. It was found that decreasing deposition temperature caused the LO band to shift towards higher wave numbers signifying increasingly tensile residual stress. Increasing MTS flow rates resulted in increased residual stress. Response to increasing hydrogen carrier gas flow showed a non linear response, decreasing only when flow was increased above a threshold value.

For perfectly crystalline samples the TO mode has a single peak. In imperfectly crystalline structures the single peak will split into two separate polarised peaks, TO₁ and TO₂. The separation between these peaks is related to the degree of imperfection. By making use of polarised Raman spectroscopy it is possible to measure the separation between the TO₁ and TO₂ peaks. The percentage hexagonal character of the sample can then be calculated using equation 81. López-Honorato [156] used this method to determine the percentage hexagonal character of deposits, this gave an indication of the stacking fault density of deposit formed under various processing conditions.

$$\%Hexagonal = 3.41\Delta TO \quad (81)$$

Where ΔTO is the separation between the TO₁ and TO₂ peaks.

Table 10. Reported wave number for Raman Si, C and SiC peaks.

Structure	Mode	Wavenumber (cm ⁻¹)	Comment
Silicon Carbide			
3C	TO	796±2 [223], 790 [231], 796 [233]	
	LO	972±2 [223], 973 [231], 972 [233]	
		1500, 1513 [233]	
		1442 [223]	Broad band assigned to C-C bonds in SiC
		508 [223]	Broad band assigned to Si-Si bonds in SiC
		200 – 600 [231]	Acoustic band
α SiC	TO ₁	794 [223]	
	TO ₂	>782 [223]	Depends on polytype
Amorphous		< 600 [225]	Acoustic phonon scattering
Silicon			
Cubic	LO	520 [223], [225] 560 [231]	Shifts by 1.88 ± 0.5 cm ⁻¹ .GPa ⁻¹
	TO	475 [231]	Strong, broad band
Nano-crystalline		510	
Amorphous		415–540 centred on 480 [223] 490 470 480 [225]	Broad band
Carbon			
Diamond		1330 [223]	Sharp, strong peak
Orientated pyrocarbon		1580 [223]	
Poorly orientated		1335 – 1340 [223] 1580 – 1590 [223] D peak: 1343 [231], 1330 [225] G peak: 1535 [231], 1600 [225]	
Amorphous		1000 – 1700 centred on 1500 1400 [225]	Broad, skewed band

8.5 MECHANICAL PROPERTIES

Measurement of the mechanical properties of TRISO silicon carbide deposits has proved to be rather difficult. The combination of a thin deposit on small spherical particles makes it very difficult to obtain sufficient material in a form amenable to testing. Some researchers resorted to including graphite disks into the fluidized bed [161][50][234]. These provided samples of material that were on a flat surface which made testing significantly easier. Unfortunately it was found that the silicon carbide deposited onto the disks was not always representative of the deposits on the particles [228].

Mechanical properties that have been measured include:

- (1) Hardness
- (2) Fracture toughness
- (3) Young's modulus
- (4) Fracture stress
- (5) Particle crush strength

Each of these will be briefly discussed in the following sections.

8.5.1 HARDNESS AND FRACTURE TOUGHNESS

Numerous methods have been developed to measure material hardness. The most commonly used methods all rely on applying a load to an indenter and measuring the penetration of the indenter into the sample. Two methods commonly used for ceramic materials are the Knoop and Vickers tests. Both have been used for measuring the hardness of CVD silicon carbide. Hardness measurements on TRISO coatings is however difficult due to the thin layer of silicon carbide deposited and the form (spherical particles) of the samples.

An alternative to Knoop and Vickers tests is nano-indentation. This technique usually makes use of a Berkovitch type indenter. Due to the low loads and small indentation size this method is well suited to the thin layers deposited by CVD. As this is a relatively new technique few researchers have reported using it for TRISO particles.

Under normal circumstances cracking of the material surrounding a hardness indent is avoided by selecting low indentation loads or using indenters, such as the Knoop indenter, that are less likely to produce cracking. Starting in the 1970's it was realised that cracking around indents could be an indicator of material toughness. This has led to the development of a number of semi-empirical methods for calculating toughness from the length of cracks originating from hardness indents, especially Vickers indents [235].

Details of the abovementioned techniques will be discussed in the following sections. Reported hardness measurements are summarised in Table 11.

Table 11. Micro- and nano- hardness of silicon carbide. Micro-hardness tests performed with Vickers or Knoop indenter. Berkovich indenter used for nano-hardness measurements.

INDENTER TYPE	HARDNESS (GPa)	LOAD (g) / DWELL (s)	MATERIAL	REF.
Berkovich	36		Bulk CVD β -SiC	[215]
Not stated	29.4	Not stated	CVD SiC on graphite	[158]
Berkovich	1: 42 2: 39		TRISO SiC deposited using: (1) MTS and C_3H_8 (2) MTS and C_2H_2	[228]
Berkovich	1: 35 - 37 2: 16.5 - 42.2 3: 36.2 - 36.8		TRISO particles. SiC deposited using (1)MTS, (2)MTS and C_3H_8 (3) MTS and C_2H_2	[156]
Vickers	58.8	50 /Not stated	CVD deposit	[132]
Vickers	22 28	> 10 000/10 50/10	6H single crystal	[67]
Knoop	29 19	> 10 000/10 50/10	Bulk CVD β -SiC Vickers and Nano indentation	[236]
Vickers	21.5	2000/15		
Berkovich	37.8		Low pressure CVD on graphite. Hardness depends on deposition temperature, maximum at 1200 °C	[137]
Vickers	22.0 36.8	Not stated		
Vickers	1: 12.3 2: 12.7 3: 15.7 4: 29.4	100/Not stated	CVD on graphite plate. Non linear increase with deposition temperature (1) 1200 °C (2) 1300 °C (3) 1400 °C (4) 1500 °C. Measured on cross section, thickness not specified	[164]
Berkovich	1: 45 2: 49 3: 45 4: 40 5: 39		TRISO particles. Deposition temperature: (1)1400 °C (2)1450 °C (3)1500 °C (4)1550 °C (5)1600 °C	[162]
Berkovich	1: 35.2 2: 39.1		(1) Poly crystalline β -SiC (2) Single crystal β -SiC	[237]

8.5.1.1 VICKERS AND KNOOP HARDNESS

Both these tests work on the principle of forcing an indenter into the surface of the sample under a controlled load and then measuring the area of the resultant indentation. Hardness is then calculated from the applied load and the contact area of the indentation. Hardness is usually quoted as a hardness number, having units of $kg.mm^{-2}$, or in SI units of GPa.

For both the Vickers and Knoop tests limitations are placed on the load that may be applied when testing brittle materials. Ideally there should be no cracking around the

indent. Due to the shape of the indenter the Knoop impression is shallower than the Vickers impression resulting in a lower propensity to crack [238]. Cracking may be avoided by making use of a lower load; however there is a minimum load below which the measured hardness increases. This effect, the Indentation Size Effect (ISE), has been analysed by a number of researchers, for example [239], [240], [241], [242]. McColm [235] also provided an analysis of the ISE.

A further problem encountered when using low indentation loads to measure hard materials is the small size of the indentation which make optical measurement of the indent inaccurate. SEM measurements can reduce this problem and are accurate enough to be used as a standard against which optical measurements may be compared [238]. Another solution is to make use of an instrumented hardness test where the applied load and displacement of the indenter are continuously measured. This in effect means that the test becomes a depth sensing type test, obviating the need to measure the indent size. It is possible to calculate the size of the indentation from the depth of penetration [238], [243].

Limitations are also placed on the distance between indents, the distance between an indent and the edge of a sample and the depth of the indent relative to the layer thickness. For thin layers this can be a severe limitation. For cracked indents, the distance between the crack tips must be at least 3 times the length of the crack. Indents should also be a minimum of 3 diagonals away from the sample edge. Layer thickness should be at least 10 times the depth of the indent, or approximately 1.5 times the length of the diagonal [244].

Several researchers have made use of Vickers and Knoop testing of silicon carbide CVD deposits. Voice [50], [175] used both Vickers and Knoop indenters to measure hardness of polished cross sections of TRISO particles. A load of 100 g was applied for 10 s. It was found that there was a considerable variation in hardness. For a deposition temperature of 1250 °C values ranged between approximately 1600 HV0.1 and 3500 HV0.1. For deposition temperatures of 1700 °C the hardness increased and the range decreased with values ranging between 3400 HV0.1 and 3700 HV0.1.

Yehekel [158] measured the hardness of CVD silicon carbide deposited onto graphite. For pure silicon carbide the hardness was found to be 3000 kg.mm⁻², this dropped to less than 1000 kg.mm⁻² when the deposit contained significant amounts of free silicon.

Kim [137] noted that Vickers hardness initially increased from 2250 kg.mm⁻² to a maximum of 3750 kg.mm⁻² then decreased with increasing deposition temperature. Hydrogen and argon carrier gas gave similar results. No details of the test method were given.

Lee [245] measured Vickers hardness using either a 1 N or 5 N load applied to the deposit surface. Deposits were too thin to remove the impact of the substrate for 5 N indents. Indents made using a 1 N load had a hardness of approximately 35 GPa for all deposit thicknesses between 30 µm and 70 µm.

Brütsch [132] measured hardness versus carbon content of silicon carbide deposited onto hard substrates. For layers deposited at 1000 °C and higher, maximum hardness was found at the stoichiometric composition with a rapid reduction in hardness with excess carbon or silicon. Vickers hardness values quoted by Brütsch [196] (up to 6000 HV50 or 58 GPa) are not consistent with other hardness values reported in the literature, even when the indentation size effect of the low (50 g) indentation load is taken into account.

8.5.1.2 NANO-INDENTATION

As an alternative to Vickers and Knoop indentation nano-indentation may be used. In this technique load and displacement are continuously measured during loading and unloading of the indenter. Typically the applied load is in the millinewton range, for silicon carbide this will result in an indent depth in the nanometer range. Hardness is calculated from the depth of penetration rather than measuring the size of the indentation which is not feasible due to the small size of the indent.

Berkovich indenters are commonly used for nano-indentation measurements. This is a 3 sided pyramidal indenter that was designed to give the same penetration depth/indent area relationship as a Vickers indenter [235]. In practice there is a difference between Berkovich and Vickers hardness measurements. Hardness measured using a Berkovich indenter can be converted to Vickers hardness using $HV = 0.927H_{\text{Nano}}$ [236].

Nano-indentation produces a very small indent making it easier to overcome the restrictions on indent positioning and layer thickness. However, nano-indentation requires careful sample preparation as the small indent is sensitive to surface roughness and condition of the surface layer. Another drawback of the small indent is the fact that properties are measured on a localised scale. This problem can be overcome by making use of an array of indents instead of a single measurement. A typical array of Berkovich indents in silicon carbide is shown in Figure 23.

Nano-indentation has been used by several researchers to measure the hardness of CVD silicon carbide, for example [156], [228], [236], [162]. Examples of hardness values may be found in Table 11.

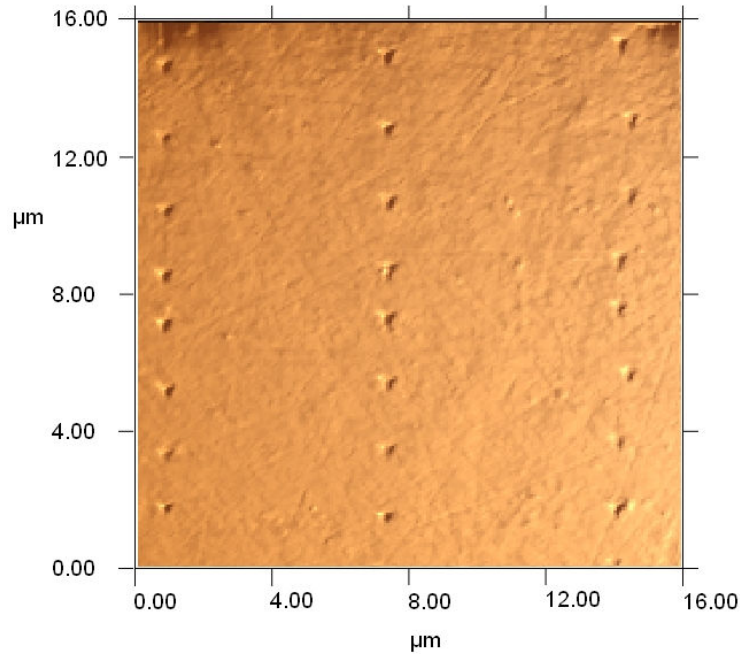


Figure 23. Berkovich indentations in TRISO silicon carbide. Indentation load = 10 mN, maximum indentation depth \approx 125 nm, final indentation depth \approx 45 nm. Surface polished with 1 μ m diamond paste.

8.5.1.3 FRACTURE TOUGHNESS

In brittle materials it is common for cracks to form around a hardness indent. These are classified as either Palmqvist cracks or median cracks. Palmqvist cracks are elliptical in form and originate at the indent corners. Median cracks are semicircular in form and run from crack tip to crack tip across the indent diagonal. These are depicted in Figure 24. A considerable amount of research has been conducted to find correlations between the size of cracks emanating from Vickers hardness indents and sample fracture toughness. A description of the development of the concepts and many of the equations is given by Ponton [246], [247] who analysed 19 of the proposed equations and compared results obtained for various materials. Sergejev [248] compared 17 equations that have been proposed. These were grouped depending on whether the equation is intended to be used with Palmqvist or median cracks. Not all the equations were applicable to the hard metal samples tested. As an alternative to the Vickers indenter a cube-corner indenter may be used. This is more likely to cause cracking so may be used at lower loads [249]. Fracture toughness equations relevant to this study are presented in Table 12. Typical fracture toughness values for silicon carbide are listed in Table 13.

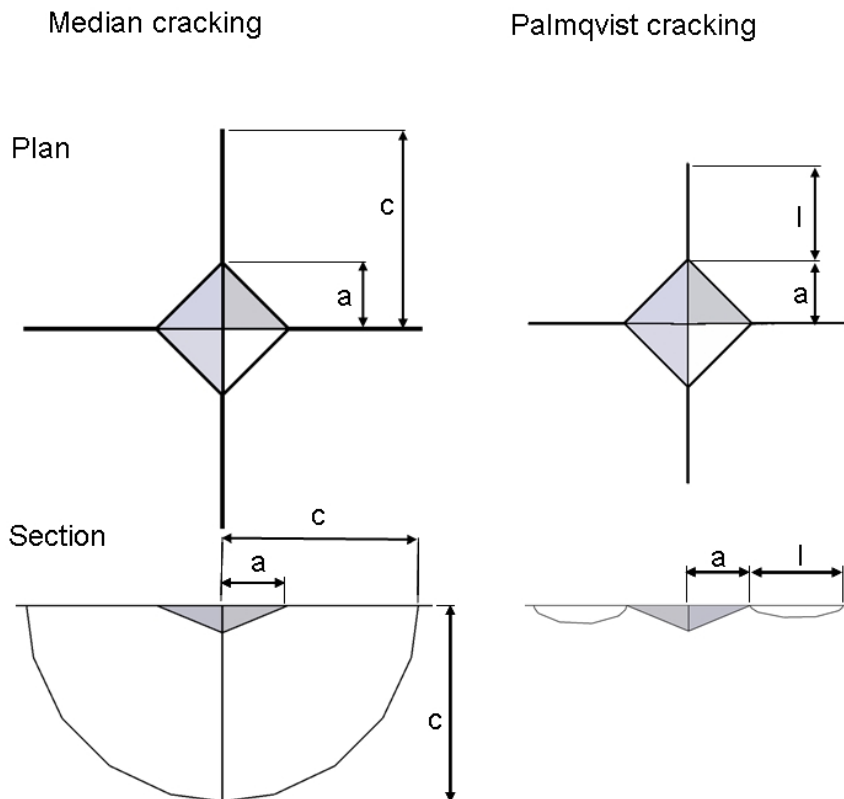


Figure 24. Median and Palmqvist cracks. Dimensions used for hardness and toughness calculations: Indent diagonal = $2a$, Palmqvist crack length = l , Median crack length = c . Adapted from [246].

For opaque materials it is not possible to determine the crack type by observation of the surface crack. There are guidelines for classifying the cracks as Palmqvist or radial depending on the crack length/indent diagonal, for example when c/a is greater than approximately 2 – 3 it is assumed that radial cracks formed. Ponton [247] concluded that even if the wrong crack type was assumed results would still be valid. Liang [250] developed a model that is claimed to be crack type independent. This model yielded results very similar to single edge notched beam tests under a wide range of loads.

Fracture toughness measurement by means of Vickers indentation has not been universally accepted. Quinn [251] is of the opinion that this method should not be accepted. Despite criticism the method still enjoys popularity, mainly due to the relative ease of use. For some samples, such as silicon carbide TRISO particles, it remains one of the only viable means of measuring fracture toughness. Ponton [247], despite claiming errors of up to 30 %, was of the opinion that indentation fracture toughness measurement is a valid method for ranking materials and is useful when other methods are not suitable.

Lee [245] used Vickers indentation together with the Anstis equation to calculate the fracture toughness of silicon carbide deposited onto graphite substrates. An indentation load of either 1 N or 5 N was used. It was found that the toughness varied with deposit thickness indicating that the layers were not thick enough to

eliminate the effect of the substrate. Despite these problems it was clear that the deposit morphology did influence the toughness measurements as deposits with faceted deposits consistently had lower fracture toughness than deposits with rounded deposits.

Zhao [252] utilised a method whereby notched cantilever beams were ion milled into the silicon carbide layer of TRISO particles. These beams were then loaded to failure using a nano-hardness indenter to apply force to the beam. Fracture toughness of the silicon carbide could be calculated from the fracture load. The procedure was repeated for different orientations, allowing for the fracture toughness in the radial and tangential direction to be measured. It was found that there was a considerable difference in fracture toughness measured in the radial and tangential directions on the TRISO particles. This is the only known report of fracture toughness being measured directly on TRISO particles.

Besides indentation toughness measurements several other techniques have been used to measure the toughness of silicon carbide. For bulk materials prepared by CVD or conventional ceramics processing methods several standard test techniques such as precracked beam, surface crack in flexure and chevron-notched beam test specimens have been utilised [253]. Cockeram [254] used these methods to measure the properties of commercial bulk CVD β -SiC. Measurements that are likely to be the most similar to TRISO particles are those performed on CVD deposits intended for microelectromechanical systems (MEMS) applications where thin layers of CVD silicon carbide have been applied to flat substrates.

Table 12. Indentation fracture toughness models applied to silicon carbide. The Liang model has not been applied to CVD silicon carbide but is of particular interest due to its applicability to Palmqvist and median cracks.

PROPOSED BY	EQUATION	REF
Evans-Davis	$K_C = 0.4636 \left(\frac{P}{a^{3/2}} \right) \left(\frac{E}{H} \right)^{2/5} 10^F$ $F = -1.59 - 0.34 - 2.02B^2 + 11.23B^3 - 24.97B^4 +$ $B = \log_{10}(c/a)$	[215] [236] [237]
Anstis	$K_C = 0.016 \left(\frac{E}{H} \right)^{0.5} \left(\frac{P}{c^{3/2}} \right)$	[245] [67] [221]
Liang	$K_C = \frac{Ha^{1/2}}{\phi\alpha} \left(\frac{E\phi}{H} \right)^{0.4} \left(\frac{c}{a} \right) \left(\left(\frac{c}{18a} \right)^{-1.51} \right)$ $\alpha = 14 \left(1 - 8 \left(\frac{4\nu - 0.5}{1 + \nu} \right)^4 \right)$	[250]

Table 13. Reported fracture toughness values of silicon carbide.

METHOD	FRACTURE TOUGHNESS (MPa.m ^{1/2})	MATERIAL	REF.
Vickers indentation (Evans-Davis)	2.8	Bulk CVD β -SiC	[215]
Vickers indentation (Anstis)	1: 5.2 to 3.8 2: 4.1 to 3.0	LPCVD β -SiC on flat graphite plate. Thickness from 30 μ m to 70 μ m. Deposition temperature (1) 1200 °C and (2) 1300 °C	[245]
Vickers indentation (Anstis)	1.8	6H single crystal	[67]
Vickers indentation (Evans-Davis)	5.08	Bulk CVD β -SiC	[236]
Notched cantilever microbeam	1: 6.72 2: 3.47	TRISO particles measured in: (1) radial (2) tangential direction	[252]
Vickers indentation (Laugier)	1: 3.51 \pm 0.42 2: 4.03 \pm 0.43 3: 4.93 \pm 0.16	TRISO particles (1) Pure SiC (2) SiC + free carbon (3) SiC + free Si	[255]
Vickers indentation (Anstis)	1: 2.36 2: 2.44	Bulk LPCVD β -SiC. (1) Parallel (2) Perpendicular to growth direction	[221]
Notched microbeam	2.8 to 3.4	LPCVD on silicon wafer	[256]
Vickers indentation (Liang)	3.2	Sintered SiC	[250]
Vickers indentation (Evans-Davis)	1: 3.46 2: 1.84 to 2.02	(1) Poly crystalline β -SiC (2) Single crystal β -SiC	[237]
Chevron-Notched beam	1: 3.64 2: 3.68	Bulk LPCVD β -SiC. (1) Parallel (2) Perpendicular to growth direction	[254]
Surface crack in flexure	4.82	Bulk LPCVD β -SiC	
Vickers indentation (Anstis)	6.60 to 7.45	Liquid phase sintered β -SiC. 10 % AlN – Y ₂ O ₃ sinter additive. Different mixtures and thermal cycles	[257]
Single Edge V-notch Beam	4.18 to 6.66		

8.5.2 YOUNG'S MODULUS AND FRACTURE STRESS

Nano-indentation provides a convenient means of measuring Young's modulus of CVD deposits. Measurement of the initial slope of the load/displacement curve during unloading of an indentation allows for the calculation of Young's modulus using equations 82 and 83. This method is described in detail by Oliver [243][258]. As can be seen from Table 14 this method has been commonly used to measure Young's modulus of TRISO silicon carbide.

$$E_r = \beta \frac{S\sqrt{\pi}}{2\sqrt{A}} \quad (82)$$

$$\frac{1}{E_s} = \frac{(1-\nu_i^2)}{E_i} + \frac{(1-\nu_s^2)}{E_r} \quad (83)$$

Where

- E_r : Reduced modulus (GPa)
- β : Indenter correction factor (dimensionless) ($\beta \approx 1$)
- S : Slope of the unload curve ($\text{N}\cdot\text{m}^{-1}$). See Figure 25.
- A : Indenter contact area (m^2)
- ν_i : Indenter Poisson ratio (Diamond = 0.07)
- E_i : Indenter Young's modulus (GPa) (Diamond = 1220 GPa)
- ν_s : Sample Poisson ratio
- E_s : Sample Young's modulus (GPa)

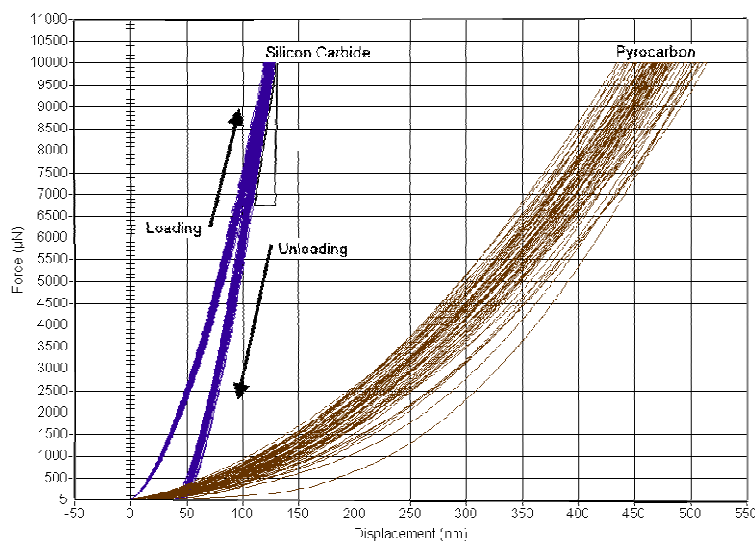


Figure 25. Load/Penetration plot for Berkovich nano-indentation in TRISO silicon carbide and inner pyrocarbon layer.

Bongartz [184], [185] used a method whereby rings of silicon carbide are produced by sequentially polishing coated particles from both sides. By controlling the polishing depth it was possible to produce rings approximately 50 μm thick from the centre of the particles. Buffer pyrocarbon was removed from the rings using a wet chemical etchant based on chromic oxide and nitric acid (see Table 17 for details); this gave a silicon carbide/dense pyrocarbon composite ring. Thermal oxidation, or etching, was used to remove carbon to make silicon carbide only rings. Rings were diametrically crushed using hard anvils. Young's modulus could be calculated from the ring dimensions and the load/deflection curve. Fracture stress was calculated from ring dimensions and fracture load. For complete rings the maximum tensile stress was on the inside of the ring adjacent to the point of contact with the anvils. By using a C shaped half ring it was possible to shift the maximum tensile stress to a point on the outside of the ring midway between the contact points. Xu [177] also used the brittle ring test, however load was applied by means of thin wire passed through complete rings.

Gilchrist [234] developed a method whereby fracture stress could be measured by means of internal pressurisation of hemispherical silicon carbide shells. The shells were prepared by polishing away half of a coated particle and then removing the remaining hemisphere from the mounting resin. After removal of the pyrocarbon layers by oxidation at 950 $^{\circ}\text{C}$ in air the silicon carbide shells were glued over a hole in a mounting plate. By applying pressure to the backside of the mounting plate the hemisphere were internally pressurised. From the pressure required to rupture the shell the fracture stress could be calculated.

Hong [259] developed a technique whereby internal pressure was applied to hollow spherical or tubular samples. Particles or rods were coated in a fluidised bed coater, polished to expose the pyrocarbon layers which were then burnt off leaving hemispherical or tubular silicon carbide shells. The samples were pressurised using a soft polyurethane insert which was compressed. Fracture stress was calculated from the internal pressure at fracture. This technique was used together with a crush test of hemispherical shells compressed between rigid anvils.

Evans [229] measured the fracture stress for fracture originating from the internal and external surfaces of TRISO coated particles by using different methods of loading hemispherical silicon carbide shells removed from coated particles. Details of the loading methods are given in Figure 26g and Figure 26h. For standard silicon carbide it was concluded that fracture strength was limited by flaws in the outer surface of the silicon carbide and not by porosity in the layer. Significant improvements in fracture strength were made by producing silicon carbide layers with a smoother surface. This also shifted the weakest point to the inner surface of the shell. Another important finding was that room temperature fracture strength could be used as a good indicator of fracture strength at operating temperatures as the strength did not decrease significantly between room temperature and 1300 $^{\circ}\text{C}$. Between 1300 $^{\circ}\text{C}$ and 1400 $^{\circ}\text{C}$ there was only a marginal decrease in fracture strength.

Voice and Lamb [50] attempted to use a 4 point bending test on 5 mm x 1 mm x 0.05 to 0.1 mm samples cut from discs coated together with TRISO particles. Problems were experienced with non-uniformity of the deposit. Thickness variation

across the discs was corrected by polishing; this was found to have little effect on modulus measurements but impacted the fracture stress measurement. Structural variation across the thickness of the silicon carbide layer had a noticeable impact on modulus measurements. As a result of these difficulties 4 point bending tests were abandoned in favour of crush tests. Price [222] used a 3 point bending test on samples cut from discs coated together with particles. As with other researchers he found that the surface finish of the test samples impacted on the fracture strength with as-deposited samples fracturing at lower loads than samples polished with 8 μm diamond paste.

Bending tests have successfully been used to measure the properties of bulk β -SiC deposited by CVD [254][221]. In these cases samples significantly larger than achievable with fluidised bed coaters are used. Importantly it has been found that the surface finish of the samples impacts on the measured strength.

Bellan [260] compared nano-indentation, acoustic microscopy and impulse excitation on β -SiC deposited onto sintered α -SiC plates that had been coated in a fluidised bed coater. Values of Young's modulus measured by means of nano-indentation were below values typically reported and was not as repeatable as acoustic microscopy, however it was concluded that nano-indentation may in fact be preferred to the other methods.

Jackson [261] [262] used micro electromechanical systems (MEMS) technology to etch 4000 μm x 600 μm tensile test samples into epitaxial and polycrystalline β -SiC deposited onto silicon wafers. Young's modulus and fracture strength were measured directly in tension using a miniaturised tensile tester. This allowed for measurement of Young's modulus as well as the tensile strength of the samples. For the epitaxial deposits it was found that there were differences in Young's modulus and tensile strength depending on the manufacturing process. In the case of the polycrystalline silicon carbide processing conditions were found to impact on the measured properties. Sharpe [263] used a similar technique but with samples of a different size (about 200 μm x 1300 μm x 150 μm) and format.

MEMS technology has also been used to produce cantilever beams. The properties of the beams could then be measured by either mechanically stressing the beam using an AFM probe [264] or from the resonant frequency of the beam [143].

Reported values of Young's modulus and fracture stress of silicon carbide measured using the techniques described above is presented in Table 14 and Table 15.

Table 14. Young's modulus of silicon carbide. Typical values reported in the literature.

METHOD	YOUNG'S MODULUS (σ)(GPa.)	MATERIAL	REF.
Nano-indentation	1: 330 2: 340 3: 330 4: 280 5: 290	TRISO β -SiC. Deposition temperature (1) 1400 (2) 1450 (3) 1500 (4) 1550 (5) 1600	[162]
Nano-indentation	1: 446 2: 474	(1) Poly crystalline β -SiC (2) Single crystal β -SiC	[237]
Nano-indentation	1: 503 (15) 2: 524 (11)	(1) Bulk CVD β -SiC (2) Single crystal β -SiC	[215]
Nano-indentation	354 (30)	β -SiC on α -SiC plates coated in a fluidized bed coater.	[260]
Acoustic microscopy	434 (19)		
Impulse excitation	360 - 425		
Brittle ring	1: 196 - 609 2: 440 - 770	TRISO particle β -SiC. Range of deposition conditions used. Ring and half ring specimen tested to initiate fracture on (1) inner and (2) outer surface	[185]
Microtensile test (Sample size: 200x4000x25 μ m)	1: 416 (45) 2: 435 (41)	Epitaxial β -SiC grown on Si wafer using SiH ₄ and C ₃ H ₈ . (1) micromoulding (2) etching	[261]
Microtensile test (Sample size: 200x4000x25 μ m)	1: 448 (13) 2: 428 (39)	Polycrystalline β -SiC deposited on Si wafer using MTS. (1) Random and (2) orientated 200 nm grain size	[262]
Microbeam. Load applied by nano-indenter	421 (24)	TRISO particle β -SiC. 3 point loading of microbeam ion milled into TRISO particle.	[252]
Pressurised diaphragm	331	Epitaxial β -SiC deposited onto silicon wafer	[265]
Cantilever beam. Load applied by AFM	470	β -SiC grown by implanting carbon into silicon	[264]
Cantilever beam resonant frequency	380	Poly crystalline β -SiC deposited from 1,3-disilabutane	[143]
Crush test	390	TRISO coated particles	[266]
3 Point bending (Sample size: 0.6x0.1x0.005 to 0.01cm)	275 - 379	β -SiC coated onto discs in a fluidised bed. Range of deposition temperatures and surface finishes.	[222]

Table 15. Fracture stress measurement of silicon carbide.

METHOD	FRACTURE STRESS (σ) (MPa)	MATERIAL	REF
Soft brass anvil on outer surface. Hard anvil on equatorial plane	330 - 650	Hemispherical shells removed from TRISO particles prepared under various conditions	[267]
Brittle ring	1: 1270 (279) 2: 980 (206)	TRISO particle β -SiC. Ring thickness (1) 30 μ m and (2) 80 μ m	[184]
Brittle ring	1: 930 - 1890 2: 980 - 2200	TRISO particle β -SiC. Wide range of deposition conditions used. Ring and half ring specimen initiate fracture on (1) inner and (2) outer surface	[185]
Microtensile test (200x4000x25 μ m)	1: 1190 (530) 2: 1650 (390)	Epitaxial β -SiC grown on Si wafer using SiH ₄ and C ₃ H ₈ . (1) micromoulding and (2) etching	[261]
Microtensile test (200x4000x25 μ m)	1: 810 (230) 2: 490 (200)	Polycrystalline β -SiC deposited on Si wafer using MTS. (1) Random and (2) orientated grain. 200 nm grain size.	[262]
Microtensile test (200x1300x150 μ m)	1: 378 (134) 2: 473 (153) 3: 785 (282)	Polycrystalline β -SiC wafer. Test samples with (1) straight (2) curved (3) notched edges	[263]
Brittle ring	1: 670 (146) 2: 1285 (223) 3: 1447 (269) 4: 783 (153) 5: 693 (214)	TRISO β -SiC. Deposited at (1)1450 (2)1500 (3)1550 (4)1600 (5)1650 °C	[177]
Internal pressurisation	1: 187 - 257 2: 263	TRISO particle or carbon rods coated in fluidised bed. Sample prepared to produce hollow (1) spheres and (2)tubes	[259]
Shell bending (1)	S ₀ = 720 m = 8.0	β -SiC shells from TRISO particles. Standard SiC, inner surface.	[229]
	S ₀ = 620 m = 3.0	β -SiC shells from TRISO particles. Standard SiC, outer surface.	
	S ₀ = 1350 m = 7.0	β -SiC shells from TRISO particles. Smooth SiC, inner surface.	
	S ₀ = 2500 m = 3.6	β -SiC shells from TRISO particles. Smooth SiC, outer surface.	
4 Point bending (5.08x0.633x0.318cm)	231 - 381 (14 - 50)	Bulk CVD β -SiC. Test from various directions relative to deposition direction. Differing machining direction and surface finish.	[254]
4 Point bending (0.3x0.4x4.5cm)	423.3 (19.6)	Bulk CVD β -SiC. As deposited value shown, thermal treatments and finer surface finish increased strength	[221]
3 Point bending (0.6x0.1x0.005 to 0.01cm)	482 - 827	β -SiC coated onto discs in a fluidised bed. Range of deposition temperatures and surface finishes.	[222]

(1) Weibull parameters reported.

8.5.3 Crush Strength

Voice [50] [175] used crush tests of complete particles in preference to bending tests performed on flat samples coated together with particles. Sapphire anvils were used, resulting in cracks initiating at the contact surface. Young's modulus and fracture stress were calculated from load/displacement data. Silicon carbide thickness measurements required for the calculations were obtained from X-Ray radiography of the particles.

Briggs [266] used crush tests to evaluate the properties of complete particles, with and without the carbon layers in place, as well as hemispherical shells. Rigid anvils were used for all tests. Results were expressed in terms of Weibull statistics. It was noted that the value of the Weibull parameter, m , for crush tests was higher than that measured using bending tests. From the tests performed on the hemispherical shells it was possible to calculate fracture stress for failure initiating from the inner and outer surface. Fracture strength of the outer surface was found to be lower than that of the inner surface. This was related to the relative roughness of the surfaces. Fracture stress was also found to be different for silicon carbide deposited onto methane and propene derived pyrocarbon. Importantly no correlation could be found between crush load of complete particles and fracture stress calculated from hemispherical shells. It was concluded that crush testing is not a suitable method for measuring the strength of individual layers.

Minato [268] crush tested complete TRISO particles after coating, after compact formation and after irradiation. For the irradiation testing both loose particles and compacts were tested. For each test 15 to 30 particles were crushed between hardened steel anvils. An instrumented system was used allowing for the load and strain to be continuously measured however only fracture load and stress was reported. It was found that particle strength was reduced by compact formation and irradiation.

Ogawa [269] used crushing strength to investigate the strength of particles with and without outer pyrocarbon as well as the impact of high temperature annealing. Annealing at 1800 °C was found to reduce the crushing strength of the particles.

Lackey [270] used a crush test using steel anvils to investigate the strength of various BISO and TRISO particles. Crush strength was measured at various stages of the particle coating process as well as on annealed particles. It was found that the strength of the particles was reduced by the deposition of 29 μm to 35 μm of silicon carbide but then increased again once the outer pyrocarbon was deposited. Annealing of the particles to simulate compact manufacturing heat treatments resulted in a reduction of the crush strength. The sensitivity of the coating process to process variables can be seen in the difference in response to particles coated using different gas distributor; use of a porous plate gas distributor resulted in a smaller decrease in strength after annealing.

Most researchers, for example [153] [162] [259] [268] [269], have used rigid anvils when performing crushing tests. In most cases complete particles, either with or without outer pyrocarbon were used for crush testing. In some cases, for example [162][259][267], hemispherical silicon carbide shells were used instead. Making use

of shells allowed for the silicon carbide to be tested without influence from pyrocarbon layers or kernels. Other researchers such as Hong [259] have used analytical solutions to calculate the fracture stress from crush test results.

When hard anvils are used to compress particles the maximum stress develops at the point of contact between the particle and anvil. This results in fracture initiating at the point of contact. Van Rooyen et al [271] used a finite element model to show that by using soft anvils the point of maximum stress can be shifted away from the contact between the anvils and particle. As a result the volume of material experiencing maximum stress would increase and the degree of stress concentration would decrease. Tests proved that measured particle crush strength increased as hardness of the anvils was reduced to approximately 38 HV. When anvil hardness was reduced below 38 HV the crush strength remained constant. Making use of soft anvils had the advantage of testing the inherent material properties rather than the stress at the contact between a particle and the anvils. Van Rooyen et al [271] reported crush load for complete TRISO coated particles. Later studies combined crush testing and finite element analysis to calculate the fracture stress of the silicon carbide layer [272].

A summary of reported crush strength, and fracture stress values derived from crush testing, using various test methods is presented in Table 16.

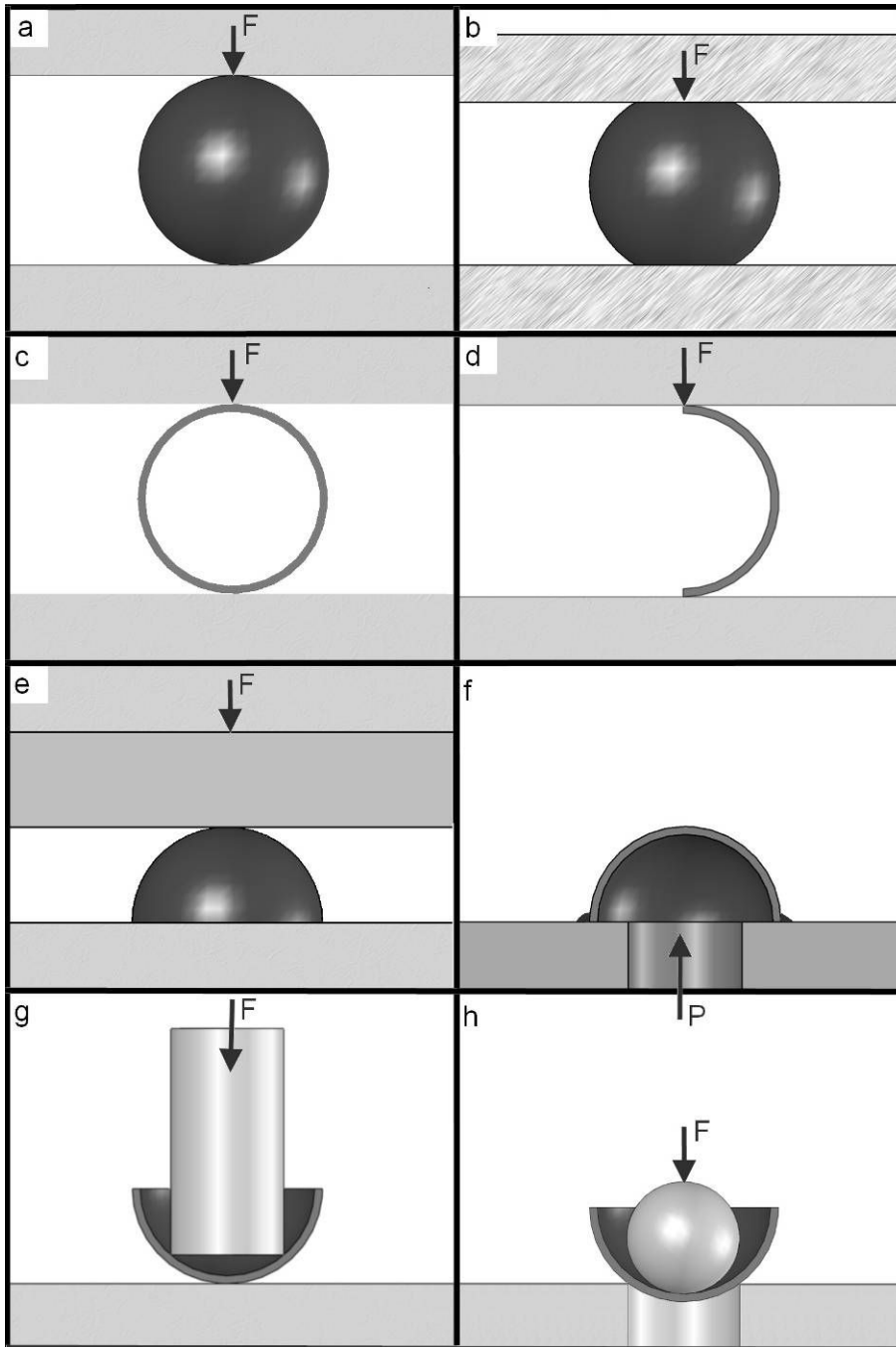


Figure 26. TRISO particle crush test configurations. (a) Whole particle crushed between hard anvils (b) Whole particle crushed between soft anvils (c) Ring test using full ring (d) Ring test using ring segment (e) Hemispherical shell crushed between hard and medium hard anvil (f) Internal pressurisation (g) Interior of hemispherical shell stressed (h) Outside of hemispherical shell stressed.

Table 16. Crush strength of silicon carbide.

METHOD	CRUSH STRENGTH (Standard Deviation)		Ref.
	(g)	(MPa)	
Hemispherical β -SiC shells prepared from TRISO particles. Soft anvil on outer surface. Hard anvil on equatorial plane. Fracture stress calculated from crush load.		330 - 650	[267]
Hemispherical β -SiC shells prepared from TRISO particles. Hard anvils. Fracture stress calculated from crush load.		638 - 822	[259]
Hemispherical β -SiC shells prepared from TRISO particles. Hard anvils. Fracture stress calculated from FEA derived equation. Samples coated at: (1)1400 °C, (2)1450 °C , (3)1500 °C, (4)1550 °C (5)1600 °C		1: 517 (73) 2: 464 (61) 3: 409 (55) 4: 471 (59) 5: 491 (59)	[162]
Hard anvil crush test Weibull parameters. Crush load and inner surface fracture stress. Methane derived pyrocarbon.	2000 m = 19 (a)	3170 m = 7.8 (a)	[266]
Outer surface fracture stress. Methane derived pyrocarbon.		1910 m = 8.4 (a)	
Crush load and inner surface fracture stress. Propene derived pyrocarbon.	2200 m = 19 (a)	2950 m = 6.6 (a)	
Weibull parameters for outer surface fracture stress. Propene derived pyrocarbon.		1870 m = 7.2 (a)	
Hard anvil crush test on complete TRISO particles. Tested before and after compact formation as well as before and after irradiation. Data for single batch (1) before and (2) after compact formation. 25 μ m SiC.	1: 2020 2: 1560		[268]
Hard anvil crush test without pyrocarbon	1100 - 740	129 - 156	[269]
Hard anvil crush test without (1) inner pyrocarbon (2) SiC (3) outer pyrocarbon (4) after anneal (approximate average reported value)	1: 1373 2: 1203 3: 2183 4: 1800		[270]
(1) Soft and (2) hard anvil crush test of complete TRISO particles (data for single batch as deposited)	1: 9439 2: 2498		[271]
Soft anvil crush test of complete TRISO particles (1) as deposited (2) after 2000 °C anneal		1: 1322 m = 3.62 2: 1201 m = 4.54 (a)	[272]

(a) Weibull characteristic strength and modulus

8.6 MICROSCOPY

8.6.1 OPTICAL MICROSCOPY

Optical microscopy has been extensively used to study silicon carbide layers within TRISO particles. However due to its limited resolution, and narrow depth of field at high magnification, its utility is restricted. Most applications have been for investigating of larger scale effects such as cracking, gross porosity and striations within the silicon carbide. Optical microscopy has also been used extensively to study complete TRISO particles. Effects such as separation of the pyrocarbon and silicon carbide layers, cracking of layers, kernel movement and swelling and interaction between the kernel and coating have been observed.

Voice [50], [175] used optical microscopy to study polished and etched silicon carbide deposits on TRISO particles. A notable feature of the deposits is the striations that form at low deposition temperatures and high MTS concentrations. It was speculated that the darker areas of the striations were regions of increased porosity but the resolution of the optical microscope was not high enough to confirm this.

Förthmann [44] measured optical anisotropy and reflectivity of TRISO silicon carbide using 546 nm light. Details of the optical anisotropy measurements were not given. Reflectivity showed a trend similar to grain size, having a minimum for deposition temperatures of 1400 °C for pure hydrogen and mixed carrier gas.

The optical properties of β -SiC and α -SiC are sufficiently different to allow for optical identification of the different phases. For example Püsche [273] identified areas of α -SiC in β -SiC grown by a physical vapour transport process by means of colour variation using dark field reflected light microscopy. Cubic β -SiC is optically isotropic whereas α -SiC exhibits birefringence (See Table 4 for optical properties of silicon carbide). de Villiers [170] used polarized transmitted light microscopy to investigate the structure and phase composition of TRISO silicon carbide. In this study features such as striations, growth cones and phase variations could clearly be seen in the silicon carbide.

Optical microscopy has been used to study palladium attack of silicon carbide. As the palladium tends to concentrate in nodules on the inner surface of the silicon carbide it is possible to see the palladium attack. This has been used by Minato [36][34] and Tiegs [35].

Low power optical microscopy has been used to measure coated particle size and shape. In combination with automated image analysis this has allowed for rapid measurement of particle size on large samples [55]. These techniques were used for example by Hunn [56] for characterising German made fuel particles.

8.6.2 SCANNING ELECTRON MICROSCOPE (SEM)

Scanning electron microscopy provides a powerful tool for investigation of the properties of TRISO silicon carbide and has been widely used. With an ability to obtain very high magnifications while maintaining a useful depth of field SEM allows for the detailed examination of the free surface, fracture surface and cross section of TRISO particles. With the ability to detect secondary electrons, backscattered electrons and X-ray detection a wide variety of analyses can be performed. This includes topographic imaging (secondary and backscatter electrons), qualitative and quantitative elemental analysis and mapping (characteristic x-rays) as well as structure analysis (backscatter electrons).

SEM samples need to be electrically conductive to prevent the build up of charge on the sample. Both silicon carbide and pyrocarbon are sufficiently conductive for this when mounted directly onto a conductive sample mount [50], [175]. Samples that have been mounted in epoxy resin need to be coated with a conductive layer, such as carbon or gold, to allow for electrical contact between the sample and the sample mount. Alternatively it is possible to mount particles in copper or carbon filled conductive compression mounting powder [47], [156], [228].

SEM imaging has been used to investigate silicon carbide fracture surfaces and, more commonly, the free surface after coating of TRISO particles. SEM has also been used to study polished, as well as polished and etched, cross sections of silicon carbide. Federer [160], Gulden [161], Minato [168], Xu [177], Voice [50], [175] and López-Honorato [47], [156], [228] all used SEM imaging to characterize silicon carbide deposits in this way.

The ability of backscatter electrons to distinguish between different elements has also allowed for rapid identification of the distribution of fission products within the TRISO layers. This was used by López-Honorato [47] [274] and MacLean [45] to study the transport of silver in silicon carbide. Elemental mapping using characteristic X-ray emission from the sample can also be used to identify the distribution of elements. Minato [26], [34] used this technique to study the behaviour of fission products within the coated particles as well as the fission product/silicon carbide interaction, especially palladium attack of the silicon carbide.

Polished sections will not display any significant contrast between the grains when secondary electron imaging is used. By etching the surface details of the structure may be highlighted. Many different etch techniques have been used in the study of silicon carbide. A list of etchants used for preparing silicon carbide for SEM and optical microscopy is presented in Table 17. Thermal etching and fused salt etching are difficult to apply to TRISO particles and have not been commonly used on coated particles. Gulden [161] used fused salt etch to etch flat samples added to a fluidized bed. Electrolytic etching and various versions of Murakami etch have been most commonly used for etching polished TRISO particles.

Backscatter electron images of polished sections will display compositional contrast. In the absence of topographic and compositional contrast, structural contrast due to electron channelling effects becomes distinguishable. This allows for backscattered electron imaging to show grain structure without the need for etching [275]. Imaging

of this sort has been used for example by Tan [179] and López-Honorato [47], [156], [228].

The structural contrast discussed above provides no information of the actual structure of the sample. By analyzing backscattered electron diffraction patterns it is possible to determine the crystallographic structure and orientation of points on the sample. In this way it is possible to map the crystallographic structure and orientation of the sample. This method, referred to as Electron Backscatter Diffraction (EBSD) provides a means of identifying the phases present, sample texture, grain size and grain boundary information. A review of the method is given by Humphreys [276]. EBSD has been used by Helary [169], [178], López-Honorato [47], [156], Tan [179] Mokoduwe [176] and van Rooyen [277]. A disadvantage of EBSD is the low throughput, analysis times between 2 [179] and 11 [277] hours have been reported for recent studies of TRISO particles.

SEM analysis has been used by numerous researchers investigating the CVD of silicon carbide not related to TRISO coated particles. Amongst these are Kostjuhin [147], Chin [180], Kim [137], Liu [181], Cheng [163], Oh [182], Zhu [135] and Oh [278]. From these studies the impact of processing conditions on the morphology of the deposits was clearly shown. Of particular interest is the 3-dimensional plot of silicon carbide structure as a function of deposition temperature, hydrogen/MTS ratio and deposition pressure developed by Chin [180].

8.6.3 TRANSMISSION ELECTRON MICROSCOPY (TEM)

Hélary [169] used TEM and High Resolution TEM to study the structure of the silicon carbides grains, grain boundaries and dislocations within the grains. Selected Area Electron Diffraction (SAED) allowed for identification of the crystal structure of the grains. From this it was concluded that little α -SiC is found in the deposits but stacking faults are common.

Förthmann [44] used a replication technique to study the surface of polished and etched surfaces. This allowed for grain size and morphology determination. From this it was concluded that deposition temperature and carrier gas composition impacted the grain structure and etch response of the deposit. Importantly these parameters could be correlated to silver release rates from the coated particles. Elongated grains orientated in a radial direction which had a non uniform etch response had the highest silver release rates.

López-Honorato has used TEM in a number of studies of silicon carbide deposited onto surrogate TRISO particles [47], [156], [274]. The presence of defects in the silicon carbide crystallites is clearly visible in TEM images as well as in the electron diffraction patterns. Of particular interest in these studies is the research into silver diffusion through the silicon carbide layer. It was concluded that silver diffuses along the grain boundaries and that processing conditions that influence the properties of the grain boundaries are likely to impact on the diffusion coefficient of silver in the silicon carbide.

The resolution of High Resolution TEM (HRTEM) is sufficient to provide details of the crystal lattice. Liu [181] used this to investigate the structure and orientation of silicon carbide deposited onto graphite from MTS and hydrogen in a LPCVD coater. It was found that initially the deposit conformed to the (002) orientation of the graphite substrate but as the layer grew the orientation changed to (111).

Kim [137] used TEM to investigate the difference in grain structure resulting from the use of pure hydrogen or hydrogen/argon mixtures as a carrier gas. It was concluded that using a mixed carrier gas resulted in grains with a higher defect density. This result is supported by the appearance of XRD diffraction patterns although Kim attributed the shape of the XRD pattern to α -SiC. When pure hydrogen was used as a carrier gas the average crystallite size was found to be 120 nm.

In a study of the effect on depletion of reactants Kim [183] used TEM to study the SiC. It was found that pure β -SiC was deposited. Stacking faults were seen on the (111) planes.

Cheng [163] used bright field TEM imaging as well as SAED to study the growth of CVD β -SiC on graphite substrates. Extra spots and streaking of the diffraction patterns indicated the presence of microtwins on the (111) planes. This was confirmed by the bright field TEM images.

In a study of TRISO silicon carbide using both TEM imaging and selected area electron diffraction De Villiers [170] found that the deposits were predominantly β -SiC with minor amounts of α -SiC present. Disordered regions as well as twinning could be identified on the electron diffraction patterns. The amount of disorder was found to be variable. It was pointed out that electron diffraction is the preferred method available for unambiguous identification of different silicon carbide phases as XRD and Raman peaks of the phases overlap making it difficult to distinguish between the various phases.

Table 17 Etch techniques applied to silicon carbide and TRISO particles.

TEMPERATURE (°C)	METHOD	NOTES	REF
THERMAL ETCH			
1200	Vacuum		
1350 – 1800	30 minutes in Argon	Sintered and reaction bonded SiC Temperature used depended on material.	[279]
MOLTEN SALT ETCH			
480	90% NaOH, 10% KNO ₃ 15 minutes	Sintered and reaction bonded SiC	[279]
600	2:1 mass ratio NaOH:KNO ₃ 10 minutes	α SiC Etches both silicon and carbon faces	[280]
950	NaHCO ₃ 10 minutes	Carbonate decomposes to form NaCO ₃ (reference states NaOH)	[281]
	KHCO ₃	Details not stated	
	Na ₂ B ₄ O ₇		
650	NaF, K ₂ CO ₃ Eutectic mixture 10 to 60 minutes	Details not stated	[161]
350	NaOH, KOH eutectic mixture	β-SiC 75 – 105 minute etch	[282]
600	KOH	β-SiC	[283]
	Na ₂ O ₂ , NaNO ₂		[282]
400	KOH	β-SiC 25 minute	[163]
500	KOH		[123]
	KOH K ₂ CO ₃		

TEMPERATURE (°C)	METHOD	NOTES	REF
ELECTROLYTIC ETCH			
100 ml H ₂ O 20g KOH	6V, 1 A.cm ⁻² , 20s		[50], [175]
120 g CrO ₃ 400 ml Acetic acid 380 ml H ₂ O 30 ml H ₂ SO ₄ 2 ml Methanol	6 V, 0.4 A, 6 s	Stain etch. Colours dependent on grain orientation	[50], [175]
10g Oxalic acid 100 ml H ₂ O	5 – 10V, 1 A, 30 s		[50], [175]
10 g CrO ₃ 0.2 ml HF 100 ml H ₂ O			[50], [175]
10 % CrO ₃ H ₂ SO ₄	6 V	Sintered and reaction bonded SiC	[279]
20 % KOH	6 V	Sintered and reaction bonded SiC	[279]
4 g K ₂ Cr ₂ O ₇ 100 ml H ₃ PO ₄	15 V 20 – 30 s	TRISO coated particles Used together with oxalic acid electrolytic etch	[168]
10 g Oxalic (C ₂ H ₂ O ₄ .2H ₂ O) 100 ml Water	15 V 30 s		
Saturated solution KF HF	No details given	TRISO silicon carbide Used as a stain etch after a NaF, K ₂ CO ₃ fused salt etch	[161]
AQUEOUS ETCH			
H ₂ CrO ₄	Not given	Polished TRISO cross section	[44]
HF K ₂ S ₂ O ₈	80 °C for 60 minutes	Polycrystalline 6H	[284]
HF Na ₂ O ₂		Polycrystalline 6H Max etch rate at 0.5 Molar Na ₂ O ₂ at 80 °C	[285]
3:1 mixture of 47 – 52% HF 70% HNO ₃	100 °C	Preferentially etched 3C leaving faulted 6H.	[174]
10 g NaOH 10 g K ₃ Fe(CN) ₆ 100 ml H ₂ O	Various temperatures reported: 110 °C to boiling.	Murakami etch. Various concentrations, including saturated solutions, have been reported. Either NaOH, KOH or mixtures have been used	[166] [160] [169] [277] [279] [274]
20 weight % CrO ₃ HNO ₃	110 °C	Used to remove pyrocarbon	[184]
0.5 g CrO ₃ 6 ml 16 mol/l HNO ₃ 6 ml 18 mol/l H ₂ SO ₄	140 °C 15 to 30 minutes	Used to remove pyrocarbon	[286]

9 COATER DESIGN AND SETUP

In chapter 6 various factors impacting on the CVD deposition of silicon carbide were discussed. Important process variables include:

1. Precursor
2. Additional reactive species (e.g. hydrocarbon, HCl)
3. Precursor concentration
4. Carrier gas composition
5. Deposition temperature
6. Operating pressure
7. Gas/Solid contacting type

The choice of a number of these variables was governed by the nature of the intended test work. Coating of TRISO has invariably been carried out in spouted bed coaters operating at atmospheric pressure. Virtually all TRISO coating has been carried out using MTS and hydrogen or hydrogen/argon mixtures. Studies on the influence of adding hydrocarbons, such as CH_4 , C_3H_6 , C_2H_2 , have indicated that minor amount of some additives may be beneficial.

Based on published data and discussions with researchers at PBMR (Pty) Ltd it was decided the coater should have the following characteristics:

1. Spouted bed coating of zirconia surrogate kernels
2. Gas supply for argon, hydrogen, acetylene (C_2H_2) and propylene (C_3H_6) and nitrogen purge to allow for pyrocarbon and SiC deposition
3. MTS to be used as the silicon carbide precursor
4. Operating temperature up to $1600\text{ }^\circ\text{C}$
5. Operating pressure at approximately atmospheric pressure with the possibility of increasing the operating pressure to approximately 100 kPa gauge pressure
6. Equipped with a differential pressure gauge to allow analysis of the fluidization behaviour during the coating process

Although all of the above mentioned features were designed into the coater not all were used in this study. No test work was carried out at elevated operating pressure while the differential pressure gauges were only used to study cold fluidization behaviour of particles prior to any coating test work. Also, pyrocarbon coated zirconia particles became available so no pyrocarbon coating was performed.

Although it was possible to use pure argon, or a hydrogen/argon mixture, as the carrier gas it was decided to restrict this study to using pure hydrogen. The final experimental matrix limited the deposition temperature to $1550\text{ }^\circ\text{C}$ and MTS concentration to 2.5 %. Based on characterisation of the fluidization behaviour of the particles the maximum total hydrogen flow was restricted to 15 slm.

9.1 SYSTEM DESIGN

In designing the coater the system was treated as several sub systems, each fulfilling a particular function. These systems were:

1. Instrumentation and control system
2. Heating system
3. Gas supply
4. MTS supply
5. Coating chamber
6. Exhaust system

Details of each of these will be discussed in the following sections. A schematic diagram of the complete coater system is given in Figure 27.

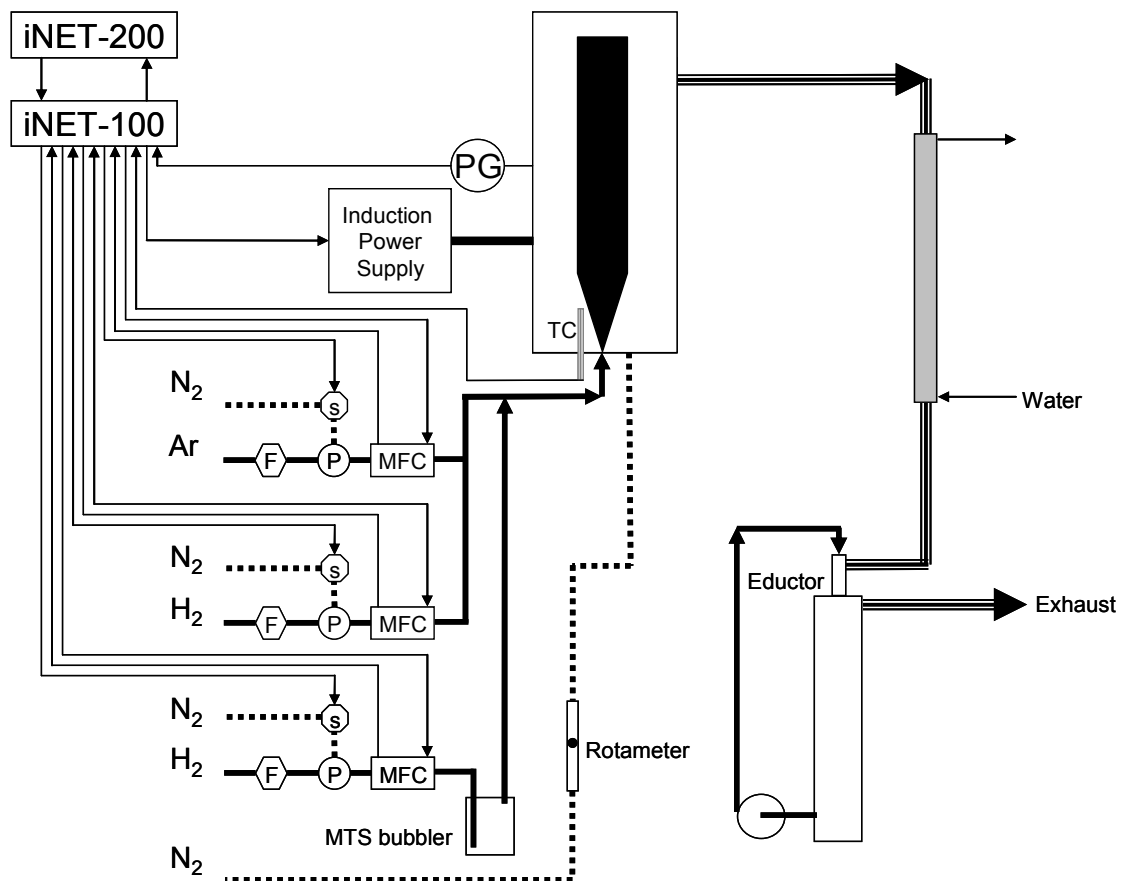


Figure 27. Simplified schematic diagram of fluidized bed coater gas supply and control system. Signal amplifiers and filters are not shown.

F: 0.5 μm filter, MFC: mass flow controller, P: pneumatic valve, S: solenoid valve, TC: type B thermocouple, PG: electronic pressure gauge

9.2 INSTRUMENTATION AND CONTROL SYSTEM

9.2.1 CONTROL HARDWARE

It was intended that the coater should be capable of completing a coating run autonomously, being capable of controlling temperature, gas flows and MTS flow without any intervention during a run. It was also required that the system would be able to measure and record process parameters for each test.

The control system was based on a desktop computer and an Omega Engineering instruNet data acquisition system consisting of an INET-100 multichannel input/output interface, an INET-200 PCI controller card and iNet-iWPLUS software. The INET-100 was capable of both analogue and digital input and output. Analogue input channels were used for measuring temperatures, pressures and gas flow rates. Analogue outputs were used for power control, gas flow control and MTS dispense rate control. Digital outputs were used for control of the gas shut off valves.

Coater temperature was measured by means of a type B thermocouple mounted adjacent to the coater tube at the point where the conical and cylindrical section join. The thermocouple was mounted in an alumina thermocouple protection sheath pressed against the coater tube. Attempts to use an uncoated thermocouple were unsuccessful due to damage to the thermocouple wire by the graphite at temperatures above approximately 1300 °C. To improve thermal contact between the thermocouple and the graphite coating tube a graphite bush was mounted over the conical section of the tube. The thermocouple, in its alumina protection tube, was inserted into the graphite bush. This arrangement was found to improve the response time significantly as well as improve the temperature uniformity within the coating tube.

Type K thermocouples were used to measure the temperature on the outer shell of the coater and at the exhaust outlet. These two measurements were used as safety checks during operation. Exceeding the maximum limit set on these temperatures resulted in the test being aborted.

The coater was designed with 2 pressure sensors, one for coater pressure and one for differential pressure across the inlet nozzle and particle bed. It was intended to use the differential pressure measurements to assess the fluidization conditions within the coater during operation. This function was never utilised during test runs due to interference caused by the induction heating system. Coater pressure was monitored during each run to check for any blockages on the exhaust system. Coater pressure measurements also were extensively used for leak testing and purging of the coater prior to each test run.

Gas flow was controlled by mass flow controllers. A 0 V to 5 V analogue signal was used to control the mass flow controller set point. Actual gas flow rates were reported by the mass flow controllers as a calibrated 0 V to 5 V analogue signal. This allowed for the gas flows, as measured by the mass flow controllers, to be recorded.

All measurement and control was done through an Omega Engineering InStrunet IO system. This allowed for 8 differential analog input channels, 8 analog output channels and 8 bidirectional digital channels. Analog input channels could be configured for various inputs, including various thermocouples. A particular problem with this system when used with a type B thermocouple was that accurate temperature measurements were not possible below a temperature of about 250 °C. Although temperatures were measured, there was a discontinuity in the reported temperature at approximately 250 °C where reported values would jump between approximately 210 °C and 250 °C.

Output current on the InStrunet digital channels was not sufficient to drive the solenoid valves directly. These outputs signals were sent to an electronic interface where the signal amplified from 5 V to 12 V and the current capacity increased. Similarly the drive current on the analog signals was increased by means of a buffer amplifier.

9.2.2 CONTROL PROGRAM

All control and data collection functions were implemented using the InStrunet scripting language. The control program consisted of a main program which handled system initiation, data file creation, calling subroutines and system shutdown under normal and emergency conditions. Specific subroutines were called for heating up, silicon carbide deposition and cooling down of the coater. Other subroutines, such as pyrocarbon deposition, could easily have been added. Each of the subroutines controlled the values and sequencing of parameters (e.g. gas flow, temperature), checked for any system errors (e.g. out of range temperature) as well as saved all measured process parameters.

Gas flows were controlled by 0 V to 5 V analog signals, the values being calculated from the required flow and the calibration curve supplied with each of the mass flow controllers. Gas shut off valves were controlled by a digital output signal, this activated the solenoid valve which then pneumatically switched the gas shut off valves.

Temperature control was by means of a Proportional Integral Differential (PID) control scheme. Due to the changing characteristics of the load and power supply characteristics with temperature different PID parameters were used for each step during heating and deposition. During the cool down step a simple proportional control algorithm was used in place of full PID control. As the temperature readings were noisy all the temperature control functions were implemented using exponentially smoothed readings. Exponential smoothing was also applied to the differential calculations and control signal.

The heating up subroutine was divided into a number of steps as listed below:

1. Fixed power of 900 W for 400 s. After this a check was done to ensure that the system was heating. A minimum temperature of 30 °C was required for the test run to continue. This was implemented to check that the thermocouple was correctly placed and that the system was operating correctly. Although this temperature was not at all accurate (see previous comments concerning the use of type B thermocouples) it did allow for the system to be tested,
2. Fixed power of 900 W until a temperature of 260 °C was achieved. At this point an accurate temperature measurement was obtained and the control system could be switched over to PID control.
3. PID control. Ramp rate: 25 °C.minute⁻¹. Target temperature: 1100 °C. PID parameters optimised for 1100 °C.
4. PID control. Ramp rate: 25 °C.minute⁻¹. Target temperature: Deposition temperature -75 °C. PID parameters optimised for target temperature.
5. PID control. Ramp rate: 10 °C.minute⁻¹. Target temperature: Deposition temperature -25 °C. PID parameters were optimised for target temperature.
6. PID control. Ramp rate: 5 °C.minute⁻¹. Target temperature: Deposition temperature. PID parameters optimised for deposition temperature.

This stepped approach allowed for system checks to be implemented, for quickly heating to deposition temperature with minimal overshoot and for accurate temperature control. During the heat up steps the argon flow was initially set to 2.8 l.minute⁻¹. Argon flow was reduced to 2.4 l.minute⁻¹ once the temperature had reached 1100 °C and finally to 2.0 l.minute⁻¹ at 75 °C below the deposition temperature. The initial flow of 2.8 l.minute⁻¹ was sufficient to prevent particles dropping out of the coater tube but not high enough for spouting. Above approximately 700 °C the argon flow of 2.4 l.minute⁻¹ was sufficient to cause the bed to slowly spout.

Once the temperature reached the desired deposition temperature the system automatically switched to the deposition step which consisted of the following steps:

1. Switch from argon to hydrogen. Argon flow was stepped down while the hydrogen flow was stepped up to the total hydrogen flow used for the deposition step. No MTS was added during this step.
2. Temperature stabilisation step of 5 minutes.
3. Switch MTS flow on. Hydrogen flow through the MTS bubbler was stepped up while the flow of hydrogen was stepped down so as to keep the total hydrogen flow constant.
4. Deposition. Temperature, hydrogen flow and bubbler flow kept constant. The deposition time was chosen to either target a specific deposit thickness or to a standard deposition time to allow for deposition rate calculation.
5. Switch from hydrogen and MTS to argon. Bubbler flow was switched off then hydrogen flow was stepped down while argon flow was stepped up to 1.6 l.minute⁻¹.
6. Purge: All gas lines, except for the bubbler supply line, were purged with argon to ensure any residual hydrogen was removed.

A typical temperature and gas flow rate history of a test run are shown in Figure 28 and Figure 29.

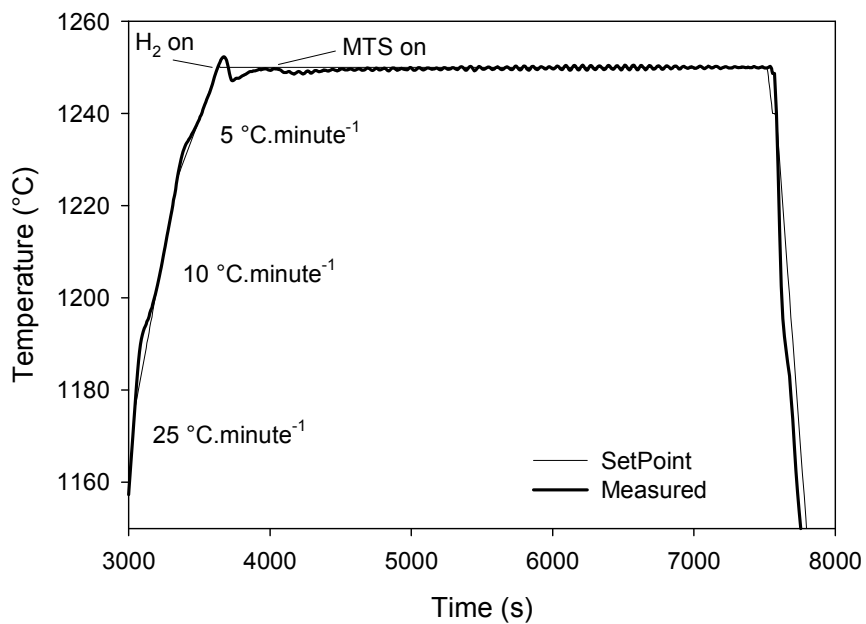


Figure 28. Temperature/time profile for a typical test run. Heating rates were constant for all test runs, temperatures at which the heating rate changed depended on deposition temperature.

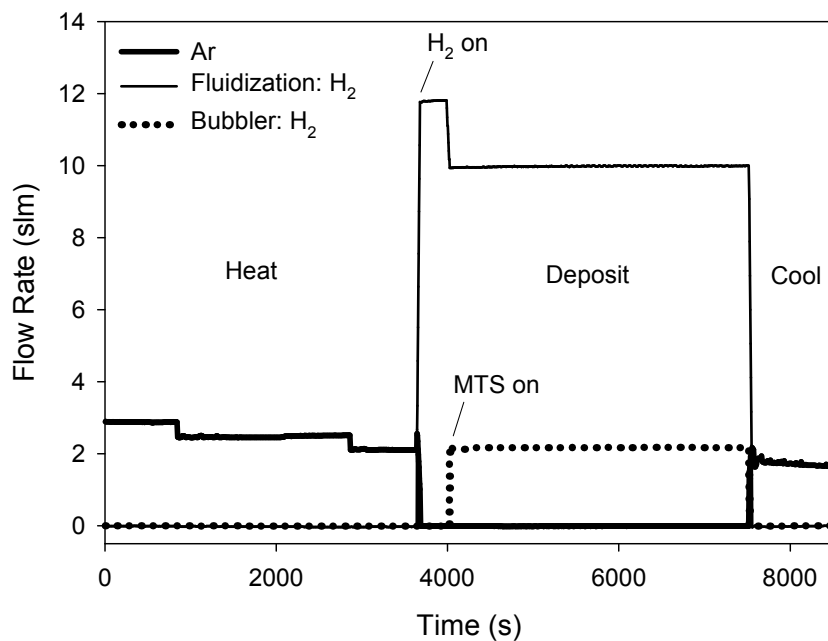


Figure 29. Gas flow sequence for a typical coating test run. Fluidization and bubbler flow rates were varied to adjust the total hydrogen flow and MTS concentration for each test run.

9.3 HEATING SYSTEM

Heating power was supplied by a 10 kW Ameritherm induction power supply capable of operating between 50 kHz and 450 kHz. An 8 turn induction coil, inner diameter of 125 mm, length of 320 mm was made of 9.53 mm (3/8") copper tubing. To prevent the coil loops from moving during operation the individual turns were bound to alumina rods with wire and epoxy adhesive. Using Wheeler's equation the coil operating frequency was estimated to be 96 kHz. Actual operating frequency of the coil was measured as 119 kHz. Results obtained using the plain coil were deemed to be quite satisfactory so no attempt was made to improve the heating uniformity by changing coil spacing or diameter.

The graphite coater tube was heated directly by the induction heater. A relatively thick wall thickness was chosen to improve heat conduction along the length of the coater tube so as to improve temperature uniformity. Also, a tube wall thicker than the skin depth ensured efficient heating of the graphite tube.

High temperature alumina fibre board discs on the inside of the coil provided insulation between the heated process tube and the water cooled copper coils. These rings also ensured that the process tube was correctly positioned in the centre of the induction coil.

A particular characteristic of the power supply was that the output voltage, not the power, was varied in proportion to the signal from the controller. This resulted in the power output being a quadratic function of the control signal. Initially it was anticipated that this would complicate the temperature control algorithm. In practice it was found that there was in fact a fairly linear temperature/control signal relationship.

9.4 GAS SUPPLY

Four gases are required to deposit all the layers making up a TRISO particle. They are:

1. Argon: used as a carrier gas during carbon deposition and as an inert fluidization gas
2. Hydrogen: carrier gas used during SiC deposition
3. Acetylene: used as a carbon precursor during buffer and dense pyrocarbon deposition
4. Propylene: used as a carbon precursor during dense pyrocarbon deposition.

Additionally nitrogen was used to purge the coater chamber prior to heating. Nitrogen was introduced into the system through a port at the bottom of the coater vessel. Nitrogen flow was controlled by a rotameter. Initially a low nitrogen flow was used for the whole test cycle; however it was found that the graphite process tube was slowly eroded during test runs. It was thought that residual oxygen in the nitrogen purge gas may contribute to the erosion so the nitrogen was used only for purging prior to heating.

Argon, hydrogen, acetylene and propylene gas lines were very similar, the only differences were the sizing of the mass flow controllers and the shut off valves. Each of the gas supply consisted of the following components:

1. 0.5 μm filter
2. Electrically operated solenoid valve. These valves were activated by signals from the control system and in turn operated the pneumatic shut off valves
3. Pneumatically operated shut off valve. Normally closed for all gasses except for Argon which was normally open. Nitrogen was used for valve activation.
4. Mass flow controller

Outside of the coating chamber the complete gas supply system was made of 6 mm stainless steel tubing. All joints in the piping were made up of Swagelok fittings.

9.4.1 MTS SUPPLY

Various options were considered for introducing MTS into the coater. Initially it was decided to use a pump to pump liquid MTS directly into the gas stream. Two pumps were tested for this purpose. Firstly a peristaltic pump with chemical resistant tubing was used. Unfortunately the repeatability of this pump was very poor due to deformation of the pump tubing. A low volume, high precision, piston pump was also tested. This failed due to the corrosive effects of MTS vapour on the pump components and a build up of silica on the pump piston.

A commonly used approach for introducing volatile compounds into a gas stream is to use a bubbler. Bubbler systems however have the disadvantage that the vapour flow rates are dependent on the temperature of the liquid as well as the pressure and flow rate of the carrier gas. A further disadvantage of bubbler systems is that when the precursor is not completely pure the composition of the vapour can change as the less volatile components are enriched in the remaining liquid. This makes accurate and predicable control of the precursor flow rates difficult. In light of the problems experienced with pumping of the liquid MTS it was decided to make use of a bubbler system.

In a bubbler the rate of evaporation can be calculated from equation 84:

$$F_l = \left(\frac{P_l}{P_s - P_l} \right) F_c \quad (84)$$

Where

- | | |
|-------|--|
| F_l | : Liquid flow rate ($\text{mol}\cdot\text{s}^{-1}$) |
| P_l | : Vapour pressure of liquid (Pa) |
| P_s | : System pressure (Pa) |
| F_c | : Carrier flow rate ($\text{mol}\cdot\text{s}^{-1}$) |

MTS vapour pressure of the liquid may be calculated using the Antoine equation:

$$P_l = 10^{\left(A - \frac{B}{C+T}\right)} \quad (85)$$

Where

P_l	: Vapour pressure of liquid (Atmosphere)
A	: 3.99703
B	: 1167.000 K
C	: -47 K
T	: Temperature (K)

Constants A, B and C are compound and state specific. The values used for liquid MTS were obtained from National Institute of Standards and Technology web site.

Bubbler temperature was controlled by placing the bubbler in an ice bath. Hydrogen flow through the bubbler was controlled by a mass flow controller. Temperature of the bubbler was measured during each test run but was not controlled except for the ice bath. It was found that during operation the temperature in the bubbler dropped by 1 °C to 2 °C.

Originally the bubbler made use of self sealing quick connects. This allowed for the bubbler to be easily removed from the coater without any leakage. Corrosion within the quick connects prevented proper operation so they were changed to Swagelok fittings and manual shut off valves for bubbler and gas line isolation.

Concentration of MTS in the feed gas was controlled by altering the fraction of hydrogen that was passed through the bubbler. An MS Excel spreadsheet was used to calculate the bubbler and main gas flows required to give the correct total gas flow and percentage MTS.

9.5 COATING CHAMBER

Details of the coating chamber are shown in Figure 30. The outer shell of the chamber consisted of a stainless steel cylinder with a removable lid. An exhaust port and pressure measurement port were attached to the cylinder close to the top end. Ports in the lid, bottom and side of the cylinder provided access and induction power feed through. Power was fed to the induction coil via 9.53 mm copper tubes attached to a Bakelite cover plate using brass Swagelok bulkhead unions. The induction coil was attached to the unions on the inside of the cover plate. Alumina fibre insulation was packed into the space between the shell and the induction coil. To ensure the coil was correctly positioned spacers were also placed between the coil and shell. Water cooled brass covers were attached to the bottom of the cylinder and on top of the lid. Normally access to the coating tube was by means of removing the bottom flange, gas feed tube and coating tube as a single assembly. Samples were loaded and unloaded through the viewing port on the top flange.

Details of the lower section of the process tube and gas inlet nozzle are shown in Figure 31. The tube consisted of a graphite tube 50 mm ID, 70 mm OD and 339 mm long. The bottom section of the tube had a conical section with a 60° included angle. A graphite ring loosely fitted onto the bottom of the tube, this included a channel for the thermocouple protection sheath to fit into. The ring improved the heat transfer between the process tube and the thermocouple, this greatly improved temperature control. The coating tube rested on the gas feed tube while the graphite ring was held in place by alumina fibre board rings fitted between the bottom flange and the process tube.

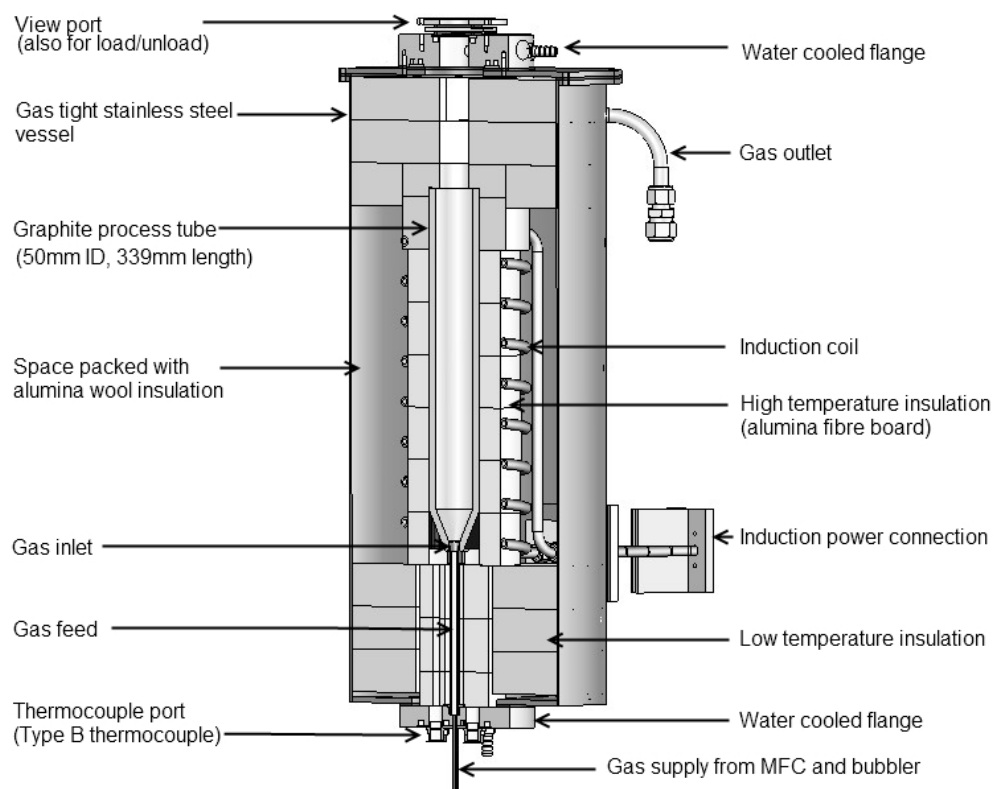


Figure 30. Cross section of coating chamber.

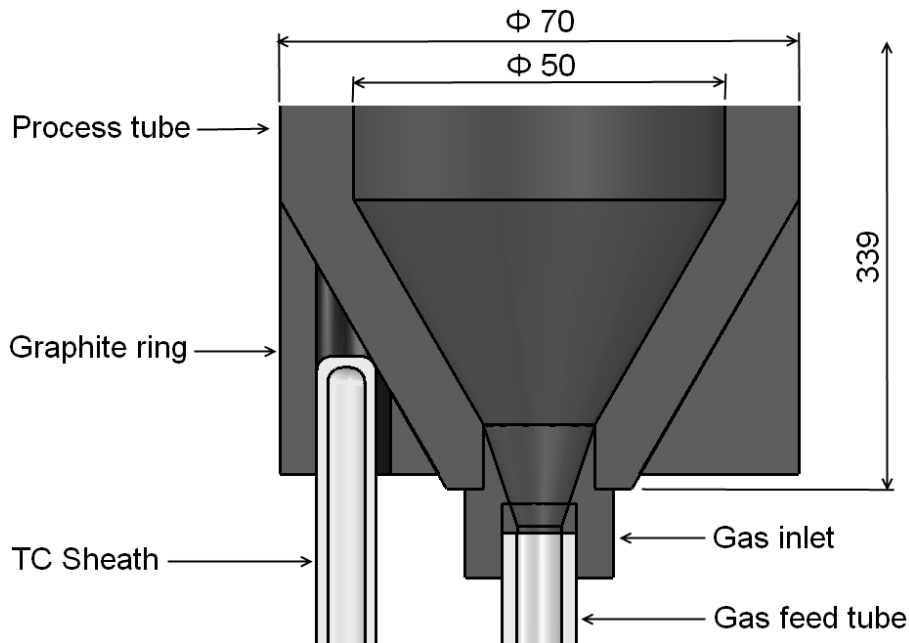


Figure 31. Details of the lower section of the process tube.

Two gas feed systems were used for introducing the gas into the process tube. Originally it was intended to use a feed tube that had no cooling. This consisted of an alumina tube 10 mm OD, 6 mm ID that was pressed into the base of the gas inlet nozzle. At the cold end the alumina tube sealed onto the bottom flange using O-rings so preventing leakage of the gas mixture into the coater chamber. Initially severe problems were experienced with this design. Heating of the feed gas resulted in silicon carbide deposition in the feed tube and, more critically, in the inlet nozzle. Heavy build up of silicon carbide in the inlet nozzle resulted in flow disturbance or complete blockage. Most of the nozzle blockage problems were overcome by making changes to the detail design of the inlet nozzle. By reducing the nozzle diameter and length the heat transfer to the alumina tube was reduced so reducing heating of the gas mixture. This reduced the deposition in the gas feed tube and nozzle. A comparison of the original and final nozzle design is shown in Figure 32. Even with the modified inlet design each inlet could only be used once due to deposition in the inlet.

As a result of the problems experienced with nozzle blockage, a cooled feed tube was also used. This consisted of a water cooled copper tube that pressed into the base of the inlet nozzle. The same design of inlet nozzle was used for non cooled and cooled gas feed. Details of the two feed systems are shown in Figure 33. No problems were experienced with the cooled gas feed system. For most test runs using the cooled gas feed the nozzle could have been used for several test runs however the nozzle was replaced after each test.

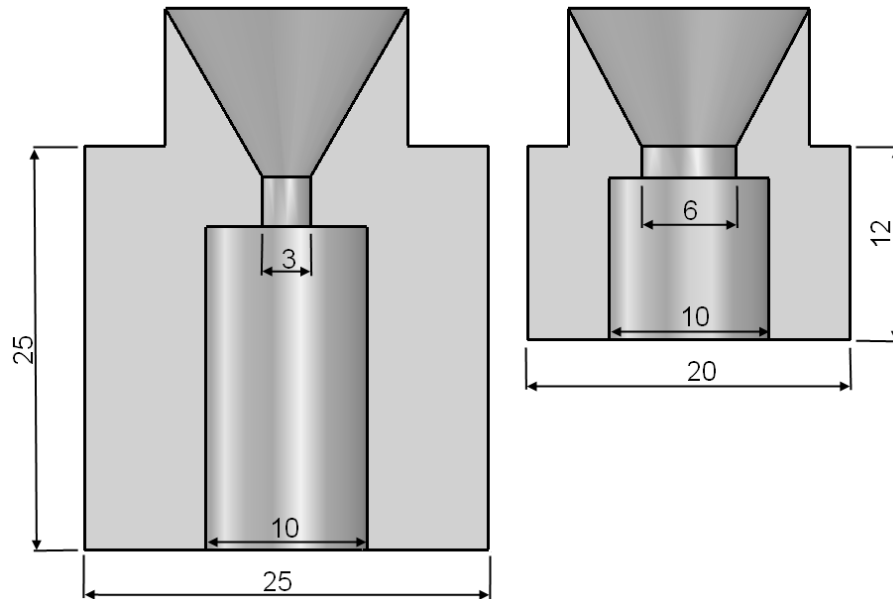


Figure 32. Comparison of original and final inlet nozzle dimension.

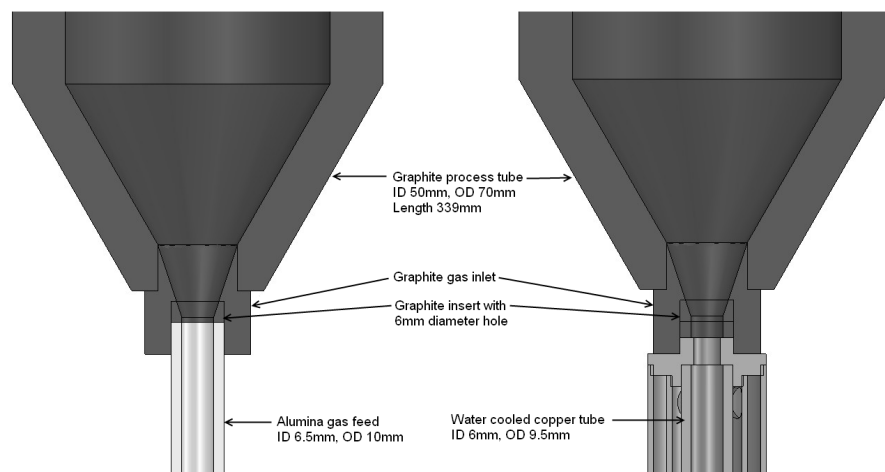


Figure 33. Comparison of non-cooled and cooled gas inlet.

The size of the inlet was determined by a hole drilled through a moulded graphite insert that was placed between the gas feed tube and the inlet nozzle. This allowed for flexibility in terms of the inlet diameter. For all experimental runs a 6 mm inlet was used. Inlet diameter was in a large part governed by the requirement of making the inlet large enough to avoid blockage of the non-cooled gas feed.

9.6 EXHAUST SYSTEM

Two requirements had to be met by the exhaust system:

1. Safely remove and dispose of the hot hydrogen from the coater
2. Ensure any HCl generated during the coating process is neutralised

To dispose of the off gas stream it was first cooled, scrubbed to remove the HCl and then dispersed to atmosphere. Cooling of the gas stream was carried out in a single tube counter current heat exchanger mounted close to the coater outlet. Dispersal of the hydrogen was achieved by exhausting the cooling/dilution air across the exhaust outlet. To minimise the risk of flashback into the scrubber a copper mesh flashback arrestors was installed on the exhaust outlet.

An eductor scrubber was used for removing HCl and any particulates from the exhaust gas. A Na_2CO_3 solution was used as the scrubber solution, this effectively neutralised the HCl in the exhaust gas. The eductor had the advantage that it would be able to remove particulates in the gas stream without the risk of clogging. A feature of the eductor scrubber was that it provided some pumping of the exhaust gas ensuring that there was no pressure build up in the coater. This characteristic may have inadvertently caused problems with the MTS bubbler system in that the coater chamber pressure was not controlled thus potentially influencing the MTS vapour flow rate. Unfortunately the exact operating pressure of the coater could not be determined during operation due to the induction power supply interfering with the electronic pressure gauge.

9.7 SYSTEM SETUP

9.7.1 MTS SUPPLY

Average MTS flow rate was calculated by weighing the MTS bubbler before and after each test run. Initially the amount of MTS delivered was very close to that predicted using equations 84 and 85. After test run DR13 the bubbler invariably delivered a higher flow than calculated. The cause of this sudden discrepancy was never determined. Other problems with the MTS feed system were caused by a faulty MFC and blockage of the gas distributor in the bubbler.

Difficulty in controlling MTS flow rate undoubtedly impacted on the results obtained. As will be shown in chapter 12, MTS flow influenced the deposition rate and a number of material properties. Variation in MTS concentration made targeting a specific silicon carbide layer thickness difficult. The impact of MTS concentration variation on the final results were expected to be minimal as the actual MTS concentration, calculated from the total mass of MTS used, was used for all analyses.

9.7.2 INSTRUMENTATION CALIBRATION

Both the absolute and differential pressure gauges were calibrated against U-tube manometers. In the case of the absolute pressure gauge a mercury column was used while a water column was used for the differential pressure gauge. Calibration data was entered into the iNET software calibration tables so that calibrated pressure readings were recorded directly.

A calibrated type S thermocouple was used to measure the offset of the type B control thermocouple and type S thermocouples used for temperature profiling. The three thermocouples were simultaneously heated in a small tube furnace and the temperature offsets calculated. Temperature offsets for the type B control thermocouple and type S profile thermocouple were entered into the iNET software calibration tables. Instrumentation bias was checked by comparing the values measured by the iNET hardware to values measured using an external instrument.

9.7.3 POWER SUPPLY SET UP

To ensure maximum power transfer between the induction power supply and the susceptor the power supply needed to be matched to the load. This is standard procedure for setting up of the power supply. Results of the voltage, current and power output as a function of set point are presented in Figure 34. These values are reported by the power supply as a percentage of maximum value. From the percentage volts versus set point it can be seen that the control signal was linear without any offset. Matching between the power supply and load was good as can be seen by the close matching between the power supply output voltage and current. Similar plots were produced for various power supply tuning options.

Due to the power supply working on voltage control the output power would theoretically increase as a quadratic function of the set point. Initially it was anticipated that this would cause problems with the ability to control the temperature accurately using a standard PID controller. From Figure 35 it can be seen that there is an approximately linear relationship between temperature and set point. This is probably as a result of the power supply current not increasing at the same rate as the voltage as well as the higher losses as the temperature increased. As expected more power, i.e. a higher set point, was required with gas flowing through the coating tube. When high volumes (14 slm) of hydrogen were used at high temperature (1490 °C) the power supply was typically operated at voltage set points of about 90 % for the cooled and 78 % for the non-cooled inlets.

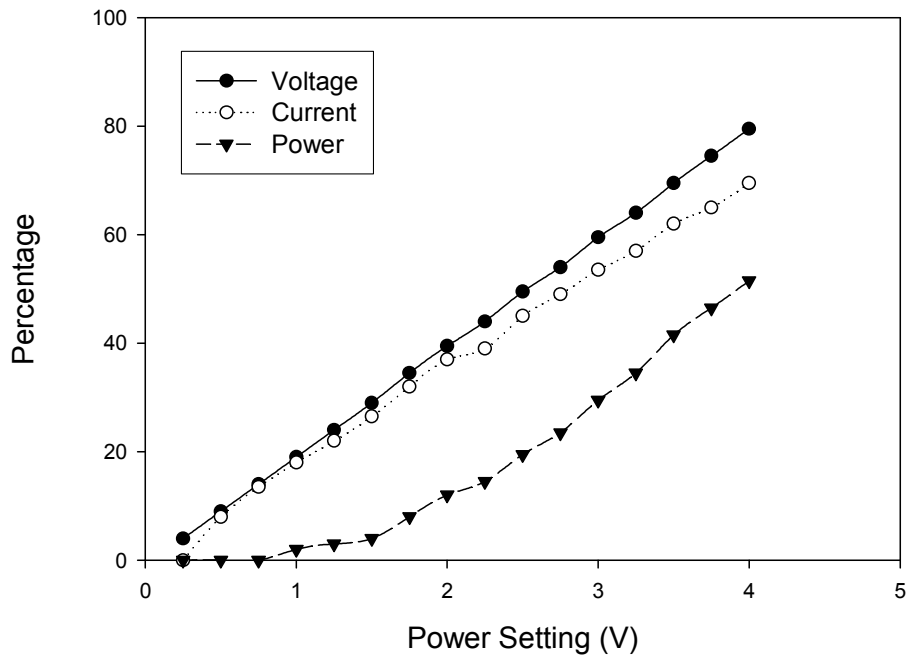


Figure 34. Power supply percentage voltage, current and power as a function of set point.

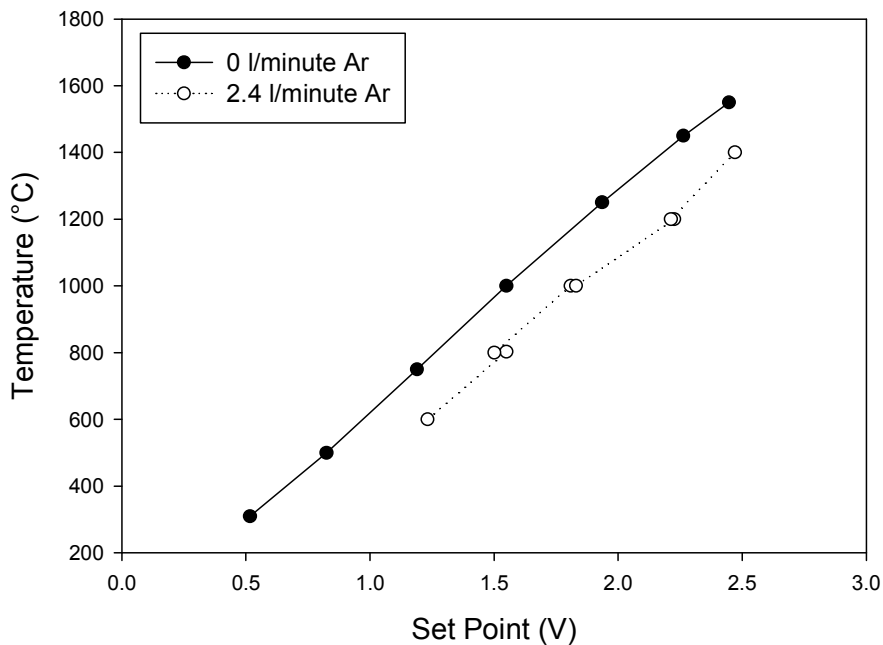


Figure 35. Measured process tube temperature versus controller set point.

9.7.4 TEMPERATURE CONTROLLER TUNING

An open loop method was used to tune the PID parameters. A dedicated control program was written to perform the tests. The procedure involved the following steps:

Using an estimated set of PID parameters the coater was heated to a set point and allowed to stabilise for 5 minutes.

Power was increased to a fixed value higher than required to maintain the set point.

Increasing temperature was recorded for 30 minutes.

A First Order Plus Dead Time (FOPDT) model was fitted to the temperature/time data using Excel. From this the process gain, dead time and time constant were obtained. Although the process gain was calculated the average process gain obtained from the slope of the data presented in Figure 35 was used in the later steps.

From the data obtained in step 4 the proportional gain, K_p , integral time, T_i , and derivative time, T_d , for each of the temperatures tested was calculated using equations 86, 87 and 88 listed below. Steps 1 to 5 were repeated for temperature set points of 600 °C, 800 °C, 1200 °C and 1400 °C.

Integral gain, K_i , and derivative gain, K_d , were calculated by multiplying the integral time and derivative time by the proportional gain.

A linear equation of integral gain and derivative gain as a function of temperature was estimated. These values were used to calculate PID values for each of the temperature set points used in the control program. A fixed proportional gain value was used as this parameter was found to be independent of temperature.

$$K_p = \frac{1.357}{K} \left(\frac{\tau}{\alpha} \right)^{0.947} \quad (86)$$

$$T_i = \frac{\tau}{0.842} \left(\frac{\alpha}{\tau} \right)^{0.738} \quad (87)$$

$$T_d = 0.381\tau \left(\frac{\alpha}{\tau} \right)^{0.995} \quad (88)$$

Where

K_p : Proportional gain ($V \cdot ^\circ C^{-1}$)

T_i : Integral time (s)

T_d : Derivative time (s)

K : Process gain ($^\circ C \cdot V^{-1}$)

α : Dead time (s)

τ : Process time (s)

Using the procedure described above allowed for PID parameters best suited to the temperature set point for each program step to be calculated.

9.7.5 FLUIDIZATION TEST

It was originally intended to determine the fluidization conditions within the coater by measuring the pressure drop across the gas inlet. It was anticipated that pressure drop information would allow for determining the minimum flow required for proper spouting as well as an assessment of the fluidization conditions within the coater. Initially cold tests were conducted using argon as a fluidizing gas. A typical plot of pressure drop across the bed of particles versus argon flow rate is shown in Figure 36.

As anticipated the pressure drop increased with increasing flow rate and then reached a point where the pressure decreased rapidly. It was expected that this would be the point where spouting would be initiated, however the fountain of particles only formed at much higher flow rates. As can be seen in Figure 36 the fountain only formed after a second smaller pressure drop was recorded. It is thought that the initial pressure drop was as a result of an internal spout forming.

Measurement of the pressure drop required to initiate spouting of a 40 g sample using hydrogen gas were not successful as the flow rate required to initiate spouting was higher than the MFC capacity. Using a 3 mm gas inlet the initial pressure drop was recorded at a hydrogen flow of approximately 24 slm. The fountain would have formed at a flow rate of more than 30 slm.

High temperature measurements using hydrogen gas were also attempted. Although the bed could be made to spout electronic interference from the power supply prevented pressure measurements. From visual observation of the bed a flow rate of 8 slm was the minimum required to form a fountain using hydrogen at high temperatures (≥ 1200 °C). The effect of temperature on gas viscosity, and so on spouting, was seen during coater heat up. For a fixed argon flow of 2.8 slm there was no movement of particles in the bed at room temperature when the test runs were started. Once the temperature had increased to approximately 700 °C a fountain would form. This remained stable at higher temperatures even when the argon flow rate was reduced to 2 slm.

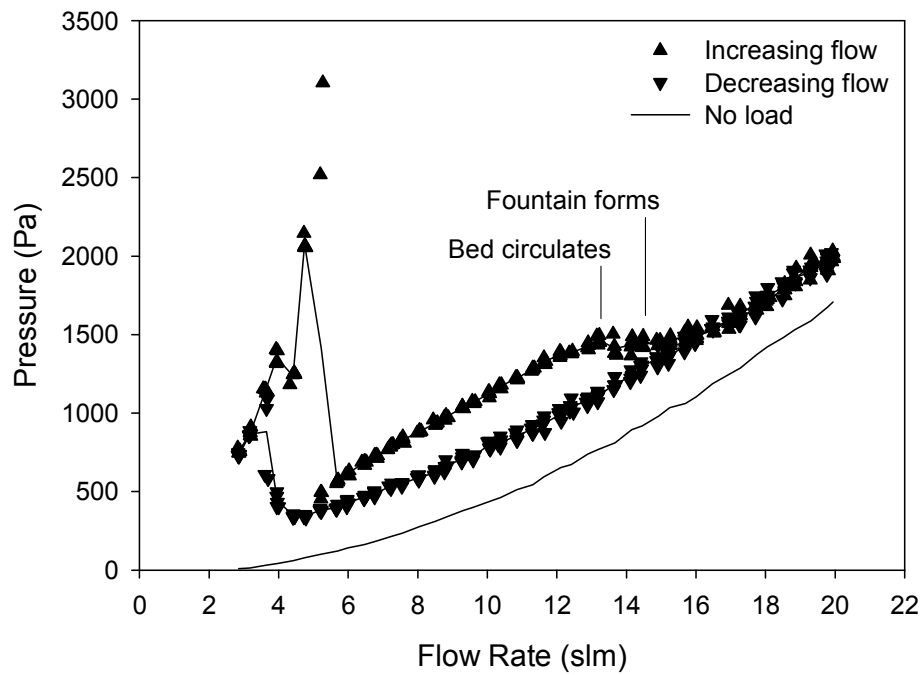


Figure 36. Pressure drop across the particle bed as a function of argon flow rate. Test conducted at room temperature using a 40 g load of carbon coated surrogate particles. No load: Pressure drop across gas piping and inlet with no particles loaded. Bed circulates: Flow rate at which the bed of particles starts to move steadily. Fountain forms: Flow at which a fountain of particle forms above the gas inlet.

10 EXPERIMENTAL PLAN AND PROCEDURES

10.1 INTRODUCTION

Coating test runs could be divided into the following groups:

1. Set up testing: used to confirm correct operation of the coater hardware and system software and to calibrate various systems, particularly MTS flow rate.
2. Deposition rate determination: A full factorial experiment used to determine the deposition rate of the hot inlet. These tests were carried out so as to be able to target a thickness of $35 \mu\text{m} \pm 5 \mu\text{m}$ for the following tests.
3. Hot inlet test matrix: A central composite experiment intended to investigate the impact of processing parameters. These test runs constituted the main group of experimental runs for the hot inlet.
4. Cold inlet deposition rate: A full factorial experiment to determine the coating rate using the cold gas inlet. Conditions for this group of test runs were chosen so that the test matrix could be expanded to give a central composite experimental design.
5. Cold inlet test matrix: A set of experiments intended to supplement the tests in group 4 above to create a central composite experiment.
6. Thickness test: A set of single parameter tests run to specifically target a variety of thicknesses. These tests were run so as to be able to check the sensitivity of crush testing to deposit thickness. They were all run using the cold gas inlet using conditions that were not part of the experimental plan of group 4 and 5 combined.

Note: For brevity the 2 inlet types will be referred to as the “hot” inlet when referring to the non-cooled inlet and “cold” when referring to the cooled inlet.

In the above schema the full factorial plans included repeated centre points while the central composite plans consisted of a full factorial, repeated centre points and axial, or star, points. The central composite design was chosen for its efficiency (i.e. ability to obtain useful data with a minimum number of test runs). Central composite design experiments provide sufficient data for interaction and second order effects to be modelled. A complete discussion of design of experiment, including the central composite design may be found in many statistical texts, for example [287]

During set up testing (Group 1) two major problems with the coater design came to light. Firstly, the MTS pumping system proved to be unusable due to frequent, and expensive, pump failures. Secondly, the hot gas inlet system resulted in blockage of the gas inlet. Problems with the MTS supply were solved by making use of a bubbler instead of pumping liquid MTS into the gas stream. Inlet nozzle blockage problems were solved by changing the design of the inlet nozzle and later by making use of a cold gas inlet. Inlet blockage problems were not fully resolved until after most of the Group 2 tests had been completed. As the gas inlet temperature could have a significant effect on the deposit properties it was decided to investigate the impact of using a hot versus a cold gas inlet. To keep the number of experimental runs

manageable it was then decided to remove load size as an experimental variable. This decision was made after the hot deposition rate tests (Group 2) had been completed.

Initially the tests in Group 2 were run using a fixed deposition time of 60 minutes. Once deposition rate data became available it was possible to adjust the deposition time to target a thickness of 35 μm . It was anticipated that for those tests that were correctly targeted the results could later be used in place of Group 3 test runs. Due to changes in the experimental plan this did not happen and these tests were only used to determine the deposition rate and crush strength. As it was found that deposition rate could be predicted accurately before the complete matrix had been completed not all the planned deposition rate tests were run.

Tests using the cold gas inlet were divided into 2 groups. The first (Group 4), a full factorial experiment, was intended to determine the deposition rate while using the cold gas inlet. For these tests the deposition rate model determined from Group 2 was initially used to calculate the deposition time to target a deposit thickness of 35 μm . As the tests proceeded the deposition rate model was updated to more accurately reflect the deposition rate using the cold inlet. Depending on the outcome of these tests it was planned to either:

1. Supplement the full factorial design with additional tests to create a central composite design. This option was to be followed if the deposit thickness obtained from the deposition rate test runs was sufficiently close to the 35 μm target thickness.
2. Complete a full central composite experiment using the deposition rate data previously obtained to target a deposit thickness of 35 μm .

As it turned out, the deposition rates achieved using the cold inlet was similar to those achieved with the hot inlet. Deposits obtained during the deposition rate experiments were approximately within the 30 μm to 40 μm thickness range targeted. As a result only the supplementary tests were required to complete a full central composite experimental plan.

10.2 EXPERIMENTAL PARAMETERS

Originally it was planned to investigate the following variables:

1. Temperature: furnace set point temperature as measured on the outside of the conical section of the process tube
2. MTS concentration: volume percentage MTS in the total gas flow
3. Hydrogen flow: total hydrogen flow through the bubbler and by-pass
4. Load: mass of pyrocarbon coated zirconia particles coated

Due to the decision to include both gas inlet types as a variable, “Load” was removed as a variable. This decision was made after Group 2 had been completed. As a result some data on the effect of load on deposition rate and efficiency was available for the hot gas inlet.

10.3 EXPERIMENTAL PLAN

A complete listing of all the planned experiments is presented in Table 18 to Table 22. All values listed in these tables are target values; these may differ from the actual values obtained. Additional calibration runs for which some response parameters were measured are listed in Table 23. In this case actual measured values for MTS concentration and hydrogen flow rate are listed. A complete list of actual experimental conditions is given in Appendix A.

Actual test run numbers are included in the tables. Data in the tables are presented in standard format, as the tests were conducted in a randomised order the run numbers are not in numeric order. For centre points, and when the deposit thickness was not acceptable, tests were repeated. In these cases 2 or more test run numbers are listed for each set of conditions. For 3 test runs (CR6, CR7, CR23) no results were obtained due to equipment problems. Test run HF2 completed but the thickness was well below target. These test runs are not listed.

Initially the test work was started with starting material CPT-T-G130. This particular lot was chosen as it had the smallest variation in particle size. Due to the decision to include test work using the cold gas inlet it was uncertain if this lot would be large enough to complete all test work. As a result of this it was decided to switch to starting material lot CPT-T-G140. While doing crush tests it was found that there were significant differences in crush strength between particles from the 2 lots of starting material. As a result of this it was decided to repeat all runs started using CPT-T-G130 using particles from CPT-T-G140. Test runs CR1, CR2, CR3, HF1, HF3, HF4, HF5 and HF6 were repeated.

A graphical representation of the experimental conditions used for the central composite design experimental matrix (i.e. hot inlet experiments in group 3 and cold inlet experiments in group 4 and 5) is shown in Figure 37.

Table 18. Group 2: Hot inlet deposition rate. Parameter values and test matrix.

PARAMETER		-★	-	0	+	+★
Temperature	°C		1350	1450	1550	
% MTS	%		0.75	1.50	2.25	
Hydrogen Flow	slm		12.5	15.0	17.5	
Load	g		20	40	60	
#	TEMPERATURE (°C)	MTS (%)	HYDROGEN (slm)	LOAD (g)	TEST #	
1	1350	0.75	12.5	20	DR18	
2	1550	0.75	12.5	20	Not run	
3	1350	2.25	12.5	20	DR6	
4	1550	2.25	12.5	20	DR24	
5	1350	0.75	17.5	20	DR23	
6	1550	0.75	17.5	20	DR12	
7	1350	2.25	17.5	20	DR19	
8	1550	2.25	17.5	20	DR22	
9	1350	0.75	12.5	20	DR20	
10	1550	0.75	12.5	60	Not run	
11	1350	2.25	12.5	60	DR25	
12	1550	2.25	12.5	60	Not run	
13	1350	0.75	17.5	60	DR3, R21	
14	1550	0.75	17.5	60	Not run	
15	1350	2.25	17.5	60	DR17	
16	1550	2.25	17.5	60	DR5, DR9	
17	1450	1.50	12.5	40	DR1, DR26	

Table 19. Group 3: Hot inlet central composite design. Parameter values and test matrix.

PARAMETER		-★	-	0	+	+★
Temperature	°C	1250	1310	1400	1490	1550
% MTS	%	0.5	0.9	1.50	2.1	2.5
Hydrogen Flow	slm	10.0	11.0	12.5	14.0	15.0
#	TEMPERATURE (°C)	MTS (%)	HYDROGEN (slm)	TEST #		
1	1310	0.9	0.9	HF11		
2	1490	0.9	0.9	HF15		
3	1310	2.1	0.9	HF1, HF21, HF22		
4	1490	2.1	0.9	HF18		
5	1310	0.9	2.1	HF7		
6	1490	0.9	2.1	HF4, HF5, HF23		
7	1310	2.1	2.1	HF8		
8	1490	2.1	2.1	HF13		
9	1250	1.5	12.5	HF19		
10	1550	1.5	12.5	HF17		
11	1400	0.5	12.5	HF14		
12	1400	2.5	12.5	HF12		
13	1400	1.5	10.0	HF6, HF24		
14	1400	1.5	14.0	HF10		
15	1400	1.5	12.5	HF3, HF9, HF16, HF20, HF25		

Table 20. Group 4: Cold inlet deposition rate. Parameter values and test matrix.

PARAMETER		-★	-	0	+	+★
Temperature	°C		1310	1400	1490	
% MTS	%		0.9	1.50	2.1	
Hydrogen Flow	slm		11.0	12.5	14.0	
#	TEMPERATURE (°C)	MTS (%)	HYDROGEN (slm)	TEST #		
1	1310	0.9	11.0	CR11		
2	1490	0.9	11.0	CR3		
3	1310	2.1	11.0	CR10		
4	1490	2.1	11.0	CR12		
5	1310	0.9	14.0	CR13		
6	1490	0.9	14.0	CR6		
7	1310	2.1	14.0	CR5		
8	1490	2.1	14.0	CR4		
9	1400	1.5	12.5	CR1, CR2, CR9		

Table 21. Group 5: Cold inlet supplementary tests. Parameter values and test matrix.

PARAMETER		-★	-	0	+	+★
Temperature	°C	1250		1400		1550
% MTS	%	0.5		1.5		2.5
Hydrogen Flow	slm	10.0		12.5		15.0
#	TEMPERATURE (°C)	MTS (%)	HYDROGEN (slm)	TEST #		
1	1250	1.5	12.5	CR18		
2	1550	1.5	12.5	CR14		
3	1400	0.5	12.5	CR16, CR17, CR25, CR26, CR27		
4	1400	2.5	12.5	CR20, CR21, CR22		
5	1400	1.5	10.0	CR19		
6	1400	1.5	15.0	CR24		
7	1400	1.5	12.5	CR15, CR28		

Table 22. Group 6: Thickness test parameter values.

TEST #	TEMPERATURE (°C)	MTS (%)	HYDROGEN (slm)	TIME (minute)
TT1	1355	1.8	11.8	39
TT2	1355	1.8	11.8	69
TT3	1355	1.8	11.8	48
TT4	1355	1.8	11.8	28
TT5	1355	1.8	11.8	55

Table 23. Additional calibration test runs.

TEST #	TEMPERATURE (°C)	MTS (%) ^(*)	HYDROGEN (slm) ^(*)	TIME (minute)
TR12	1200	2.1	11.1	28
TR13	1200	1.3	10.2	30
TR14	1200	0.7	9.5	30
MTS1	1200	2.2	12.1	60

(*)Measured values

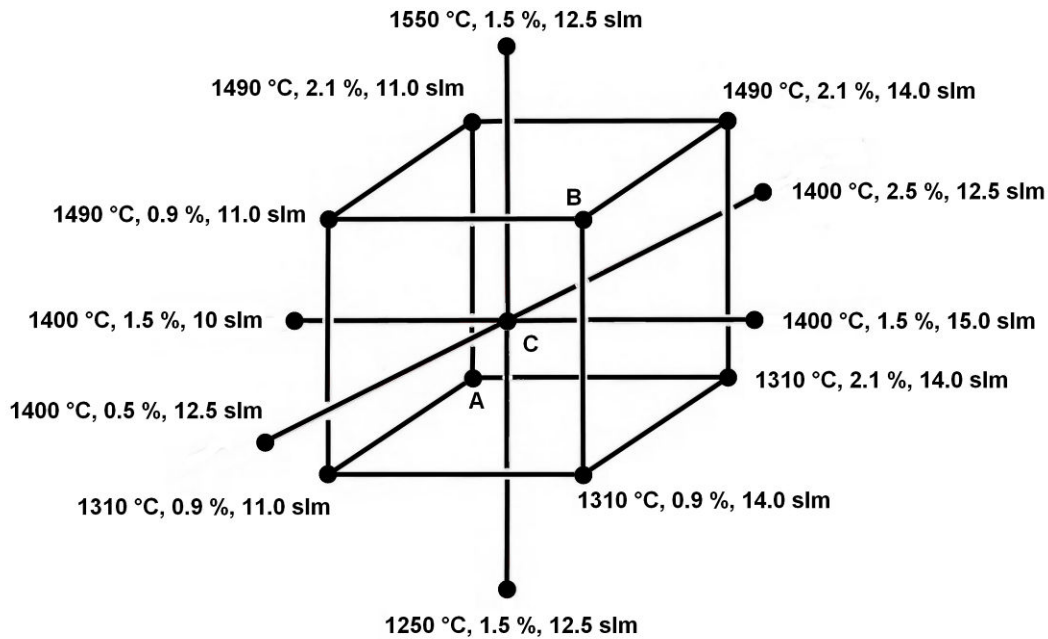


Figure 37. Graphical presentation of experimental plan. Full factorial points are represented by the cube corners, centre points by C and axial points by the points outside of the cube. Planned values are shown, actual experimental values obtained are presented in Appendix A. Values not shown in the diagram:

A : 1310 °C, 2.1 %, 11.0 slm
B : 1490 °C, 0.9 %, 14.0 slm
C: 1400 °C, 1.5 %, 12.5 slm

10.4 TEST RUN PROCEDURE

All tests were carried out using zirconia surrogate particles that had previously been coated with a buffer and inner pyrolytic carbon coating. Three separate lots of starting material were used:

1. CPT-T-G133: used only for set up testing
2. CPT-T-G130: deposition rate and runs CR1 to CR3 and HF1 to HF6
3. CPT-T-G140: all remaining experimental runs

As the starting material was pre-coated with carbon no carbon deposition steps were carried out.

Prior to starting the tests aliquots of approximately 50 g each were split from the starting material batch by repetitively splitting using a riffle splitter. Enough aliquots were split out for all the tests to be carried out prior to the start of test runs. These were used randomly. Immediately prior to each test run a sample of 40.0 g was weighed out from one of the portions.

For each test run the amount of MTS used was calculated by weighing the bubbler immediately before and after the test run. After the initial weighing the bubbler was placed into an ice bath so that the MTS temperature could equalise prior to the start of the deposition step. During each test run the bubbler temperature was controlled by an ice bath.

A fresh gas scrubber solution of NaCO_3 was made up for each test run. Based on the expected MTS consumption the amount of NaCO_3 required to neutralise the HCl released during the deposition step was calculated. An excess of approximately 20 % NaCO_3 was used to ensure that all the HCl released would be absorbed by the exhaust scrubber. As a check, the pH of the solution was measured before and after each run. Except for test runs with known MTS supply problems the wash solution had a pH of approximately 9 after each run.

As the coater was opened between each test run so that new gas inlets could be installed it was necessary to purge any air from the system before commencing a test run. This was achieved by repetitively pressurising and depressurising the coater chamber with inert gas. At least 5 cycles were used. In addition to the purging the leak testing also served as an additional purge cycle.

After purging the integrity of the coater chamber was checked before each run by conducting a leak test on the system. This involved pressurising the coater to 100 kPa using argon gas then isolating the chamber. The pressure drop was then measured over a period of time. Initially a procedure was used where the actual leak rate was calculated. For later test runs a simpler approach was used whereby the coater was deemed to be gas tight if the pressure remained above 95 kPa after 40 minutes. This procedure proved to be very effective at checking the integrity of the system; a number of problems were picked up in this way. Problems were however experienced with the exhaust shut off valve leaking during the leak tests resulting in a false test failure. The shut off valve was open during a test run so a leaking valve was of no consequence for the test run.

For each test run a new copy of the control program with the test parameters applicable to the test was created. Before conducting the tests the parameter values in the control program were checked by running a test routine that recorded the test parameter values. These were then checked against the intended parameter values. This procedure provided a means of double checking the test parameters and recording the actual parameters used for each test.

Once the coater and control program had been verified the sample was loaded into the process tube. To do this the nitrogen chamber purge valve was opened and argon flow manually set to maximum. The top port was then opened and the sample poured into the process tube through a tube inserted into the port. Once the sample was loaded the port was sealed and the run started. After starting the run the nitrogen purge was shut off. Although the coater was opened to atmosphere while the particles were being loaded the high gas flow ensured that this would be minimised. Any air which did enter would be purged out by the argon flow during the heat up. Heating up to deposition temperature took at least 1 hour.

After starting the control program the test run proceeded automatically without requiring any further actions. In practice some intervention was required. To improve safety the hydrogen supply valves were only opened shortly before hydrogen was required by the system. Similarly the MTS bubbler isolation valves were only opened immediately prior to deposition. Both hydrogen and MTS would be turned off immediately after completion of the deposition step. It was also standard for the exhaust scrubber to be run only during the deposition step, normally the scrubber would be turned on a few minutes before the hydrogen flow was activated and then left on until the test run ended.

After the test run ended the system was allowed to cool down to the point where the sample could be removed from the coater. Most of the sample was removed from the top of the coater with a vacuum system. Some sample was removed from the bottom via the vent tube; this portion of sample was kept separate as it often contained particles that had dropped out of the bed without being coated.

Although the test runs were randomised it was normal to alternate test runs using the hot and cold gas inlet. This was a practical matter as the alternate inlet system could be prepared while a test run was in progress. A single process tube was used at a time, so although the inlet system was alternated the same process tube would be used.

11 SAMPLE PREPARATION AND ANALYSIS

In this chapter the procedures used for preparing and analysing samples will be described. All raw results are presented in the appendices. Theoretical aspects of the test methods used are discussed in Chapter 8.

11.1 SAMPLE PREPARATION

11.1.1 SAMPLE MOUNTING

Samples that were to be used for hardness, fracture toughness and optical thickness measurements were mounted in epoxy resin. For each test run approximately 30 to 40 particles were mounted together. The procedure used ensured that all the samples were mounted on the same plane and in a regular pattern. This made it easier to ensure that the particles were all polished to the same cross section and made it easier to identify particles that had been indented. It was also desirable to have the samples level and on the same thickness to make focussing under the microscope and in the SEM easier. Several methods were tried before a reliable mounting method was developed; some of these are briefly discussed below.

Initially it was attempted to stick particles onto a piece of graph paper, paste the graph paper onto the base of a standard 25 mm mounting mould and then cast the epoxy resin into the assembled mould. The graph paper served as a template to create an array of evenly spaced particles. By pasting the graph paper with the attached particles onto the mould base it was intended to get all the particles onto a flat plane. Three problems were experienced with this method. Firstly, the paper invariably lifted off of the mould base resulting in the particles not all being on plane. This problem was experienced using both epoxy resin and stationary glue stick as the adhesive. Secondly, it was difficult to ensure that exactly the same amount of epoxy resin was used for each set of samples. As a result the sample mount thickness varied making microscope and SEM work more difficult. Finally, it was also difficult to ensure that the samples were perfectly horizontal while the epoxy resin was setting. This resulted in the ends of the sample mounts not being parallel. This made maintaining focus while moving sample under the microscope tedious, especially in the SEM.

The following method was found to give very good results: Perspex rings, 25 mm outside diameter and 15 mm length, were used as a mould for the mounting resin. A strip of graph paper was stuck to the back of a microscope slide – this made it possible to arrange the particles into a regular pattern. A circle the same diameter as the inside diameter of the Perspex ring was marked on the graph paper to make it easier to ensure that all the particles were placed so as to fit into the ring. A strip of double sided tape was mounted to the front of the microscope slide and the particles stuck onto the tape. A Perspex ring was then stuck onto the double sided tape forming a mould into which the epoxy resin could be cast. Struers Epofix or Akasel Aka-cure epoxy resin was used. The resin was heated to approximately 40 °C to 50 °C to reduce the viscosity, degassed under vacuum and then cast into the Perspex

rings while still under vacuum. Samples were then held under vacuum for several minutes to ensure that gas bubbles were removed from the samples before the vacuum was released. Samples were cured at 50 °C until the resin had set completely.

Despite the care taken in trying to eliminate bubbles in the sample mounts it was found that small bubbles were often trapped around the particles. These were filled with resin after grinding, prior to polishing. An advantage of re-impregnating the sample after grinding was that the kernels were also bonded into the coated particle, thus preventing the kernels from breaking free during polishing.

Samples for electron microprobe analysis were mounted using Buehler Probemet, a conductive copper filled compression mounting resin. Making use of a conductive mounting resin allowed for SEM and microprobe analysis without the need for coating the particles. Two particles from each test run were stuck to a piece of graph paper which was then stuck to the piston of the mounting press. Samples were heated to 150 °C for 9 minutes and then cooled for 10 minutes. Mounting pressure was set to 100 kPa. The recommended pressure for this type of resin is 420 kPa but it was found that the particles fractured if the mounting pressure was higher than approximately 100 kPa.

11.1.2 POLISHING

Samples were ground and polished on a ATM Saphir 550 automatic polishing machine. Grinding and polishing parameters are listed in Table 24.

Table 24. Grinding and polishing method

Step	Grit	Disc	Lubricant	Time (minutes)
1	600 mesh Diamond	AKA Piato 600	Water	20+
2	1200 mesh Diamond	AKA Piato 1200	Water	8
3	9 µm Diamond	AKA Plaran	Aka-Lube Blue	10
4	3 µm Diamond	AKA Paran	Aka-Lube Blue	10
5	1 µm Diamond	AKA Napal	Aka-Lube Blue	5
6	0.1 µm Colloidal silica	AKA Chemal	None	5
7	0.05 µm Colloidal silica	AKA Chemal	None	5

All grinding and polishing was carried out with a force of 25 N applied to each sample and a platen speed of 150 rpm. Grinding was initially done in steps of 4 minutes with a microscopic inspection after each 4 minutes cycle. The intention being to coarse grind to a point where fine grinding and polishing would result in the particles polished to mid-way through the particle. This was not always easy to control. To ensure that the sample surface was ground square it was found best to grind in multiple short steps rather than a single long step.

11.1.3 ETCHING

To investigate grain structure samples mounted in epoxy resin and polished using the full sequence listed in Table 24 were etched using a Murakami etch. Etch solution was made up of equal parts of hot saturated solutions of NaOH and $K_3Fe(CN)_6$ heated to boiling point. Samples were floated in the solution face down while the solution was continuously heated in a microwave oven. Etch time was 20 minutes.

Etch response of the deposits formed under differing process conditions varied significantly. As samples from each group of tests (hot inlet, cold inlet and thickness tests) were mounted together, samples for each group were etched identically.

11.1.4 POWDER SAMPLES

For X-ray diffraction and direct measurement of the density silicon carbide was separated from the pyrocarbon and zirconia kernels using the following method:

1. Coated particles were coarsely crushed to expose the pyrocarbon. To avoid breaking the zirconia kernels, and keep the surface area of the silicon carbide to a minimum, care was taken to avoid crushing the particle to a fine powder.
2. Pyrocarbon was removed by oxidation at 700 °C for approximately 24 hours.
3. The mixture of silicon carbide and zirconia kernels were then screened into 3 size fractions: + 520 μm , -520 μm + 420 μm and -420 μm . Zirconia kernels would report to the -520 μm + 420 μm with very few reporting to the +520 μm fraction. Some of the silicon carbide shells in the +520 μm were put aside for density measurement using a density gradient column, this technique was ultimately not used.
4. Zirconia kernels were then separated from the silicon carbide shells by making use of the difference in shape factor. The spherical zirconia kernels would roll across a flat surface while the silicon carbide fragments would not roll. Separation was achieved by placing small quantities of the mixture on a piece of paper and then gently tilting and shaking the paper until the zirconia kernels rolled off leaving the silicon carbide fragments behind.
5. Except for the shells separated for density measurement the various size fractions were recombined once the kernels had been removed. Helium pycnometry was used to measure the density of the fragments without grinding. The samples were lightly pressed into the sample cup, this tended to crush the fragments. For powder X-ray diffraction analysis the silicon carbide fragments were ground to a fine powder using an agate mortar and pestle.

While the silicon carbide fragments were being ground in preparation for powder X-ray diffraction analysis it was found that for some of the samples not all the kernels had been removed. In the worst case there were about 5 to 10 kernels in the sample. These kernels were picked from the sample by hand.

11.2 MICROSCOPY

Scanning electron microscopy was used to investigate surface structure, grain structure, etch response as well as measure micro-hardness and fracture strength of the silicon carbide deposits.

11.2.1 SURFACE STRUCTURE

SEM imaging of the surface structure allowed for an evaluation of the grain structure and size.

All images were recorded using a Jeol 5800LV electron microscope. Working distance was set to 14 mm, acceleration voltage to 10 kV.

Whole particles were mounted onto a 20 mm x 20 mm aluminium plate using silver loaded adhesive. A total of 20 particles, 2 each from 10 test runs, could be mounted onto each plate. The aluminium plates were mounted onto the SEM sample mount using conductive carbon tape. To achieve a flat field of view the particle was centred in the field of view. For each of the particles images were recorded at magnifications of 500, 1000, 2500 and 10 000. All images were recorded without moving the particles i.e. the centre point of images at different magnifications remained fixed. It was often difficult to obtain satisfactory images at a magnification of 10 000.

11.2.2 POLISHED SECTION

Back scatter electron images were recorded using a JEOL 5800LV SEM equipped with a Centaurus electron detector. Samples were mounted in Buehler Probemet conductive compression mounting resin and were polished using the full sequence listed in Table 24. Making use of the finely polished samples allowed for the grain structure of the silicon carbide to be viewed using backscatter electron imaging. Images from 2 particles from each of the accepted test runs and the thickness tests were recorded.

A fixed magnification of 2000 was used for all images. Best results were obtained using an acceleration voltage of 14 kV and a working distance of 13 mm.

11.2.3 POLISHED AND ETCHED SECTION

Etched samples were gold coated. Samples were viewed using a JEOL 5800LV SEM. Working distance was set to 14 mm and acceleration voltage to 5 keV. Images from a single particle from each of the hot inlet, cold inlet and thickness test matrices were recorded. Little difference was seen between particles from the same test run.

11.3 DENSITY

Initially density was measured using a pycnometer bottle. Once a helium pycnometer became available this was used in preference to the pycnometer bottle. All batches that had been measured using the pycnometer bottle were then remeasured using the gas pycnometer.

Two methods were used to determine silicon carbide density: calculated density and direct measurement. Initially the calculated density method was used as this was relatively fast. For more accurate measurements, direct measurement using a low volume helium pycnometer was used. Indirect measurement involved calculating the silicon carbide density from the particle mass gain and change in particle density during deposition.

Density of the starting material was measured using both the pycnometer bottles and gas pycnometer. It was found that there was a significant difference in measured density between the techniques. Pycnometer bottle measurements report envelope density while gas pycnometer measurements report absolute density. As the pyrocarbon is porous the difference between the two measurements is significant. Although it was measurable, the difference between the two measurement techniques was significantly less when measuring coated particles as the silicon carbide is non-porous. Silicon carbide density measurements on complete particles using the helium pycnometer were corrected to give the same average density as measured by the water pycnometer bottle. This was necessary as the calculation method assumed envelope density whereas the helium pycnometer measure absolute density.

For all the measurement methods used, the repeatability of the measurement technique was assessed by repeatedly measuring a sample. For the pycnometer bottle distilled water and a sample of starting material was measured. In the case of the 100 ml helium pycnometer samples of batches CPT-T-G130 and CPT-T-G140 of the starting material were used while for the 10 ml pycnometer one of the test runs (CR15) was used. Results for the repeatability tests are presented in Table 25. For CR15 the first 3 measurements yielded results that were inconsistent with all subsequent measurements; data for all measurements and an edited data set with the first 3 measurements removed is presented.

11.3.1 PYCNOMETER BOTTLE

A nominally 10 ml pycnometer bottle with an integrated thermometer was used for measuring the density of whole particles. The certified volume of the bottle was 9.735 ml at 20 °C, thermometer graduations were 0.2 °C. Water density versus temperature data based on that published in the CRC Handbook of Chemistry and Physics, 53rd edition, was used for determining the actual water density for each measurement.

The general procedure for measuring the density was as follows:

1. Clean and dry the pycnometer bottle
2. Measure the weight of the empty bottle (m_{empty})
3. Fill the bottle with particles and measure the dry mass (m_{dry})
4. Fill the bottle with distilled water
5. Dry the outside of the bottle
6. Measure the wet mass and temperature of the bottle (m_{wet})

Particle density was then calculated as follows:

$$\rho = \frac{(m_{dry} - m_{empty})}{\left(v - \left((m_{wet} - m_{dry}) / \rho_{water} \right) \right)} \quad (89)$$

Where:

- ρ : Particle density ($\text{g}\cdot\text{cm}^{-3}$)
- m_{dry} : Dry mass of pycnometer bottle with particles (g)
- m_{empty} : Mass of empty pycnometer bottle (g)
- m_{wet} : Mass of pycnometer filled with particles and water (g)
- v : Volume of pycnometer bottle = 9.735 for pycnometer used (cm^3)
- ρ_{water} : Density of water at test temperature ($\text{g}\cdot\text{cm}^{-3}$)

Initially problems were experienced with ensuring the particles wet completely and ensuring that all the air was removed from the pycnometer bottle. By putting the filled bottle under vacuum it was possible to remove bubbles from between the particles. It was uncertain to what extent air was removed from open porosity in the particle.

For each test run the density of the distilled water was also measured. This data was used to collect data on the accuracy and reproducibility of the measurements. Similarly the density of the starting material was measured repeatedly; however these measurements were not repeated for all test runs. As the water density measurements were performed at different temperatures the water density results reported in Table 25 are for the density error (reported density – measured density), not absolute density. Water density measurement errors were not normally distributed; the distribution approximated two overlapping normal distributions with peaks at $0.0011 \text{ g}\cdot\text{cm}^{-3}$ and $0.0037 \text{ g}\cdot\text{cm}^{-3}$.

11.3.2 HELIUM PYCNOMETER

Two different Micromeritics AccuPyc II 1340 systems were used. One instrument was set up for a sample cup of 100 ml, 35 ml or 10 ml. For smaller samples an instrument with sample sizes of 35 ml, 10 ml or 1 ml was used. When measuring the density of complete coated particles, or starting material, the larger sample cups could be used, typically a 35 ml or 10 ml sample cup could be completely filled. For SiC powder (see section 11.1.4 for details of preparation method) the available sample size was below the minimum required for accurate measurement using the larger capacity pycnometer. For these samples the 1 ml sample cup was used. Powdered samples were pressed into the sample cup to ensure as large a sample as possible was measured. Normally the sample cup was filled with a sample of 0.75 g to 1.25 g.

For all measurements the pycnometer was set up for 10 purge cycles followed by 10 measurement cycles. Initial chamber pressure was set to 134.4 kPa (19.5 psi on the instrument). The system was set up for pressure equilibration before switching between measurement steps; an equilibration pressure change rate of 0.005 psi.minute⁻¹ was used. A calibration was performed on the instrument each day before using the instrument. Room temperature was not controlled, a problem which may have contributed significantly to run to run variation, especially where several measurements were performed over a long period on a day.

Table 25 Comparison of density measurement repeatability.

Material	Test Method	Average (g.cm ⁻³)	Standard Deviation (g.cm ⁻³)	Range (g.cm ⁻³)	Count
Distilled water	Pycnometer bottle	0.0022 (1)	0.0013	0.0053	58
CPT-T-G140	Pycnometer bottle	2.1781	0.0079	0.0284	18
CPT-T-G130	He pycnometer 35 ml	2.3642	0.0013	0.0065	22
CPT-T-G140	He pycnometer 35 ml	2.5071	0.0015	0.0284	18
CR15 SiC shells (2)	He pycnometer 1 ml	3.1379	0.0129	0.0361	11
CR15 SiC shells (3)	He pycnometer 1 ml	3.1311	0.0065	0.0169	8

(1) Density error: Actual Density – Measured Density

(2) All measurements

(3) Edited data

11.4 HARDNESS AND FRACTURE TOUGHNESS

Vickers micro-hardness was measured on samples mounted in epoxy resin and polished to midway through the particle. A Future-Tech FV-700 hardness tester was used to make 4 indents evenly spaced around the particle. Each indent was made in the middle of the silicon carbide layer with the indent diagonals in the radial and tangential direction as shown in Figure 38. Prior to indentation the samples were sputter coated with a gold/palladium alloy to allow for SEM measurement of the indents. All samples were first indented before the indents were measured, resulting in a considerable (several days) time difference between indentation and measurement. Samples were stored in a desiccator between indentation and measurement.

Due to the high hardness of the silicon carbide, and low indentation load used, the indents were too small to measure reliably using the filar micrometer on the hardness tester. To overcome this problem all measurements were made using SEM secondary electron images. A standard magnification of 3000 was used for measuring 100 g indents. For indents made using a 50 g load magnifications of between 6000 and 9000 were used. Image contrast tended to be very poor, making measurement of some indents difficult, especially in the case of the 50 g indents. SEM operating conditions were standardized with a working distance of 14 mm and acceleration voltage of 15 kV.

Calibration of the SEM was checked using test structures etched into a gold plated silicon chip. SEM measurements were compared to measurements made using a calibrated optical microscope. It was estimated that the difference between the SEM and optical microscope measurements for a 10 μm structure (the smallest feature available on the test chip) were 0.070 μm in the horizontal direction and 0.217 μm in the vertical direction. Differences between the horizontal and vertical direction would not have influenced the measurements as the radial and tangential cracks were both measured in the horizontal and vertical directions due to their positioning around the particle. SEM measurements were not corrected to compensate for the differences in measurement.

In virtually all cases the 100 g load resulted in cracking around the indent. The severity of the cracking ranged from short cracks running from the corners of the indent to complete shattering of the silicon carbide layer. For hardness measurement any cracking should be considered unacceptable, however if it is intended to measure fracture toughness by means of indentation cracking it is obviously a requirement that the indent should crack. For fracture toughness measurement an ideal crack would be straight and run from the corner of the indent. Many of the cracks formed were unacceptable resulting in the indent being rejected. Typical examples of unacceptable cracks are shown in Figure 39. When a 50 g load was used cracks would not form on all indents, those that did were normally acceptable for fracture toughness measurement.

As both hardness and fracture toughness were being measured, diagonal length and crack lengths were both measured. All measurements were made on SEM images using a combination of ImageJ and MS Excel. Coordinates for the indent corners and

crack tips were measured using ImageJ and transferred to Excel where the indent diagonal lengths and crack lengths were calculated. Crack lengths were calculated as the straight line distance between the indent corner and the crack tip.

Initially a single batch was used as a pilot study. For this batch particles were indented with a range of loads. For the pilot study additional indents were made at 45 °, 135 °, 225 ° and 315 ° positions. For these indents the corner cracks tended to run across the striations, the average crack length being intermediate between that of the radial and circumferential cracks. From the pilot study results it was found that indent loads below 50 g were hardly visible, even under high magnification in the SEM. Loads higher than 100 g resulted in shattering of the silicon carbide layer.

Partially based on the pilot study, and partially on consideration of the effort involved in performing the measurements it was decided to make a total of 44 indents, 4 indents on each of 11 particles. Ten of the particles were indented using a 100 g load while the 11th particle was indented using a 50 g load. For each test, SEM images were recorded for later analysis. Initially all indents were assessed, this however proved to be too time consuming to be practical. For the remaining test runs images were recorded until a total of 20 acceptable indents had been found. For some test runs it was not possible to find 20 acceptable indents, in these cases as many good indents as could be found were used. The total number of indents inspected was recorded to allow for the fraction acceptable indents to be calculated. For test runs having a thin silicon carbide thickness very few acceptable indents were found. However, for test runs from group HF and CR having a thickness below 30 µm the test were repeated. This improved the number of acceptable indents for those test conditions. Low acceptable indent counts impacted on the confidence of the hardness and fracture toughness measures.

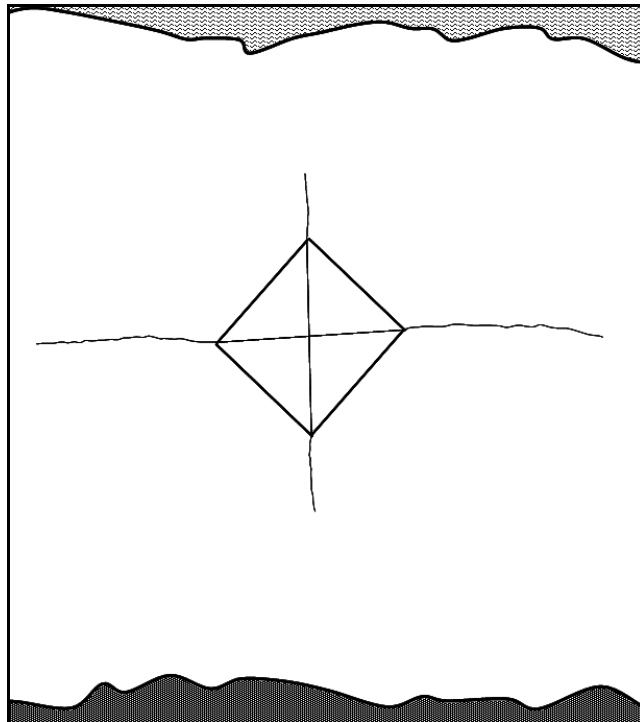


Figure 38 Typical good Vickers indent with straight cracks emanating from each corner. Indents were placed approximately midway across the silicon carbide layer. For all indents the diagonals were aligned in the radial and circumferential directions. Radial cracks were often shorter than circumferential cracks.

Vickers hardness was calculated as:

$$HV = \frac{1854.4F}{L_r L_t} \quad (90)$$

Where:

HV : Vickers hardness number (GPa)

F : Indenter load (N)

L_r, L_t : Diagonal length in radial and tangential direction (μm)

Equation 90 expresses hardness in SI units of GPa, it is however more common for Vickers hardness to be expressed in units of $\text{kg}\cdot\text{mm}^{-2}$. Units of GPa were chosen over $\text{kg}\cdot\text{mm}^{-2}$ as these units are required for calculating fracture toughness. The numerical values of the two units differ by a factor of 101.973 ($\text{kg}\cdot\text{mm}^{-2}$)/(GPa).

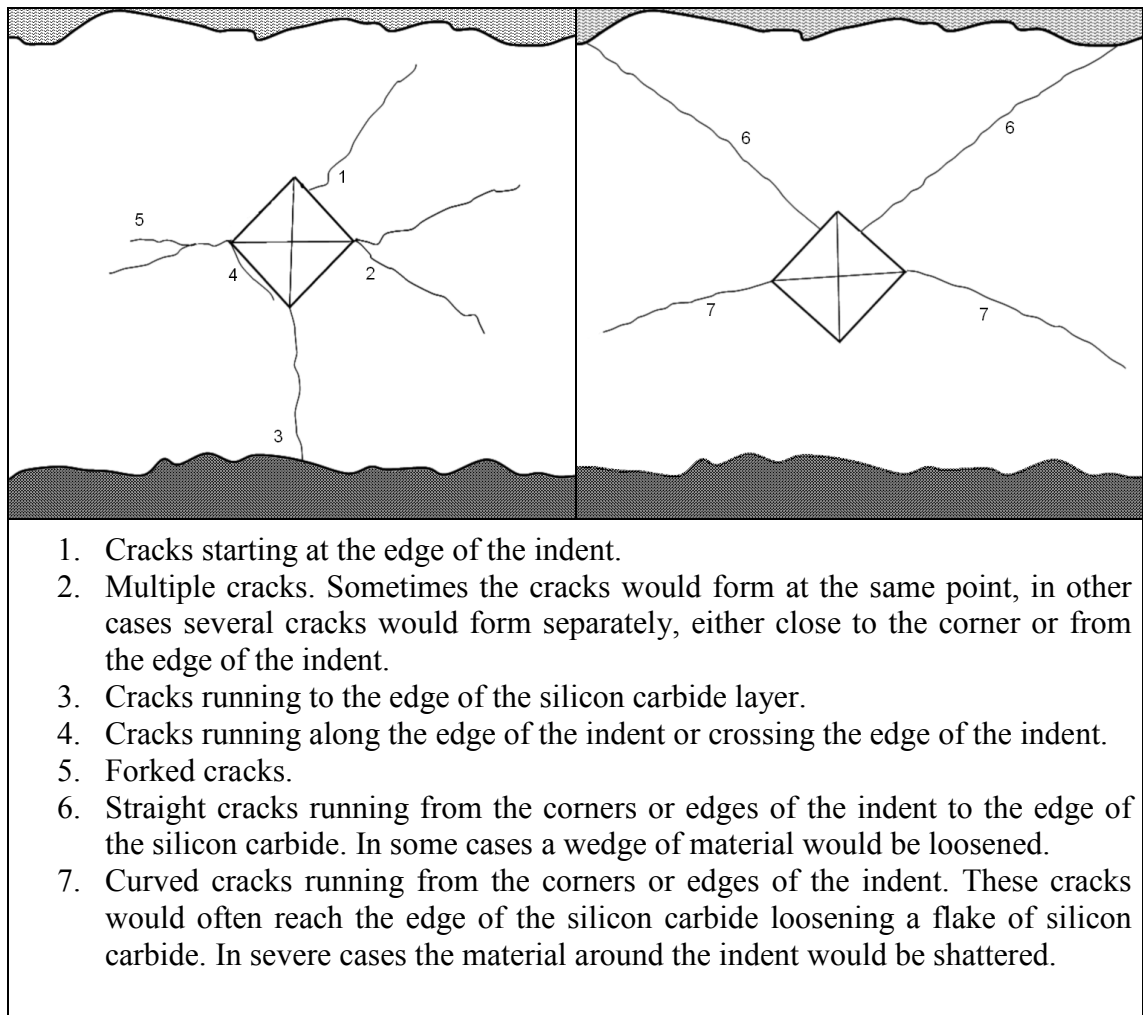


Figure 39. Unacceptable cracks resulting in the rejection of an indent.

11.5 NANO-INDENTATION

Nano-indentation tests were performed on sets of samples mounted in resin, as described in section 11.1.1, and polished to a 0.05 μm finish using the procedure described in section 11.1.2. Separate mounts were prepared for samples from the various groups of tests. Two particles from each test run were mounted.

Nano-indentation tests were performed at Nelson Mandela Metropolitan University using a CSM Instruments Nano Hardness Tester equipped with a Berkovich indenter. A total of 60 indentations were made on a single particle from each test run.

Hardness and Young's modulus were reported by the instrument. Young's modulus was calculated using the method described in 8.5.1.2. A Poisson ratio of 0.16 was used for the calculations.

11.6 CRUSH STRENGTH

Crush strength was measured on whole particles without an outer pyrocarbon coating. All test runs from the deposition rate, non-cooled inlet, cooled inlet and thickness tests were measured using soft anvils. Particles prepared using the cooled inlet were also tested using hard anvils.

Details of the crush test apparatus are shown in Figure 40. The crush test apparatus consisted of a long pivoted arm which was counter weighted so as to balance the mass of the arm. Load was applied to the arm manually using an adjustable screw. The applied load was measured using a strain gauge and peak recording digital voltmeter.

Particles were crushed between two plates 20 mm X 20 mm made of either annealed aluminium or alumina. Aluminium anvils were annealed to give a hardness of approximately 23 HVN. When using the soft aluminium anvils each particle indented the anvil requiring each particle to be differently positioned. Particles were positioned so that the indents were closely spaced but did not touch. Anvils needed to be replaced once the surface was covered by indents. Top and bottom anvils were held in place on the set up using a thin layer of stationary glue; this prevented the anvils from moving but allowed easy removal.

Each time the crush tester was used the calibration was checked. This was done by loading the load arm with known weights and recording the strain gauge reading. No adjustments were made to the setup however the load applied to the particles was calculated from the latest calibration data.

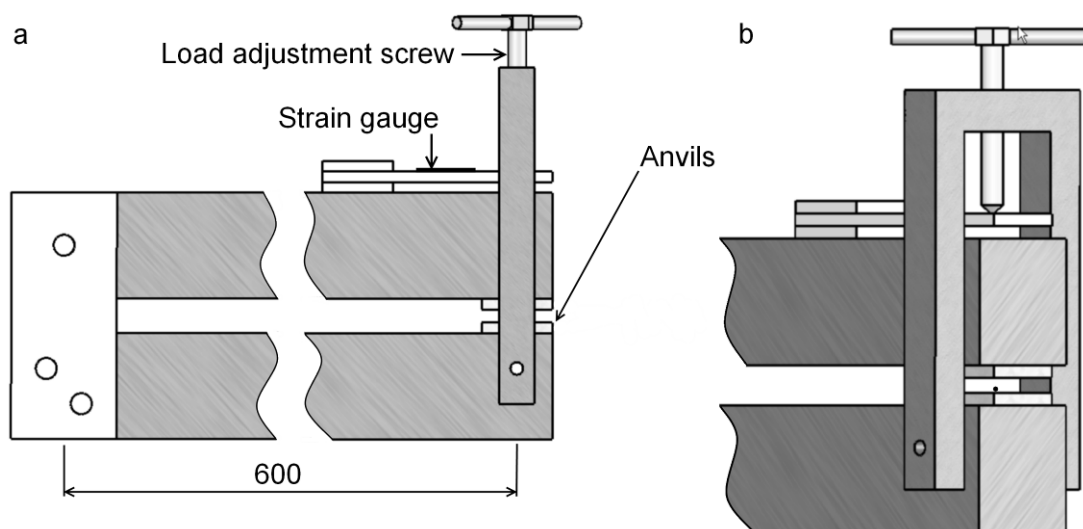


Figure 40. Crush test apparatus. (a) General view of the set up. The counter weight used to balance the weight of the arm is not shown. (b) Detail view of anvils, load adjustment and load measurement set up.

11.6.1 CHARACTERISATION OF CRUSH TEST APPARATUS

Several tests were carried out to characterise the tester. These are discussed in detail in the following sections. All the tests listed below were carried out with coated particles from test run CR4. From the characterisation tests it could be concluded that the test equipment was stable over the time period over which the tests were carried out and that differences in measurement position on the anvils, between the anvil sets and daily set up of the tester did not result in statistically significant differences in the measured crush strength.

11.6.1.1 IMPACT OF PARTICLE POSITION ON ANVILS

To test whether particle position on the anvil had any influence on the measured crush strength, particles from a single test run were measured at various positions on a single set of anvils. The anvils were divided into a 3 X 3 matrix giving 9 equally sized zones. Particles were crushed in the 4 corner zones and the centre zone. All test conditions were identical except for position on the anvil. A summary of the results are presented in Table 26. ANOVA yielded a P-value = 0.162.

Table 26. Crush strength of particles tested at various positions on the soft anvils.

Position	Count	Average Strength (g)	Standard Deviation (g)
Top Left	36	6452	750
Bottom Left	36	6046	645
Centre	60	6279	703
Top Right	36	6316	673
Bottom Right	36	6239	632

11.6.1.2 IMPACT OF DIFFERENT ANVIL SETS

The impact of different anvil sets was assessed by measuring crush strength of particles from a single batch using two anvil sets. Measurements were performed on the second set immediately after completion of the first set of measurements. All measurements were carried out at approximately similar positions on the two anvil sets.

A summary of results is presented in Table 27. An equal variance t-test yielded a P-value = 0.194.

Table 27. Crush strength for 2 different anvil sets. All other parameters kept constant.

Anvil	Count	Average Strength (g)	Standard Deviation (g)
19	54	6434	593
20	54	6282	619

11.6.1.3 DAY TO DAY VARIATION

Day to day variation was tested by measuring particles using the same anvil set but with different calibrations. The time between the two sets of measurements was approximately 1 day. During this time the equipment was switched off. Generally there was little difference in the calibration data for different days, so it was not expected that significant differences would be found.

A summary of results is presented in Table 28. An equal variance t-test yielded a P-value = 0.502.

Table 28. Impact of set up calibration on crush strength results. The same set of anvils was used for both tests.

Test	Count	Average Strength (g)	Standard Deviation (g)
4.2	51	6515	636
4.3	54	6434	593

11.6.1.4 LONG TERM STABILITY

A long term stability test was carried out by comparing results of measurements made at the time of the first crush test measurements to measurements carried out after all other tests had been completed. As with the previous tests no statistically significant differences could be found between the tests (Equal variance t-test, P-values = 0.176). Results are summarised in Table 29.

Table 29. Comparison of results from the start of testing to results obtained at the end of testing.

Test	Count	Average Strength (g)	Standard Deviation (g)
4	50	6420	796
4.5	204	6268	689

11.6.2 STANDARD DEVIATION OF MEANS

A total of 14 groups of coated particles from CR4 were measured. The standard deviation of the means of these tests was 150.5 g.

11.6.2.1 ANALYSIS OF RESULTS

Crush load of all test runs from group DR, HF, CR and TT were measured using soft anvils. Test runs from group CR that had used starting material CPT-T-G140 were also measured using hard anvils. This allowed for a comparison between the hard and soft anvils. Data analysis focused on test runs that had used CPT-T-G140 and had been tested using soft anvils.

Most of the crush load data analysis was performed assuming that the data could be described by a normal distribution. As an alternative, data could have been regarded as having a Weibull distribution. However the difference between the 2 distributions was found to be negligible. Goodness of fit between the 2 distributions was evaluated using Probability-Probability (P-P) plots. Numerically the fit was expressed as the coefficient of determination, R^2 , for the linear fit of the measured and predicted probabilities plotted on a P-P plot. A comparison between the test run with the best and the worst fit is shown in Figure 41. Despite the apparently poor fit to a normal distribution for test HF20 this would have passed the Kalmogorov-Smirnov goodness of fit test at a 99 % confidence limit.

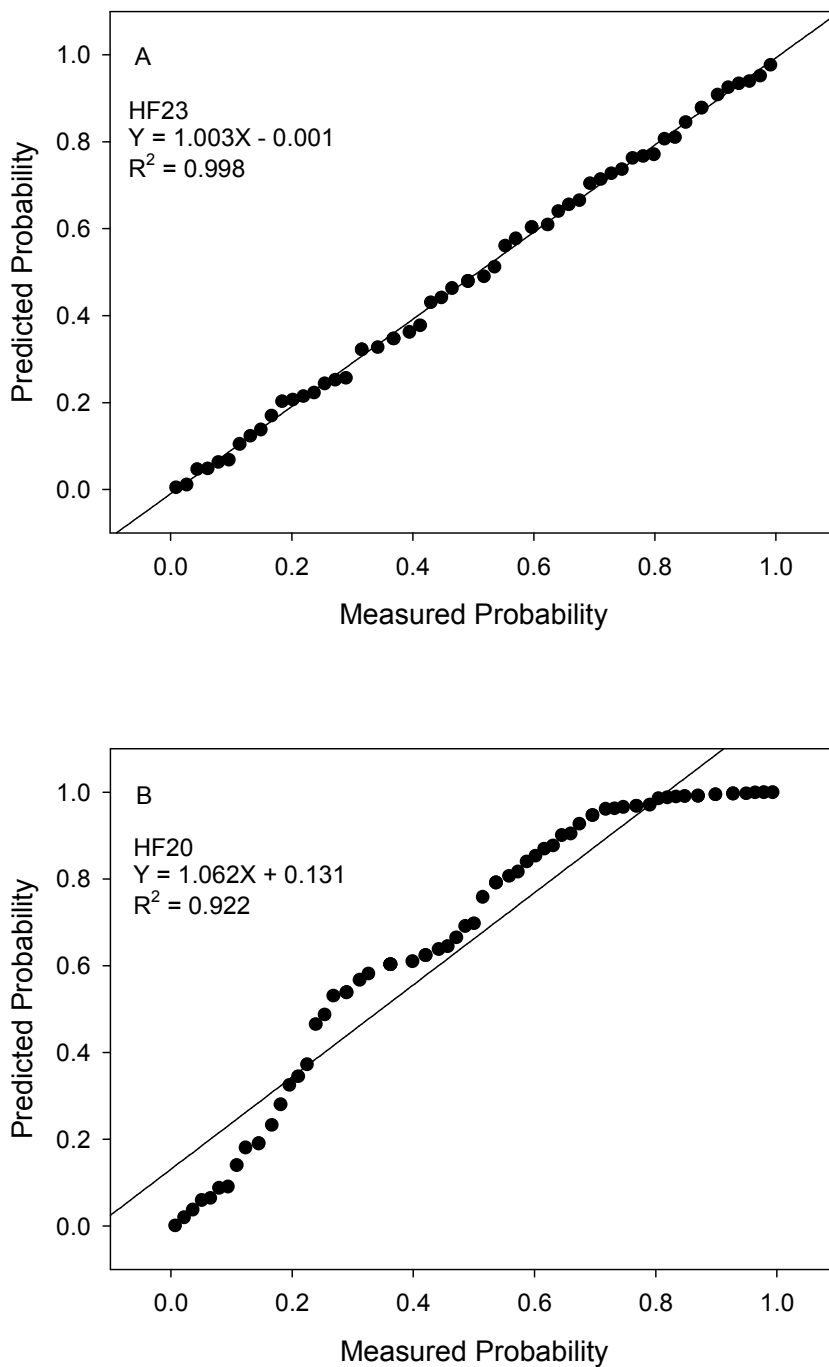


Figure 41. . Example of typical P-P plots used to test the goodness of fit of measured data to Weibull and normal distributions. Test run (A) HF23 and (B) HF20 represent the best and worst fit for test run using particles from lot CPT-T-G140 measured using soft anvils.

11.7 GRAIN SIZE

11.7.1 SURFACE GRAIN SIZE

Analysis of the size of the free surface of the grain has the advantage of not requiring any sample preparation, except the removal of the outer pyrocarbon layer in completely coated TRISO particles. Surface grain size was measured on backscatter electron SEM images of the particle surface. Details of sample mounting and microscopy are given in section 11.2.1.

Grain size was measured on SEM images using a line intercept method. Using ImageJ “Grid” plug-in a grid was overlaid onto 1000 magnification images. The grid size was selected so as to give a randomly positioned 6x6 grid on the image. This resulted in 5 vertical and 5 horizontal lines crossing the image. Using the “Cell Counter” plug-in, points where the grid lines crossed grain boundaries were marked. The XY coordinates of each point was then measured and transferred to Excel. Grain size was calculated as the distance between each point measured. Measurements were made on a single image from each of 2 particles per batch.

It was often difficult to accurately determine grain boundaries. For the deposits that formed grains with domed surfaces, boundaries between the rounded grains were quite clear. However, within the rounded surface there were often features which may be interpreted as grain boundaries. These features tended to be less distinct than the boundaries between the domes. The methodology adopted for this study was to treat the less distinct feature as grain boundaries.

Another feature of viewing the top surface of the deposit is that newly formed grains could appear as small grains on top of larger grains. Due to the methodology used to calculate the grain size this would result in the larger grains being counted as multiple smaller grains instead of a single large grain. No attempt was made to compensate for this potential error; grain size as measured by the method described above was used in all further analyses.

11.7.2 SEM GRAIN SIZE

Cross sectional grain size was measured on backscatter electron images using a line intercept method similar to that described for surface grain size. The only significant differences in the method being that a finer grid was overlaid onto the SEM images and that separate measurements were made in directions parallel and perpendicular to the growth direction. Due to the aspect ratio of the cross sectional images lines perpendicular to the growth direction intercepted the layer image over a much longer distance than lines parallel to the growth direction. Approximately 10 lines were used for the perpendicular measurements while 20 lines were used for measurement of grain size in a direction parallel to the growth direction.

Measurement could only be performed on a selection of samples. For the majority of images the grain size was too small or indistinct to be measurable. On images where grains could be clearly seen it was often difficult to distinguish all grain boundaries clearly making the accuracy of this method doubtful.

11.7.3 X-RAY DIFFRACTION CRYSTALLITE SIZE

X-ray diffraction patterns were analysed using AutoQuan software; this reported sample crystallite size directly. These values were accepted as is.

11.8 THICKNESS

As discussed in chapter 8 several methods are available for measuring deposit thickness. Direct measurement methods, such as optical microscopy and SEM techniques, have the disadvantage of requiring a representative cross section of the deposit. In the case of polished samples it was necessary to ensure that the samples are polished to midway through the particle. In cases where the polishing stopped before, or after, the centre of the particle reported thickness would be greater than the actual thickness. Figure 42 indicates the sensitivity of reported thickness as a function of polish height error. It can be seen that for small polish height errors there was a relatively small error in measured thickness. SEM measurement of fractured particles suffered from a similar problem – it was difficult to find radial fracture sections which could be viewed perpendicularly. Any deviation from radial fracture direction would result in reported layer thickness being greater than actual thickness. When the viewing angle deviated from perpendicular the measured thickness would be less than the actual thickness.

After testing optical and SEM measurements it was decided to standardise on the calculated thickness method described in section 11.8.1.5. Although, as with the other methods, the absolute accuracy of this method cannot be guaranteed without extensive calibration it has the advantage of allowing for a large sample volume, is easy to perform and is relatively fast. The last mentioned advantage was especially important while test runs were being conducted.

11.8.1 OPTICAL MEASUREMENT

Several optical methods of thickness measurement were tested. In principle most of these methods could have been used on SEM images. All these methods were found to be very time consuming due to the need to prepare polished cross sections and/or the need to record and analyse images of the particles. Automated versions of these methods could however be viable options for routine measurements on a large scale.

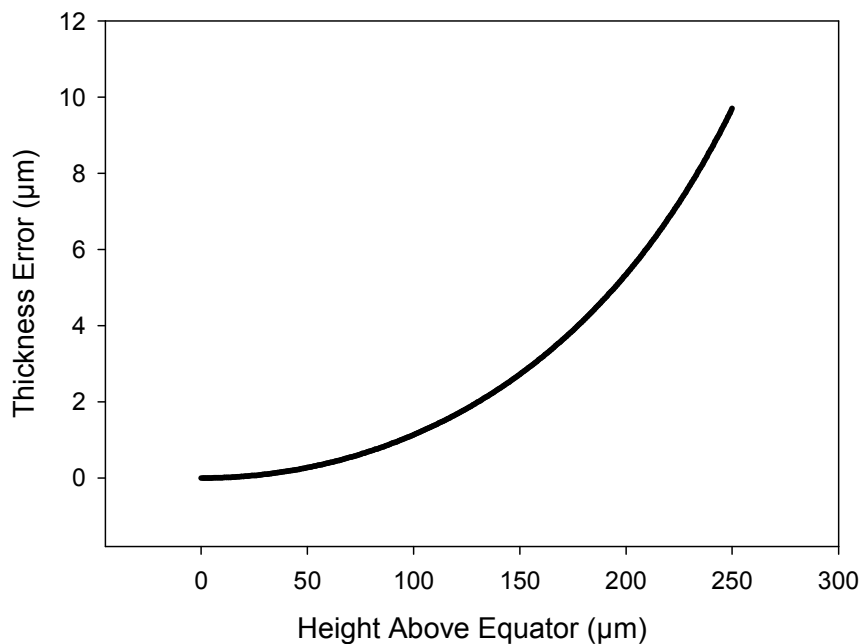


Figure 42. Thickness measurement error due to polish height error. Error values calculated for a layer thickness of 35 µm.

11.8.1.1 LINE INTERCEPT METHOD

ImageJ software was used for all image manipulation required for this method. As part of the measurement process an image consisting of a large number of thin, parallel, vertical lines was created. This image was used to analyse all the images. The following procedure was used to measure the thickness:

1. ImageJ was calibrated using the scale bar recorded on the image.
2. A segmented line was drawn along the centre of the silicon carbide layer. Line width was chosen as 200 pixels.
3. Using the “Straighten” function the selected zone was straightened out to form a rectangular image 200 pixels wide and the length of the selected line.
4. The selected strip was then converted to a binary image using the “Threshold” function.
5. Spots and holes were removed from the image using the “Fill Holes” function.
6. Using the “Image calculator” function the intercept between the binary image of the deposit and the measurement line image was determined. This resulted in a number of parallel lines, the length of each line being the thickness of the deposit at that point.

Line lengths were measured using the “Analyze Particles” function. Limits on the minimum and maximum line lengths were set to ensure that unreasonably short or long lines were excluded.

This method is capable of measuring the thickness as well as the thickness uniformity of the deposit. The number of measurements obtained depended on the length of deposit sampled and the number of sampling lines used. Typically approximately 500 measurements were obtained per image analysed.

This method required high magnification images resulting in a short length of deposit being sampled. As a result several images needed to be analysed to obtain a reasonable sample size. In practice images of several particles were used. Low resolution images introduced errors due to the threshold function used to convert the gray scale image to a binary image as the exact boundary depended on the threshold setting. Using higher resolution images reduced the percentage error introduced; however SEM secondary electron images were not suitable due to the low contrast of the images. Optical images were used for all the measurements performed in investigating this method.

A potential problem with this technique is distortion introduced by the ImageJ “Straighten” function. Careful positioning of the segmented line along a constant radius, and making use of short segment lengths, resulted in minimal distortion. However, considerable errors could be introduced if the segmented line was not carefully placed. Errors due to placement of the segmented line could be minimised by placing it along the smooth silicon carbide / IPyC interface. Using the standard ImageJ functions this however resulted in only half the selected area intersecting the silicon carbide layer.

As the calculated thickness method, as described in section 11.8.1.5, was used in preference to this method the potential errors introduced by any distortion were not analysed in detail.

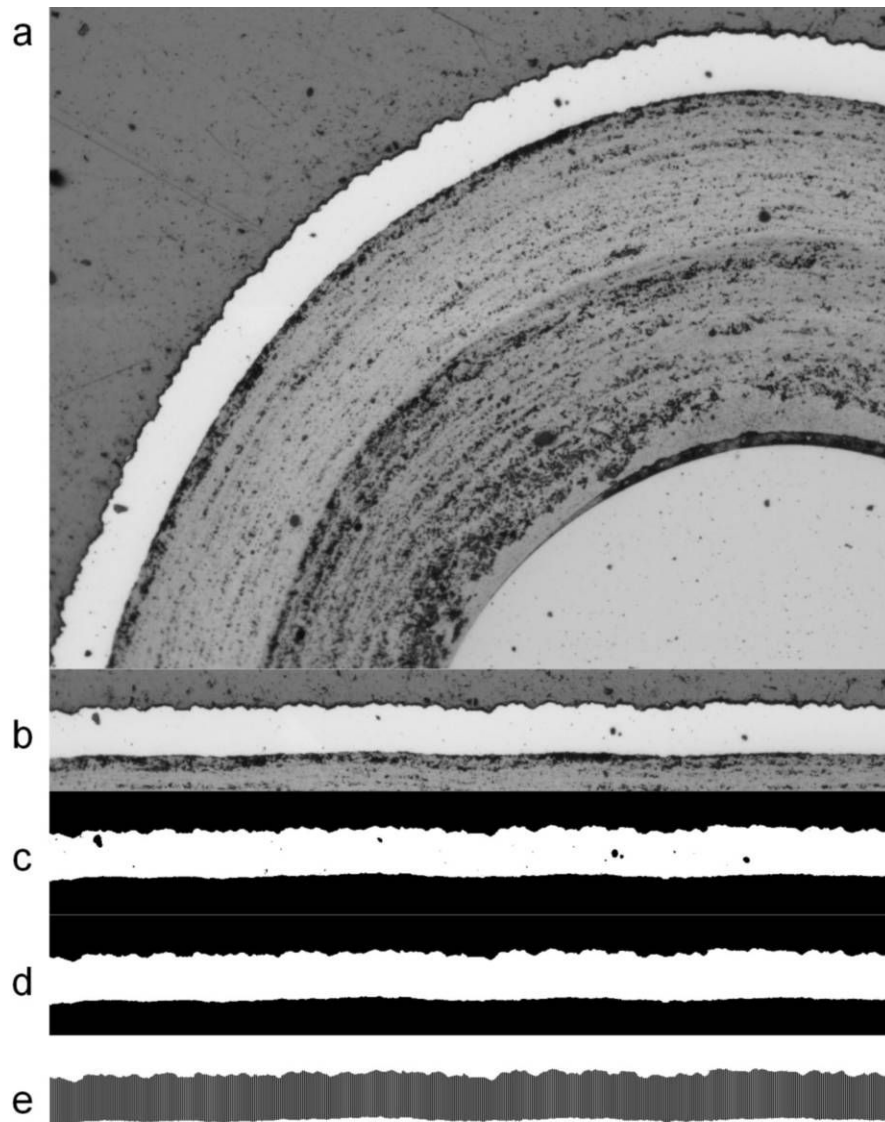


Figure 43. Line intercept method of measuring layer thickness. (a) Original image (b) Selected area straightened (c) Straightened image converted to a binary image (d) spots and holes removed (e) intercept between lines and cleaned image. Note that in image (e) individual lines are too finely spaced to be individually resolved.

11.8.1.2 DIFFERENCE IN RADIUS

In this method the thickness was calculated as the difference in radius between the inside and outside of the deposit. The following procedure was used:

1. Using ImageJ the X Y coordinates of a series of points marked along the inside surface of the deposit was measured. Coordinates were transferred to MS Excel.
2. Using Excel solver function, the best fit circle was found using a routine that minimised the sum square error between the circle and actual measured points.
3. Steps 1 and 2 above were repeated for the outside surface of the deposit.
4. Deposit thickness was calculated as the difference in radius between the 2 circles calculated above.

This method yielded an average thickness. As with the line intercept method it required high magnification images of the deposit cross section for accurate measurement.

11.8.1.3 SILHOUETTE METHOD

This method was only used to initially measure size and size distribution of the starting material. Attempts to measure deposit thickness were unsuccessful due to a lack of accuracy. Changes to the detail of the method may have yielded more accurate results but it was decided to make use of faster alternatives instead of refining the method. This method was useful in that it allowed for the most uniform batch of starting material to be selected.

The following procedure was used:

1. Particles were mounted onto a microscope slide using double sided tape. Care was taken to ensure that the particles were not touching each other.
2. Images of the particles were recorded using a stereo microscope. Illumination was by placing the microscope slide with the particles on a light box. All images were recorded with the same microscope set up.
3. Images were converted to binary images using ImageJ software.
4. The area of each particle was measured using the ImageJ “Analyze Particles” function. Severely misshapen particles or particles touching the edge of the image or other particles were excluded automatically by ImageJ by placing limits on particle size, circularity.
5. Particle radius was calculated in MS Excel based on the assumption that each particle image was circular.

The method was calibrated by using images of a vernier calliper scale. Except for the illumination used, no changes were made to the microscope set up between recording the calibration images and particle images. As with the line intercept method this method was sensitive to the threshold procedure when converting the images to binary format.

It was initially intended to use the above procedure before and after coating to allow for the deposit thickness to be calculated. However this did not yield accurate results and the method was not developed further. An ANOVA test on repeated measures of a batch of starting material indicated that there were significant differences between the results, with a P-value of 2.2×10^{-5} . The difference of $9 \mu\text{m}$ between the 2 sets of measurements represents 25 % of the targeted deposit thickness of $35 \mu\text{m}$. Probability plots of the measured particle are presented in Figure 45. A low magnification was used so as to allow for a number of particles to be analysed on each image. This reduced the number of images processed in ImageJ at the cost of accuracy. Higher magnification could have yielded more accurate results at the cost of having to analyse a larger number of images. This method is most likely well suited to an automated measurement system where no images are recorded and a higher magnification could be used.

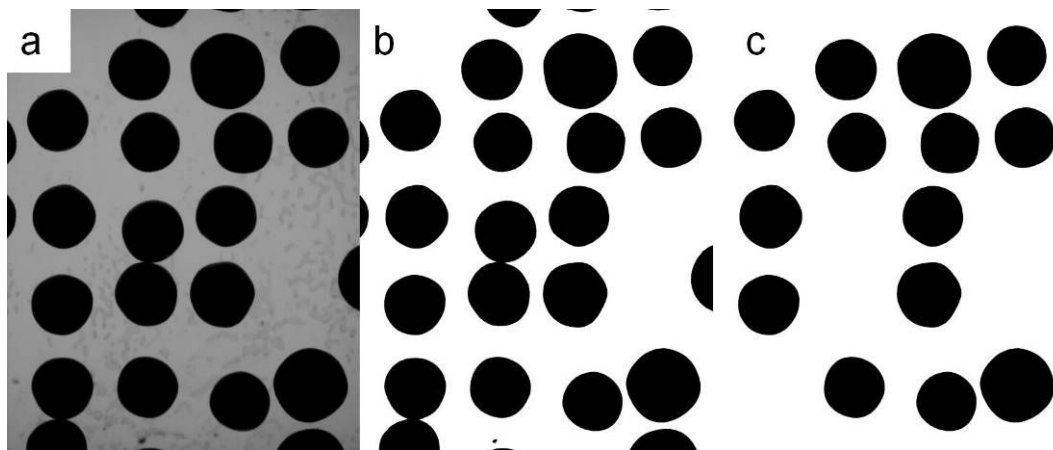


Figure 44. Silhouette method. (a) original image (b) binary image with particles touching the edge and each other (c) measured image with edge, touching and misshapen particles removed. Particle from batch CPT-T-G133, note the larger particles found in this batch of material.

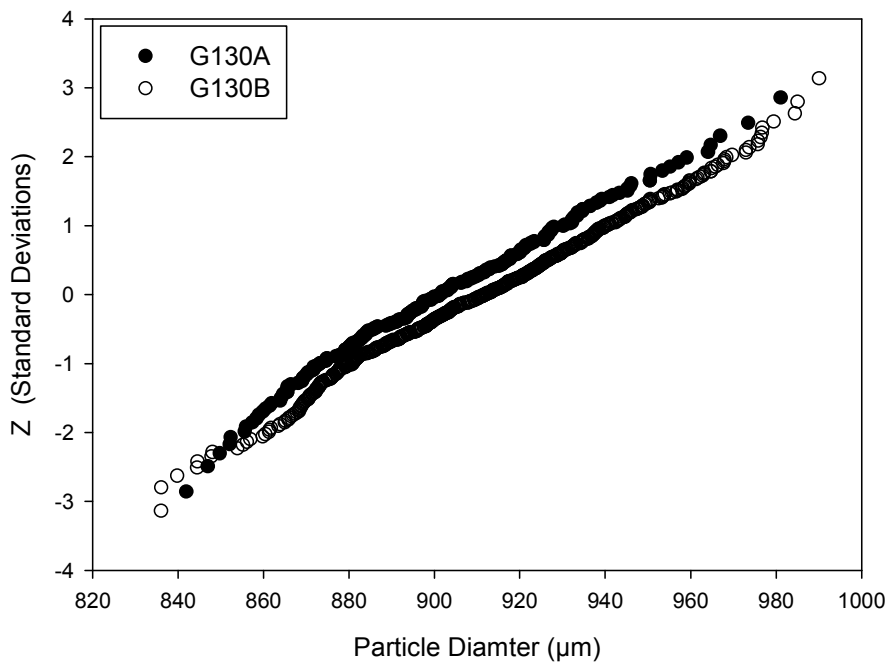


Figure 45. CPT-T-G130 starting material particle diameter. Normal probability plot of repeated measurement of particle diameter using the silhouette method. Average diameter for test A: 902 µm. Average diameter for test B: 912 µm. Average diameter from repeated density measurements: 930 µm

11.8.1.4 SEM MEASUREMENT

Direct measurement of the deposit thickness on SEM images was performed on the backscatter electron images taken to investigate grain structure. ImageJ was used to superimpose lines onto the SEM images. Line lengths were estimated using the ImageJ measure function calibrated to the SEM calibration bar. For most of the test runs measured, 20 lines were measured on each of 2 images.

A severe limitation of this method was the very small sample size. Deposit thickness was measured over a distance of approximately 60 µm on each image. Due to the high magnification used compared to optical methods it is expected that this method would be less sensitive to errors in estimation of the edge of the deposit. Also, as no manipulation of the images was required it is expected that there would be very little bias in the measurements. Differences in length of each of the lines allowed for an estimation of the deposit uniformity.

11.8.1.5 CALCULATED THICKNESS

Particle volume could be calculated from the particle density and mass. By assuming that the particles are spherical it is possible to calculate the particle radius. By repeating these calculations for particles before and after coating the layer thickness can be calculated as the difference between the coated and uncoated particle diameter.

The assumption of the particles being spherical is not completely correct. However the errors in deposit thickness are likely to be very small due to the fact that the thickness is calculated as the difference in diameter between the starting particles and coated particles. Due to the SiC layer being thin compared to the particle dimensions (approximately 35 μm SiC on 470 μm radius particles) the errors due to non-sphericity are likely to be small. As the same non-sphericity would be expected across all starting material (all samples taken from a single lot of starting material) any errors would also be constant for all test runs.

11.9 PHASE COMPOSITION

11.9.1 X-RAY DIFFRACTION

Powder X-Ray diffraction was used to analyse the phase composition of each of the accepted test runs. Only a single repeat of each centre point was measured. In addition to the experimental matrices the 5 test runs with varying thickness were tested to investigate whether thickness had any influence on silicon content. If, as had been observed on earlier test runs, any silicon was concentrated close to the pyrocarbon/silicon carbide interface then a thicker layer of silicon carbide would appear to contain less silicon.

Powder samples were prepared as described in Section 11.1.4. Finely ground powder was manually pressed into a standard 10 mm sample ring. Two of the samples were ground in ethanol. These samples did not bind effectively when pressed into the sample holders. This, combined with the increased sample preparation time and success of dry grinding, led to the rest of the samples being ground dry.

A PANalytical X'Pert PRO diffractometer equipped with a cobalt X-ray tube was used for all powder X-ray diffraction analyses. Highscore Plus (PANalytical X'Pert Highscore Plus, version 2.2b) software was used to identify the phases present in each of the samples. Quantitative analysis of the diffraction patterns was carried out using AutoQuan (GE Inspection Technologies GmbH, Autoquan Version 2.70) software. Quantitative analysis was performed using only 3 phases; silicon, β -SiC and quartz. No other silicon carbide phases beside β -SiC were found to have a reasonable fit to the measured peaks.

Analysis of silicon carbide powders in the as received, heat treated and milled condition proved that the quartz found in the samples was as a result of milling the

samples using an agate mortar and pestle. Tests were performed on two materials, one a coarse powder of uncertain origin and the other a very fine β -SiC powder. For each material XRD analysis was performed on the initial powder, after heating in air at 700 °C for 48 hours and after grinding in an agate mortar and pestle. The β -SiC powder was very fine to start with so grinding had very little effect. Heat treating of the samples did not introduce any quartz due to oxidation of the silicon carbide. Milling introduced quartz into the coarse powder. From this it was concluded that the quartz detected in the samples was as a result of milling and not burning off of the carbon.

X-ray diffraction results are presented in Appendix B.

11.9.2 RAMAN SPECTROSCOPY

Raman analysis was carried out using a Horiba Jobin Yvon T64000 spectrometer equipped with a 514.5 nm argon laser. A 50X, 0.75 NA objective lens was used for viewing and analysis. Laser spot size was approximately 2 μm diameter. For each test run 1 point on a single particle was measured at the centre of the silicon carbide layer. Samples used for the Raman spectroscopy had been mounted in Buehler Probemet compression mounting resin (samples had been prepared for other test work, the conductive properties of the Probemet resin were not required for these tests) and polished to a 1 μm finish.

Spectra were measured between 50 cm^{-1} and 1600 cm^{-1} . Each scan was repeated to allow for elimination of random noise spikes. Raman spectra were analysed using Labspec 5 software. This allowed for peak position, height and width to be measured.

11.10 ELEMENTAL COMPOSITION

Microprobe analysis was performed using a Cameca SX100 Electron Probe Micro Analyser. Samples were mounted in conductive Buehler Probemet resin and polished to a 1 μm finish. The conductive mounting allowed for analysis without any sample coating.

Two particles from each test run together with particles from MTS calibration runs were mounted together. A separate sample mount was prepared for tests carried out using the cold and hot inlets. One measurement was performed per particle. It was originally intended that only the particle from each of the good test runs be measured, however the analyst measured all of the particles in each of the sample mounts. This resulted in additional data being available for statistical analysis of the results. Due to an error (missed particles) in measurement of the sample mount containing particles coated using the cooled inlet these samples were measured a second time.

Calibration of the equipment was performed using a sample of single crystal silicon carbide as well as silicon and carbon standards. Best results were obtained using the single crystal silicon carbide standard with a measurement time of 10 s.

11.11 DATA ANALYSIS

MS Excel was used for data storage and basic statistical analysis, such as calculation of average, standard deviations, t-test, ANOVA, linear regression and calculation of probabilities. Graphical analysis was also carried out using Excel.

Determination of Weibull distribution parameters of the crush load tests was also performed using MS Excel. Instead of the conventional method of determining Weibull parameters, by using a line fit to linearised data, a direct fit method using Excel's "Solver" function was developed. This was based on minimising the sum of residuals squared. This method has the advantage of not requiring any form of linearization of the data.

DataFit (Oakdale Engineering, DataFit version 9.0.59) was used for non linear regression analysis. This allowed for multiple regression analysis. DataFit results included a statistical analysis of the results obtained including t-tests, F-test and an estimate of parameter confidence intervals. DataFit included numerous built in models, however user defined models were often used.

In reporting the results of statistical tests, probability values of the tests, "P-values", are reported rather than assigning a simple pass/fail at a specific confidence level. The "P-value" of a statistical test, for example a t-test, is the probability of the calculated test statistic being equal to the calculated value assuming the null hypothesis is true. It may be interpreted as the level of confidence where the null hypothesis would be accepted. In this study, the t-test null hypothesis was always taken as $\bar{x}_A = \bar{x}_B$ (i.e. there is no difference between the sample means).

In the context of curve fitting, the t-test null hypothesis was taken as being that a parameter value is zero i.e. the parameter has no influence. A low P-value implies the null hypothesis is unlikely, leading to the rejection of the null hypothesis i.e. there is statistical support that a parameter has a no-zero value. In the following sections P values calculated by DataFit are listed as "P(t)" in the parameter tables.

DataFit also reported coefficient of multiple determination, R^2 , and adjusted coefficient of multiple determination, R_a^2 . The adjusted coefficient of multiple determination adjusted the R^2 values to take into account the sample size and number of parameters included in the model. In assessing the goodness of fit of the models preference was given to R_a^2 as this reduced the risk of overparameterization.

Graphics were prepared using SigmaPlot (Systat Software Inc., SigmaPlot version 11). Some statistical analysis, for example calculating data median and standard deviation as well linear regression, was performed within SigmaPlot. This was however only used for graphics purposes. All statistics presented were derived from either MS Excel or DataFit.

12 RESULTS

In this chapter results obtained from the experimental runs will be presented and discussed. Results will mostly be presented in aggregated form. Raw data is presented in Appendix A.

12.1 DEPOSITION CHARACTERISTICS

12.1.1 DEPOSITION RATE

Deposition rate can be expressed in several different formats. Those found to be the most useful for this study were $\mu\text{m}\cdot\text{minute}^{-1}$ and $\text{mol}\cdot\text{s}^{-1}\cdot\text{m}^{-2}$. The first measure makes intuitive sense when dealing with layer thickness and is commonly used in the literature. A more fundamental way of expressing deposition rate is $\text{mol}\cdot\text{s}^{-1}\cdot\text{m}^{-2}$. Models based on the Arrhenius rate equation were developed using both of these units. The first model, expressing deposition rate in terms of $\mu\text{m}\cdot\text{minute}^{-1}$, was developed to enable targeting a specific deposit thickness for each of the tests. This model was used to calculate the deposition rate from the temperature, % MTS, hydrogen flow rate and weight of particles coated. These parameters could be directly used on the coater when conducting test runs. This model is given by equation 91; fitted parameters are given in Table 30.

$$\text{Rate} = k(L^l)(\%MTS)^m(H^h)e^{\frac{-Q}{RT}} \quad (91)$$

Where:

Rate : Deposition rate ($\mu\text{m}\cdot\text{minute}^{-1}$)

k : Rate constant

L : Load (g)

%MTS : MTS concentration in gas stream (%)

H : Hydrogen flow rate (slm)

Q : Activation energy ($\text{J}\cdot\text{mol}^{-1}$)

R : Universal gas constant ($8.314 \text{ J}\cdot\text{K}^{-1}\cdot\text{mol}^{-1}$)

T : Deposition temperature (K)

l, m, h : Reaction order with respect to load, MTS concentration and hydrogen flow

In the case of the cold inlet, load was not used as a variable, 40 g of particles being used for all tests. In this case the impact of the load is taken up into the constant *k*. In all other respects the parameter sets are similar. A comparison of the measured deposition rates to those predicted using equation 91 and parameter values listed in Table 30 are presented in Figure 46. The 2 outliers with high deposition rates were for test runs from Group 1 which used a 20 g load and high MTS concentration.

Table 30. Deposition rate model parameters used to fit equation 91 to measured deposition rate. Deposition rate expressed as $\mu\text{m}\cdot\text{minute}^{-1}$.

Parameter	Estimated Value	P(t)	95 % Confidence Interval (\pm)
All Data (72 tests)			
k	13.815	0	5.854
l	-0.893	0	0.037
m	1.032	0	0.040
h	0.743	0	0.086
Q	27929.418	0	3824.000
R^2	0.990	R_a^2	0.990
Hot Inlet (41 tests)			
k	14.322	0.0029	9.073
l	-0.880	0	0.047
m	1.029	0	0.058
h	0.736	0	0.119
Q	28699.301	0	5882.000
R^2	0.991	R_a^2	0.990
Cold Inlet (31 tests)			
k	0.542	0.0005	0.282
l	NA	NA	NA
m	1.015	0	0.054
h	0.605	0	0.017
Q	24055.341	0	4890.923
R^2	0.988	R_a^2	0.987

From Figure 46 it can be seen that there is a good correlation between the predicted and measured deposition rates. Also, there is little difference between the models set up using the cold, hot and combined data. The good fit between the predicted and measured deposition rates is also evident from the coefficient of multiple determination, R^2 , and adjusted coefficient of multiple determination, R_a^2 , listed in Table 30.

Equation 91 was used to determine the deposition rate from the initial deposition rate tests. The model parameters were continuously updated after results from each test run became available. This proved to be successful in targeting a thickness of $35 \mu\text{m}$ for the tests in groups 3, 4 and 5. Errors in controlling the MTS flow rate accounted for a larger source of thickness variation than inaccuracies in the model. Inspection of equation 91 reveals that several of the parameters can be combined, for example the combination of %MTS and hydrogen flow rate gives the MTS flow rate. This was used to simplify the model.

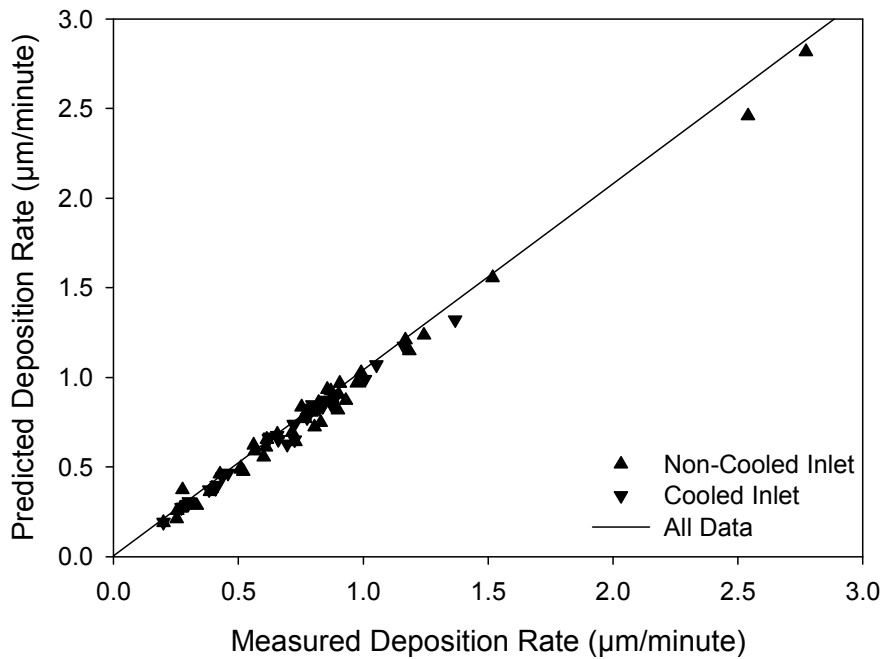


Figure 46. Measured deposition rate versus deposition rate calculated from equation 91.

An alternative form of equation 91 may also be used to calculate the deposition rate in terms of the amount of silicon carbide deposited per unit time per unit area of particles. This form of the model is given by equation 92:

$$Rate = k(M^m)(H^h)e^{\frac{-Q}{RT}} \quad (92)$$

Where:

Rate : Deposition rate ($\text{mol.m}^{-2}.\text{minute}^{-1}$)

k : Rate constant

M : MTS flux ($\text{mol.m}^{-2}.\text{minute}^{-1}$)

H : Hydrogen flow rate ($\text{mol.m}^{-2}.\text{minute}^{-1}$)

Q : Activation energy (J.mol^{-1})

R : Universal gas constant ($8.314 \text{ J.K}^{-1}\text{mol}^{-1}$)

T : Deposition temperature (K)

m, h : Reaction order with respect to MTS and hydrogen flux

Parameters for equation 92 are given in Table 31. Goodness of fit between measured and predicted values is shown in Figure 47.

Table 31. Deposition rate model parameters used to fit equation 92 to measured deposition rate. Deposition rate expressed as $\text{mol}\cdot\text{s}^{-1}\cdot\text{m}^{-2}$.

Parameter	Estimated Value	P(t)	95 % Confidence Interval (\pm)
All Data			
k	6.227	0	1.759
m	0.982	0	0.035
h	-0.136	0	0.044
Q	27070.214	0	3474.542
R^2	0.991	R_a^2	0.990
Hot Inlet			
k	6.407	0	2.751
m	0.990	0	0.055
h	-0.132	0.00043	0.069
Q	27479.546	0	5571.247
R^2	0.990	R_a^2	0.990
Cold Inlet			
k	5.911	0.0005	1.283
m	0.951	0	0.027
h	-0.161	0.00014	0.075
Q	26713.882	0	2530.921
R^2	0.988	R_a^2	0.987

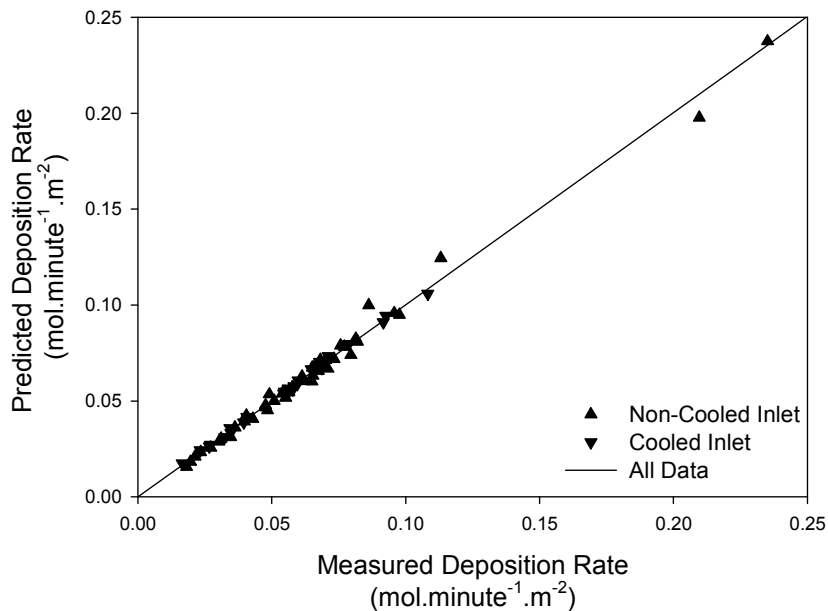


Figure 47. Measured deposition rate versus deposition rate calculated from equation 92.

Load size, measured in terms of the area of particles per test run, was originally included into equation 92 but it was found to be unimportant i.e. the exponent was found to be zero. MTS flux was found to be the strongest determinant of deposition rate, having a 1st order relationship to deposition rate. This relationship is shown in Figure 48. From the parameters fitted to equation 92 it can be seen that, over the range of temperatures and hydrogen flows used in the test work, the deposition rate has an almost linear dependence on both temperature and hydrogen flux. Hydrogen flux was found to have a larger impact than deposition temperature.

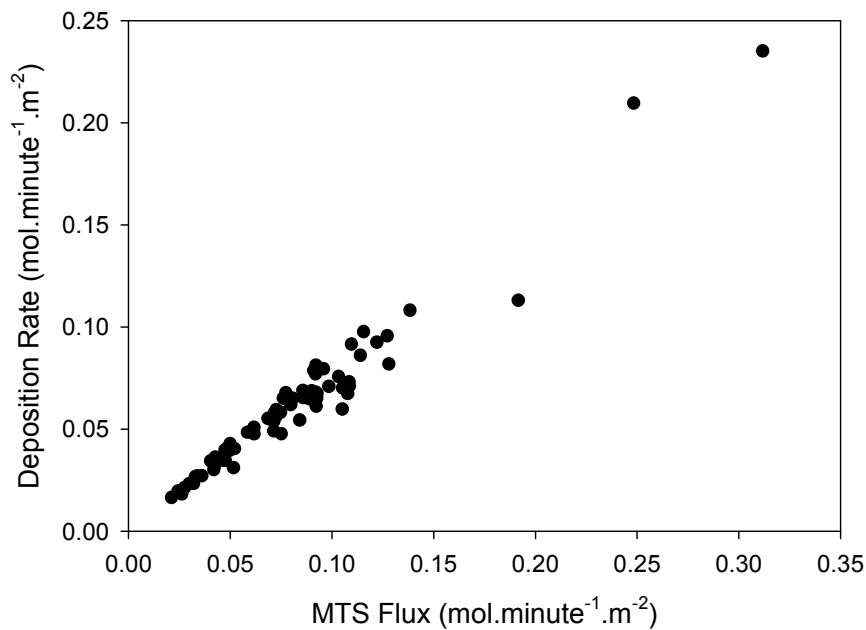


Figure 48. Influence of MTS flux on deposition rate. Data from all test runs.

12.1.2 DEPOSITION EFFICIENCY

Deposition efficiency was defined as the total mass increase of the particles divided by the expected mass increase assuming all the MTS was converted to silicon carbide deposited onto the particles. MTS converted to silicon carbide but not deposited onto the particles, by for example depositing onto the coater tube or forming dust in the gas stream, is specifically excluded from the efficiency calculations.

It would be expected that any process variable that increases deposition rate and contact time between the MTS vapour and the particle surface would result in increased deposition efficiency, thus increasing deposition temperature would be expected to increase deposition rate and so increase deposition efficiency. Interaction between parameters will however make the situation more complex.

Deposition efficiency will be constrained between 0 % and 100 %. It is expected that a sigmoid function between these limits would most realistically describe the measured efficiency. Although linear models may adequately describe the measured deposition efficiency over a narrow range it must be borne in mind that any linear model must be constrained between 0 % and 100 %.

Deposition temperature was found to be the most important parameter in determining deposition efficiency. Equation 93 was found to adequately describe the deposition rate as a function of temperature. Equation parameters are presented in Table 32. The poor fit for the data for deposition at 1355 °C is due to a single value of MTS concentration and hydrogen flow rate being used for all of these tests. From Figure 49 it can be seen that deposition efficiency increases asymptotically with increasing temperature. In Figure 49 the average value for each deposition temperature is plotted.

$$Efficiency = \frac{a}{1 + \left(\frac{T}{c}\right)^b} \quad (93)$$

Where:

- a : Maximum achievable efficiency (%)
- b : Logistic function shape parameter
- c : Logistic function position parameter (°C)
- T : Deposition temperature (°C)

Table 32. Equation 93 parameter values.

Parameter	Hot Inlet	Cold Inlet
a	98.545	99.4987
b	-6.100	-6.5746
c	1133.973	1144.111
R_a^2	0.997	0.994

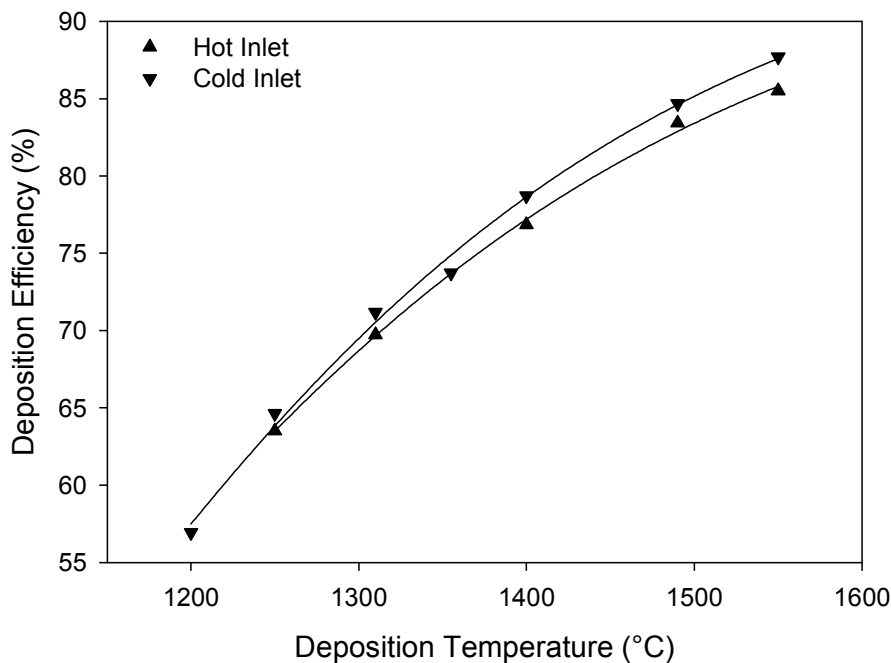


Figure 49. Influence of deposition temperature on deposition efficiency. Each data point represents the average deposition efficiency for the particular temperature. Logistic function fitted to each curve.

At all temperatures investigated the cold inlet resulted in higher deposition efficiency, also the predicted maximum deposition efficiency for the cold inlet was higher (99.5 %) than that of the hot inlet (98.5%). This is somewhat surprising as it would be expected that the higher temperature of the gas entering the bed of particles in the case of the hot gas inlet would have resulted in higher deposition efficiency due to the higher reaction rates. A possible explanation for the lower deposition efficiency may be the increased amount of the silicon carbide deposited onto the coater gas feed tube and inlet nozzle. Any deposition in the gas feed system would reduce the amount of precursor available for depositing onto the particles.

As can be seen from Figure 50A and Figure 50B there is considerable spread in the deposition efficiency around the average values for a particular temperature. This is due to the combined impact of MTS concentration and hydrogen flow rate. The impact of MTS concentration and hydrogen flow is displayed in Figure 51A and Figure 51B. In Figure 51 the impact of each parameter is shown for data grouped by deposition temperature. Data from the hot and cold inlet system has been pooled. Lines fitted to the data represent the best fit linear equation.

From Figure 51A it can be seen that the influence of MTS concentration is dependent on deposition temperature. At lower temperatures increasing MTS concentration resulted in a reduction in deposition efficiency. As deposition temperature increased this effect became weaker until at 1550 °C MTS concentration had virtually no effect on deposition efficiency.

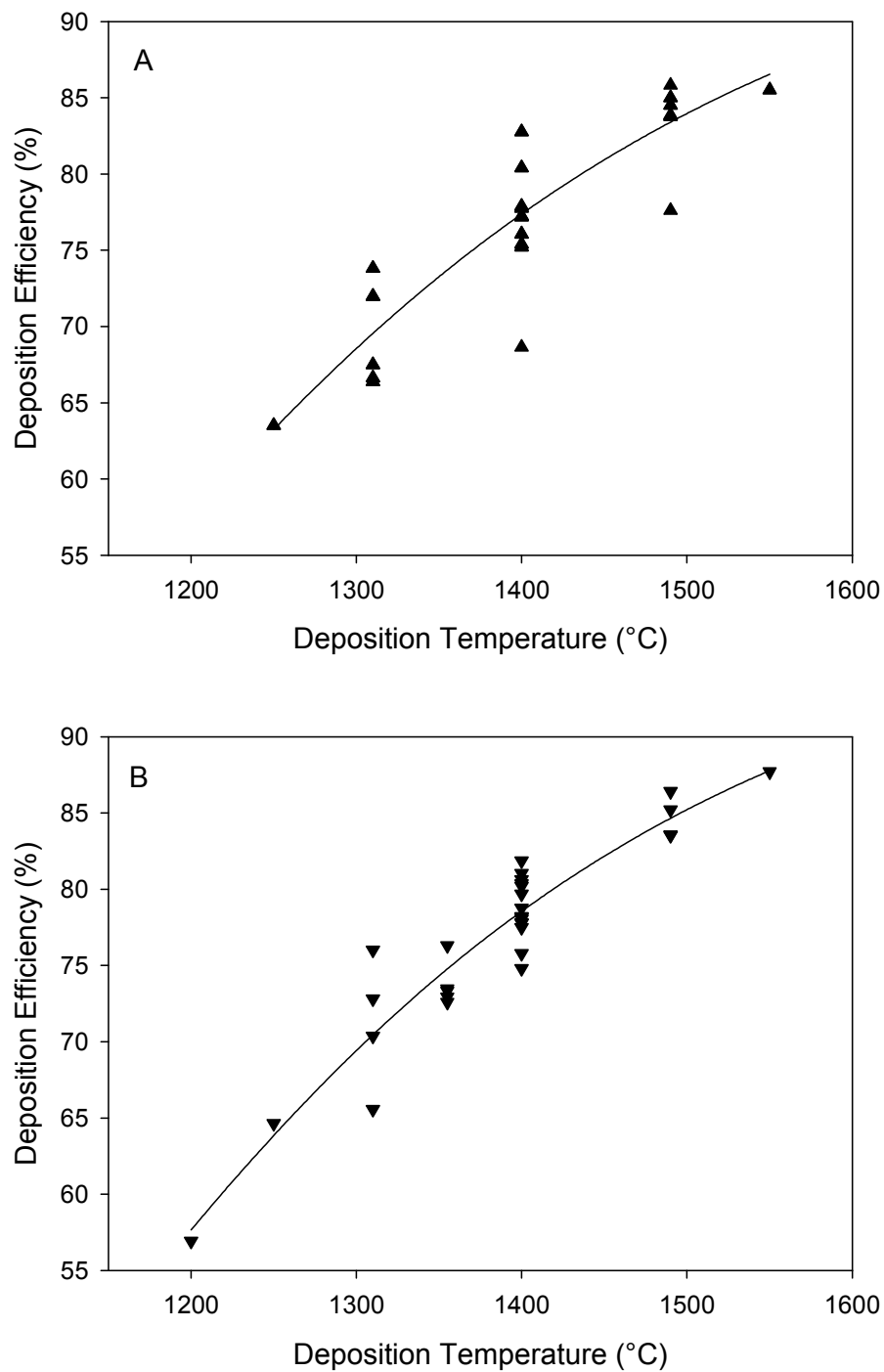


Figure 50. Spread of efficiency values due to influence of MTS concentration and hydrogen flow rate at each deposition temperature for (A) hot, (B) cold inlet.

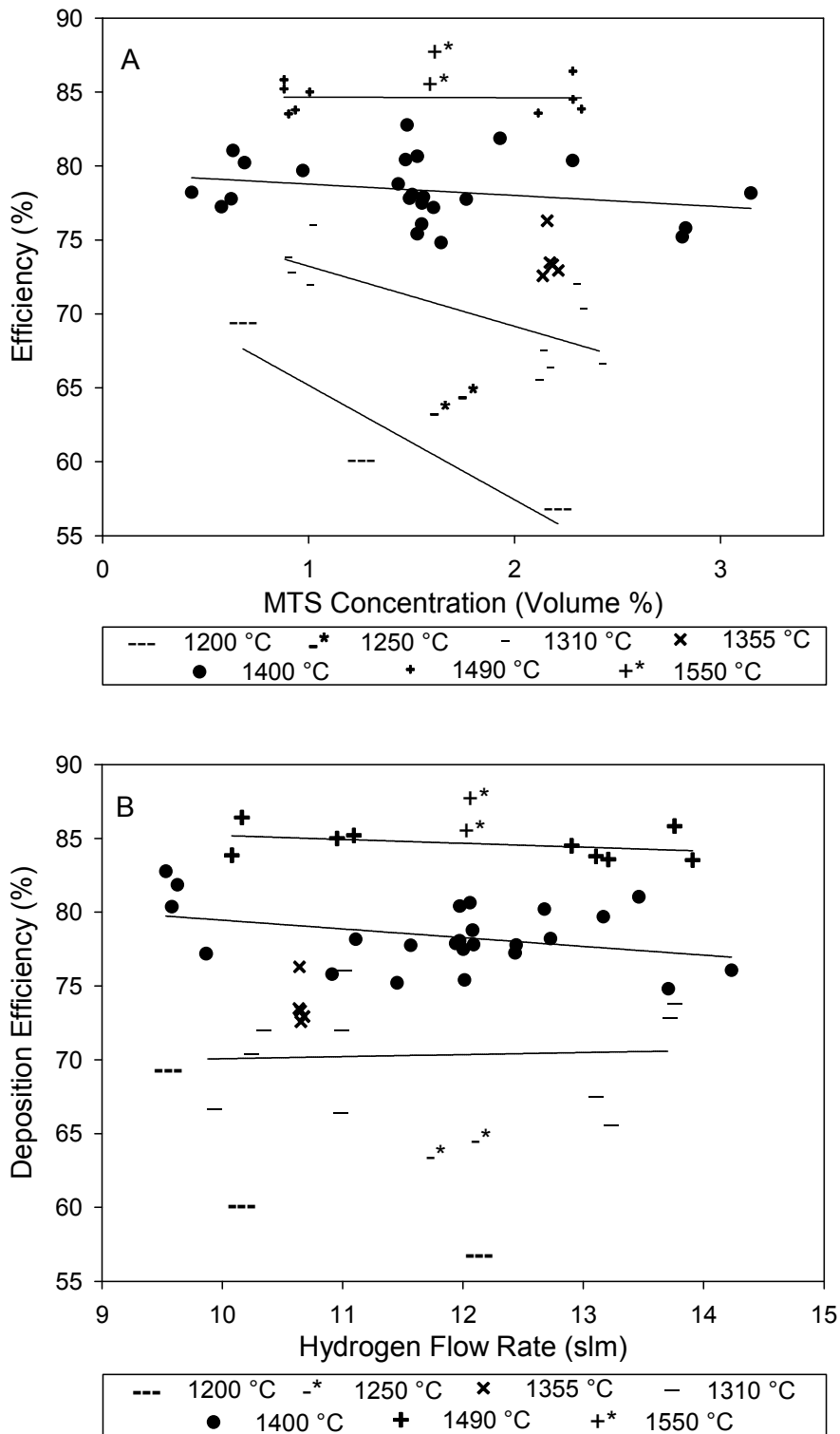


Figure 51. Influence of (A) MTS concentration, (B) hydrogen flow rate on deposition efficiency. Pooled data for hot and cold inlet.

Hydrogen flow appears to have very little impact on deposition efficiency. From Figure 51B it can be seen that deposition efficiency changes little with changes in flow. There is no clear trend in response to changes in flow rate as temperature is changed.

From the limited data available from the deposition rate tests, it was possible to investigate the impact of load size on deposition efficiency. Data from accepted test runs from this group is presented in Figure 52. Data for all MTS concentrations and hydrogen flow rates are shown for each load size. As the full experimental matrix was not run and some of the test runs experienced problems, such as gas leakage, that may impact the calculated deposition efficiency it is not possible to calculate a meaningful average for the MTS concentration and hydrogen flows. From Figure 52 it can be seen that deposition efficiency increased with an increase in load. This effect is more pronounced at a lower deposition temperature. This is in line with expectation as a larger load would result in a longer contact time between the gas and particles resulting in a higher efficiency. This effect would also become less important as the deposition rate increased with increasing temperature.

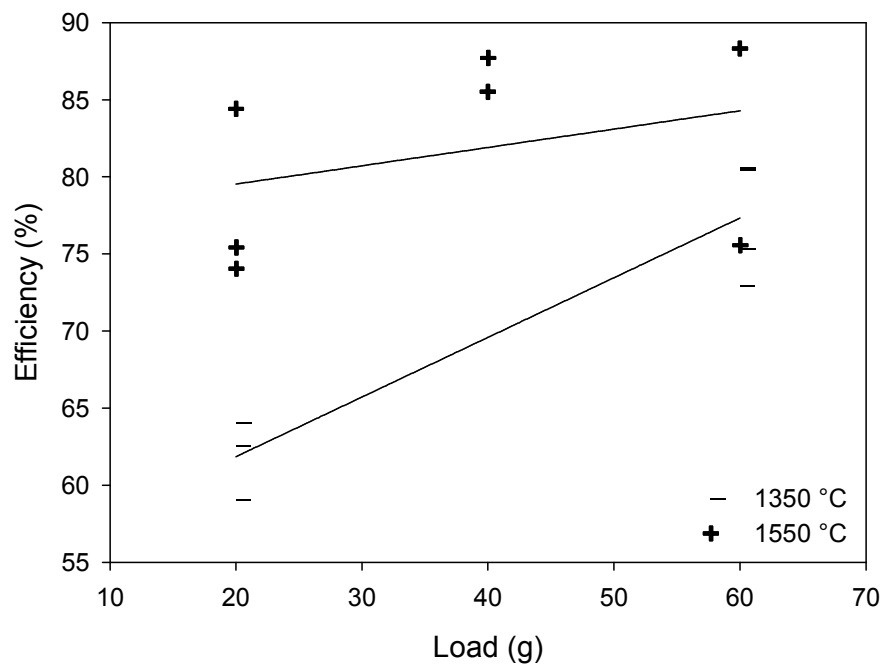


Figure 52. Influence of load size on deposition efficiency. Data from coating rate test runs using a hot gas inlet.

12.2 DENSITY

The following analysis was performed on density values measured on powdered samples using a helium pycnometer as described in section 11.3.2. All density measurements, including those determined by other methods, are presented in Appendix A.

Regression analysis indicated that deposit density was determined by deposition temperature, MTS flux and gas inlet type. Over the temperature range investigated, deposit density does not have an obviously non-linear dependence on temperature. However, as discussed in section 6.6, a quadratic relationship has often been reported in the literature. Density cannot increase linearly with temperature over an extended temperature range as this would result in a density of greater than theoretical density (3.217 g.cm^{-3}) being predicted for high deposition temperatures. Based on the above it was decided to use a quadratic rather than a linear function to model the effect of temperature on density. Density was found to decrease linearly as MTS flux was increased. Use of the hot inlet system was found to result in a higher density than the cold inlet.

Equation 94, together with parameter values in Table 33, was used to model the deposit density as a function of process parameters:

$$\rho = a + bT^2 + cT + dM + eI \quad (94)$$

Where:

- ρ : Deposit density (g.cm^{-3})
- a, b, c, d, e : Model parameters
- T : Deposition temperature ($^{\circ}\text{C}$)
- M : MTS flux ($\text{mol.m}^{-2}.\text{minute}^{-1}$)
- I : Inlet type (Hot inlet = 0; Cold inlet = 1)

Table 33. Equation 4 parameter values.

Parameter	Value	P(t)	95 % Confidence Interval (\pm)
a	0.0346		
b	-1.257×10^{-6}	0	1.077×10^{-7}
c	4.006×10^{-3}	0	1.597×10^{-4}
d	-0.720	0.0004	0.382
e	-2.307×10^{-2}	0.03196	2.100×10^{-2}
R^2	0.637		
R_a^2	0.615		

The relationship between deposit density and process parameters is shown in Figure 53 and Figure 54. In both figures the model values are plotted for a cold inlet. Plots for the hot inlet would be parallel to the cold inlet plots but shifted upwards by $0.002307 \text{ g.cm}^{-3}$ (value of parameter e in equation 94). In Figure 53, the MTS values used to calculate the displayed model values are $0.02 \text{ mol.m}^{-2}.\text{minute}^{-1}$ (upper line) and $0.14 \text{ mol.m}^{-2}.\text{minute}^{-1}$ (lower line). In Figure 54 the upper and lower lines were calculated for a temperature of $1550 \text{ }^\circ\text{C}$ and $1250 \text{ }^\circ\text{C}$ respectively.

In Figure 53 there is considerable uncertainty as to the exact influence of temperatures above $1550 \text{ }^\circ\text{C}$. Based on published data it is assumed that the density will decrease when the temperature increases above a critical value. With the available data it is not known at what temperature this will occur. When viewed individually the hot and cold inlets behave differently. When the hot inlet is used there is a definite quadratic relationship with a maximum density at approximately $1450 \text{ }^\circ\text{C}$. For the cold inlet density increases almost linearly up to $1550 \text{ }^\circ\text{C}$. It is not known if the density would have shown a maximum and started to decrease at higher deposition temperatures.

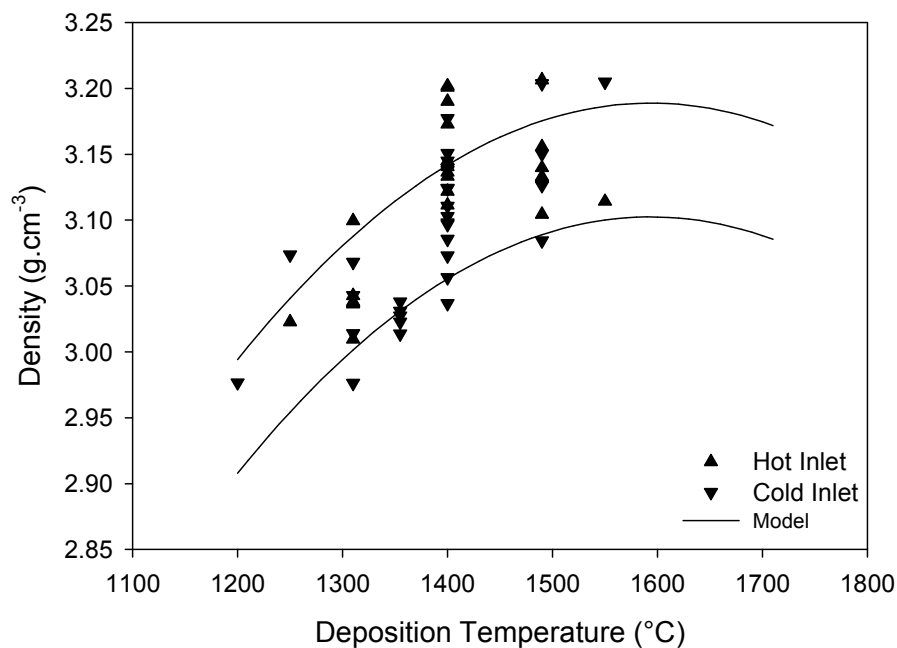


Figure 53. Deposit density as a function of deposition temperature. Model values calculated for MTS values of $0.02 \text{ mol.m}^{-2}.\text{minute}^{-1}$ and $0.14 \text{ mol.m}^{-2}.\text{minute}^{-1}$ for the upper and lower lines respectively.

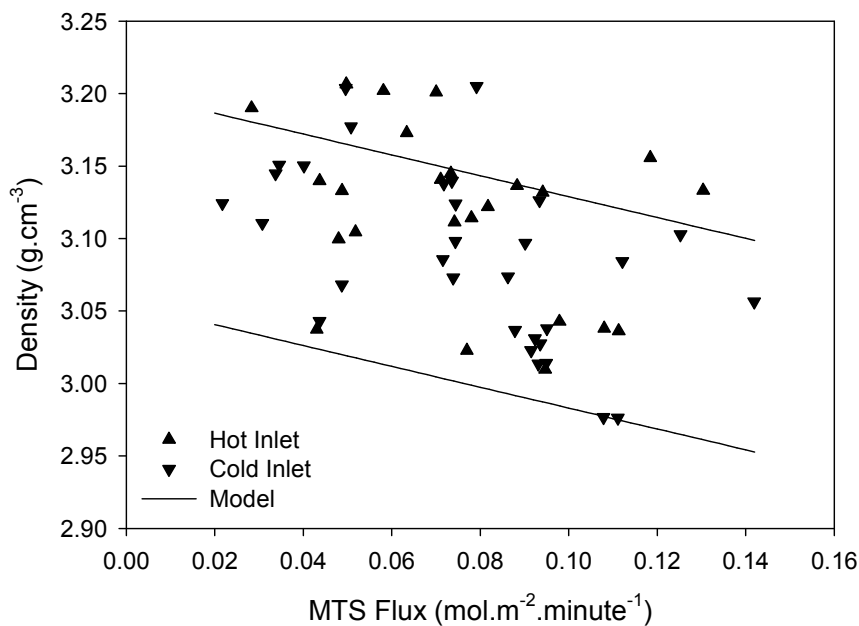


Figure 54. Deposit density as a function of MTS flux. Model values calculated for deposition temperatures of 1550 °C and 1250 °C for the upper and lower lines.

12.3 SEM GRAIN SIZE

12.3.1 SURFACE GRAIN SIZE

Grain size was measured on the surface of the deposits using secondary electron images and in cross section using backscatter electron images. Initially it was anticipated that the dome like structures seen on the surface of the deposit was the top surface of columnar grains. Once the backscatter electron images of the deposit grain structure became available it was realised that the dome structures were not related to individual grains but rather to microcrystalline grain structures. The dome structures appear to be the top of polycrystalline growth cones; their size therefore does not have any significance in terms of grain size. Only in cases where individual, faceted, grains are visible can the grain size be determined from images of the deposit surface. The transition from a structure consisting of growth cones to one of individual grains was not sharp, there being a transition structure consisting of growth cones made up of grains coarse enough for individual grains to be discernable. In the current study only a portion of the deposits had morphology where true grain size could be determined. Examples of the observed structures are shown in Figure 55.

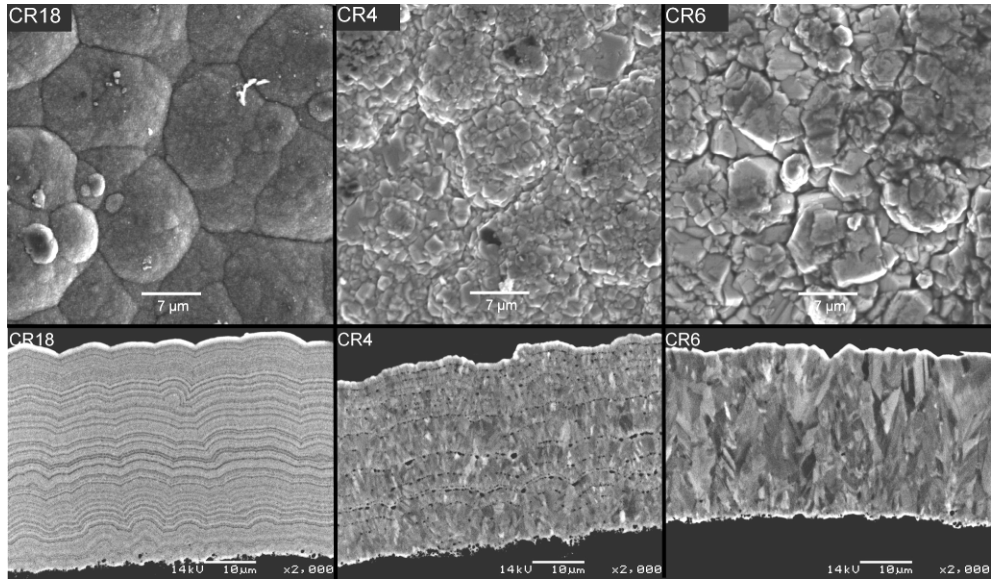


Figure 55. Typical surface and cross sectional view of deposits showing variation in growth structure and grain size. Secondary electron images of surface structure and backscatter electron images of cross sections.

In Figure 56 the structures type and size are shown as a function of deposition temperature and MTS flux. Surface features were classified as “Domes”, “Clusters” and “Facets”. An example of “Domes”, “Clusters” and “Facets” are shown by runs CR18, CR4 and CR6 respectively in Figure 55.

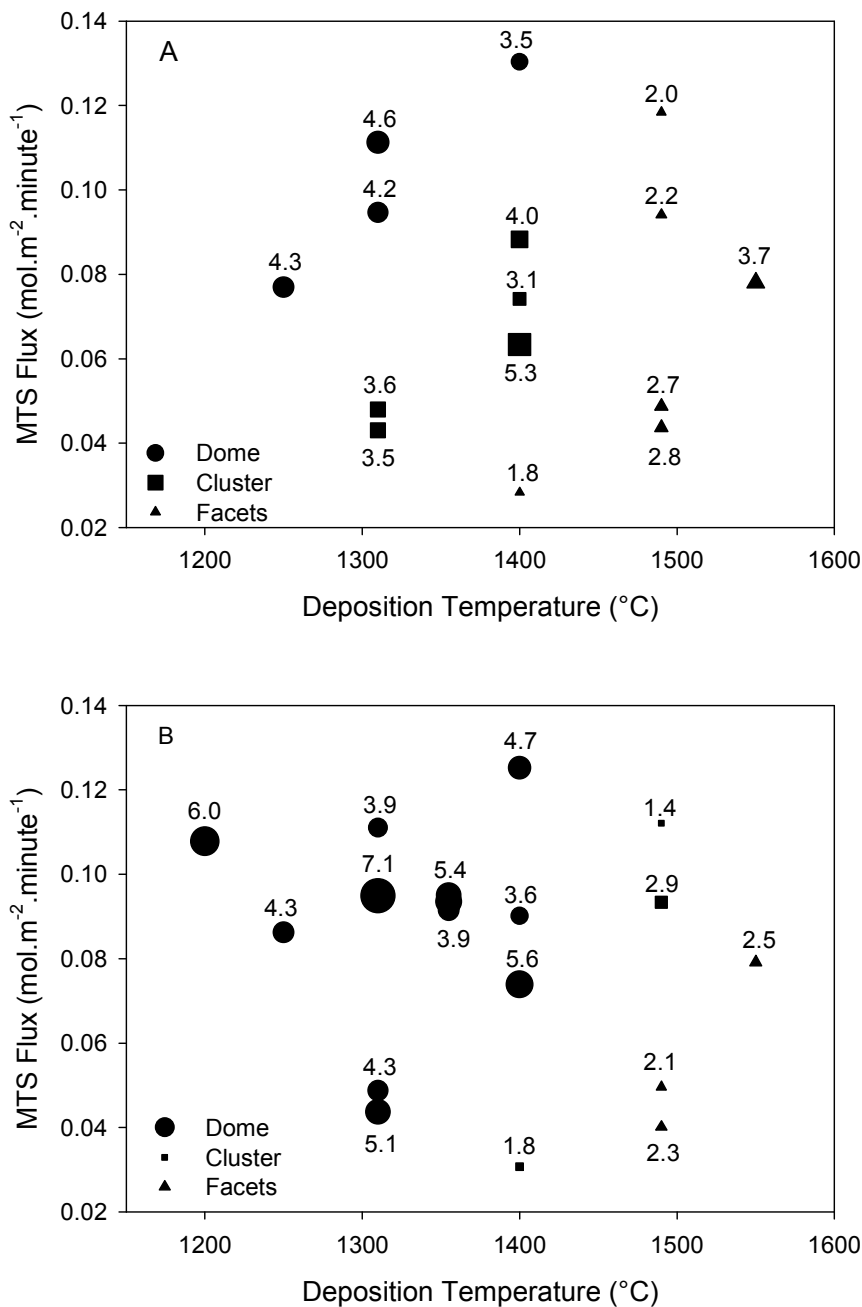


Figure 56. Influence of deposition temperature and MTS flux on surface structure. A: Hot inlet. B: Cold inlet. Symbol size is proportional to feature size, actual values are shown next to each symbol.

In classifying the surface structure type the distinction between “Domes” and “Clusters” is somewhat arbitrary with no clear cut difference between the two structures. In the case of samples which had a clear faceted grain structure it was not uncommon to see clusters of small faceted grains. Details of the measurement method used to determine the data in Figure 56 can be found in section 11.7.1. In the above analysis average dimensions were used. Grain sizes had a lognormal distribution and were therefore not evenly distributed around the average value.

12.3.2 CROSS SECTIONAL GRAIN SIZE

Backscatter electron images clearly revealed the grain structure of the deposits. For tests conducted at high temperature and low MTS flux the grains were clear enough to be measured. The temperature and MTS flux conditions required for measureable grains to develop corresponded, approximately, to the conditions required to form clusters or faceted structure as discussed in the previous section. At lower temperatures and higher MTS flux conditions the grains became too small or indistinct to measure. At sufficiently low temperatures no crystals were visible, the cross section appearing as even bands. This change in structure can be seen in Figure 55. Further details of deposit structure may be found in section 13.2.3 and Appendix C.

Grain size was found to be dependent on deposition temperature, MTS flux and inlet type. The relationship between these parameters and grain size is given by Equation 95 and the values listed in Table 34.

$$L = a + bT + cM + dMI \quad (95)$$

Where:

- L : Grain size (Intercept length) (μm)
- a, b, c, d : Constants
- T : Deposition temperature ($^{\circ}\text{C}$)
- M : MTS flux ($\text{mol}\cdot\text{m}^{-2}\cdot\text{minute}^{-1}$)
- I : Inlet type (Hot Inlet = 0; Cold Inlet = 1)

Table 34. Equation 95 parameter values.

Parameter	Value	P(t)	95 % Confidence Interval (\pm)
A	-9.321	0.00002	2.388
b	7.875×10^{-3}	0	1.640×10^{-3}
c	-3.125	0.02404	3.776
d	-6.042	0.00005	2.610
R^2	0.952		
R_a^2	0.933		

Similarly to the surface structure, grain size measurements were found to fit a lognormal distribution. The deposit was found to be textured with grains elongated in the radial direction. An example of the grain size distribution in the radial and tangential direction is shown in Figure 57. Larger grains tended to be more elongated in the radial direction than smaller grains. The aspect ratio ($D_{\text{Radial}}/D_{\text{Tangential}}$) of the grains as a function of average grain size is shown in Figure 58.

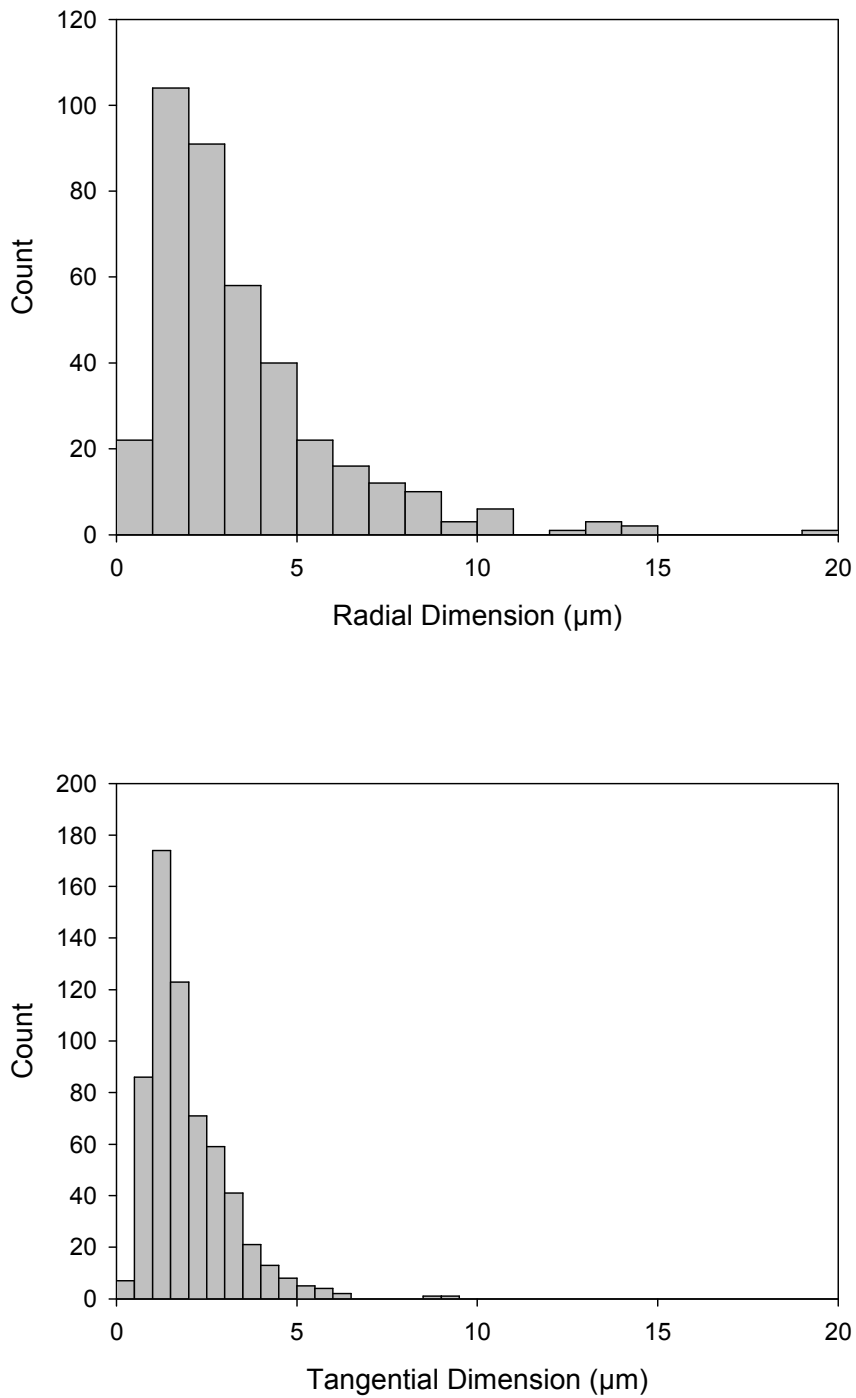


Figure 57. Grain size distribution in the radial and tangential direction for HF17. Test run HF17 had the largest and most elongated grains.

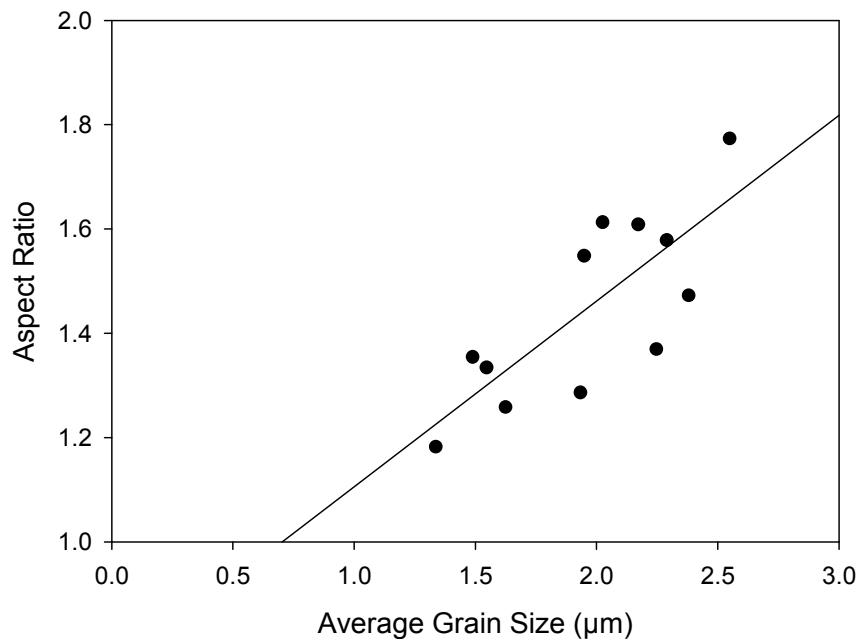


Figure 58. Aspect ratio of grains as a function of grain size. Grains are elongated in the radial direction.

From equation 95 it can be seen that the grain size increases linearly with deposition temperature and decreases linearly with increasing MTS flux. The impact of MTS flux is dependent on the type of gas inlet used with the cold inlet being more sensitive to changes in MTS flux than the hot inlet. The dependence of grain size on deposition temperature and MTS is shown in Figure 59 and Figure 60. From Figure 61 it can be seen that there is a good correlation between predicted and actual values. This is also reflected in the R^2 value in Table 34.

In Figure 60 the change in slope of the line representing the model indicates that there is an interaction between MTS flux and inlet type. When the cold inlet was used the grain size decreases more rapidly with an increase in MTS flux.

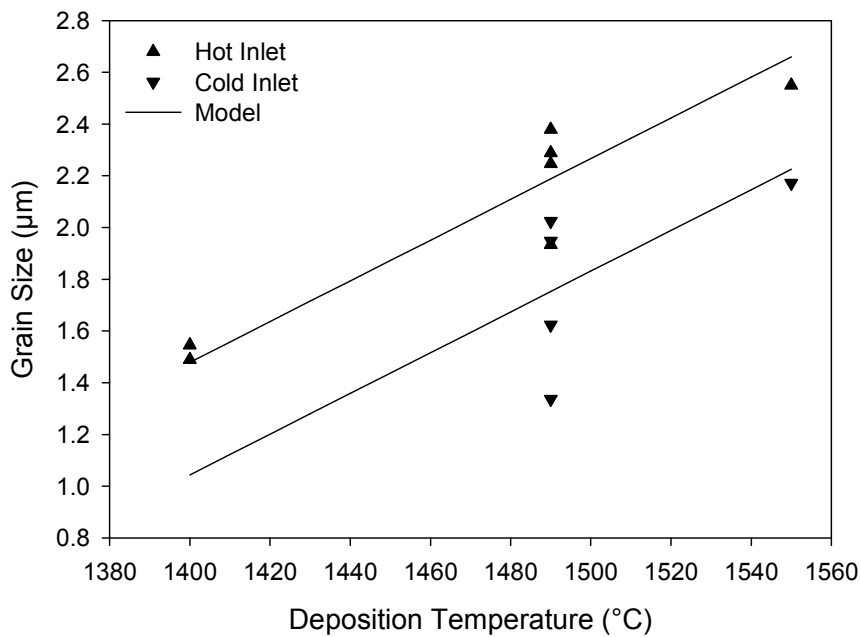


Figure 59. Grain size as a function of deposition temperature. Predicted values are plotted for a MTS concentration of $0.072 \text{ mol.m}^{-2}.\text{minute}^{-1}$ for a hot (upper line) and cold inlet (lower line).

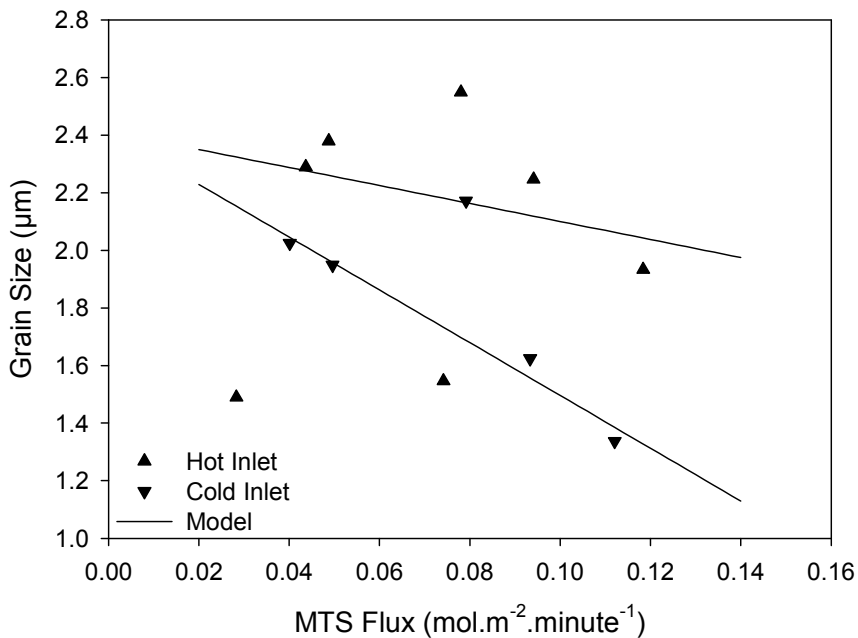


Figure 60. Grain size as a function of MTS flux. Predicted values are plotted for a temperature of $1490 \text{ }^\circ\text{C}$ for a hot (upper line) and cold inlet (lower line).

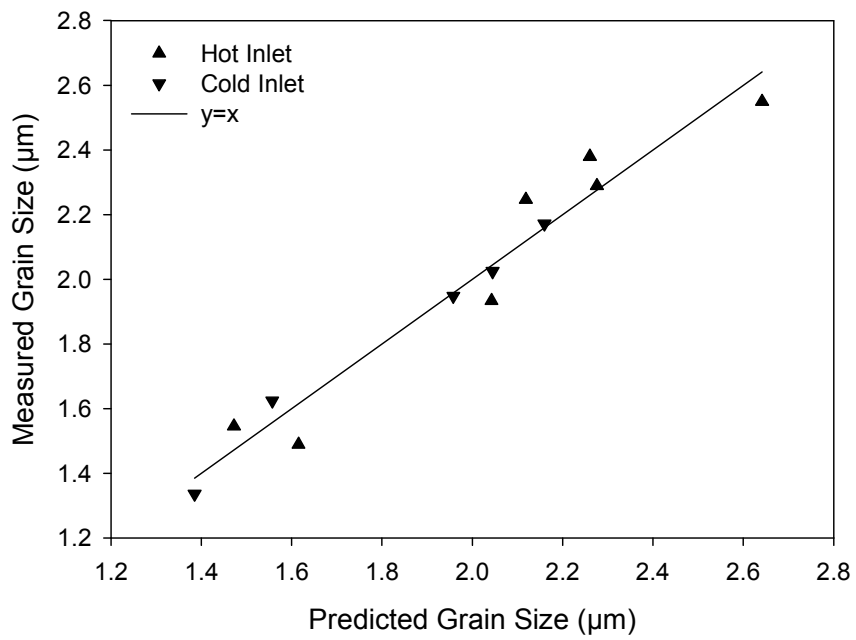


Figure 61. Correlation between actual grain size and grain size predicted by equation 95.

12.4 MECHANICAL PROPERTIES

12.4.1 CRUSH LOAD

A summary of crush load data may be found in Appendix A.

For all test runs it was found that measured crush loads could be described using either a Weibull or normal distribution. For the majority of test runs it was found that the fit to a Weibull distribution was marginally better than to a normal distribution, however the differences were small enough to warrant regarding the data as being normally distributed.

Initial testing revealed significant differences in crush load between particles from starting material CPT-T-G130 and CPT-T-G140. This resulted in several test runs from group HF (HF1, HF3, HF4, HF5, HF6) and CR (CR1, CR2, CR3) that had been coated using particles from CPT-T-G130 being repeated using CPT-T-G140 as the starting material. This allowed for a direct comparison between test runs. The differences between the two lots of starting material were also apparent when testing uncoated particles. From

Figure 62 it can be seen that, using soft anvils, there was a significant difference in crush load between uncoated particles from CPT-T-G130 and CPT-T-G140. This large difference was however not seen when hard anvils were used.

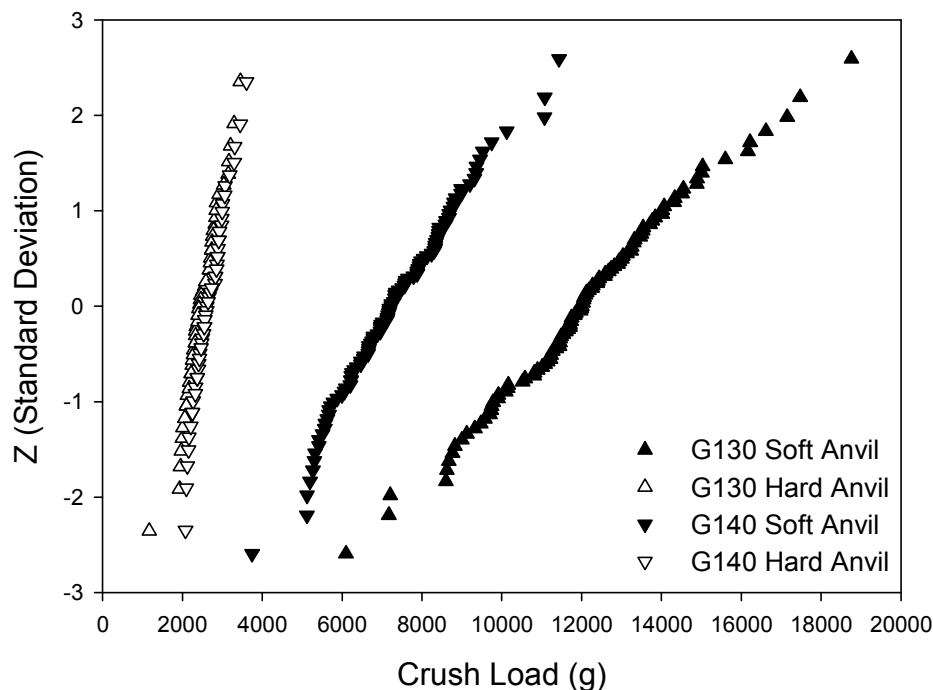


Figure 62. Normal probability plot of starting material crush load using soft aluminium anvils and alumina anvils.

G130 Soft: $\bar{x} = 12072$ g, $\sigma = 2203$ g

G130 Hard: $\bar{x} = 2508$ g, $\sigma = 417$ g

G140 Soft: $\bar{x} = 7346$ g, $\sigma = 1572$ g

G140 Hard: $\bar{x} = 2681$ g, $\sigma = 364$ g

For coated particles, the difference between the starting particles can be seen in Figure 63. In the figure, crush test results from test runs processed using similar conditions, but using different lots of starting material, are compared. The test runs chosen had similar coating thicknesses. As was the case with the uncoated particles, coated particles from lot CPT-T-G130 have a higher crush load than particles from CPT-T-G140.

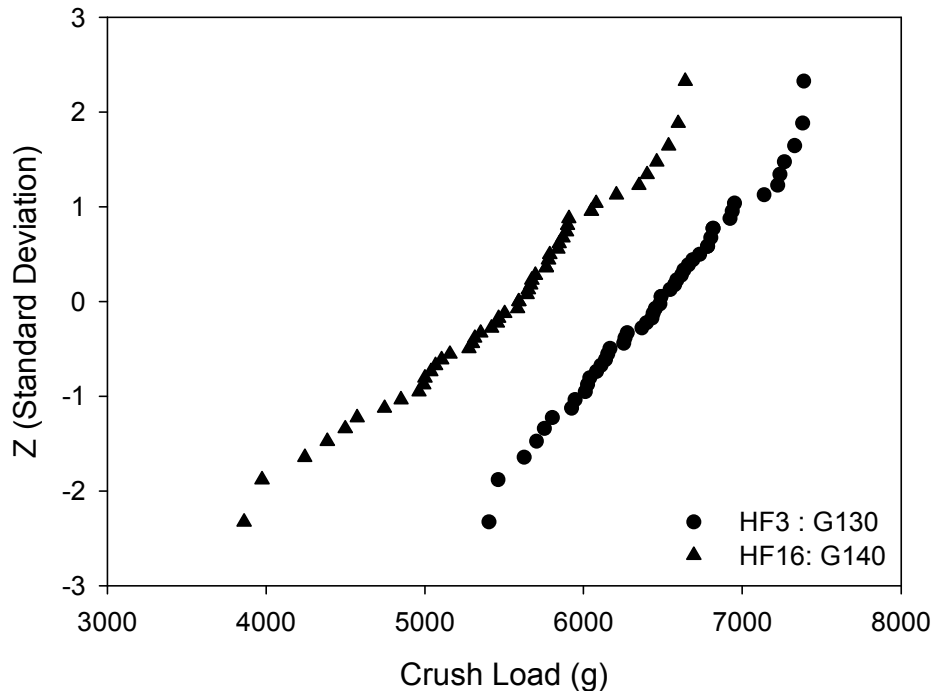


Figure 63. Impact of starting material on crush load. Batches HF3 and HF16 processed under similar condition but used particles from lots CPT-T-G130 and CPT-T-G140 respectively. Soft anvils used for both sets of particles. Deposit thickness was 33 μm for test run HF3 and 32 μm for test run HF16.

From

Figure 62, Figure 64 and Figure 65 it can be seen that there is a significant difference between the measured crush load when using soft anvils and hard anvils. From Figure 65 it is seen that the differences are consistent across all test runs. These differences reflect the difference in failure mechanism between the two test methods.

As expected, deposit thickness was found to have a large influence on crush load. Test runs TT1 to TT5 were specifically intended to investigate the influence of thickness on crush load. These tests were conducted under similar process conditions with only deposition time being varied in order to obtain a range of deposit thicknesses. Crush load data from these test runs is presented in Figure 64. The data is well represented by a linear fit with a R_a^2 value of 0.979 when averaged data is considered. The effect of thickness together with all other factors, such as process conditions, is shown in Figure 65. It can clearly be seen that deposit thickness plays a major role in determining crush load.

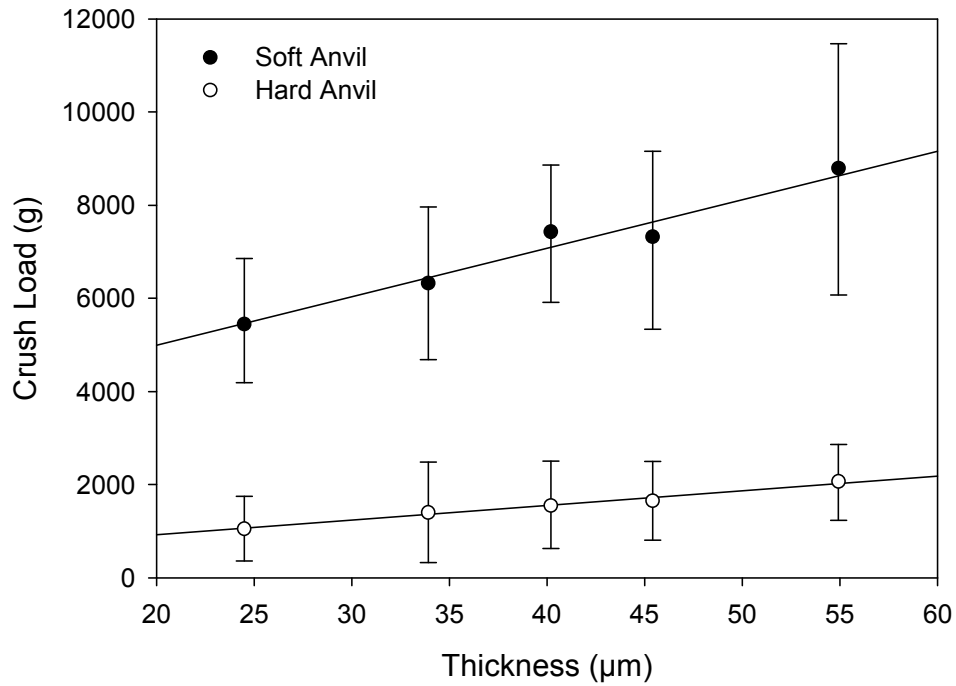


Figure 64. Crush load of particles from test runs TT1 to TT5. All test runs were processed under similar conditions. Markers represent median value, error bars represent 3σ values.

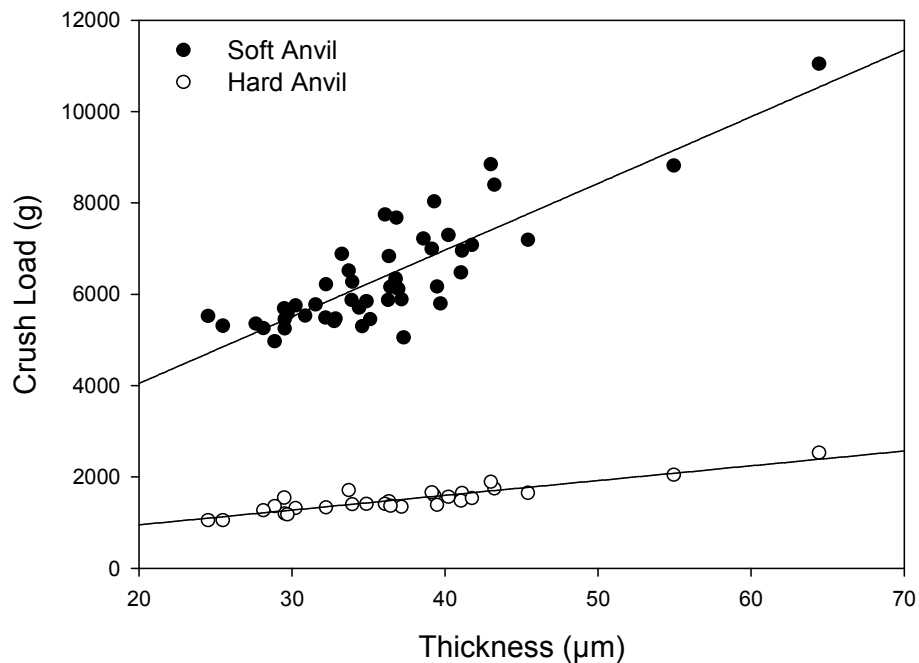


Figure 65. Test average crush load of each test runs using CPT-T-G140 particles as a function of deposit thickness. Variation is due to different processing conditions of the various tests as well as measurement and random errors.

Based on the results presented in Figure 65, for CPT-T-G140 particles the soft anvil crush strength dependence on silicon carbide thickness may be expressed as:

$$\text{CrushLoad} = 1.185 t_{\text{SiC}}^2 + 48.553 t_{\text{SiC}} + 3046 \quad (96)$$

Where Crush Load is expressed in gram and silicon carbide thickness, t_{SiC} , in micrometer. R_a^2 for this fit is 0.710. Deviation from the model is due to differences in process conditions and random measurement errors. As will be shown in subsequent paragraphs deposition temperature and inlet type influence crush load while MTS concentration and hydrogen flow have insignificant influence. As was discussed in section 11.6.2 the expected standard deviation of means is approximately 150 g, this will contribute to the scatter of data.

Using a crush load of 7346 g for uncoated CPT-T-G140 particles and equation 96 it can be seen that for a coating thickness of less than approximately 43 μm the coated particles fail at a load less than the uncoated particles. When hard anvils are used a coating thickness of at least 87 μm is required before the strength of the coated CPT-T-G140 particles increases above that of the uncoated particles. A similar analysis reveals that, when soft anvils are used, CPT-T-G130 particles would require a coating of about 110 μm before the particle strength increased above that of the uncoated particles. For this model R_a^2 was only 0.52, placing considerable doubt on the accuracy of the analysis. It should however be noted that all the test runs, including DR6 which had a thickness of 91 μm , failed at a load less than the crush load of the uncoated particles. No coated CPT-T-G130 particles were tested using hard anvils.

Analysis of the impact of process conditions was performed using crush load data that had been normalised to a thickness of 35 μm . This was done by calculating the crush load using crush load / thickness relationship determined by fitting a straight line through all of the data points used for an analysis. This procedure was repeated for each group (i.e. test group CR and HF) of tests as it was found that there were differences in the crush load/thickness relationship between the various groups. Corrected crush load data for all tests is presented in Figure 66. In the case of tests using particles from lot CPT-T-G130 no statistically significant relationship between any of the process variables and crush load could be found. This was also the case for CPT-T-G140 particles from the CR group that were tested with hard anvils. It should be noted that the lowest deposition temperature used for coating of CPT-T-G130 particles was 1310 $^{\circ}\text{C}$, which was higher than the temperature where temperature effects were noticed for other tests. It is therefore possible that the lack of measured effect of temperature is due to the temperature range investigated rather than a real lack of influence. Only tests using particles from lot CPT-T-G140, and tested using soft anvils, showed any systematic variation with deposition parameters. Unless noted otherwise the following analysis is limited to tests from group CR and HF, which used particles from CPT-T-G140, and were tested using soft anvils.

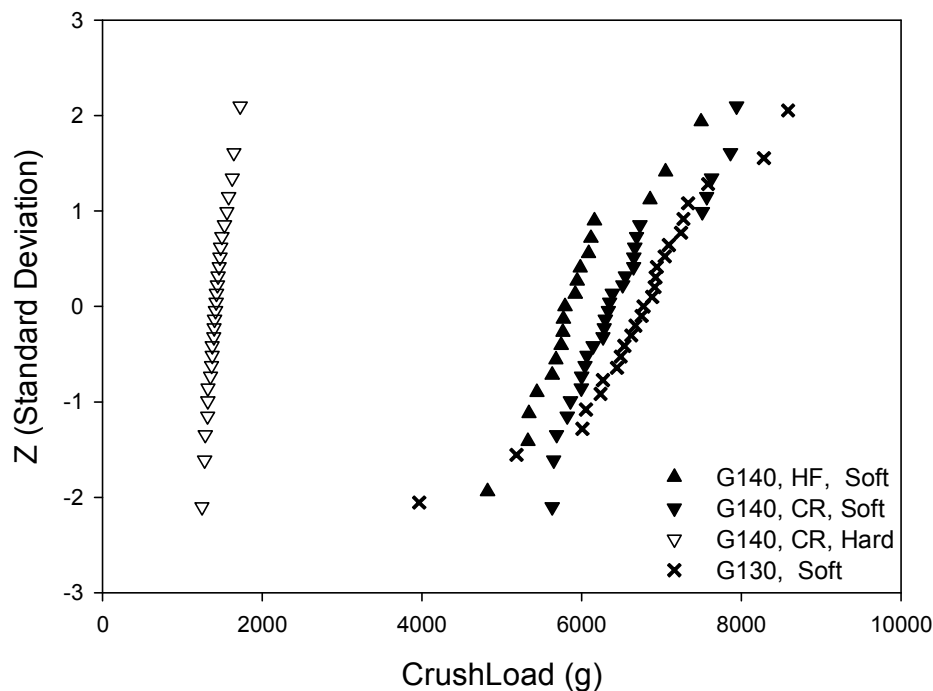


Figure 66. Normal probability plot of corrected crush load for all test runs. Each data point represents the average value of the crush load, corrected to a thickness of 35 μm , for a test run. Marker type indicate test starting material (CPT-T-G130 or CPT-T-G140), test group (DR, CR or HF) and anvil type (Soft or hard). For tests using CPT-T-G130 starting material test runs from group CR and HF were tested using soft anvils only.

For each of the groups of data presented in Figure 66 it was found that the data fitted a normal distribution. A summary of the results are given in Table 35. In the case of test runs tested using soft anvils each of the groups had several outliers. For test runs using CPT-T-G130 particles the outliers were found at both the low and high end of the distribution. For CPT-T-G140 particles outliers were only found at the high end of the distribution.

Table 35. Corrected crush load average, and standard deviation, for each group of test runs.

Test	Average Crush Load (g)	Standard deviation (g)
G140, HF, Soft anvil	5944	629
G140, CR, Soft anvil	6493	660
G140, CR, Hard anvil	1433	116
G130, DR, CR, HF, Soft anvil	6725	902

Only deposition temperature was found to have a statistically significant influence on crush load. A model including a quadratic term for temperature, a first order term

for MTS concentration and an interaction term between temperature and MTS concentration could be fitted to the group CR tests with a R_a^2 of 0.81. This model however completely failed to fit the data from group HF. Analysis of the crush load revealed that only deposition temperature had any significant systematic. As can be seen from Figure 67(A) there is considerable variation in crush loads measured for each deposition temperature. From the data available no systematic explanation for this variation could be found.

Several functions could be fitted to the data shown in Figure 67 (A) however it was assumed that, over the temperature range of interest, the data could be described by a decreasing sigmoid function as given in equation 97.

$$CrushLoad = a - \frac{b}{\left(1 + \left(\frac{T}{c}\right)^d\right)} \quad (97)$$

Where a , b , c and d are constants and T is the deposition temperature measured in degrees Celsius. Values of the model parameters are presented in Table 36. When fitting the model to the data from group HF it was assumed that the maximum strength would be the same as for group CR, it therefore follows that the value of parameter a will be the same for the two models. Without this assumption the curve fitting software (DataFit) would not converge to a solution when fitting the data to equation 97. In Table 36, R^2 and R_a^2 values in parenthesis are for models fitted to the average value for each deposition temperature.

Table 36. Parameter values for fitting equation 97 to measured crush strength. Model fitted to all data for each temperature. Values in parenthesis are for a model fitted to data averaged for each temperature.

Parameter	CR			HF		
	Estimate	P(t)	95 % CI	Estimate	P(t)	95 % CI
a	7942	0	1214	7942	NA	NA
b	1550	0.0171	1249	2205	0	307
c	1262	0	150	1278	0	37
d	-140	0.8628	1654	-59	0.096	71
R^2	0.309 (0.957)			0.434 (0.997)		
R_a^2	0.223 (0.914)			0.363 (0.994)		

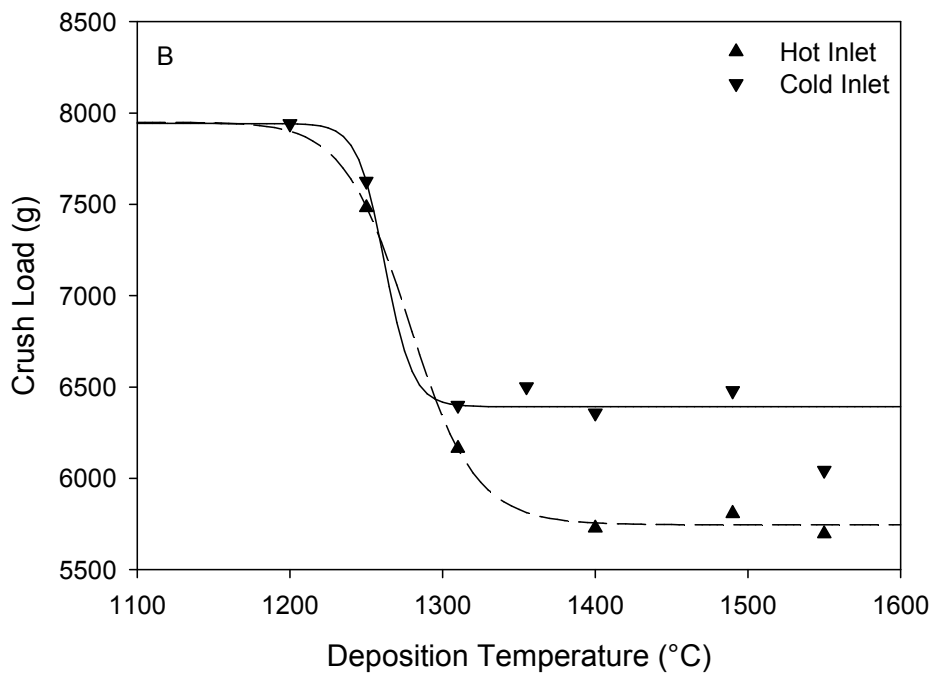
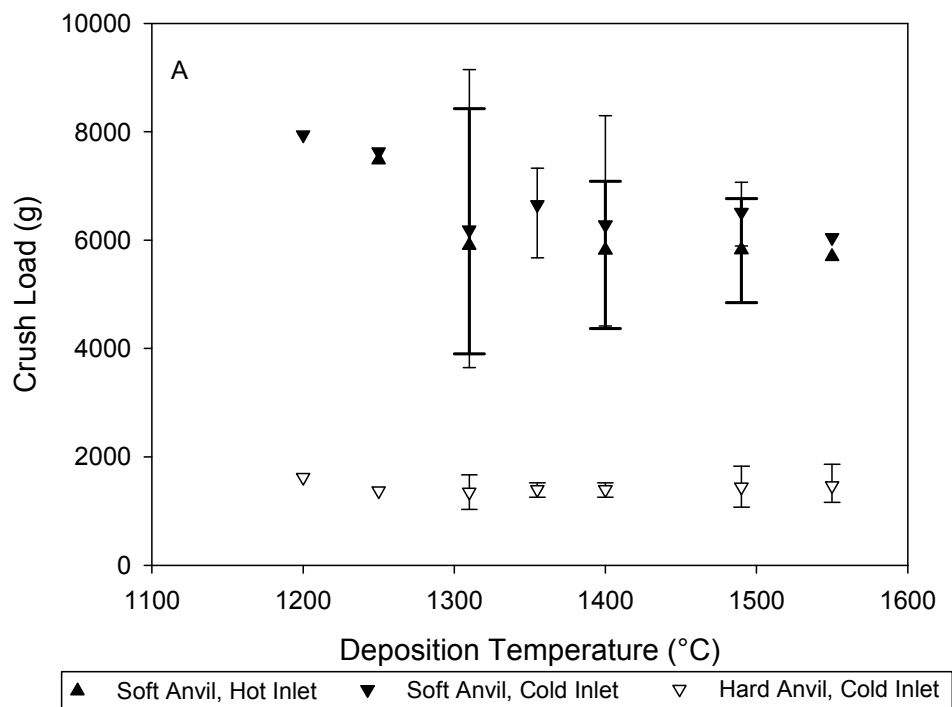


Figure 67. Crush load as a function of temperature for coated CPT-T-G140 particles. All data normalised to a deposit thickness of 35 μm . (A) Distribution of individual test runs tested using hard and soft anvils. Points represent median value, error bars estimated 3 σ value of individual test means. Heavy error bars represent data for group HF. (B) Fit of models to average soft anvil crush load for each deposition temperature. Model fitted to all tests, average values for each temperature shown.

12.4.2 HARDNESS

12.4.2.1 VICKERS MICROHARDNESS

Vickers micro-hardness test results are presented in Appendix A.

Average hardness for all batches measured is shown in Table 37. For the 100 g indents the average within lot (i.e. across measurement position and particles) standard deviation was found to be 1.829 GPa. The difference of 1.282 GPa between the 50 g and 100 g load was found to be statistically significant (Paired t-test, $P(t) = 4 \times 10^{-6}$). This indicates that for these measurements the indentation size effect may have influenced the results obtained.

Table 37. Vickers micro-hardness of all test runs measured using 50 g and 100 g indentation load.

Load (g)	Test Runs Measured	Average Hardness (GPa)	Standard Deviation (GPa)
50	53	28.826	1.713
100	52	27.545	1.496

As there was a significant difference in indentation crack lengths in the radial and tangential direction, the dimensions of the indents in the radial and tangential direction were compared. Results are presented in Table 38. It should be noted that these differences are not due to imperfections in the Vickers indenter or SEM astigmatism. Indenter imperfections and SEM astigmatism would have been averaged out due to changing orientation for different measurement positions around the particle. Indent diagonals in the tangential direction were found to be 0.07 μm longer than those in the radial direction. This difference was found to be statistically significant (Paired t-test, $P(t) = 1.5 \times 10^{-6}$). Although this difference is most likely real it becomes insignificant when considering other sources of variation and was not investigated further. In all further analysis hardness values were calculated using both the radial and tangential diagonal dimensions.

Table 38. Vickers indent diagonal length dependence on direction. Load: 100 g.

Diagonal Direction	Count	Length (μm)	Standard Deviation (μm)
Radial	52	8.14	0.21
Tangential	52	8.21	0.23

It was found that the hardness obtained using the hot gas inlet was higher than that obtained when using the cold gas inlet system. Hardness data for the hot and cold inlets are presented in Table 39. The difference between the two coating systems is statistically significant (One sided t-test of means, $P(t) = 0.027$) with a difference of 1.028 GPa. A normal probability plot of the Vickers hardness results of all test runs is presented in Figure 68. In this case the difference in hardness is 1.216 GPa with a one sided t-test $P(t) = 0.003$.

Table 39. Vickers hardness of hot and cold gas inlet system. Data from HF and CR experimental matrix only.

	Count	Average (GPa)	Standard Deviation (GPa)
Hot	16	28.140	1.466
Cold	16	27.112	2.040

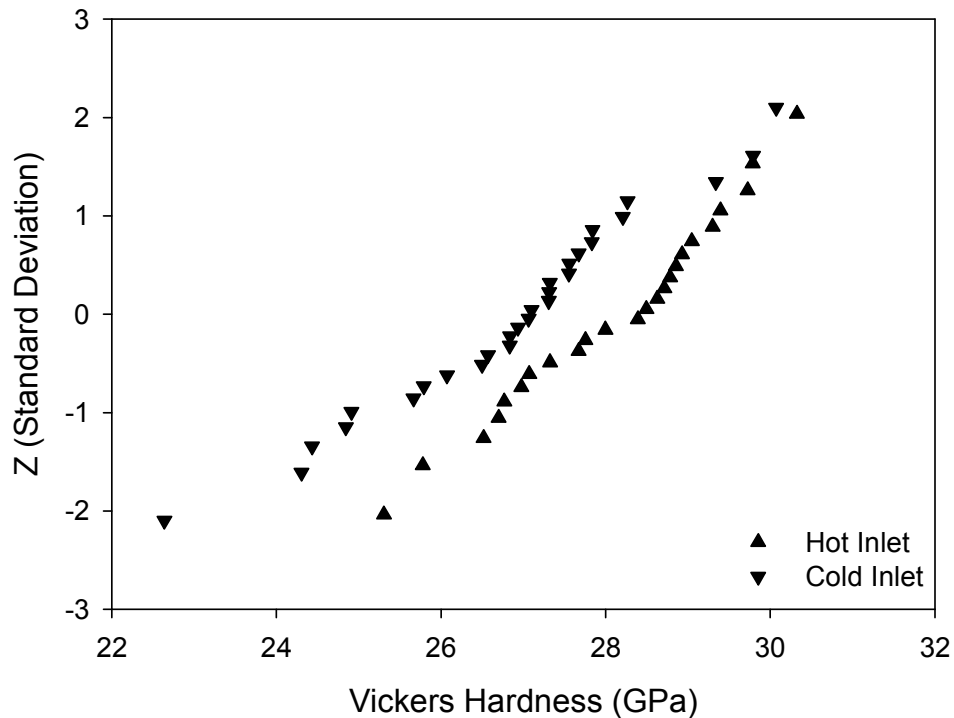


Figure 68. Vickers micro-hardness normal probability plot for all test runs measured.

As can be seen from Figure 69, Figure 70 and Figure 71 no single process parameter was found to have a significant influence on the Vickers microhardness. One test (MTS1) processed at 1200 °C may indicate that the hardness falls off rapidly when the deposition temperature is decreased below approximately 1250 °C. However there is insufficient data to draw a general trend.

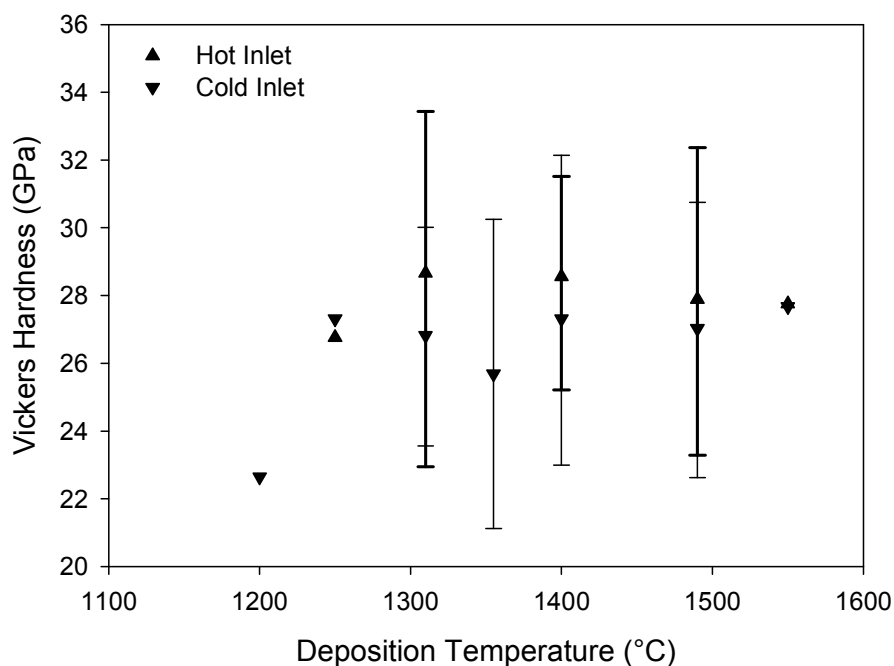


Figure 69. Influence of deposition temperature on Vickers micro-hardness. Markers indicate median value, error bars are estimated 3σ values. Heavy error bars indicate hot inlet.

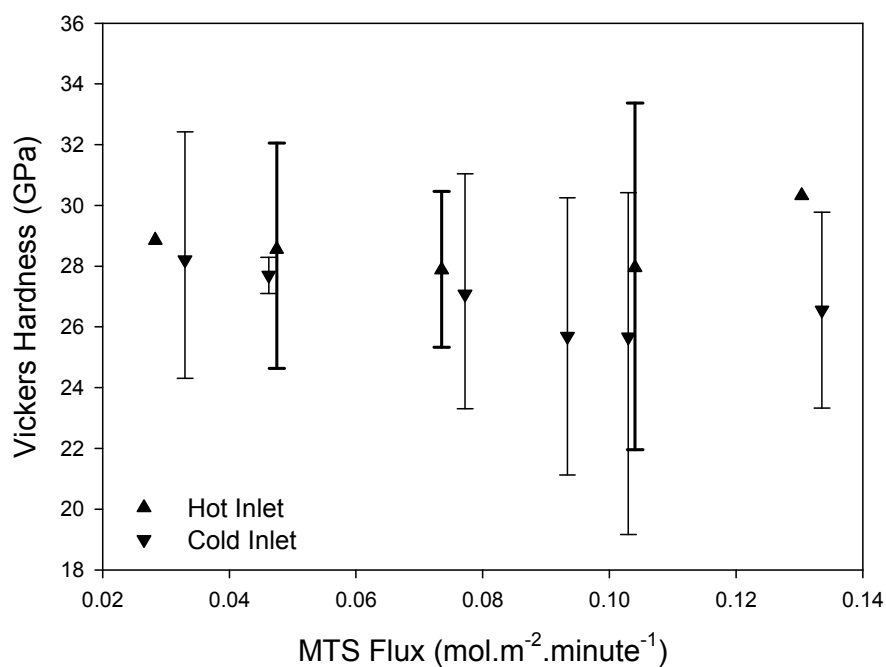


Figure 70. Influence of MTS flux on Vickers micro-hardness. Markers indicate median value, error bars estimated 3σ values.

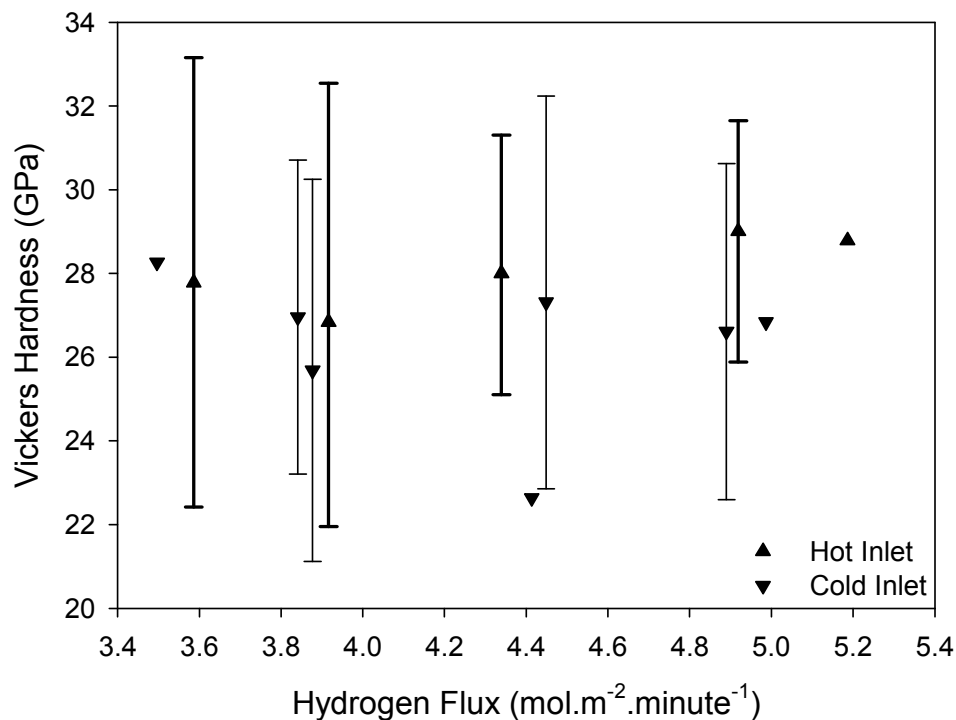


Figure 71. Influence of hydrogen flux on the Vickers micro-hardness. Markers indicate median value, error bars estimated 3σ values.

In Figure 69 to Figure 71 the error bars are based on the standard deviations calculated for each subgroup. This resulted in an exaggerated estimate of the expected spread of data. The true spread of data may be seen in the normal probability plots of the data, Figure 68, where individual batch averages are plotted. Due to the reasonably large sample size (24 and 28 test runs for HF and CR respectively) there is a high confidence that there is a difference in hardness between groups HF and CR.

12.4.2.2 VICKERS INDENTATION CRACKING

Crack length data may be found in Appendix A. Crack lengths from the indent corner to the crack tip are reported.

For the majority of test runs a portion of the indents were rejected. Typical reasons for rejecting of indents are discussed in section 11.4. It was found that the percentage of cracks rejected was strongly correlated to deposit thickness. This can be seen in Figure 72. For test runs with a deposit thickness below approximately 25 μm none of the 40 indents were acceptable. The fraction acceptable indents increased with thickness to approximately 40 μm at which point close to 100 % of the indents were acceptable. Use of a 50 g indentation load resulted in fewer reject indents however

the indents and cracks were difficult to measure and a significant portion of the indents did not crack at all.

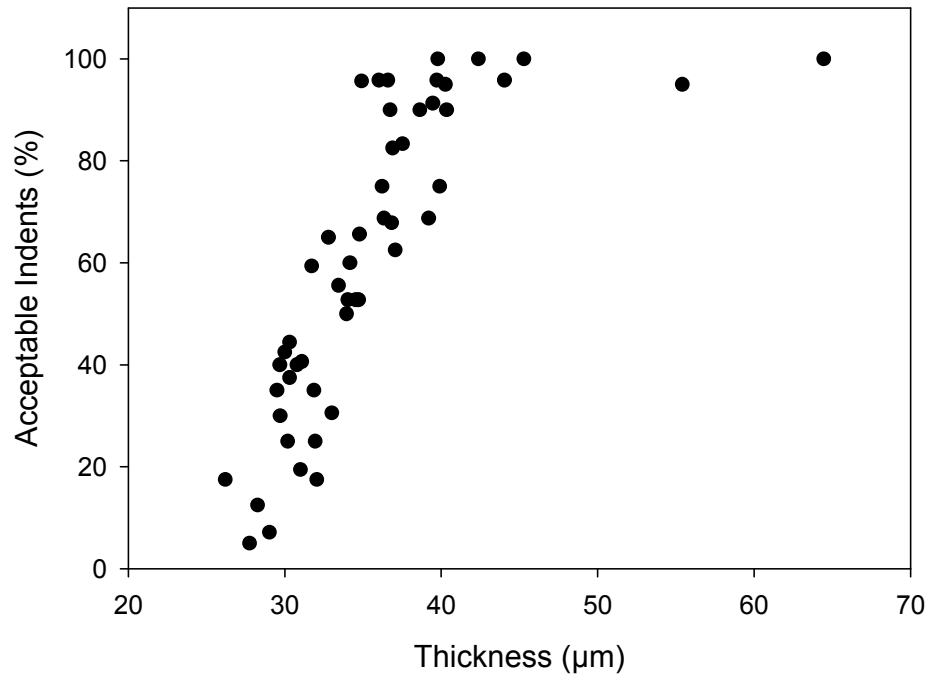


Figure 72. Percentage of acceptable indents as a function of deposit thickness. Data for all test runs measured.

It was found that there were substantial differences in crack length between radial (i.e. cracks running across the thickness of the deposit) and tangential cracks (i.e. cracks approximately parallel to the deposit surface). Radial crack length tended to be independent of deposit thickness while the length of tangential cracks was dependent on deposit thickness. This can be seen from Figure 73(A). Tangential crack length was found to decrease as deposit thickness increased up to about 45 μm. For deposits thicker than 45 μm the crack length no longer depended on deposit thickness. This correlates to the fraction acceptable cracks as discussed in the previous paragraph.

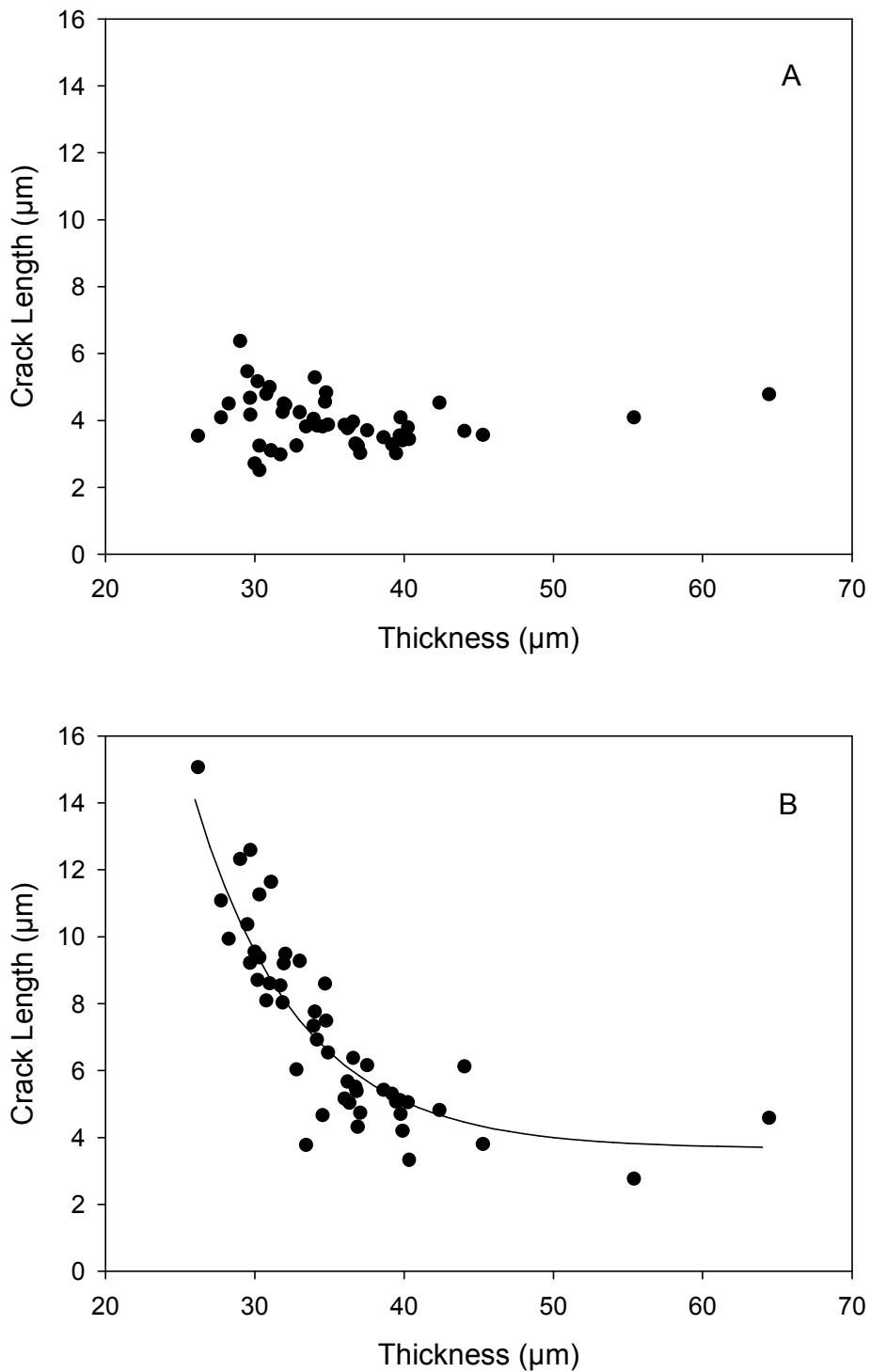


Figure 73. Crack length dependence on deposit thickness. A: Radial crack length was found to be independent of deposit thickness. B: Tangential crack length was found to increase as deposit thickness decreases below 40 μm. Below 25 μm few indents were acceptable. Line represents equation 99 at a temperature of 1400 °C and a MTS flux of 0.078 mol.m⁻².minute⁻¹.

The differences in distribution of radial and tangential cracks is shown in Figure 74 and Table 40. Differences in crack length between the radial and tangential direction were found to be statistically significant (Paired t-test, $P(t) = 2.9 \times 10^{-11}$).

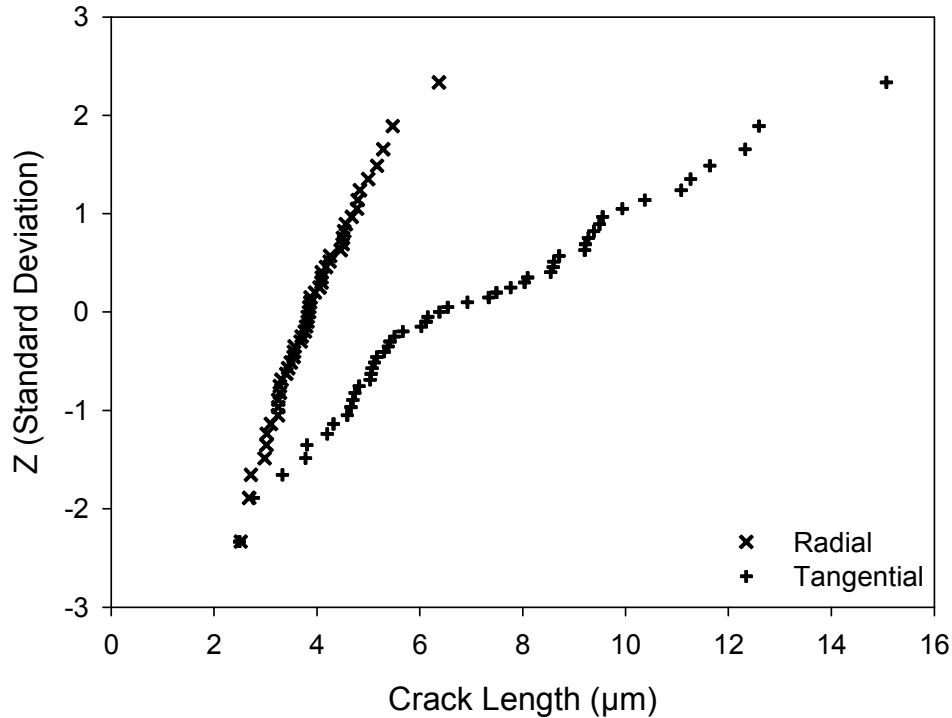


Figure 74. Normal probability plot of radial and tangential crack length. Average crack length value for test runs.

Table 40. Summary of crack length characteristics.

Crack Direction	Count	Average (μm)	Standard Deviation (μm)
Radial	51	3.933	0.774
Tangential	51	7.112	2.809

Regression analysis revealed that there was a linear relationship between radial crack length and deposition temperature. MTS flux, hydrogen flux and gas inlet type were found to have no statistically significant influence. Radial crack length may be modelled by equation 98 and parameter values in Table 41. Radial crack length, as a function of deposition temperature, is shown in Figure 75.

$$l_r = a + bT \quad (98)$$

Where:

- l_r : Radial crack length - corner of indent to crack tip (μm)
- a, b : Model parameters
- T : Deposition temperature ($^{\circ}\text{C}$)

Table 41. Radial crack length model parameters. Parameter values calculated for all data, values in parenthesis are for model fitted to average crack length values for each deposition temperature.

Parameter	Value	P(t)	95 % Confidence Interval (\pm)
a	-4.033	0.00991	3.018
b	5.688×10^{-3}	0.00000	2.158×10^{-3}
R^2	0.374 (0.872)		
R_a^2	0.361 (0.840)		

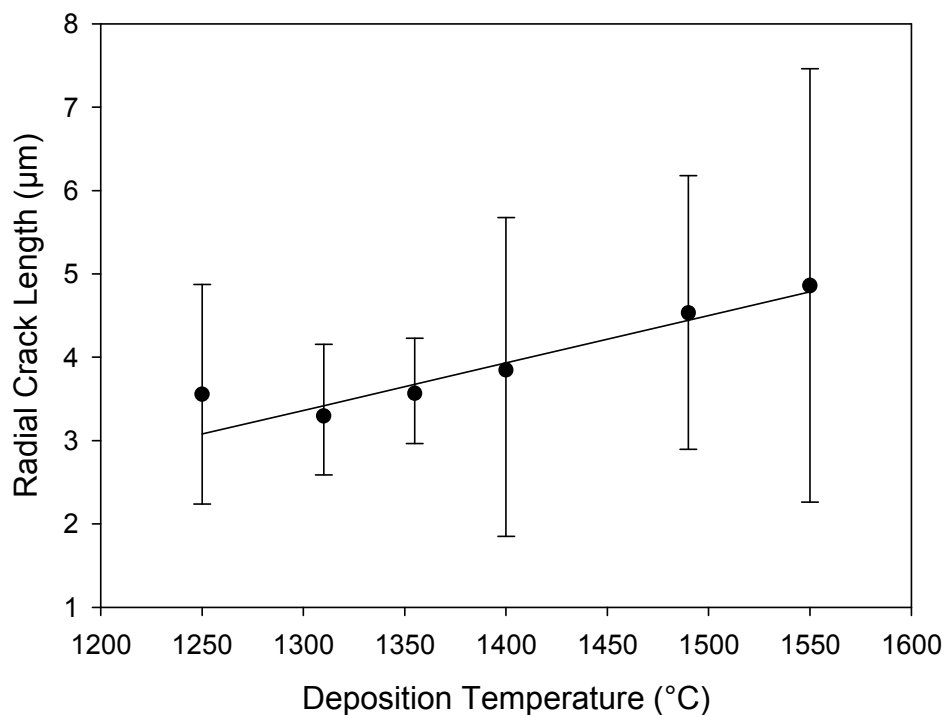


Figure 75. Radial crack length as a function of deposition temperature. Markers indicate median value, error bars estimated 3σ values. Fitted line represents equation 98 and parameter values in Table 41.

The low coefficient of determination of the model based on individual crack lengths indicates that there is considerable variability in the radial crack length that is not explained by deposition temperature alone. As only deposition temperature plays a significant role in determining radial crack length, the variability in crack length must be related to measurement variability and inherent material properties. Other process parameters (MTS concentration, hydrogen flow rate, inlet type) may play a role, however there is insufficient evidence to prove any influence. Despite the poor fit to individual data points it is reasonable certain that deposition temperature does influence radial crack length, this is seen by the significantly improved coefficient of determination when the model is fitted to the average data for each deposition

temperature. Crack length uncertainty will introduce uncertainty into any estimation of fracture toughness, K_{IC} , based on crack length.

In addition to deposit thickness, tangential crack length was found to be dependent on both deposition temperature and MTS flux. Hydrogen flux and gas inlet type had no statistically significant influence on crack length. Tangential crack length could be modelled using the following equation:

$$l_t = a + be^{ct} + dT + eM \quad (99)$$

Where:

- l_t : Tangential crack length (corner of indent to crack tip) (μm)
 a, b, c, d, e : Model parameters
 t : Deposit thickness (μm)
 T : Deposition temperature ($^{\circ}\text{C}$)
 M : MTS flux ($\text{mol}\cdot\text{m}^{-2}\cdot\text{minute}^{-1}$)

Values of the constants a, b, c, d and e used to fit tangential crack length data to equation 99 are given in Table 42. Predicted crack length as a function of deposit thickness is plotted in Figure 73.

Table 42. Tangential crack length model parameters.

Parameter	Value	P(t)	95 % CI
a	-4.800	0.163	6.813
b	425.468	0.160	599.423
c	-0.143	0	5.353×10^{-2}
d	6.868×10^{-3}	0.00748	4.938×10^{-3}
e	-14.809	0.022	12.580
R^2	0.858		
R_a^2	0.845		

The impact of deposition temperature on tangential crack length is shown in Figure 76.

It was not possible to determine whether the cracks were of the Palmqvist or radial type. Based on crack length:indent diagonal ratios it is assumed that radial cracks were of the Palmqvist type ($c/a < 2$). The situation is less clear in the case of tangential cracks as the c/a ratio for these cracks varies across the Palmqvist to median crack transition range c/a of between 2 and 3.

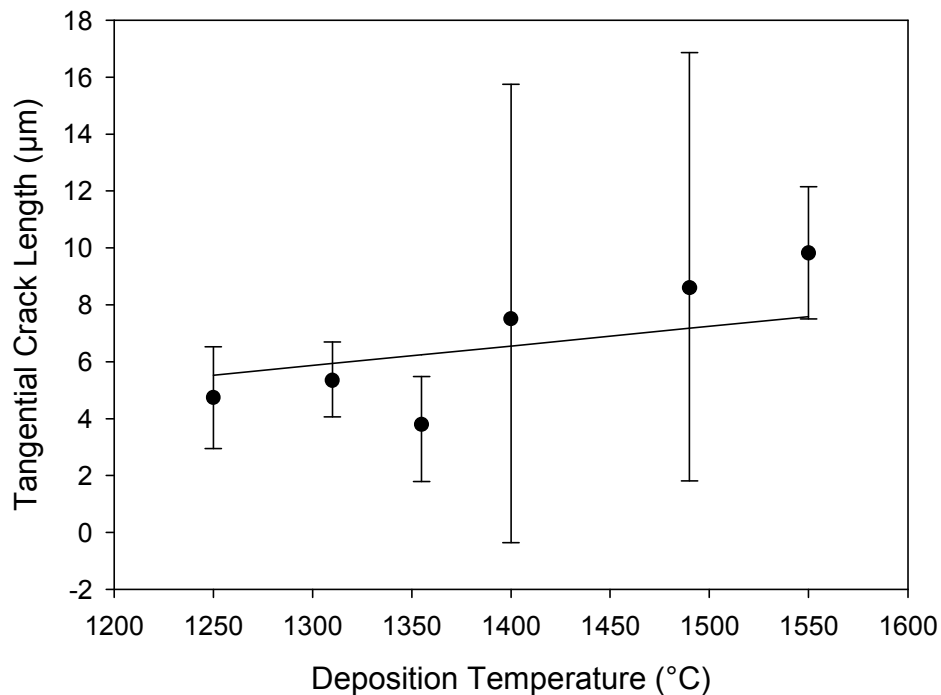


Figure 76. Tangential crack length as a function of deposition temperature. Markers indicate median value, error bars estimated 3σ values. Fitted line represents equation 99 and parameter values in Table 42 for a deposit thickness of $35 \mu\text{m}$ and a MTS of $0.075 \text{ mol.m}^{-2}.\text{minute}^{-1}$. The apparent poor fit and wide spread of crack length values is as a result of the strong influence of thickness and the influence of MTS concentration on the tangential crack length.

12.4.3 NANO-INDENTATION

Nano-indentation hardness data is presented in Appendix A.

Normal probability plots of the average hardness of each test from group HF and CR particles are shown in Figure 77. For each test runs 60 indents were made on a single particle. Hardness values from individual indents were normally distributed with an average standard deviation of 1.835 GPa. No statistically significant difference could be found between the average hardness of the HF and CR groups (2 sample t-test, $P(t) = 0.791$) or between the test using CPT-T-G130 and CPT-T-G140 particles (2 sample t-test, $P(t) = 0.356$).

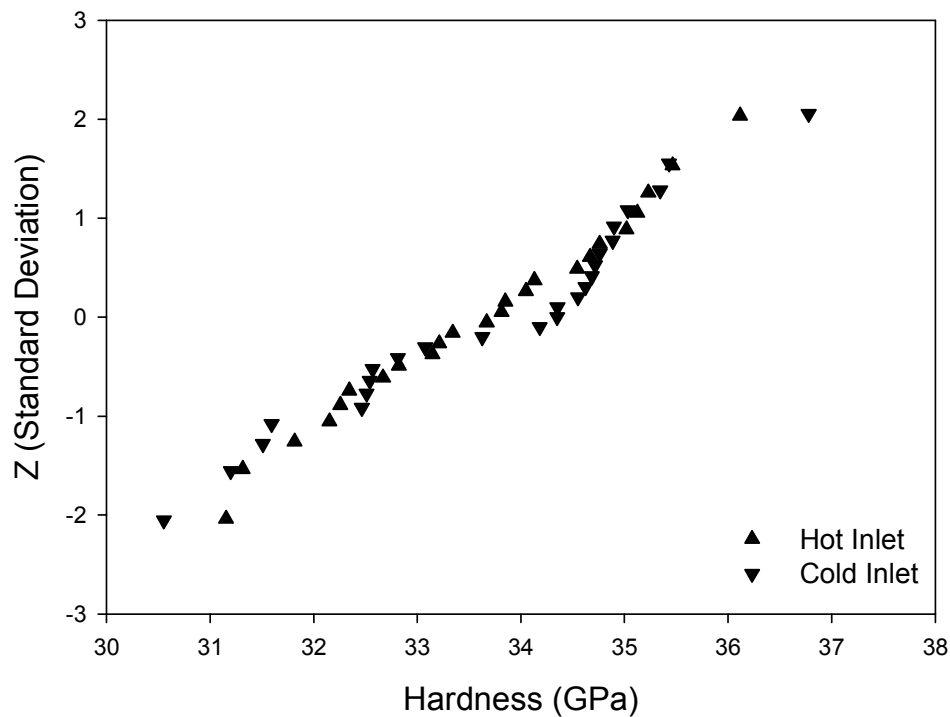


Figure 77. Normal probability plot of nano-indentation hardness of particles from group HF and CR. Each point is the average of 60 measurements on a single particle from each test run.

Deposition temperature was the only parameter that was found to have a significant influence on nano-hardness. This is shown in Figure 78. Nano-indentation hardness changed from approximately 32 GPa to 35 GPa as deposition temperature was increased from 1250 °C to 1550 °C.

As can be seen from Figure 79 and Figure 80 hardness values did not vary significantly with changing MTS or hydrogen flux over the range investigated. Considering the small effect and the large spread of data there is insufficient evidence that, over the range of values investigated, MTS and hydrogen flux had any significant influence on nano-indentation hardness.

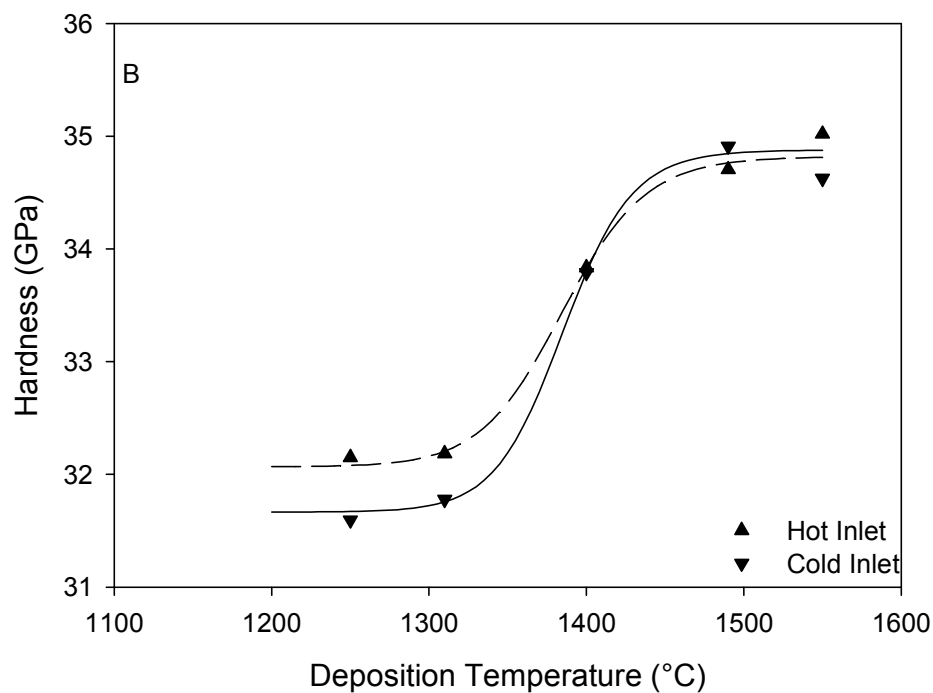
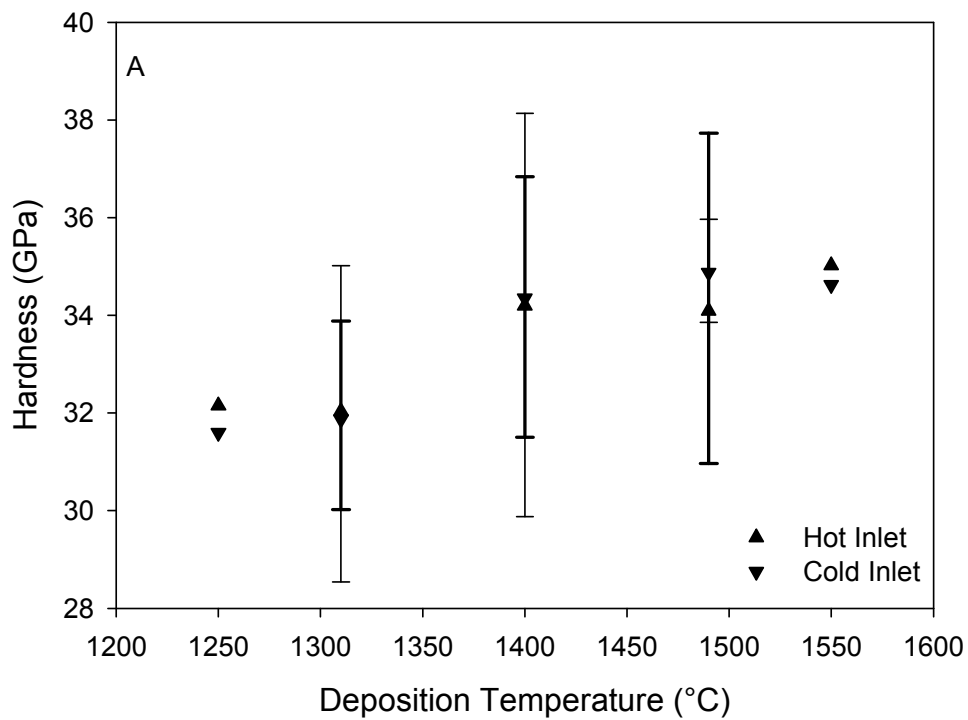


Figure 78. A: Influence of deposition temperature on nano-indentation hardness. Symbols represent median hardness value for each temperature, error bars estimated 3σ values. Group HF data represented by heavy error bars. B: Median hardness values showing the fit of equation 100 using parameters values listed in Table 43.

Nano-indentation hardness may be modelled using equation 100:

$$Hardness = a + \frac{b}{1 + \left(\frac{T}{c}\right)^d} \quad (100)$$

Where:

- a : Constant. Hardness value at low deposition temperatures. (GPa)
- b : Constant. Hardness range between low and high temperature. (GPa)
- T : Deposition temperature (°C)
- c : Constant (°C)
- d : Constant (dimensionless)

Fit parameters for this model are given in Table 43. A plot of equation 100 using the parameter values listed in Table 43 is shown in Figure 78(B). In Table 43, values given in parenthesis are for a model fitted to the average hardness value for each deposition temperature. As can be seen from the table there is considerable uncertainty in the values of some of the parameters, especially the exponent term, d . Alternative linear and linear interaction models, which included terms for MTS and hydrogen flux, could also have been fitted to the data with a marginally better coefficient of determination. However those models could not account for asymptotic behaviour at the extremes of the deposition temperature range.

Table 43. Nano-indentation hardness fit parameters for equation 100.

Parameter	HF			CR		
	Estimate	P(t)	95 % CI	Estimate	P(t)	95 % CI
a	32.066	0	2.213	31.666	0	2.550
b	2.753	0.075	3.074	3.211	0.064	3.424
c	1384.821	0	82.568	1385.242	0	121.245
d	-52.776	0.663	256.974	-63.459	0.771	464.828
R^2	0.640 (0.967)			0.633 (0.995)		
R_a^2	0.549 (0.872)			0.541 (0.979)		

The high coefficient of multiple determination of the model fitted to averaged data indicates that the model is a reasonably good description of nano-indentation hardness as a function of deposition temperature. Variability of individual data points for each deposition temperature results in a significantly reduced coefficient of multiple determination when the model is fitted to individual test run results. Model coefficients are effectively determined for averaged values for each deposition temperature, hence it is possible to fit the model despite the variability of the data. As was the case for other measures the poor fit when individual data points are analyzed may be due to measurement error or the influence of deposition parameters either not controlled during the tests or which may influence the silicon carbide properties to some extent but there is insufficient data to prove an effect i.e. the sample size is too small relative to the size of the effect for there to be sufficient statistical proof of the effect.

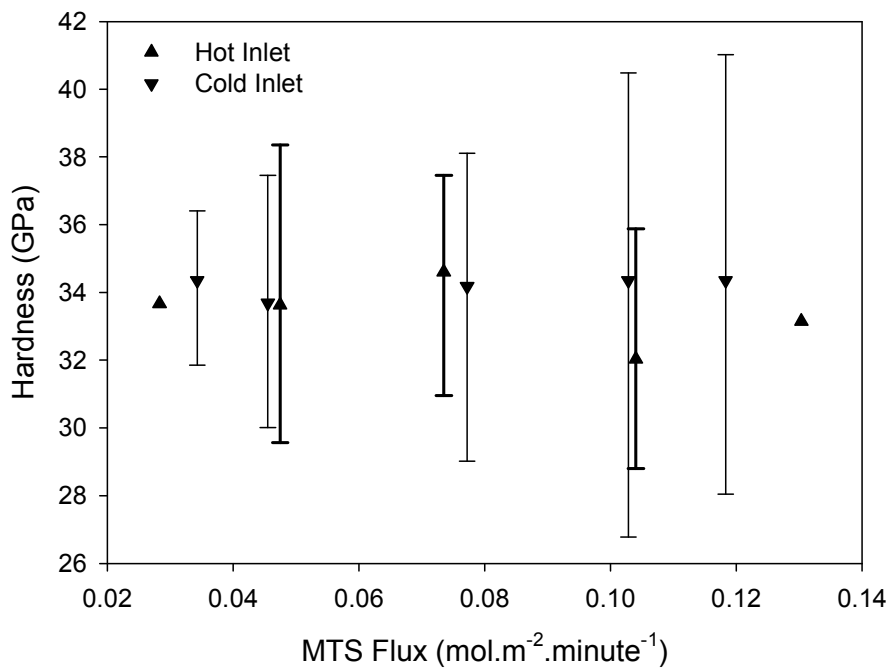


Figure 79. Nano-indentation hardness as a function of MTS flux. MTS flux has no influence on the SiC deposit hardness. Symbols represent median value, errors bars estimated 3σ values.

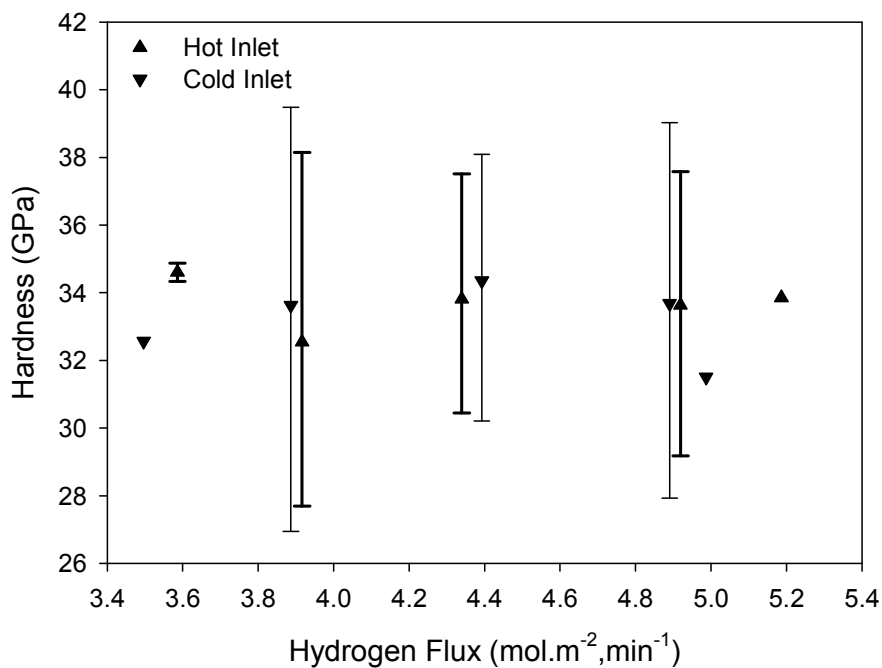


Figure 80. Nano-indentation hardness as a function of hydrogen flux. Hydrogen flux has no influence on the SiC deposit hardness. Symbols represent median value, errors bars estimated 3σ values.

12.4.4 YOUNG'S MODULUS

Young's modulus data can be found in Appendix A.

From Figure 81 it can be seen that there is a difference in Young's modulus between particles coated using the cold inlet and the hot inlet. These results are summarised in Table 44. The difference in Young's modulus between particles coated using the cold and hot gas inlet was found to be $19.91 \text{ GPa} \pm 11.96 \text{ GPa}$ at a 95% confidence level. The confidence interval was calculated assuming normally distributed data and unknown population variance.

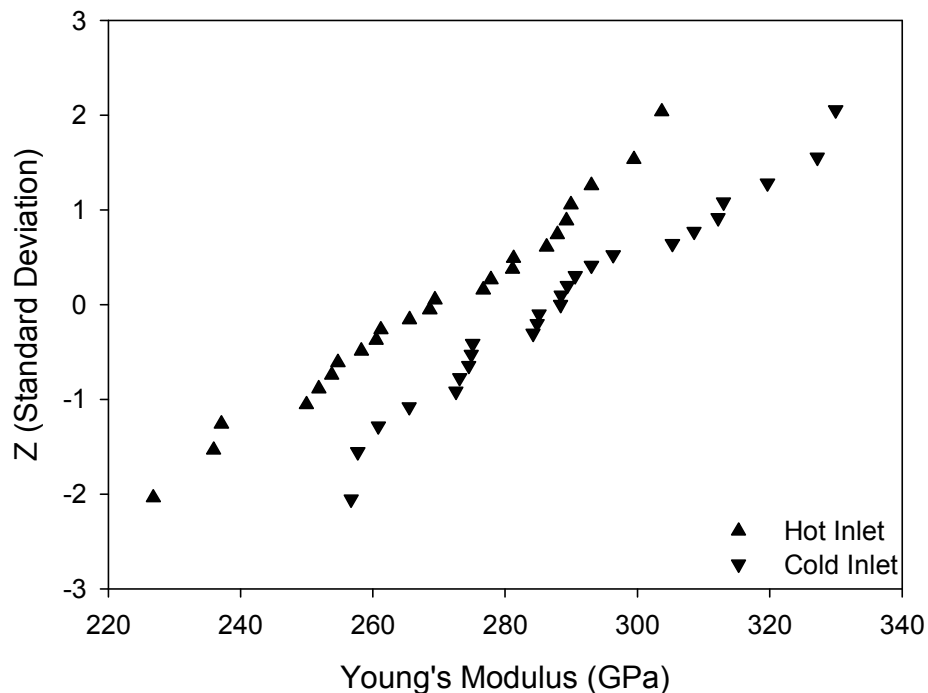


Figure 81. Normal probability plot of Young's modulus for particles prepared using the hot and cold gas inlet.

Table 44. Nano-indentation determination of Young's modulus.

	Hot Inlet	Cold Inlet
Average (GPa)	269.17	289.08
Standard Deviation (GPa)	20.737	20.876
Count	24	25
95 % Confidence Interval	8.737	8.601

Young's modulus as a function of process parameters is depicted in Figure 82, Figure 83 and Figure 84.

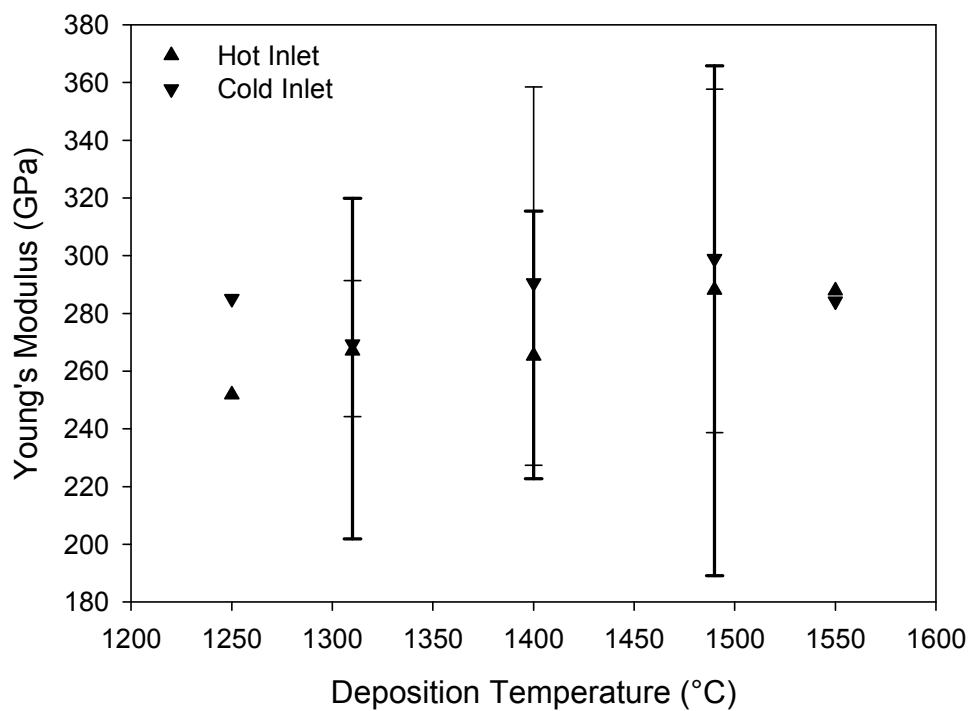


Figure 82. Young's modulus dependence on deposition temperature. Markers indicate median value, error bars 3σ values. Heavy error bars represent data for hot inlet.

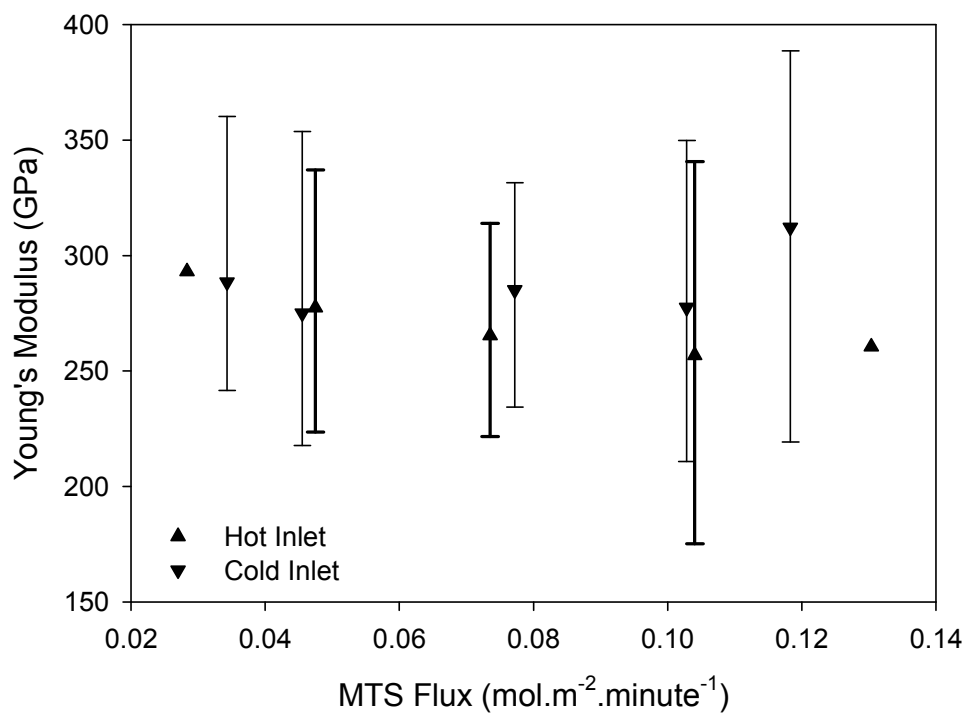


Figure 83. Young's modulus dependence on MTS flux. Markers indicate median value, error bars 3σ values.

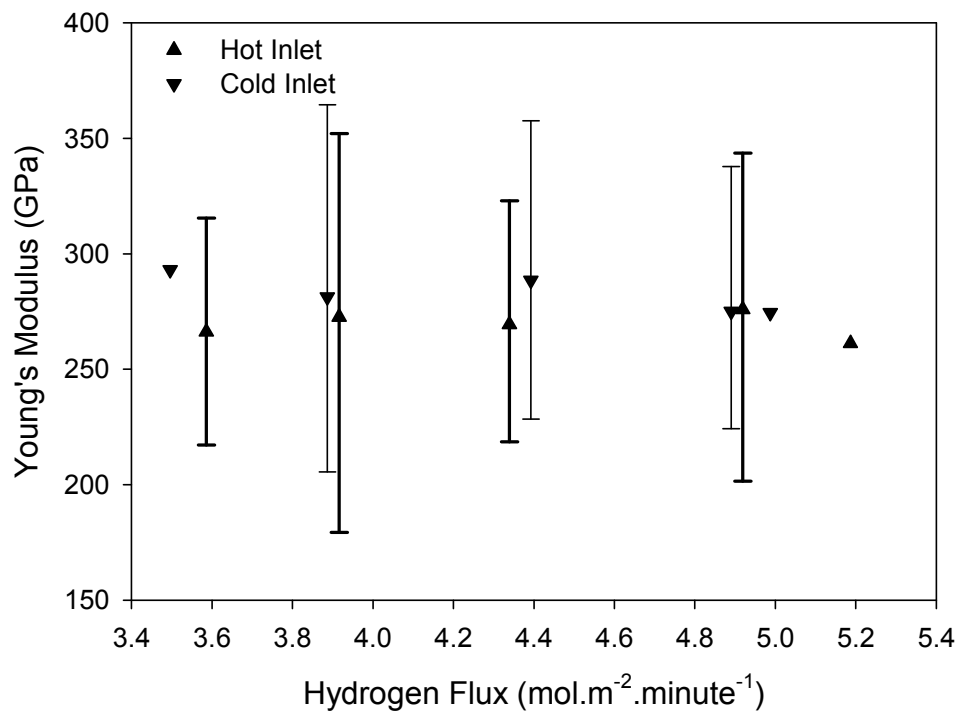


Figure 84. Young's modulus dependence on hydrogen flux. Markers indicate median value, error bars 3 σ values.

12.4.5 FRACTURE TOUGHNESS

Fracture toughness was calculated using the Liang, Anstis and Evans-Davis correlations. These correlations can be found in section 8.5.1.3, Table 12. Hardness and Young's modulus values as measured by nano-indentation were used in the calculations in preference to Vickers hardness and published values of Young's modulus. Due to the differences in crack length in the radial and tangential direction the calculations were repeated for each crack direction. Tangential crack lengths were recalculated using equation 99 so as to eliminate the effect of deposit thickness. Calculated fracture toughness values are presented in Appendix A.

It was found that there were no statistically significant differences in fracture toughness between samples coated using the hot and cold gas inlets for cracks in both the radial (Two sample t-test, $P(t) = 0.216$) and tangential directions (Two sample t-test, $P(t) = 0.268$). No statistically significant difference in fracture toughness was found between the radial and tangential directions (Two sample t-test, $P(t) = 0.244$) when the tangential crack length had been corrected for the influence of layer thickness. All t-test results reported here are based on fracture toughness results obtained from the Liang correlation.

Normal probability plots of fracture toughness calculated using the Liang, Anstis and Evans-Davis correlations are shown in Figure 85. Data for both inlet types and both crack directions were pooled for each of the plots. A summary of the data is presented in Table 45. Fracture toughness values calculated using the Evans-Davis correlation were consistently higher than those calculated using the Liang and Anstis correlations. Results obtained using the Evans-Davis correlation were also less widely distributed than those of obtained using the Liang and Anstis correlations. This reflects a lower sensitivity to changes in crack length and therefore a lower sensitivity to changes in material properties. This effect is also seen in Figure 86 where it can be seen that the fracture toughness calculated using the Evans-Davis has a lowest sensitivity to deposition temperature.

Table 45. Summary of fracture toughness calculated using the Liang, Anstis and Evans-Davis correlations. All data pooled for each calculation.

	Average (MPa.m ^{0.5})	Standard Deviation (MPa.m ^{0.5})	95 % Confidence Interval (MPa.m ^{0.5})
Liang	2.276	0.132	± 0.076
Anstis	2.141	0.160	± 0.084
Evans-Davis	2.814	0.040	± 0.042

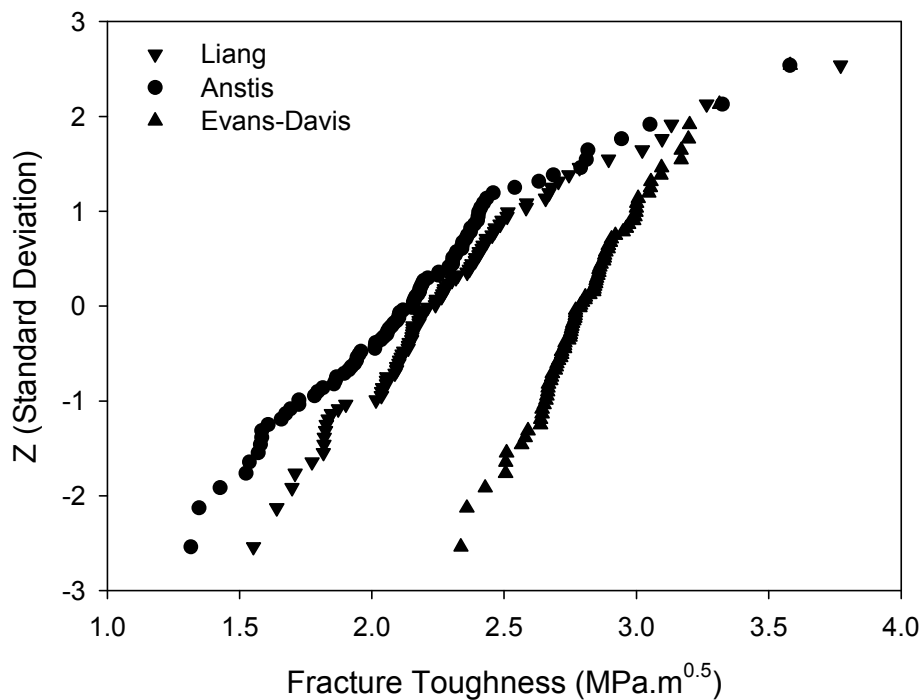


Figure 85. Normal probability plot of fracture toughness calculated using Liang, Anstis and Evans-Davis correlations. Data for all tests pooled for each calculation method.

The influence of processing conditions on fracture toughness is shown in Figure 86, Figure 87 and Figure 88. Only deposition temperature appears to have any influence on fracture toughness. The influence of deposition temperature is most strongly reflected by fracture toughness calculated using the Anstis correlation. The apparent increase in fracture toughness at high values of MTS flux was strongly influenced by result from a single test run, CR22. Test run HF11, which had a similarly high MTS flux, had a fracture toughness value close to average. Only 2 test runs were conducted at this extreme value, one for each of the gas inlets. The high fracture toughness of CR22 resulted from a combination of values, no individual measurement (i.e. crack length, hardness, Young's modulus) was particularly extreme, and hence it would seem unreasonable to disregard this data.

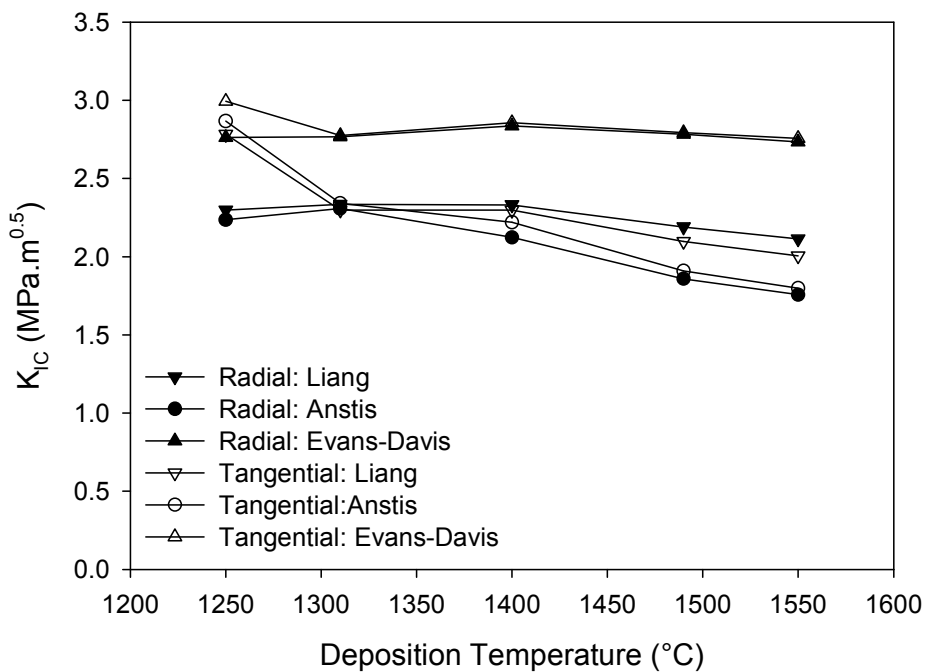


Figure 86. Influence of deposition temperature on fracture toughness calculated using the Liang, Anstis and Evans-Davis correlations. Average value for each temperature shown.

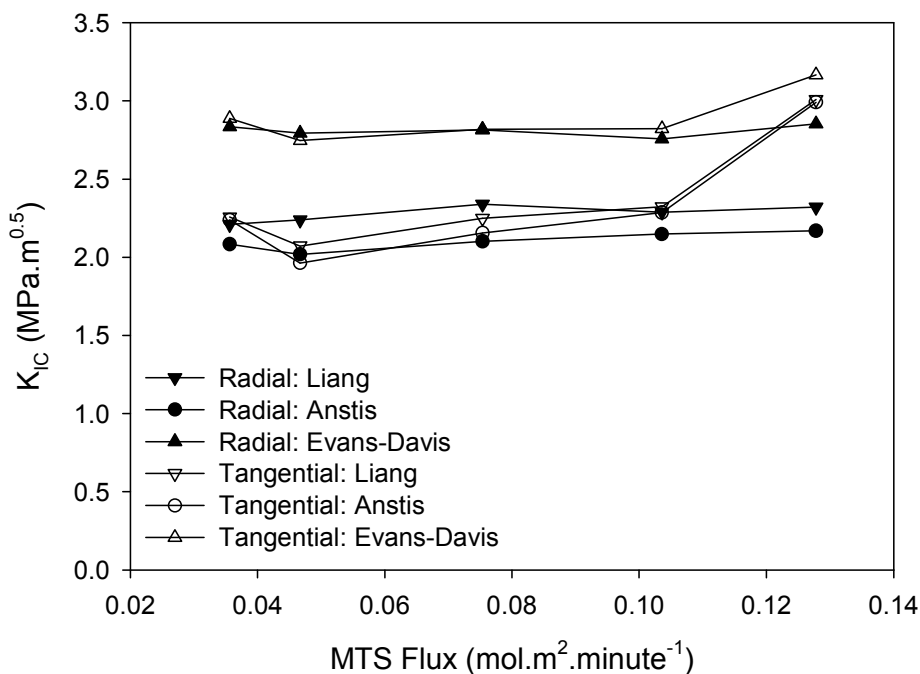


Figure 87. Influence of MTS flux on fracture toughness calculated using the Liang, Anstis and Evans-Davis correlations. Average value for each MTS flux shown.

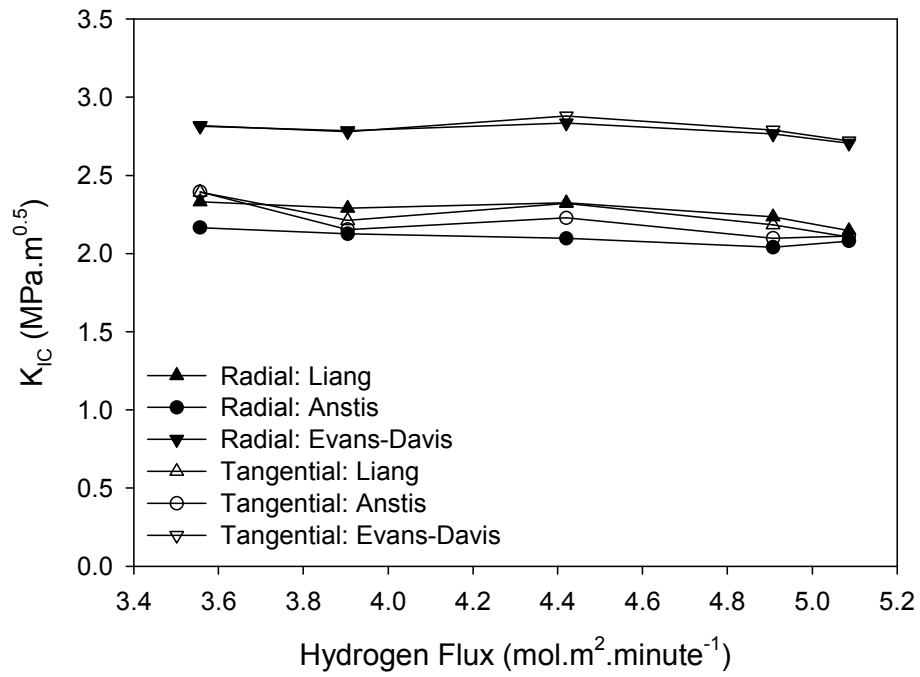


Figure 88. Influence of hydrogen flux on fracture toughness calculated using the Liang, Anstis and Evans-Davis correlations. Average value for each hydrogen flux shown.

12.5 X-RAY DIFFRACTION ANALYSIS

In this section results of the XRD diffraction analysis will be discussed. All XRD patterns may be found in Appendix B. Tables containing data derived from the XRD patterns are presented in Appendix A. Crystallite size was also measured using XRD; results may be found in Appendix A and are discussed in section 12.5.3.

12.5.1 PHASE COMPOSITION

A XRD pattern displaying the peaks found in the samples is shown in Figure 89. In all samples analysed only 3C SiC, silicon and quartz peaks were identified. The relative intensity of the various peaks was dependent on the processing conditions. At high deposition temperatures the deposits consisted of 3C silicon carbide with a small quantity of quartz contamination. It was established that the quartz was present as a result of grinding the deposit in an agate mortar and pestle in preparation for XRD analysis. In calculating the free silicon content of the deposit the quartz content was excluded from the composition. Silicon was only detected in samples prepared at relatively low deposition temperatures. This can be seen in Figure 90. No free carbon was identified in any of the samples.

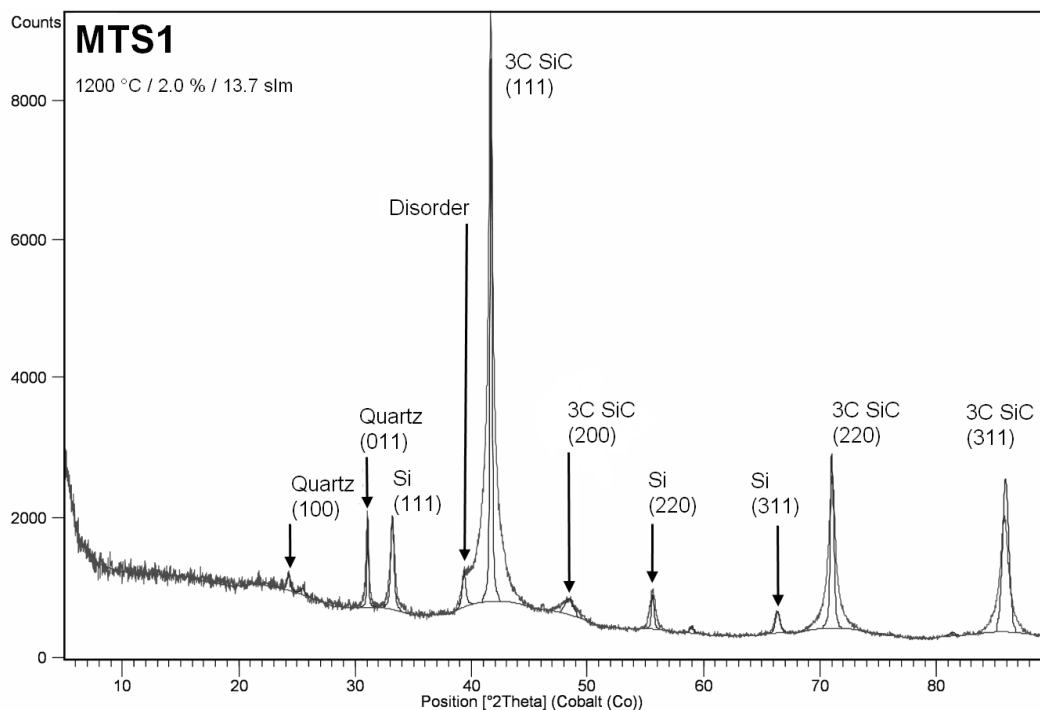


Figure 89. XRD pattern showing peaks detected in samples. Not all peaks were observed in every sample, silicon only being detected at deposition temperatures below 1400 °C.

In the case of the hot inlet, free silicon was only detected in small quantities (0.045 %) in a single sample that was deposited at 1250 °C. For samples prepared using the cold gas inlet silicon was detected in samples prepared at 1400 °C (0.088 %), 1310 °C (0.124 %), 1250 °C (0.725 %) and 1200 °C (6.849 %). From the above it would appear that the maximum temperature for deposition of free silicon is lower when the hot gas inlet is used. It is also apparent that the free silicon content remains at a low level until deposition temperature is reduced below a critical point after which the silicon content of the deposit increases rapidly.

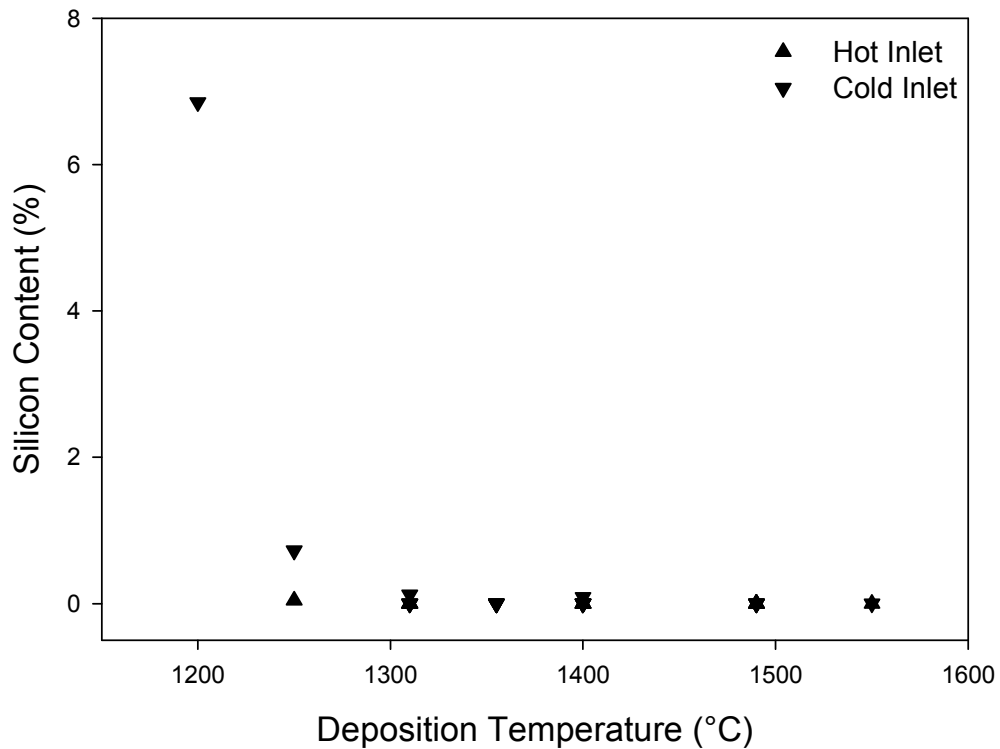


Figure 90. Free silicon content of the deposit as a function of deposition temperature.

12.5.2 DISORDERED PHASE

Apart from the 3C polytype no other silicon carbide polytypes were detected in the deposits. In a number of the samples, especially those deposited at the lower temperatures, evidence of disordered silicon carbide was found. This was evidenced as a shoulder and small peak on the low angle side of the 3C silicon carbide (111) peak. This effect can be seen in Figure 91 where XRD diffraction patterns of silicon carbide deposited at 1250 °C and 1550 °C are compared. The higher level of disorder in the material deposited at 1250 °C is manifest as the small peak and shoulder between approximately 39 ° and the large 3C (111) peak at 41.6 °.

The degree of disorder was assessed by means of the intensity ratio of the 2 peaks. As can be seen from Figure 92 this ratio is strongly dependent on temperature. Regression analysis revealed that MTS flux, hydrogen flux and inlet type do not have a statistically significant effect. Peak intensity ratio could be modelled as:

$$Ratio = e^{(aT+b)} \quad (101)$$

Where:

- Ratio* : Intensity ratio $I_{\text{disorder}}/I_{111}$ (%)
a : Constant (°C⁻¹)
T : Deposition temperature (°C)
b : Constant (unit less)

Values of constants *a* and *b* are given in Table 46.

Table 46. Parameter values and model fit parameters for equation 101.

	Value	P(t)	95% Confidence Interval (±)
<i>a</i>	8.726×10^{-3}	0	8.357×10^{-4}
<i>b</i>	12.267	0	0.893
R^2	0.936		
R_a^2	0.934		

Crystallographic disorder was also assessed by considering the separation between the (111) and (200) peaks. It was found that MTS and hydrogen flux did not have any statistically significant influence on peak separation. It was expected that a decrease in deposition temperature would result in an increase in crystallographic disorder. This in turn would result in a decrease in the separation between the (111) and (200) peaks at lower deposition temperatures. As can be seen in Figure 93 this relationship was not supported by the available data.

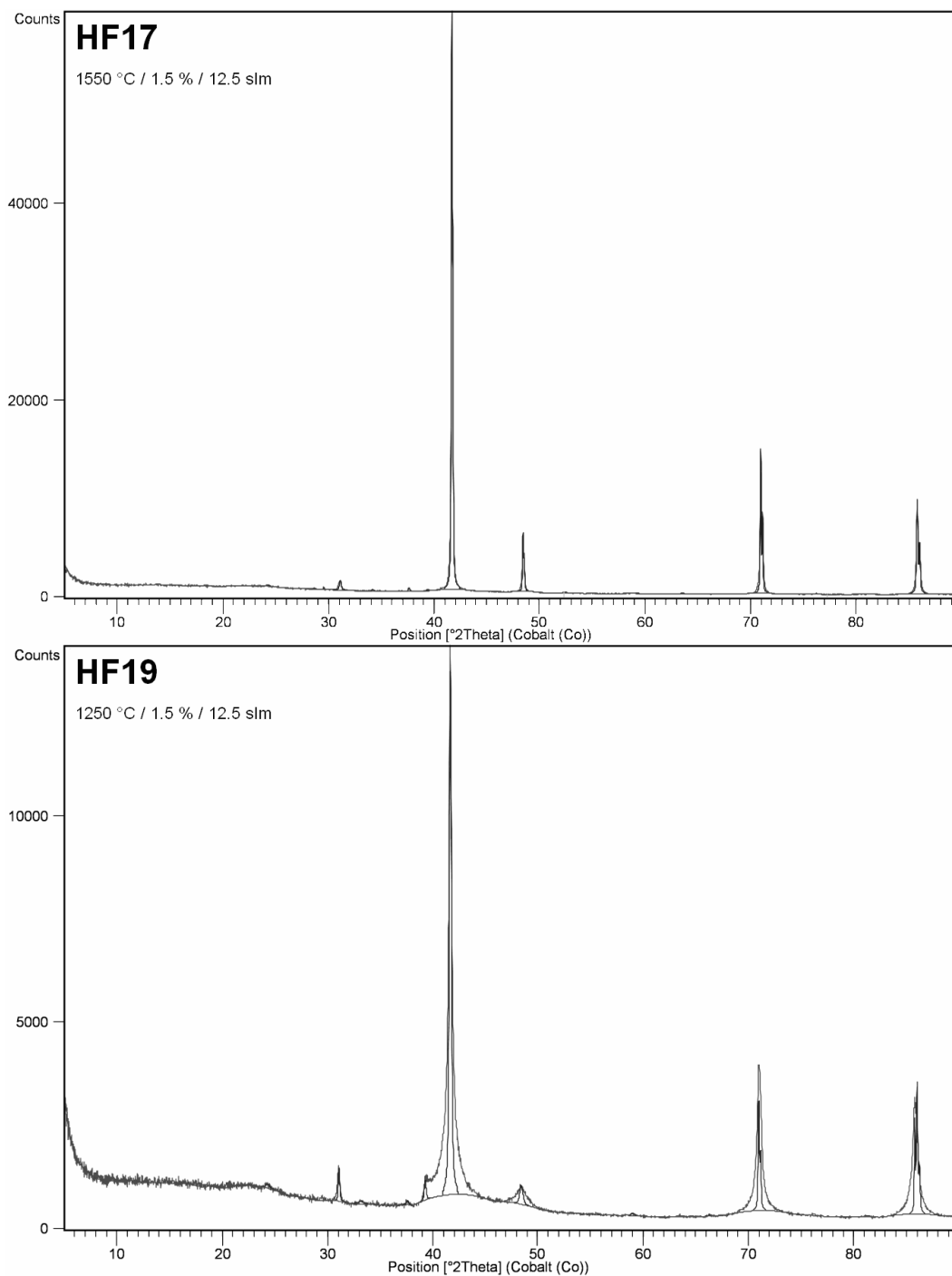


Figure 91. Comparison of XRD pattern of deposit prepared using a relatively low and high deposition temperature. MTS and hydrogen flow were similar. Increased crystal disorder at low deposition temperatures can be seen as an increase in intensity between approximately 39 ° and 41 °.

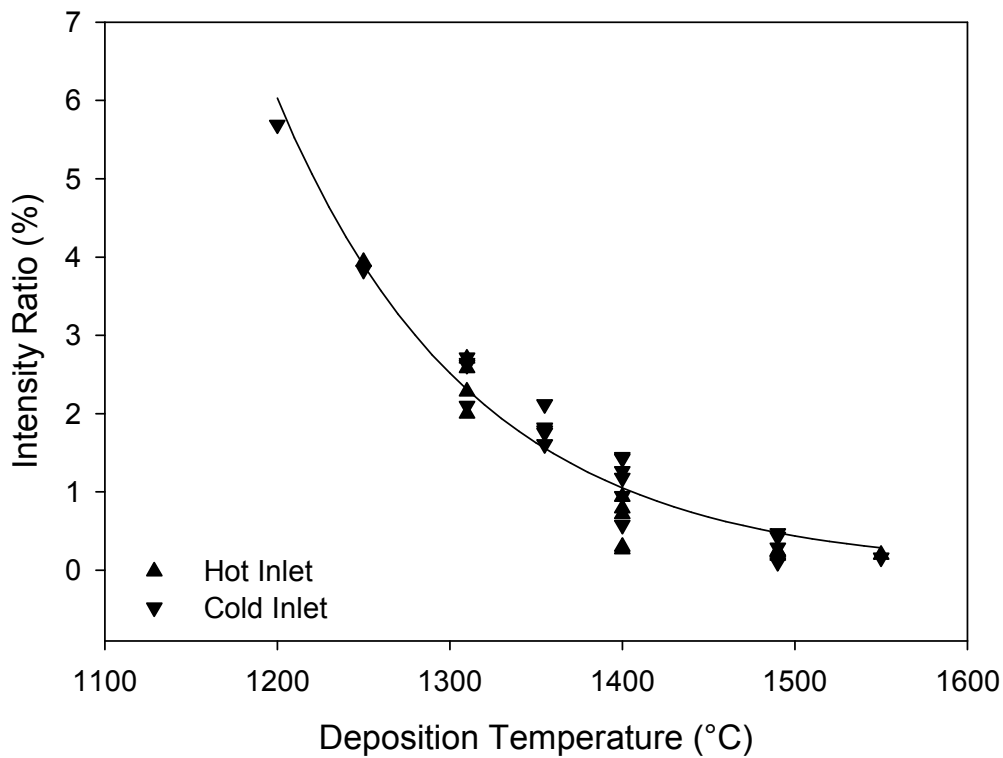


Figure 92. Intensity ratio ($100 \times I_{\text{Disorder}}/I_{111}$) as a function of deposition temperature. Data for all XRD samples analysed. Curve plotted from equation 101 using values in Table 46.

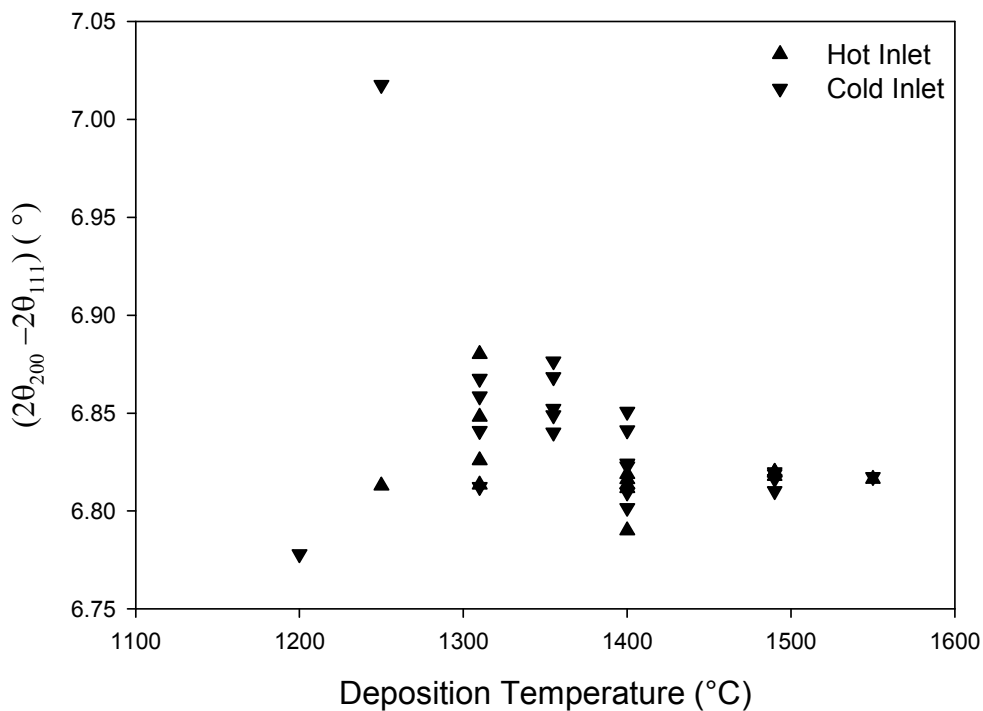


Figure 93. Separation between (111) and (200) XRD peaks as a function of deposition temperature.

12.5.3 CRYSTALLITE SIZE

Crystallite size data, as reported by Autoquan, is presented in Appendix A.

Regression analysis revealed that temperature, MTS flux and inlet type all influenced deposit crystallite size. Equation 102 can be used to describe the available data. Fit parameters for this equation are presented in Table 47.

$$Size = e^{(a+bT+cMTS+dInlet)} \quad (102)$$

Where

- Size* : Crystallite size (nm)
a, b, c, d : Constants
T : Temperature (°C)
MTS : MTS flux (mol.m⁻².s⁻¹)
Inlet : Inlet type (Hot inlet =0, Cold inlet = 1)

Table 47. Parameters for fitting equation 102 to crystallite size measurements.

	Value	P(t)	95% Confidence Interval (±)
<i>a</i>	-4.753	0	±1.186
<i>b</i>	6.358×10 ⁻³	0	7.693×10 ⁻⁴
<i>c</i>	-2.371	0.032	2.149
<i>d</i>	-0.205	0.0007	0.111
R ²	0.915		
R _a ²	0.907		

Measured crystallite sizes, together with values predicted using equation 95, are shown in Figure 94. It can be seen that crystallite size increases rapidly as deposition temperature increased from 1200 °C to 1550 °C. The cold gas inlet resulted in smaller crystallites than the hot inlet under all conditions. This effect was stronger at high deposition temperatures than at low temperatures. All else constant, increasing MTS flux reduced crystallite size, this effect being almost linear for the range investigated.

It should be noted that the crystallite size measured by XRD is quite different to the grain size observed using SEM imaging.

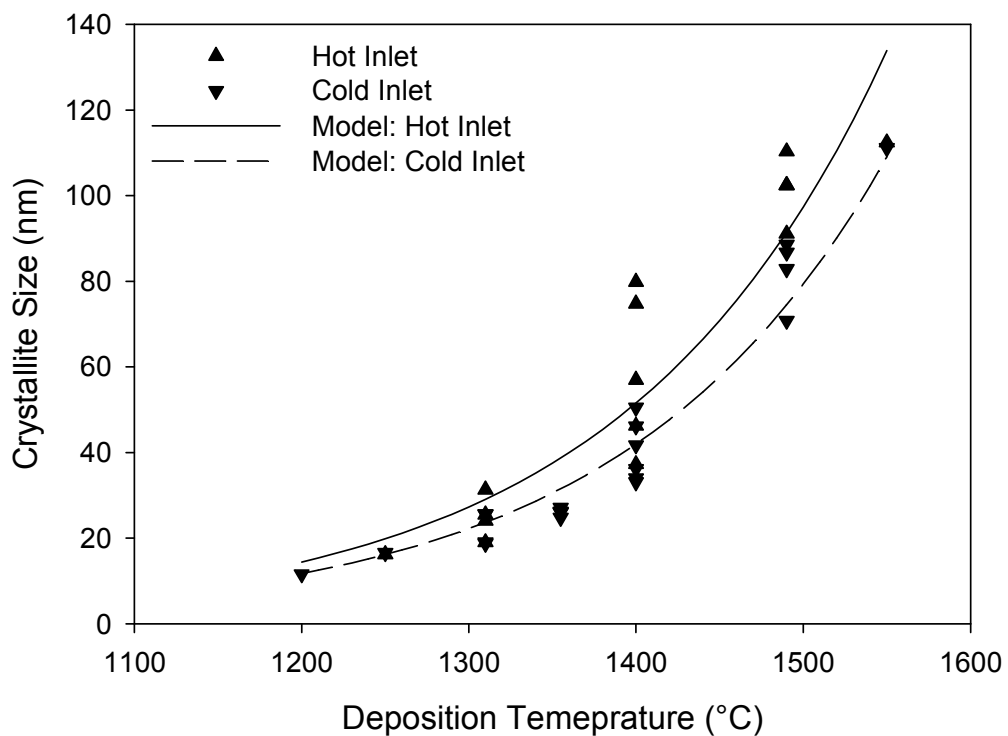


Figure 94. Crystallite size as a function of deposition temperature and type of gas inlet. Predicted values are for a MTS flux of $0.088 \text{ mol.m}^{-2}.\text{minute}^{-1}$.

12.5.4 LATTICE PARAMETER

It was found that deposition temperature had a significant influence on the silicon carbide lattice parameter. Increasing deposition temperature resulted in an increase in the lattice parameter. In modelling the relationship between deposition temperature and lattice parameter it was assumed that a sigmoidal type function would best describe the data. A linear relationship was tested; this however resulted in a slightly worse fit. The influence of MTS and hydrogen flux was assumed to be linear. Inlet type was found to have no statistically significant influence on the lattice parameter. Lattice parameter may be modelled using Equation 103 and parameter values listed in Table 48.

$$a = b + \left(\frac{c}{1 + \left(\frac{T}{d} \right)^e} \right) + fMTS + gH \quad (103)$$

Where:

- a : Cubic lattice parameter (nm)
- b, c, d, e, f, g : Model parameters
- MTS : MTS flux ($\text{mol.m}^{-2}.\text{minute}^{-1}$)
- H : Hydrogen flux ($\text{mol.m}^{-2}.\text{minute}^{-1}$)

Table 48. Parameter values for fitting equation 103 to measured lattice parameters.

	Estimate	P(t)	95% Confidence Interval (\pm)
b	0.43573	0	1.556×10^{-4}
c	2.401×10^{-4}	0	1.067×10^{-4}
d	1368.044	0	37.446
e	-35.075	0.0036	30.556
f	-7.741×10^{-4}	0.0022	6.356×10^{-4}
g	3.025×10^{-5}	0.0447	3.966×10^{-5}
R^2	0.859		
R_a^2	0.836		

Measured lattice parameters as a function of deposition temperature are shown in Figure 95. The horizontal line represents a lattice parameter of 0.43589 nm. Test runs with a lattice parameter value below the line have a compressive strain while those with values above the line have tensile strain.

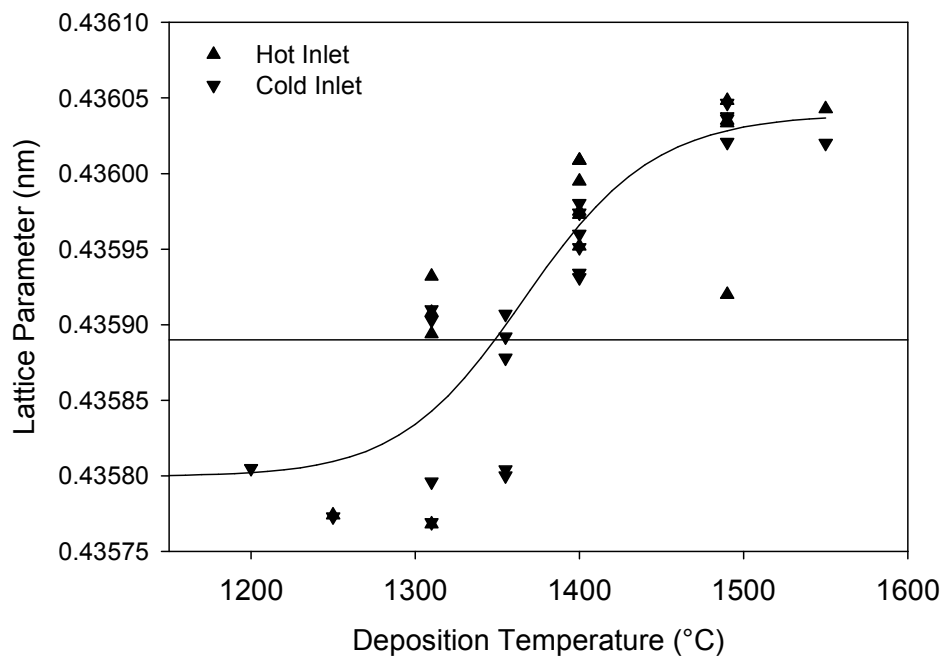


Figure 95. β -SiC lattice parameter as a function of deposition temperature. The horizontal line represents the standard room temperature lattice parameter. Equation 103 is plotted for MTS flux of $0.078 \text{ mol.m}^{-2}.\text{minute}^{-1}$ and a hydrogen flux of $0.078 \text{ mol.m}^{-2}.\text{minute}^{-1}$.

Although the change in lattice parameters is small (total range of 0.00028 nm) it is still significant when compared to the average 95 % confidence interval of $\pm 0.0000576 \text{ nm}$ estimated by Autoquan.

12.6 RAMAN SPECTROSCOPY

Raman spectrographs of all samples tested may be found in Appendix B. A discussion of Raman spectroscopy and the factors influencing the Raman spectrum is presented in section 8.4.2.

Features typically seen in Raman spectrographs of the deposits are shown in Figure 96. In the case of high temperature deposits only the TO (796 cm^{-1}), LO (972 cm^{-1}) and the resonance peak at approximately 1513 cm^{-1} were significant. At low deposition temperatures these peaks were either significantly reduced or not present while the peaks due to crystalline silicon (520 cm^{-1}), amorphous silicon (415 cm^{-1} to 540 cm^{-1}) and amorphous silicon carbide (below 600 cm^{-1}) increased in intensity.

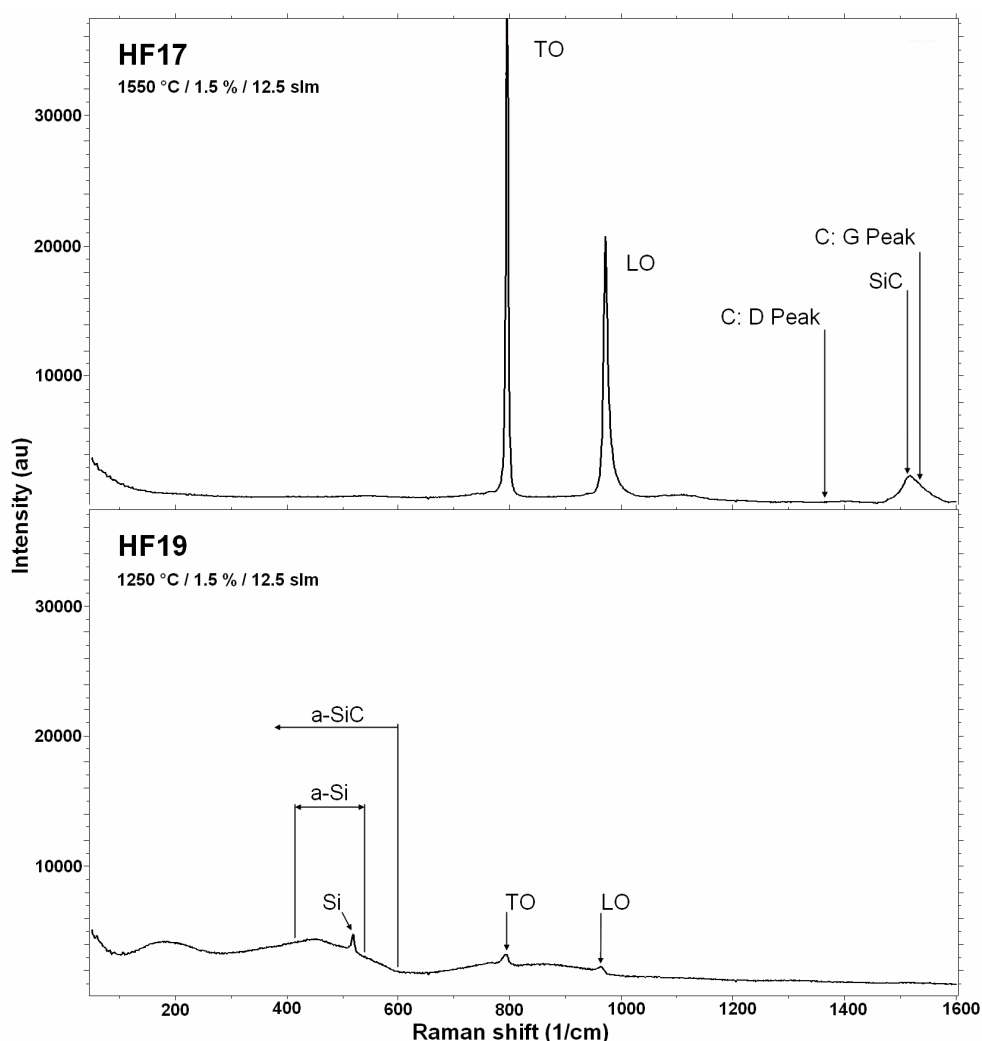


Figure 96. Raman spectrum showing features present in deposits formed at high and low temperatures. Peaks related to crystalline silicon (Si) and amorphous silicon (a-Si) and possibly amorphous SiC (a-SiC) only appear at low deposition temperatures. Silicon carbide resonance peaks and peaks possibly related to carbon D and G peaks only appear at high deposition temperatures.

At high deposition temperature 2 broad, low intensity, peaks become apparent at approximately 1310 cm^{-1} and 1400 cm^{-1} . These peaks may be related to the formation of free carbon in the deposit, however the intensity is so low ($< 500\text{ a.u.}$) that they would fall below the background level of deposits formed at lower temperatures where carbon formation is unlikely. An additional feature of deposits formed at high temperatures is the broad low intensity peak that forms at approximately 1110 cm^{-1} . The 1050 cm^{-1} to 1450 cm^{-1} spectrum of deposits formed at low (HF17) and high (HF19) temperatures are compared in Figure 97.

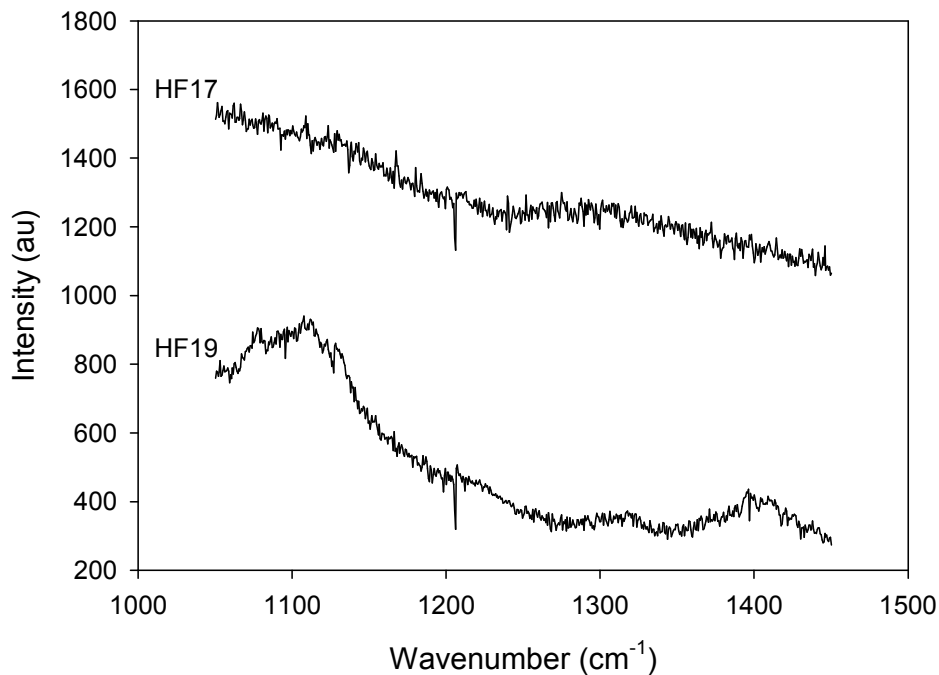


Figure 97. Detail of low intensity peaks formed at high deposition temperatures. HF19 deposited at $1550\text{ }^{\circ}\text{C}$, HF17 deposited at $1250\text{ }^{\circ}\text{C}$, all other deposition conditions similar. The features present at approximately 1110 cm^{-1} , 1310 cm^{-1} and 1400 cm^{-1} are not present when the deposition temperature is below $1490\text{ }^{\circ}\text{C}$.

Intensity of the TO, LO and silicon peaks were found to be sensitive to deposition conditions. For these peaks the response to processing conditions could be described using equation 104. Parameter values for the TO, LO and silicon peaks are given in Table 49. The response of the TO and LO peaks was very similar except that the TO peak was found to be insensitive to hydrogen flux. For both peaks the deposits formed using the cold gas inlet system resulted in lower peak intensity. As the TO and LO peaks decreased in intensity the silicon peak increased in intensity. For the processing conditions used, and the Raman spectrometer set up, peak intensities increase exponentially. It should be noted that there will be a maximum limit to the intensity and that over a broader range of processing conditions the peak intensity will not continue to increase exponentially.

$$Intensity = e^{(a+bT+cM+dH+eI)} \quad (104)$$

Where

- Intensity* : Peak intensity (arbitrary units)
a, b, c, d : Constant
T : Temperature (°C)
M : MTS flux (mol.m⁻².minute⁻¹)
H : Hydrogen flux (mol.m⁻².minute⁻¹)
I : Inlet type (Hot inlet = 0, Cold inlet = 1)

Table 49. Parameter values for fitting equation 104 to measured Raman peak intensities.

	Value	P(t)	95% Confidence Interval (±)
TO Peak			
<i>a</i>	0		
<i>b</i>	7.047×10 ⁻³	0	1.699×10 ⁻⁴
<i>c</i>	-3.616	0.0275	3.185
<i>d</i>	0		
<i>e</i>	-0.184	0.0285	0.163
R ²	0.869		
R _a ²	0.861		
LO Peak			
<i>a</i>	-3.142	0.0063	2.181
<i>b</i>	7.877×10 ⁻³	0	1.314×10 ⁻³
<i>c</i>	-9.617	0	3.287
<i>d</i>	0.392	0.0004	0.199
<i>e</i>	-0.130	0.0960	0.154
R ²	0.903		
R _a ²	0.890		
Si Peak			
<i>a</i>	16.095	0	0.662
<i>b</i>	7.877×10 ⁻³	0.0001	7.877×10 ⁻³
<i>c</i>	3.302	0.0003	1.650
<i>d</i>	0		
<i>e</i>	0.279	0	7.719×10 ⁻²
R ²	0.972		
R _a ²	0.969		

In Table 49 a parameter value of 0 indicates that the parameter was found to have no statistically significant influence on the peak intensity.

Measured peak intensity, together with values estimated using equation 104 and the parameter values listed in Table 49, as a function of deposition temperature are shown in Figure 98 to Figure 100. In all cases the model values are for average MTS

and hydrogen fluxes. Plotting the model for extreme values of MTS and hydrogen flux would have resulted in a somewhat better fit between the model and measured values.

In Figure 100 solid symbols are used where an actual silicon peak formed. Hollow symbols were used where no silicon peak formed. This represents a background value, as for example in the Raman plot for HF17 in Figure 96, or the side of the peak formed due to amorphous phases as for example in the plot for HF19 in Figure 96.

Test run CR18, deposited at 1250 °C, was reported as having an unusually intense silicon peak. Although the high value is plotted in Figure 100 the value was not used in determining the model parameters. Including data for CR18 into the model did not change the parameters significantly but did decrease the goodness of fit. It may be speculated that this high value was as a result of a non uniform distribution of silicon and that an area with a higher than average silicon content was viewed during measurement. This effect was however not noticed on any of the other samples.

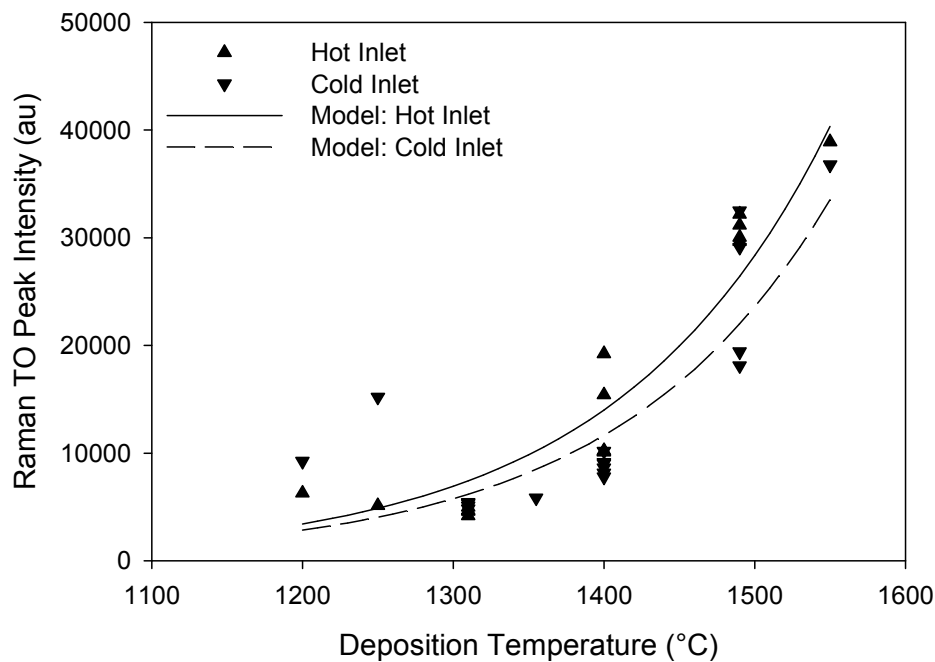


Figure 98. Raman TO peak intensity as a function of deposition temperature. Model values plotted for an average MTS flux ($0.088 \text{ mol.m}^{-2}.\text{minute}^{-1}$).

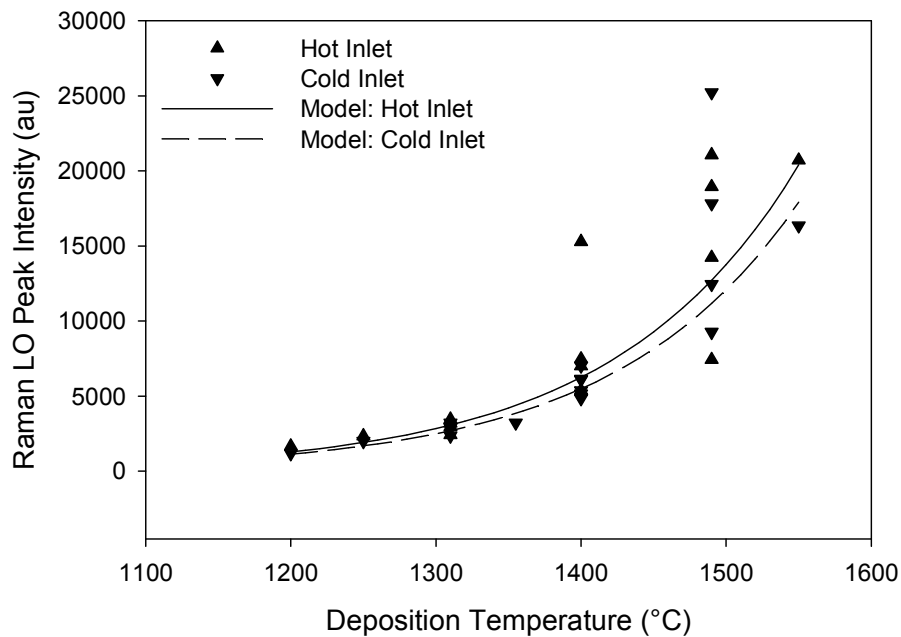


Figure 99. Raman LO peak intensity as a function of deposition temperature. Model values plotted for an average MTS ($0.088 \text{ mol.m}^{-2}.\text{minute}^{-1}$) and hydrogen flux ($4.344 \text{ mol.m}^{-2}.\text{minute}^{-1}$).

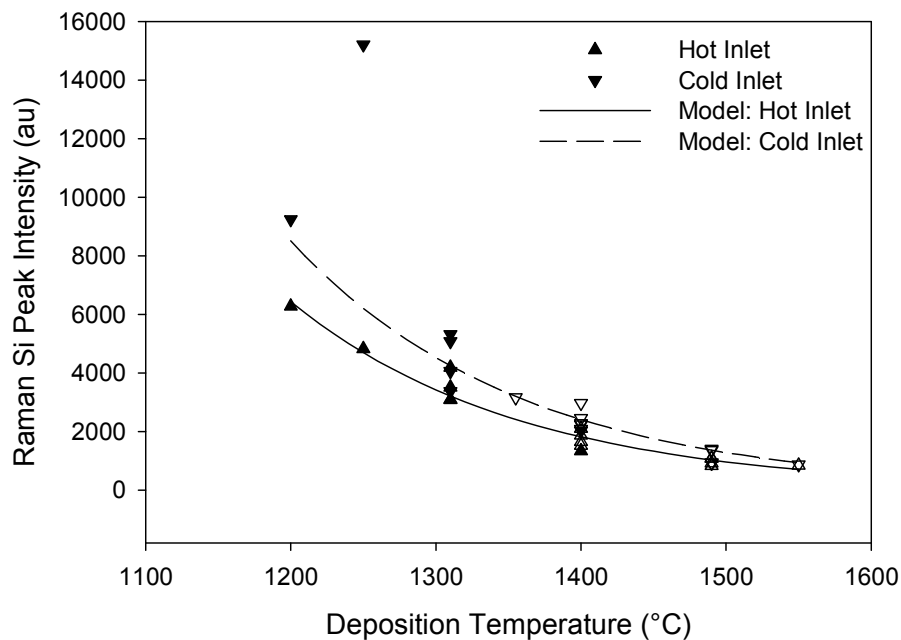


Figure 100. Raman silicon peak intensity as a function of deposition temperature. Solid symbols used where an actual silicon peak formed, unfilled symbols used to depict the intensity value of the background where no silicon peak formed. Model values plotted for an average MTS ($0.088 \text{ mol.m}^{-2}.\text{minute}^{-1}$) and hydrogen flux ($4.344 \text{ mol.m}^{-2}.\text{minute}^{-1}$).

Process conditions were found to influence the position of the silicon carbide TO and LO peaks. This is most likely due to the influence of crystallite size or crystal perfection. The position of the peaks was modelled using a sigmoidal function such as equation 105. An alternative model based on exponential growth to a maximum value was also tested; however this resulted in a marginally worse fit. It was found that deposition temperature was the key determinant of peak position. For the TO peak; MTS flux, hydrogen flux and inlet type had no statistically significant influence. For the LO peak MTS flux was found to have a significant influence while hydrogen flux and inlet type had no statistically significant influence.

$$Position = \frac{a}{\left(1 + \left(\frac{T}{b}\right)^c\right)} + dM \quad (105)$$

Where

Position : Wavenumber of the peak (cm⁻¹)
a, b, c, d : Constants
T : Temperature (°C)
M : MTS flux (mol.m⁻².minute⁻¹)

	Value	P(t)	95% Confidence Interval (±)
TO Peak			
<i>a</i>	795.679	0	0.415
<i>b</i>	870.081	0	102.749
<i>c</i>	-16.041	0	7.903
<i>d</i>	0		
R ²	0.826		
R _a ²	0.815		
LO Peak			
<i>a</i>	973.803	0	1.301
<i>b</i>	883.177	0	44.615
<i>c</i>	-12.825	0	2.131
<i>d</i>	-11.724	0.0403	11.172
R ²	0.968		
R _a ²	0.965		

Plots of TO and LO peak position as a function of temperature as shown in Figure 101 and Figure 102. In both cases the peak position shifts to a lower wave number as deposition temperature is decreased. In the case of the LO peak increasing MTS flux shifts the peak to a lower wave number. Comparing Figure 101 to Figure 102 it can be seen that the LO peak position is significantly more sensitive to changing process conditions than the TO peak. At deposition temperatures above approximately 1400 °C the effect of deposition temperature on the peak position become less significant.

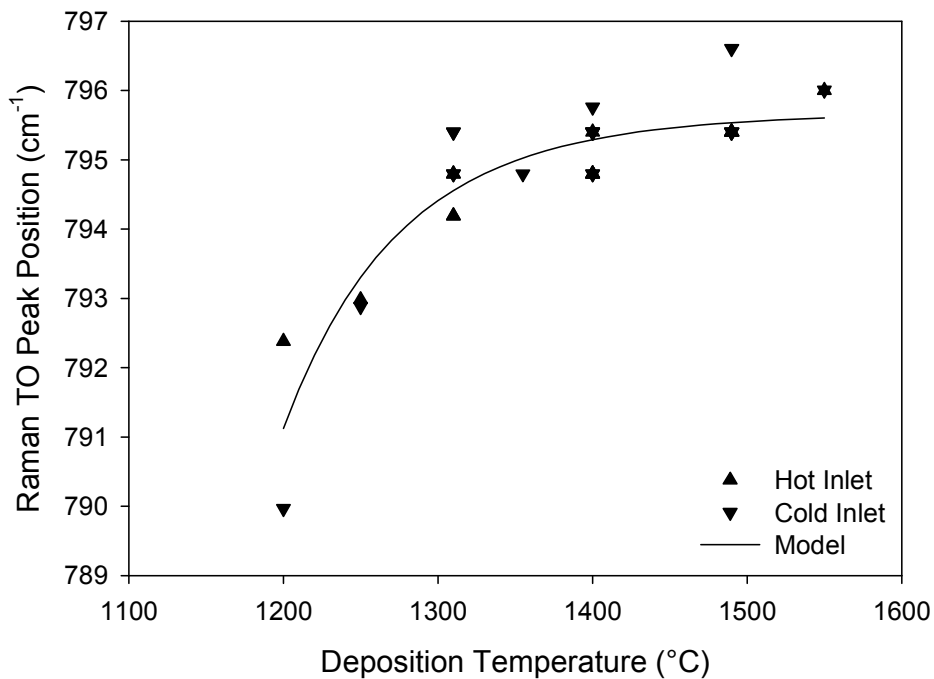


Figure 101. Silicon carbide TO peak position as a function of deposition temperature.

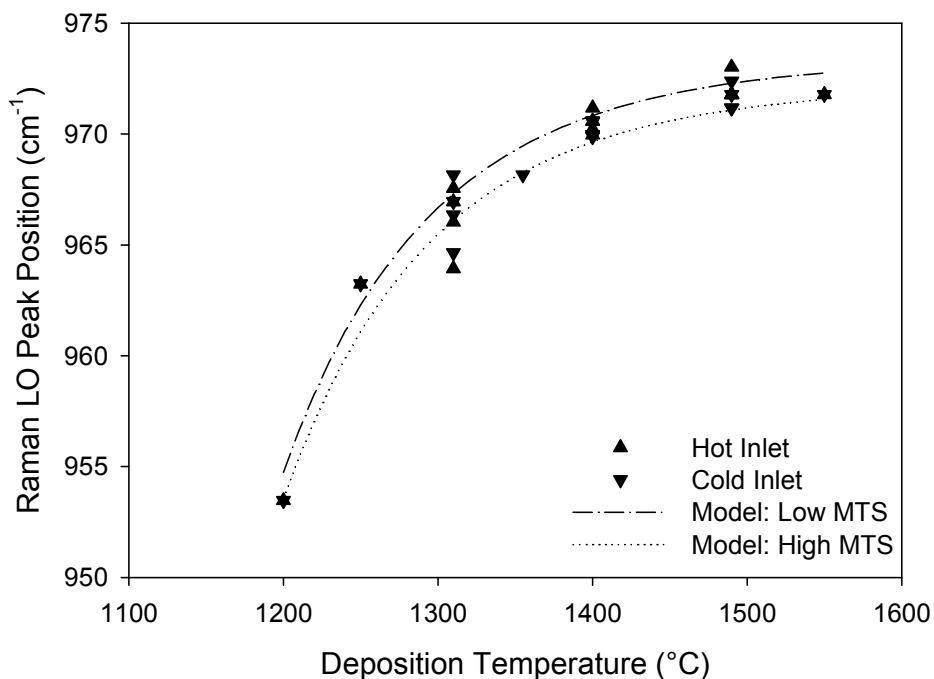


Figure 102. Silicon carbide LO peak position as a function of deposition temperature. Equation 105 plotted using values listed in Table 49 and MTS flux values of $0.028 \text{ mol.m}^{-2}.\text{minute}^{-1}$ and $0.130 \text{ mol.m}^{-2}.\text{minute}^{-1}$.

12.7 MICROPROBE ANALYSIS

A summary of all microprobe analysis results is presented in Appendix A.

Total silicon and total carbon content of the deposits was measured to determine if any free silicon or free carbon was present in the deposits. Stoichiometric silicon carbide contains 70.03 % silicon on a mass basis. As silicon carbide is a stoichiometric compound any deviation from a silicon content of 70.03 % represents either free silicon or free carbon in the deposit.

A normal probability plot of the average silicon content of all the test runs is shown in Figure 103. With the exception of 3 test runs (TR12, TR13, TR14) coated using the hot gas inlet system and 2 test runs (CR18, MTS1) using the cold inlet the silicon content of the various test runs is approximately normally distributed. All the test runs with high silicon content were deposited at either 1250 °C (CR18) or 1200 °C (MTS1, TR12, TR13, TR14).

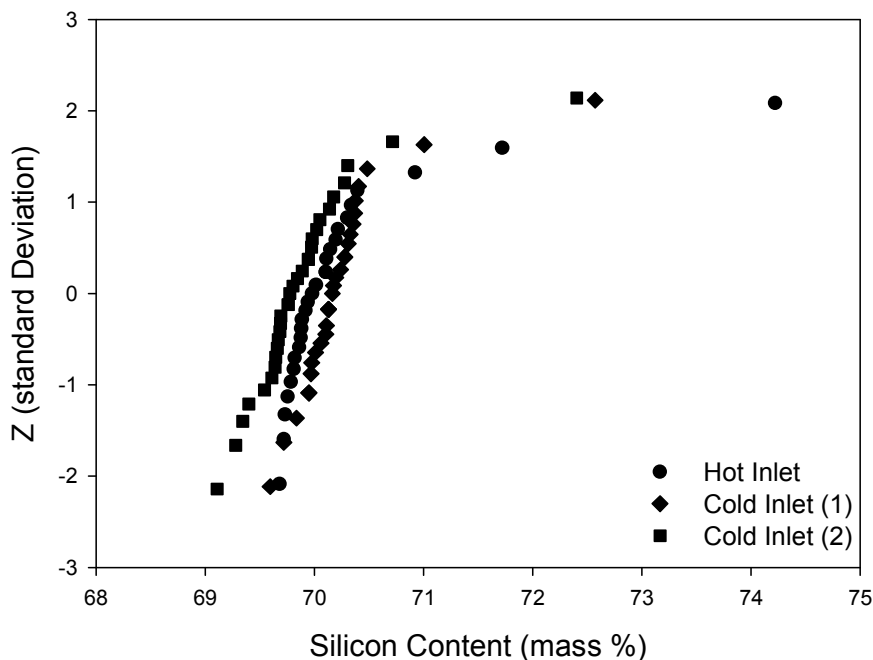


Figure 103. Silicon content normal probability plot. Cold Inlet (1) and Cold Inlet (2) represent the original and repeated measurements of test runs coated using the cold gas inlet system. Only test runs coated at 1200 °C and 1250 °C had a silicon content of more than 70.5 %.

A summary of the silicon content of the deposits is presented in Table 50. Data from all test runs coated at 1200 °C is excluded from this summary. The difference of 0.352 % Si between the two sets of measurements performed on the samples prepared using the cold gas inlet was found to be statistically significant (Paired t-test, $P(t) = 2.95 \times 10^{-5}$). When the hot inlet is compared to the cold inlet there are statistically significant differences in silicon content when the 2 sets of measurements performed on the cold inlet samples are considered separately. If the

repeated measurements are pooled there is no significant difference in silicon content between test runs coated using the cold and hot inlets (Paired t-test, $P(t) = 0.994$).

Table 50. Silicon content of deposits formed between 1250 °C and 1550 °C.

	Average (Mass %)	Std Deviation (Mass %)	Count	95% Confidence Interval (±)
Hot Inlet	69.981	0.208	24	0.088
Cold Inlet (Combined)	69.982	0.347	58	0.091
Cold Inlet (1 st Measure)	70.166	0.266	28	0.103
Cold Inlet (2 nd Measure)	69.811	0.239	30	0.123

The effect of process conditions on deposit silicon content is shown in Figure 104, Figure 105 and Figure 106. Above 1250 °C deposition temperature was found to have no effect on silicon content. When the deposition temperature was below 1250 °C the silicon content of the deposit increases rapidly with decreasing deposition temperature. Both MTS flux and hydrogen flux were found to have a negligible influence on the silicon content of the deposit. In both Figure 105 and Figure 106 the only test runs with a significantly higher than normal silicon content were those coated at 1200 °C.

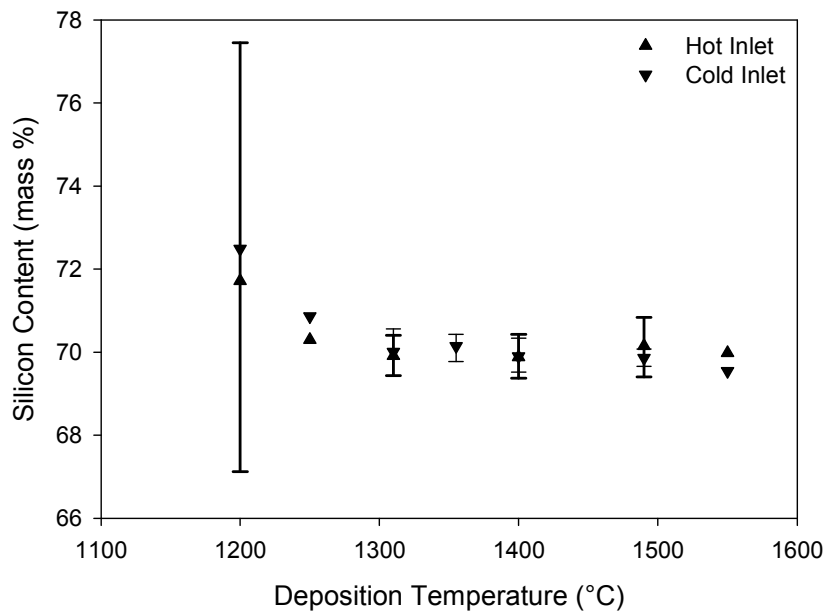


Figure 104. Silicon content dependence on deposition temperature. Markers represent median value, error bars estimated 3σ values. Heavy error bars represent data for hot inlet. The wide range of the estimated error for hot inlet test runs coated at 1200 °C are due to the small sample size (2 test runs) and wide range of silicon content(71.72 % to 74.22 %) of runs coated at 1200 °C. The large difference between the 2 test runs may be as a result of the non uniform distribution of any elemental silicon in the layer.

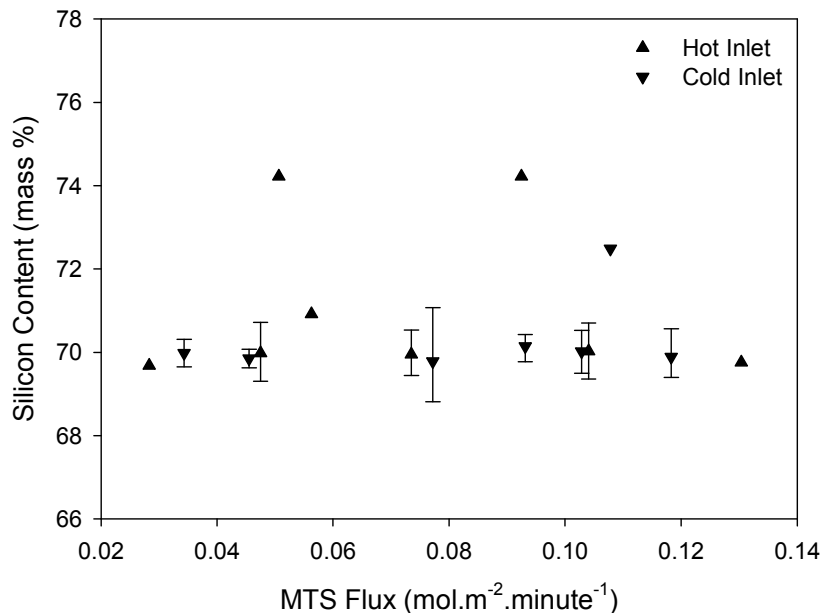


Figure 105. Silicon content dependence on MTS flux. Error bar markers represent median value, error bars estimated 3σ values. Only test runs coated at 1250 °C and 1200 °C have silicon contents higher than expected for normally distributed data.

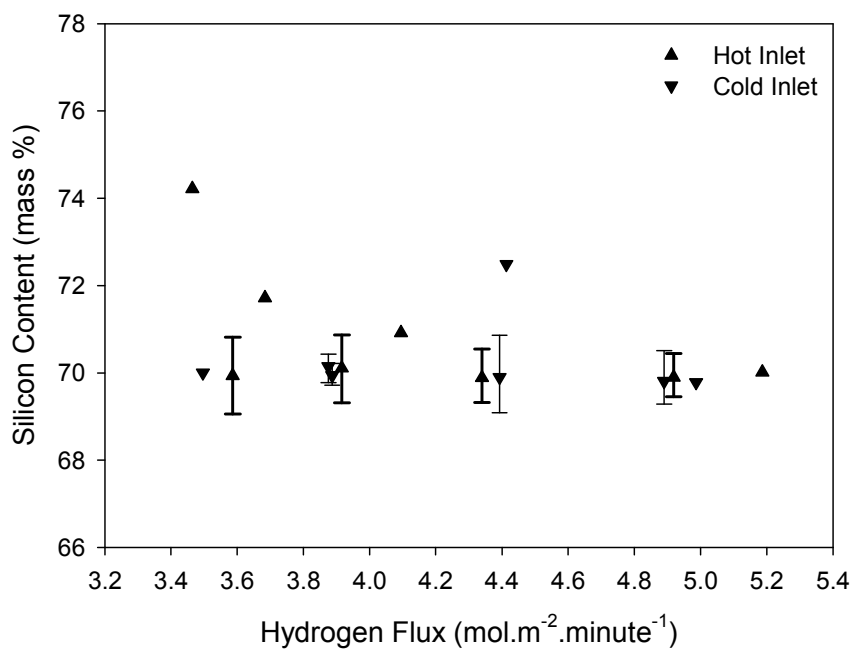


Figure 106. Silicon content dependence on hydrogen flux. Error bar markers represent median value, error bars estimated 3σ values. Only test runs coated at $1250\text{ }^{\circ}\text{C}$ and $1200\text{ }^{\circ}\text{C}$ have silicon contents higher than expected for normally distributed data.

12.8 SEM MICROSCOPY

The microstructure of the deposits was investigated by means of SEM imaging. Three separate techniques were used; secondary electron imaging of the free surface, backscatter electron imaging of polished cross sections, secondary electron imaging of polished and etched cross sections. A summary of the findings will be presented in the following 3 sections. Appendix C contains a complete set of images.

12.8.1 SURFACE STRUCTURE

Deposit surface structure was found to be sensitive to processing conditions with deposition temperature; MTS concentration and hydrogen flow rate all influencing deposit morphology. These effects can be seen in Figure 107, Figure 108 and Figure 109. At deposition temperatures below 1400 °C the deposit consisted of grains with rounded, dome like, tops. At 1400 °C the deposit morphology depended on the MTS concentration, hydrogen flow rate and the inlet type used. Low MTS concentration coupled with low hydrogen flow rates resulted in a faceted deposit. This effect was more pronounced when the hot gas inlet system was used. Increasing the deposition temperature to 1490 °C resulted in faceted grains under all combinations of MTS concentration and hydrogen flow tested.

The transition from domed grains to faceted grains was not sharp. At the lowest deposition temperatures (MTS1 at 1200 °C) the domes were well defined and appeared relatively smooth being, covered by very fine nodules. As deposition temperature increased the nodules became more pronounced, the smooth domes changing to domes covered by nodules with a wide range of sizes. This resulted in a domed structure with a rough surface (e.g. HF11, CR13). Further changes in deposition conditions resulted in the nodules becoming faceted. At this stage the deposit appeared to consist of domed structures made up of clusters of small faceted grains (e.g. CR12, CR14). Further increases in temperature resulted in large faceted grains together with clusters of smaller grains and finally, at the highest deposition temperatures, individual faceted grains.

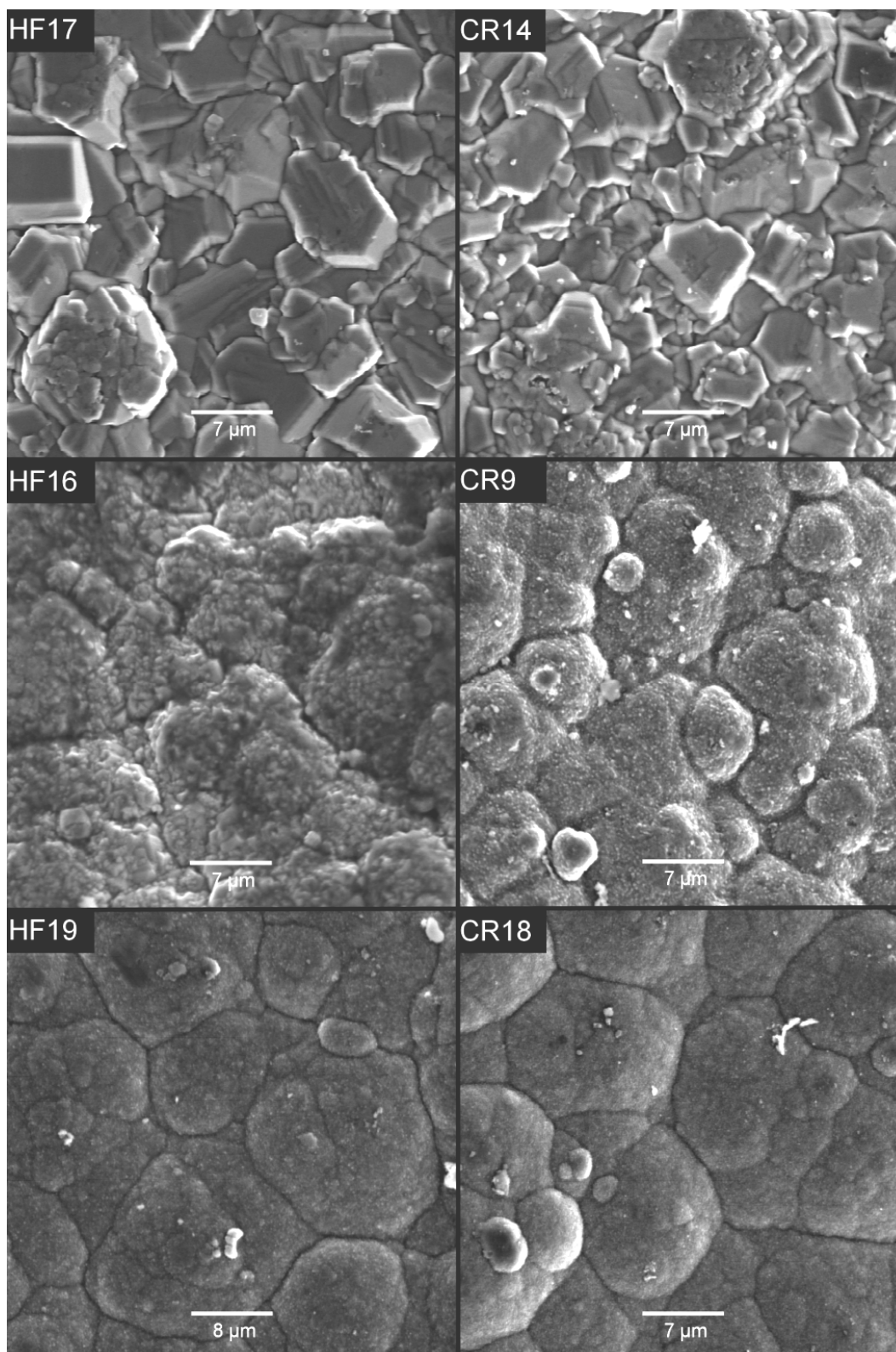


Figure 107. Influence of deposition temperature on deposit surface morphology.
Process conditions: MTS: 1.5 %, Hydrogen flow: 12.5 slm, Temperature:
HF19, CR18 : 1250 °C
HF16, CR9 : 1400 °C
HF17, CR14 : 1550 °C

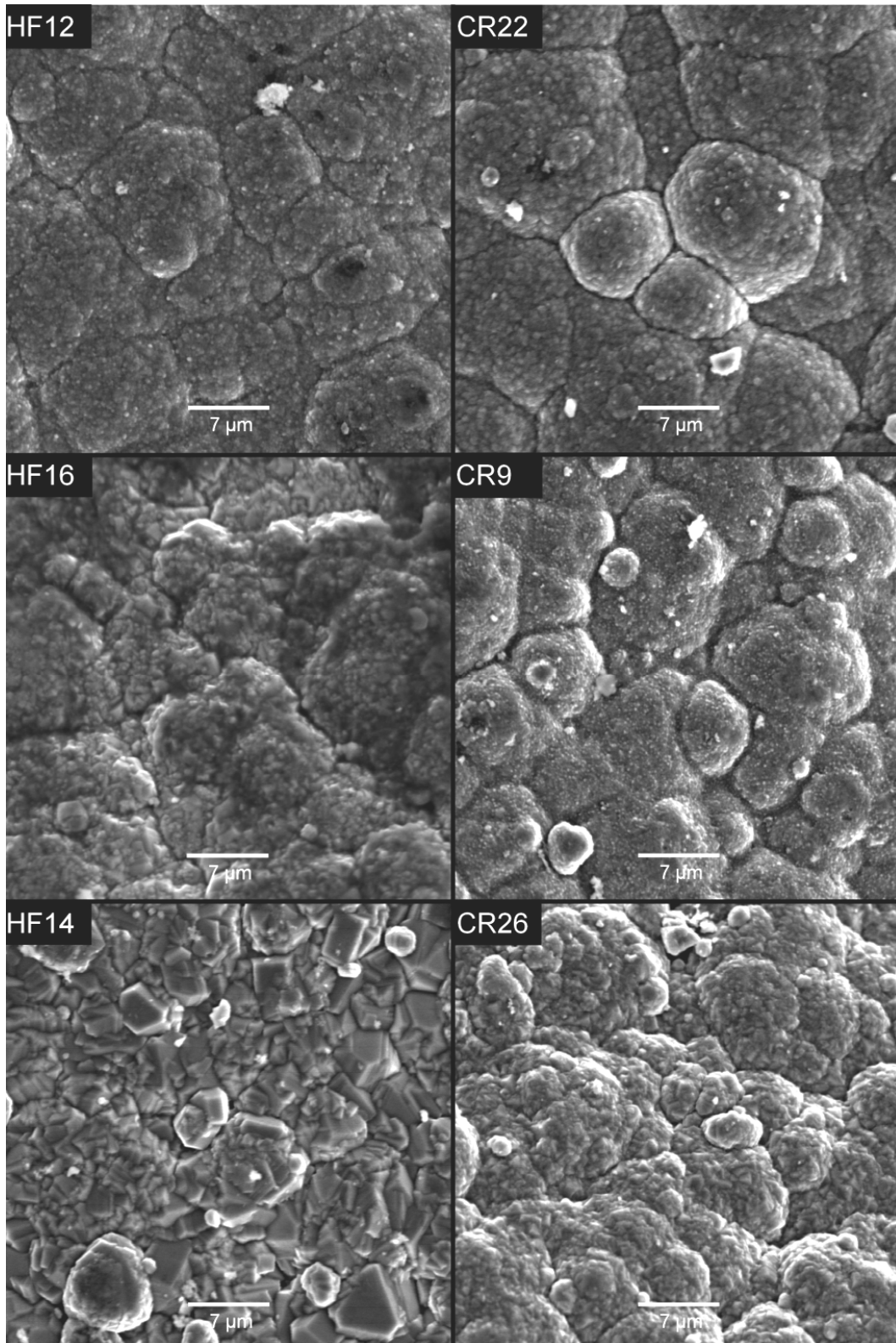


Figure 108. Influence of MTS concentration on deposit surface morphology. Process conditions: Temperature: 1400 °C, Hydrogen flow: 12.5 slm, MTS concentration:
HF14, CR26 : 0.5 %
HF16, CR9 : 1.5 %
HF12, CR22 : 2.5 %

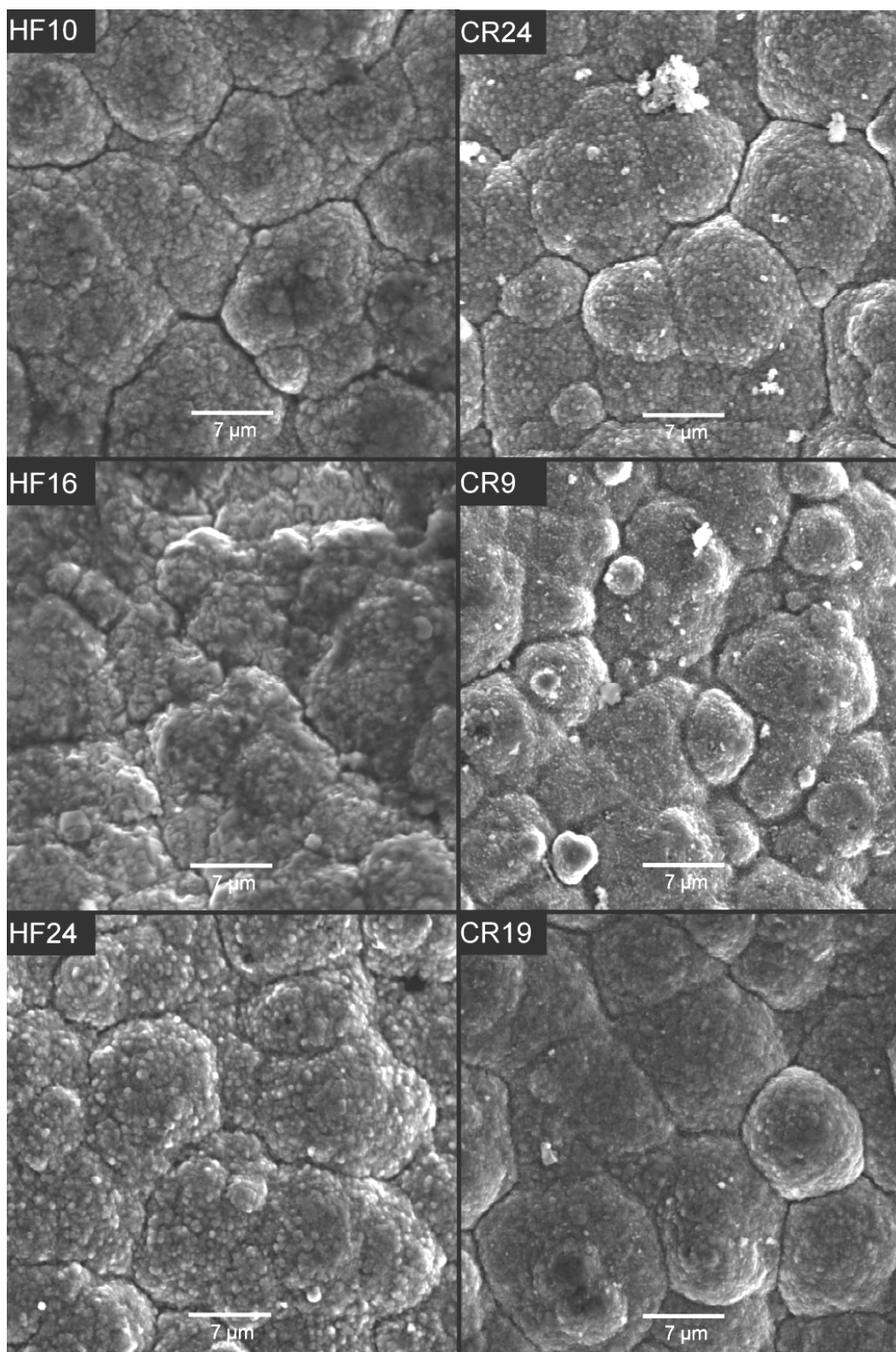


Figure 109. Influence of hydrogen flow rate on deposit surface morphology.

Process conditions: Temperature: 1400 °C, MTS concentration: 1.5 %

Hydrogen flow:

HF24, CR19 : 10 slm

HF16, CR9 : 12.5 slm

HF10, CR24 : 14 slm

12.8.2 BACKSCATTER ELECTRON IMAGING

Backscatter electron images allowed for viewing of the grain structure of the deposit cross section. From Figure 110, Figure 111 and Figure 112 it can be seen that the grain structure of the deposit was dependent on process conditions. When viewed in cross section the grain size varied from being too small to be resolved at 2000 × magnification up to an approximate maximum size of 10 μm width and 30 μm length.

A notable feature of most of the deposits is the striations within the deposit. These are obvious in the very fine grained deposits formed at low deposition temperatures (e.g. HF19, CR18). At higher deposition temperatures the striations appear as bands of finely crystalline material. In each band new grains appear to be nucleated at the interface with very few grains growing across the interface. Under backscatter electron imaging the interface between the bands appears to have a high density of pores. Although secondary electron imaging does reveal some porosity along the bands it is not clear that all the dark spots seen on the backscatter electron images are in fact due to porosity. It may be possible that the bands consist of regions of dispersed porosity that is too fine to resolve. It is unlikely that there is a significant difference in composition between the “porous” regions and the interspersed crystalline bands as excess silicon was only detected in test runs coated at 1250 °C and below. As will be seen later these bands tended to etch at a higher rate than the rest of the material.

From the backscatter electron images it is apparent that the domed structure seen on many of the deposits originate at the initial stages of the deposition process. The majority of the domes are formed by a build up of layers starting on an initial point – either a site where the deposit started forming or starting material surface. Only very rarely were points observed where a new dome was initiated once deposition had progressed beyond the initial stages. The striations follow the surface of the deposit giving rise to parallel bands. In cases where the surfaces consisted of faceted clusters of fine particles forming a domed surface, small well defined grains formed within the striations. This gave rise to the faceted clusters while the underlying domed structure remained intact.

Test run HF14 (and to a lesser extent CR26) is of note as it was deposited at a temperature where all other test runs had a striated structure; however it had a clearly crystalline structure without any striations. This is consistent with the faceted surface structure as seen in the previous section. Although similar in structure the grain size of HF14 is clearly smaller than seen on HF17 which was deposited at 1550 °C. The impact of using a cooled inlet is clearly demonstrated by comparing test run HF14 to CR26 which was coated under similar conditions. As seen in Figure 111 test run HF14, coated using a hot gas inlet, has clearly defined grains and no bands of porosity whereas CR26 has very fine indistinct grains and bands of porosity. In this respect it appears as if the use of a hot gas inlet has the same effect as a higher deposition temperature.

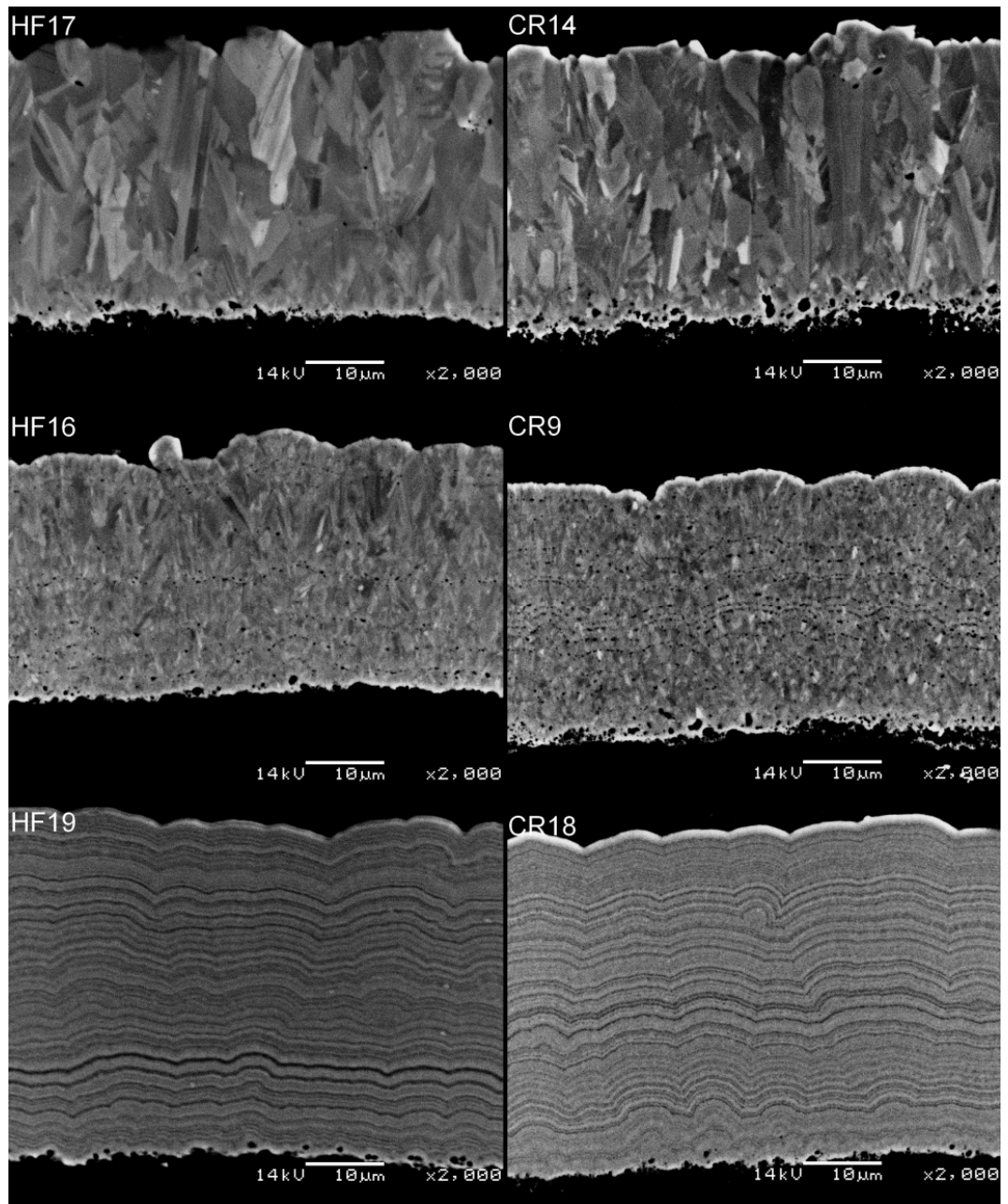


Figure 110. Influence of deposition temperature on deposit grain structure.
Process conditions: MTS: 1.5 %, Hydrogen flow: 12.5 slm, Temperature:
HF19, CR18 : 1250 °C
HF16, CR9 : 1400 °C
HF17, CR14 : 1550 °C

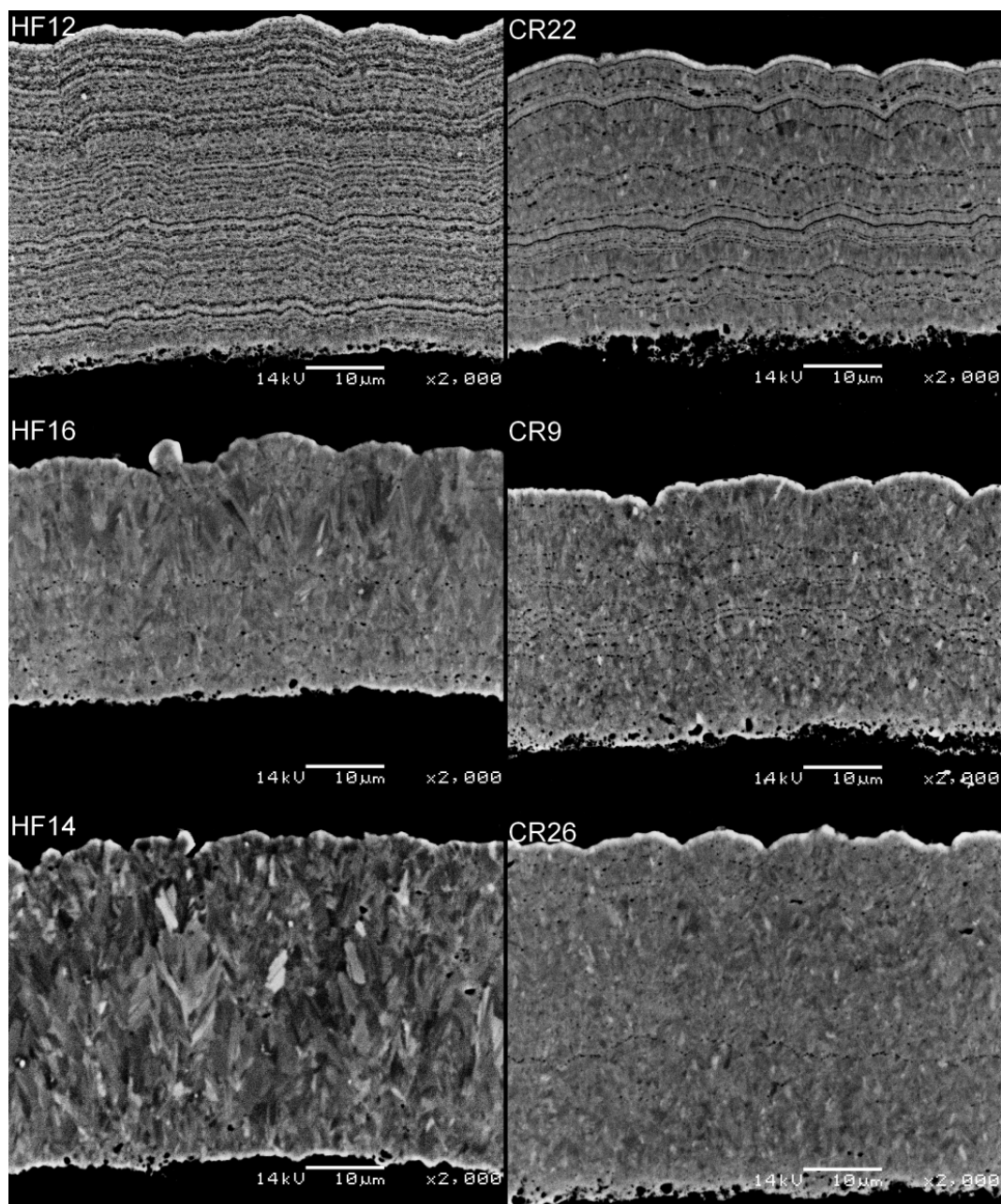


Figure 111. Influence of MTS concentration on deposit grain structure.
Process conditions: Temperature: 1400 °C, Hydrogen flow: 12.5 slm,
MTS concentration:
HF14, CR26 : 0.5 %
HF16, CR9 : 1.5 %
HF12, CR22 : 2.5 %

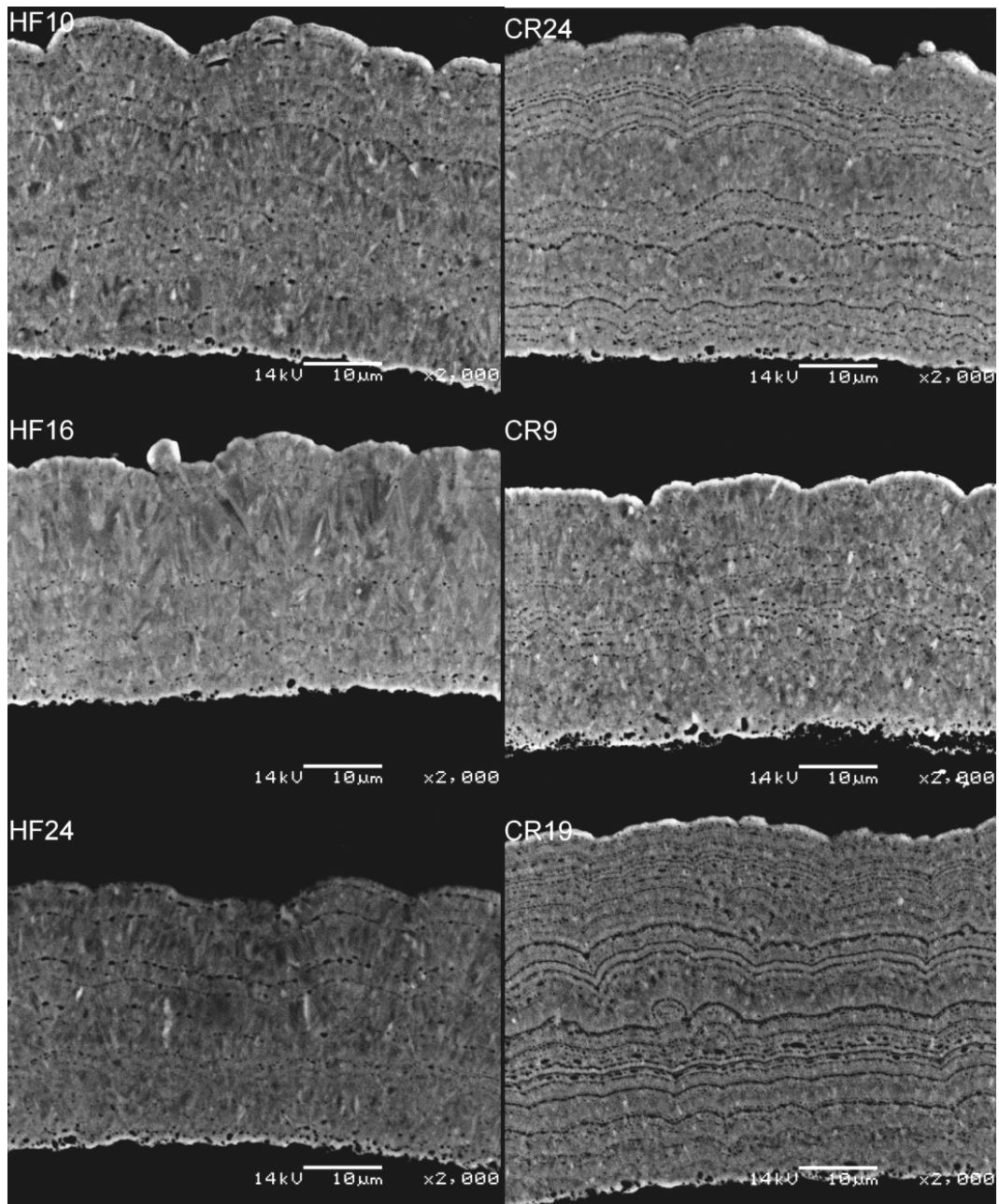


Figure 112. Influence of hydrogen flow rate on deposit grain structure.
Process conditions: Temperature: 1400 °C, MTS concentration: 1.5 %
Hydrogen flow:
HF24, CR19 : 10.0 slm
HF16, CR9 : 12.5 slm
HF10, CR24 : 14.0 slm

12.9 POLISHED AND ETCHED SAMPLES

Etching highlighted the differences in the deposits seen using backscatter electron imaging. Coarse grained deposits and fine grained bands in striated deposits were found to be virtually immune to attack. Porous bands in striated deposits etched rapidly leaving more resistant layers standing free. The effect of process conditions is shown in Figure 113 to Figure 116.

The influence of MTS concentration and hydrogen flow rate is shown in Figure 116. It can be seen that the highest resistance to etch is achieved at low MTS concentrations and high hydrogen flow rates. Test run CR13 is notable in that the etch attack appears to be fairly uniform across the whole surface rather than being restricted to specific bands. This left the whole surface pitted.

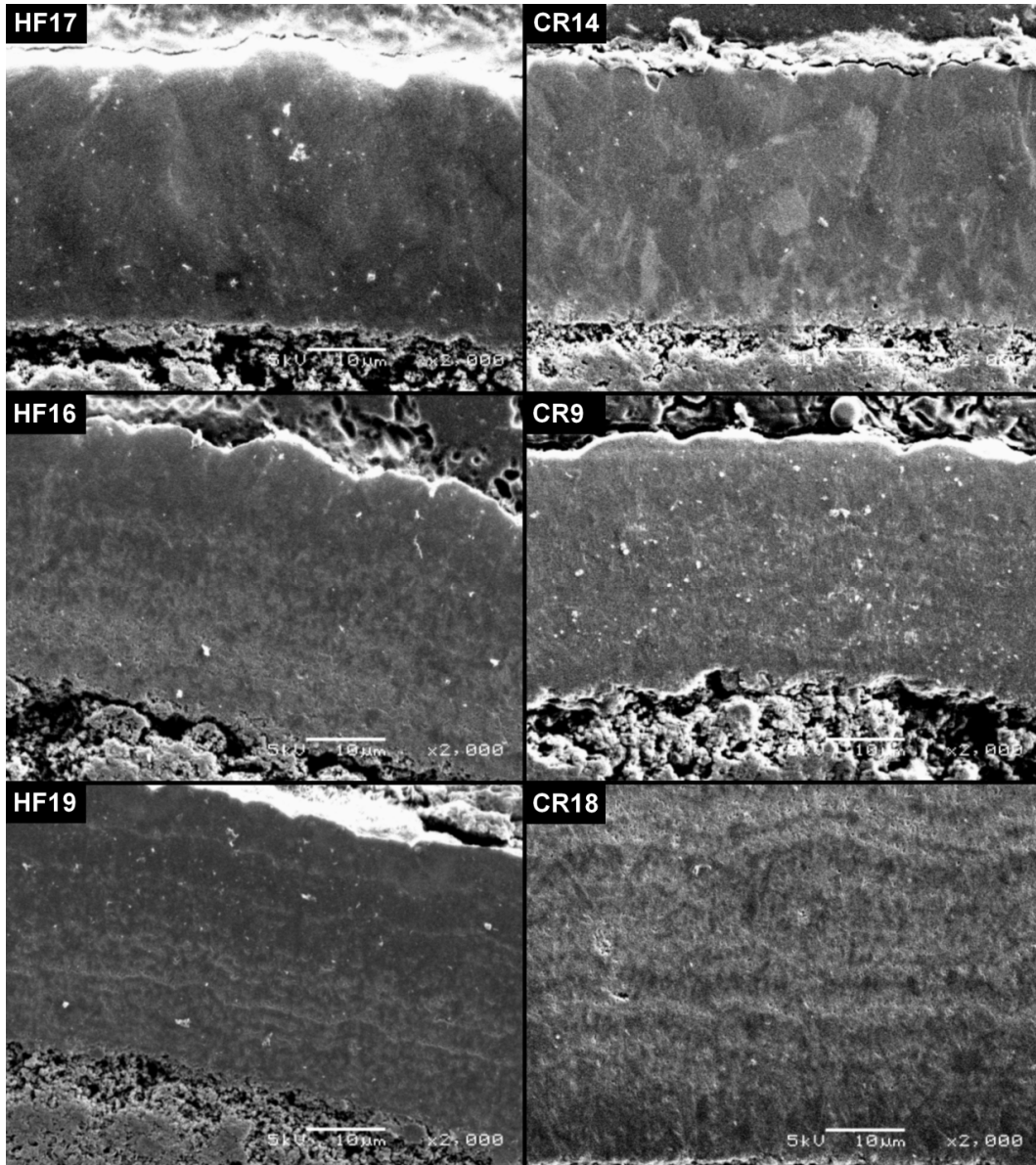


Figure 113. Influence of deposition temperature on deposit etch resistance.
Process conditions: MTS: 1.5 %, Hydrogen flow: 12.5 slm,
Temperature:
HF19, CR18 : 1250 °C
HF16, CR9 : 1400 °C
HF17, CR14 : 1550 °C

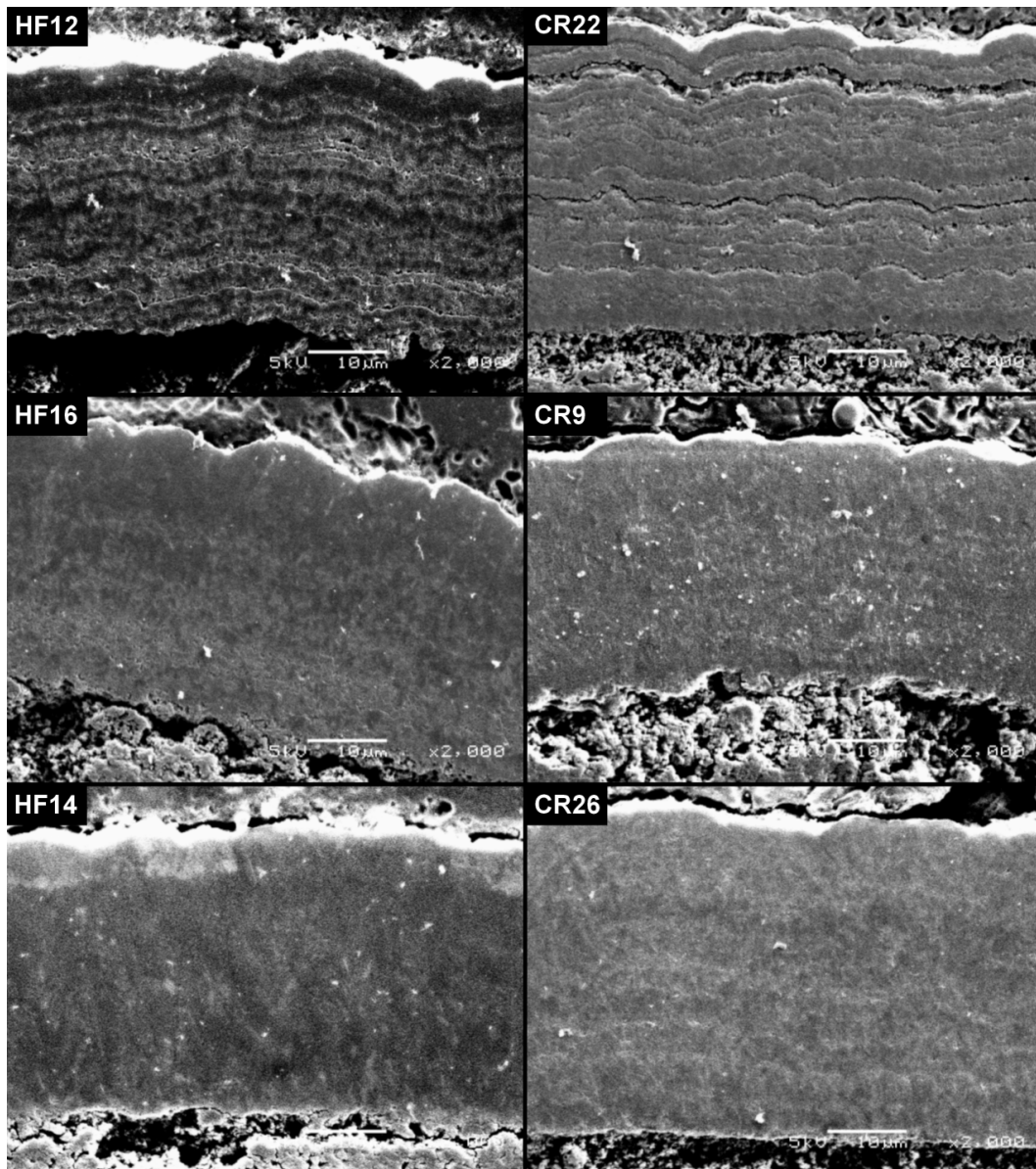


Figure 114. Influence of MTS concentration on deposit etch resistance.
Process conditions: Temperature: 1400 °C, Hydrogen flow: 12.5 slm,
MTS concentration:
HF14, CR26 : 0.5 %
HF16, CR9 : 1.5 %
HF12, CR22 : 2.5 %

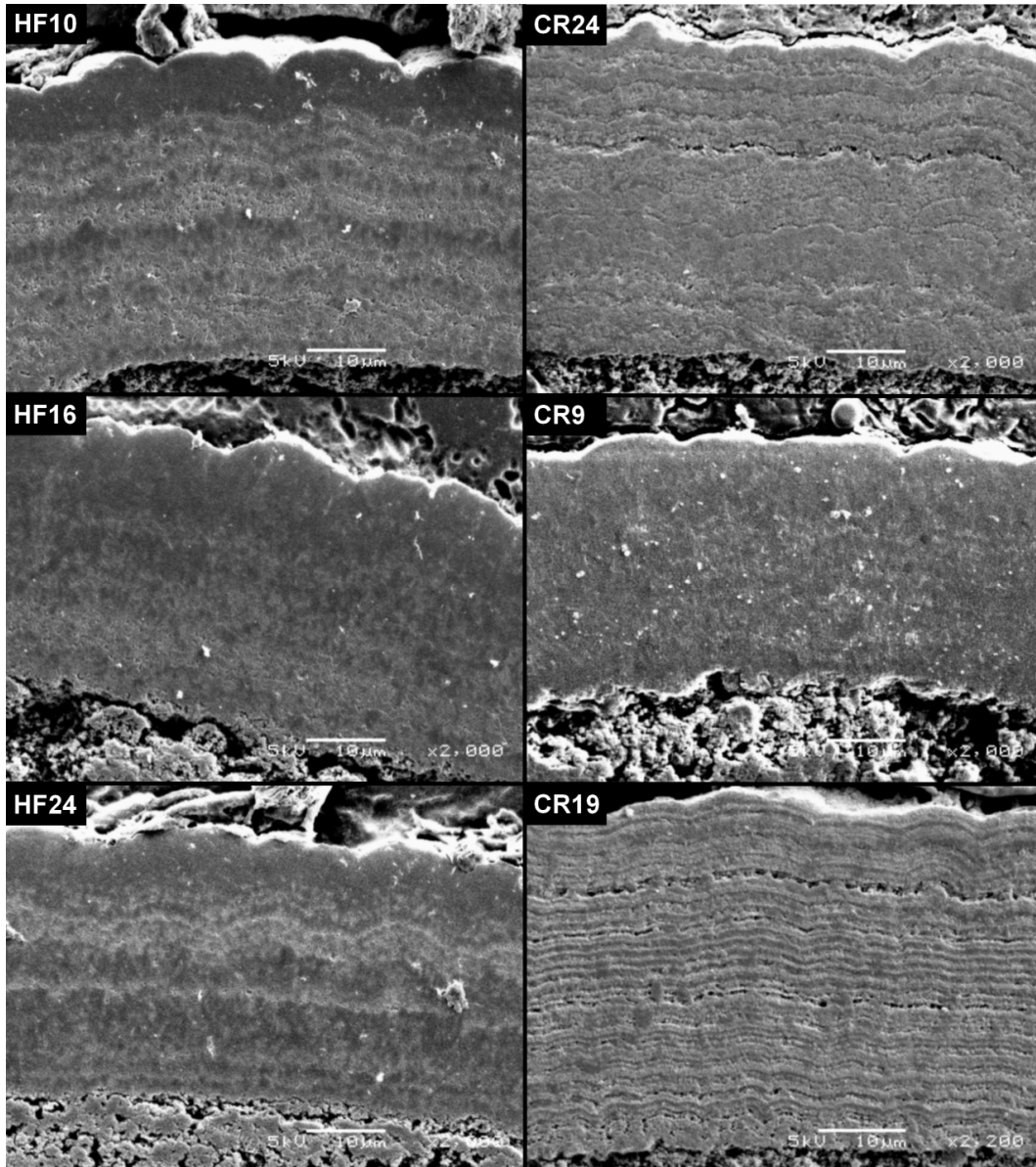


Figure 115. Influence of hydrogen flow rate on deposit etch resistance.
Process conditions: Temperature: 1400 °C, MTS concentration: 1.5 %
Hydrogen flow:
HF24, CR19 : 10.0 slm
HF16, CR9 : 12.5 slm
HF10, CR24 : 14.0 slm

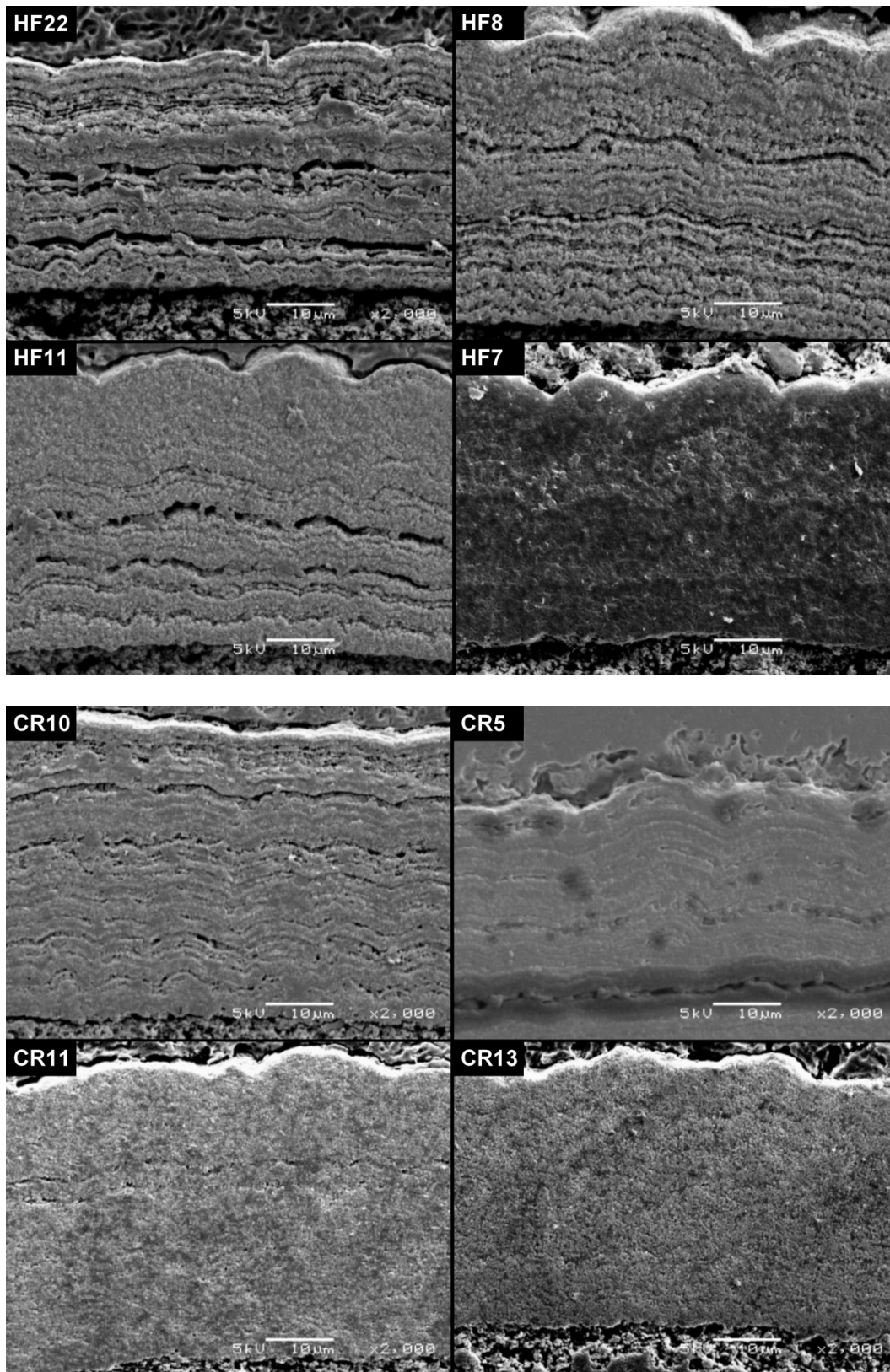


Figure 116. Influence of MTS concentration and hydrogen flow rate on deposit resistance to etching. All deposits formed at 1310 °C. MTS concentration varied between 0.9 % (bottom row) and 2.1 % (top row). Hydrogen flow rate varies between 11.0 slm (left column) and 14.0 slm (right column).

13 DISCUSSION

13.1 DEPOSITION CHARACTERISTICS

13.1.1 DEPOSITION RATE

Deposition rate models developed in this study are in agreement with the model (equation 42) published by Minato and Fukuda [153][155] being dependent on MTS flow, temperature and hydrogen flow. Apparent activation energy values measured in this study ranged between 21 kJ.mol^{-1} and 29 kJ.mol^{-1} . This is lower than the 49.8 kJ.mol^{-1} to 68 kJ.mol^{-1} reported in the literature for atmospheric pressure coaters [162][159][157] which were operating under conditions of mass transport control. As a comparison, Kim et al [183] measured an activation energy of 120 kJ.mol^{-1} using a low pressure CVD coater. Under these conditions the process was under activation or mixed control. From a comparison of the activation energy values it is clear that this particular process operated under conditions of mass transport control. The low sensitivity to deposition temperature may explain why Gulden [161] found no relationship between deposition rate and deposition temperature.

In agreement with Gulden [161] and Federer [160] deposition rate was found to have linear dependence on MTS flux. This would be expected for a process operating under conditions of mass transport control. This implies that deposition rate may be controlled by changing MTS concentration, hydrogen flow rate and/or load.

The interpretation of activation energy and dependence on deposition rate on MTS flux needs to be interpreted with caution. In this particular type of CVD coater the majority of the precursor is reacted. As a result there will be a very strong depletion effect along the length of the coater. MTS concentration will decrease from the set point value to very close to zero while HCl concentration will increase as the gas moves away from the inlet. No matter what the control mechanism at the inlet, with sufficient depletion, a mass transport mechanism will predominate by the time the gas stream exits the bed of particles. In this regard the process will always appear to be mass transport controlled. In very shallow particle beds and at low deposition temperatures, where the deposition efficiency is low, the depletion effects will have a lower impact on the process.

Due to the depletion effects in a spouted bed coater, care should be exercised when comparing experimental results obtained from spouted beds to results obtained in conventional tube furnaces where precursor depletion is minimal.

13.1.2 DEPOSITION EFFICIENCY

Efficiency values obtained ranged between 57 % and 88 %. These were very similar to those reported by Stinton and Lackey [166] but higher than those reported by Voice [175]. The predicted maximum efficiency using equation 93 is somewhat higher than the maximum theoretical efficiency predicted by Minato and Fukuda [168] (99 % versus 95 %).

Deposition efficiency was found to be dependent on deposition temperature, inlet type, MTS flux and load. Unlike the results reported by Stinton and Lackey [166] deposition efficiency was not found to decrease at high temperatures. It was found that there was an interaction effect between deposition temperature and MTS concentration. At low temperature, an increase in MTS concentration reduced efficiency. This effect reduced with increasing temperature so that at 1490 °C MTS concentration had virtually no effect on deposition efficiency. An explanation for these observations is as follows: at low temperatures, the reaction rate is low enough for a portion of the MTS to escape the particle bed before it has reacted. In this case, increasing the MTS concentration only allows more MTS to escape so reducing the efficiency. Increasing the temperature will result in an increase in the reaction rate, resulting in less MTS escaping the particle bed. This will result in higher deposition efficiency. At sufficiently high temperatures, all the MTS can react within the particle bed; in this case increasing the MTS concentration will have virtually no effect on the deposition efficiency. Under conditions where the MTS is fully depleted in the bed deposition efficiency will be high, reducing the extent of depletion will reduce the deposition efficiency. The exact combination of deposition temperature and MTS concentration resulting in complete depletion will depend on the particle bed depth. The above finding contradicts the findings of Voice [175] and Stinton and Lackey [166].

Similarly to the findings of Gulden [161], it was found that deposition efficiency increased with increasing load size. This effect was more pronounced for deposition at low (1350 °C) temperatures than at high (1550 °C) temperatures. This may be explained by considering that the deposition rate will increase at higher temperatures resulting in a higher amount of deposition in the lower portions of the bed of particles.

The impact of bed depth (equivalent to load) on deposition efficiency has implications for the design of coaters; to improve deposition efficiency it would be best to use a deep bed. For a fixed coater capacity deposition efficiency will depend, up to a limit, on the length:diameter ratio of the tube. Increasing the depth of the bed beyond the point where the gas flow is fully depleted will obviously have no further impact on deposition efficiency. In making this choice it must also be borne in mind that other factors, such as coating uniformity, will come into play. Although it is economically advantageous to have high deposition efficiency, for TRISO particles quality of the coating will override other considerations.

13.2 PHYSICAL PROPERTIES

13.2.1 DENSITY

Measured density ranged between 2.977 g.cm^{-3} (92.5 % theoretical) to 3.207 g.cm^{-3} (99.7 % theoretical). For most test runs the density was significantly below 3.217 g.cm^{-3} , this is to be expected as many of the test runs were not close to optimal deposition conditions. Density was found to be dependent on deposition temperature, MTS flux and type of gas inlet used.

Only in the case of the hot gas inlet system was the density found to reach a maximum value with increasing temperature and decrease with a further increase in temperature. Federer [161] and Voice [175] reported that density reached a maximum value at a deposition temperature of $1650 \text{ }^\circ\text{C}$ and $1575 \text{ }^\circ\text{C}$ respectively. These values are above the maximum temperature used for the current tests; this may explain why the cold inlet (as used by other researchers) did not show a maximum. The hot inlet behaved similarly to a cold inlet operating at a higher temperature. This may explain why a maximum density was seen when using the hot inlet but not with the cold inlet. On average the hot inlet resulted in densities 0.023 g.cm^{-3} higher than when the cold inlet was used.

It should be noted that comparison of results between different coater designs is not easy. Differences in the method used to measure the temperature (e.g. pyrometer or thermocouple), difference in measurement position (e.g. side of coater tube, base of tube, particle bed) as well as the detail design of the gas inlet will all impact on the actual temperature, and temperature variation, of the particle bed. These difficulties may in part explain differences in reported results.

The deposition of silicon together with silicon carbide at low deposition temperatures has been reported by several researchers. This has been used to explain the decrease in density of deposits formed as the deposition temperature is reduced. Assuming the deposit is a mixture of full density silicon carbide and silicon it would require a mass fraction of 18 % silicon to reduce the deposit density from 3.217 g.cm^{-3} to 3.000 g.cm^{-3} , the approximate minimum density measured in this study. Such a high level of free silicon should have been reliably detected. In this study significant amounts of silicon were not found in deposits formed above $1200 \text{ }^\circ\text{C}$. Therefore free silicon cannot be the cause of the reduction in density seen when the deposition temperature is reduced below $1500 \text{ }^\circ\text{C}$. A reduction in density to 3.000 g.cm^{-3} can be explained by a porosity mass fraction of 0.002 %. This equated to a porosity volume fraction of 6.7 %. For this calculation a gas density of 0.001 g.cm^{-3} was assumed. Actual density of the gas in the pores will have little impact on the density of the deposit at low levels of porosity.

The hypothesis that the decrease in density at low deposition temperatures is due to an increase in porosity is not supported by porosity measurements reported by Kim et al [162]. They reported a constant porosity of approximately 0.4 % for deposition temperatures between $1400 \text{ }^\circ\text{C}$ and $1500 \text{ }^\circ\text{C}$. In their study porosity was measured on SEM images, pores smaller than the resolution of the SEM images would have been missed. Kim did present data showing that the deposit composition remained stoichiometric for deposition temperatures between $1400 \text{ }^\circ\text{C}$ and $1550 \text{ }^\circ\text{C}$.

This supports the hypothesis that low density of deposits formed in this temperature range is not due to the deposition of free silicon. Using X-ray techniques Voice [175] estimated 3 % porosity in a low temperature deposit. Pore size was estimated to be 17.9 nm. López-Honorato et al [47] presented images in which nano-scale pores could be seen on grain boundaries and circumferential bands in addition to bands of micron scale pores. Obviously a large number of these nano-pores would be required in order to have a significant impact on the deposit density.

13.2.2 GRAIN SIZE

Measurement of the surface grain size of the domed structures formed at low deposition temperatures is considered to be of little value as the size of these structures does not reflect the actual size of grains or crystallites. For situations where faceted grains could be identified it was found that grain size increased with increasing temperature and decreasing MTS flux. Gas inlet type had a strong effect with the hot inlet resulting in a larger grain size than the cold inlet. Measured surface grain size ranged between 1.8 μm to 3.7 μm for the hot inlet and 2.1 μm to 2.5 μm for the cold inlet.

When grain size was measured on deposit cross sections, average grain size varied between approximately 1.5 μm and 2.3 μm . Grains were found to be elongated in the radial direction. The length/width ratio depended on the average grain size, varying from 1.2 for small grains to 1.8 for the largest grains. In both the radial and tangential direction the size distribution was approximately log normal, some of the grains being significantly larger than the average.

Crystallite sizes, as measured by XRD, were considerably smaller than the grains sizes measured by the line intercept method used to determine the grain sizes mentioned above. Similarly to surface grain size, crystallite size was found to depend on deposition temperature, MTS flux and inlet type. Crystallite size ranged from 12 nm to 112 nm. Obviously the micron scale grains measured using the line intercept method must consist of a large number of smaller crystallites.

XRD crystallite size did correlate to average grain size measured on backscatter electron SEM images with grain size increasing approximately linearly with increasing crystallite size. There was however considerable scatter in the data, the correlation coefficient being 0.64.

Although not a direct measure of grain size Raman spectroscopy is sensitive to grain size. Under deposition conditions resulting in small crystallite sizes, as measured by XRD, the position of the Raman TO and LO peaks was shifted to lower wave numbers. This effect was found to be stronger for the LO peak than for the TO peak. Similarly to XRD crystallite size measurement the position of the Raman LO peak was found to be sensitive to deposition temperature and MTS concentration. The Raman peak position was however not sensitive to gas inlet type. It was found that at high deposition temperatures the position of both the TO and LO peaks asymptotically approached 796 cm^{-1} and 972 cm^{-1} respectively. At low deposition temperatures the peak positions were more sensitive to deposition temperature.

13.2.3 MICROSTRUCTURE AND MORPHOLOGY

Changes in the surface morphology with changing process conditions were found to be similar to those reported in the literature with a transition from a botryoidal structure to a faceted structure with increasing deposition temperature and, at sufficiently high temperatures, a decrease in MTS flux. Hydrogen flux was found to have little effect on the surface structure.

Changes in the surface structure reflected changes in the microstructure of the deposits. Botryoidal surface structures were associated with deposits with a very fine grain size, often too fine to be distinguishable at $2000\times$ magnification. These structures often appeared to be striated when viewed using backscattered electron imaging. They were also readily attacked by Murakami reagent leaving a very clearly striated structure. The etch solution selectively attacked specific layers within these deposit while leaving other layers relatively intact. Layers which were rapidly attacked may have been microcrystalline or amorphous resulting in a lower etch resistance. Another possibility is that the bands that etched away rapidly were more porous than the surrounding layers. Voice [175] contended that the striations were more porous and had a higher silicon content than the surrounding areas. He found that heat treatment of low temperature deposits at $2100\text{ }^{\circ}\text{C}$ resulted in rapid grain growth, development of macro-porosity and segregation of elemental silicon. The first two of these findings is consistent with microcrystalline deposits which have significant micro-porosity. These striated structures have been shown to perform poorly when used in TRISO applications, this may be related to the presence of porosity.

Increasing deposition temperature resulted in the deposit becoming more crystalline. The striated structure initially changed to a structure consisting of bands of fine grains separated by thin bands of porosity, to small evenly distributed grains and finally large orientated grains. The bands of porosity appeared to follow lines parallel to the surface of the deposit which still had a rounded structure. In this respect the lines of porosity appeared almost as remnants of striations. At intermediate temperatures the surface of the deposit changed to clusters of fine grains, these became more faceted as temperature increased and MTS flux was reduced. The outline of the clusters resembled the shape of the rounded domes seen at lower deposition temperatures. In the case of the hot inlet a deposition temperature of $1400\text{ }^{\circ}\text{C}$ and an MTS concentration of 0.5 % resulted in a deposit with no indication of striations, intermediate sized grains and little porosity. This type of structure is regarded as the ideal for TRISO applications.

Increasing grain size resulted in an increasingly faceted surface structure. In the case of the largest grains the surface was made up of clearly distinguishable, faceted grains. Twins could easily be identified lending support to the claims that growth is by a twin plane re-entrant edge (TPRE) mechanism. These large grains were elongated with the long axis in a radial direction. The length of the largest grains often crossed a significant portion of the deposit thickness. In TRISO applications these through layer grains are regarded as undesirable [24] and should be avoided.

Comparison of the XRD crystallite size to the surface structure size did not show any clear correlation. Neither the “domed” nor the “faceted” structure size correlated to crystallite size. There was however a correlation between the crystallite size and the type of structure; “domes” always consisted of crystallites smaller than approximately 40 nm while “faceted” structures always consisted of crystallites larger than about 80 nm. Structures classified as “clusters” fell into the 40 nm to 80 nm size range and showed a general trend of decreasing size as the XRD crystallite size increased.

Comparing the results obtained using the hot and cold inlets it appeared as if the only difference was that the hot inlet effectively operated at a higher temperature for the same deposition temperature set point. As a result, the hot inlet system produced larger crystallites and grains at each deposition temperature. The differences in microstructure for similar operating condition, but different gas inlet types, has significant implications for the transfer of operations between different coater designs. Obviously each coater design would need to be characterised so as to enable a specific microstructure to be produced rather than a fixed coating recipe being transferred between coater types.

13.2.4 PHASE COMPOSITION

X-ray diffraction results indicated that the silicon carbide consisted exclusively of cubic β -SiC. This finding was supported by Raman spectroscopy for deposits formed above 1400 °C. At lower temperatures there is a possibility that some of the silicon carbide was amorphous, although there is some ambiguity as to whether amorphous silicon carbide or amorphous silicon formed. The fact that very little silicon was detected using microprobe analysis lends support to the view that amorphous silicon carbide was formed.

Several researchers, for example [137][151], reported detecting α -SiC using XRD techniques. It is likely that the peak assigned to α -SiC is in fact due to disordered β -SiC. In this study no α -SiC was detected using either XRD or Raman spectroscopy.

Although it is assumed that reports of α -SiC being detected in β -SiC CVD deposits using XRD are due to mistaken interpretation of peaks, it is possible that the deposits do contain small amounts of α -SiC. This has been confirmed by SAED studies [170][169] leaving no doubt as to the presence of α -SiC. The amounts present is however very small.

13.2.5 DISORDER

Using XRD analysis disordered silicon carbide was indicated by the presence of a shoulder on the (111) peak. The degree of disorder was quantified by considering the ratio of peak heights of the disordered phase relative to the (111) peak height. It was found that the degree of disorder decreased exponentially with increasing deposition temperature. MTS flux, hydrogen flow and inlet type were found to have no influence on the level of disorder.

Assessment of the degree of disorder by the separation of the silicon carbide (111) and (200) XRD peaks did not yield significant results. It was found that MTS and hydrogen flux had no significant influence. The influence of temperature was more difficult to assess. At temperatures above 1300 °C there is a weak effect with separation between the peaks decreasing with increasing temperature. Below 1300 °C the data is too scattered to draw any conclusion. Due to the very clear effect seen by comparing the height of the “disorder peak” to the height of the (111) peak this technique was not pursued further.

In the literature, disorder in silicon carbide has been identified using both electron diffraction [170][169][156] and Raman spectroscopy [156]. Stacking faults are also visible in most TEM images of TRISO silicon carbide presented in the literature. López-Honorato [156] found that stacking faults, expressed as a fraction hexagonal structure, in TRISO silicon carbide increased as MTS volume fraction increased from 0.36 % to 9.1 %. This contrasts with the findings of this study which indicated that MTS concentration had no significant effect, albeit over a MTS concentration range of only 0.5 % to 2.5 %.

13.2.6 LATTICE PARAMETERS

It was found that the lattice constant of the β -SiC deposit is dependent on deposition temperature, MTS and hydrogen flux. Inlet type was found to have no significant influence. Deposition temperature was found to be the most significant factor. From measured lattice parameters and reported lattice parameters, strain was calculated to vary between -2.065×10^{-4} compressive and 3.671×10^{-4} tensile strain.

13.3 ELEMENTAL COMPOSITION

Microprobe analysis showed that for deposition temperatures above approximately 1310 °C no free silicon was deposited. Lower deposition temperatures resulted in increasing excess silicon as the deposition temperature decreased. Tests carried out using the hot inlet resulted in a lower free silicon content than those using the cold inlet. This trend is in general agreement with previously reported ([92], [156], [158], [159], [160], [170],) results however the minimum deposition temperature required to ensure no free silicon is lower than previously reported.

In this study there was considerable variation in the silicon content of deposits formed at 1200 °C. A possible explanation for this is the fact that the free silicon

may not be uniformly distributed within the silicon carbide. De Villiers et al [170] reported layers of free silicon within TRISO coated particles when the layer cross section was viewed using backscattered electron imaging. For the same samples microprobe analysis could not detect any excess silicon. The non-uniform distribution of the silicon could contribute to a large standard deviation in measured silicon values. The fact that excess silicon was not detected by the microprobe calls into doubt the suitability of this technique for analysis of silicon carbide deposits.

XRD analysis and Raman spectroscopy confirmed the general trends noted in the previous paragraph: decreasing deposition temperature results in more free silicon and the hot inlet results in lower free silicon than the cold inlet. Raman spectroscopy appears to be more sensitive than either XRD or microprobe measurements, being able to detect free silicon at higher deposition temperatures. Unfortunately Raman spectroscopy could not quantitatively determine the free silicon content of the samples. Raman spectroscopy may also be susceptible to a non-uniform distribution of free silicon as the volume sampled is relatively small with a spot size of approximately 2 μm .

13.4 MECHANICAL PROPERTIES

13.4.1 CRUSH LOAD

Crush load was found to be highly dependent on the test method used. Testing with hard anvils resulted in a crush load significantly less than when soft anvils were used. When hard anvils were used it was also found that the difference between the test runs was significantly less. This was clearly seen when different batches of starting material were tested using the two methods. No difference between the batches could be seen when hard anvils were used whereas with soft anvils the two batches were clearly different. The differences between the soft and hard anvil is due to the difference in the stress distribution during crushing. In the case of hard anvils fracture takes place close to the point of contact. Use of soft anvils shifts the point of maximum stress away from the point of contact towards the particles equator resulting in tensile failure of a larger volume of material [271].

When using soft anvils it was found that there is a large difference in crush load between the two lots of starting material used. This difference was not apparent when hard anvils were used. The reason for the difference in crush strength between CPT-T-G130 and CPT-T-G140 is uncertain, it may however be related to the density of the inner pyrocarbon layer. Unfortunately, the inner pyrocarbon density of CPT-T-G130 was not measured. The estimated density of CPT-T-G130 is 2.08 $\text{g}\cdot\text{cm}^{-3}$ compared to the measured density of 1.58 $\text{g}\cdot\text{cm}^{-3}$ for CPT-T-G140. The estimated density of CPT-T-G130 is based on particle mass, particle size, thickness and density of the buffer and the thickness of the inner pyrocarbon layer. There may be considerable error in this estimate, but a higher density of the pyrocarbon layer could explain the higher crush strength of the CPT-T-G130 particles.

It was found that the crush load of coated particles was dependent on the starting material used. A higher crush strength starting material resulted in higher strength

coated particles. Surprisingly, the crush load of coated particles was in most cases lower than for the non-coated particles. When soft anvils were used the coating needed to be at least 43 μm thick to achieve the same strength as uncoated starting material. This is thicker than the upper specification limit for most TRISO silicon carbide coatings. In the case of hard anvils the silicon carbide layer would need to be about 87 μm before a strength equivalent to carbon coated particles was achieved. The reduction in strength is most likely due to the brittle nature of the silicon carbide coating. Relatively small deformation of the particle will result in cracking of the silicon carbide; these cracks can then propagate through the pyrocarbon coating resulting in failure. Stinton et al [270] reported a similar reduction in strength of silicon carbide coated particles.

In order to assess the material properties the crush load of the particles was normalised to an equivalent thickness of 35 μm . Specific test runs (TT1 to TT5), all coated using the same conditions, were run to determine the impact of silicon carbide layer thickness. It was however found that the crush load/thickness relationship of the different test groups (CR, HF and TT) were not consistent, so each test group was normalised using data specific to that group. For the normalised data it was found that only deposition temperature had any statistically significant influence on crush load.

Crush load of the carbon coated starting material as well as the silicon carbide coated particles was found to be highly variable, especially when soft anvils were used. In the case of silicon carbide coated particles the within lot standard deviation of the crush load was significantly lower than for the uncoated particles. This may reflect a difference in failure mechanism as previously discussed. In addition to the within lot variation there was also considerable lot to lot variation. Due to the within lot variation the use of crush testing as a quality control test would require large samples. Even then there would still be uncertainty due to lot-to-lot variation. Due to the considerable uncertainty it is unlikely that crush testing would be of much value as a quality control test despite its attractiveness due to its relative simplicity. Crush testing would only be able to detect gross errors.

The increase in crush load at low deposition temperatures is not reflected by any significant changes in Vickers hardness or in fracture toughness. Nano-indentation hardness decreased over the temperature range where crush load increased.

13.4.2 HARDNESS

Vickers hardness values ranged between 23 GPa and 30 GPa. This is within the range of Vickers hardness values for silicon carbide reported in the literature. None of the process variables were found to have a significant effect on Vickers hardness. Despite this there were statistically significant, albeit small, differences between the two types of inlet. On average the hot inlet resulted in a 1 GPa higher hardness than the cold inlet. In most situations differences between the two types of inlet could be attributed to differences in particle and gas temperature. This can only apply when the property being measured is sensitive to temperature. In the case of Vickers hardness this is not the situation. One possible explanation is that gas entering the particle bed may be slightly different in composition due to deposition in the gas

feed tube. This would result in the feed gas containing some HCl and other reaction products which may impact hardness. If this was the case, it would be expected that there would be some other characteristics, such as grain structure or composition, which would also be affected.

In the case of the cold gas inlet a single test run (MTS1) had a hardness which may be low compared to other values in the normal distribution. This test run was the only one which had a significant amount (mass fraction: 6.8 %) of free silicon. Large amounts of free silicon have been shown to reduce deposit hardness (for example [158]).

Nano-indentation hardness values ranged between 30.6 GPa and 36.8 GPa. This is within the range reported in the literature. Unlike Vickers hardness, inlet type was found to have no statistically significant influence on nano-hardness. Deposition temperature was found to have a significant influence on hardness. Nano-hardness increased from approximately 32 GPa to 35 GPa as deposition temperature increased from 1250 °C to 1550 °C. MTS and hydrogen flux were found to have no influence on nano-hardness.

The mechanisms underlying the change in hardness with temperature are uncertain. Several material properties, such as crystallite size, grain size, residual stress and composition have been shown to be impacted by deposition temperature; changes in hardness could be impacted by these properties. None of these factors have a response to temperature that correlates to the response of hardness to temperature. For example, grain size and crystallite size both increase with increasing deposition temperature. It would be expected that this would result in a reduction in hardness with increasing deposition temperature. Also, the free silicon content increases as the deposition temperature is reduced below 1300 °C; it would therefore be expected that nano-hardness would decrease to the hardness of silicon as temperature decreased and not reach a minimum level of 32 GPa.

13.4.3 YOUNG'S MODULUS

Young's modulus values measured by nano-indentation were considerably below the values reported in the literature for nano-indentation as well as other methods. There is some question as to the validity of the measurements. The fact that the values are lower than expected, and there was a significant difference between the two gas inlet types but no other dependence on process conditions raises serious concerns. As all samples for each of the gas inlet types were mounted into a single sample mount it is feasible that the observed differences in Young's modulus are in fact due to the sample mount. Without further experimental tests to confirm the results and investigate whether the sample mount had any influence the current results will have to be treated with considerable reservation.

It was expected that there would be at least some correlation between Young's modulus and process parameters. It is known for example that porosity, or a second phase such as silicon, influences Young's modulus of a material. For silicon carbide it has been shown that porosity will result in a reduction of Young's modulus [49]. In the present study it was shown that density is influenced by process condition,

either due to porosity or free silicon. This effect is however not reflected in any change in Young's modulus measurements placing further doubt on the results obtained.

13.4.4 FRACTURE TOUGHNESS

Vickers indentation cracking was shown to be highly dependent on deposit thickness. Below a thickness of 40 μm the length of tangential cracks increased as the layer thickness was decreased. For radial cracks deposit thickness had virtually no influence on the crack length. The influence of deposit thickness was also clearly seen when considering the fraction of indents that were acceptable. If the deposit was thicker than 40 μm close to 100 % of indents were regarded as acceptable, below 40 μm the fraction of acceptable indents decreased linearly with decreasing deposit thickness. When the deposit thickness was below 25 μm all indents were regarded as unacceptable.

Radial crack length was found to be sensitive to deposition temperature, increasing linearly as deposition temperature increased. MTS flux or hydrogen flux was found to have no influence on radial crack length. There was considerable variation in the length of the radial cracks resulting a poor fit to the model. Only approximately 37 % of the variation could be explained by the model.

In addition to deposit thickness, tangential crack length was found to increase with increasing deposition temperature and decreasing MTS flux. In this case the impact of random variation was much less than for radial cracks, 85 % of the variation being explained by the model.

Conventionally a low MTS concentration and high (within the temperature range investigated in this study) deposition temperature would be selected for coating TRISO particles. This choice is primarily driven by fission product release through intact coatings. From fracture toughness consideration the optimal conditions would be low deposition temperature and high MTS flux. Reports in the literature indicate that pressure vessel failure is not a major failure mechanism of TRISO coated particles whereas release of fission products from intact particles is a serious concern, especially at high temperatures. It is therefore understandable that TRISO particles are coated at high deposition temperatures and low MTS flux, conditions selected for low fission product release rather than high mechanical strength. For non TRISO applications, where mechanical properties may be the primary consideration, the choice of process operating conditions may be different to the optimum for coating TRISO particles.

The equations devised by Liang, Anstis as well as Evans and Davis were used to calculate fracture toughness. Nano-indentation hardness and Young's modulus values were used for all the fracture toughness calculations. For calculating the fracture toughness in the tangential direction the crack lengths were recalculated to eliminate the effect of deposit thickness. There was good agreement between the fracture toughness values predicted by the Liang and Anstis equations. The

Evans-Davis equation resulted in fracture toughness values significantly higher than both the Liang and Anstis equations.

Despite doubts as to the accuracy of the Young's modulus values determined by nano-indentation, these were the only estimates of actual Young's modulus of the deposits available. The low Young's modulus values would have contributed to the low fracture toughness values determined in this study. However, in all the equations used the fracture toughness is proportional to $E^{0.4}$. Large changes in Young's modulus would be required to significantly impact the calculated fracture toughness values.

Fracture toughness was found to be similar in the radial and tangential directions. This may appear somewhat surprising at first as there were distinct differences in crack lengths in the two directions. Two factors should be considered. Firstly; for tangential cracks, crack lengths were corrected to remove the impact of layer thickness. This eliminated much of the difference between the crack lengths in the radial and tangential direction. Secondly; in all the equations used to calculate fracture toughness the dependence on crack length is not very strong. For example, in the Anstis equations fracture toughness is proportional to $c^{-1.5}$, where c is the crack length measured from the centre of the indent. Although it is not as obvious to see from the Liang equation the response of the Liang equation to changes in c is very similar. The Evans-Davis equation is less sensitive to changes in crack length than the Anstis and Liang equations. Large changes in crack length are therefore required to have significant effects on calculated fracture toughness.

Eliminating the effect of layer thickness on the length of the tangential cracks was necessary to ensure that the material properties, and not the layer thickness, was being assessed. This also allowed for a comparison of the properties in the radial and tangential directions. It may be argued that normalising the crack lengths masked a real difference in fracture toughness between the radial and tangential directions, however from Figure 73 it can be seen that layer thickness largely determines the tangential crack length. This effect must be eliminated to assess intrinsic material properties. The validity of this approach is supported by the fact that when the layer thickness is more than 40 μm radial and tangential crack lengths are very similar (see Figure 73).

Deposition temperature was found to be the only process parameter that had any significant influence on the fracture toughness. This is most strongly seen in the fracture toughness values calculated using the Anstis equation where fracture toughness changed from an average value of 2.8 $\text{MPa}\cdot\text{m}^{0.5}$ to 1.8 $\text{MPa}\cdot\text{m}^{0.5}$ as deposition temperature changed from 1250 $^{\circ}\text{C}$ to 1550 $^{\circ}\text{C}$. In the case of the Liang and Evans-Davis equations the influence of deposition temperature is sufficiently weak to cast doubts on the actual effect of deposition temperature on fracture toughness.

Comparing the results obtained in this study to fracture toughness values listed in Table 13 it can be seen that results of this study are similar to, but slightly lower than, published results. Measurements performed by Zhao et al [252] using a notched microbeam showed a clear difference in fracture toughness between the radial and tangential direction. Values measured in the radial direction were

significantly higher than values measured in this study ($6.72 \text{ MPa}\cdot\text{m}^{0.5}$ versus $2.09 \text{ MPa}\cdot\text{m}^{0.5}$ to $2.80 \text{ MPa}\cdot\text{m}^{0.5}$) and reported in the literature. For tangential cracks Zhao et al [252] obtained a fracture toughness of $3.47 \text{ MPa}\cdot\text{m}^{0.5}$ compared to $2.19 \text{ MPa}\cdot\text{m}^{0.5}$ to $2.83 \text{ MPa}\cdot\text{m}^{0.5}$ measured in this study. Zhan et al [255] used Vickers indentation cracking to measure fracture toughness of TRISO silicon carbide for longitudinal cracks originating from indents made on the outside of the particles. Crack lengths measured in this way were between those measured in the radial and tangential direction. For pure silicon carbide fracture toughness values of $3.51 \text{ MPa}\cdot\text{m}^{0.5}$ were measured. It should be noted that as Zhan et al [255] used data from Zhao et al [252] to calibrate their measurements it would be expected that these studies would yield similar results. Cockeram [254] found that fracture toughness of bulk CVD silicon carbide was not dependant on fracture direction relative to growth direction but that different test methods gave different results. For chevron notch bar measurements the average K_{IC} value was $3.658 \text{ MPa}\cdot\text{m}^{0.5}$ while for Surface Crack in Flexure tests the average K_{IC} value was $4.824 \text{ MPa}\cdot\text{m}^{0.5}$.

13.5 IMPACT OF INLET TYPE

A unique feature of this study was the investigation of the impact of gas inlet design. A conventional cooled inlet was compared to an inlet without any cooling. In the case of the hot gas inlet, two effects are important: Firstly, the most obvious effect is that the gas entering the particle bed is considerably hotter than in the case of the cooled inlet. This resulted in less cooling of the particles in the spout and a more uniform temperature distribution in the particle bed. Secondly, deposits formed in the gas feed tube below the gas inlet. Microscopic examination of the deposits revealed 2 phases, most likely silicon carbide together with elemental silicon. As a result of the reactions in the gas feed tube the composition of the gas would have changed; MTS concentration would be reduced, HCl concentration increased and the C:Si ratio increased (assuming free silicon was deposited). It can be expected that these changes in the feed gas would have influenced the microstructure and composition of the deposits.

Details of the impact of the hot inlet were discussed in the previous sections. These effects are briefly summarised as follows:

1. Deposition efficiency: Use of the hot inlet results in lower deposition efficiency. The predicted maximum efficiency for the hot inlet is 98.5 % compared to for the cold 99.5 % inlet.
2. Density: Density values obtained using the hot inlet were $2.307 \times 10^{-2} \text{ g}\cdot\text{cm}^{-3}$ higher than when the cold inlet was used. It was also noted that when a hot inlet was used the density reached a maximum value at a deposition temperature of $1450 \text{ }^\circ\text{C}$. No maximum value was reached for the cold inlet using the deposition temperatures investigated in this study.
3. Grain size and structure: For the hot inlet, the temperature at which faceted surface structure formed was lower than for the cold inlet. In addition, for a particular deposition temperature, the sizes of the faceted grains were larger when a hot inlet was used. When viewed in cross section the grains formed using the hot inlet were larger than when a cold inlet was used.

4. Crystallite size: Use of the hot inlet resulted in a larger crystallite size. This effect was more pronounced at high deposition temperatures.
5. Raman peak intensity: the intensity of both the LO and TO peak increased while the intensity of the silicon peak reduced when the hot inlet was used. In cases where no distinct silicon peak was detected the background value in the region of 520 cm^{-1} decreased when a hot gas inlet was used.
6. Hardness: Vickers hardness increased by 1.027 GPa when a hot inlet was used. In contrast, nano-hardness was not impacted by inlet type.
7. Young's modulus: Although the results indicate that the hot inlet resulted in a lower Young's modulus there is considerable doubt as to the significance of these differences.

Considering the impact of the gas inlet design seen in this study at least some of the differences in the reported literature may be explained. Few researchers have reported sufficient details of the gas inlet systems used to enable an effective comparison. Lackey et al [270] compared the crush strength of particles coated using a conical inlet compared to those coated using a porous frit inlet. It was noted that the crush strength of TRISO coated particles coated using the conical inlet were more sensitive to annealing than particles coated using the frit. Stinton and Lackey [166] found that use of the frit inlet resulted in higher silicon carbide density at high deposition rates. From the results of this study, and the work of Lackey et al [270] and Stinton and Lackey [166], it is apparent that gas inlet conditions are important. It is however uncertain how sensitive the coating process is to inlet design.

Use of a hot inlet did result in several operational problems. The original gas inlet design used a 3 mm or 6 mm diameter inlet port, was longer and larger in diameter. These inlets rapidly blocked due to the deposition of silicon carbide in the inlet. This was especially true for the 3 mm inlet. These problems were reduced by using a shorter, smaller diameter inlet with a 6 mm port. The modified design allowed for a single run to be completed without the inlet blocking. It is likely that the build up of silicon carbide in the inlet port influenced the gas flow patterns in the particle bed.

The importance of gas flow patterns may be seen by the complexity of the gas inlets used in large scale coaters. Multiple inlet ports of different sizes and orientation are typically used in large coaters. An example of this may be seen in [214] where multiple inlet ports are used. López-Honorato et al [156] have also noted that multiport gas inlets resulted in improved particle sphericity.

In the design of large commercial coaters two important aspects to consider are the uniformity of the coating and selection of the coating process to achieve the required pyrocarbon and silicon carbide properties. Coating uniformity will be influenced by particle and gas flow patterns which are determined by the design of the coater. Detailed design of the coater will also impact the deposition process by influencing inlet gas temperature, heat transfer rates, gas/particle contact time etc. Results of this study have highlighted the fact that careful characterisation of the combination of coating process and coater will be required to develop a process that can reliably produce the required coatings. It is unlikely that a coating process will be transferable between different coater designs.

14 CONCLUSIONS

Models have been developed allowing for accurate prediction of deposition rate and deposition efficiency of a fluidised bed chemical vapour deposition process. It was found that deposition rate was largely governed by MTS flux but that deposition temperature and hydrogen flux also played a role. Deposition rate was found to be directly proportional to MTS flux allowing for a very simple means of controlling the deposition rate. Deposition temperature and, to a lesser extent, MTS concentration were also found to determine the properties of the silicon carbide. Hydrogen flow rate was found to have a significantly smaller impact on the properties of the deposit. While deposition rate and deposition efficiency are both important when considering the economics of TRISO particle manufacturing these factors are significantly less important than the properties of the silicon carbide and controllability of the deposition process.

The dependence of material properties on process parameters was determined for density, grain size, crush strength, hardness, Young's modulus, fracture toughness, elemental composition and crystallographic characteristics such as crystallite size, lattice parameters and degree of disorder. It was found that deposition temperature is the most critical of the process parameters considered, influencing all the properties that were dependent on process conditions. This has considerable implication for the design and operation of spouted bed coaters in that the temperature must be accurately controlled in order to ensure consistent deposit properties. As the measured temperature and temperature uniformity of a coater depends on the coater design optimal operating condition will also be design dependent. Factors such as temperature measurement position and gas flow patterns may have a considerable effect on the properties of the deposits obtained in a particular coater.

Density was found to be dependent on deposition temperature, MTS concentration and gas inlet type. To obtain a maximum density high deposition temperature and low MTS concentration should be used. Using a non-cooled gas inlet system also resulted in increased density for a particular deposition temperature. The impact of deposition temperatures above 1550 °C is uncertain. Based on published data it was assumed that higher temperatures would result in a decreasing density due to increasing levels of porosity. In the current study there is however no evidence to support this. SEM imaging of deposits formed at 1550 °C did not reveal significant porosity in the deposit. In the published literature it is often stated that the decrease in density with decreasing deposition temperature is due to the deposition of free silicon together with the silicon carbide. This is not supported by results obtained in this study. An alternative explanation for the decreasing density is that the deposits become more porous as deposition temperature decreases.

The differences in free silicon content between this study and those reported in the literature for low temperature deposition are most likely related to the temperature distribution within the coater. Coating properties will be dependent on the actual temperature of the particles and gas; this may differ considerably from the coater set point temperature. Another aspect that may play a role is the movement and circulation rate of the particles within the coater. This will depend on the detail design of the coater tube and gas inlet system. As most coaters are operated with a

high level of precursor depletion it is unlikely that depletion effects are responsible for the differences in free silicon content.

Secondary electron SEM images of the deposit surface revealed a change in morphology with changing deposition temperature, MTS concentration and gas inlet type. It was found that the surface structure correlated with the cross sectional structure viewed using backscattered electron imaging. Deposits consisting of well formed grains that did not have any striations had a surface a structure that consisted of faceted grain. Surface structures consisting of rounded domes correlated to striated deposits formed at lower deposition temperature or high MTS concentrations. The correlation between surface morphology and grain structure may allow for a convenient means of assessing the deposit structure without the need for preparation of polished cross sections. This may be particularly important in a production environment.

This is the first systematic study of the impact of process parameters on particle crush strength measured using soft anvils. It was shown that there is a considerable difference in crush strength depending on the measurement techniques. Soft anvils resulted in considerably higher crush strength than when hard anvils were used. Results obtained using soft anvils were also shown to be sensitive to processing conditions whereas hard anvils showed little response to process conditions. For investigating the impact of process conditions, crush tests using soft anvils have a definite advantage in that the test appears to be more sensitive to material properties.

Crush tests using soft anvils highlighted the fact that the particle crush strength is dependent on the strength of the pyrocarbon coated kernel. Unless the strength of the underlying pyrocarbon is controlled crush testing will be of little value in studying the properties of the silicon carbide. In the current study the majority of the tests were performed with the same batch of starting material. This allowed for the elimination of pyrocarbon properties as a variable. Due to the sensitivity of the particle crush strength on the properties of both the pyrocarbon and silicon carbide layer this is not an effective test for investigation the properties of the silicon carbide layer in situations where the pyrocarbon properties are variable. Crush testing may however be a convenient quality control measure to test complete coated particle where the properties of the pyrocarbon and silicon carbide are measured together. The considerable variation in crush strength of the inner pyrocarbon layers will however make this a very insensitive test only suitable for detecting gross errors.

It was found that the crush strength of the particles decreased when silicon carbide was deposited onto pyrocarbon coated kernels. A silicon carbide layer considerably thicker than the standard thickness of 35 μm was required for the particle crush strength to match that of the pyrocarbon coated particle. This result highlighted the brittle nature of the silicon carbide and resulting risk of damage to the silicon carbide layer during coating and manufacture of fuel elements. Of particular concern is the potential for damage to the particles during the silicon carbide coating step where a thin, partially formed, silicon carbide layer may be damaged due to energetic spouting.

Crush strength was found to be insensitive to MTS concentration and hydrogen flow rate. Deposition temperatures below 1300 $^{\circ}\text{C}$ resulted in an increase in particle crush

strength. This finding is of little practical importance for coating of TRISO particles as other properties, such as density, are degraded at low deposition temperatures. For deposition temperatures above 1300 °C crush strength was not dependent on process conditions. As expected crush strength was found to be sensitive to layer thickness. Under typical process conditions increasing layer thickness may be the only practical means of increasing the strength of TRISO particles.

Hardness was measured using Vickers indentation and a Berkovich indenter. In the case of the Vickers hardness only gas inlet type was found to have any impact on the deposit hardness. Nano-indentation was found to be dependent on only deposition temperature. The lack of sensitivity of hardness measurements means that hardness testing will be of little value in evaluating deposits in either a production or research context.

Although not the first study to use indentation cracking to determine the fracture toughness of TRISO silicon carbide (a paper was published in 2012 [255]), this was the first systematic study to apply indentation cracking to investigate the impact of a variety of process parameters. Several important factors came to light. It was found that silicon carbide layer thickness was the most important factor in determining tangential crack length. Radial crack lengths were found to be independent of deposit thickness. Using a 100 g load, a minimum layer thickness of approximately 45 μm is required to ensure that layer thickness does not influence crack length. For thinner layers, it is possible to recalculate the crack length to eliminate the effect of deposit thickness. This requires knowledge of the relationship between crack length and layer thickness. It was found that for the Liang, Anstis and Evans-Davis correlations fracture toughness was lower than typically reported in the literature.

Fracture toughness sensitivity to process variables was found to depend on the calculation method used, only the equation proposed by Anstis showing any dependence on process conditions. Only deposition temperature was found to have any influence on fracture toughness. Within the range of process conditions typically used for depositing TRISO silicon carbide it is not possible to improve the fracture toughness of the silicon carbide using process variables. If TRISO particles are to be used under conditions where pressure vessel failure becomes a significant risk the only available options to mitigate the risk would be to change the design of the particle, for example making use of a thicker silicon carbide layer or smaller diameter particle.

The value of this type of fracture toughness measurement is doubtful. The procedure is very time consuming, requiring careful sample preparation and a considerable amount of time to accurately measure the crack lengths. Due to the small size of the indents and cracks this is best done using a SEM. The results obtained are somewhat doubtful as there is considerable doubt as to the validity of the techniques. However, in the absence of any viable alternatives this is currently the only method available.

A surprising aspect of this study was the low free silicon content of the deposits. Previous studies have indicated that free silicon forms at deposition temperature below 1500 °C. Using XRD and microprobe analysis it was found that significant amounts free silicon were only deposited at temperatures below 1300 °C. Raman spectroscopy detected free silicon at 1300 °C but not at 1355 °C. The differences in

measured silicon content between various studies may be due to differences in actual particle temperature for a given temperature set point. As the majority of coaters are controlled using a thermocouple outside of the coater tube and do not directly measure the temperature of the particles it is likely that the actual particle temperature and control temperature may be significantly different. Actual particle temperature in the spout and fountain is expected to be lower than the control temperature due to the stream of relatively cold gas flowing through the particle bed. Particle temperature will depend on the exact design of the coater, especially the position where temperature is measured and the details of the gas inlet.

Raman spectroscopy proved to be a very useful technique for assessing the quality of the deposits, being capable of detecting low levels of silicon. Raman spectroscopy was also found to be sensitive to the crystallinity of the deposit. For the silicon carbide TO and LO Raman peaks the intensity and position of the peaks were sensitive to deposition conditions. Peak intensity followed a trend very similar to crystallite size as measured using XRD. Raman spectroscopy may provide a very convenient method of assessing the quality of coated TRISO particles. The method appears to be sensitive to both the composition, being able to detect low levels of free silicon, and microstructure of the deposit. Although not used in this study, it is also possible to use Raman spectroscopy without the need to mount and polish the particles. Eliminating the requirement for slow and destructive sample preparation could be a major benefit of Raman spectroscopy in a production environment.

XRD analysis of the deposit showed that β -SiC is the only silicon carbide phase deposited in detectable quantities. It was also shown that the crystallinity of the deposit increased with increasing deposition temperature. By analysing features of the XRD pattern associated with disordered structures it was possible to quantify the level of disorder in the deposit. Lattice constant and crystallite size of the β -SiC were also measured. Lattice parameters changed from a value less than the standard value to a value greater than the standard value as deposition temperature increased. This indicated a change from compressive to tensile strain with increasing deposition temperature. Crystallite size was found to be dependent on process conditions and type of gas inlet used. Increasing the deposition temperature, or making use of a non-cooled gas inlet, resulted in larger crystallites.

Etch response of the deposits varied significantly with differing process conditions. For deposits formed at low temperatures the layers within the deposit were readily attacked by Murakami reagent. Deposits formed at high temperatures were uniformly resistant to the reagent showing virtually no sign of attack. Etch resistance may prove to be a very quick and effective means to assess the quality of the deposit. Although the details of the etched structure require a SEM to be viewed it is possible to see whether the sample had been severely attacked under an optical microscope. Etching highlighted the striated structure of some of the deposits. Deposits formed at high temperatures had a uniform and low etch rate. The low etch resistance of layers within the striated structure indicate that these layers are somehow different to the more resistant layers, possibly containing porous or amorphous material. It is known that striated deposits perform poorly in TRISO applications. It was found that the most uniformly etch resistant deposits were formed at high temperatures, low MTS concentrations and high hydrogen flow rates.

Backscatter electron imaging of polished cross sections revealed the grain structure of the deposits. Striated deposits were also easily identifiable. High deposition temperature and low MTS concentration resulted in larger grains. There were also clear differences between the two gas inlets systems used with the non-cooled gas inlet resulting in larger grains. Under some conditions grains large enough to extend across the entire layer were formed. Such large grains are potentially undesirable. To ensure an optimal grain size deposition temperature and MTS concentration must be optimised for a particular coater design.

An aspect of this study not considered in previous studies was the impact of gas inlet temperature. This was assessed by making use of a conventional cooled gas inlet and an inlet that had no cooling. In most respects making use of a hot gas feed system had a similar effect to operating at a higher deposition temperature. The hot inlet system did suffer from numerous problems with blockage of the inlet port, a problem not experienced when using a cooled gas inlet. It is recommended that cooled inlets be used as the advantages of using a hot inlet are minimal while there are significant disadvantages. The use of the hot inlet did highlight the importance of the detail design of the gas inlet system. Even if using a cooled inlet, the temperature of the gas entering the particle bed will depend on the exact design of the inlet. This makes comparing the optimal operating conditions of various coaters difficult. The difficulty in comparing coater designs highlights the importance of being able to specify the process in terms of material properties rather than process parameters. This may be particularly important when characterising a new coater design where process conditions need to be selected to obtain specific material properties. This may reduce the time and cost of qualifying new designs.

For a number of the models developed there was a considerable variance in the properties measured. This may be due to actual variation in the material properties induced by uncontrolled process conditions or measurement error. Either of these sources of variation have a significant impact on the ability to control the process. This will have a serious effect on product quality in a production environment. The lack of control over some of the material properties counters the argument for specifying the product in terms of material properties. A more practical method of control may be to specify process parameters, such as deposition temperature and MTS concentration, which are easily measureable and controllable. Fortunately some of the key process outputs, such as deposition rate and silicon carbide density, can be effectively controlled allowing high quality silicon carbide to be deposited.

One possible source of process variation is the coater operating pressure. The eductor system used for gas cleaning reduced the pressure in the coater, the extent of which was not controlled nor measured. It is strongly suspected that variation in operating pressure was responsible for some of the difficulty in controlling the MTS feed rate. It is unknown what other impact operating pressure would have on deposition characteristics. It is well established that low pressure CVD behaves quite differently to atmospheric pressure CVD. However, it is unknown how sensitive the process is to pressure variation around atmospheric pressure. This may be a meaningful factor to investigate in future.

In this study a number of material properties were investigated. It was found that crush strength (using soft and hard anvils), Vickers hardness, fracture toughness

(measured by means of Vickers indentation cracking), nano-indentation hardness, Young's modulus (as measured by nano-indentation) and microprobe analysis showed very little, or no, response to process conditions typically encountered during coating of TRISO particle. As such these techniques are of little value in investigating the silicon carbide deposition process or as a manufacturing control measurement.

Powder XRD measurements proved to be a useful technique for measuring crystallite size and the degree of disorder within the silicon carbide deposit. Both these characteristics were found to be dependent on deposition conditions. A disadvantage of the XRD method is that, as used in this study, it is a destructive technique. It is also unknown how, if at all, crystallite size and disorder relate to performance of TRISO particles.

Raman spectroscopy proved to be a very useful method in that it allowed for assessment of material properties in addition to been capable of detecting very low levels of free silicon. This technique has the potential for very quick assessment of the material characteristics with minimal sample preparation. This would be a major advantage in a production environment. As for XRD the relationship between measured Raman spectra and TRISO particle performance is not known. Further studies will need to be carried out to determine if any direct links exist and set target and limit values for measured parameters (i.e. Raman peak intensity or position).

SEM imaging provides a very powerful technique for evaluating the silicon carbide layer. The microstructure of the deposit was found to be sensitive to process conditions as well as the coater used. Although viewing of finely polished cross sections of the deposit provided the most information, viewing of the surface of the silicon carbide also provided very useful information. Viewing of the surface structure has the advantage that minimal sample preparation is required. Further investigation will need to be conducted to establish the optimal grain structure and grain size and establish production control limits for these parameters. High resolution imaging combined with automated image analysis may prove to be a very powerful tool in controlling TRISO particle coating processes.

15 REFERENCES

- [1] “IAEA-TECDOC-1198: Current status and future development of modular high temperature gas cooled reactor technology,” Vienna, 2001.
- [2] J. Kupitz and M. Podest, “Nuclear heat applications: World overview,” *IAEA Bulletin*, vol. 26, no. 4, pp. 9-12, 1984.
- [3] “IAEA-TECDOC-1236 Design and evaluation of heat utilization systems for the high temperature engineering test reactor,” 2001.
- [4] “GIF and Generation-IV.” [Online]. Available: http://www.gen-4.org/PDFs/GIF_Overview.pdf. [Accessed: 22-Sep-2009].
- [5] C. Tang, “Design and manufacture of the fuel element for the 10 MW high temperature gas-cooled reactor,” *Nuclear Engineering and Design*, vol. 218, no. 1–3, pp. 91-102, Oct. 2002.
- [6] H. Zhao, T. Liang, J. Zhang, J. He, Y. Zou, and C. Tang, “Manufacture and characteristics of spherical fuel elements for the HTR-10,” *Nuclear Engineering and Design*, vol. 236, no. 5–6, pp. 643-647, Mar. 2006.
- [7] S. Shiozawa, S. Fujikawa, T. Iyoku, K. Kunitomi, and Y. Tachibana, “Overview of HTTR design features,” *Nuclear Engineering and Design*, vol. 233, no. 1–3, pp. 11-21, Oct. 2004.
- [8] J. Cleveland, “Country Nuclear Power Profiles Annex 1: Overview of Global Development of Advanced Nuclear Power Plants,” International Atomic Energy Agency, Vienna, 2003.
- [9] “Global development of advanced nuclear power plants , and related IAEA activities,” Vienna, 2006.
- [10] M. T. Simnad, “The early history of high-temperature helium gas-cooled nuclear power reactors,” *Energy*, vol. 16, no. 1–2, pp. 25–32, 1991.
- [11] R. P. Hammond, H. M. Busey, K. R. Chapman, F. P. Durham, J. D. Rogers, and W. R. Wykoff, “Turret High temperature gas-cycle reactor proposal,” 1958.
- [12] R. . Simon and P. . Capp, “Operating experience with the dragon high temperature reactor experiment,” in *HTR-2002: Proceedings of the conference on high temperature reactors*, 2002, p. 695.
- [13] W. C. Birely, “Operating experience of the peach bottom atomic power station,” *Nuclear Engineering and Design*, vol. 26, no. 1, pp. 9–15, 1974.

- [14] H. Nabielek, G. Kaiser, H. Huschka, H. Ragoss, M. Wimmers, and W. Theymann, "Fuel for pebble-bed HTRs," *Nuclear Engineering and Design*, vol. 78, no. 2, pp. 155-166, Apr. 1984.
- [15] E. . Parma, P. . Pickard, and A. . Suo-Anttila, "Very High Efficiency Reactor (VHER) Concepts for Electrical Power Generation and Hydrogen Production," 2003.
- [16] J. Finseth, "Overview of ROVER Engine Tests: Final Report," George C. Marshall Space Flight Center, 1991.
- [17] H. Nickel, H. Nabielek, G. Pott, and A. . Mehner, "Long time experience with the development of HTR fuel elements in Germany," *Nuclear Engineering and Design*, vol. 217, no. 1–2, pp. 141-151, Aug. 2002.
- [18] Y. Xu, "Overview of the 10 MW high temperature gas cooled reactor—test module project," *Nuclear Engineering and Design*, vol. 218, no. 1–3, pp. 13-23, Oct. 2002.
- [19] J. M. Kendall and R. Bullock, "Advanced coated particle fuel options," in *Proc. HTR2004, 2nd Int. Topical Meeting on HTR Technology, Beijing (China)*, 2004, vol. 22, no. 24.09, pp. 1-9.
- [20] C. Rodriguez, A. Baxter, D. McEachern, M. Fikani, and F. Venneri, "Deep-Burn: making nuclear waste transmutation practical," *Nuclear Engineering and Design*, vol. 222, no. 2–3, pp. 299-317, Jun. 2003.
- [21] IAEA, Ed., "IAEA-TECDOC-1645: High Temperature Gas Cooled Reactor Fuels and Materials," International Atomic Energy Agency, Vienna, 2010.
- [22] D. L. Hanson and J. . Saurwein, "Development Plan for Advanced High Temperature Coated-Particle Fuels," San Diego, 2001.
- [23] H. Nabielek, W. Kuhnlein, W. Schenk, W. Heit, a Christ, and H. Ragoss, "Development of advanced HTR fuel elements," *Nuclear Engineering and Design*, vol. 121, no. 2, pp. 199-210, Jul. 1990.
- [24] D. . Petti, J. Buongiorno, J. . Maki, R. . Hobbins, and G. . Miller, "Key differences in the fabrication, irradiation and high temperature accident testing of US and German TRISO-coated particle fuel, and their implications on fuel performance," *Nuclear Engineering and Design*, vol. 222, no. 2–3, pp. 281-297, Jun. 2003.
- [25] G. . Horsley, G. . Weldrick, J. . Turnbull, and R. Shipp, "Influence of irradiation temperature, burnup, and fuel composition on gas pressure (Xe, Kr, CO, CO₂) in coated particle fuels," *Journal of the American Ceramic Society*, vol. 59, no. 1, pp. 1-4, 1976.

- [26] K. Minato, T. Ogawa, K. Fukuda, and M. Shimizu, "Fission product behavior in Triso-coated UO₂ fuel particles," *Journal of Nuclear Materials*, vol. 208, pp. 266-281, 1994.
- [27] G. K. Miller and R. G. Bennett, "Analytical solution for stresses in TRISO-coated particles," *Journal of nuclear materials*, vol. 206, no. 1, pp. 35-49, 1993.
- [28] J. L. Kaae, "A mathematical model for calculating silicon carbide-coated stresses in a pyrocarbon-and silicon carbide-coated fuel particle," *Journal of Nuclear Materials*, vol. 29, pp. 249-266, 1969.
- [29] C. Lu, R. Danzer, and F. Fischer, "Fracture statistics of brittle materials: Weibull or normal distribution," *Physical Review E*, vol. 65, no. 6, pp. 1-4, Jun. 2002.
- [30] G. K. Miller and D. C. Wadsworth, "Treating asphericity in fuel particle pressure vessel modeling," *Journal of Nuclear Materials*, vol. 211, pp. 57 - 69, 1994.
- [31] G. . Miller, D. A. Petti, J. T. Maki, and L. Knudson, D, "An evaluation of the effects of SiC layer thinning on failure of TRISO-coated fuel particles," *Journal of Nuclear Materials*, vol. 355, no. 1-3, pp. 150-162, Sep. 2006.
- [32] G. . Miller, D. . Petti, and J. . Maki, "Consideration of the effects of partial debonding of the IPyC and particle asphericity on TRISO-coated fuel behavior," *Journal of Nuclear Materials*, vol. 334, no. 2-3, pp. 79-89, Sep. 2004.
- [33] "TEC-DOC-978 CH3 Normal Operation TRISO Fuel Performance Under Irradiation."
- [34] K. Minato, T. Ogawa, S. Kashimura, and K. Fukuda, "Fission product palladium-silicon interaction in HTGR fuel particles," *Journal of Nuclear Materials*, vol. 172, pp. 184-196, 1990.
- [35] T. N. Tieg, "Fission product Pd-SiC interaction in irradiated coated particle fuels," 1980.
- [36] K. Minato, K. Fukuda, A. Ishikawa, and N. Mita, "Advanced coatings for HTGR fuel particles against corrosion of SiC layer," *Journal of Nuclear Materials*, vol. 246, no. 2-3, pp. 215-222, Aug. 1997.
- [37] E. López-Honorato, K. Fu, P. J. Meadows, J. Tan, and P. Xiao, "Effect of Microstructure on the Resilience of Silicon Carbide to Palladium Attack," *Journal of the American Ceramic Society*, vol. 93, no. 12, pp. 4135-4141, Dec. 2010.

- [38] K. Minato, T. Ogawa, S. Kashimura, and K. Fukuda, "Carbon monoxide-silicon carbide interaction in HTGR fuel particles," *Journal of Materials Science*, vol. 26, pp. 2379-2388, 1991.
- [39] E. Proksch, A. Strigl, and H. Nabielek, "Carbon monoxide formation in UO₂ kerneled HTR fuel particles containing oxygen getters," *Journal of Nuclear Materials*, vol. 139, pp. 83-90, 1986.
- [40] E. Proksch, A. Strigl, and H. Nabielek, "Production of CO during burnup of (Th, U)O₂ kerneled HTR fuel particles," *Journal of Nuclear Materials*, vol. 136, pp. 129-135, 1985.
- [41] K. Verfondern, H. Nabielek, and J. M. Kendall, "Coated Particle Fuel for High Temperature Gas Cooled Reactors," *Nuclear Engineering and Technology*, vol. 39, no. 5, pp. 603-616, Oct. 2007.
- [42] R. E. Bullock and J. L. Kaae, "Performance of coated UO₂ particles gettered with ZrC," *Journal of Nuclear Materials*, vol. 115, pp. 69-83, 1983.
- [43] W. Amian and D. Ströver, "Diffusion of silver and cesium in silicon-carbide coatings of fuel particles for high-temperature gas-cooled reactors," *Nuclear Technology*, vol. 61, no. 3-4, pp. 475-486, 1983.
- [44] R. Förthmann, E. Gyarmati, J. Linke, and E. Wallura, "Influence of material properties on the retention of fission products by silicon carbide coatings," *High Temperature - High Pressure*, vol. 14, no. 4, pp. 477-485, 1982.
- [45] H. J. MacLean and R. G. Ballinger, "Silver Ion Implantation and Annealing in CVD Silicon Carbide: The Effect of Temperature on Silver Migration," in *Second International Meeting on High Temperature Reactor Technology, Beijing, China*, 2004, pp. 1-20.
- [46] E. Friedland, N. van der Berg, and J. Malherbe, "Diffusion of Fission Products through Silicon Carbide," in *International Topical Meeting on Nuclear Research Applications and Utilization of Accelerators*, 2009.
- [47] E. López-Honorato, H. Zhang, D. Yang, and P. Xiao, "Silver Diffusion in Silicon Carbide Coatings," *Journal of the American Ceramic Society*, vol. 94, no. 9, pp. 3064-3071, Sep. 2011.
- [48] S. Fujikawa et al., "Achievement of Reactor-Outlet Coolant Temperature of 950.DEG.C. in HTTR," *Journal of Nuclear Science and Technology*, vol. 41, no. 12, pp. 1245-1254, 2004.
- [49] L. Snead, T. Nozawa, Y. Katoh, T.-S. Byun, S. Kondo, and D. Petti, "Handbook of SiC properties for fuel performance modeling," *Journal of Nuclear Materials*, vol. 371, no. 1-3, pp. 329-377, Sep. 2007.
- [50] E. H. Voice and D. N. Lamb, "The deposition and structure of pyrolytic silicon carbide," 1969.

- [51] K. Minato, H. Kikuchi, K. Fukuda, N. Suzuki, H. Tomimoto, and N. Kitamura, "Failure mechanisms of fuel particle coating for high-temperature gas-cooled reactors during the coating process," *Nuclear Technology*, vol. 111, pp. 260-269, 1995.
- [52] K. Minato et al., "Internal flaws in the silicon carbide coating of fuel particles for high-temperature gas-cooled reactors," *Nuclear Technology*, vol. 106, pp. 342-349, 1994.
- [53] E. Proksch, A. Strigl, and H. Nabielek, "Production of carbon monoxide during burn-up of UO₂ kerneled HTR fuel particles," *Journal of Nuclear Materials*, vol. 107, no. 2-3, pp. 280-285, 1982.
- [54] G. Miller, "Consideration of the effects on fuel particle behavior from shrinkage cracks in the inner pyrocarbon layer," *Journal of Nuclear Materials*, vol. 295, no. 2-3, pp. 205-212, Jun. 2001.
- [55] A. . Kercher, J. . Hunn, and J. . Price, "Advanced characterization methods for TRISO fuels," in *Proceedings of the Advanced Reactors with Innovative Fuels Workshop (ARWIF-2005)*, 2005.
- [56] J. . Hunn, "Results From ORNL Characterization of German Reference Fuel From EUO 2358-2365 Composite," 2004.
- [57] A. Ishikawa and E. Oeda, "Deterioration of ZrC-coated fuel particle caused by failure of pyrolytic carbon layer," *Journal of Nuclear Materials*, vol. 252, no. 1-2, pp. 13-21, Jan. 1998.
- [58] E. G. Acheson, "Production of artificial carbonaceous materials," U.S. Patent 492 7671893.
- [59] Y. M. Tairov and V. F. Tsvetkov, "General principles of growing large-size single crystals of various silicon carbide polytypes," *Journal of Crystal Growth*, vol. 52, pp. 146-150, 1981.
- [60] A. . Powell and L. . Rowland, "SiC materials-progress, status, and potential roadblocks," *Proceedings of the IEEE*, vol. 90, no. 6, pp. 942-955, Jun. 2002.
- [61] S. Müller, "The status of SiC bulk growth from an industrial point of view," *Journal of Crystal Growth*, vol. 211, no. 1-4, pp. 325-332, Apr. 2000.
- [62] M. Bhatnagar and B. J. Baliga, "Comparison of 6H-SiC, 3C-SiC, and Si for power devices," *Electron Devices, IEEE Transactions on*, vol. 40, no. 3, pp. 645-655, 1993.
- [63] M. Ruff, H. Mitlehner, and R. Helbig, "SiC devices: physics and numerical simulation," *IEEE Transactions on Electron Devices*, vol. 41, no. 6, pp. 1040-1054, Jun. 1994.

- [64] G. Brezeanu, "Silicon carbide (SiC): A short history. An analytical approach for SiC power device design," *CAS 2005 Proceedings. 2005 International Semiconductor Conference, 2005.*, pp. 345-348, 2005.
- [65] G. L. Harris, Ed., *Properties of silicon carbide*. London: Institution of Electrical Engineers, 1995.
- [66] H. O. Pierson, *Handbook of Refractory Carbides and Nitrides Properties, Characteristics, Processing and Applications*. Westwood: Noyes Publications, 1996.
- [67] J. Qian, L. L. Daemen, and Y. Zhao, "Hardness and fracture toughness of moissanite," *Diamond and Related Materials*, vol. 14, no. 10, pp. 1669-1672, Oct. 2005.
- [68] K. Nassau, "Moissanite: a new synthetic gemstone material," *Journal of Gemmology*, vol. 26, no. 7, pp. 425-438, 1999.
- [69] Y. Zhang, "Large-scale fabrication of lightweight Si/SiC ceramic composite optical mirror," *Materials Letters*, vol. 58, no. 7-8, pp. 1204-1208, Mar. 2004.
- [70] J.-an Xu, H.-kwang Mao, R. J. Hemley, and E. Hines, "The moissanite anvil cell: a new tool for high-pressure research," *Journal of Physics: Condensed Matter*, vol. 14, no. 44, pp. 11543-11548, Nov. 2002.
- [71] Z. Liu, J. Xu, H. P. Scott, Q. Williams, H.-kwang Mao, and R. J. Hemley, "Moissanite (SiC) as windows and anvils for high-pressure infrared spectroscopy," *Review of Scientific Instruments*, vol. 75, no. 11, p. 5026, 2004.
- [72] N. N. Ault, "Silicon Carbide Ceramics, Structure and Properties of," in *Encyclopedia of Materials: Science and Technology*, 2nd ed., and P. V. K. H. Jürgen Buschow, Robert W. Cahn, Merton C. Flemings, Bernard Ilshner, Edward J. Kramer, Subhash Mahajan, Ed. Oxford: Elsevier, 2001, pp. 8502-8508.
- [73] G. Dhanaraj, X. . Huang, M. Dudley, V. Prasad, and R. . Ma, "Silicon Carbide Crystals — Part I: Growth and Characterization," in *Crystal Growth Technology*, K. Byrappa and T. Ohachi, Eds. Berlin, Heidelberg, New York: Springer-Verlag, 2003, pp. 181-225.
- [74] D. Barrett, "SiC boule growth by sublimation vapor transport," *Journal of Crystal Growth*, vol. 109, no. 1-4, pp. 17-23, Feb. 1991.
- [75] N. Ohtani, "Growth of large high-quality SiC single crystals," *Journal of Crystal Growth*, vol. 237-239, pp. 1180-1186, Apr. 2002.
- [76] Y. Tairov, "Investigation of growth processes of ingots of silicon carbide single crystals," *Journal of Crystal Growth*, vol. 43, pp. 209-212, 1978.

- [77] R. C. Glass, D. Henshall, V. F. Tsvetkov, and C. H. Carter, "SiC Seeded crystal growth," *physica status solidi (b)*, vol. 202, no. 1, pp. 149 - 162, 1997.
- [78] R. E. Smallman and R. J. Bishop, *Modern Physical Metallurgy and Materials Engineering Science, process, applications*, 6th ed. OXFORD: Butterworth-Heinemann, 1999, pp. 334-337.
- [79] S. Ding, S. Zhu, Y. Zeng, and D. Jiang, "Fabrication of mullite-bonded porous silicon carbide ceramics by in situ reaction bonding," *Journal of the European Ceramic Society*, vol. 27, no. 4, pp. 2095-2102, 2007.
- [80] S. Moustafa, M. Morsi, and a Almeldin, "Formation of silicon carbide from rice hulls," *Canadian Metallurgical Quarterly*, vol. 36, no. 5, pp. 355-358, Dec. 1997.
- [81] V. Martinez, M. Valencia, J. Cruz, J. Mejia, and F. Chejne, "Production of β -SiC by pyrolysis of rice husk in gas furnaces," *Ceramics International*, vol. 32, no. 8, pp. 891-897, 2006.
- [82] C. Vix-Guterl, "SiC material produced by carbothermal reduction of a freeze gel silica-carbon artefact," *Journal of the European Ceramic Society*, vol. 19, no. 4, pp. 427-432, Apr. 1999.
- [83] Y.-W. Kim, S.-H. Kim, I.-H. Song, H.-D. Kim, and C. B. Park, "Fabrication of Open-Cell, Microcellular Silicon Carbide Ceramics by Carbothermal Reduction," *Journal of the American Ceramic Society*, vol. 88, no. 10, pp. 2949-2951, Oct. 2005.
- [84] G. Jin, "Synthesis and characterization of mesoporous silicon carbide," *Microporous and Mesoporous Materials*, vol. 60, no. 1-3, pp. 207-212, Jun. 2003.
- [85] J. Qian, "Preparation of porous SiC ceramic with a woodlike microstructure by sol-gel and carbothermal reduction processing," *Journal of the European Ceramic Society*, vol. 24, no. 10-11, pp. 3251-3259, Sep. 2004.
- [86] J. Johnson and K. Grobsky, "Rapid fabrication of lightweight silicon-carbide mirrors," *Proceedings of SPIE*, vol. 4771, pp. 243-253, 2002.
- [87] K. Choy, "Chemical vapour deposition of coatings," *Progress in Materials Science*, vol. 48, no. 2, pp. 57-170, 2003.
- [88] A. Elutin and L. Ivanov, "Effective Method of Producing Gas-Impermeable SiC-Coatings," *Advanced Performance Materials*, vol. 188, pp. 183-188, 1997.
- [89] Y. Kajikawa, S. Noda, and H. Komiyama, "Preferred Orientation of Chemical Vapor Deposited Polycrystalline Silicon Carbide Films," *Chemical Vapor Deposition*, vol. 8, no. 3, pp. 99-104, May 2002.

- [90] T. Takeuchi, "A Kinetic Study of the Chemical Vapor Deposition of Silicon Carbide from Dichlorodimethylsilane Precursors," *Journal of The Electrochemical Society*, vol. 145, no. 4, p. 1277, 1998.
- [91] H. Komiyama, Y. Shimogaki, and Y. Egashira, "Chemical reaction engineering in the design of CVD reactors," *Chemical Engineering Science*, vol. 54, no. 13–14, pp. 1941-1957, Jul. 1999.
- [92] G. D. Papasouliotis and S. V. Sotirchos, "Experimental study of atmospheric pressure chemical vapor deposition of silicon carbide from methyltrichlorosilane," *Journal of Materials Research*, vol. 14, no. 08, pp. 3397-3409, Jan. 1999.
- [93] R. Masel, *Chemical kinetics and catalysis*. New York: Wiley, 2001.
- [94] R. Moene, J. . Dekker, M. Makkee, J. Schoonman, and J. A. Moulijn, "Evaluation of Isothermal Chemical Vapor Infiltration with Langmuir-Hinshelwood Type Kinetics," *Journal of The Electrochemical Society*, vol. 141, no. 1, pp. 282-290, 1994.
- [95] I. Langmuir, "The constitution and fundamental properties of solids and liquids," *Journal of the Franklin Institute*, vol. 39, no. 9, pp. 1848 - 1906, 1917.
- [96] R. Gasser, *An introduction to chemisorption and catalysis by metals*. Oxford University Press, 1985.
- [97] H. Sone, T. Kaneko, and N. Miyakawa, "In situ measurements and growth kinetics of silicon carbide chemical vapor deposition from methyltrichlorosilane," *Journal of Crystal Growth*, vol. 219, no. 3, pp. 245-252, Oct. 2000.
- [98] T. Kaneko, "Growth kinetics of vapor-grown SiC," *Journal of Crystal Growth*, vol. 128, no. 1–4, pp. 354-357, Mar. 1993.
- [99] Y. Akiyama, "Modeling Thermal CVD," *Journal of Chemical Engineering of Japan*, vol. 35, no. 8, pp. 701-713, 2002.
- [100] N. Imaishi, T. Sato, M. Kimura, and Y. Akiyama, "Micro/macro modeling of CVD synthesis," *Journal of Crystal Growth*, vol. 180, no. 3–4, pp. 680-690, Oct. 1997.
- [101] C. V. Thompson, "Structure evolution during processing of polycrystalline films," *Annual Review of Materials Science*, vol. 30, pp. 159 - 190, 2000.
- [102] V. Hlavacek, J. J. Thiart, and D. Orlicki, "Morphology and Film Growth in CVD Reactions," *Le Journal de Physique IV*, vol. 05, no. C5, pp. C5-3-C5-44, Jun. 1995.

- [103] D. P. Stinton, T. M. Besmann, and R. A. Lowden, “Advanced ceramics by chemical vapour deposition techniques,” *Ceramic Bulletin*, vol. 67, no. 2, 1988.
- [104] N. Hwang and D. Yoon, “Driving force for deposition in the chemical vapour deposition process,” *Journal of materials science letters*, vol. 13, no. 19, pp. 1437–1439, 1994.
- [105] D. Lespiaux, F. Langlais, and R. Naslain, “Correlations between gas phase supersaturation, nucleation process and physico-chemical characteristics of silicon carbide deposited from Si-CH-Cl system on silica,” *Journal of materials*, vol. 30, no. 6, pp. 1500–1510, 1995.
- [106] T. Liu, D. Raabe, and W.-M. Mao, “A review of crystallographic textures in chemical vapor-deposited diamond films,” *Frontiers of Materials Science in China*, vol. 4, no. 1, pp. 1-16, Jan. 2010.
- [107] J. Zhang and J. B. Adams, “Modeling and visualization of polycrystalline thin film growth,” *Computational Materials Science*, vol. 31, no. 3–4, pp. 317-328, Nov. 2004.
- [108] J. Yun, “Model of morphology evolution in the growth of polycrystalline β -SiC films,” *Diamond and Related Materials*, vol. 9, pp. 439 - 445, 2000.
- [109] P. Smereka, X. Li, G. Russo, and D. J. Srolovitz, “Simulation of faceted film growth in three dimensions: microstructure, morphology and texture,” *Acta Materialia*, vol. 53, no. 4, pp. 1191-1204, Feb. 2005.
- [110] X. Jiang, G. Yu, and S. T. Lee, “Simulation of polycrystalline 3D film growth: An investigation of the evolution of grain size and texture in diamond films,” *Applied Physics A: Materials Science & Processing*, vol. 74, no. 2, pp. 217-224, Feb. 2002.
- [111] M. Bloomfield and T. Cale, “Formation and evolution of grain structures in thin films,” *Microelectronic Engineering*, vol. 76, no. 1–4, pp. 195-204, Oct. 2004.
- [112] C. Wild et al., “Chemical vapour deposition and characterization of smooth {100}-faceted diamond films,” *Diamond and Related Materials*, vol. 2, no. 2–4, pp. 158–168, 1993.
- [113] P. Van der Sluis and J. Kroon, “The development and prediction of needle habits,” *Journal of crystal growth*, vol. 104, no. 2, pp. 310–314, 1990.
- [114] E. Granneman, “Thin films in the integrated circuit industry: requirements and deposition methods,” *Thin Solid Films*, vol. 228, no. 1–2, pp. 1-11, May 1993.
- [115] J. . Mullin, *Crystallisation*, 2nd ed. Butterworth, 1972.

- [116] T. Ohachi and K. Byrappa, Eds., *Crystal Growth Technology*. Berlin: Springer Verlag, 2003.
- [117] W. K. Burton, N. Cabrera, and F. C. Frank, "The Growth of Crystals and the Equilibrium Structure of their Surfaces," *Philosophical Transactions of the Royal Society A: Mathematical, Physical and Engineering Sciences*, vol. 243, no. 866, pp. 299-358, Jun. 1951.
- [118] B. W. van de Waal, "Cross-twinning model of fcc crystal growth," *Journal of Crystal Growth*, vol. 191, no. 1-2, pp. 339-165, Jan. 1996.
- [119] R. Jagannathan, R. Mehta, J. Timmons, and D. Black, "Anisotropic growth of twinned cubic crystals," *Physical review. B, Condensed matter*, vol. 48, no. 18, pp. 13261-13265, Nov. 1993.
- [120] N. Ming and I. Sunagawa, "Twin lamellae as possible self-perpetuating step sources," *Journal of crystal growth*, vol. 87, pp. 13 - 17, 1988.
- [121] J.-W. Lee, U.-J. Chung, N. Hwang, and D.-Y. Kim, "Growth process of the ridge-trough faces of a twinned crystal," *Acta crystallographica. Section A, Foundations of crystallography*, vol. 61, no. Pt 4, pp. 405-10, Jul. 2005.
- [122] M. A. Lovette, A. R. Browning, D. W. Griffin, J. P. Sizemore, R. C. Snyder, and M. F. Doherty, "Crystal shape engineering," *Industrial and Engineering Chemistry Research*, vol. 47, no. 24, pp. 9812 - 9833, 2008.
- [123] N. Sugiyama, A. Okamoto, K. Okumura, T. Tani, and N. Kamiya, "Step structures and dislocations of SiC single crystals grown by modified Lely method," *Journal of Crystal Growth*, vol. 191, no. 1-2, pp. 84-91, Jul. 1998.
- [124] M. Kitamura, S. Hosoya, and I. Sunagawa, "Re-investigation of the re-entrant corner effect in twinned crystals," *Journal of Crystal Growth*, vol. 47, pp. 93-99, 1979.
- [125] R. Boistelle, "Crystallization mechanisms in solution," *Journal of crystal growth*, vol. 90, no. 1-3, pp. 14-30, 1988.
- [126] I. Sunagawa, "Growth and morphology of crystals," *FORMA-TOKYO-*, vol. 14, no. 1/2, pp. 147-166, 1999.
- [127] G. Chichignoud, M. Ucar-Morais, M. Pons, and E. Blanquet, "Chlorinated silicon carbide CVD revisited for polycrystalline bulk growth," *Surface and Coatings Technology*, vol. 201, no. 22-23, pp. 8888-8892, Sep. 2007.
- [128] "COMPOSITE MATERIALS HANDBOOK," *MIL-HDBK-17-5*, vol. 5, 2002.
- [129] X. Wei, L. Cheng, L. Zhang, Y. Xu, and Q. Zeng, "Numerical Simulation of Effect of Methyltrichlorosilane Flux on Isothermal Chemical Vapor Infiltration Process of C/SiC Composites," *Journal of the American Ceramic Society*, vol. 89, no. 9, pp. 2762 -2768, Jun. 2006.

- [130] D. Jaglin, J. Binner, B. Vaidhyathan, C. Prentice, B. Shatwell, and D. Grant, "Microwave Heated Chemical Vapor Infiltration: Densification Mechanism of SiCf/SiC Composites," *Journal of the American Ceramic Society*, vol. 89, no. 9, pp. 2710 - 2717, Jun. 2006.
- [131] K. Appiah, "Texturing of polycrystalline SiC films on graphitic carbon in laminated composites grown by forced-flow chemical vapor infiltration," *Thin Solid Films*, vol. 371, no. 1-2, pp. 114-118, Aug. 2000.
- [132] R. Brutsch, "Chemical vapour deposition of silicon carbide and its applications," *Thin Solid Films*, vol. 126, pp. 313 - 318, Jan. 1985.
- [133] J. I. Kim, W.-J. Kim, D. J. Choi, and J. Y. Park, "Deposition of compositionally graded SiC/C layers on C-C composites by low pressure chemical vapor deposition," *Journal of Nuclear Materials*, vol. 307-311, pp. 1084-1087, Dec. 2002.
- [134] J. N. Pring and W. Fielding, "The preparation at high temperatures of some refractory metals from their chlorides," *J. Chem. Soc., Trans.*, vol. 95, pp. 1497-1506, 1909.
- [135] D. Zhu, P. Hing, P. Brown, and Y. Sahai, "Characterization of silicon carbide coatings grown on graphite by chemical vapor deposition," *Journal of materials processing technology*, vol. 48, no. 1, pp. 517-523, 1995.
- [136] G. Chung and K. Kim, "Heteroepitaxial Growth of 3C-SiC Thin Films on Si (100) Substrates by Single Source Chemical Vapor Deposition for MEMS Applications," *Sensors, 2006. 5th IEEE Conference on*, no. 100, pp. 1231-1234, 2006.
- [137] H. S. Kim and D. J. Choi, "Effect of diluent gases on growth behavior and characteristics of chemically vapor deposited silicon carbide films," *Journal of the American Ceramic Society*, vol. 82, no. 2, pp. 331-337, 1999.
- [138] K. Yagi, "3C-SiC growth by alternate supply of SiH₂Cl₂ and C₂H₂," *Journal of Crystal Growth*, vol. 174, no. 1-4, pp. 653-657, Apr. 1997.
- [139] N. Nordell, "Influence of H₂ Addition and Growth Temperature on CVD of SiC Using Hexamethyldisilane and Ar," *Journal of The Electrochemical Society*, vol. 142, no. 2, p. 565, 1995.
- [140] B. J. Choi, D. W. Park, and D. R. Kim, "Chemical vapour deposition of silicon carbide by pyrolysis of methylchlorosilanes," *Journal of materials science letters*, vol. 16, no. 1, pp. 33-36, 1997.
- [141] T. Kaneko and T. Okuno Hisami, "Growth kinetics of silicon carbide CVD," *Journal of crystal growth*, vol. 91, no. 4, pp. 599-604, 1988.

- [142] Y. Avigal, M. Schieber, and R. Levin, "The growth of hetero-epitaxial SiC films by pyrolysis of various alkyl-silicon compounds," *Journal of Crystal Growth*, vol. 24–25, no. 1974, pp. 188-192, Oct. 1974.
- [143] C. R. Stoldt, M. C. Fritz, C. Carraro, and R. Maboudian, "Micromechanical properties of silicon-carbide thin films deposited using single-source chemical-vapor deposition," *Applied Physics Letters*, vol. 79, no. 3, p. 347, 2001.
- [144] B. C. Kang, S. B. Lee, and J. H. Boo, "Growth of β -SiC nanowires on Si (100) substrates by MOCVD using nickel as a catalyst," *Thin solid films*, vol. 464, pp. 215–219, 2004.
- [145] G. S. Fischman and W. T. Petuskey, "Thermodynamic Analysis and Kinetic Implications of Chemical Vapor Deposition of Sic from Si-C-C1-H Gas Systems," *Journal of the American Ceramic Society*, vol. 68, no. 4, pp. 185-190, Apr. 1985.
- [146] F. Kobayashi, "Formation of carbon-excess SiC from pyrolysis of CH₃SiCl₃," *Journal of Crystal Growth*, vol. 28, no. 3, pp. 395-396, Apr. 1975.
- [147] I. M. Kostjulin and S. V. Sotirchos, "Codeposition of SiC and C from Mixtures of Methyltrichlorosilane and Ethylene in Hydrogen," *Industrial & Engineering Chemistry Research*, vol. 40, no. 12, pp. 2586-2596, Jun. 2001.
- [148] H. Nagasawa and Y. Yamaguchi, "Mechanisms of SiC growth by alternate supply of SiH₂Cl₂ and C₂H₂," *Applied Surface Science*, vol. 82–83, no. 94, pp. 405-409, Dec. 1994.
- [149] M. D. Allendorf, T. H. Osterheld, and C. F. Melius, "The decomposition of methyltrichlorosilane: Studies in a high-temperature flow reactor," Livermore, CA (United States), 1994.
- [150] W. G. Zhang and K. J. Hüttinger, "CVD of SiC from Methyltrichlorosilane. Part I: Deposition Rates," *Chemical Vapor Deposition*, vol. 7, no. 4, pp. 167-172, Jul. 2001.
- [151] W. G. Zhang and K. J. Hüttinger, "CVD of SiC from Methyltrichlorosilane. Part II: Composition of the Gas Phase and the Deposit," *Chemical Vapor Deposition*, vol. 7, no. 4, pp. 173-181, Jul. 2001.
- [152] A. I. Kingon, L. J. Lutz, P. Liaw, and R. F. Davis, "Thermodynamic calculations for the chemical vapor deposition of silicon carbide," *Journal of the American Ceramic Society*, vol. 66, no. 8, pp. 558-566, 2006.
- [153] K. Minato and K. Fukuda, "Chemical vapor deposition of silicon carbide for coated fuel particles," *Journal of Nuclear Materials*, vol. 149, no. 2, pp. 233–246, 1987.

- [154] T. M. Besmann, B. W. Sheldon, T. S. Moss, and M. D. Kaster, “Depletion Effects of Silicon Carbide Deposition from Methyltrichlorosilane,” *Journal of the American Ceramic Society*, vol. 75, no. 10, pp. 2899-2903, Oct. 1992.
- [155] K. Minato and K. Fukuda, “SiC coating of small particles in a fluidized bed reactor,” *Materials and Manufacturing Processes*, vol. 3, no. 4, pp. 617-641, 1988.
- [156] E. López-Honorato, P. Meadows, J. Tan, and P. Xiao, “Control of stoichiometry, microstructure, and mechanical properties in SiC coatings produced by fluidized bed chemical vapor deposition,” *Journal of Materials Research*, vol. 23, no. 6, pp. 1785–1796, 2008.
- [157] A. Van Kemenade and C. Stemfoort, “On the formation of β -SiC from pyrolysis of CH_3SiCl_3 in hydrogen,” *Journal of Crystal Growth*, vol. 12, no. 1, pp. 13-16, Jan. 1972.
- [158] J. Yeheskel and M. S. Dariel, “Codeposition of Free Silicon during CVD of Silicon Carbide,” *Journal of the American Ceramic Society*, vol. 78, no. 1, pp. 229-232, Jan. 1995.
- [159] T. M. Besmann, B. W. Sheldon, and M. D. Kaster, “Temperature and concentration dependence of SiC deposition on Nicalon fibres,” *Surface and Coatings Technology*, vol. 43, no. 1, pp. 167-175, May 1990.
- [160] J. I. Federer, “Parametric study of silicon carbide coatings deposited in a fluidized bed,” *Thin Solid Films*, vol. 40, pp. 89-96, Jan. 1977.
- [161] T. D. Gulden, “Deposition and microstructure of vapor-deposited silicon carbide,” *Journal of the American Ceramic Society*, vol. 51, no. 8, pp. 424-427, Nov. 1968.
- [162] W.-J. Kim, J. N. Park, M. S. Cho, and J. Y. Park, “Effect of coating temperature on properties of the SiC layer in TRISO-coated particles,” *Journal of Nuclear Materials*, vol. 392, no. 2, pp. 213-218, Jul. 2009.
- [163] D. J. Cheng, W. J. Shyy, K. DH, and M. Hon, “Growth Characteristics of CVD Beta-Silicon Carbide,” *Journal of The Electrochemical Society*, vol. 134, no. 12, pp. 3145 - 3149, 1987.
- [164] B. J. Choi and D. R. Kim, “Growth of silicon carbide by chemical vapour deposition,” *Journal of materials science letters*, vol. 10, no. 14, pp. 860-862, 1991.
- [165] M. G. So and J. S. Chun, “Growth and structure of chemical vapor deposited silicon carbide from methyltrichlorosilane and hydrogen in the temperature range of 1100 to 1400 °C,” *Journal of Vacuum Science & Technology A: Vacuum, Surfaces, and Films*, vol. 6, no. 1. p. 5, Jan-1988.

- [166] D. P. Stinton and W. J. Lackey, "Effect of deposition conditions on the properties of pyrolytic SiC coatings for HTGR fuel particles," *American Ceramic Society Bulletin*, vol. 57, no. 6, pp. 568-573, 1978.
- [167] F. Charollais et al., "CEA and AREVA R&D on HTR fuel fabrication and presentation of the CAPRI experimental manufacturing line," *Nuclear Engineering and Design*, vol. 236, no. 5–6, pp. 534-542, Mar. 2006.
- [168] K. Minato and K. Fukuda, "Structure of chemically vapour deposited silicon carbide for coated fuel particles," *Journal of Material Science*, vol. 23, no. 2, pp. 699-706, 1988.
- [169] D. Helary, X. Bourrat, O. Dugne, G. Maveyraud, M. Perez, and P. Guillermier, "Microstructures of silicon carbide and pyrocarbon coatings for fuel particles for high temperature reactors (HTR)," in *HTR2004, Beijing*, 2004, pp. 1-12.
- [170] J. de Villiers, J. Roberts, and N. Ngoepe, "Evaluation of the Phase Composition, Crystallinity, and Trace Isotope Variation of SiC in Experimental TRISO Coated Particles," *Journal of Engineering for Gas Turbines and Power*, vol. 131, no. 6, p. 062904, 2009.
- [171] V. . Pujar and J. D. Cawley, "Computer Simulations of Diffraction Effects due to Stacking Faults in β -SiC: I, Simulation Results," *Journal of the American Ceramic Society*, vol. 80, no. 7, pp. 1653–1662, 1997.
- [172] V. . Pujar and J. . Cawley, "Computer Simulations of Diffraction Effects due to Stacking Faults in β -SiC: II, Experimental Verification," *Journal of the American Ceramic Society*, vol. 84, no. 11, pp. 2645–2651, 2001.
- [173] S. Shinozaki and K. . Kinsman, "Aspects of 'one dimensional disorder' in silicon carbide," *Acta Metallurgica*, vol. 26, no. 5, pp. 769 - 776, 1978.
- [174] G. Z. Cambaz, G. N. Yushin, Y. Gogotsi, and V. G. Lutsenko, "Anisotropic etching of SiC whiskers.," *Nano letters*, vol. 6, no. 3, pp. 548-51, Mar. 2006.
- [175] E. H. Voice, "The formation and structure of silicon carbide pyrolytically deposited in a fluidised bed of microspheres," Winfrith, 1970.
- [176] M. Mokoduwe, S. I. . Van Rooyen, J. . Neethling, A. Janse van Vuuren, and J. Olivier, E, "Effect of high temperature annealing on the grain size of CVD-grown SiC and experimental PBMR TRISO coated particles," in *HTR2010*, 2010.
- [177] S. Xu, J. Zhou, B. Yang, and B. Zhang, "Effect of deposition temperature on the properties of pyrolytic SiC," *Journal of nuclear materials*, vol. 224, no. 1, pp. 12–16, 1995.

- [178] D. Helary, O. Dugne, X. Bourrat, P. Jouneau, and F. Cellier, “EBSD investigation of SiC for HTR fuel particles,” *Journal of Nuclear Materials*, vol. 350, no. 3, pp. 332-335, May 2006.
- [179] L. Tan, T. R. Allen, J. . Hunn, and J. H. Miller, “EBSD for microstructure and property characterization of the SiC-coating in TRISO fuel particles,” *Journal of Nuclear Materials*, vol. 372, no. 2–3, pp. 400-404, Jan. 2008.
- [180] J. Chin, P. K. Gantzel, and R. G. Hudson, “The structure of chemical vapor deposited silicon carbide,” *Thin Solid Films*, vol. 40, pp. 57-72, Jan. 1977.
- [181] R. Liu, C. Zhang, X. Zhou, and Y. Cao, “Structural analysis of chemical vapor deposited -SiC coatings from CHSiCl–H gas precursor,” *Journal of Crystal Growth*, vol. 270, no. 1–2, pp. 124-127, Sep. 2004.
- [182] J. H. Oh, B. J. Oh, D. J. Choi, G. H. Kim, and H. S. Song, “The effect of input gas ratio on the growth behavior of chemical vapor deposited SiC films,” *Journal of materials science*, vol. 36, no. 7, pp. 1695–1700, 2001.
- [183] D.-J. Kim, D.-J. Choi, and Y.-W. Kim, “Effect of reactant depletion on the microstructure and preferred orientation of polycrystalline SiC films by chemical vapor deposition,” *Thin Solid Films*, vol. 266, no. 2, pp. 192-197, Oct. 1995.
- [184] K. Bongartz, E. Gyarmati, H. Nickel, H. Schuster, and W. Winter, “Measurement of Young’s modulus and fracture stress on HTR particle coatings by the brittle ring test,” *Journal of Nuclear Materials*, vol. 45, pp. 261-264, Jan. 1972.
- [185] K. Bongartz et al., “The brittle ring test□: a method for measuring on coatings of htr fuel particles,” *Journal of Nuclear Materials*, vol. 62, pp. 123-137, 1976.
- [186] C. Vahlas, B. Caussat, P. Serp, and G. Angelopoulos, “Principles and applications of CVD powder technology,” *Materials Science and Engineering: R: Reports*, vol. 53, no. 1–2, pp. 1-72, Jul. 2006.
- [187] D. Geldart, “Types of gas fluidization,” *Powder Technology*, vol. 7, no. 5, pp. 285-292, May 1973.
- [188] K. . Mathur and N. Epstein, *Spouted Beds*. New York: Academic Press, 1974.
- [189] J. Piña, V. Bucalá, N. S. Schbib, P. Ege, and H. I. de Lasa, “Modeling a silicon CVD spouted bed pilot plant reactor,” *International Journal of Chemical Reactor Engineering*, vol. 4, 2006.
- [190] D. Sathiyamoorthy, V. Rao, P. Rao, and P. Mollick, “Development of pyrolytic carbon coated zirconia pebbles in a high temperature spouted bed,” *Indian Journal of Engineering and Material Science*, vol. 17, no. October, pp. 349-352, 2010.

- [191] R. . Daugherty and J. . Franzini, *Fluid Mechanics with Engineering Applications*, 7th ed. McGraw-Hill Book Company.
- [192] R. Niven, “Physical insight into the Ergun and Wen & Yu equations for fluid flow in packed and fluidised beds,” *Chemical Engineering Science*, vol. 57, no. 3, pp. 527-534, Feb. 2002.
- [193] M. Leva, *Fluidization*. New York: McGraw-Hill Book Company, 1974.
- [194] R. L. C. Flemmer and C. L. Banks, “On the drag coefficient of a sphere,” *Powder Technology*, vol. 48, no. 3, pp. 217-221, Nov. 1986.
- [195] R. Turton and N. Clark, “An explicit relationship to predict spherical particle terminal velocity,” *Powder Technology*, vol. 53, no. 6, pp. 127 - 129, Jun. 1987.
- [196] P. . Rowe, “A convenient empirical equation for estimation of the Richardson-Zaki exponent,” *Chemical Engineering Science*, vol. 42, no. 11, pp. 2795 - 2796, 1987.
- [197] M. Olazar, M. J. San Jose, A. T. Aguayo, J. M. Arandes, and J. Bilbao, “Stable operation conditions for gas-solid contact regimes in conical spouted beds,” *Industrial & Engineering Chemistry Research*, vol. 31, no. 7, pp. 1784-1792, Jul. 1992.
- [198] W. R. A. Goossens, “Classification of fluidized particles by Archimedes number,” *Powder technology*, vol. 98, no. 1, pp. 48–53, 1998.
- [199] J. R. Grace, “Contacting modes and behaviour classification of gas-solid and other two-phase suspensions,” *The Canadian Journal of Chemical Engineering*, vol. 64, no. 3, pp. 353-363, Jun. 1986.
- [200] W.-C. Yang, “Modification and re-interpretation of Geldart’s classification of powders,” *Powder Technology*, vol. 171, no. 2, pp. 69-74, Feb. 2007.
- [201] B. Kozanoglu, “Hydrodynamics of large particle fluidization in reduced pressure operations: an experimental study,” *Powder Technology*, vol. 125, no. 1, pp. 55-60, May 2002.
- [202] V. Sangeetha, R. Swathy, N. Narayanamurthy, C. M. Lakshmanan, and L. R. Miranda, “Minimum Fluidization Velocity At High Temperatures Based on Geldart Powder Classification,” *Chemical Engineering & Technology*, vol. 23, no. 8, pp. 713-719, Aug. 2000.
- [203] J. Zhou, D. D. Bruns, C. E. A. Finney, C. S. Daw, S. Pannala, and D. I McCollum, “Hydrodynamic correlation with experimental results from cold mockup spouted beds for nuclear fuel particle coating,” in *Annual Meeting - ACE International*, 2005.

- [204] M. Sanjose, “Correlation for calculation of the gas dispersion coefficient in conical spouted beds,” *Chemical Engineering Science*, vol. 50, no. 13, pp. 2161-2172, Jul. 1995.
- [205] M. Olazar, M. J. San Jose, M. A. Izquierdo, A. O. de Salazar, and J. Bilbao, “Effect of operating conditions on solid velocity in the spout, annulus and fountain of spouted beds,” *Chemical engineering*, vol. 56, pp. 3585-3594, 2001.
- [206] M. Olazar et al., “Solid Trajectories and Cycle Times in Spouted Beds,” *Industrial & Engineering Chemistry Research*, vol. 43, no. 1, pp. 3433-3438, Jun. 2004.
- [207] M. Olazar, M. J. S. Jose, M. A. Izquierdo, S. Alvarez, and J. Bilbao, “Fountain geometry in shallow spouted beds,” *Industrial & Engineering Chemistry Research*, vol. 43, no. 1, pp. 1163-1168, 2004.
- [208] M. J. S. José, M. Olazar, M. A. Izquierdo, S. Alvarez, and J. Bilbao, “Spout Geometry in Shallow Spouted Beds,” *Industrial & Engineering Chemistry Research*, vol. 40, no. 1, pp. 420-426, 2001.
- [209] S. Davidson and M. Perkin, “An investigation of density determination methods for porous materials , small samples and particulates,” in *IMEKO 2010 Metrology in modern contex*, 2010, pp. 69-72.
- [210] I. M. Jánosi, G. Szabó, and T. Tél, “High precision balance from salt and water and the slow swelling of ping-pong balls,” *European Journal of Physics*, vol. 25, no. 2, pp. 303-310, Mar. 2004.
- [211] N. Pratten, “The precise measurement of the density of small samples,” *Journal of Materials Science*, vol. 16, pp. 1737-1747, 1981.
- [212] J. M. Brown, B. M. Kadlubowski, L. J. Forney, and J. T. Sommerfeld, “Density gradient columns: Dynamic modeling for linear profiles,” *Review of scientific instruments*, vol. 67, no. 11, pp. 3973–3980, 1996.
- [213] C. H. Lindsley, “Preparation of density-gradient columns,” *Journal of Polymer Science*, vol. 46, no. 148, pp. 543–545, 1960.
- [214] J. T. Keeley, B. L. Tomlin, W. C. Richardson, C. Barnes, and D. Marshall, “Development of a continuous process for TRISO coating of AGR fuel,” in *4th International Topical Meeting on High Temperature Reactor Technology HTR2008*, 2008, pp. 1-6.
- [215] M. . Osborne, J. . Hay, L. Snead, and D. Steiner, “Mechanical-and Physical-Property Changes of Neutron-Irradiated Chemical-Vapor-Deposited Silicon Carbide,” *Journal of the American Ceramic Society*, vol. 82, no. 9, pp. 2490–2496, 1999.

- [216] O. Gal and P. Premović, “Density determination of plastics by a volumetric titration method,” *Die Angewandte Makromolekulare Chemie*, vol. 84, no. 1, pp. 1–6, 1980.
- [217] M. Viana, P. Jouannin, C. Pontier, and D. Chulia, “About pycnometric density measurements.,” *Talanta*, vol. 57, no. 3, pp. 583-93, May 2002.
- [218] S. Tamari, “Optimum design of the constant-volume gas pycnometer for determining the volume of solid particles,” *Measurement Science and Technology*, vol. 15, no. 3, pp. 549-558, Mar. 2004.
- [219] J. Park, “Application of statistics to oil density measurement,” *Measurement*, vol. 30, pp. 95-103, 2001.
- [220] C. K. Jo, Y. Kim, J. M. Noh, and F. Venneri, “TRU self-recycling in a high temperature modular helium reactor,” *Nuclear Engineering and Design*, vol. 242, pp. 215-220, Jan. 2012.
- [221] H. Wang, R. N. Singh, and J. S. Goela, “Effects of Postdeposition Treatments on the Mechanical Properties of a Chemical-Vapor-Deposited Silicon Carbide,” *Journal of the American Ceramic Society*, vol. 78, no. 9, pp. 2437–2442, 1995.
- [222] R. Price, “Structure and properties of pyrolytic silicon carbide,” *Journal of the American Ceramic Society*, vol. 48, no. 9, pp. 859 - 862, 1969.
- [223] P. Krautwasser, G. Begun, and P. Angelini, “Raman spectral characterization of silicon carbide nuclear fuel coatings,” *Journal of the American Ceramic Society*, vol. 66, no. 6, pp. 424–434, 1983.
- [224] Y. Lu and M. Hon, “Stacking fault probability in β -SiC grown by chemical vapour deposition,” *Materials Science and Engineering: B*, vol. 8, pp. 241-244, 1991.
- [225] Y. Ward, R. J. Young, and R. A. Shatwell, “Application of Raman microscopy to the analysis of silicon carbide monofilaments,” *Journal of Materials Science*, vol. 39, no. 22, pp. 6781-6790, Nov. 2004.
- [226] D. Olego and M. Cardona, “Pressure dependence of the optical phonons and transverse effective charge in 3C-SiC,” *Physical Review B*, vol. 25, no. 2, pp. 3878 - 3888, 1982.
- [227] G. Gouadec and P. Colomban, “Raman Spectroscopy of nanomaterials: How spectra relate to disorder, particle size and mechanical properties,” *Progress in Crystal Growth and Characterization of Materials*, vol. 53, no. 1, pp. 1-56, Mar. 2007.
- [228] E. López-Honorato, P. J. Meadows, J. Tan, Y. Xiang, and P. Xiao, “Deposition of TRISO Particles With Superhard SiC Coatings and the

- Characterization of Anisotropy by Raman Spectroscopy,” *Journal of Engineering for Gas Turbines and Power*, vol. 131, no. 4, p. 042905, 2009.
- [229] A. Evans, C. Padgett, and R. Davidge, “Strength of Pyrolytic SiC Coatings of Fuel Particles for High-Temperature Gas-Cooled Reactors,” *Journal of the American Ceramic Society*, vol. 56, no. 1, pp. 36–41, 1973.
- [230] Y. Ward, R. J. Young, and R. A. Shatwell, “Effect of excitation wavelength on the Raman scattering from optical phonons in silicon carbide monofilaments,” *Journal of Applied Physics*, vol. 102, no. 2, p. 023512, 2007.
- [231] B. Jin and N. Shi, “Analysis of microstructure of silicon carbide fiber by Raman spectroscopy,” *Journal of Materials Science and Technology*, vol. 24, no. 2, p. 261, 2008.
- [232] G. Gouadec and P. Colomban, “Non-destructive mechanical characterization of SiC fibers by Raman spectroscopy,” *Journal of the European Ceramic Society*, vol. 21, no. 9, pp. 1249-1259, Sep. 2001.
- [233] Y. M. Lu and I. C. Leu, “Qualitative study of beta silicon carbide residual stress by Raman spectroscopy,” *Thin solid films*, vol. 377, no. 1–2, pp. 389–393, Dec. 2000.
- [234] K. E. Gilchrist and J. E. Brocklehurst, “A technique for measuring the strength of high temperature reactor fuel particle coatings,” *Journal of Nuclear Materials*, vol. 43, pp. 347-350, 1972.
- [235] I. McColm, *Ceramic hardness*. New York: Plenum Press, 1990.
- [236] S. Nogami, A. Hasegawa, and L. Snead, “Indentation fracture toughness of neutron irradiated silicon carbide,” *Journal of Nuclear Materials*, vol. 307–311, pp. 1163-1167, Dec. 2002.
- [237] M. Pharr, Y. Katoh, and H. Bei, “Dependence of fracture toughness on crystallographic orientation of single-crystalline cubic (β) silicon carbide,” *U.S. Department of Energy Journal of Undergraduate Research*, 2005.
- [238] G. Quinn, “Hardness testing of ceramics,” *Advanced Materials and Processes*, vol. 154, no. 2, pp. 5-10, 1998.
- [239] P. C. Jindal and D. T. Quinto, “Load dependence of microhardness of hard coatings,” *Surface and Coatings Technology*, vol. 36, no. 3–4, pp. 683-694, Dec. 1988.
- [240] X. Ren, R. Hooper, C. Griffiths, and J. Henshall, “Indentation size effect in ceramics: Correlation with H/E,” *Journal of materials science letters*, vol. 22, no. 15, pp. 1105–1106, 2003.

- [241] J. Quinn and G. Quinn, “Indentation brittleness of ceramics: a fresh approach,” *Journal of materials Science*, vol. 32, no. 16, pp. 4331–4346, 1997.
- [242] J. Gong, J. Wu, and Z. Guan, “Examination of the indentation size effect in low-load Vickers hardness testing of ceramics,” *Journal of the European Ceramic Society*, vol. 19, no. 15, pp. 2625–2631, 1999.
- [243] W. Oliver and G. M. Pharr, “An improved technique for determining hardness and elastic modulus using load and displacement sensing indentation experiments,” *Journal of Materials Research*, vol. 7, no. 6, pp. 1564–1583, 1992.
- [244] “Standard Test Method for Vickers Indentation Hardness of Advanced Ceramics,” *October*. ASTM International, 2003.
- [245] K. S. Lee, J. Y. Park, W. J. Kim, and G. W. Hong, “Effect of microstructure of SiC layer on the indentation properties of silicon carbide–graphite system fabricated by LPCVD method,” *Journal of materials science letters*, vol. 20, no. 13, pp. 1229–1231, 2001.
- [246] C. . Ponton and R. . Rawlings, “Vickers indentation fracture toughness test Part 1 Review of literature and formulation of standardised indentation toughness equations,” *Materials Science and Technology*, vol. 5, no. 9, pp. 865 - 872, 1989.
- [247] C. . Ponton and R. . Rawlings, “Vickers indentation fracture toughness test Part 2 Application and critical evaluation of standardised indentation toughness equations,” *Materials Science and Technology*, vol. 5, no. 10, pp. 961–976, 1989.
- [248] F. Sergejev and M. Antonov, “Comparative study on indentation fracture toughness measurements of cemented carbides,” *Proceedings of the Estonian Academy of Sciences. Engineering*, vol. 12, no. 4, pp. 388–398, 2006.
- [249] D. Harding, G. Pharr, and W. Oliver, “Cracking during nanoindentation and its use in the measurement of fracture toughness,” in *MRS Proceedings: Volume 356 - Symposium B2 – Thin Films: Stresses and Mechanical Properties V*, 1994.
- [250] K. Liang, G. Orange, and G. Fantozzi, “Evaluation by indentation of fracture toughness of ceramic materials,” *Journal of materials science*, vol. 25, no. 1, pp. 207–214, 1990.
- [251] G. D. Quinn and R. C. Bradt, “On the Vickers Indentation Fracture Toughness Test,” *Journal of the American Ceramic Society*, vol. 90, no. 3, pp. 673–680, Mar. 2007.

- [252] X. Zhao, R. M. Langford, J. Tan, and P. Xiao, "Mechanical properties of SiC coatings on spherical particles measured using the micro-beam method," *Scripta Materialia*, vol. 59, no. 1, pp. 39-42, Jul. 2008.
- [253] "ASTM C 1421 – 01b: Standard Test Methods for Determination of Fracture Toughness of Advanced Ceramics." ASTM, 2002.
- [254] B. V. Cockeram, "Fracture Toughness and Flexural Strength of Chemically Vapor-Deposited Silicon Carbide As Determined Using Chevron-Notched and Surface Crack in Flexure Specimens," *Journal of the American Ceramic Society*, vol. 87, no. 6, pp. 1093-1101, Jun. 2004.
- [255] H. Zhang, E. López-Honorato, A. Javed, I. Shapiro, and P. Xiao, "A Study of the Microstructure and Vickers Indentation Fracture Toughness of Silicon Carbide Coatings on TRISO Fuel Particles," *Journal of the American Ceramic Society*, vol. 95, no. 3, pp. 1086 - 1092, Jan. 2012.
- [256] J. J. Bellante, H. Kahn, R. Ballarini, C. A. Zorman, M. Mehregany, and A. H. Heuer, "Fracture toughness of polycrystalline silicon carbide thin films," *Applied Physics Letters*, vol. 86, no. 7, p. 071920, 2005.
- [257] K. Strecker, S. Ribeiro, and M.-J. Hoffmann, "Fracture toughness measurements of LPS-SiC: a comparison of the indentation technique and the SEVNB method," *Materials Research*, vol. 8, no. 2, pp. 121-124, Jun. 2005.
- [258] W. C. Oliver and G. M. Pharr, "Measurement of hardness and elastic modulus by instrumented indentation: Advances in understanding and refinements to methodology," *Journal of Materials Research*, vol. 19, no. 1, pp. 3-20, Jan. 2004.
- [259] S.-G. Hong, T.-S. Byun, R. Lowden, L. Snead, and Y. Katoh, "Evaluation of the Fracture Strength for Silicon Carbide Layers in the Tri-Isotropic-Coated Fuel Particle," *Journal of the American Ceramic Society*, vol. 90, no. 1, pp. 184-191, Jan. 2007.
- [260] C. Bellan and J. Dhers, "Evaluation of Young modulus of CVD coatings by different techniques," *Thin Solid Films*, vol. 469–470, pp. 214-220, Dec. 2004.
- [261] K. M. Jackson, J. Dunning, C. a. Zorman, M. Mehregany, and W. N. Sharpe, "Mechanical properties of epitaxial 3C silicon carbide thin films," *Journal of Microelectromechanical Systems*, vol. 14, no. 4, pp. 664-672, Aug. 2005.
- [262] K. M. Jackson, "Fracture strength, elastic modulus and Poisson's ratio of polycrystalline 3C thin-film silicon carbide found by microsample tensile testing," *Sensors and Actuators A: Physical*, vol. 125, no. 1, pp. 34-40, Oct. 2005.

- [263] W. N. Sharpe, O. Jadaan, G. M. Beheim, G. D. Quinn, and N. N. Nemeth, "Fracture strength of silicon carbide microspecimens," *Journal of Microelectromechanical Systems*, vol. 14, no. 5, pp. 903-913, Oct. 2005.
- [264] C. Serre, "Determination of micromechanical properties of thin films by beam bending measurements with an atomic force microscope," *Sensors and Actuators A: Physical*, vol. 74, no. 1-3, pp. 134-138, Apr. 1999.
- [265] M. Mehregany, L. G. Matus, and D. J. Larkin, "Internal stress and elastic modulus measurements on micromachined 3C-SiC thin films," *IEEE Transactions on Electron Devices*, vol. 44, no. 1, pp. 74-79, 1997.
- [266] A. Briggs, R. Davidge, C. Padgett, and S. Quickenden, "Crushing behaviour of high temperature reactor coated fuel particles," *Journal of Nuclear Materials*, vol. 61, no. 3, pp. 233-242, 1976.
- [267] T.-S. Byun, J. . Hunn, J. . Miller, L. Snead, and J. W. Kim, "Evaluation of Fracture Stress for the SiC Layer of TRISO-Coated Fuel Particles Using a Modified Crush Test Method," *International Journal of Applied Ceramic Technology*, vol. 7, no. 3, pp. 327-337, Nov. 2009.
- [268] K. Minato, K. Fukuda, K. Ikawa, H. Matsushima, and S. Kurobane, "Crushing strength of irradiated Triso coated fuel particles," *Journal of nuclear materials*, vol. 119, no. 2-3, pp. 326-332, 1983.
- [269] T. Ogawa and K. Ikawa, "Crushing strengths of SiC-Triso and ZrC-Triso coated fuel particles," *Journal of Nuclear Materials*, vol. 98, no. 1-2, pp. 18-26, 1981.
- [270] W. J. Lackey, D. P. Stinton, L. E. Davis, and R. L. Beatty, "Crushing strength of high-temperature gas-cooled reactor fuel particles," *Nuclear Technology*, vol. 31, no. 2, pp. 191-201, 1976.
- [271] G. T. van Rooyen, R. D. Preez, J. D. Villiers, and R. Cromarty, "The fracture strength of TRISO-coated particles determined by compression testing between soft aluminium anvils," *Journal of Nuclear Materials*, vol. 403, no. 1-3, pp. 126-134, Aug. 2010.
- [272] I. . van Rooyen, J. H. Neethling, and P. M. van Rooyen, "The influence of annealing temperature on the strength of TRISO coated particles," *Journal of Nuclear Materials*, vol. 402, no. 2-3, pp. 136-146, Jul. 2010.
- [273] R. Püsche et al., "Temperature induced polytype conversion in cubic silicon carbide studied by Raman spectroscopy," *Journal of Applied Physics*, vol. 96, no. 10, p. 5569, 2004.
- [274] E. López-Honorato, D. Yang, J. Tan, P. J. Meadows, and P. Xiao, "Silver Diffusion in Coated Fuel Particles," *Journal of the American Ceramic Society*, vol. 93, no. 10, pp. 3076-3079, Oct. 2010.

- [275] J. Goldstein et al., *Scanning electron microscopy and X-ray microanalysis*, 3rd ed. New York: Springer Science + Media Incorporated, 2003.
- [276] F. Humphreys, “Review grain and subgrain characterisation by electron backscatter diffraction,” *Journal of materials science*, vol. 36, no. 16, pp. 3833–3854, 2001.
- [277] I. . van Rooyen et al., “Effects of phosphorous-doping and high temperature annealing on CVD grown 3C-SiC,” *Nuclear Engineering and Design*, vol. 251, pp. 191 - 202, Nov. 2011.
- [278] J. Oh and D. Choi, “Fabrication of multi-layer CVD-SiC films with different microstructures by manipulating the input gas ratio,” *Journal of materials science letters*, vol. 19, no. 22, pp. 2043–2046, 2000.
- [279] S. G. Cook, J. A. Little, and J. E. King, “Etching and microstructure of engineering ceramics,” *Materials characterization*, vol. 34, no. 1, pp. 1–8, 1995.
- [280] U. Ram and G. Singh, “The growth and defect structure of SiC polytypes studied by chemical etching and x–ray diffraction,” *Journal of Crystal Growth*, vol. 32, no. 2, pp. 197–204, 1976.
- [281] R. Chinn, *Ceramography: Preparation and Analysis of Ceramic Microstructures*, 1st ed. ASM International, 2002, p. 214.
- [282] P. Nordquist, H. Lessoff, and R. Gorman, “A eutectic hydroxide etch for - SiC,” *Materials Letters*, vol. 7, no. 9,10, pp. 316 - 317, 1989.
- [283] K. Shibahara and S. Nishino, “Surface morphology of cubic SiC (100) grown on Si (100) by chemical vapor deposition,” *Journal of crystal growth*, vol. 78, pp. 538-544, 1986.
- [284] K. Bourenane, A. Keffous, G. Nezzal, A. Boukezzata, and S. Naama, “Chemical etching of hot-pressed p-type polycrystalline SiC surfaces by HF/K₂S₂O₈ solutions,” *Surface and Interface Analysis*, vol. 39, no. 5, pp. 392–396, 2007.
- [285] N. Gabouze, A. Keffous, T. Kerdja, and Y. Belaroussi, “Chemical etching investigation of polycrystalline p-type 6H-SiC in HF/Na₂O₂ solutions,” *Applied Surface Science*, vol. 255, no. 15, pp. 6751-6756, May 2009.
- [286] K. P. Skolo, P. Jacobs, J. H. Venter, W. Klopper, and P. L. Crouse, “Wet-chemical dissolution of TRISO-coated simulated high-temperature-reactor fuel particles,” *Journal of Nuclear Materials*, vol. 420, no. 1–3, pp. 342-346, Jan. 2012.
- [287] D. C. Montgomery, *Design and analysis of experiments*, 4th ed. John Wiley & Sons, Inc., 1997.

APPENDIX A: DATA TABLES

1	EXPERIMENTAL CONDITIONS.....	302
2	DEPOSIT MASS AND DEPOSITION EFFICIENCY	304
3	DEPOSIT THICKNESS	306
4	DEPOSITION RATE.....	308
5	DENSITY	310
6	SEM GRAIN SIZE	312
6.1	SURFACE STRUCTURE	312
6.2	CROSS SECTION	313
7	CRUSH STRENGTH	314
8	MICROINDENTATION	317
8.1	HARDNESS.....	317
8.2	FRACTURE TOUGHNESS	319
9	NANO-INDENTATION.....	323
9.1	HARDNESS.....	323
9.2	YOUNG'S MODULUS	325
10	X-RAY DIFFRACTION.....	327
11	RAMAN SPECTROSCOPY	328
12	ELECTRON MICROPROBE ANALYSIS	329

1 EXPERIMENTAL CONDITIONS

Table 1. Experimental conditions for test runs using hot gas inlet.

Test #	Temp. (°C)	Load (g)	Methyltrichlorosilane			Hydrogen		
			Set (vol. %)	Actual (vol. %)	Actual flux(a)	Set (vol. %)	Actual (vol. %)	Actual flux (a)
TR12	1200	40.01	NA	2.047	0.092	NA	11.146	4.095
TR13	1200	40.02	NA	1.257	0.051	NA	10.154	3.684
TR14	1200	40.00	NA	0.682	0.026	NA	9.545	3.465
DR1	1450	40.00	1.50	1.643	0.103	15.0	15.120	5.688
DR3	1350	60.00	0.75	0.796	0.032	17.5	15.062	3.777
DR4	1450	40.06	1.50	1.461	0.061	15.0	10.177	3.823
DR5	1550	60.00	2.25	2.173	0.091	17.5	15.181	3.807
DR6	1350	20.02	2.25	2.271	0.190	12.5	10.081	7.577
DR9	1550	60.04	2.25	2.301	0.113	17.5	17.726	4.442
DR12	1550	20.04	0.75	0.741	0.091	17.5	15.083	11.325
DR17	1350	60.01	2.25	3.676	0.184	17.5	17.765	4.454
DR18	1350	20.04	0.75	1.209	0.127	12.5	12.794	9.606
DR19	1350	20.02	2.25	3.388	0.507	17.5	17.750	13.341
DR20	1350	60.01	0.75	0.722	0.024	12.5	12.313	3.087
DR21	1350	60.01	0.75	0.764	0.036	17.5	17.180	4.308
DR22	1550	20.04	2.50	2.337	0.310	17.5	15.804	11.866
DR23	1350	20.00	0.75	0.761	0.107	17.5	17.152	12.904
DR24	1550	20.01	2.50	2.561	0.247	12.5	11.541	8.679
DR25	1350	60.01	2.50	2.505	0.080	12.5	11.528	2.891
DR26	1450	40.04	1.50	1.625	0.095	15.0	14.190	5.333
HF1	1310	40.01	2.10	2.286	0.098	11.0	10.283	3.867
HF3	1400	40.02	1.50	1.447	0.071	12.5	11.901	4.475
HF4	1490	40.00	0.90	0.919	0.052	14.0	13.733	5.166
HF5	1490	40.01	0.90	0.881	0.050	14.0	13.758	5.174
HF6	1400	40.00	1.50	1.478	0.058	10.0	9.530	3.583
HF7	1310	40.00	0.90	0.885	0.048	14.0	13.701	4.970
HF8	1310	40.00	2.10	2.124	0.111	14.0	13.044	4.747
HF9	1400	40.00	1.50	1.472	0.070	12.5	11.973	4.334
HF10	1400	40.00	1.50	1.550	0.088	15.0	14.231	5.187
HF11	1310	40.00	0.90	0.992	0.043	11.0	10.931	3.976
HF12	1400	40.01	2.50	2.815	0.130	12.5	11.452	4.162
HF13	1490	40.01	2.10	2.284	0.118	14.0	12.902	4.688
HF14	1400	40.03	0.50	0.578	0.028	12.5	12.433	4.512
HF15	1490	40.01	0.90	1.006	0.044	11.0	10.953	3.977
HF16	1400	40.00	1.50	1.558	0.074	12.5	11.940	4.336
HF17	1550	40.00	1.50	1.617	0.078	12.5	12.074	4.386
HF18	1490	40.00	2.10	2.325	0.094	11.0	10.079	3.659
HF19	1250	40.00	1.50	1.639	0.077	12.5	11.774	4.277
HF20	1400	40.00	1.50	1.767	0.082	12.5	11.565	4.202
HF21	1310	35 (b)	2.10	2.412	0.108	11.0	9.879	4.045
HF22	1310	40.00	2.10	2.156	0.095	11.0	10.921	3.974
HF23	1490	40.00	0.90	0.936	0.049	14.0	13.104	4.768
HF24	1400	40.00	1.50	1.607	0.063	10.0	9.865	3.590
HF25	1400	40.00	1.50	1.528	0.073	12.5	12.014	4.372

(a) $\text{mol.m}^{-2}.\text{minute}^{-1}$

(b) Test run started with 40.00 g. Gas flow problems resulted in lost particles.

Table 2. Experimental conditions for test runs using cold gas inlet.

Test #	Temp. (°C)	Load (g)	Methyltrichlorosilane			Hydrogen		
			Set (vol. %)	Actual (vol. %)	Actual flux(a)	Set (vol. %)	Actual (vol. %)	Actual flux(a)
CR1	1400	40.04	1.50	1.44	0.072	12.5	12.080	4.540
CR2	1400	40.01	1.50	1.49	0.074	12.5	12.088	4.546
CR3	1490	40.00	0.90	0.88	0.040	11.0	11.093	4.173
CR4	1490	40.02	2.10	2.12	0.112	14.0	13.207	4.788
CR5	1310	40.02	2.10	2.10	0.111	14.0	13.175	4.779
CR6	1490	40.01	0.90	0.90	0.050	14.0	13.908	5.033
CR9	1400	40.05	1.50	1.55	0.074	12.5	12.001	4.338
CR10	1310	40.02	2.10	2.32	0.095	11.0	10.184	3.702
CR11	1310	40.00	0.90	1.01	0.044	11.0	10.955	3.981
CR12	1490	40.01	2.10	2.28	0.093	11.0	10.162	3.692
CR13	1310	40.02	0.90	0.90	0.049	14.0	13.667	4.961
CR14	1550	40.02	1.50	1.64	0.079	12.5	12.106	4.391
CR15	1400	40.01	1.50	1.50	0.072	12.5	11.971	4.346
CR16	1400	40.01	0.50	0.69	0.035	12.5	12.677	4.603
CR17	1400	40.00	0.50	0.97	0.051	12.5	13.167	4.781
CR18	1250	40.00	1.50	1.77	0.086	12.5	12.150	4.412
CR19	1400	40.00	1.50	1.93	0.074	10.0	9.627	3.497
CR20	1400	40.00	2.50	2.28	0.088	12.5	9.580	3.480
CR21	1400	40.00	2.50	3.15	0.142	12.5	11.109	4.039
CR22	1400	40.00	2.50	2.83	0.125	12.5	10.913	3.969
CR24	1400	40.00	1.50	1.64	0.090	15.0	13.707	4.987
CR25	1400	40.00	0.50	0.63	0.034	12.5	13.462	4.898
CR26	1400	40.00	0.50	0.62	0.031	12.5	12.443	4.528
CR27	1400	40.00	0.50	0.43	0.022	12.5	12.728	4.632
CR28	1400	40.00	1.50	1.53	0.074	12.5	12.058	4.388
TT1	1355	40.00	1.80	2.21	0.095	11.8	10.679	3.886
TT2	1355	40.00	1.80	2.19	0.094	11.8	10.650	3.875
TT3	1355	40.00	1.80	2.16	0.092	11.8	10.640	3.872
TT4	1355	40.00	1.80	2.17	0.093	11.8	10.636	3.870
TT5	1355	40.00	1.80	2.14	0.091	11.8	10.653	3.876
MTS1	1200	40.00	1.97	2.21	0.108	13.7	12.129	4.413

 (a) mol.m⁻².minute⁻¹

2 DEPOSIT MASS AND DEPOSITION EFFICIENCY

Table 3. Deposit mass and deposition efficiency: Hot gas inlet system.

Test	MTS Used (g)	SiC Deposited (g)	Percentage Efficiency (%)
TR12*	43.29	5.03	43.31
TR13	25.87	4.18	60.23
TR14	13.13	2.45	69.48
DR1	101.11	19.88	73.30
DR3	47.14	9.22	72.93
DR4	60.50	13.37	82.38
DR5	135.20	32.03	88.31
DR6	93.84	14.86	59.03
DR9	83.78	16.98	75.55
DR12	37.61	7.47	74.04
DR17	99.19	15.59	58.59
DR18	65.93	11.32	64.00
DR19*	70.89	8.32	43.75
DR20	71.79	15.49	80.43
DR21	101.52	20.52	75.35
DR22	38.21	7.73	75.41
DR23	48.34	8.11	62.54
DR24	32.42	7.34	84.40
DR25	106.84	23.09	80.56
DR26	65.74	14.63	82.96
HF1	73.94	14.28	71.99
HF3	52.52	9.67	68.63
HF4	45.10	9.39	77.61
HF5	56.34	12.97	85.81
HF6	52.52	11.66	82.76
HF7	75.19	14.89	73.82
HF8	77.38	14.01	67.49
HF9	53.78	11.60	80.40
HF10	67.34	13.74	76.06
HF11	75.31	14.54	71.97
HF12	66.47	13.41	75.20
HF13	58.37	13.23	84.49
HF14	69.45	14.39	77.24
HF15	55.00	12.54	84.99
HF16	56.77	11.86	77.88
HF17	53.06	12.17	85.50
HF18	52.91	11.90	83.84
HF19	85.11	14.50	63.51
HF20	62.52	13.04	77.75
HF21	73.40	13.12	66.63
HF22	67.50	12.02	66.38
HF23	57.09	12.83	83.77
HF24	59.17	12.25	77.17
HF25	56.02	11.33	75.39

(*)Possible leaks on gas feed tube due to inlet blockage

Table 4. Deposit mass and deposition efficiency: Cold gas inlet system.

Test	MTS Used (g)	SiC Deposited (g)	Percentage Efficiency (%)
CR1	52.91	11.18	78.77
CR2	54.96	11.47	77.80
CR3	49.44	11.3	85.20
CR4	61.11	13.70	83.57
CR5	77.55	13.62	65.47
CR6	55.88	12.54	83.65
CR9	56.82	11.81	77.48
CR10	77.41	14.61	70.35
CR11	76.51	15.60	76.01
CR12	50.78	11.77	86.40
CR13	75.47	14.74	72.81
CR14	51.22	12.05	87.70
CR15	54.93	11.50	78.04
CR16	84.04	18.08	80.20
CR17	127.91	27.34	79.68
CR18	85.08	14.75	64.63
CR19	72.14	15.84	81.85
CR20	44.81	9.66	80.36
CR21	72.31	15.16	78.15
CR22	63.8	12.97	75.78
CR24	71.92	14.43	74.79
CR25	80.28	17.45	81.03
CR26	75.11	15.67	77.77
CR27	53.15	11.15	78.20
CR28	56.22	12.16	80.63
TT1	62.92	12.31	72.93
TT2	109.57	21.55	73.32
TT3	75.25	15.40	76.29
TT4	44.25	8.72	73.46
TT5	85.42	16.63	72.57
MTS1	109.81	16.77	56.93

3 DEPOSIT THICKNESS

Table 5. Deposit thickness: Hot gas inlet.

Test #	Deposit Thickness (μm) (1)						
	He Pycn. (Particle)	He Pycn. (Powder)	Water Pycn.	SEM	Filar Microm.	Line Intercept	Radius Diff.
TR12	13.2		11.8				
TR13	8.3		7.5				
TR14	6.0		6.5				
DR1	52.2		51.2				
DR3	16.1		16.1				
DR4	36.6		42.9				
DR5	54.4		53.7				
DR6	91.1		89.4				
DR9	35.5		34.9				
DR12	37.7		37.1				
DR17	30.9		29.7				
DR18	61.4		60.5				
DR19	47.1		46.1				
DR20	30.4		29.5				
DR21	38.3		37.8				
DR22	41.6		40.6				
DR23	45.6		44.8				
DR24	40.7		40.4				
DR25	43.5		43.8				
DR26	39.1		38.5				
HF1	41.3	39.5	40.5			35.4	
HF3	32.8	31.7	32.3			30.7	
HF4	27.0	26.2	25.9		25.4	25.4	
HF5	35.9	34.0	36.0		33.3	31.6	
HF6	33.1	31.1	33.0			28.0	
HF7	36.3	36.7	36.8	41.7			
HF8	37.0	37.1	31.3	38.3			
HF9	27.6	27.7	28.4		28.4		
HF10	34.4	34.9	34.6	38.7		33.3	
HF11	39.7	39.7	39.1	41.9			
HF12	37.3	36.2	37.8	41.2			
HF13	33.9	33.9	34.2	36.7		31.1	
HF14	36.8	36.3	36.7	37.2			
HF15	31.5	31.9	31.5	31.4			
HF16	32.2	32.1	31.4	32.2			
HF17	32.9	33.0	32.3	34.2			
HF18	32.8	31.0	30.0	33.1			
HF19	36.8	36.9	36.7	41.0			
HF20	34.6	34.2		34.1	31.7		
HF21	38.6	38.6					
HF22	33.3	32.8		34.0		30.1	
HF23	35.1	34.7		33.8	30.5		
HF24	30.9	30.8		33.1			
HF25	29.5	29.0					

Table 6. Deposit thickness: Cold gas inlet.

Test #	Deposit Thickness (μm) (1)						
	He Pycn. (Particle)	He Pycn. (Powder)	Water Pycn.	SEM	Filar Microm.	Line Intercept	Radius Diff.
CR1	31.3	30.3	30.6				
CR2	32.7	30.0	32.4				
CR3	30.9	29.7	29.7	36.0			
CR4	33.7	34.8	34.7	34.4			
CR5	36.3	36.8	36.0	37.3			
CR6	30.2	30.2	31.0	32.5			
CR9	29.5	30.3	30.4	29.9			
CR10	39.3	39.2	39.2	42.0			
CR11	39.5	40.3	40.2	42.6			
CR12	32.2	31.9	31.8	32.0			
CR13	37.2	37.5	36.4	39.4			
CR14	29.5	29.5	29.4	32.1			
CR15	29.7	29.7	30.1				
CR16	43.2	44.0	42.9				
CR17	64.4	64.5	64.4		63.7		
CR18	36.1	36.0	35.5	41.2			
CR19	41.1	40.3	40.2	42.8			
CR20	25.5	25.7			24.7		
CR21	41.0	41.0					
CR22	34.9	34.5		36.4	33.8		
CR24	36.4	36.6		38.3			
CR25	41.8	42.4					
CR26	39.1	39.8		42.6			
CR27	28.9	29.0					
CR28	28.1	28.3			30.1		
TT1	33.9	33.4		36.2	32.4	32.8	37.1
TT2	54.9	55.4		59.0	53.8	53.4	54.7
TT3	40.2	39.9		41.4	38.8	38.6	42.0
TT4	24.5	24.3		22.6	22.6	21.9	25.8
TT5	45.4	45.3		47.7	43.4	43.7	43.0
MTS1	43.4	44.4		45.7	44.2	44.2	

(1) Abbreviation used for the thickness measurement methods:

- He Pycn. (Particle) Calculated from the particle density and particles mass change.
Density of whole particles measured using a helium pycnometer
- He Pycn. (Powder) Thickness calculated from the deposit density and particle mass change. Powdered deposit density measured using a helium pycnometer.
- Water Pycn. Calculated from the particle density and particles mass change.
Density of whole particles measured using a pycnometer bottle
- SEM Thickness measured directly on SEM images of polished cross section
- Filar Microm. Thickness measured on polished cross section using a microscope mounted filar micrometer
- Line Intercept Line intercept method using optical micrograph of polished cross section
- Radius Diff. Difference in radius measured on optical micrographs of polished cross section

4 DEPOSITION RATE

Table 7. Deposition rate: Hot gas inlet.

Test #	Deposition Rate ($\mu\text{m}\cdot\text{minute}^{-1}$)	Deposition Rate ($\text{g}\cdot\text{m}^{-2}\cdot\text{minute}^{-1}$)	Deposition Rate ($\text{mol}\cdot\text{m}^{-2}\cdot\text{minute}^{-1}$)
TR12	0.472	1.619	0.040
TR13	0.277	1.248	0.031
TR14	0.200	0.731	0.018
DR1	0.870	3.037	0.076
DR3	0.268	0.939	0.023
DR4	0.610	2.039	0.051
DR5	0.906	3.262	0.081
DR6	1.518	4.536	0.113
DR9	1.184	3.456	0.086
DR12	0.753	2.733	0.068
DR17	1.410	4.349	0.108
DR18	0.974	3.287	0.082
DR19	2.772	8.963	0.224
DR20	0.253	0.789	0.020
DR21	0.333	1.090	0.027
DR22	2.773	9.428	0.235
DR23	0.830	2.703	0.067
DR24	2.541	8.405	0.210
DR25	0.805	2.609	0.065
DR26	0.931	3.190	0.080
HF1	0.898	2.845	0.071
HF3	0.729	1.969	0.049
HF4	0.509	1.624	0.040
HF5	0.520	1.722	0.043
HF6	0.601	1.943	0.048
HF7	0.394	1.390	0.035
HF8	0.902	2.937	0.073
HF9	0.614	2.213	0.055
HF10	0.764	2.622	0.065
HF11	0.385	1.212	0.030
HF12	1.243	3.837	0.096
HF13	1.169	3.916	0.098
HF14	0.255	0.857	0.021
HF15	0.426	1.455	0.036
HF16	0.715	2.263	0.056
HF17	0.822	2.613	0.065
HF18	0.992	3.092	0.077
HF19	0.566	1.915	0.048
HF20	0.769	2.488	0.062
HF21	0.856	2.814	0.070
HF22	0.792	2.457	0.061
HF23	0.509	1.597	0.040
HF24	0.561	1.913	0.048
HF25	0.656	2.162	0.054

Table 8. Deposition rate: Cold gas inlet.

Test	Deposition Rate ($\mu\text{m}\cdot\text{minute}^{-1}$)	Deposition Rate ($\text{g}\cdot\text{m}^{-2}\cdot\text{minute}^{-1}$)	Deposition Rate ($\text{mol}\cdot\text{m}^{-2}\cdot\text{minute}^{-1}$)
CR1	0.695	2.275	0.057
CR2	0.726	2.336	0.058
CR3	0.412	1.381	0.034
CR4	1.053	3.674	0.092
CR5	0.886	2.851	0.071
CR6	0.458	1.631	0.041
CR9	0.655	2.251	0.056
CR10	0.819	2.612	0.065
CR11	0.383	1.301	0.032
CR12	1.007	3.158	0.079
CR13	0.408	1.390	0.035
CR14	0.777	2.722	0.068
CR15	0.660	2.194	0.055
CR16	0.302	1.085	0.027
CR17	0.435	1.586	0.040
CR18	0.622	2.184	0.054
CR19	0.721	2.386	0.060
CR20	0.850	2.765	0.069
CR21	1.368	4.339	0.108
CR22	1.162	3.712	0.093
CR24	0.775	2.636	0.066
CR25	0.298	1.070	0.027
CR26	0.272	0.934	0.023
CR27	0.200	0.665	0.017
CR28	0.625	2.320	0.058
TT1	0.870	2.710	0.068
TT2	0.796	2.682	0.067
TT3	0.838	2.755	0.069
TT4	0.876	2.674	0.067
TT5	0.826	2.596	0.065
MTS1	0.723	2.400	0.060

5 DENSITY

Table 9. Deposit density: Hot gas inlet.

Test #	Pycnometer Bottle (g.cm ⁻³)	Helium Pycnometer (Whole particles) (g.cm ⁻³)	Helium Pycnometer (Powdered deposit) (g.cm ⁻³)
TR12	3.130	2.811	
TR13	3.147	2.910	
TR14		2.724	
DR1	3.153	3.104	
DR3	3.153	3.188	
DR4	3.035	3.225	
DR5	3.177	3.155	
DR6	3.019	2.970	
DR9	3.073	3.032	
DR12	3.141	3.112	
DR17	2.985	2.880	
DR18	3.002	2.971	
DR19	2.984	2.934	
DR20	3.036	2.967	
DR21	3.038	3.011	
DR22	3.117	3.056	
DR23	2.995	2.955	
DR24	3.060	3.061	
DR25	2.950	2.989	
DR26	3.107	3.079	
HF1	2.966	2.917	3.043
HF3	3.074	3.044	3.141
HF4	3.128	3.018	3.104
HF5	3.020	3.053	3.207
HF6	3.011	3.022	3.202
HF7	3.109	3.136	3.100
HF8	3.193	3.045	3.036
HF9	3.164	3.212	3.201
HF10	3.128	3.181	3.136
HF11	3.063	3.039	3.037
HF12	2.991	3.049	3.133
HF13	3.112	3.160	3.156
HF14	3.157	3.155	3.190
HF15	3.173	3.177	3.140
HF16	3.170	3.099	3.111
HF17	3.175	3.128	3.114
HF18	3.257	2.973	3.132
HF19	3.030	3.029	3.023
HF20		3.087	3.122
HF21		3.041	3.038
HF22		2.970	3.010
HF23		3.100	3.133
HF24		3.164	3.173
HF25		3.095	3.145

Table 10. Deposit density: Cold gas inlet.

Test	Pycnometer Bottle (g.cm ⁻³)	Helium Pycnometer (Whole particles) (g.cm ⁻³)	Helium Pycnometer (Powdered deposit) (g.cm ⁻³)
CR1	3.027	2.971	3.086
CR2	2.973	2.964	3.098
CR3	3.143	3.035	3.150
CR4	3.102	3.175	3.084
CR5	3.041	3.014	2.976
CR6	3.157	3.199	3.204
CR9	3.107	3.153	3.073
CR10	3.076	3.007	3.014
CR11	3.028	3.098	3.043
CR12	3.119	3.094	3.126
CR13	3.157	3.096	3.068
CR14	3.222	3.203	3.205
CR15	3.081	3.136	3.138
CR16	3.218	3.206	3.151
CR17	3.167	3.178	3.177
CR18	3.115	3.069	3.074
CR19	3.132	3.070	3.124
CR20		3.064	3.037
CR21		3.052	3.056
CR22		3.076	3.103
CR24		3.108	3.097
CR25		3.188	3.145
CR26		3.157	3.111
CR27		3.136	3.124
CR28		3.153	3.140
TT1		2.996	3.038
TT2		3.050	3.027
TT3		3.008	3.031
TT4		2.990	3.014
TT5		3.015	3.023
MTS1		3.043	2.977

6 SEM GRAIN SIZE

6.1 SURFACE STRUCTURE

Table 11. Size of surface features measured by line intercept method applied to secondary electron images.

Test #	Dimension (μm)	Standard Deviation (μm)	Count
HF7	3.562	1.954	477
HF8	4.573	2.708	353
HF10	3.981	2.081	425
HF11	3.520	1.803	479
HF12	3.489	1.944	477
HF13	1.998	1.078	869
HF14	1.846	0.940	928
HF15	2.793	1.674	606
HF16	3.084	1.683	542
HF17	3.668	2.069	233
HF18	2.181	1.187	790
HF19	4.300	2.464	390
HF22	4.224	2.609	394
HF23	2.708	1.559	634
HF24	5.342	2.997	305
CR3	2.284	1.314	745
CR4	1.379	0.567	1258
CR5	3.919	2.445	422
CR6	2.110	1.118	813
CR9	5.615	3.057	309
CR10	7.146	4.985	243
CR11	5.071	2.655	347
CR12	2.935	1.815	581
CR13	4.259	2.224	355
CR14	2.472	1.597	694
CR18	4.307	2.513	386
CR19	4.356	2.578	375
CR22	4.693	3.106	349
CR24	3.647	2.160	463
CR26	1.760	1.723	960
TT1	5.103	2.842	156
TT2	5.373	3.456	305
TT3	4.402	2.740	376
TT4	3.878	2.321	430
TT5	4.278	2.881	388
MTS1	5.963	3.328	274

6.2 CROSS SECTION

Table 12. Cross section grain size as measured by line intercept method applied to backscatter electron images.

Test #	Dimension (µm)	Standard Deviation (µm)	Count
Combined			
HF13	1.934	1.059	1391
HF14	1.489	0.745	1812
HF15	2.290	1.683	1135
HF16	1.546	0.723	754
HF17	2.549	1.984	1007
HF18	2.247	1.362	1116
HF23	2.380	1.595	1047
CR3	2.025	1.396	1076
CR4	1.337	0.596	1928
CR6	1.949	1.262	1239
CR12	1.624	0.831	1484
CR14	2.172	1.554	1105
Radial			
HF13	2.186	1.223	670
HF14	1.733	0.862	839
HF15	2.916	2.196	470
HF16	1.809	0.827	317
HF17	3.477	2.594	391
HF18	2.644	1.681	494
HF23	2.919	2.028	444
CR3	2.696	1.857	371
CR4	1.450	0.639	954
CR6	2.457	1.592	516
CR12	1.822	0.938	698
CR14	2.791	1.996	457
Tangential			
HF13	1.699	0.813	721
HF14	1.279	0.545	973
HF15	1.847	0.978	665
HF16	1.356	0.567	437
HF17	1.961	1.130	616
HF18	1.931	0.929	622
HF23	1.983	1.011	603
CR3	1.672	0.894	705
CR4	1.226	0.527	974
CR6	1.586	0.780	723
CR12	1.448	0.677	786
CR14	1.735	0.921	648

7 CRUSH STRENGTH

Table 13. Soft anvil crush strength of test runs using CPT-T-G130 particles as starting material.

Test	Count	Average Strength (g)	Standard Deviation (g)	Characteristic Strength (g)	Weibull Modulus	Rejects
G130	105	12072	2203	12732	7.03	0
DR1	51	8522	727	8858	13.42	1
DR3	50	4747	507	4928	12.26	2
DR4	53	6994	755	7503	10.21	3
DR5	55	9925	776	10161	12.93	1
DR6	53	10915	1064	11512	12.58	1
DR9	55	6951	563	7149	13.30	0
DR12	52	8467	576	8909	13.48	6
DR17	53	6659	432	7005	13.64	4
DR18	53	7006	697	7410	13.08	0
DR19	53	7075	589	7265	11.87	0
DR20	54	6926	502	7120	13.71	0
DR21	54	7813	735	8003	13.92	0
DR22	55	6724	759	6956	11.99	0
DR23	55	4701	367	5028	12.23	0
DR24	53	6400	754	6935	11.80	1
DR25	54	7032	633	7539	11.31	0
DR26	54	6818	518	7251	12.55	0
HF1	50	7712	778	8060	10.38	0
HF3	50	6470	503	6651	13.68	1
HF4	50	5937	526	6103	15.37	0
HF5	50	7153	647	7415	11.80	1
HF6	50	6644	560	6876	16.49	0
CR1	50	6671	375	6850	18.88	2
CR2	50	6514	513	6705	15.57	0
CR3	50	6471	435	6700	16.34	1

Table 14. Soft anvil crush strength of test runs using CPT-T-G140 particles as starting material.

Test	Count	Average Strength (g)	Standard Deviation (g)	Characteristic Strength (g)	Weibull Modulus	Rejects
G140	105	7346	1572	7779	5.77	0
HF7	50	5872	480	6040	14.59	0
HF8	50	6116	581	6349	11.01	1
HF9	50	5354	570	5584	12.03	0
HF10	50	5710	587	5936	11.22	0
HF11	50	5798	525	5967	14.52	0
HF12	50	5053	560	5187	11.39	1
HF13	52	5874	458	6114	15.98	0
HF14	50	6338	472	6520	14.33	0
HF15	50	5773	390	5892	16.86	0
HF16	50	5487	651	5745	10.74	0
HF17	50	5465	529	5685	12.12	0
HF18	50	5410	505	5593	12.93	1
HF19	50	7678	732	7993	12.73	0
HF20	69	5300	387	5773	10.54	3
HF21	50	7216	534	7490	13.22	0
HF22	50	6880	532	7143	13.93	2
HF23	57	5453	523	5639	11.71	0
HF24	55	5534	617	5794	9.80	0
HF25	51	5248	520	5439	11.19	3
CR4	50	6420	796	4000	3.95	0
CR5	50	6833	723	7136	10.59	0
CR6	50	5754	631	6009	11.67	0
CR9	48	5690	505	5905	12.17	4
CR10	50	8031	573	8293	15.32	2
CR11	50	6171	695	6470	10.57	0
CR12	50	6216	620	6481	11.58	0
CR13	50	5885	547	6083	12.84	1
CR14	50	5452	411	5602	14.27	0
CR15	50	5573	472	5715	16.33	0
CR16	50	8399	893	8779	10.84	1
CR17	50	11045	865	11321	15.90	0
CR18	50	7743	734	8008	12.06	0
CR19	50	6956	644	7217	10.64	4
CR20	50	5309	463	5532	15.15	1
CR21	50	6474	616	6666	12.96	1
CR22	50	5847	689	6169	10.73	2
CR24	50	6158	623	6354	11.60	0
CR25	50	7081	677	7358	12.72	0
CR26	50	6995	466	7179	17.63	0
CR27	56	4970	459	5182	14.68	0
CR28	56	5254	524	5495	10.98	0
TT1	57	6272	537	6540	13.25	1
TT2	55	8820	823	9141	11.89	0
TT3	56	7296	431	7607	17.54	0
TT4	50	5521	445	5656	14.36	5
TT5	52	7192	612	7537	14.45	2
MTS1	74	8845	881	9211	10.33	0

Table 15. Hard anvil crush strength of test runs using CPT-T-G140 particles as starting material.

Test	Count	Average Strength (g)	Standard Deviation (g)	Characteristic Strength (g)	Weibull Modulus	Rejects
G140	53	2681	364	2795	7.91	1
CR4	202	1680	462	1860	4.39	0
CR5	55	1468	335	1549	5.52	0
CR6	56	1316	262	1405	5.34	0
CR9	50	1547	506	1593	4.47	4
CR10	54	1599	358	1706	4.93	0
CR11	56	1390	329	1483	5.39	0
CR12	55	1333	311	1407	4.91	0
CR13	56	1348	209	1425	7.48	1
CR14	55	1197	311	1262	4.93	0
CR15	56	1181	291	1261	4.88	0
CR16	56	1745	265	1840	7.11	0
CR17	57	2529	384	2686	6.89	0
CR18	55	1408	323	1502	4.96	0
CR19	59	1643	333	1722	5.84	0
CR20	59	1056	181	1094	6.74	0
CR21	56	1480	274	1597	6.36	0
CR22	57	1411	313	1505	4.91	0
CR24	60	1366	294	1468	4.79	0
CR25	55	1536	262	1627	6.44	0
CR26	57	1662	364	1804	4.93	0
CR27	56	1360	328	1461	4.64	0
CR28	63	1273	280	1344	6.76	0
TT1	55	1404	360	1546	4.01	0
TT2	56	2048	272	2144	9.26	0
TT3	54	1566	313	1659	5.89	0
TT4	54	1054	231	1105	5.96	0
TT5	55	1653	281	1767	6.42	0
MTS1	54	1895	379	1984	6.03	0

8 MICRO-INDENTATION

8.1 HARDNESS

Table 16. Vickers microhardness: Hot gas inlet.

Test #	Load: 50 g		Load: 100 g			
	Count	Hardness (GPa)	Count	Radial Diagonal (μm)	Tangential Diagonal (μm)	Average Hardness (GPa)
HF1	0		21	8.241	8.181	26.978
HF3	4	29.934	19	8.207	8.267	28.496
HF4	4	31.535	7	7.997	8.174	28.713
HF5	4	28.048	19	7.998	8.144	29.395
HF6	3	30.551	13	8.223	8.275	26.519
HF7	4	27.899	36	8.070	8.083	28.393
HF8	4	31.095	20	7.991	8.119	29.727
HF9	6	27.511	3	8.163	8.179	27.998
HF10	4	28.516	22	7.902	8.005	28.784
HF11	4	31.985	23	7.732	7.874	29.787
HF12	3	32.126	18	7.903	7.646	30.325
HF13	4	29.515	20	8.101	8.049	29.300
HF14	4	30.368	22	7.949	8.019	28.856
HF15	4	27.668	10	8.193	8.282	26.701
HF16	4	29.361	7	8.015	8.103	28.627
HF17	4	28.464	11	8.203	8.227	27.755
HF18	4	29.868	7	8.202	8.391	25.780
HF19	4	26.972	33	8.112	8.290	26.769
HF20	3	28.755	24	8.129	8.195	27.326
HF21	4	28.259	18	7.761	8.038	28.928
HF22	3	27.912	26	8.301	8.425	25.307
HF23	4	27.442	19	8.271	8.220	27.072
HF24	4	30.832	16	7.781	7.855	29.049
HF25	4	28.470	2	8.131	8.097	27.672

Table 17. Vickers micro-hardness: Cold inlet.

Test #	Load: 50 g		Load: 100 g			
	Count	Hardness (GPa)	Count	Radial Diagonal (μm)	Tangential Diagonal (μm)	Average Hardness (GPa)
CR1	4	29.013	15	8.242	8.251	26.834
CR2	4	28.597	17	8.128	8.177	27.323
CR3	3	25.501	12	8.274	8.363	26.498
CR4	4	28.891	21	8.057	8.174	27.834
CR5	2	29.177	19	8.458	8.505	25.667
CR6	4	30.162	10	8.328	8.405	24.844
CR9	4	27.308	16	7.870	8.031	29.339
CR10	3	29.778	22	8.401	8.467	26.073
CR11	4	30.088	19	8.087	8.089	27.841
CR12	3	28.437	14	8.108	8.167	27.555
CR13	4	30.031	20	8.029	8.162	27.559
CR14	4	31.695	14	8.170	8.198	27.672
CR15	4	28.542	16	8.198	8.351	24.912
CR16	4	26.135	23	7.939	8.089	28.210
CR17	4	30.814	20	7.874	7.808	30.073
CR18	4	28.251	23	8.129	8.226	27.308
CR19	3	26.058	18	8.007	8.068	28.265
CR20	4	29.013	0			
CR21	4	29.308	21	8.228	8.108	27.313
CR22	4	27.160	19	8.234	8.392	25.792
CR24	3	26.476	23	8.145	8.238	26.840
CR25	4	30.782	20	8.209	8.213	27.100
CR26	4	26.599	20	7.815	7.842	29.789
CR27	3	27.654	0			
CR28	4	30.664	5	8.216	8.161	26.571
TT1	4	24.928	20	8.204	8.333	26.938
TT2	4	26.967	19	8.607	8.664	24.306
TT3	4	28.458	18	8.482	8.729	24.433
TT4	4	30.458	0			
TT5	4	28.407	20	8.242	8.353	27.066
MTS1			40	8.938	8.987	22.639

8.2 FRACTURE TOUGHNESS

Table 18. Vickers indent crack length. Hot gas inlet.

Test #	Radial				Tangential			
	l (μm)	σ (μm)	c/a	Count	l (μm)	σ (μm)	c/a	Count
HF1	3.019	0.999	1.735	29	5.069	1.700	2.235	39
HF3	2.984	0.828	1.724	28	8.542	2.805	3.074	35
HF4	3.544	0.697	1.877	10	15.071	6.252	4.728	14
HF5	5.288	5.119	2.308	8	7.765	2.578	2.921	32
HF6	3.104	1.011	1.753	6	11.640	4.244	3.822	24
HF7	3.310	0.850	1.820	68	5.508	1.320	2.364	70
HF8	3.026	0.825	1.751	30	4.738	1.379	2.176	30
HF9	4.087	0.596	2.000	2	11.083	3.891	3.713	4
HF10	3.878	0.939	1.975	37	6.543	2.470	2.645	41
HF11	3.551	0.956	1.910	32	5.119	1.704	2.312	37
HF12	3.767	1.279	1.969	27	5.670	2.199	2.458	30
HF13	4.050	1.160	2.003	33	7.339	2.370	2.818	38
HF14	3.847	1.243	1.964	31	5.036	1.631	2.261	37
HF15	4.501	1.193	2.093	8	9.207	2.046	3.235	18
HF16	4.463	0.685	2.107	7	9.491	3.418	3.355	14
HF17	4.246	1.743	2.034	7	9.278	2.866	3.259	21
HF18	4.996	1.021	2.204	12	8.606	3.374	3.075	14
HF19	3.245	1.190	1.791	49	4.321	1.245	2.054	54
HF20	3.851	1.260	1.944	36	6.927	2.824	2.697	42
HF21	3.495	0.712	1.885	36	5.420	1.376	2.372	33
HF22	3.251	0.871	1.778	42	6.031	1.849	2.442	47
HF23	4.560	1.232	2.106	18	8.596	2.813	3.085	32
HF24	4.794	1.742	2.226	27	8.094	2.443	3.071	29
HF25	6.372	0.800	2.571	2	12.324	3.947	4.038	4

Table 19. Vickers indent crack length. Cold gas inlet.

Test #	Radial				Tangential			
	l (µm)	σ (µm)	c/a	Count	l (µm)	σ (µm)	c/a	Count
CR1	2.519	0.911	1.611	22	11.265	4.119	3.732	30
CR2	2.718	0.665	1.667	21	9.556	4.011	3.344	33
CR3	4.177	1.429	2.004	17	12.594	3.315	4.028	24
CR4	4.838	1.422	2.192	37	7.489	1.915	2.846	42
CR5	3.280	0.916	1.773	26	5.386	1.743	2.270	27
CR6	5.168	1.517	2.235	13	8.710	2.257	3.082	20
CR9	3.244	1.315	1.816	20	9.383	4.336	3.360	32
CR10	3.281	1.068	1.778	42	5.307	1.347	2.259	43
CR11	3.793	0.836	1.938	37	5.053	1.028	2.249	35
CR12	4.257	1.265	2.046	20	8.034	2.548	2.975	28
CR13	3.703	1.273	1.915	38	6.157	1.497	2.521	36
CR14	5.472	1.377	2.337	16	10.373	3.209	3.535	28
CR15	4.677	1.181	2.130	28	9.219	3.531	3.228	31
CR16	3.685	1.105	1.920	36	6.124	2.175	2.528	35
CR17	4.781	1.269	2.220	34	4.588	1.158	2.170	32
CR18	3.866	0.913	1.946	33	5.165	2.170	2.263	32
CR19	3.441	1.159	1.856	22	3.332	1.373	1.829	22
CR20	No acceptable indents							
CR21	3.621	1.481	1.887	37	4.058	1.709	1.994	37
CR22	3.820	1.479	1.919	25	4.662	1.899	2.122	25
CR24	3.962	1.227	1.967	37	6.381	2.214	2.558	33
CR25	4.531	0.920	2.104	33	4.820	1.713	2.174	37
CR26	4.090	1.094	2.045	37	4.699	1.345	2.200	37
CR27	No acceptable indents							
CR28	4.504	2.106	2.100	4	9.939	2.553	3.428	7
TT1	3.821	1.065	1.924	23	3.779	1.898	1.914	17
TT2	4.091	1.210	1.947	37	2.765	1.257	1.640	18
TT3	3.402	0.769	1.791	28	4.203	1.248	1.977	22
TT4	No acceptable indents							
TT5	3.565	0.911	1.859	36	3.805	1.270	1.917	22
TT5	2.519	0.911	1.611	22	11.265	4.119	3.732	30

Table 20. Fracture toughness: Hot gas inlet. Fracture toughness calculated using the Liang, Anstis and Evans-Davis model. Calculations performed using hardness and Young's modulus values determined by nano-indentation. Tangential cracks corrected to compensate for thickness effects.

Test #	Fracture Toughness - Radial (MPa.m ^{0.5})			Fracture Toughness - Tangential (MPa.m ^{0.5})		
	Liang	Anstis	Evans-Davis	Liang	Anstis	Evans-Davis
HF1	2.417	2.340	2.730	2.121	2.105	2.637
HF3	2.657	2.341	2.905	2.111	1.943	2.729
HF4	2.302	2.175	2.767	1.774	1.692	2.509
HF5	1.873	1.658	2.580	2.016	1.913	2.750
HF6	2.785	2.374	3.055	1.552	1.316	2.359
HF7	2.360	2.344	2.796	2.318	2.373	2.807
HF8	2.287	2.388	2.661	2.464	2.631	2.744
HF9	2.094	1.944	2.643	2.455	2.435	2.854
HF10	2.155	2.057	2.714	2.178	2.165	2.764
HF11	2.155	2.292	2.717	2.105	2.250	2.699
HF12	2.055	2.157	2.651	2.242	2.402	2.752
HF13	2.268	2.065	2.843	2.184	2.095	2.858
HF14	2.273	2.191	2.847	2.745	2.811	3.093
HF15	2.369	1.867	2.949	2.094	1.795	2.902
HF16	2.151	1.863	2.770	1.847	1.674	2.643
HF17	2.326	1.935	2.879	1.817	1.584	2.638
HF18	1.836	1.537	2.429	2.187	2.015	2.694
HF19	2.392	2.291	2.769	2.895	2.944	2.998
HF20	2.485	2.083	2.971	2.378	2.156	3.007
HF21	2.155	2.411	2.717	2.087	2.316	2.679
HF22	2.583	2.355	2.921	3.097	3.051	3.170
HF23	2.282	1.857	2.880	1.825	1.571	2.668
HF24	1.821	1.724	2.506	2.491	2.540	2.893
HF25	1.640	1.347	2.337	1.710	1.525	2.506

Table 21. Fracture toughness: Cold gas inlet tests. Fracture toughness calculated using the Liang, Anstis and Evans-Davis model. Calculations performed using hardness and Young's modulus values determined by nano-indentation. Tangential cracks corrected to compensate for thickness effects.

Test #	Fracture Toughness - Radial (MPa.m ^{0.5})			Fracture Toughness - Tangential (MPa.m ^{0.5})		
	Liang	Anstis	Evans-Davis	Liang	Anstis	Evans-Davis
CR1	3.265	2.816	3.314	1.819	1.584	2.664
CR2	3.022	2.687	3.197	2.375	2.212	3.000
CR3	2.514	2.045	3.047	1.698	1.427	2.566
CR4	2.154	1.815	2.824	2.114	1.922	2.894
CR5	2.511	2.305	2.839	2.433	2.362	2.861
CR6	2.040	1.608	2.666	2.679	2.404	3.095
CR9	2.432	2.321	2.850	2.141	2.101	2.754
CR10	2.404	2.306	2.759	2.138	2.118	2.682
CR11	2.211	2.152	2.749	2.179	2.196	2.769
CR12	2.264	1.959	2.846	2.406	2.253	2.994
CR13	2.274	2.186	2.789	2.037	2.013	2.706
CR14	1.902	1.579	2.590	2.194	2.012	2.876
CR15	2.243	1.783	2.840	2.705	2.422	3.169
CR16	2.466	2.306	3.000	1.828	1.725	2.658
CR17	2.056	1.952	2.806	2.056	2.035	2.858
CR18	2.203	2.182	2.757	2.669	2.790	2.990
CR19	2.391	2.399	2.884	3.132	3.325	3.200
CR22	2.585	2.181	3.053	3.772	3.580	3.582
CR24	2.137	2.103	2.697	2.036	2.059	2.676
CR25	2.102	1.896	2.728	2.240	2.161	2.867
CR26	2.150	2.075	2.787	2.420	2.459	2.961

9 NANO-INDENTATION

9.1 HARDNESS

Table 22. Nano-indentation hardness: Hot gas inlet

TEST	INDENTS	HARDNESS (GPa)	STANDARD DEVIATION (GPa)
HF1	60	31.816	1.479
HF3	60	33.812	1.712
HF4	60	33.212	2.107
HF5	60	34.049	2.023
HF6	60	34.668	2.289
HF7	60	32.343	1.355
HF8	60	31.315	1.284
HF9	60	32.668	1.742
HF10	60	33.850	1.587
HF11	60	32.823	1.662
HF12	60	33.147	1.629
HF13	60	34.131	1.913
HF14	60	33.670	2.150
HF15	60	36.117	2.600
HF16	60	35.125	1.867
HF17	60	35.020	1.907
HF18	60	33.342	1.840
HF19	60	32.151	1.710
HF20	60	35.464	2.059
HF21	60	31.153	1.445
HF22	60	32.257	1.756
HF23	60	35.231	2.426
HF24	60	34.543	1.896
HF25	60	34.760	2.136

Table 23. Nano-indentation hardness: Cold gas inlet.

TEST	INDENTS	HARDNESS (GPa)	STANDARD DEVIATION (GPa)
CR1	60	34.887	1.388
CR2	60	34.760	1.173
CR3	60	35.032	1.881
CR4	60	35.345	1.741
CR5	60	31.199	2.257
CR6	60	34.551	2.232
CR9	60	34.182	2.487
CR10	60	30.553	1.596
CR11	60	32.542	1.747
CR12	60	34.718	1.775
CR13	60	32.813	1.227
CR14	60	34.625	1.668
CR15	60	35.431	2.278
CR16	60	34.350	1.519
CR17	60	34.899	1.547
CR18	60	31.595	1.299
CR19	60	32.570	1.808
CR20	60	32.465	1.772
CR21	60	36.779	2.305
CR22	60	34.353	2.010
CR24	60	31.509	1.679
CR25	60	33.077	1.555
CR26	60	34.685	2.453
CR27	60	33.628	1.890
CR28	60	32.510	2.059

9.2 YOUNG'S MODULUS

Table 24. Nano-indentation Young's modulus: Hot gas inlet.

TEST	INDENTS	YOUNG'S MODULUS (GPa)	STANDARD DEVIATION (GPa)
HF1	60	237.102	6.091
HF3	60	249.967	8.279
HF4	60	258.278	11.078
HF5	60	286.257	10.949
HF6	60	277.863	10.621
HF7	60	265.548	6.012
HF8	60	235.929	5.625
HF9	60	253.787	8.490
HF10	60	261.223	7.369
HF11	60	268.600	7.362
HF12	60	260.511	7.895
HF13	60	289.944	12.155
HF14	60	293.039	14.321
HF15	60	303.690	16.691
HF16	60	281.120	12.570
HF17	60	287.896	12.988
HF18	60	226.818	10.147
HF19	60	251.830	5.832
HF20	60	289.260	10.426
HF21	60	281.270	7.576
HF22	60	276.684	10.690
HF23	60	299.470	12.742
HF24	60	254.708	8.692
HF25	60	269.395	11.056

Table 25. Nano-indentation Young's modulus: Cold gas inlet.

TEST	INDENTS	YOUNG'S MODULUS (GPa)	STANDARD DEVIATION (GPa)
CR1	60	305.293	11.389
CR2	60	296.334	10.809
CR3	60	319.650	16.435
CR4	60	308.566	9.699
CR5	60	265.479	12.135
CR6	60	275.089	12.050
CR9	60	260.844	8.278
CR10	60	257.719	7.909
CR11	60	273.127	6.850
CR12	60	289.402	11.149
CR13	60	274.872	6.823
CR14	60	284.220	11.534
CR15	60	290.573	11.457
CR16	60	313.010	9.343
CR17	60	329.974	10.268
CR18	60	285.123	6.166
CR19	60	293.038	9.309
CR20	60	272.567	8.259
CR21	60	327.174	16.327
CR22	60	312.189	10.887
CR24	60	274.486	10.641
CR25	60	288.391	10.608
CR26	60	288.453	14.302
CR27	60	284.829	10.506
CR28	60	256.705	7.890

10 X-RAY DIFFRACTION

Table 26. Powder X-Ray diffraction analysis: hot gas inlet

Test #	Si (%)	$I_{\text{Disorder}}/I_{111}$	$2\Theta_{220} - 2\Theta_{111}$ (°)	Crystallite Size (nm)	Lattice Parameter (nm)
HF7	0	2.004	6.826	31.360	0.43593
HF8	0	2.706	6.814	24.100	0.43589
HF9	0	0.269	6.819	79.830	0.43601
HF10	0	0.792	6.812	46.250	0.43597
HF11	0	2.585	6.880	25.530	0.43591
HF12	0	0.938	6.790	37.280	0.43595
HF13	0	0.230	6.820	110.300	0.43605
HF14	0	0.304	6.814	74.790	0.43601
HF15	0	0.190	6.818	102.400	0.43604
HF16	0	0.719	6.816	56.960	0.43599
HF17	0	0.201	6.816	112.400	0.43604
HF18	0	0.246	6.820	102.400	0.43592
HF19	0.045	3.942	6.813	16.260	0.43577
HF22	0	2.283	6.848	19.050	0.43577
HF23	0	0.238	6.820	91.100	0.43603
HF24	0	2.004	6.826	47.250	0.43598

Table 27. Powder X-Ray diffraction analysis: cold gas inlet.

Test #	Si (%)	$I_{\text{Disorder}}/I_{111}$	$2\Theta_{220} - 2\Theta_{111}$ (°)	Crystallite Size (nm)	Lattice Parameter (nm)
CR3	0	0.103	6.816	88.550	0.43605
CR4	0	0.473	6.820	70.800	0.43602
CR5	0.124	2.625	6.841	18.750	0.43580
CR6	0	0.291	6.819	86.730	0.43604
CR9	0	0.946	6.824	46.130	0.43597
CR10	0	2.715	6.868	19.070	0.43577
CR11	0	2.098	6.859	25.630	0.43591
CR12	0	0.428	6.810	82.840	0.43604
CR13	0	2.646	6.812	25.580	0.43590
CR14	0	0.159	6.817	111.100	0.43602
CR15	0	1.178	6.841	41.700	0.43596
CR18	0.725	3.837	7.018	16.590	0.43577
CR19	0	1.445	6.851	34.000	0.43593
CR22	0	1.427	6.810	33.100	0.43593
CR24	0	1.263	6.802	36.170	0.43595
CR26	0.088	0.579	6.823	50.510	0.43598
TT1	0	1.821	6.868	26.050	0.43589
TT2	0	1.785	6.840	27.100	0.43580
TT3	0	1.757	6.877	26.020	0.43588
TT4	0	1.610	6.852	24.800	0.43580
TT5	0	2.118	6.849	26.200	0.43591
MTS1	6.849	5.691	6.778	11.580	0.43581

11 RAMAN SPECTROSCOPY

Table 28. Raman peak position and intensity for sample prepared using a cooled gas inlet.

TEST #	SiC TO Peak		SiC LO Peak		Si Peak
	Intensity (au)	Shift (cm ⁻¹)	Intensity (au)	Shift (cm ⁻¹)	Intensity (au)
CR2	795.401	8156.258	970.575	5152.505	2446.133
CR3	796.605	32494.510	972.389	17820.875	930.493
CR4	795.401	19413.010	971.181	12450.138	1358.249
CR5	795.401	5318.899	966.348	2361.022	5318.899(a)
CR6	795.401	29102.396	971.785	25227.021	929.978
CR9	795.401	10175.830	970.577	7027.204	2079.677
CR10	795.401	5075.583	964.64	2916.804	5075.583(a)
CR11	794.797	5431.789	968.161	3220.402	4055.930(a)
CR12	795.401	18112.445	971.181	9267.798	1399.227
CR13	794.797	4818.935	966.952	2944.111	3372.963(a)
CR14	796.006	36769.586	971.785	16354.278	871.159
CR18	792.883	15202.478	963.243	2004.329	15202.478(a)
CR19	794.797	8992.851	969.973	6133.807	2970.591
CR22	795.401	8622.733	969.973	6097.830	2238.953
CR24	794.797	9119.924	970.577	5366.962	2272.087
CR26	795.401	7783.337	970.577	4838.587	2032.527(a)
MTS1	789.965	9240.526	953.468	1181.834	9240.526(a)
TT2	794.797	5836.265	968.161	3230.612	3161.428

(a) Test runs exhibiting a silicon peak above the background level

Table 29. Raman peak position and intensity for sample prepared using a non-cooled gas inlet.

TEST #	SiC TO Peak		SiC LO Peak		Si Peak
	Intensity (au)	Shift (cm ⁻¹)	Intensity (au)	Shift (cm ⁻¹)	Intensity (au)
HF7	794.7974	4701.007	966.036	3187.672	3081.592(a)
HF8	794.1933	5008.368	966.952	3458.580	3512.960(a)
HF10	794.7974	10229.508	970.577	7003.224	1867.679
HF11	794.1933	4597.632	967.557	2960.684	3097.833
HF12	794.7974	10106.231	969.973	5382.814	2101.683
HF13	795.4014	31168.352	971.785	14238.389	1080.498
HF14	795.4014	19221.234	971.181	15294.384	1336.496(a)
HF15	795.4014	32200.154	971.785	18942.535	830.443
HF16	794.7974	15416.475	970.225	5347.442	1519.563
HF17	796.0054	38904.449	971.785	20712.174	848.690
HF18	795.4014	30047.070	973.018	7429.721	1082.874
HF19	792.9852	5128.897	963.243	2347.993	4822.620(a)
HF22	794.7974	4191.697	963.932	2437.529	4191.697(a)
HF23	795.4014	29657.863	971.785	21063.916	927.840
HF24	794.7974	10161.997	970.5768	7473.539	1649.690
TR12	792.3812	6281.735	953.468	1680.237	6281.735(a)

(a) Test runs exhibiting a silicon peak above the background level

12 ELECTRON MICROPROBE ANALYSIS

Table 30. Electron microprobe analysis of silicon carbide deposit.

Test #	Count	Si Average Weight %	Si Standard Deviation	C Average Weight %	C Standard Deviation
CR1	1	69.950		27.960	
CR2	2	70.195	0.092	27.735	1.039
CR3	2	70.165	0.134	28.375	1.831
CR4	2	69.970	0.042	28.620	0.000
CR5	2	70.130	0.240	29.145	0.742
CR6	2	69.720	0.354	30.440	0.085
CR9	2	69.835	0.544	27.625	0.771
CR10	2	70.130	0.099	29.845	0.460
CR11	2	70.175	0.078	29.435	1.817
CR12					
CR13					
CR14	2	69.975	0.049	29.305	2.595
CR15	2	70.130	0.226	29.045	1.308
CR16	2	70.110	0.156	29.095	0.346
CR17	2	70.355	0.035	29.855	2.666
CR18	2	71.005	0.148	27.715	0.375
CR19	2	70.060	0.014	29.540	1.584
CR20	2	69.595	0.573	29.760	0.877
CR21	2	69.950	0.184	27.825	0.827
CR22	2	70.105	0.148	29.060	2.150
CR24	2	70.280	0.042	29.740	2.376
CR25	2	70.405	0.021	30.055	3.231
CR26	2	70.375	0.078	29.870	1.131
CR27	2	70.370	0.311	27.800	0.057
CR28	2	70.010	0.269	27.240	1.061
HF1	2	70.110	0.382	28.960	2.560
HF3	2	69.920	0.325	28.925	1.153
HF4	2	70.105	0.262	29.540	2.008
HF5	2	69.860	0.552	30.390	0.453
HF6	2	70.145	0.007	28.900	2.036
HF7	2	69.785	0.375	29.145	1.973
HF8	2	69.940	0.339	28.560	0.707
HF9	2	69.885	0.346	28.705	0.799
HF10	2	70.015	0.445	28.675	0.049
HF11	2	70.105	0.431	28.550	1.428
HF12	2	69.755	0.474	27.090	1.160
HF13	2	70.195	0.120	28.035	2.171
HF14	2	69.680	0.410	27.825	1.549
HF15	2	70.395	0.064	29.205	0.106
HF16	2	69.810	0.721	27.725	0.672
HF17	2	69.980	0.184	27.970	1.230
HF18	2	70.335	0.163	28.340	0.523
HF19	2	70.300	0.792	29.075	2.157
HF20	2	69.875	0.403	27.760	1.556
HF21	2	69.880	0.948	27.910	1.457
HF22	2	69.720	0.127	29.380	0.948
HF23	2	69.820	0.651	29.940	0.636
HF24	2	69.730	0.622	27.145	0.573
HF25	2	70.215	0.078	29.100	0.962

Test #	Count	Si Average Weight %	Si Standard Deviation	C Average Weight %	C Standard Deviation
TT1	2	70.485	0.247	29.690	1.386
TT2	4	70.240	0.255	28.548	0.602
TT3	4	70.310	0.073	29.578	0.924
TT4	4	70.330	0.101	30.095	1.045
TT5	4	70.280	0.076	28.800	0.665
TR12	18	70.921	0.814	28.967	5.637
TR13	2	71.720	0.000	27.945	0.983
TR14	1	74.220		24.390	
MTSI	10	72.572	1.434	27.881	1.686

Table 31. Repeated measurements of CR, TT and MTS1 particles.

Test #	Count	Si Average Weight %	Si Standard Deviation	C Average Weight %	C Standard Deviation
CR1	2	69.610	0.255	27.625	0.573
CR2	2	69.845	0.559	26.495	1.223
CR3	1	69.640		28.520	
CR4	2	69.645	0.431	28.155	1.322
CR5	2	70.275	0.247	26.835	0.120
CR6	2	69.890	0.552	29.780	1.457
CR9	2	69.670	0.396	27.905	0.686
CR10	2	70.050	0.580	26.650	2.206
CR11	2	69.685	0.573	27.125	2.708
CR12	2	69.945	0.233	29.260	0.396
CR13	2	69.775	0.757	27.100	1.952
CR14	2	69.110	0.297	28.620	0.820
CR15	2	69.400	0.184	26.670	0.693
CR16	2	69.690	0.226	27.925	1.181
CR17	2	69.660	0.042	27.380	0.424
CR18	2	70.715	0.021	26.665	2.567
CR19	2	69.945	0.021	27.595	1.039
CR20	2	70.175	0.078	30.120	3.352
CR21	2	69.760	0.255	27.955	1.648
CR22	2	70.305	0.021	26.805	1.421
CR24	2	69.280	0.226	30.400	1.697
CR25	2	69.345	0.290	27.650	0.368
CR26	2	69.805	0.092	29.600	3.111
CR27	2	69.760	0.127	27.100	0.000
CR28	2	69.975	0.078	28.300	0.976
TT1	4	69.543	0.675	28.870	1.887
TT2	4	69.693	0.633	28.453	0.762
TT3	4	69.980	0.242	28.423	1.364
TT4	4	70.138	0.218	28.760	1.223
TT5	4	70.020	0.353	27.750	1.956
MTS1	10	72.403	1.308	25.734	2.050

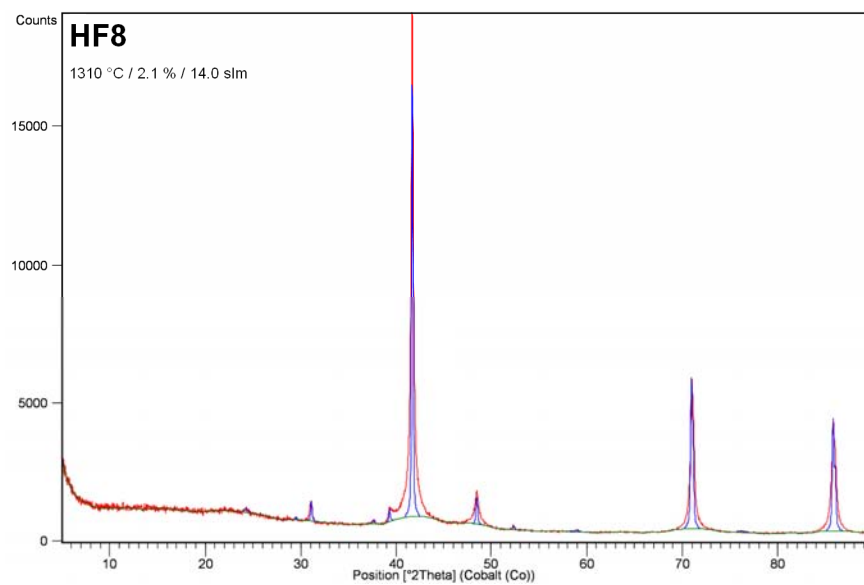
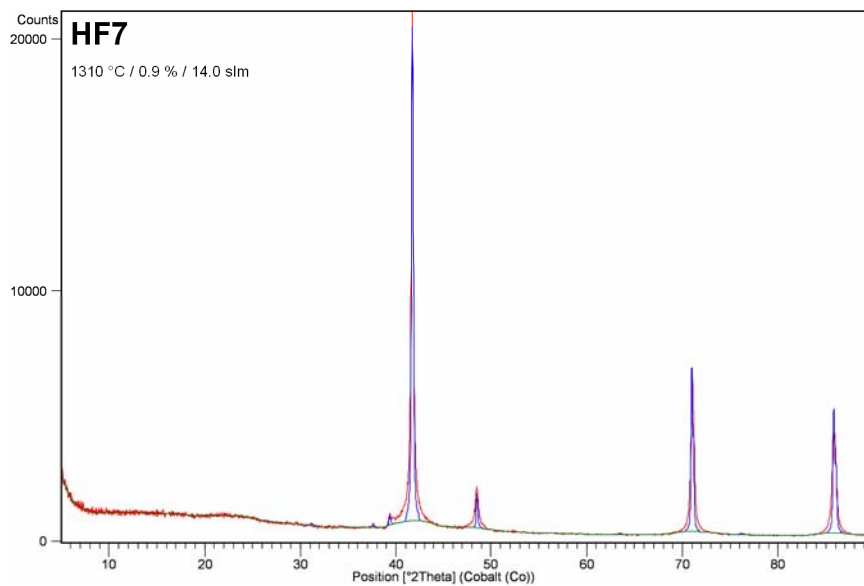
Estimated standard deviation for each of the measurements, as reported by the instrument, was on average 0.98 weight percent and 6.80 weight percent for silicon and carbon respectively.

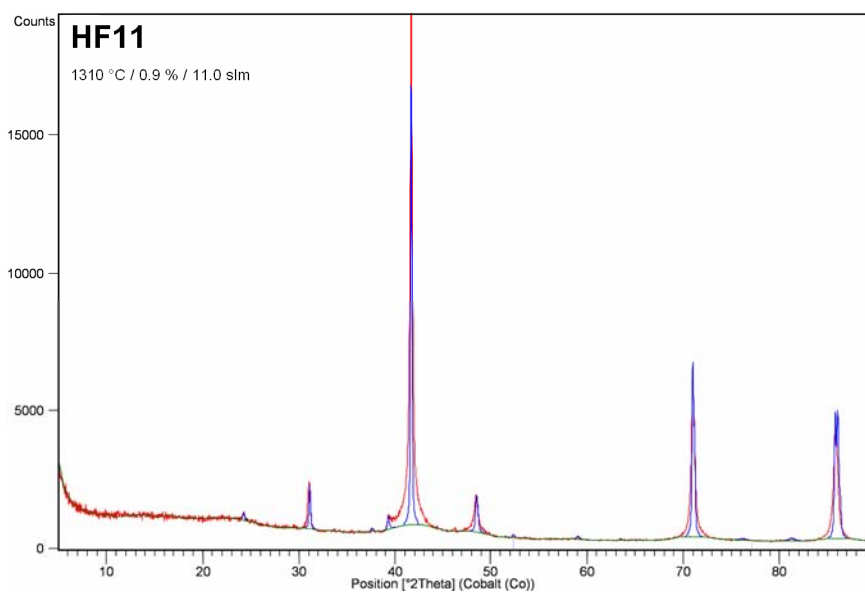
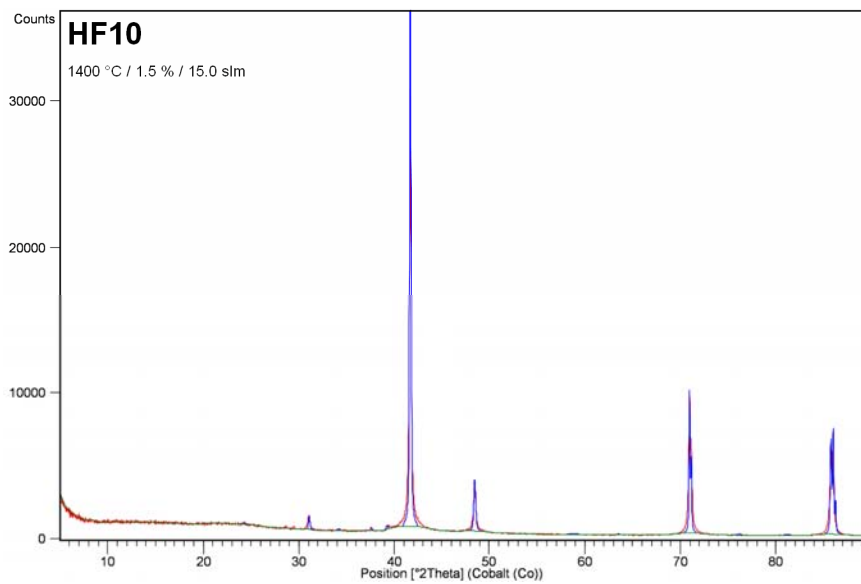
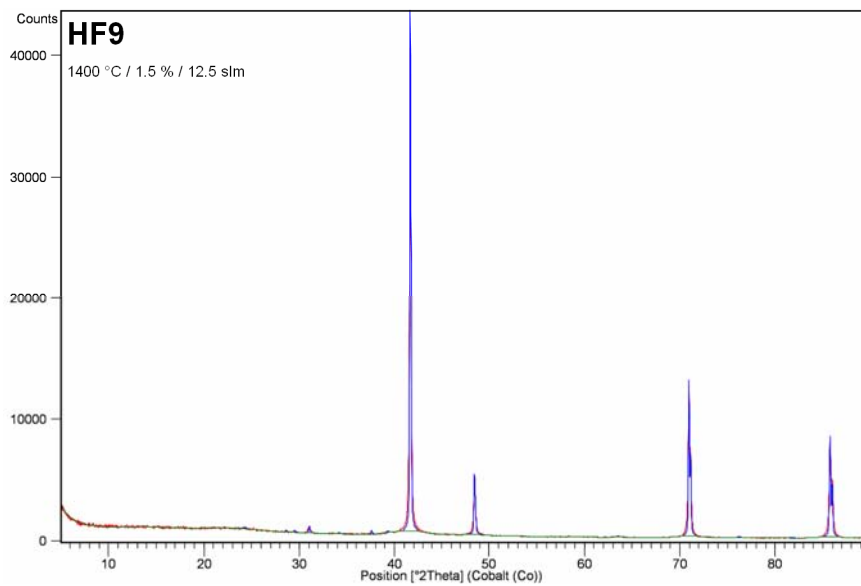
APPENDIX B: X-RAY DIFFRACTION PATTERNS AND RAMAN SPECTRA

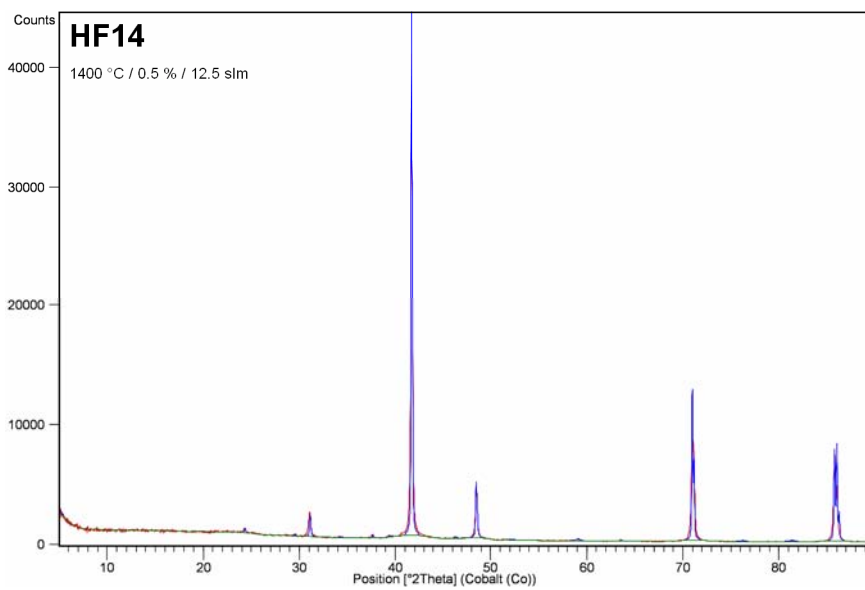
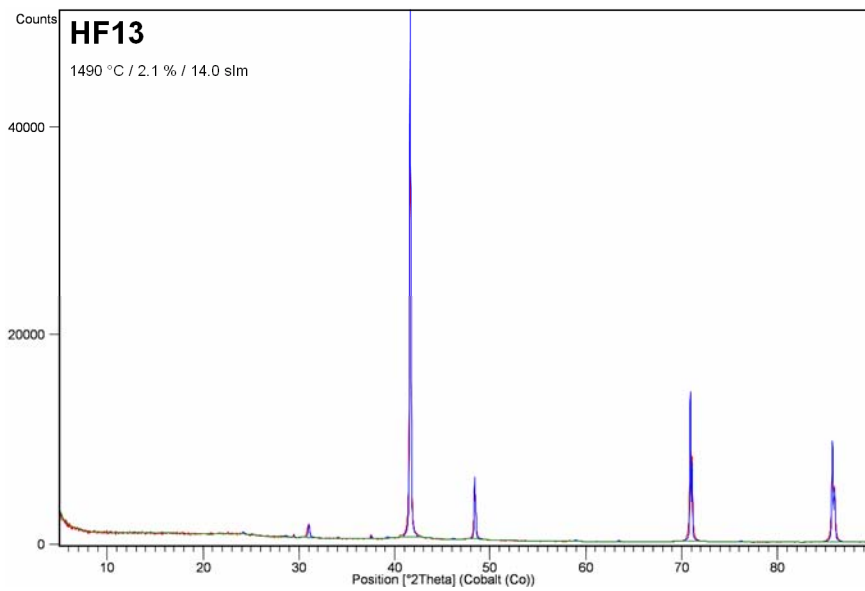
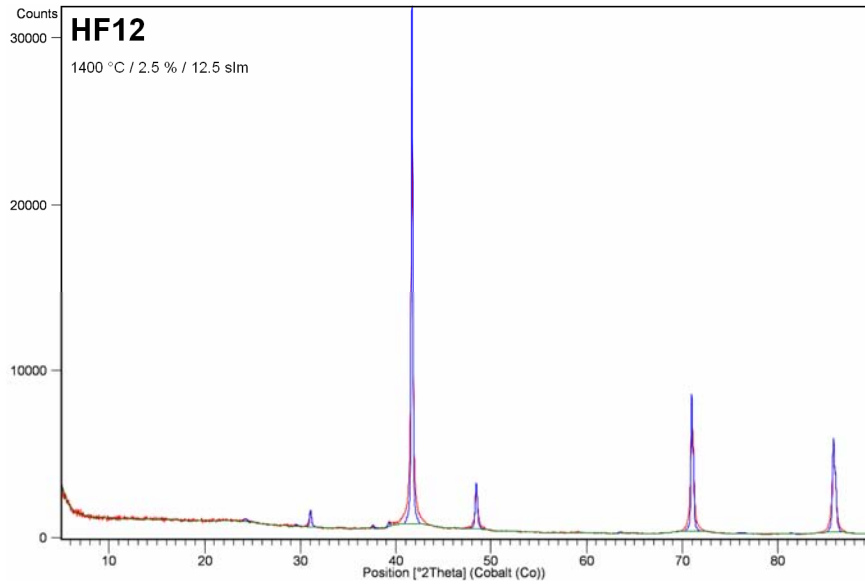
1	X-RAY DIFFRACTION PATTERNS	332
1.1	X-RAY DIFFRACTION PATTERNS: HOT INLET	332
1.2	X-RAY DIFFRACTION PATTERNS: COLD INLET	337
2	RAMAN SPECTROSCOPY	343
2.1	RAMAN SPECTRA: HOT INLET	343
2.2	RAMAN SPECTRA: COLD INLET	349

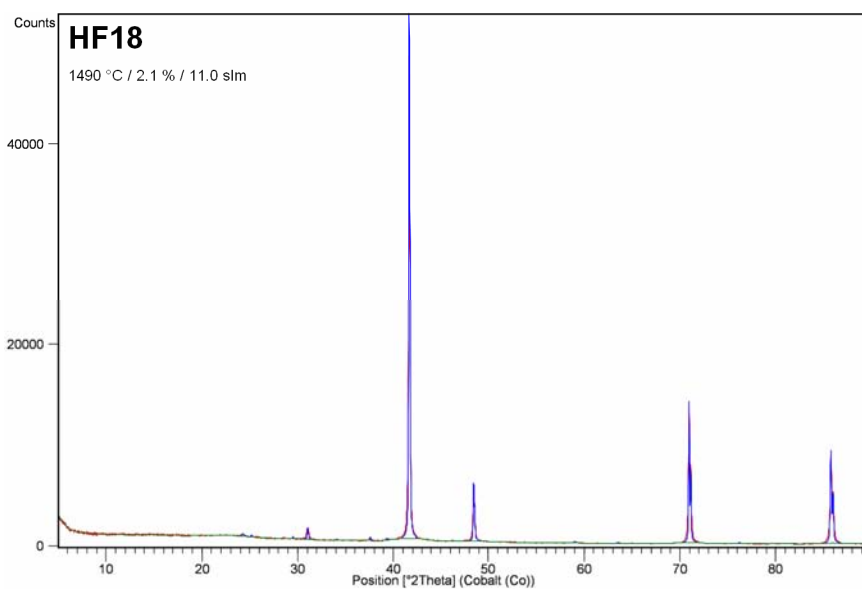
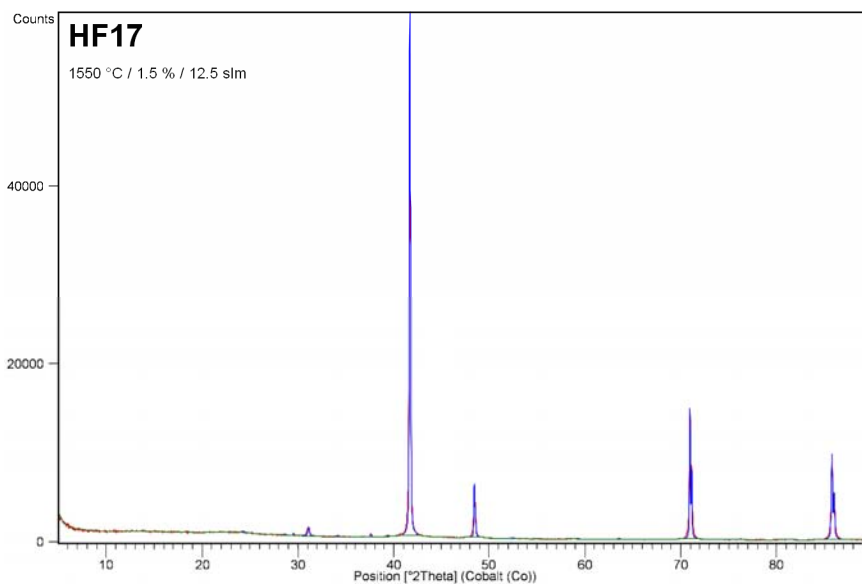
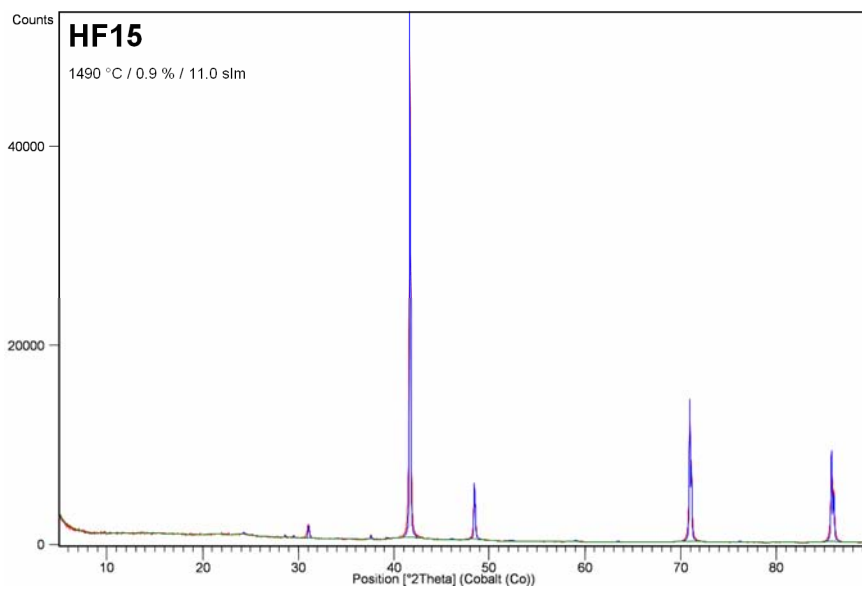
1 X-RAY DIFFRACTION PATTERNS

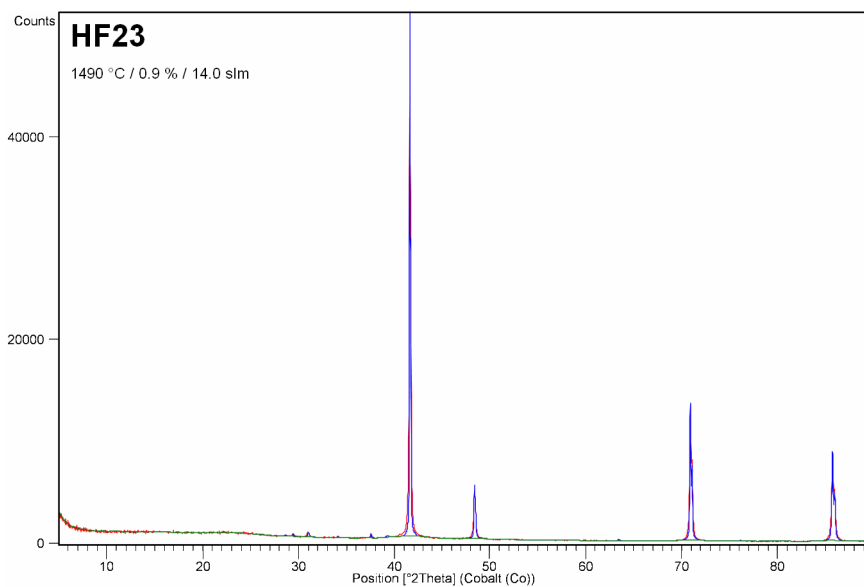
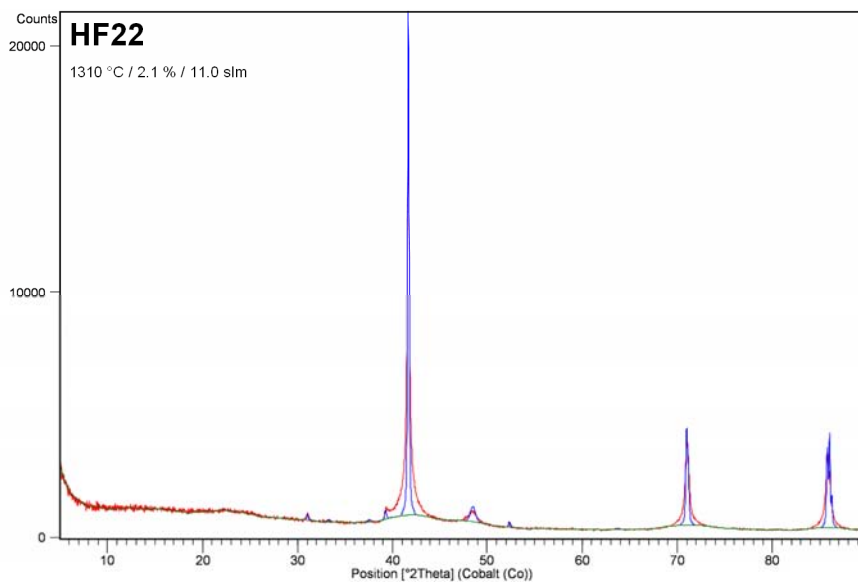
1.1 X-RAY DIFFRACTION PATTERNS: HOT INLET



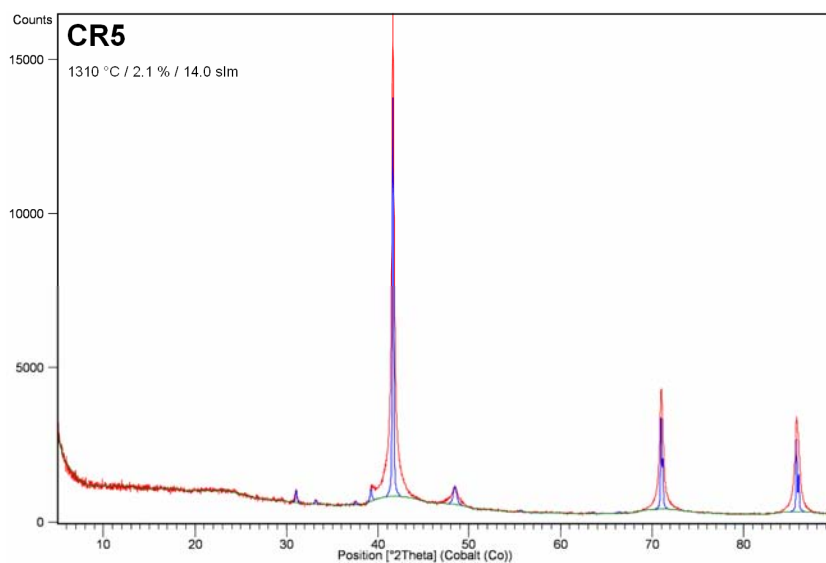
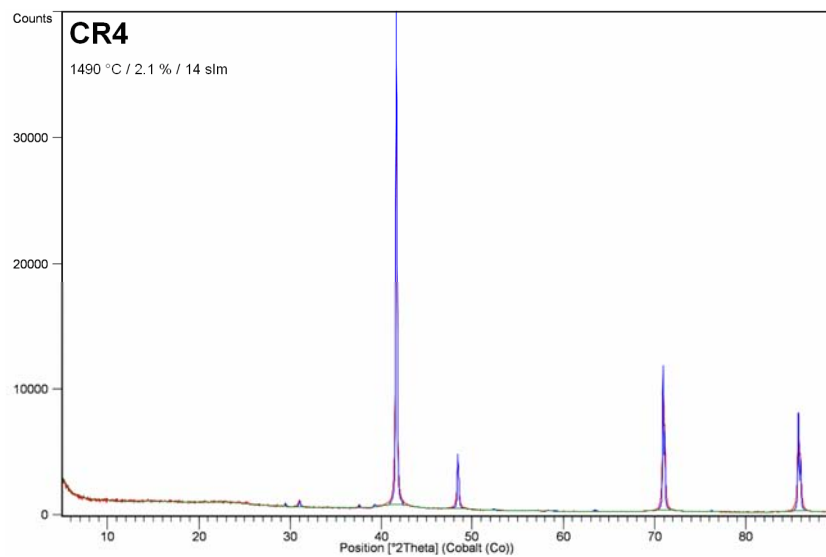
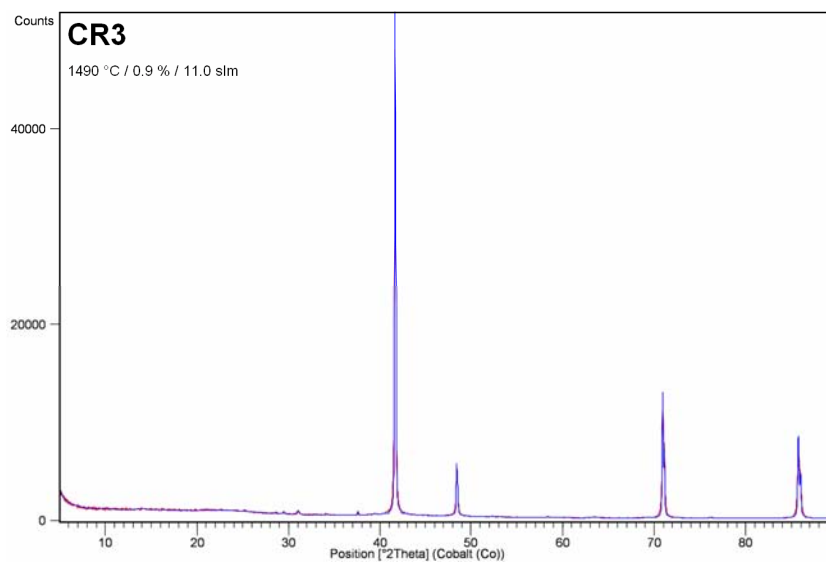


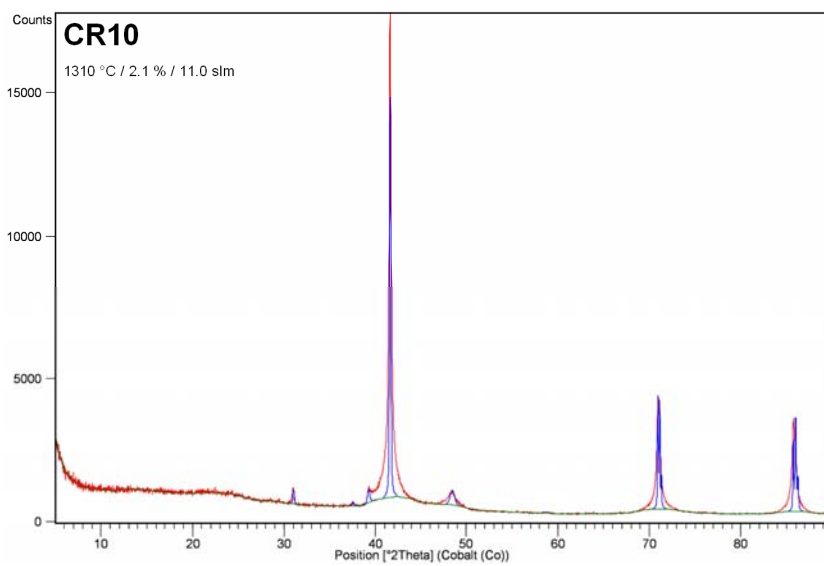
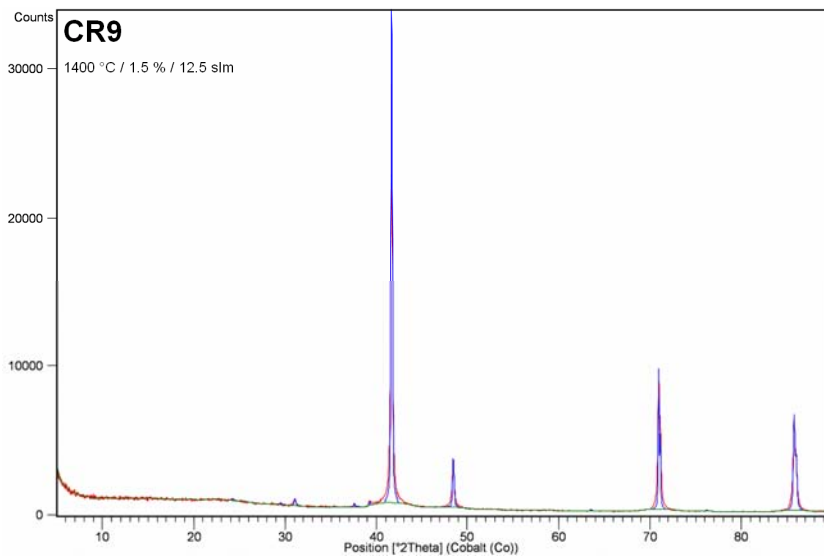
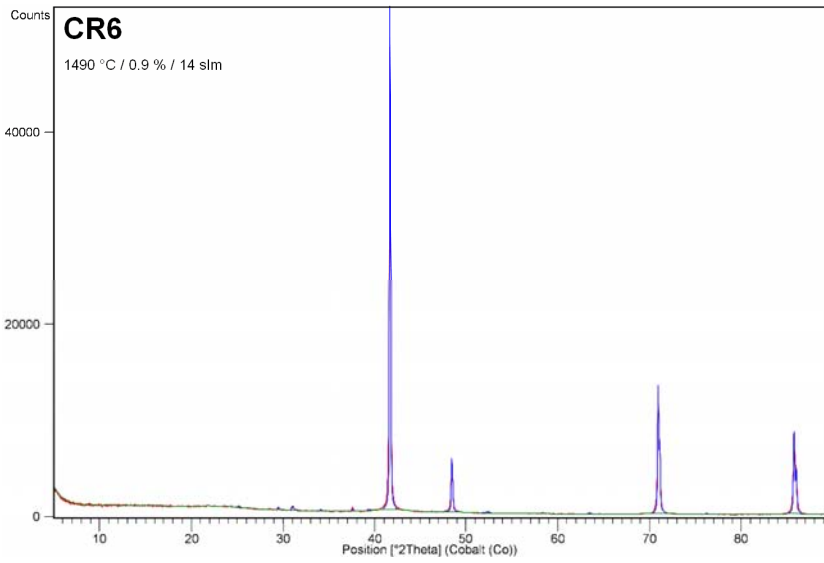


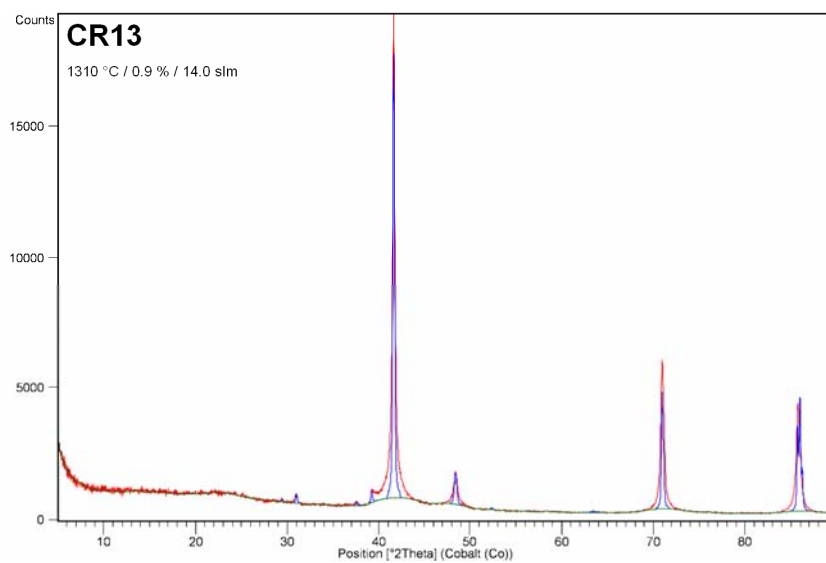
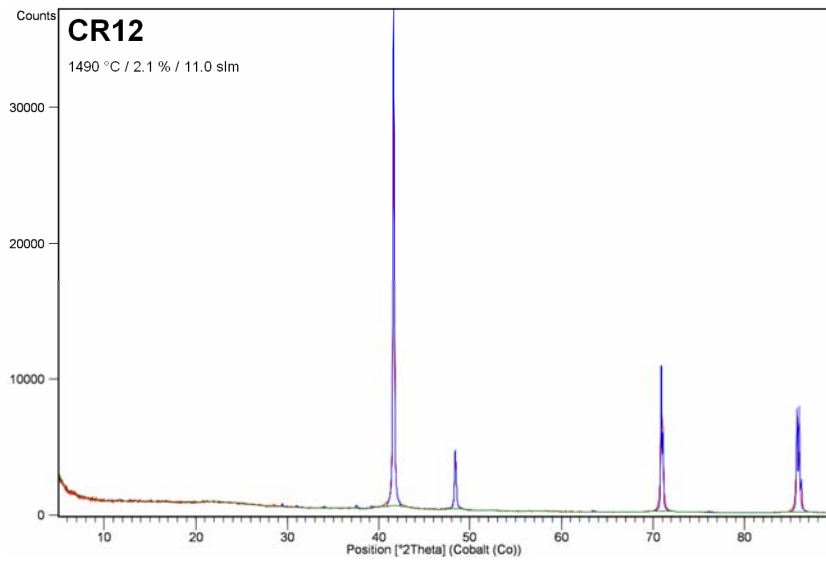
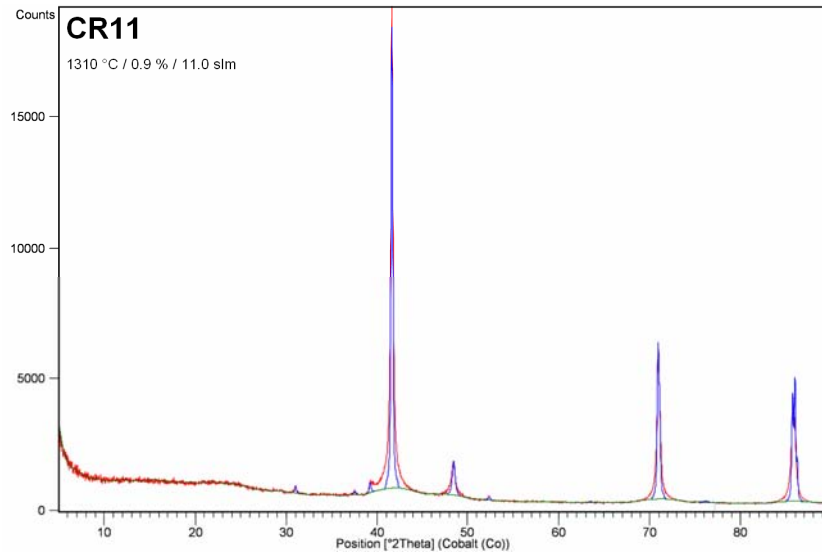


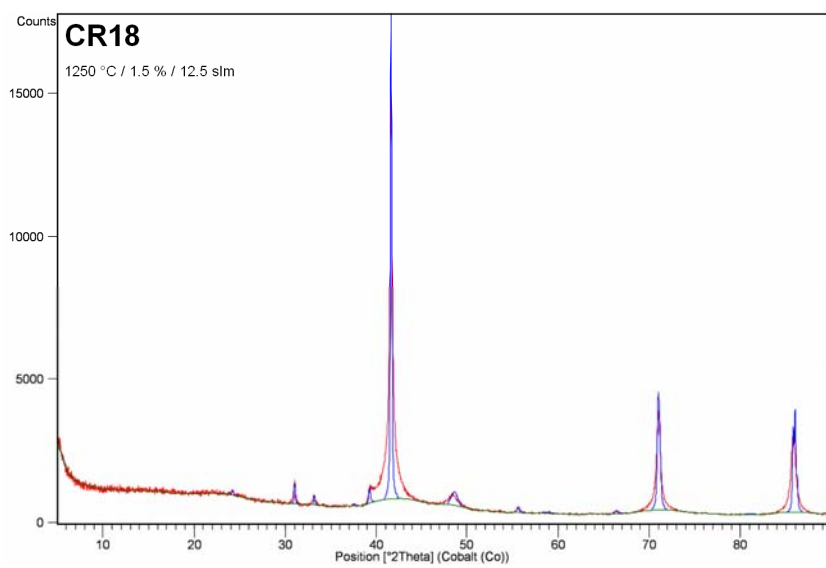
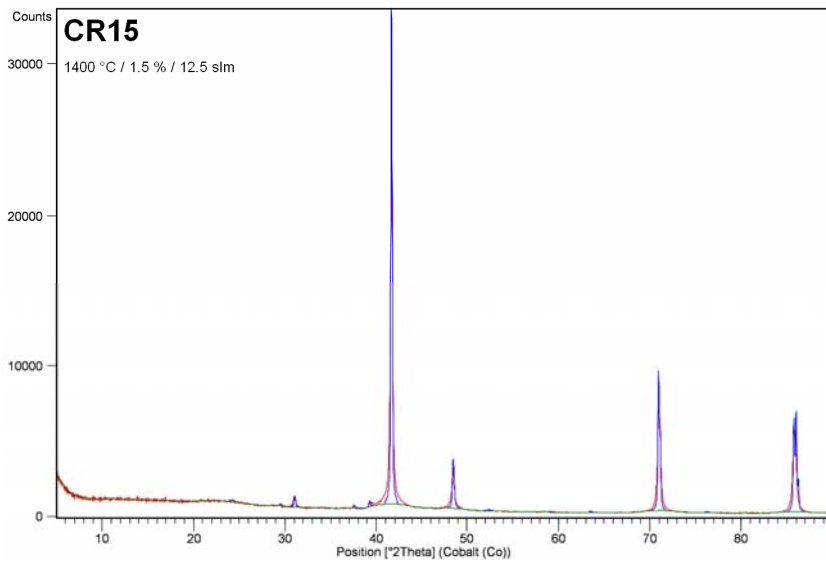
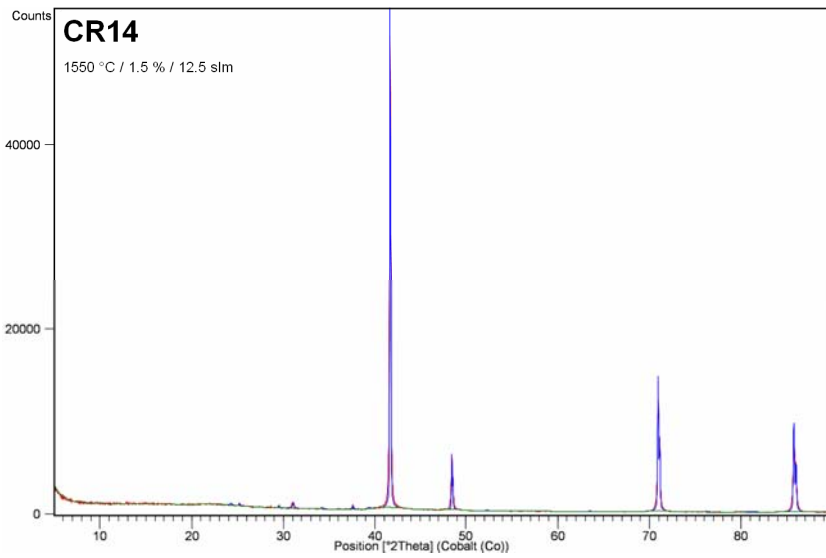


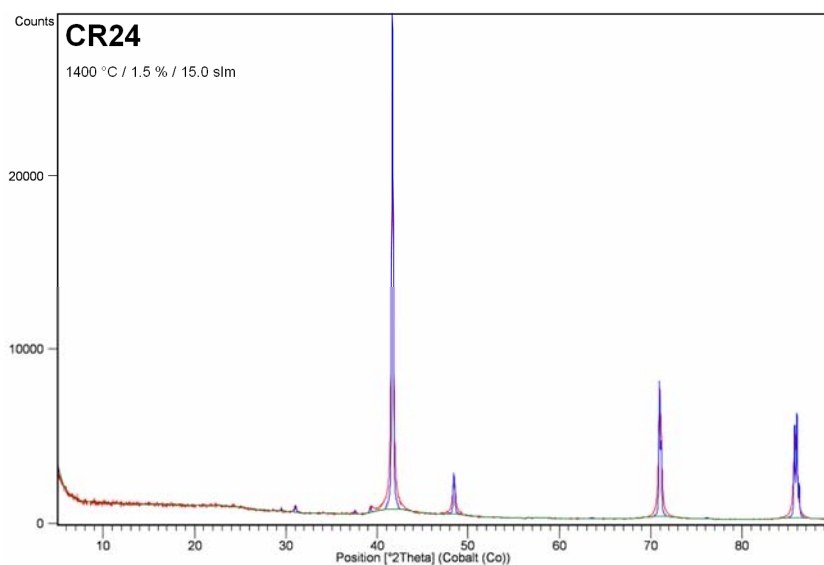
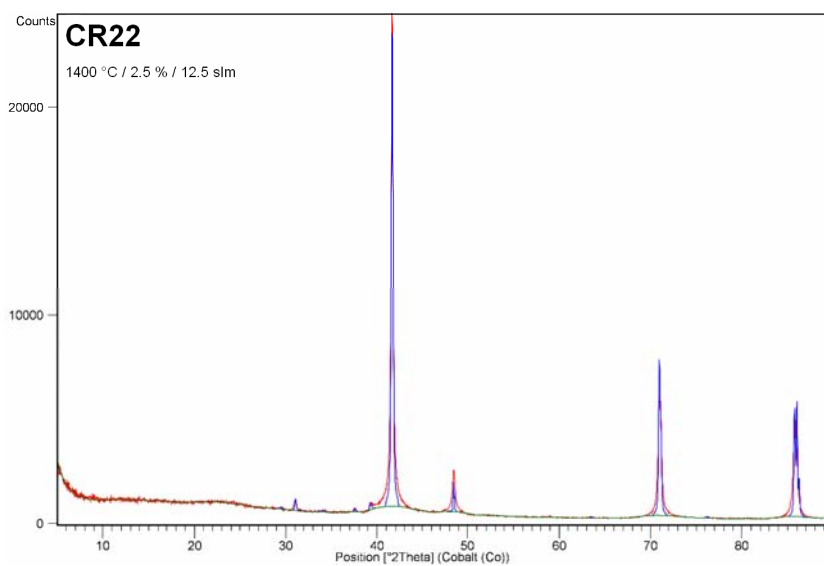
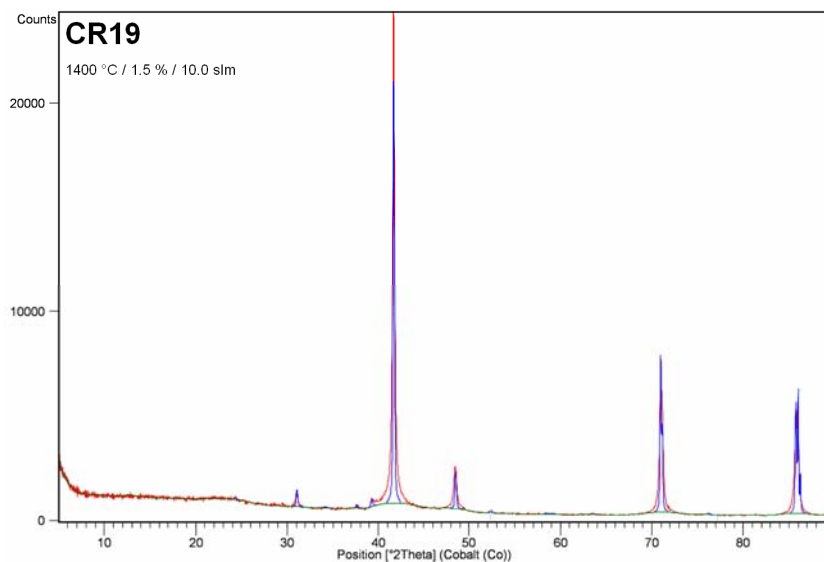
1.2 X-RAY DIFFRACTION PATTERNS: COLD INLET

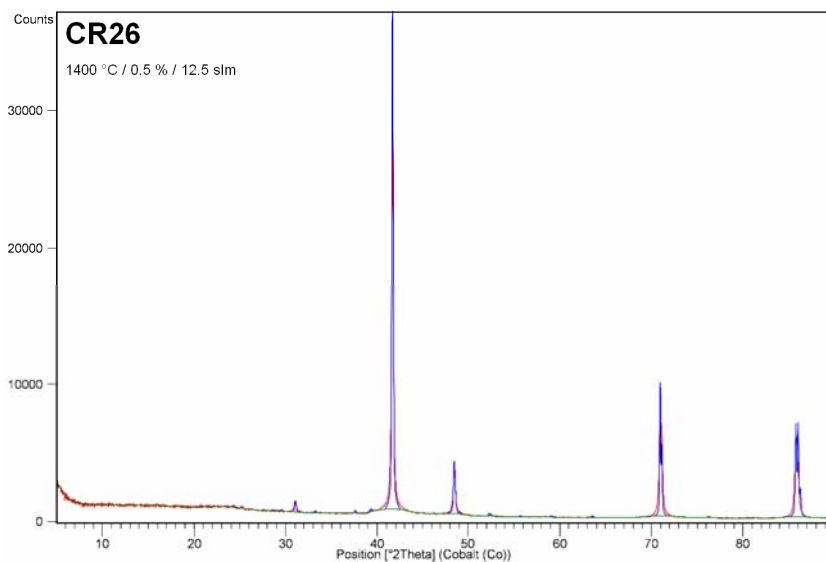






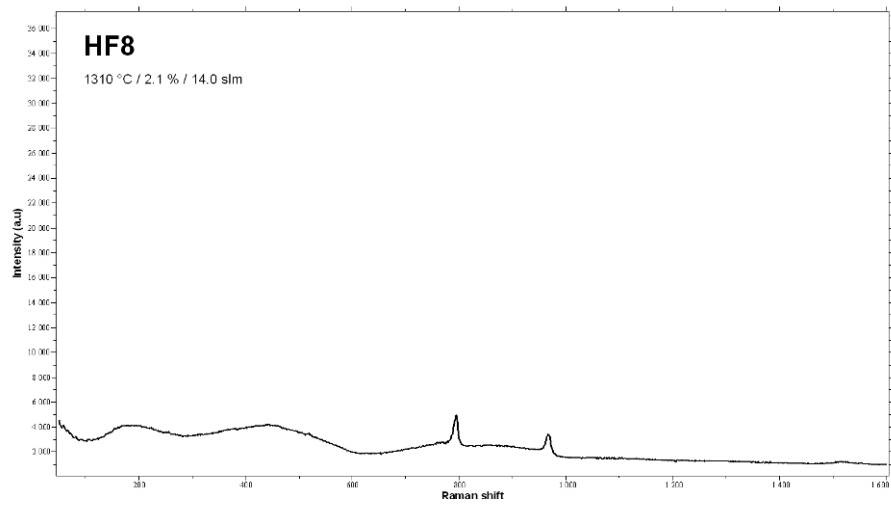
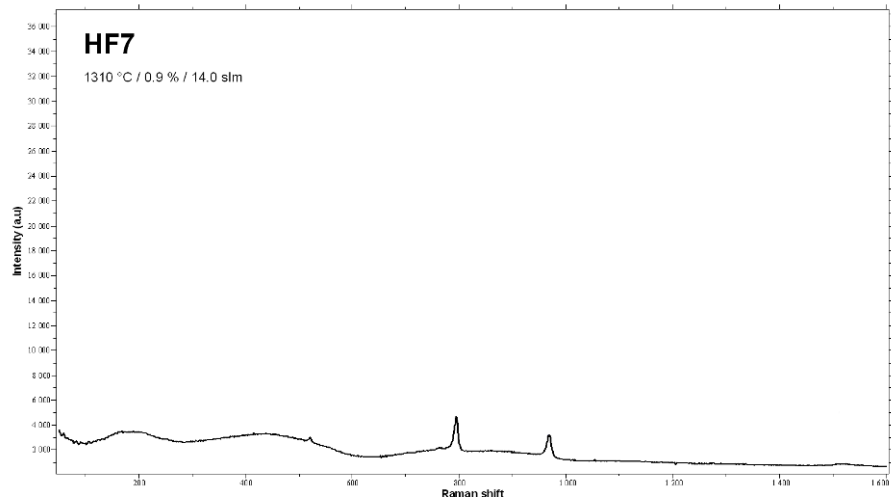


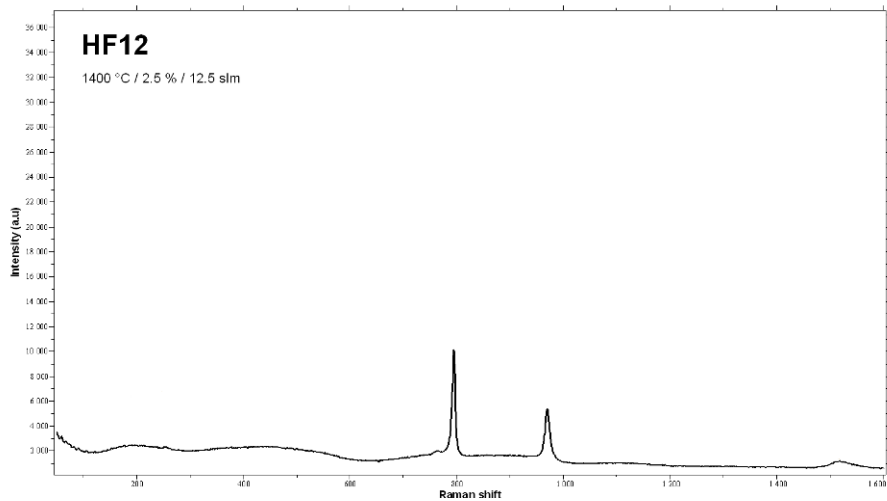
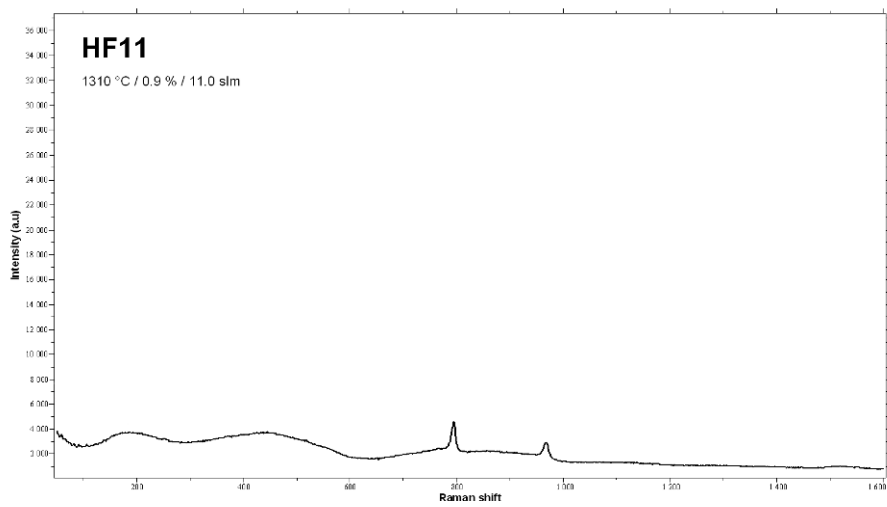
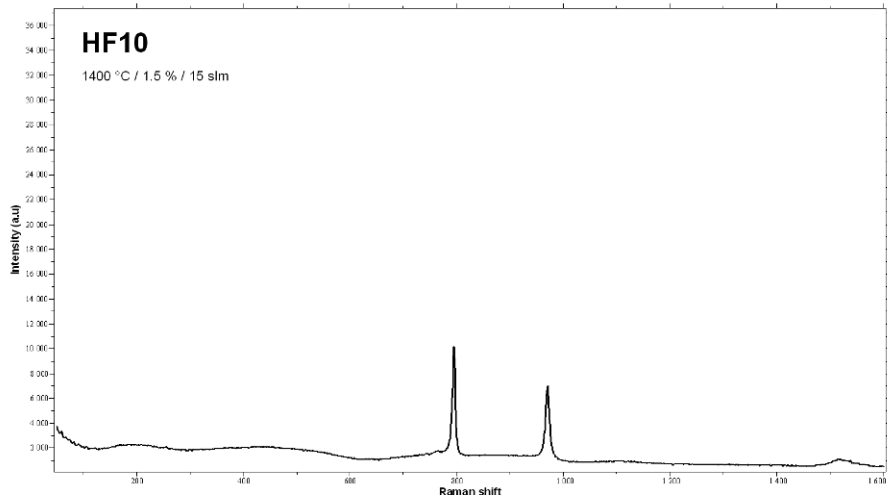


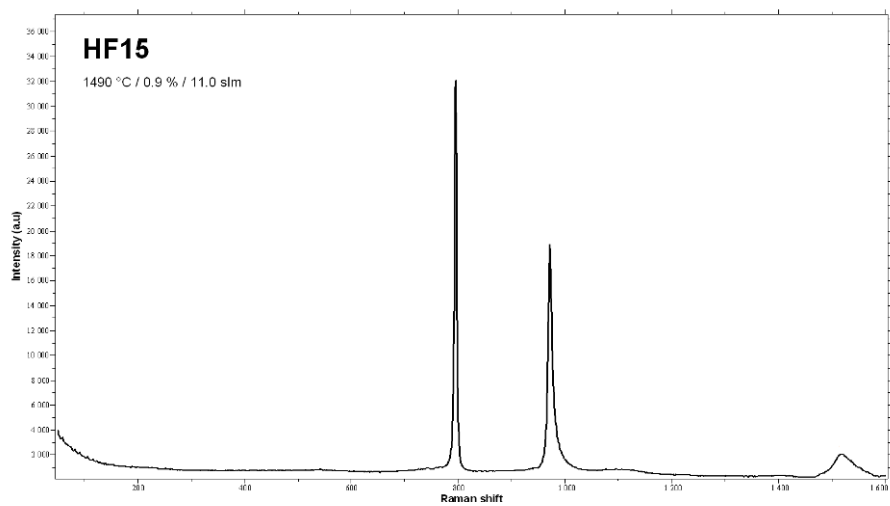
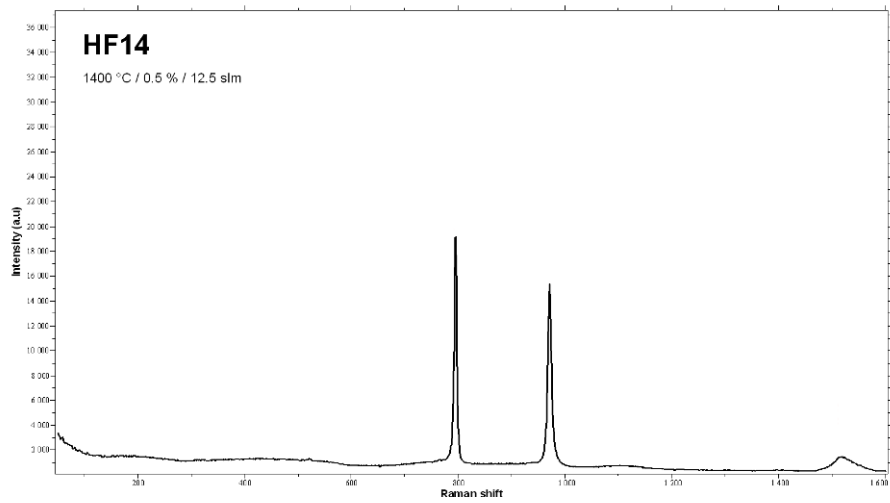
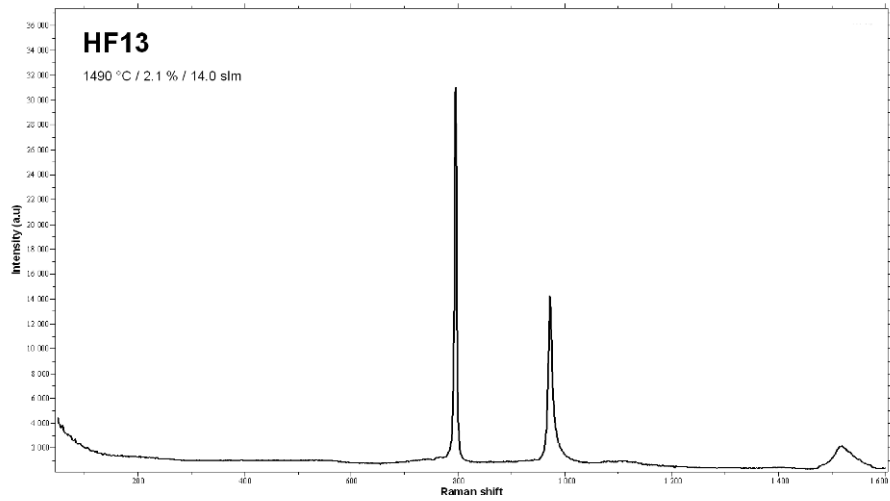


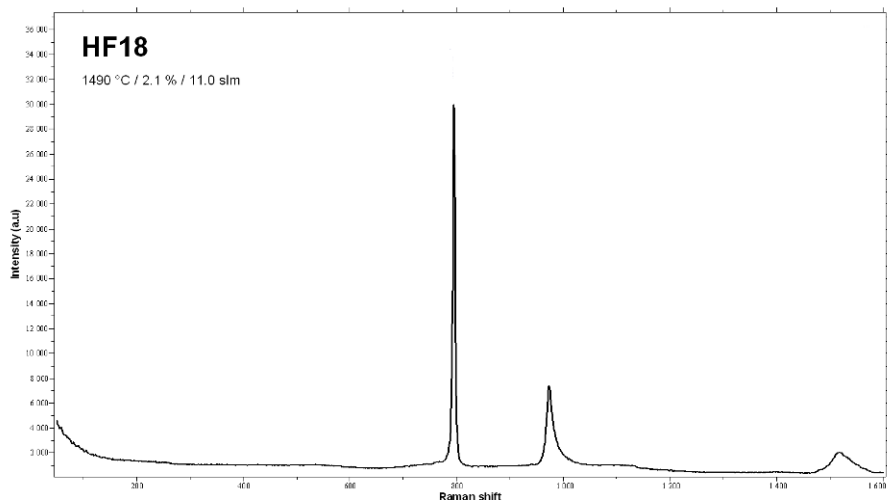
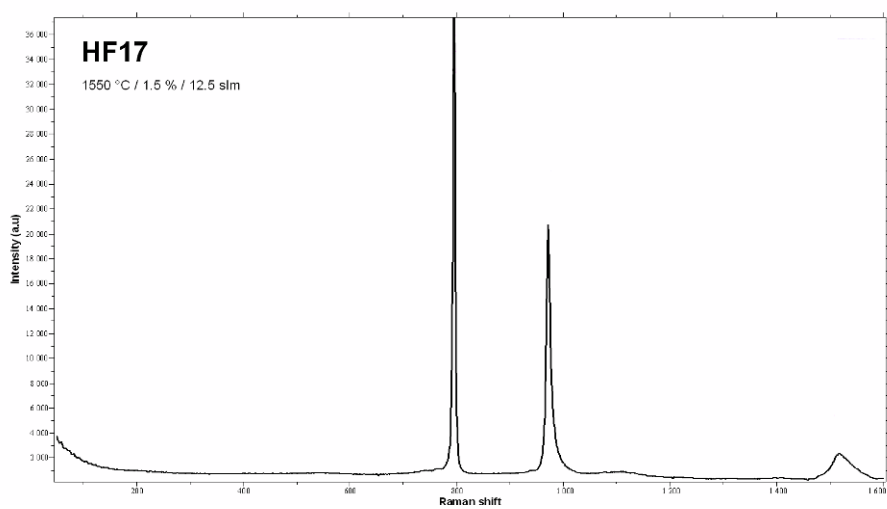
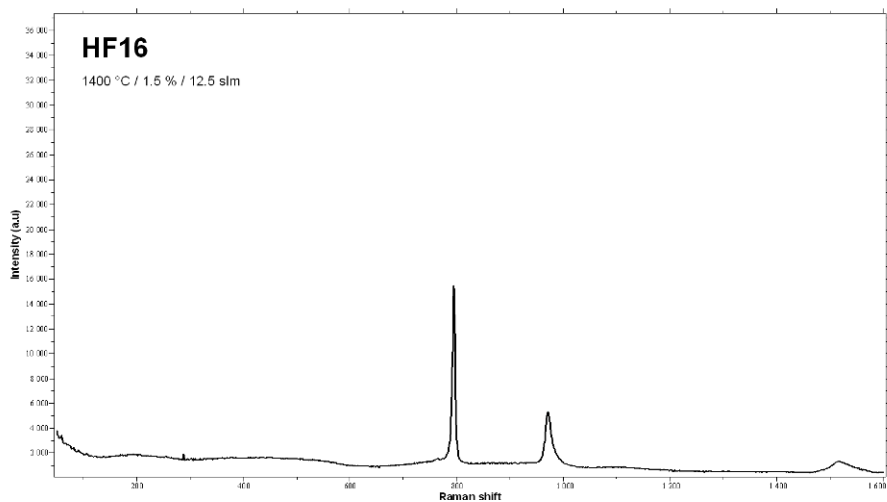
2 RAMAN SPECTROSCOPY

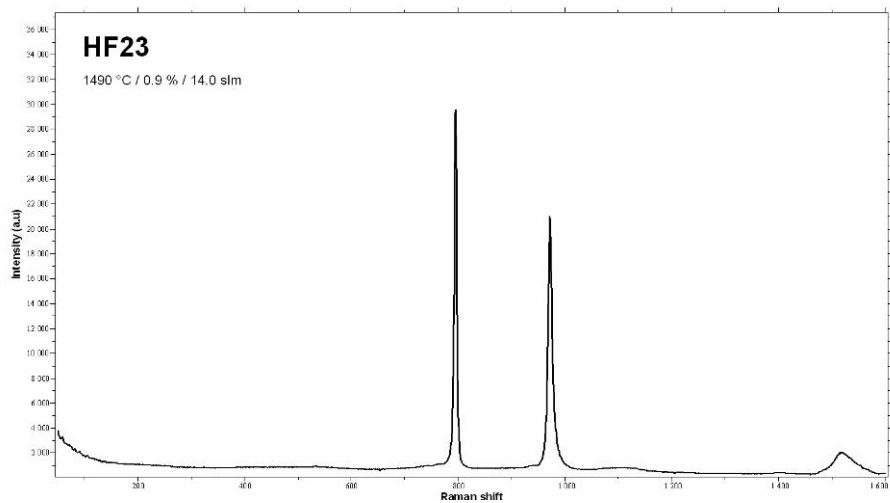
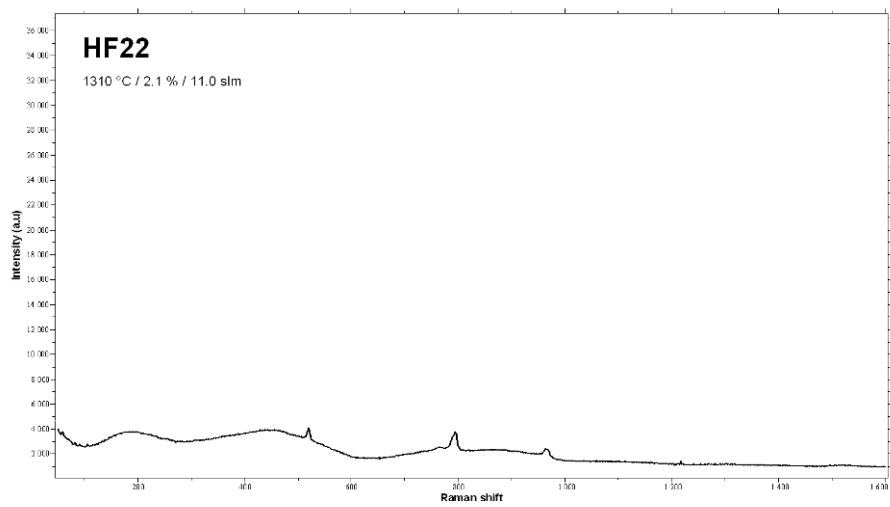
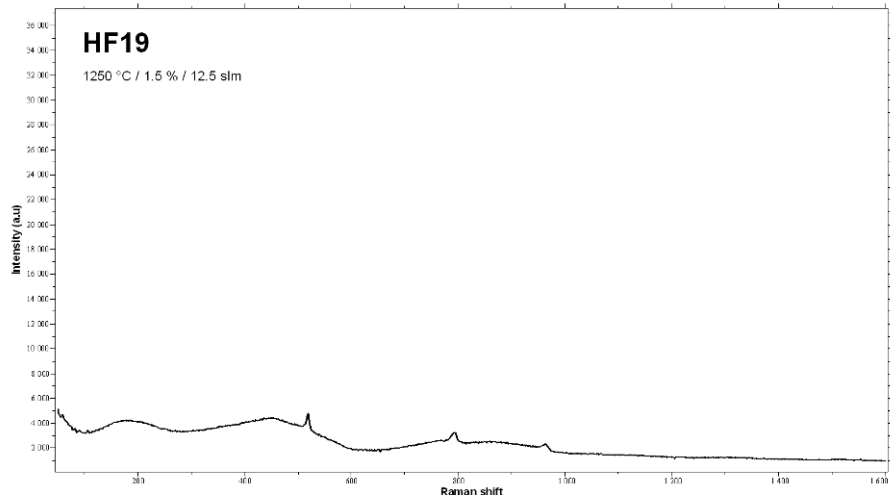
2.1 RAMAN SPECTRA: HOT INLET

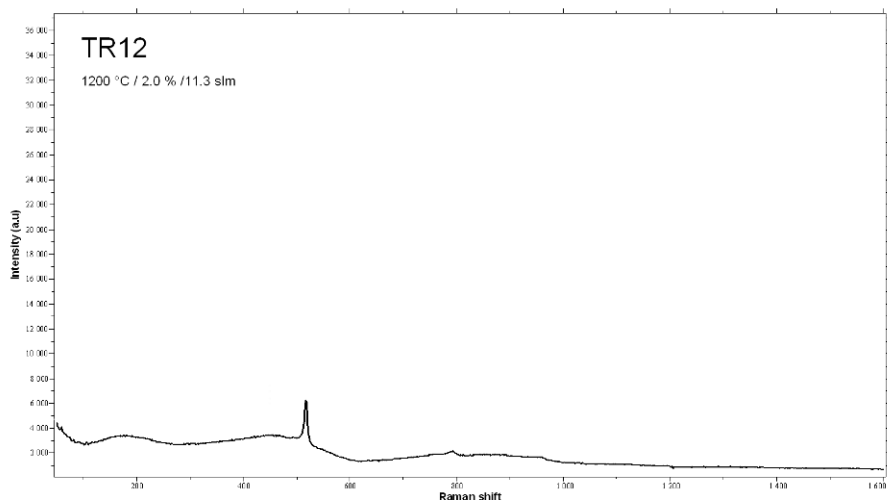




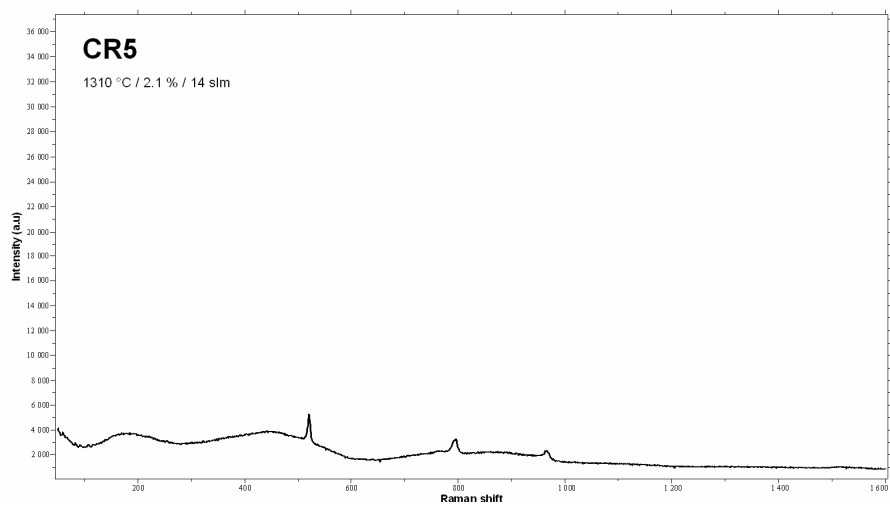
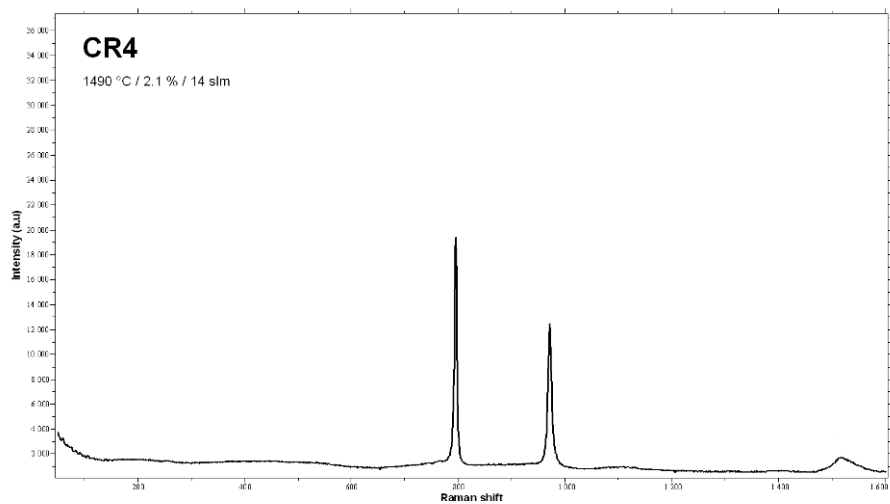
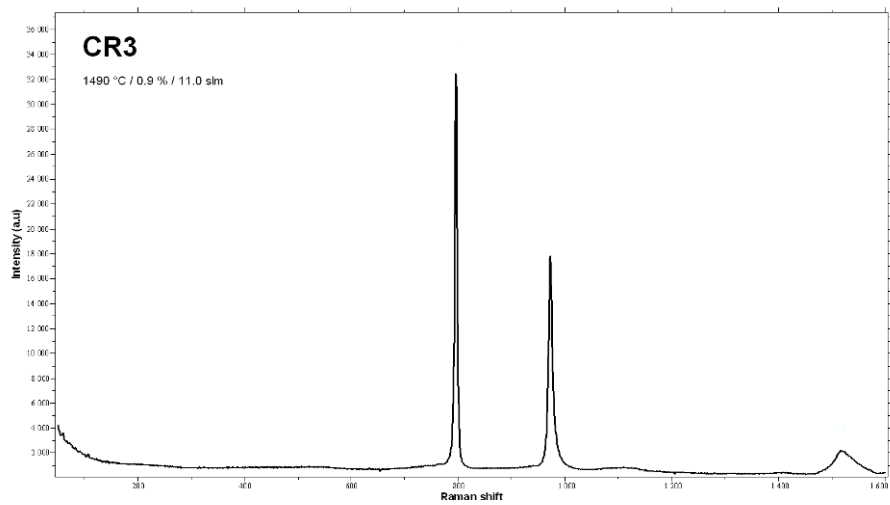


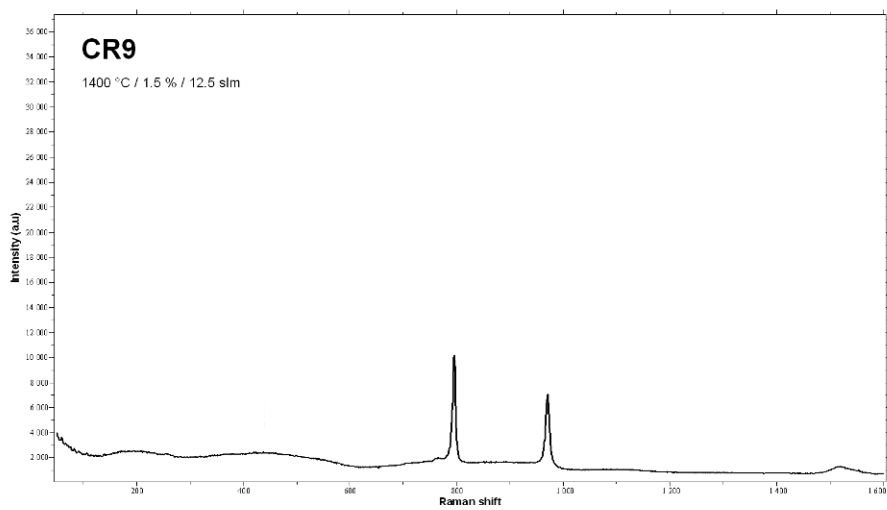
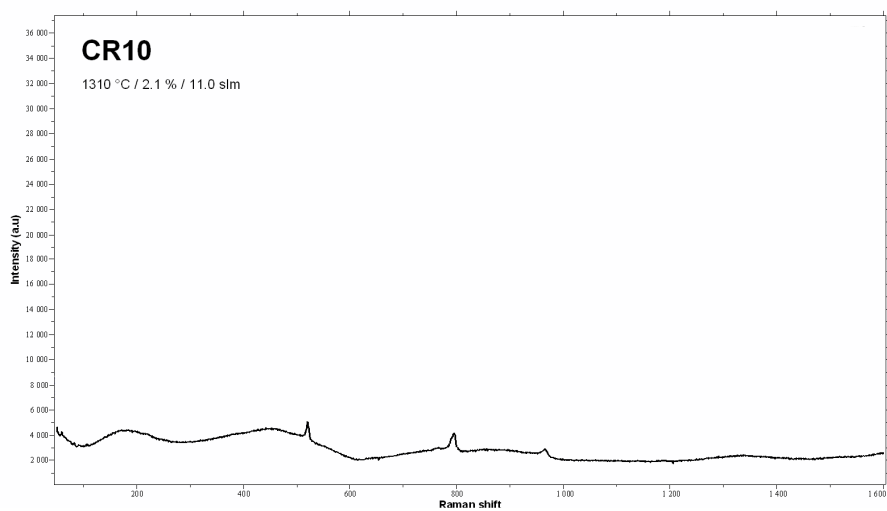
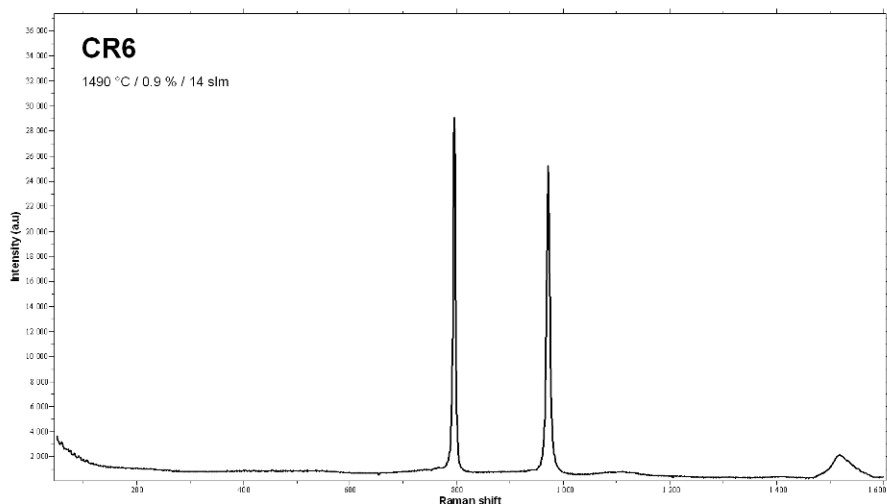


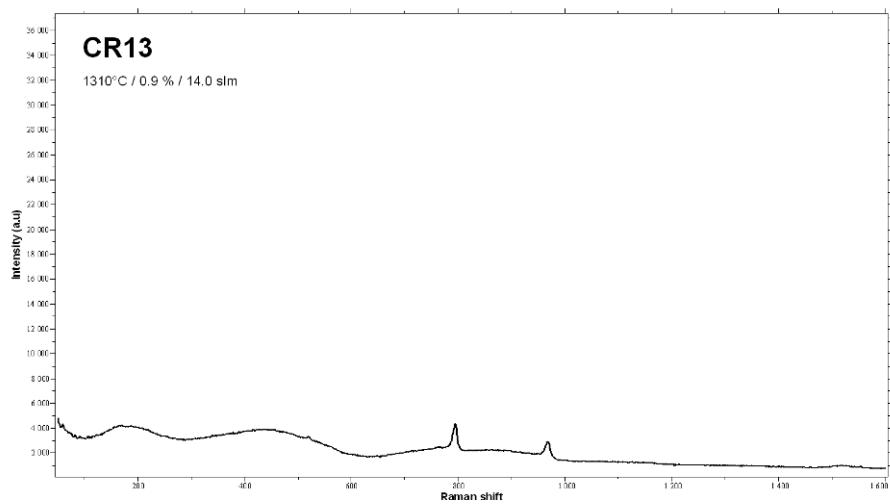
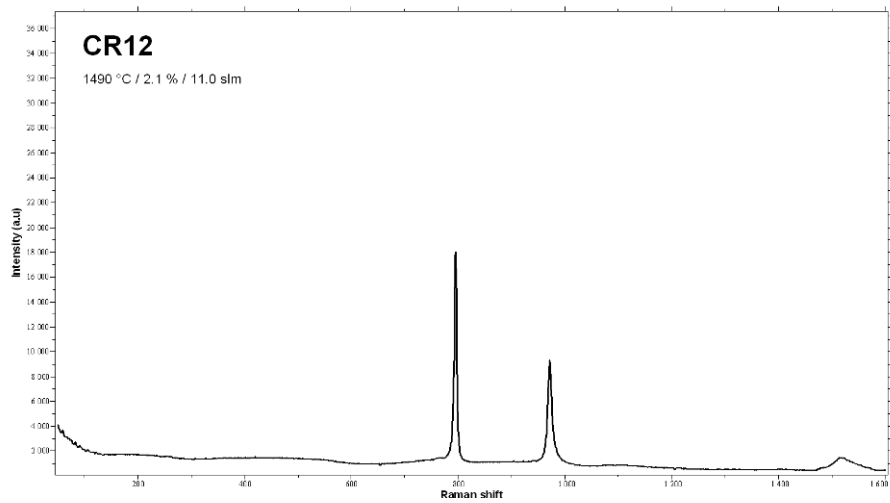
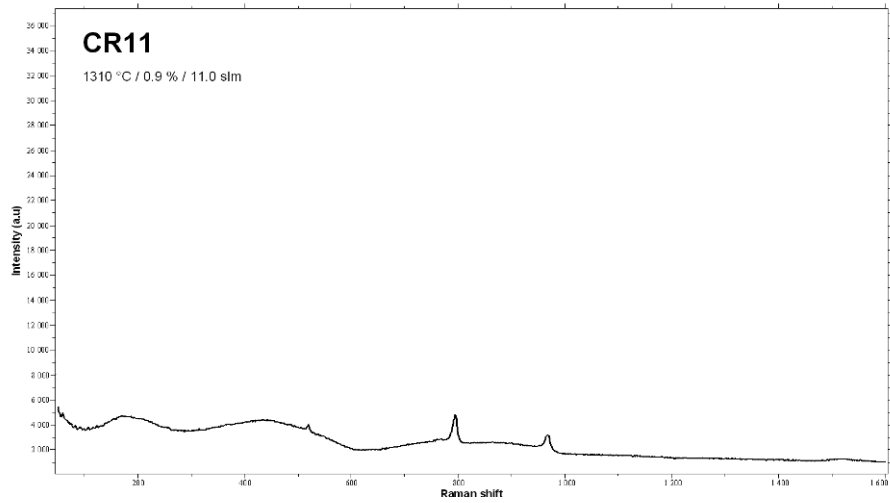


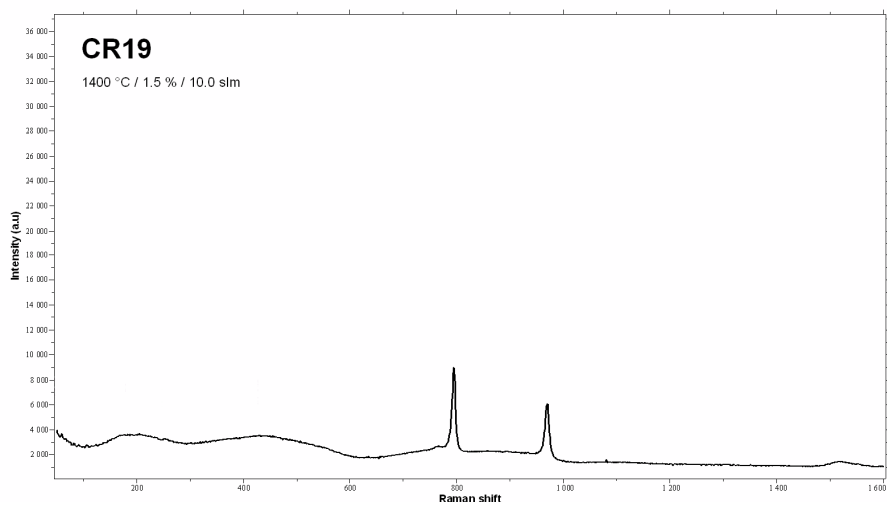
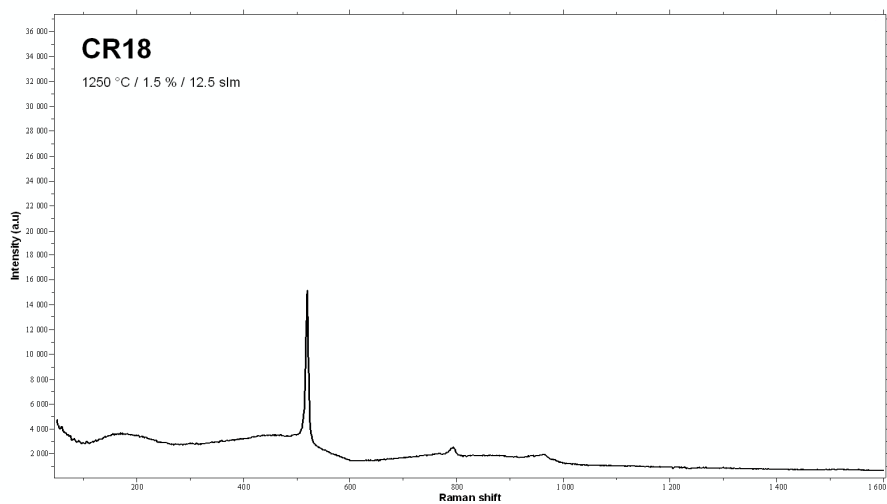
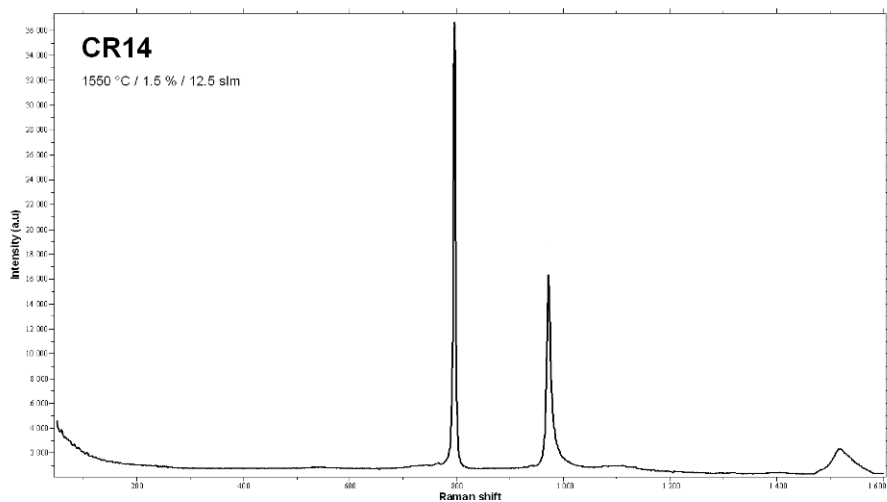


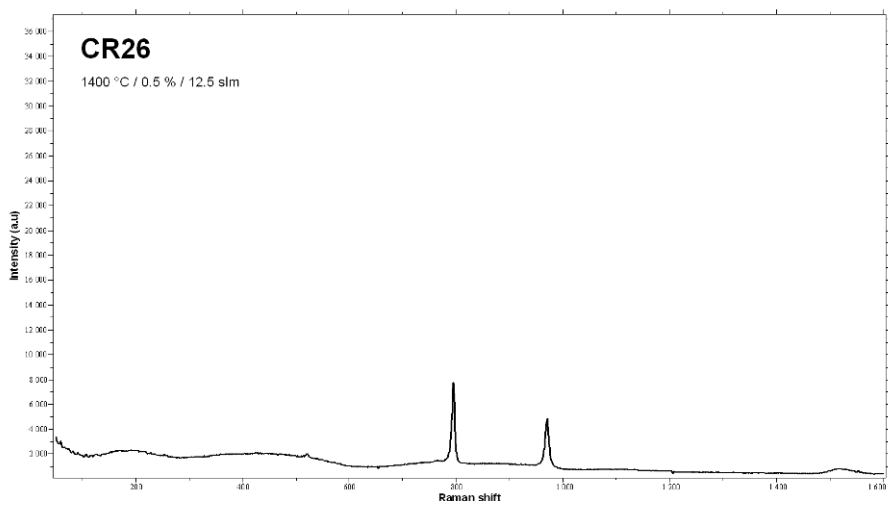
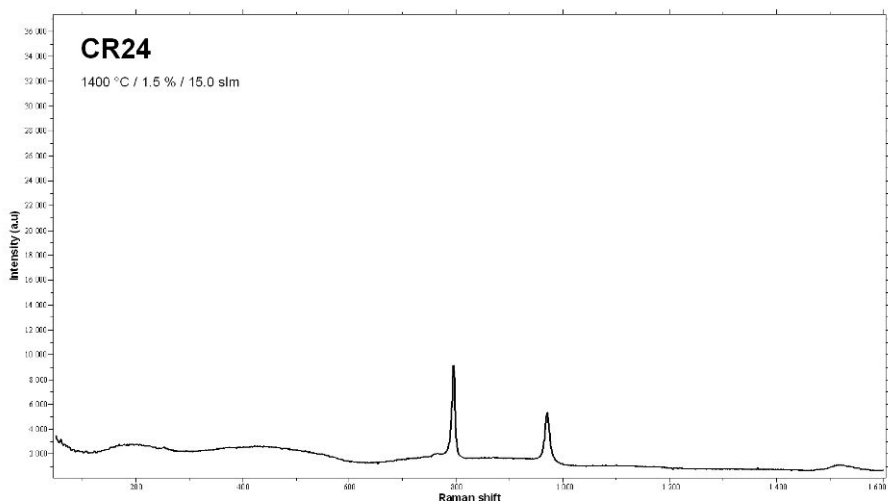
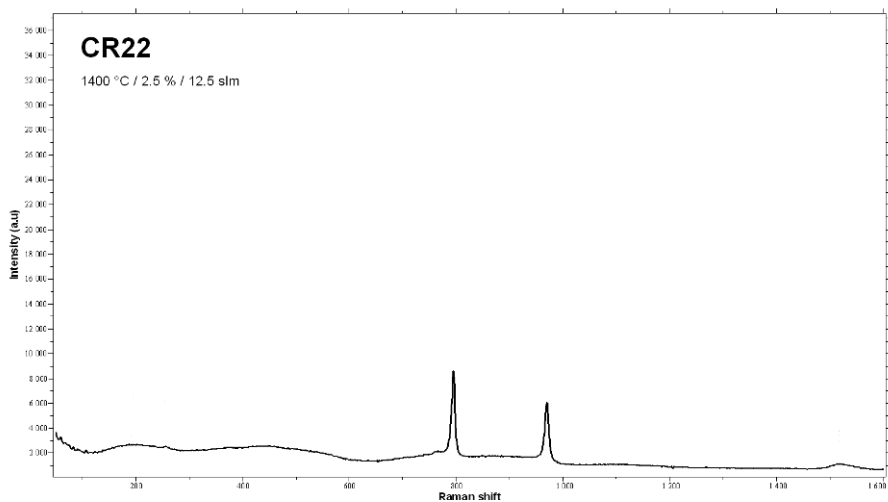
2.2 RAMAN SPECTRA: COLD INLET

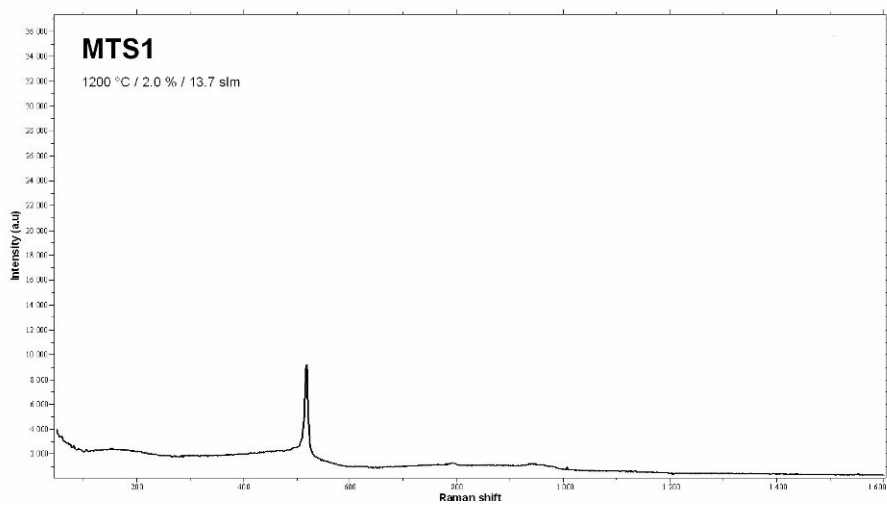
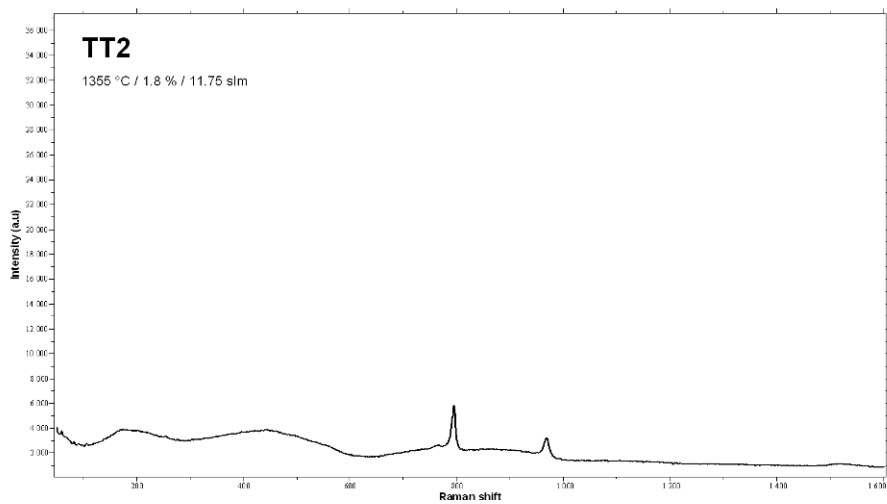










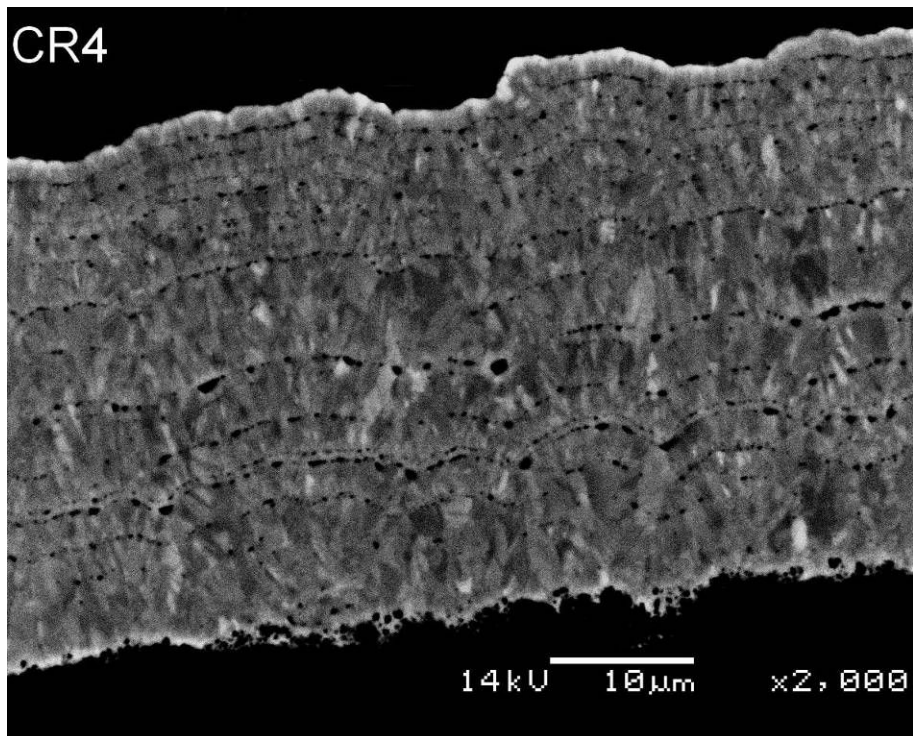
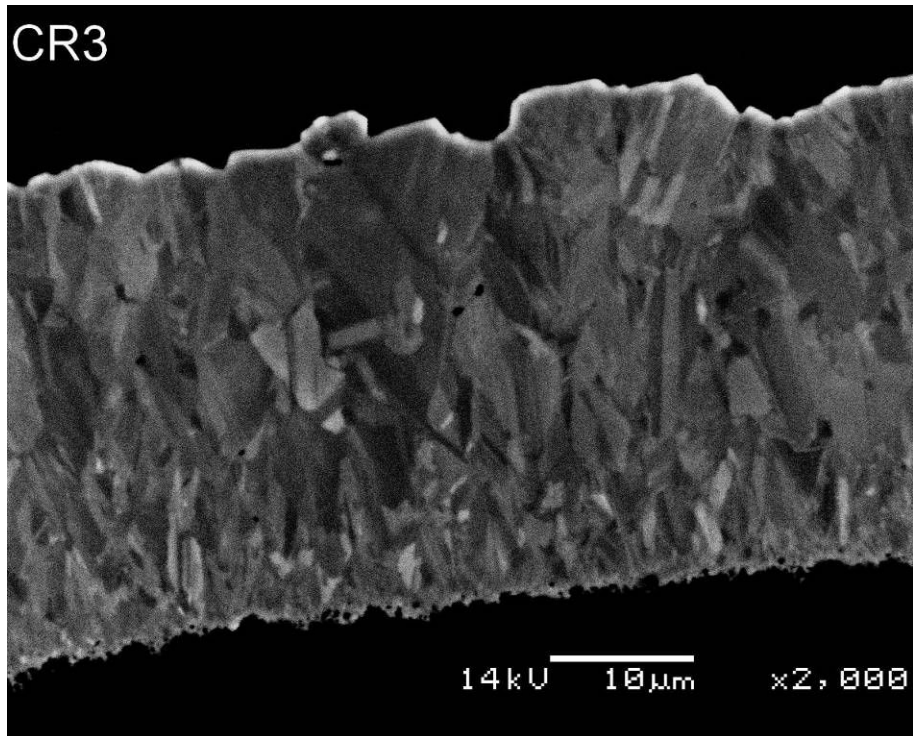


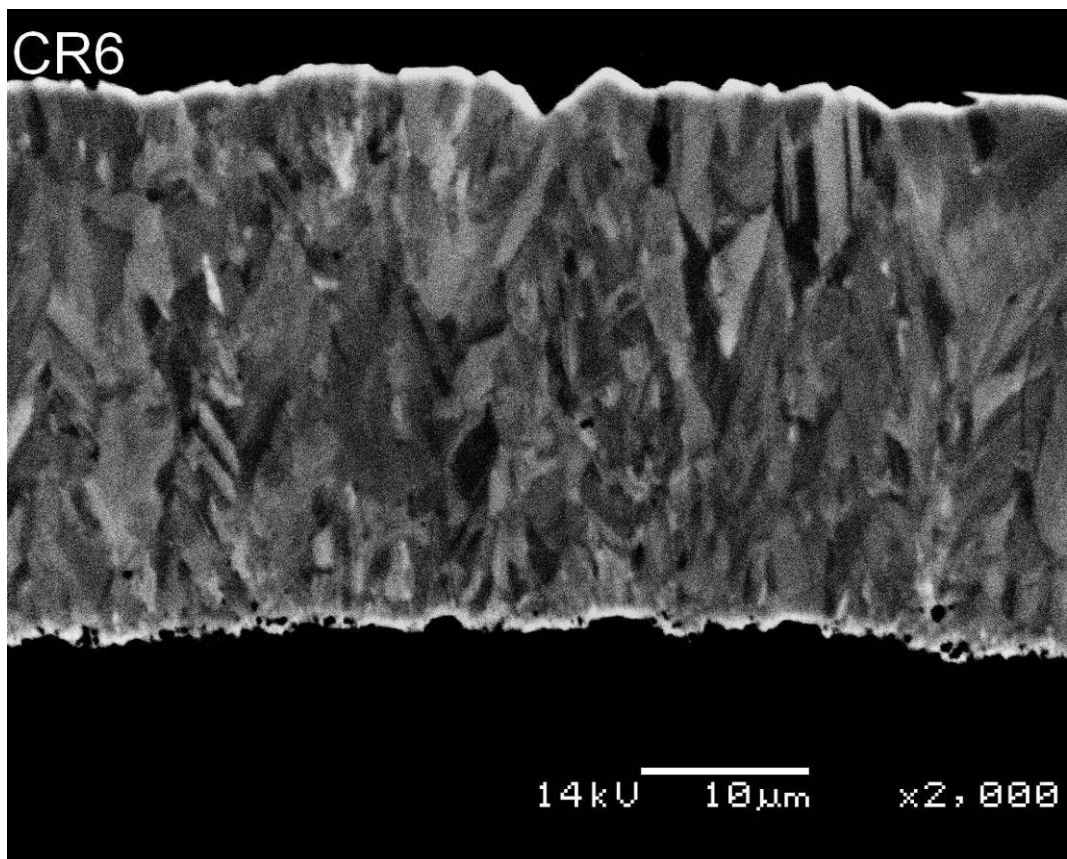
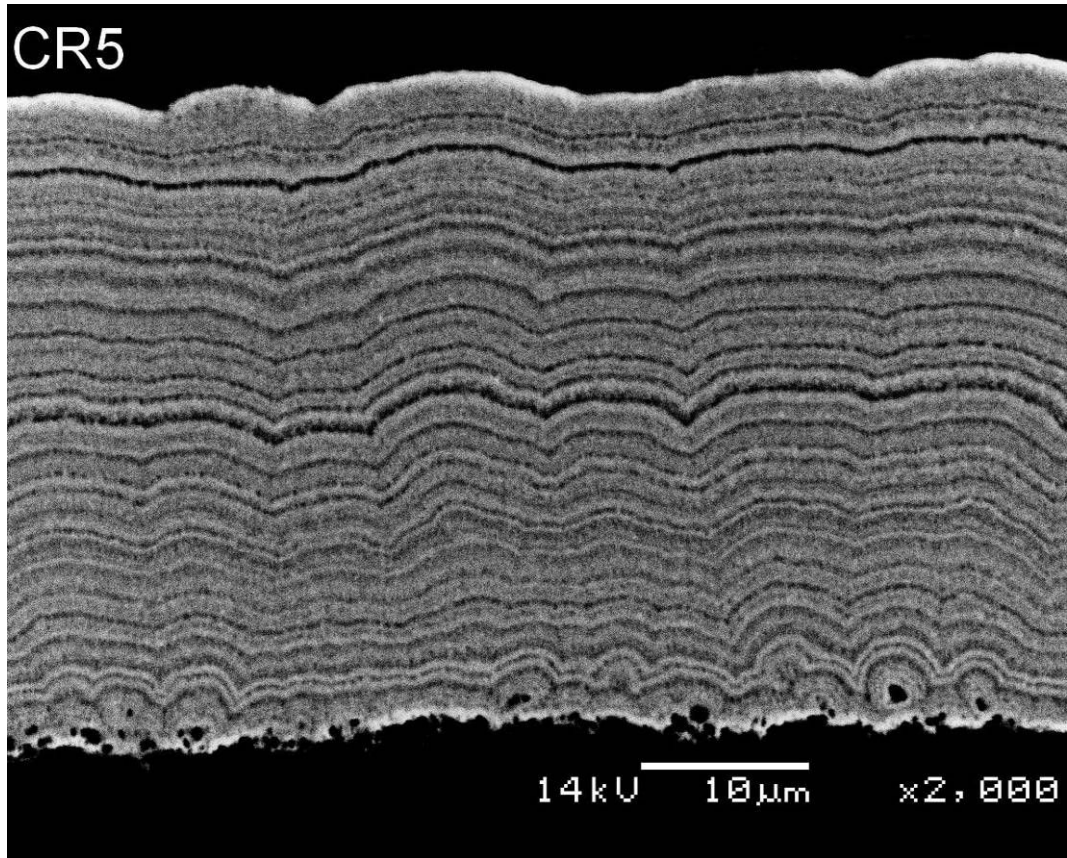
APPENDIX C: ELECTRON MICROSCOPY IMAGES

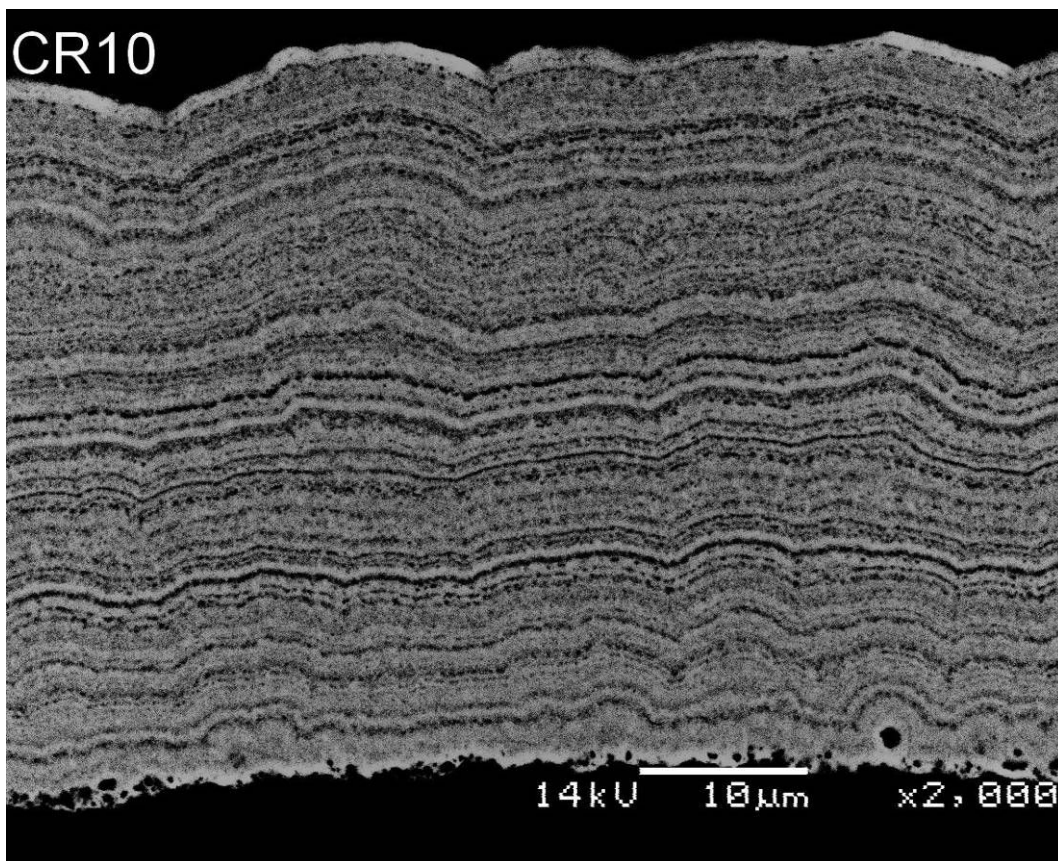
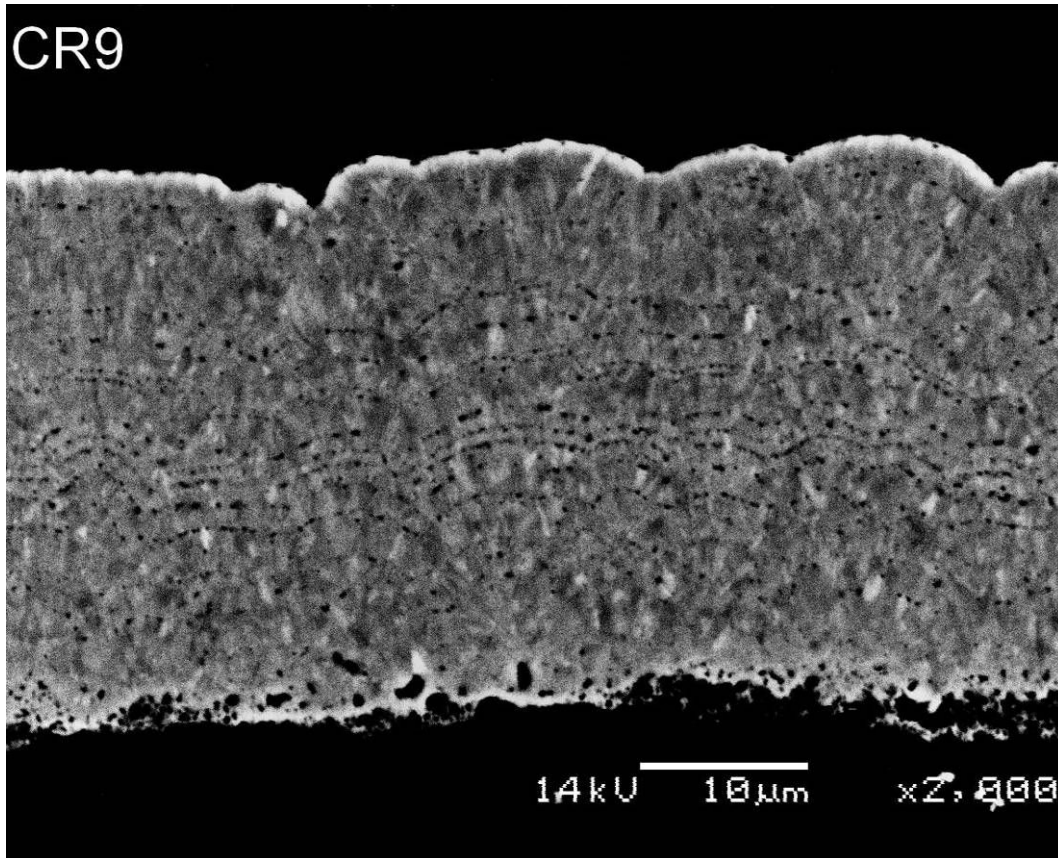
1	POLISHED SAMPLE: BACKSCATTER ELECTRON.....	356
1.1	COLD INLET	356
1.2	HOT INLET	367
2	ETCHED SAMPLE SECONDARY ELECTRON IMAGES.....	374
2.1	COLD INLET	374
2.2	HOT INLET	384
3	SURFACE STRUCTURE SECONDARY ELECTRON IMAGE.....	393
3.1	COLD INLET.....	393
3.2	HOT INLET	401

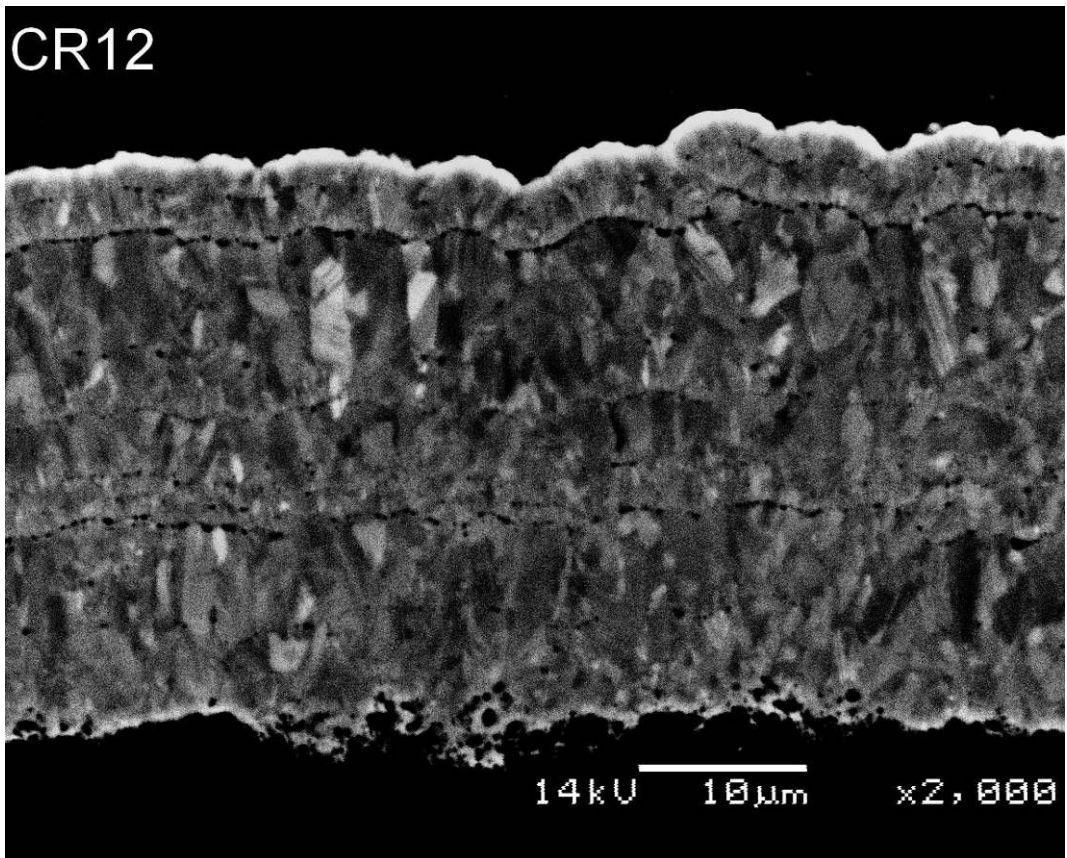
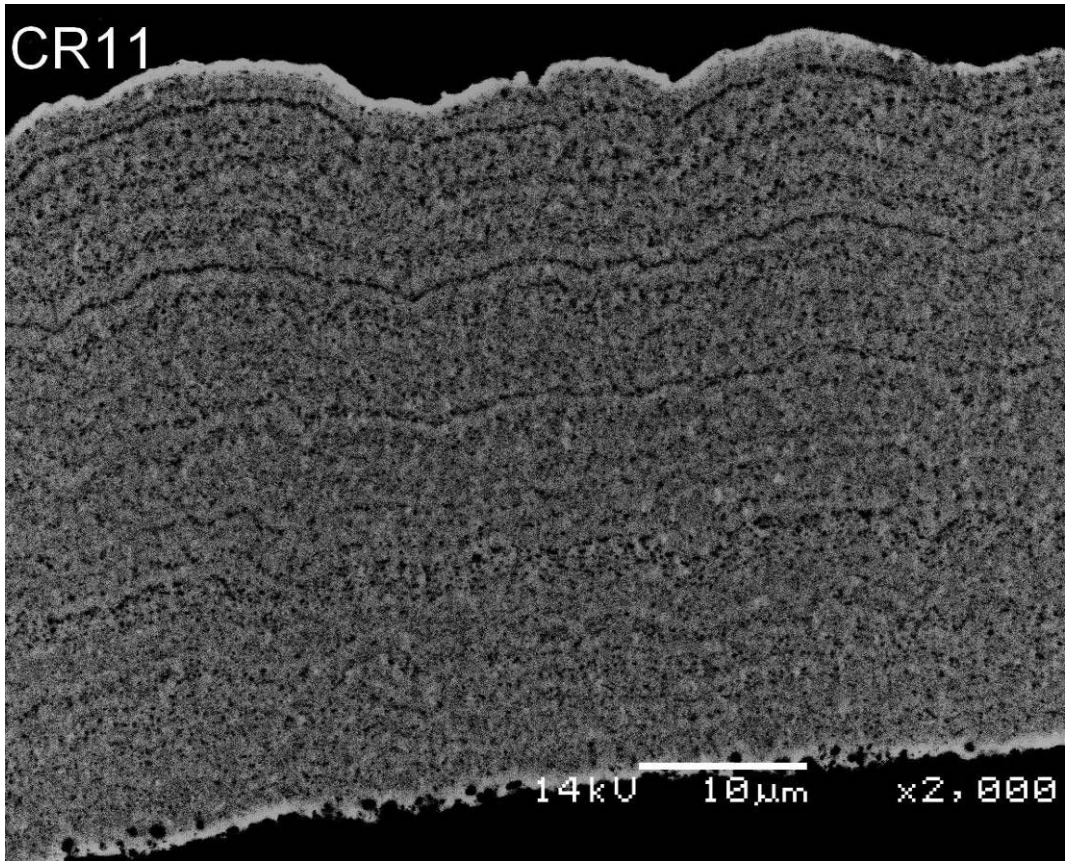
1 POLISHED SAMPLE: BACKSCATTER ELECTRON IMAGES

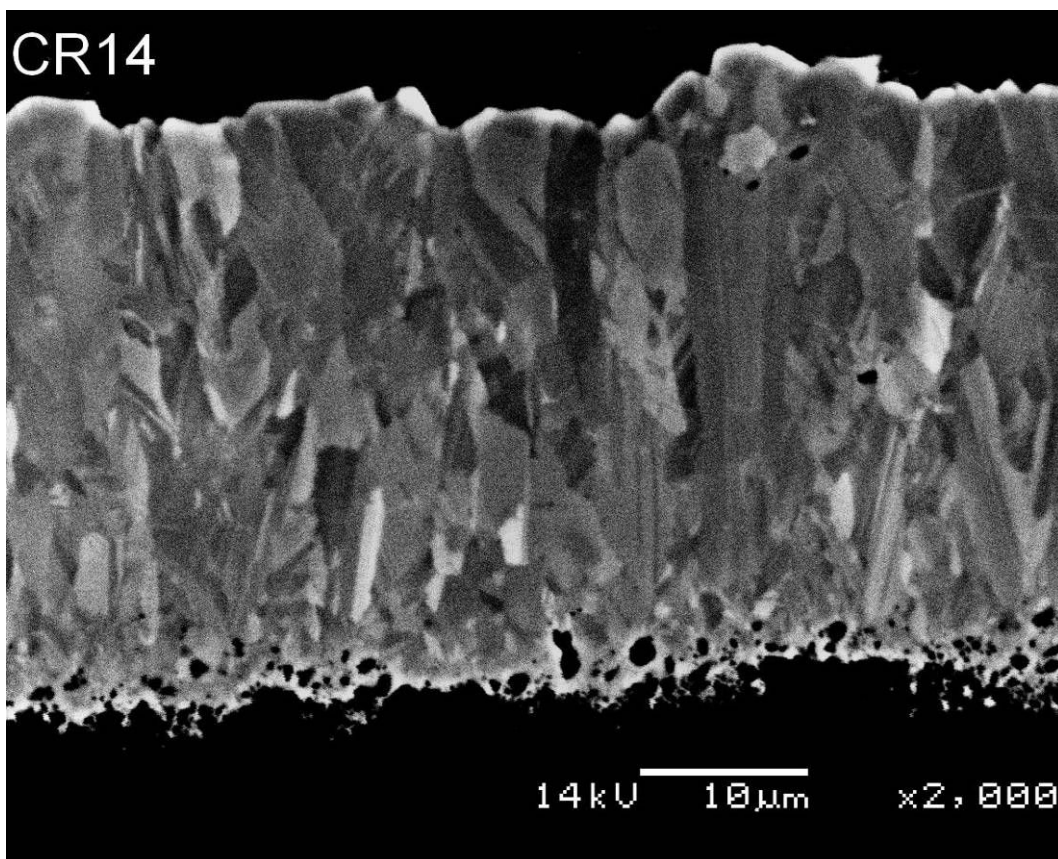
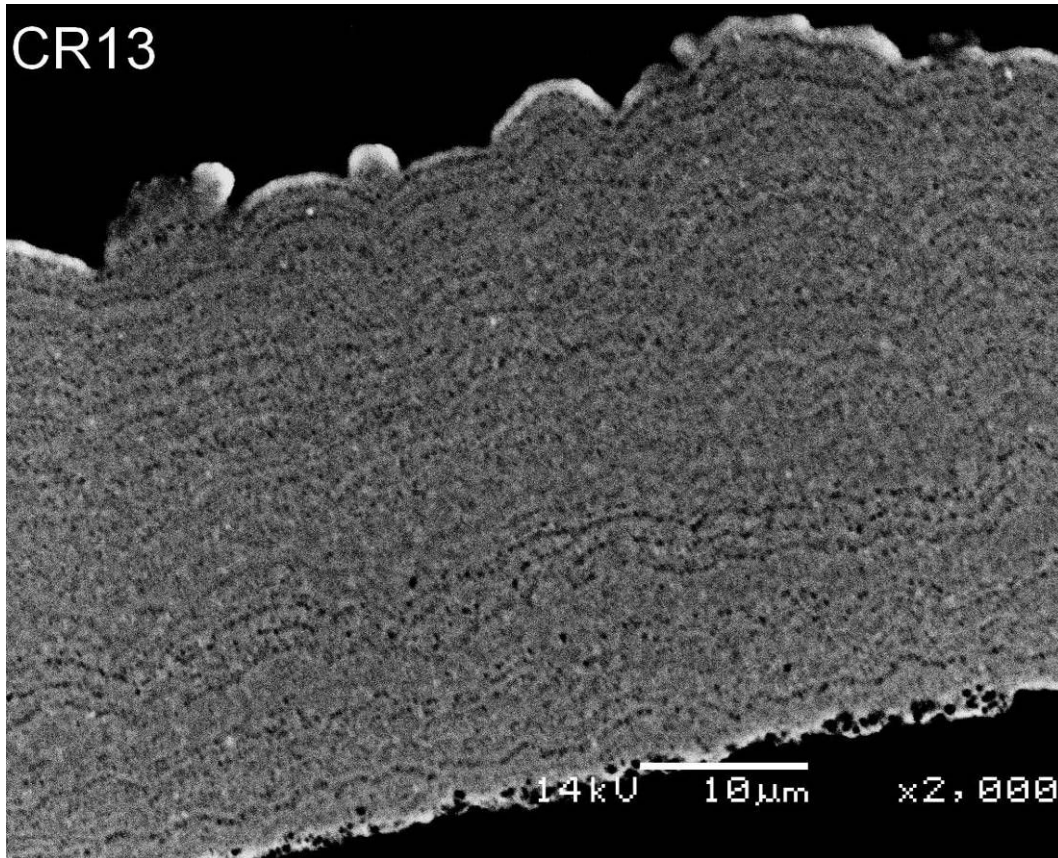
1.1 COLD INLET

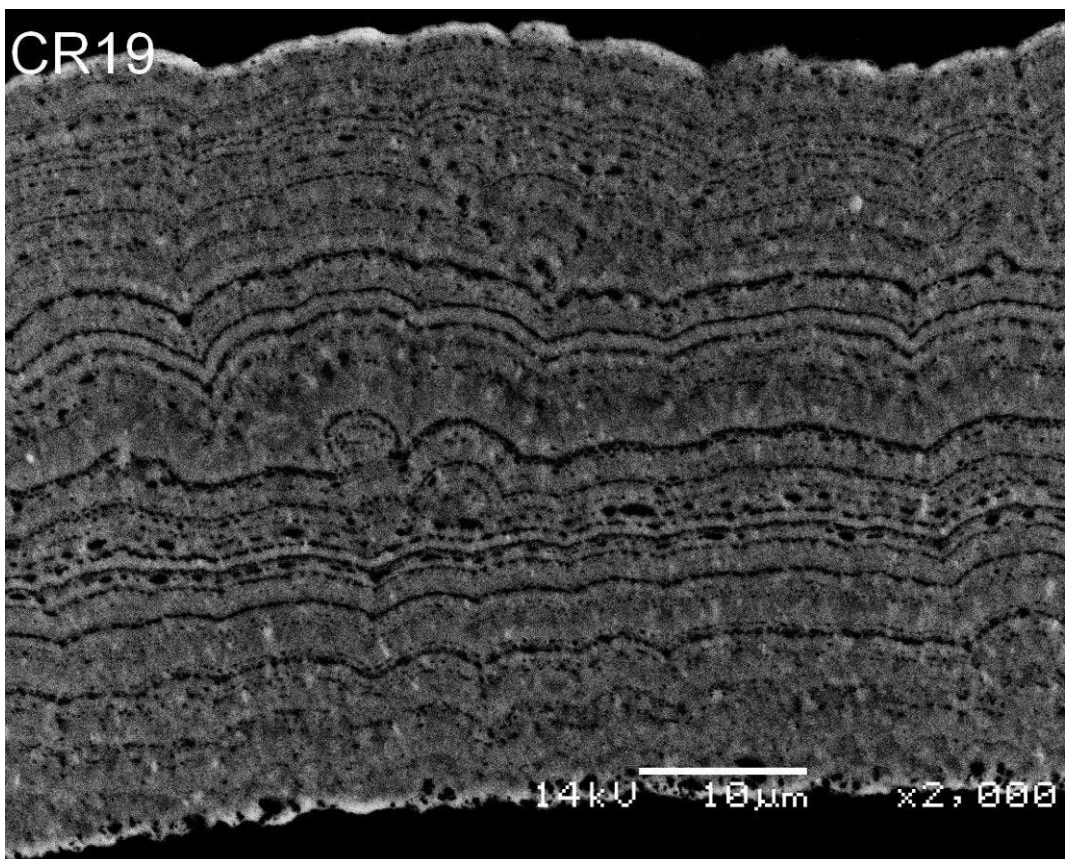
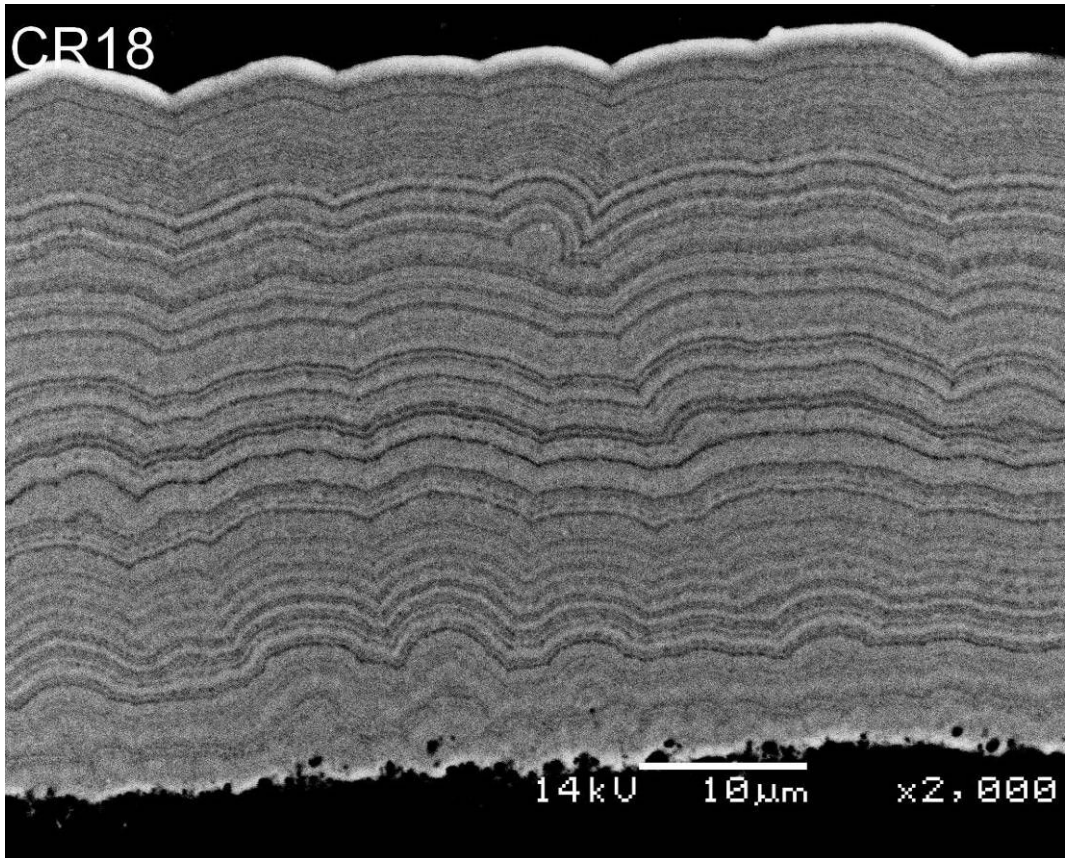


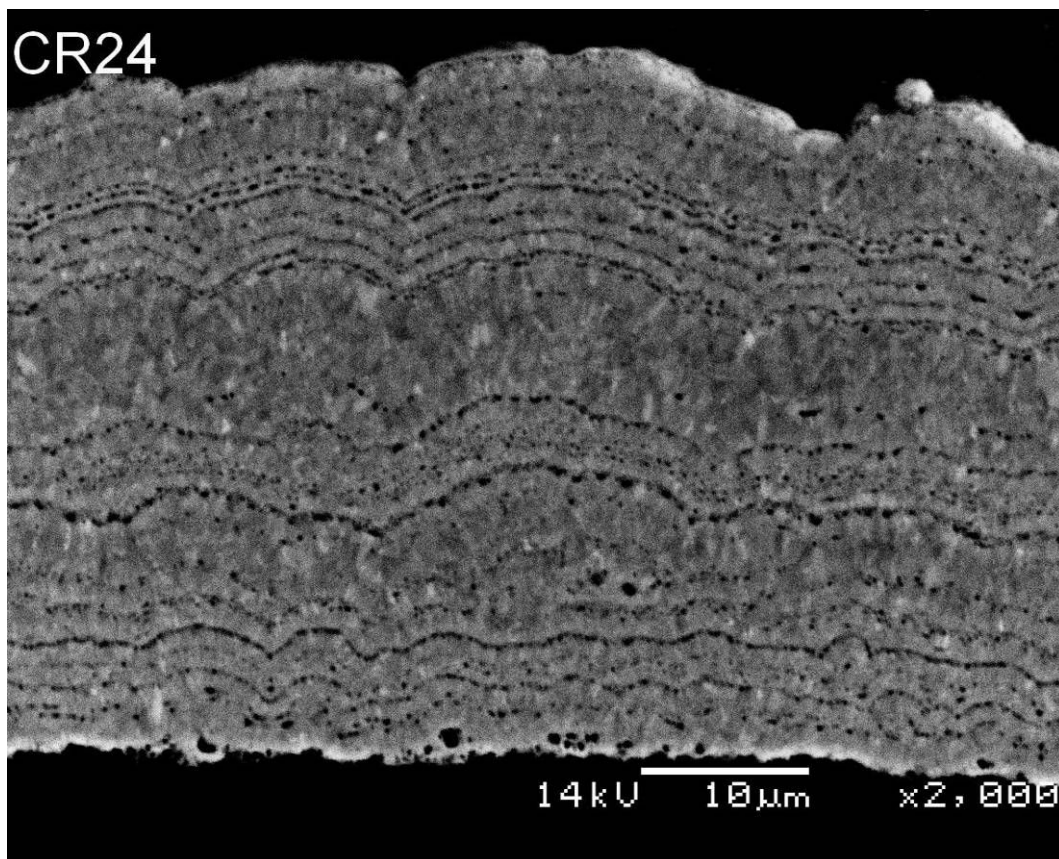
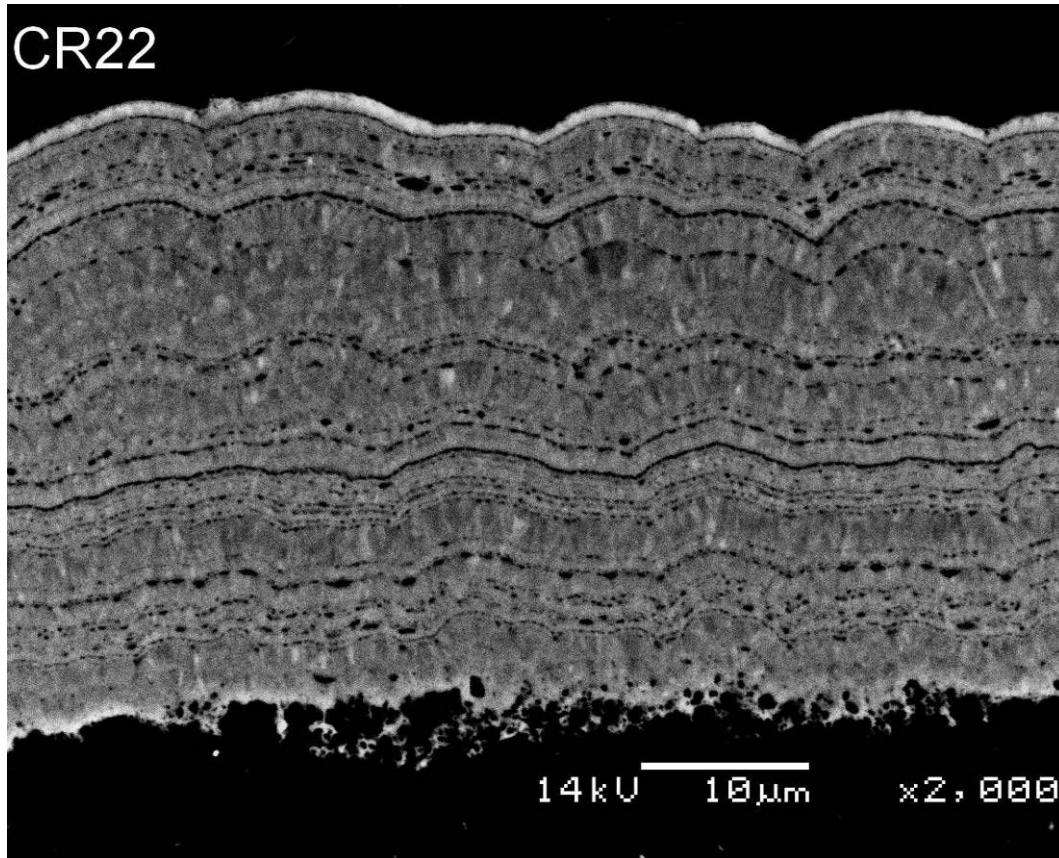


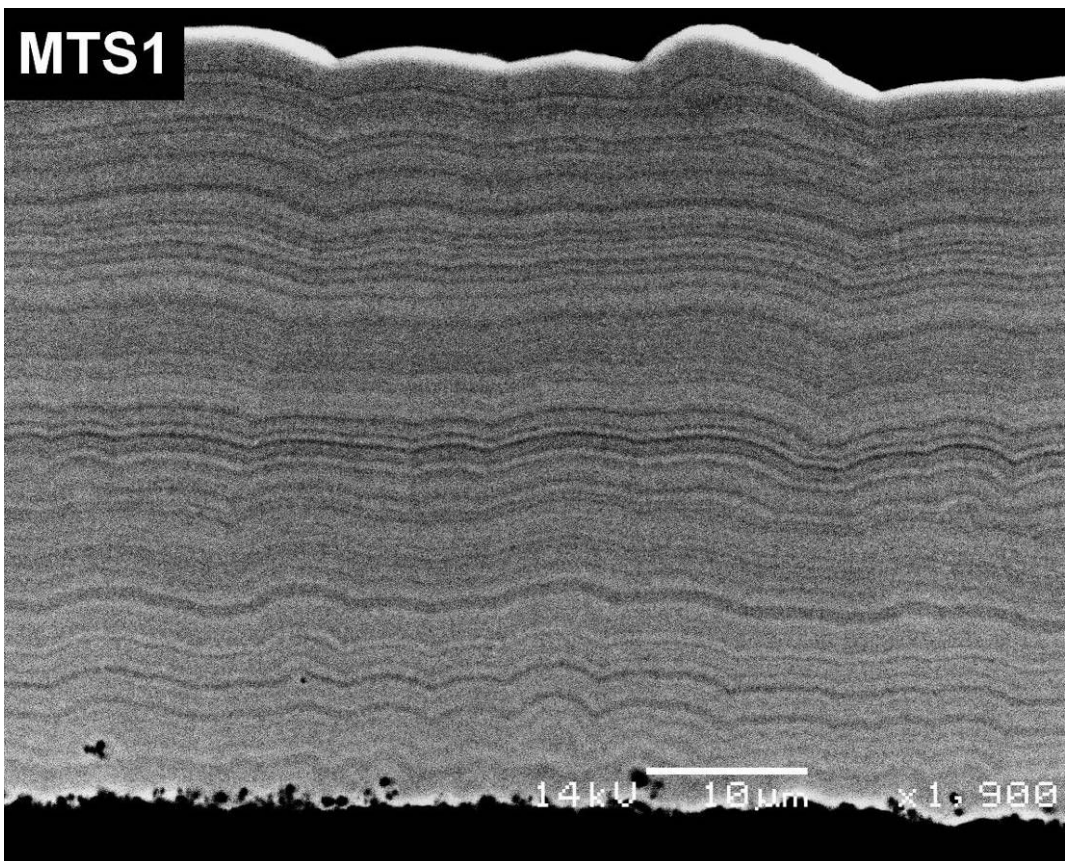
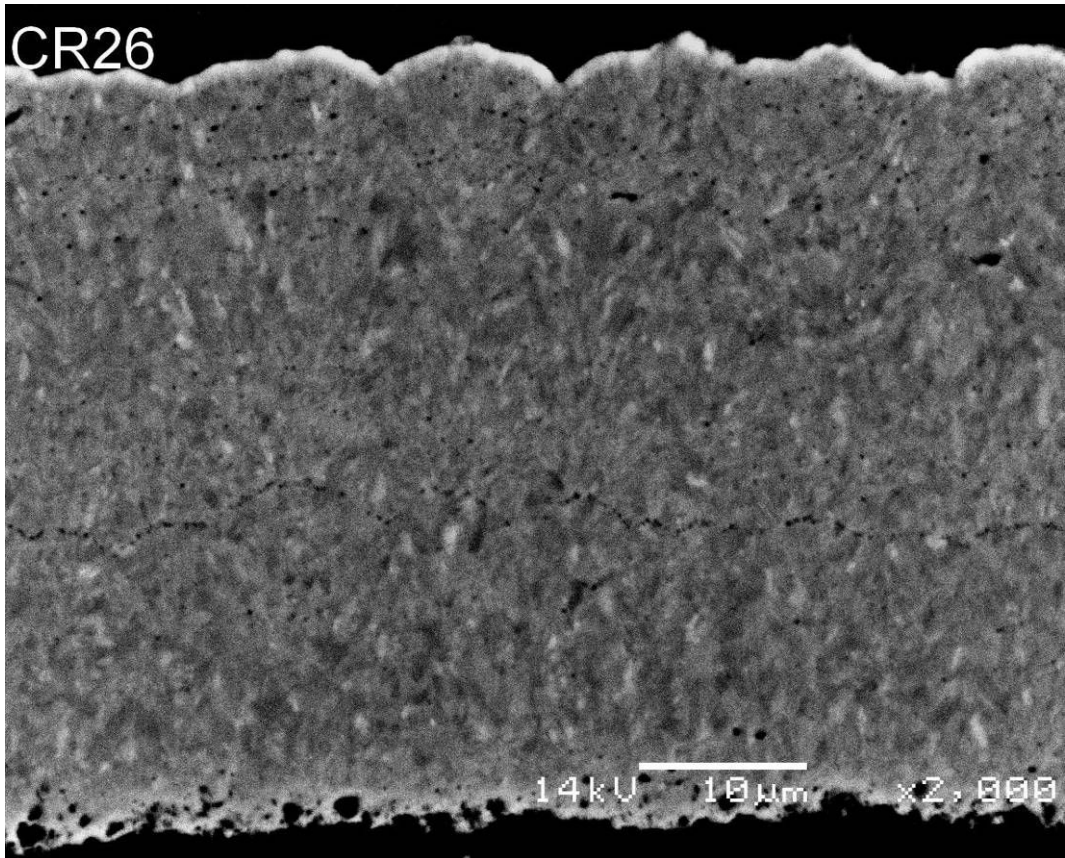


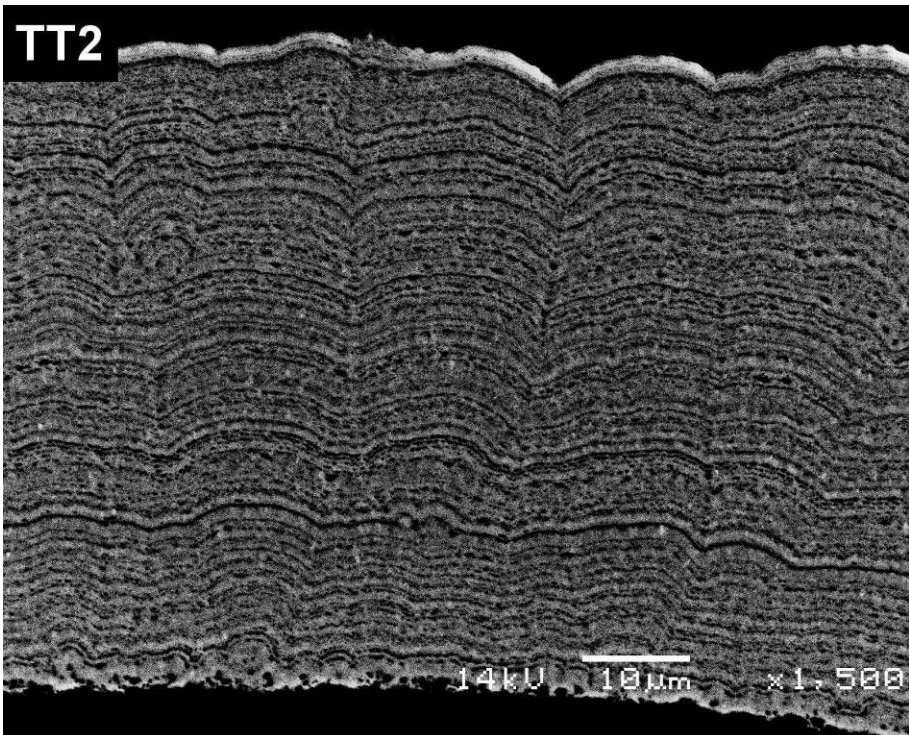
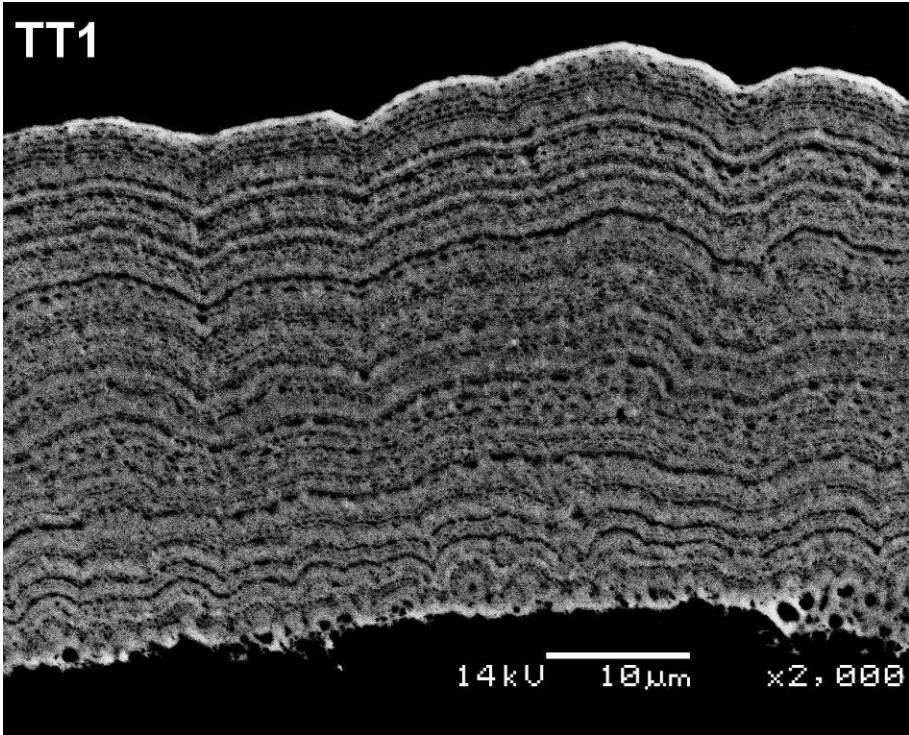


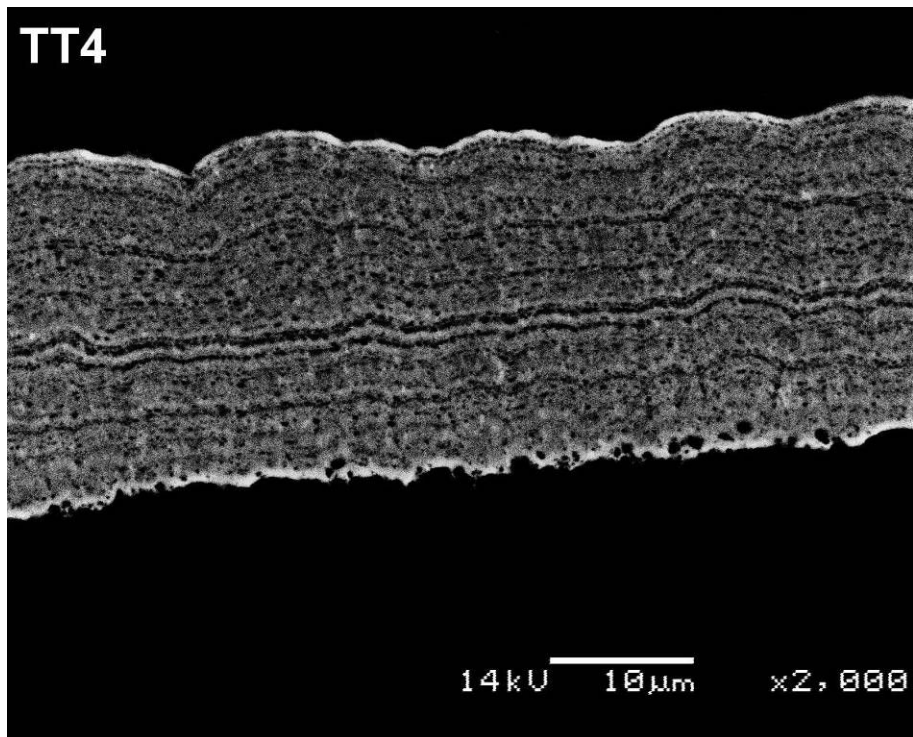
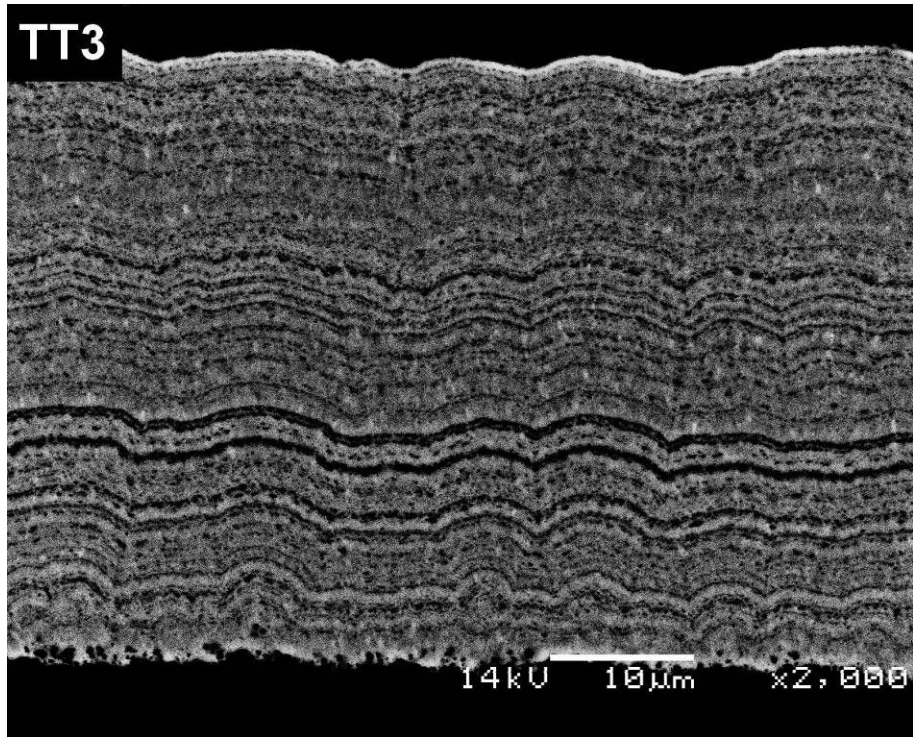


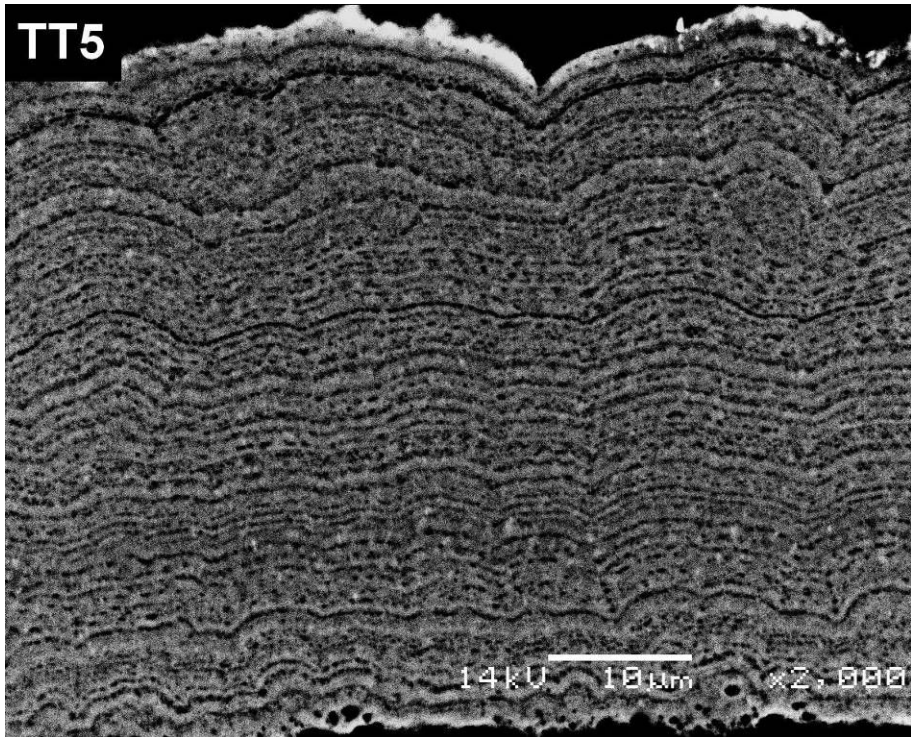




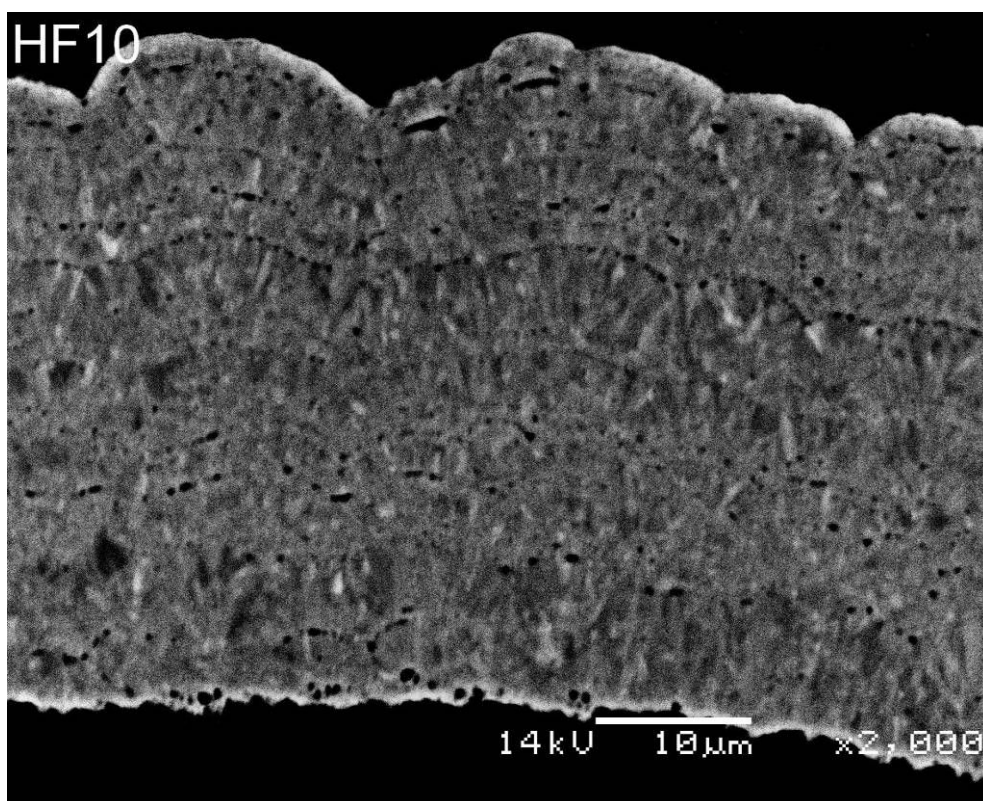
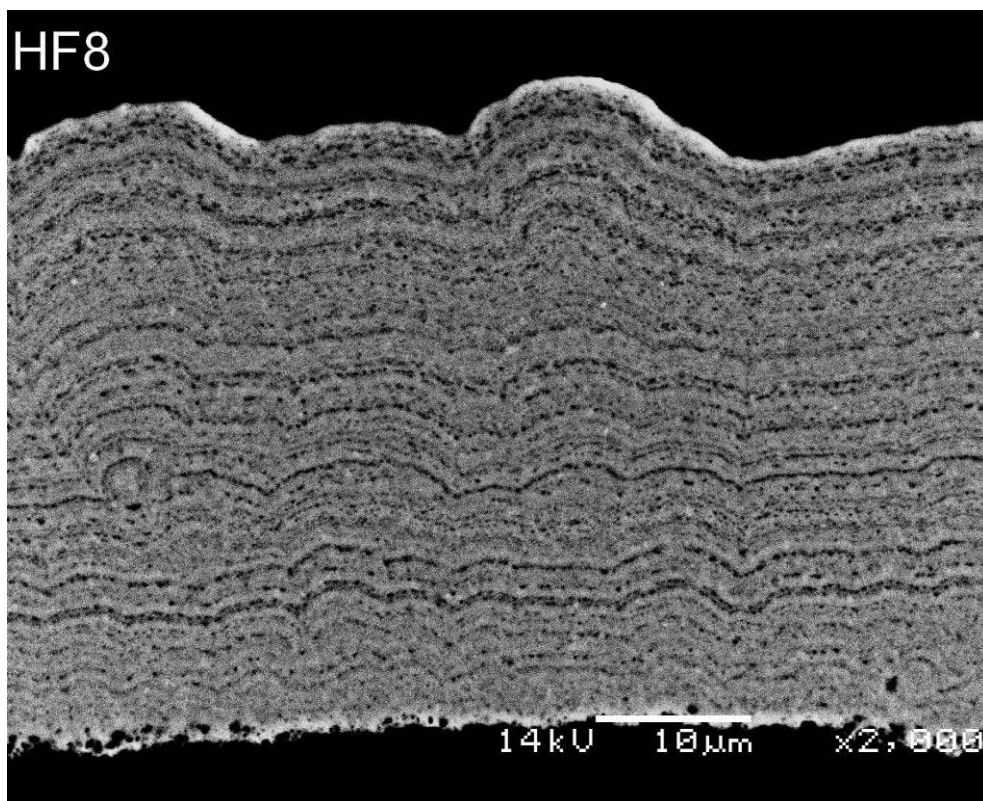


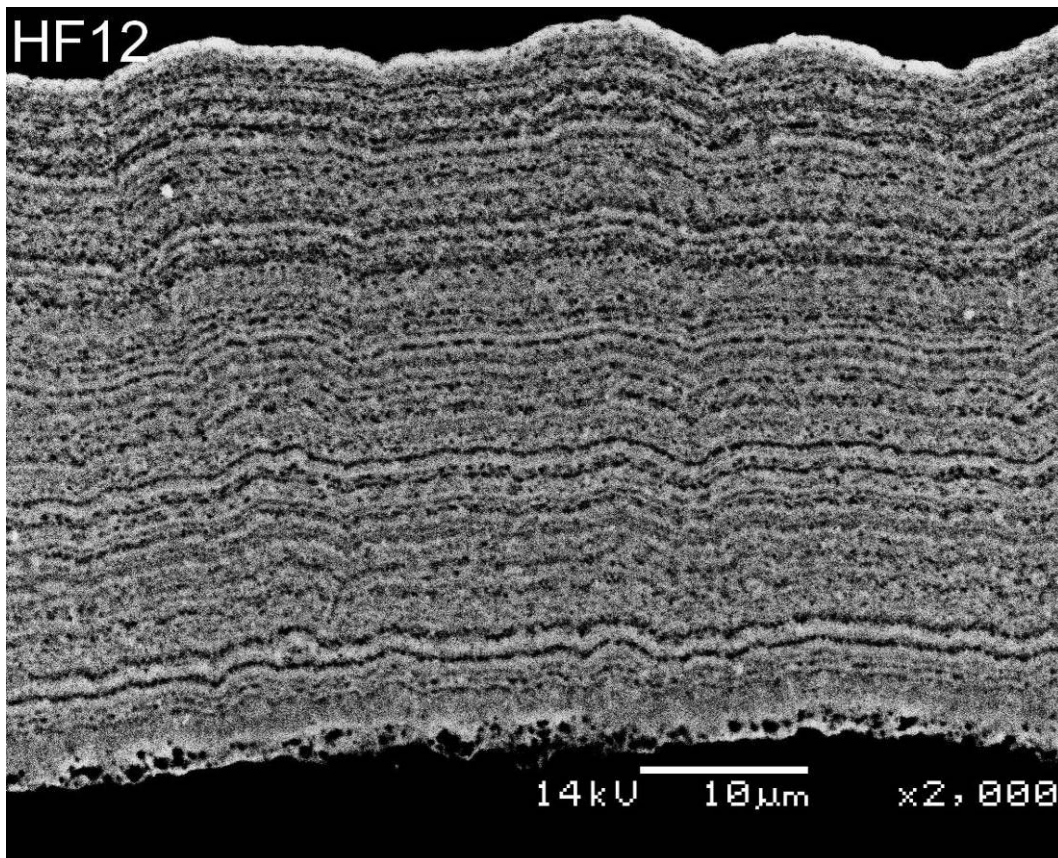
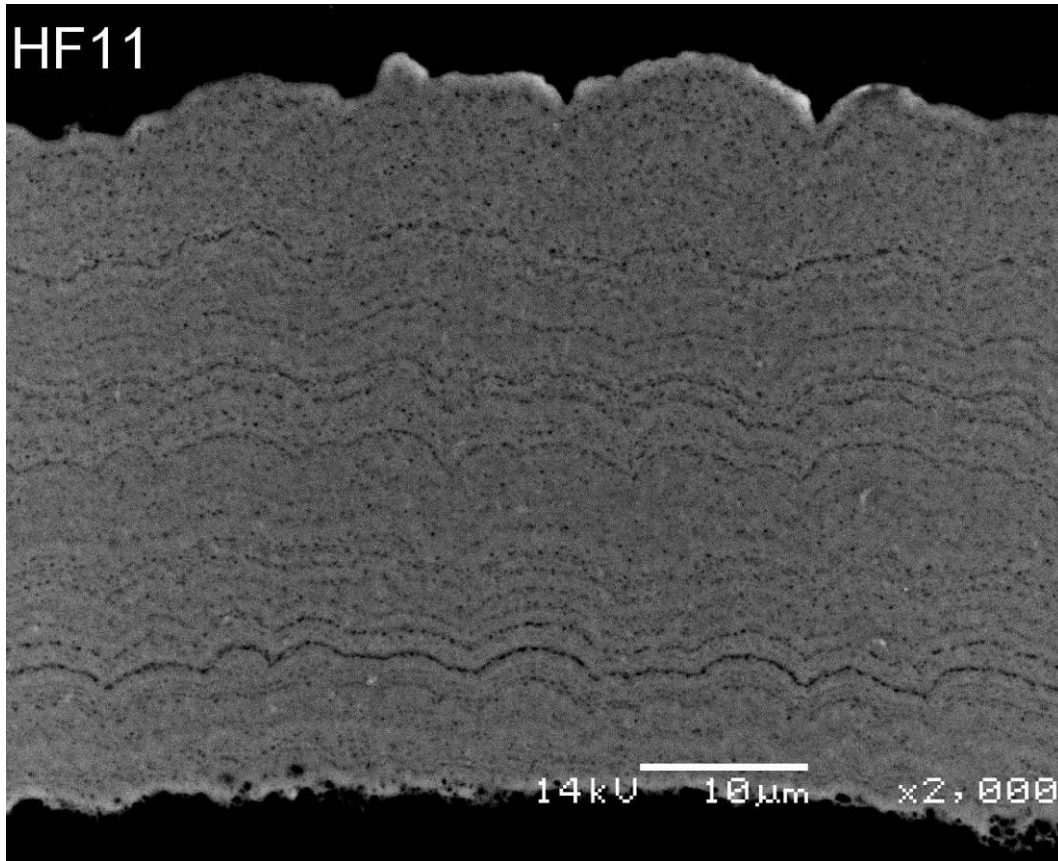


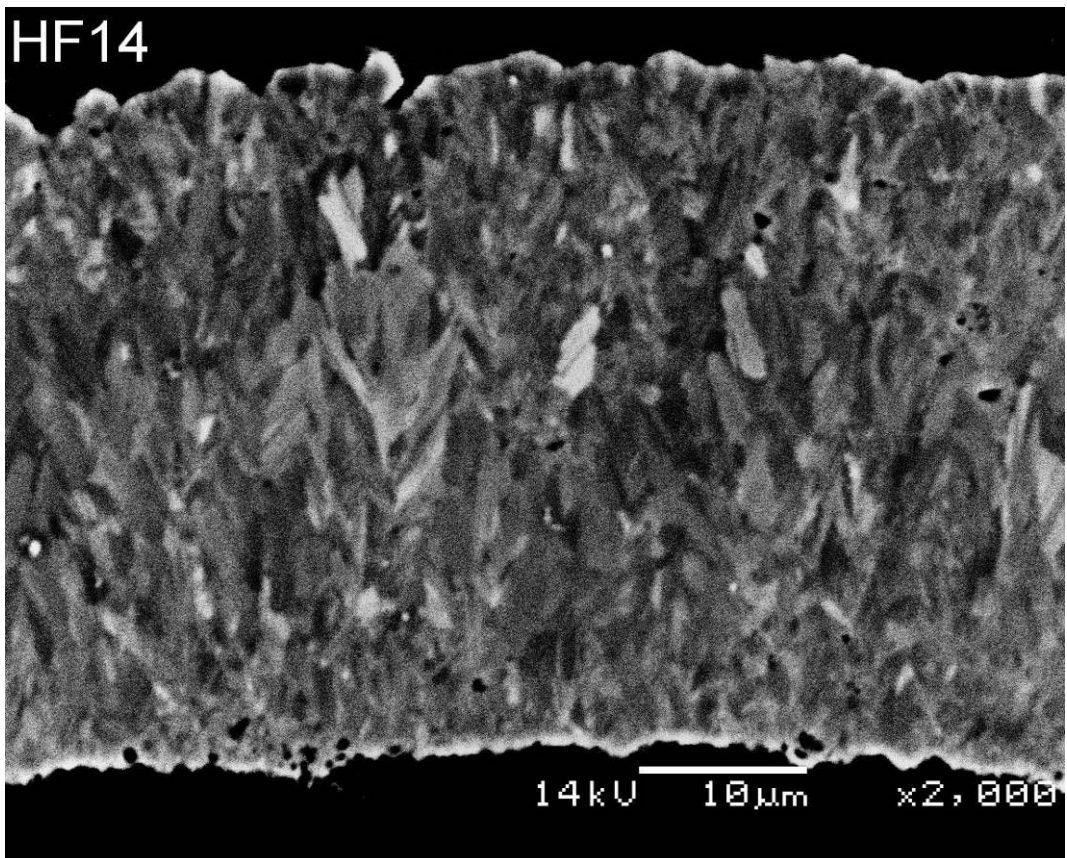
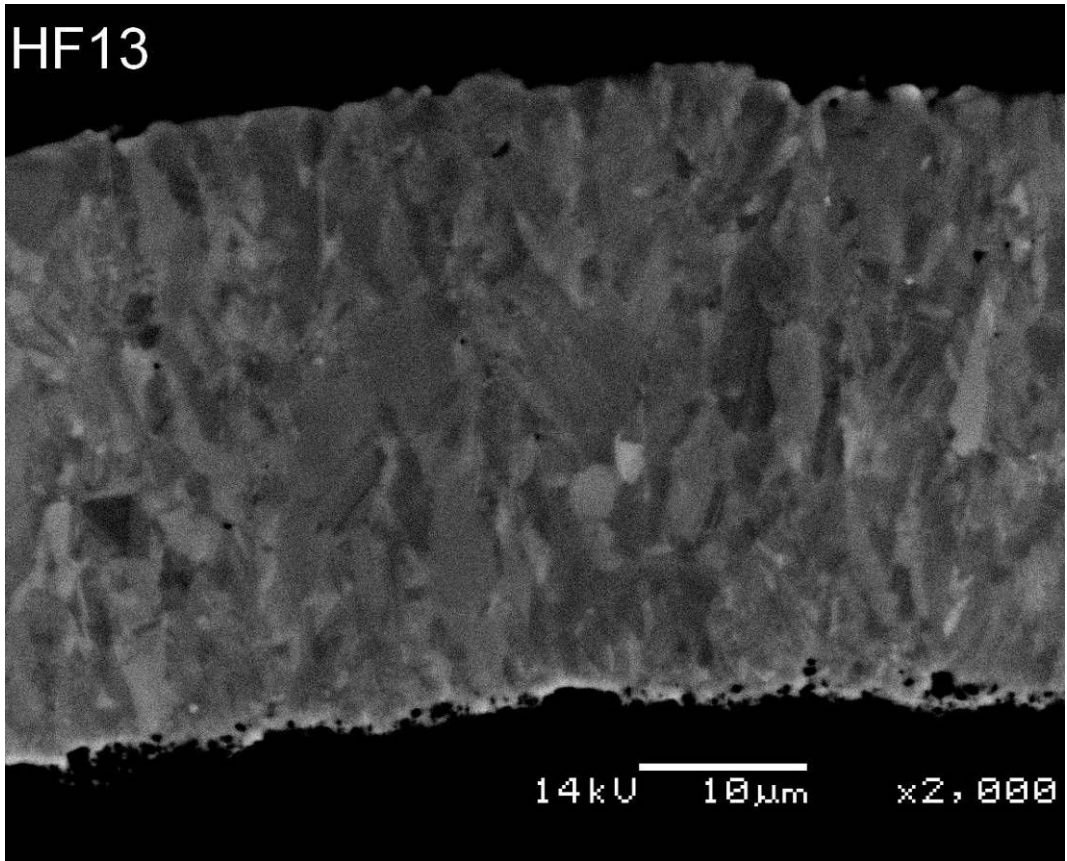


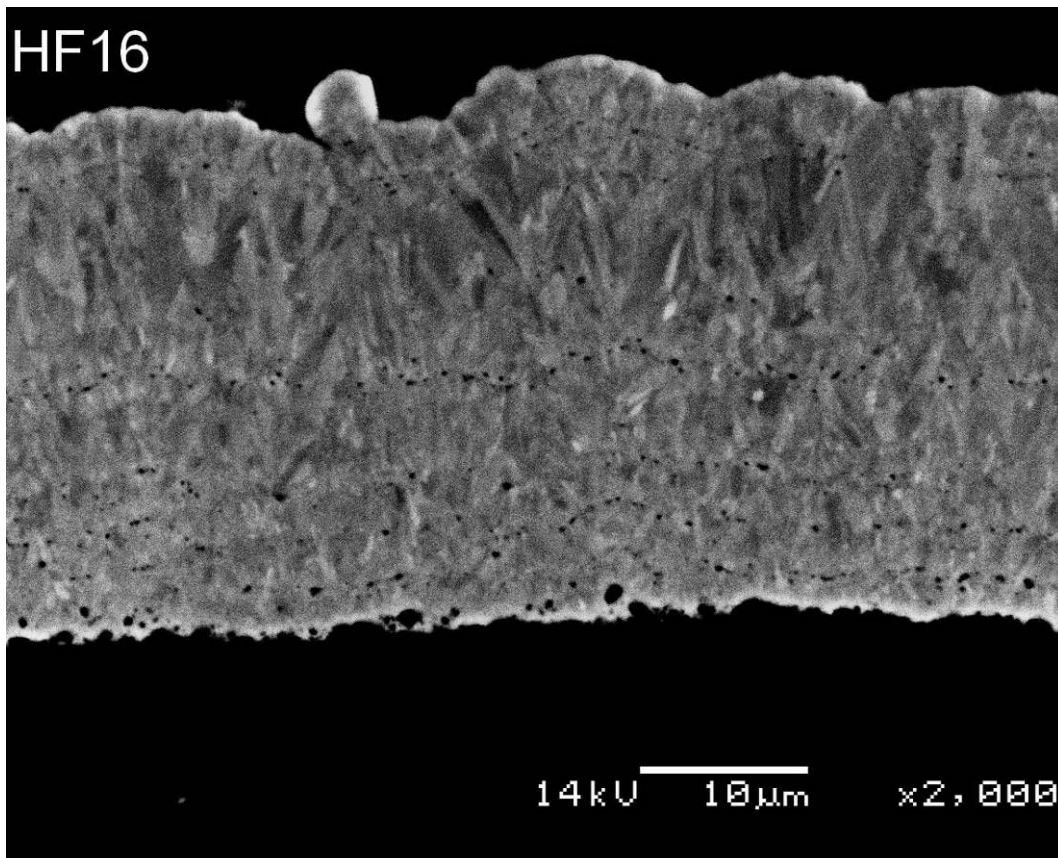
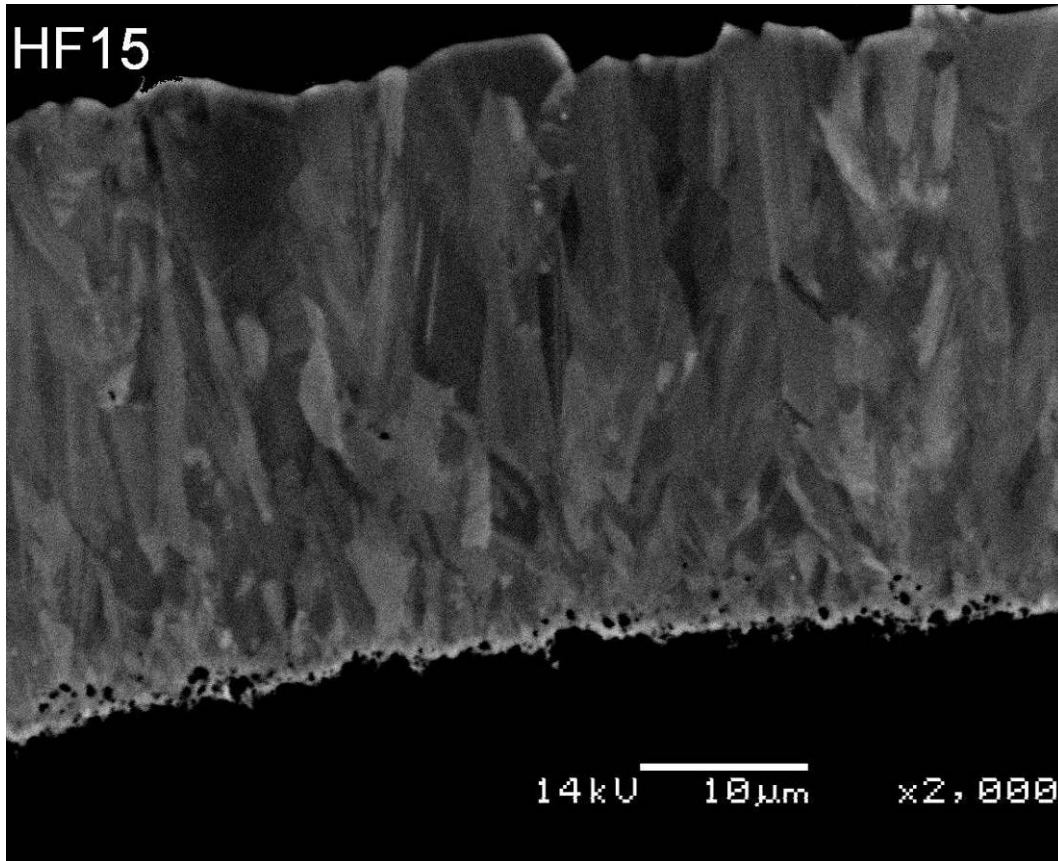


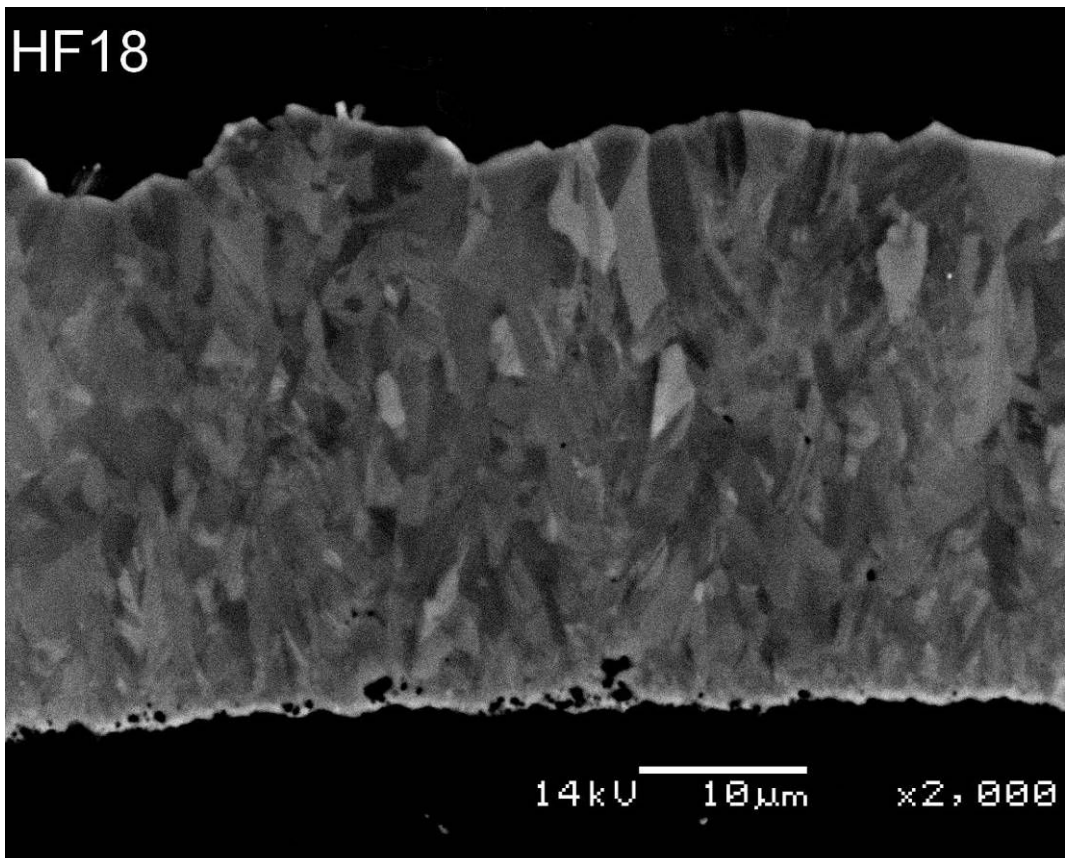
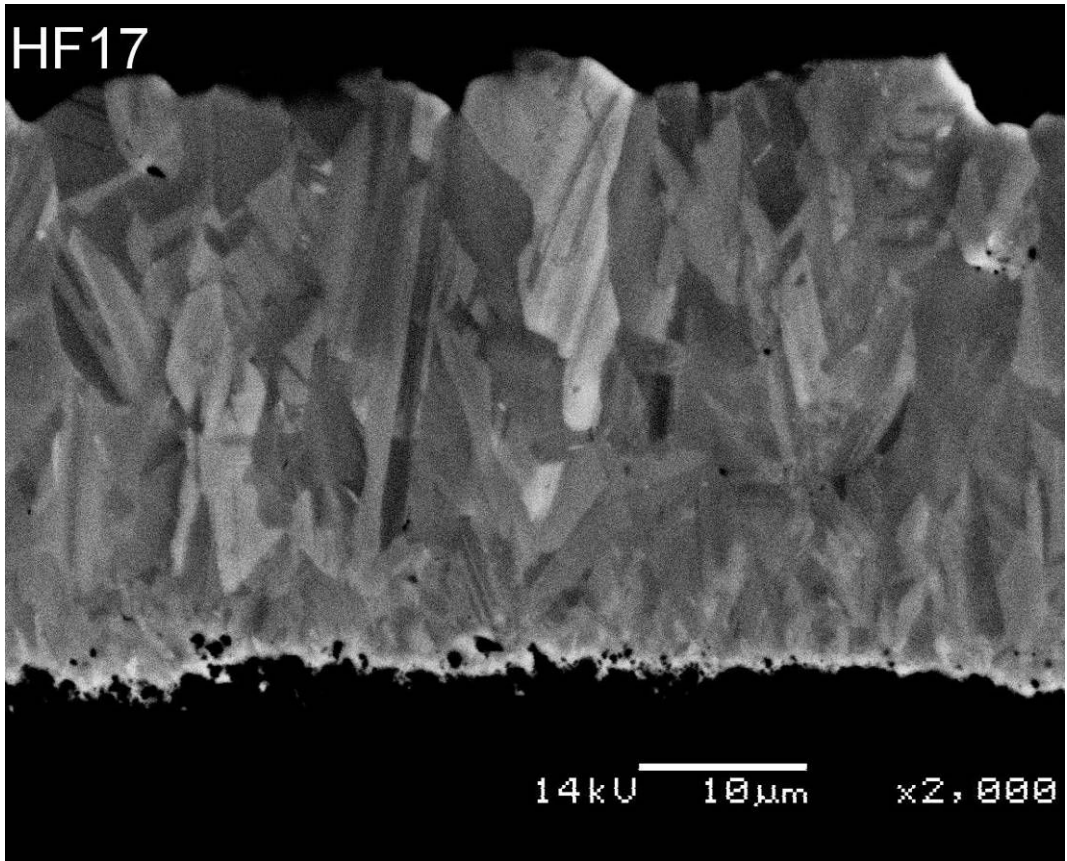
1.2 HOT INLET

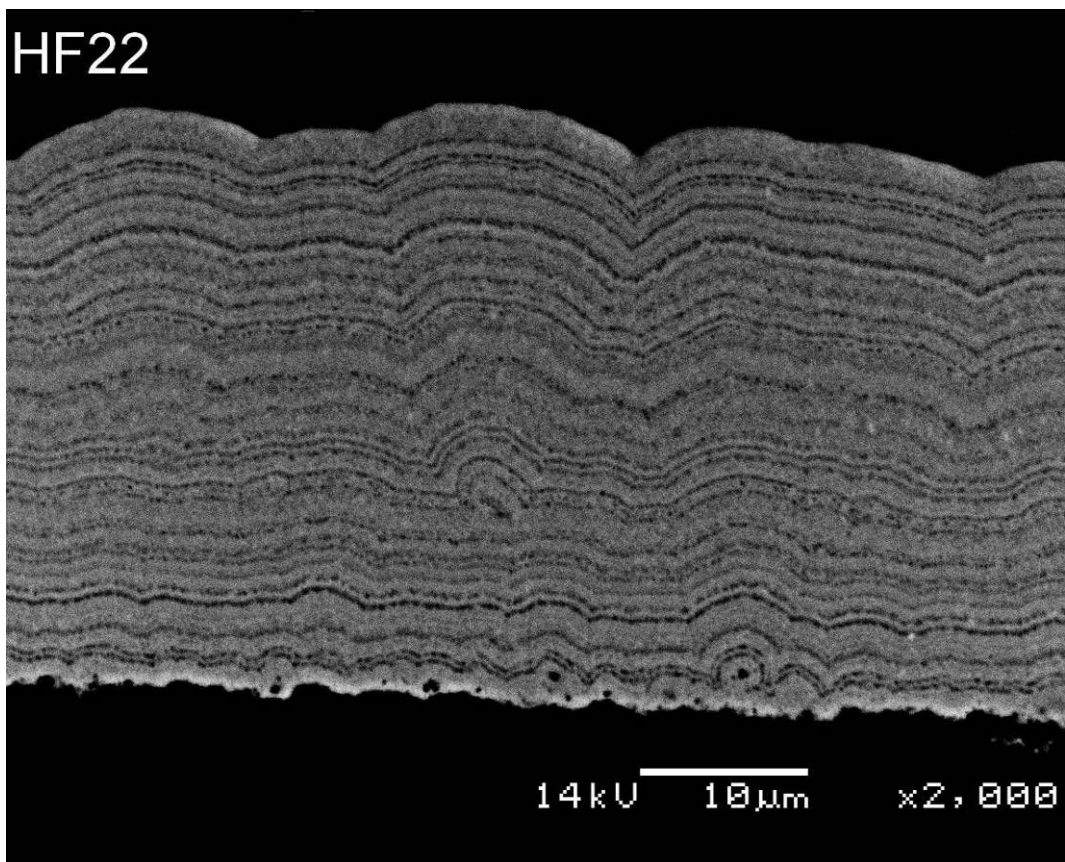
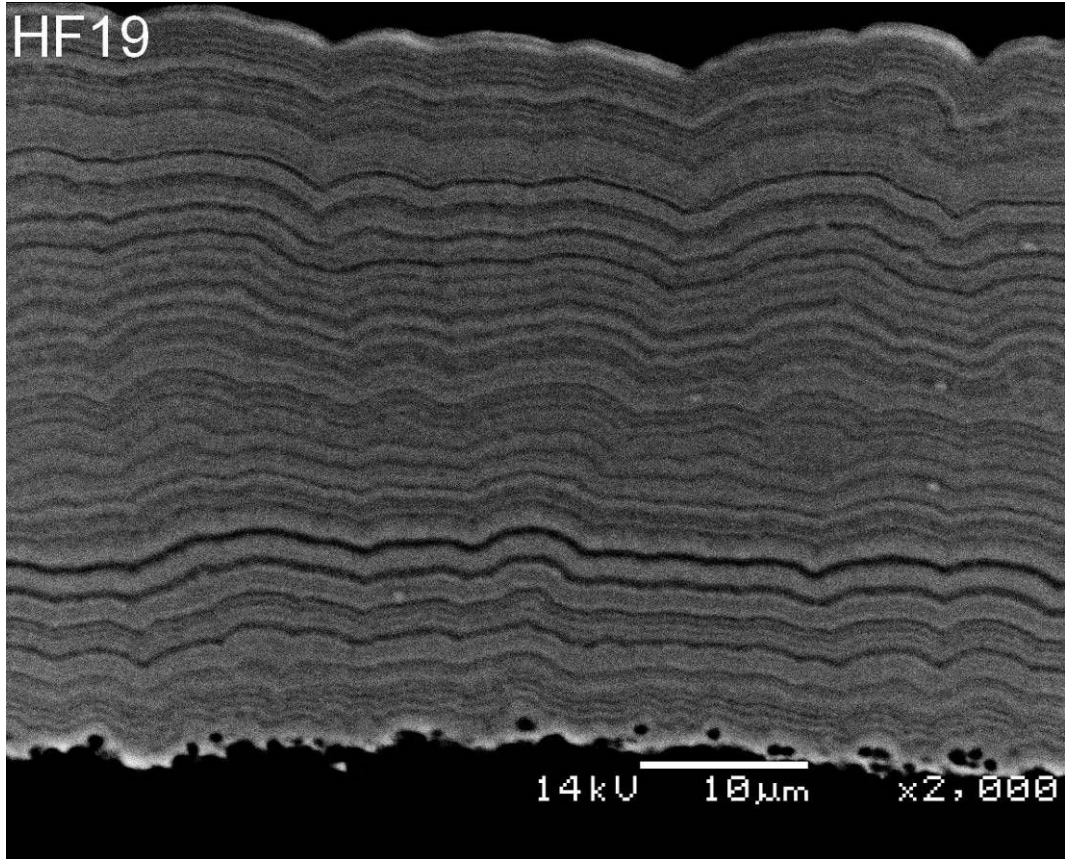


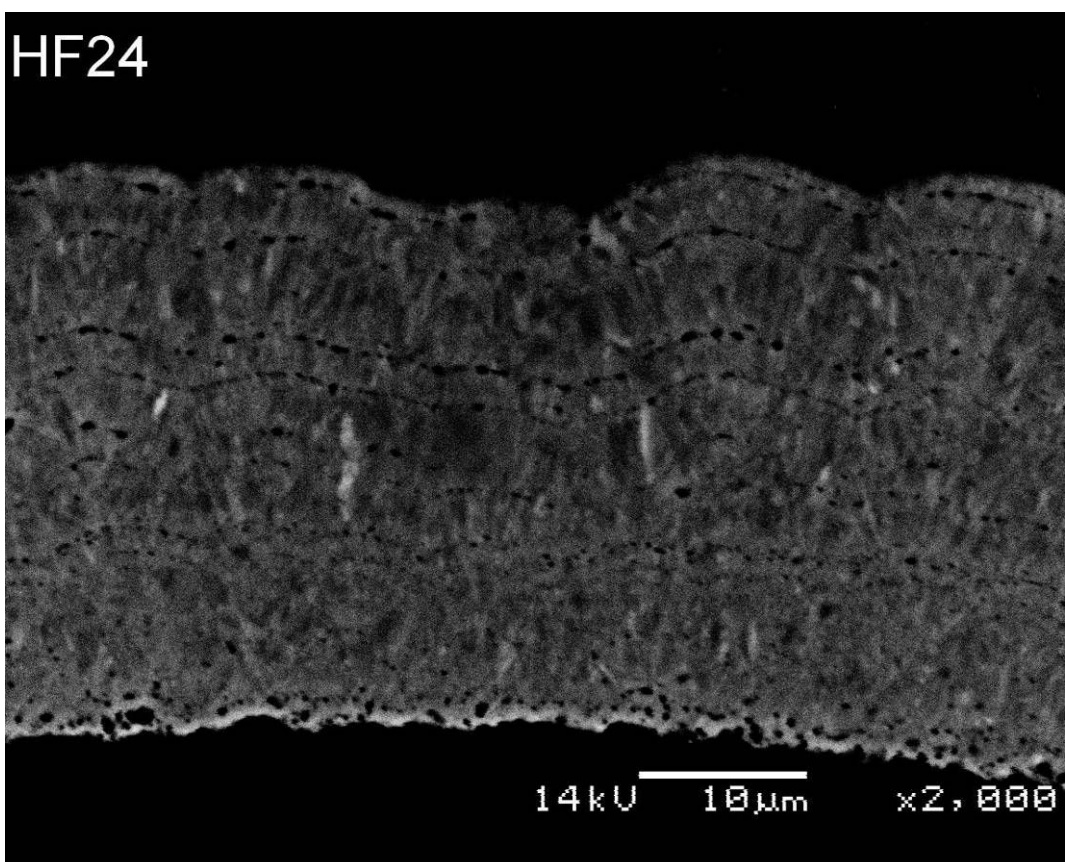
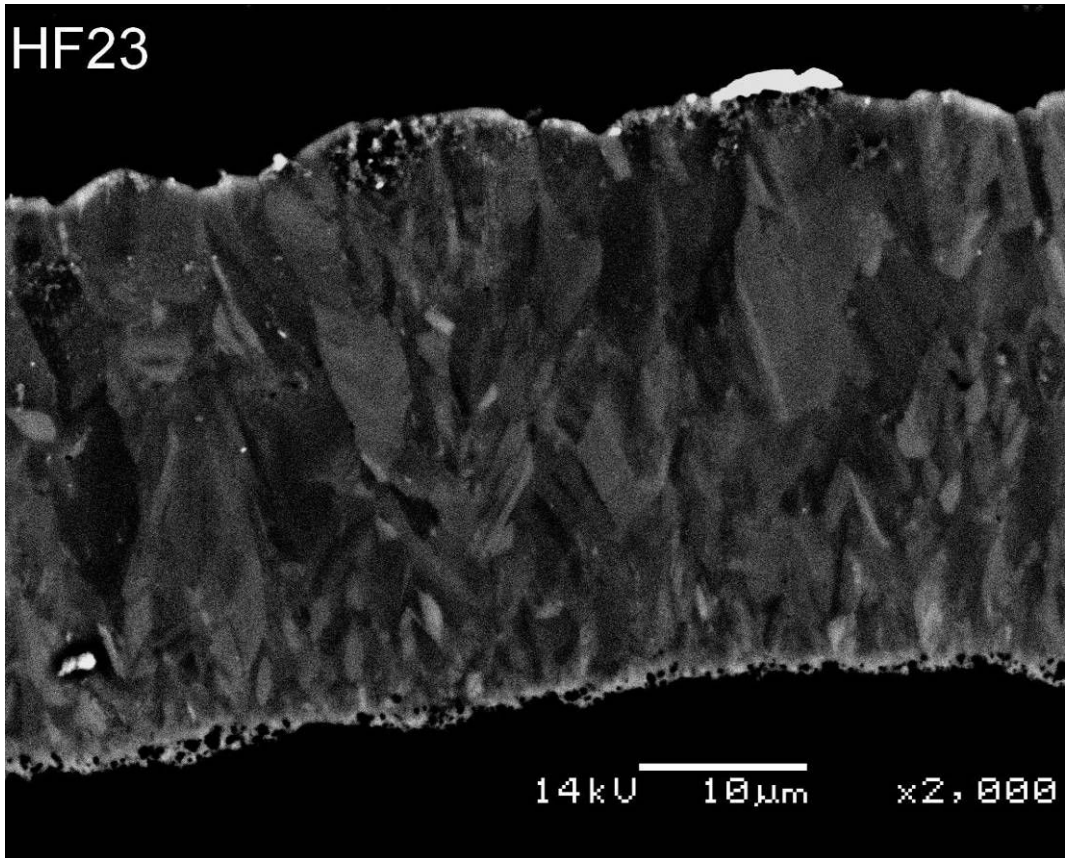






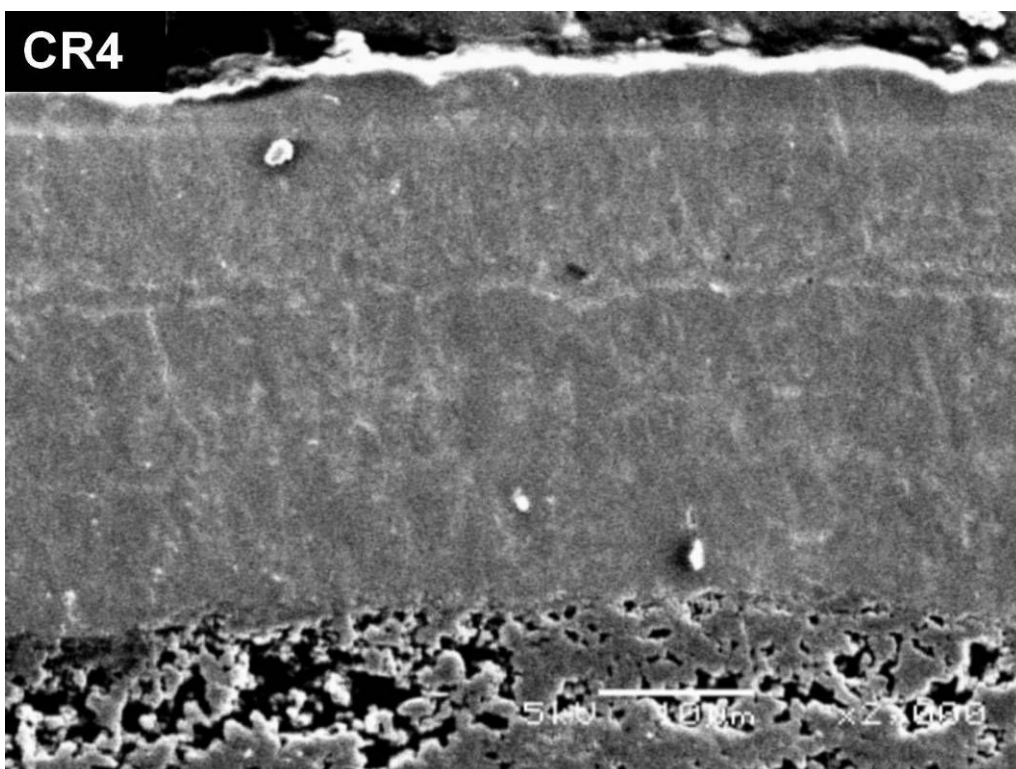
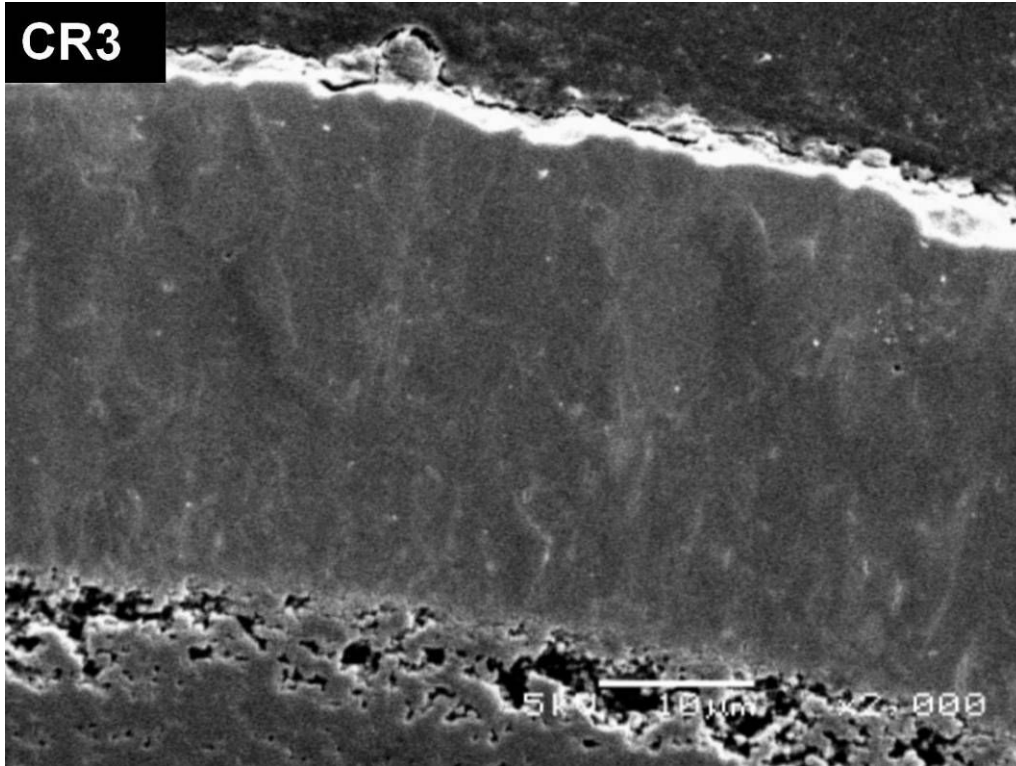


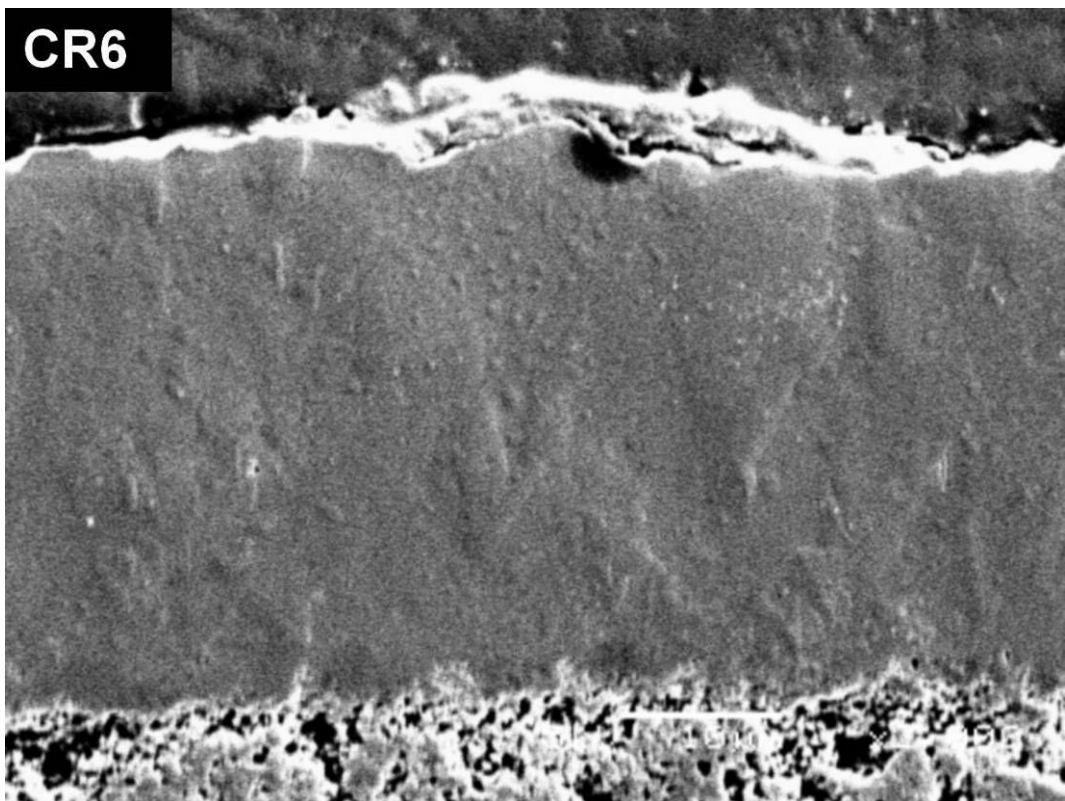
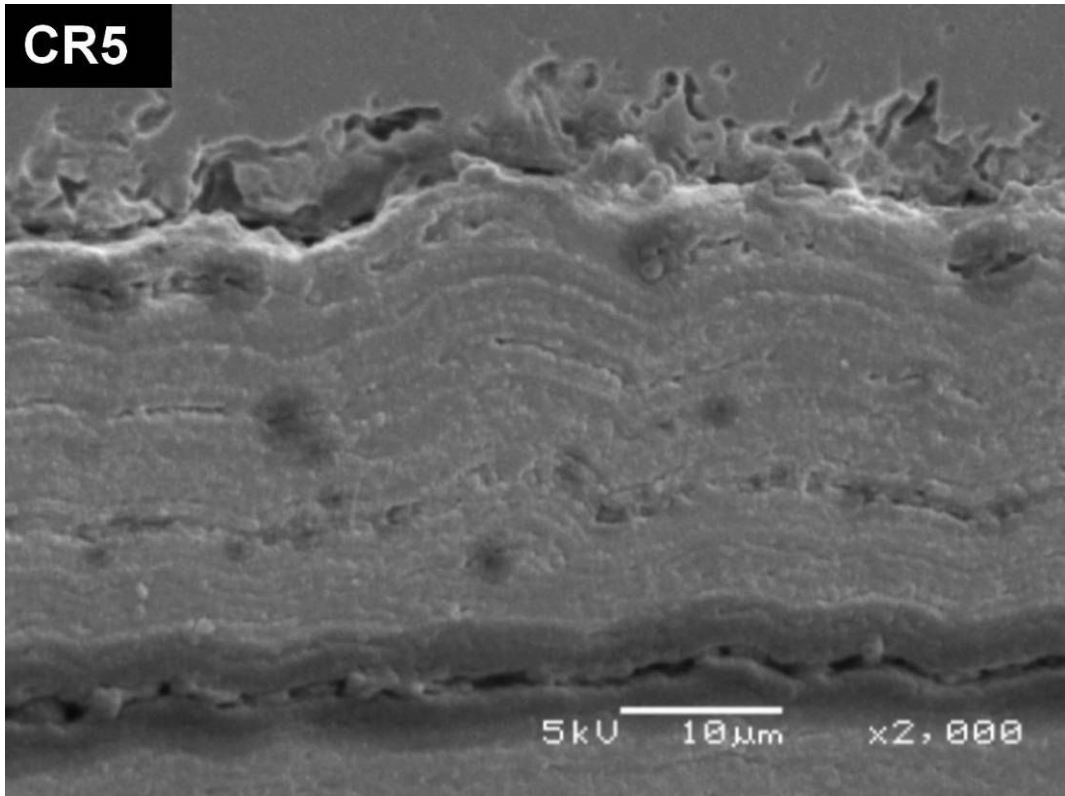


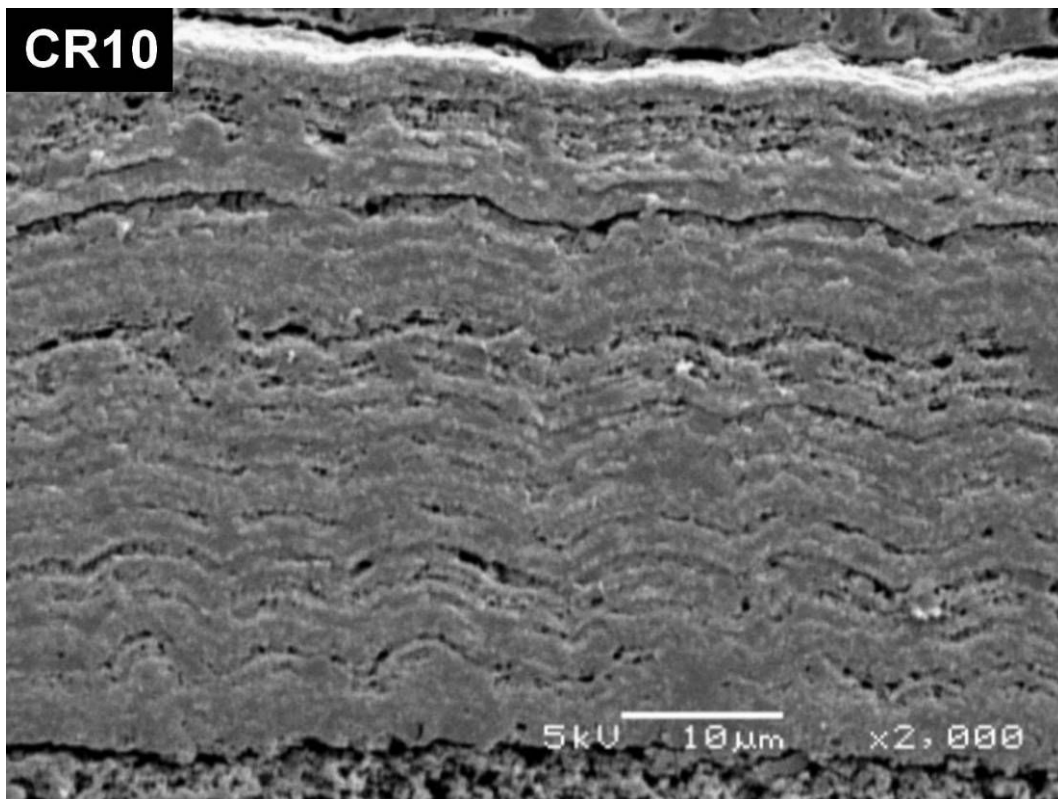
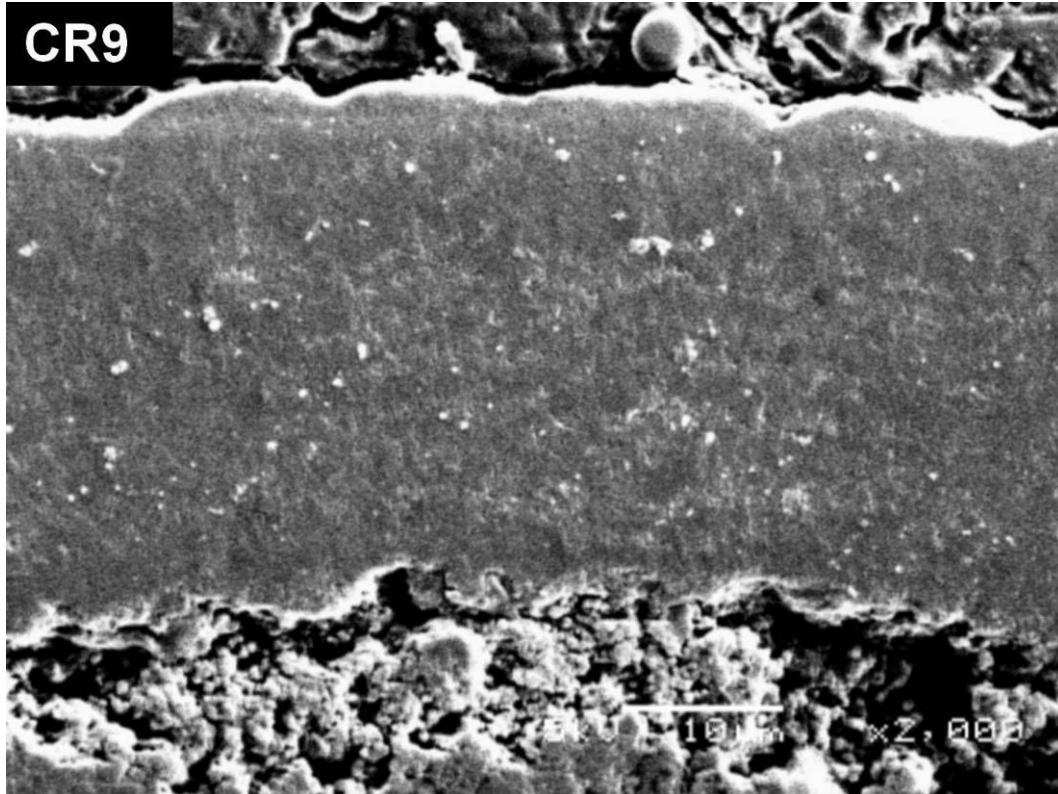


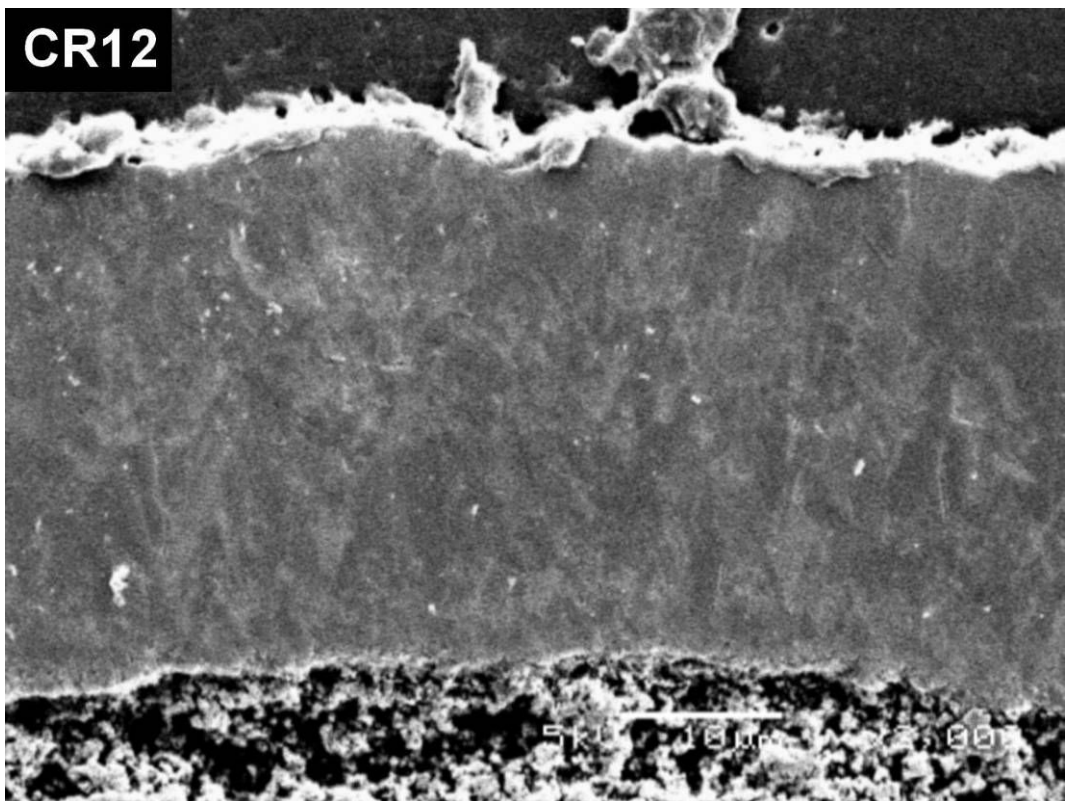
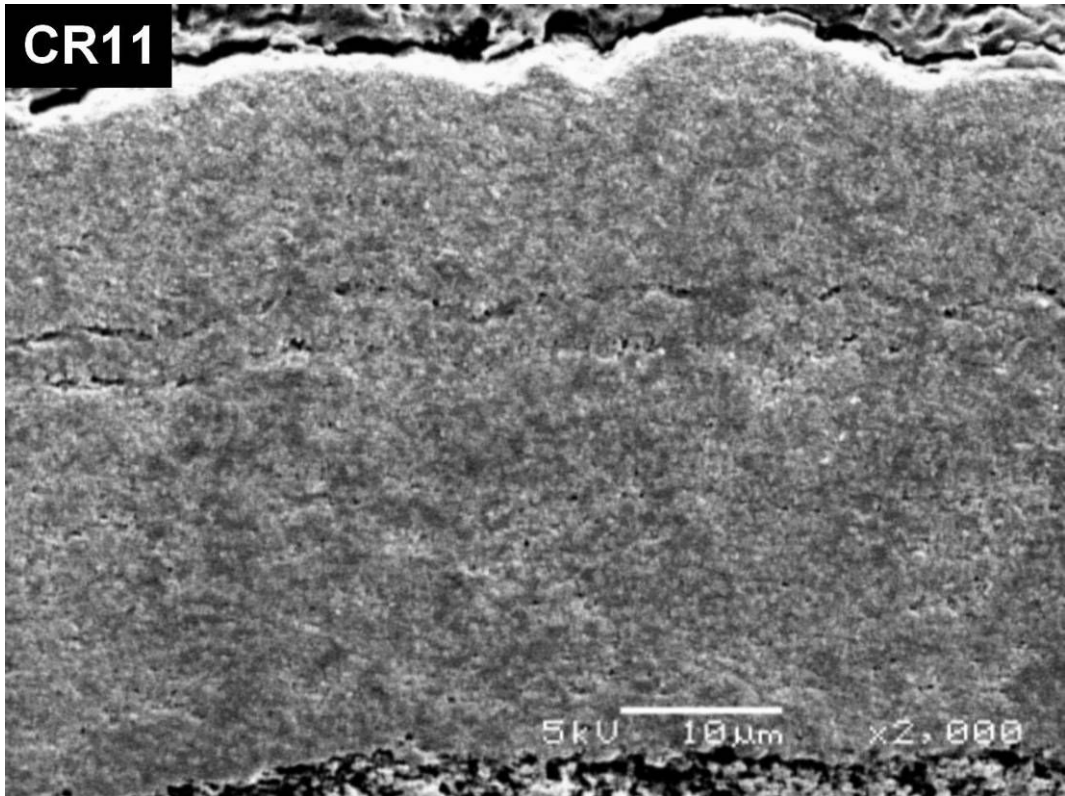
2 ETCHED SAMPLE SECONDARY ELECTRON IMAGES

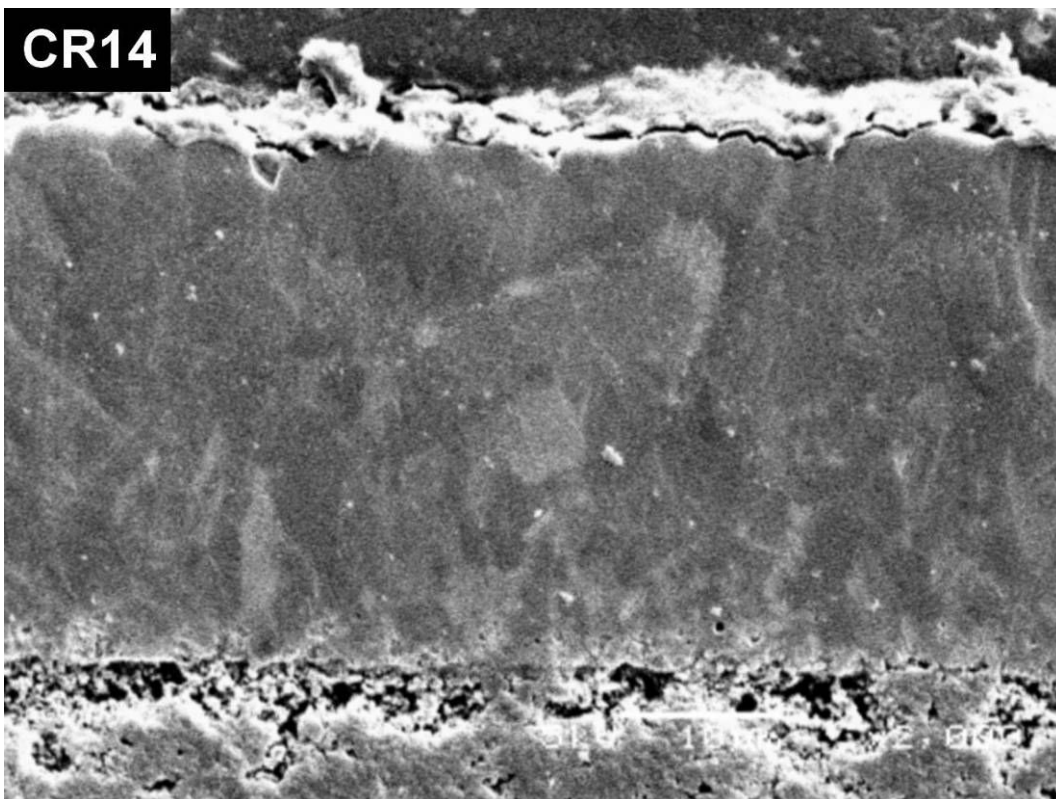
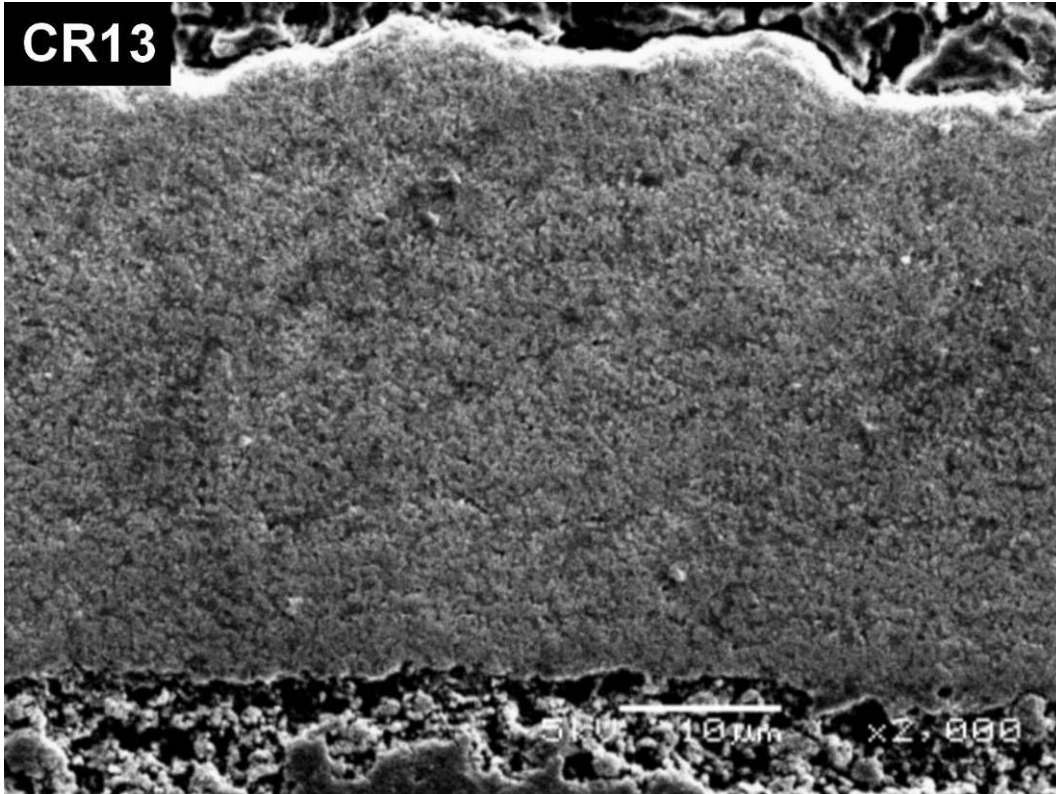
2.1 COLD INLET



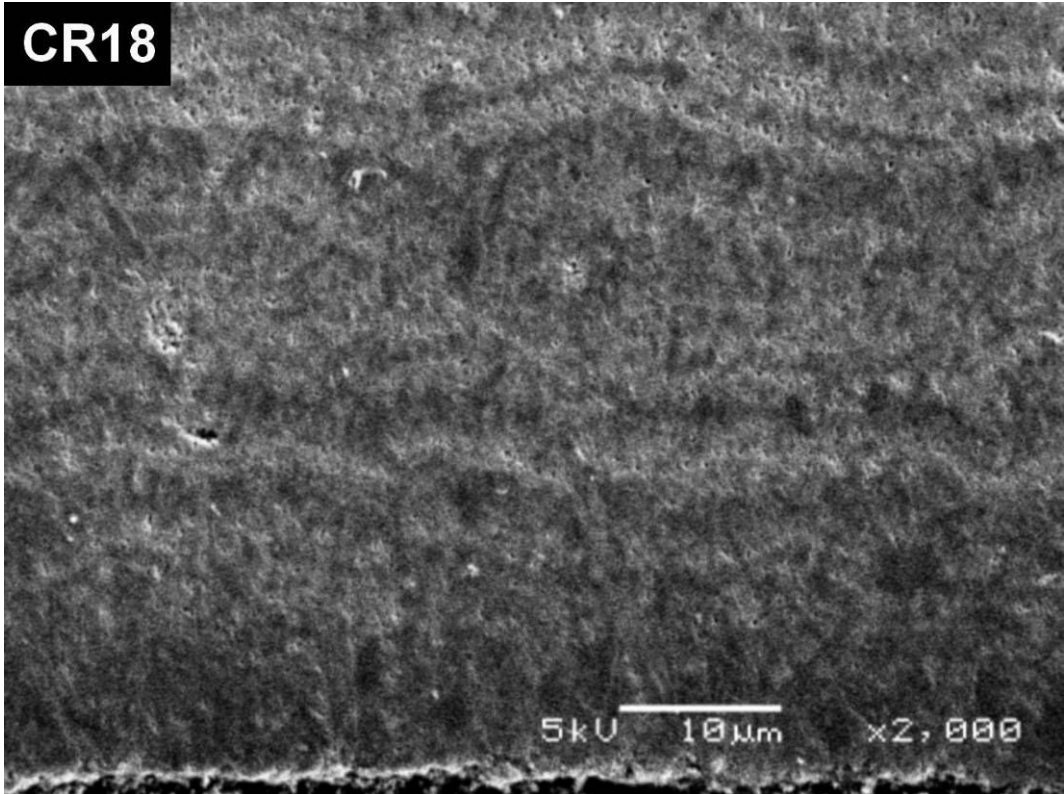




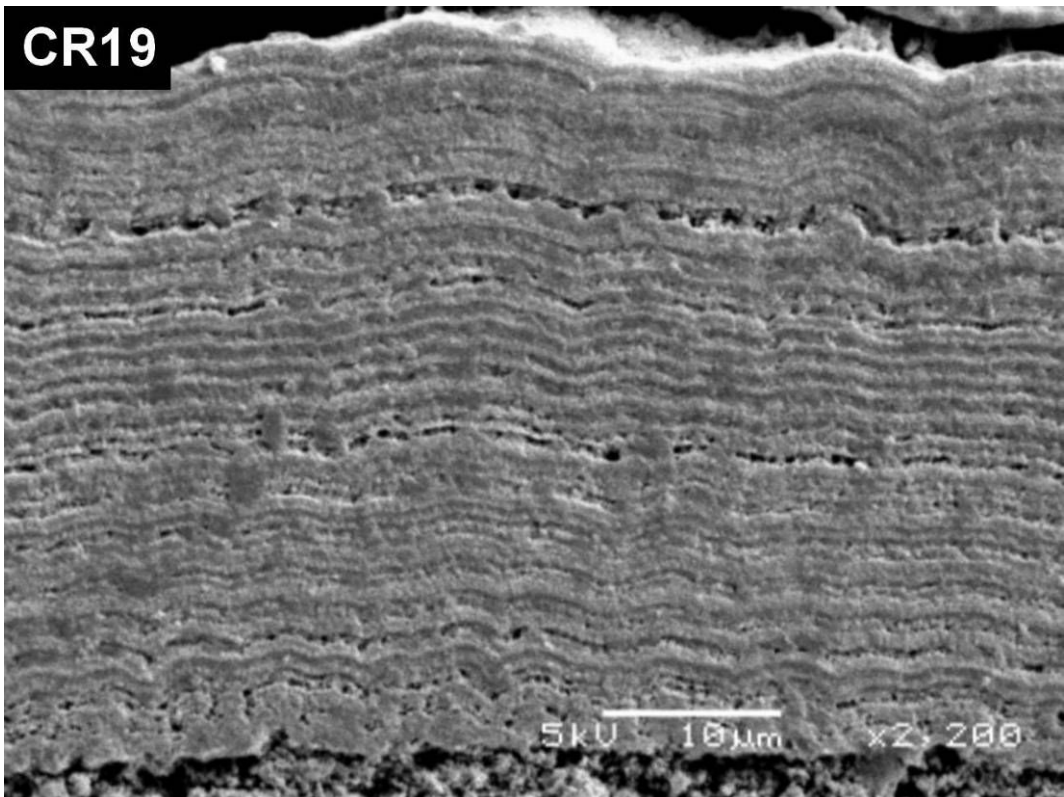


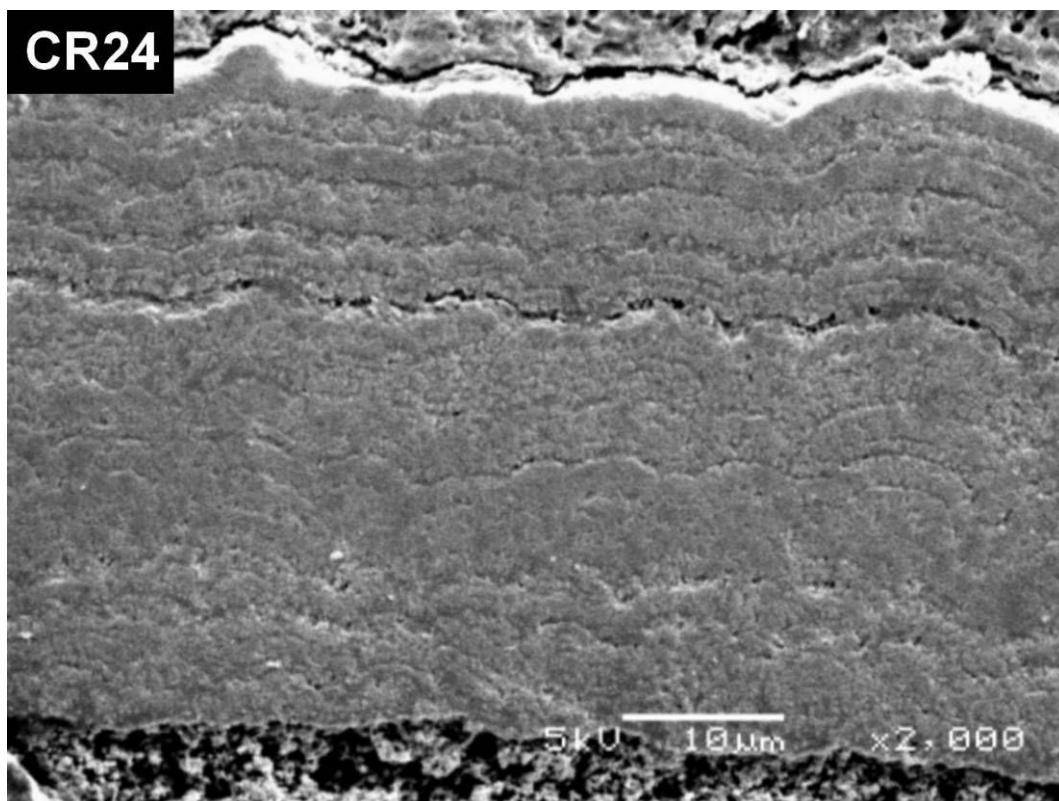
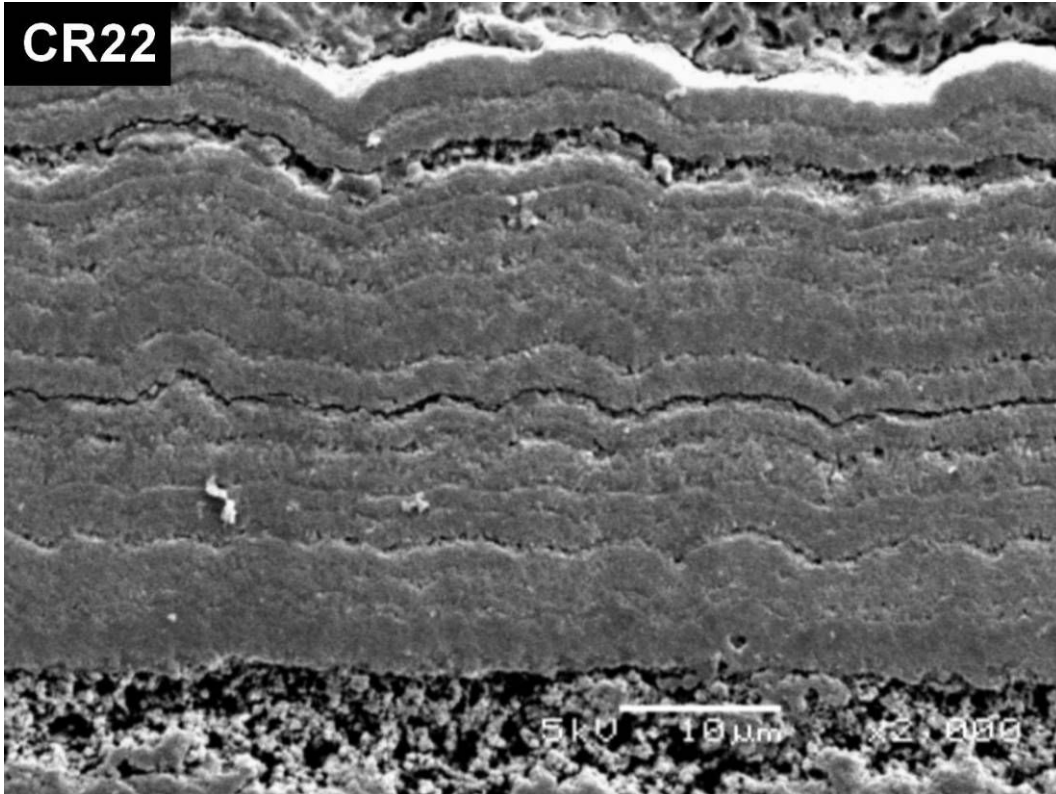


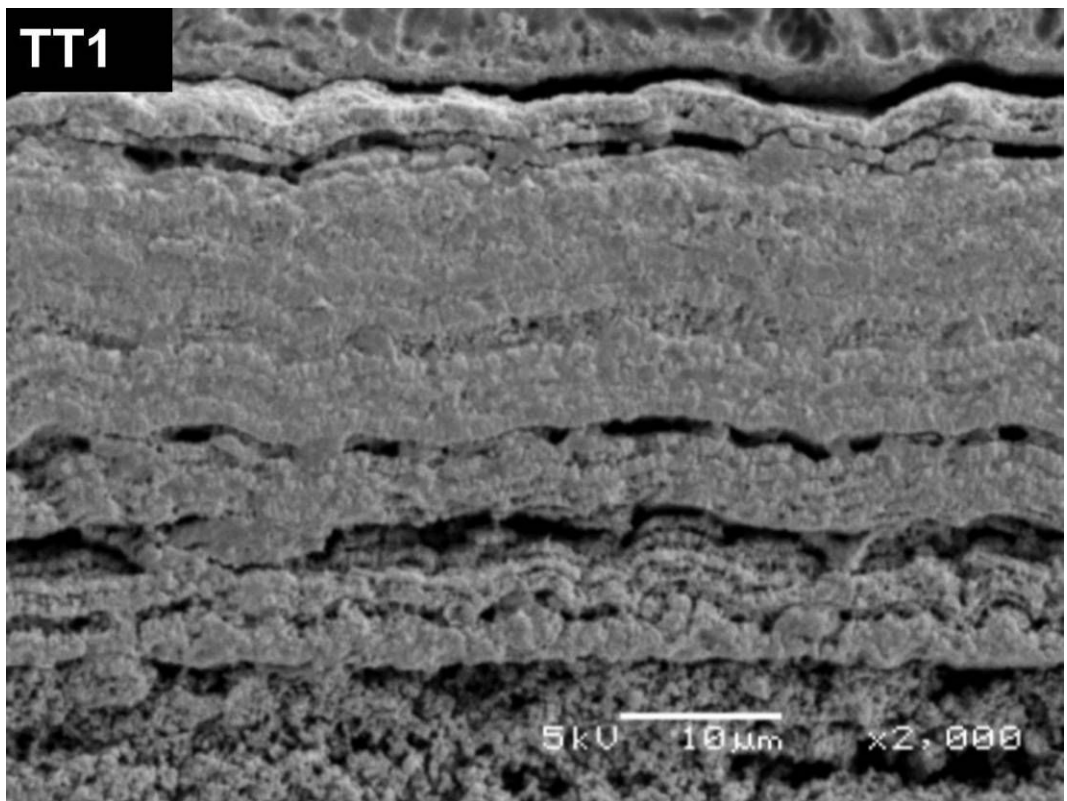
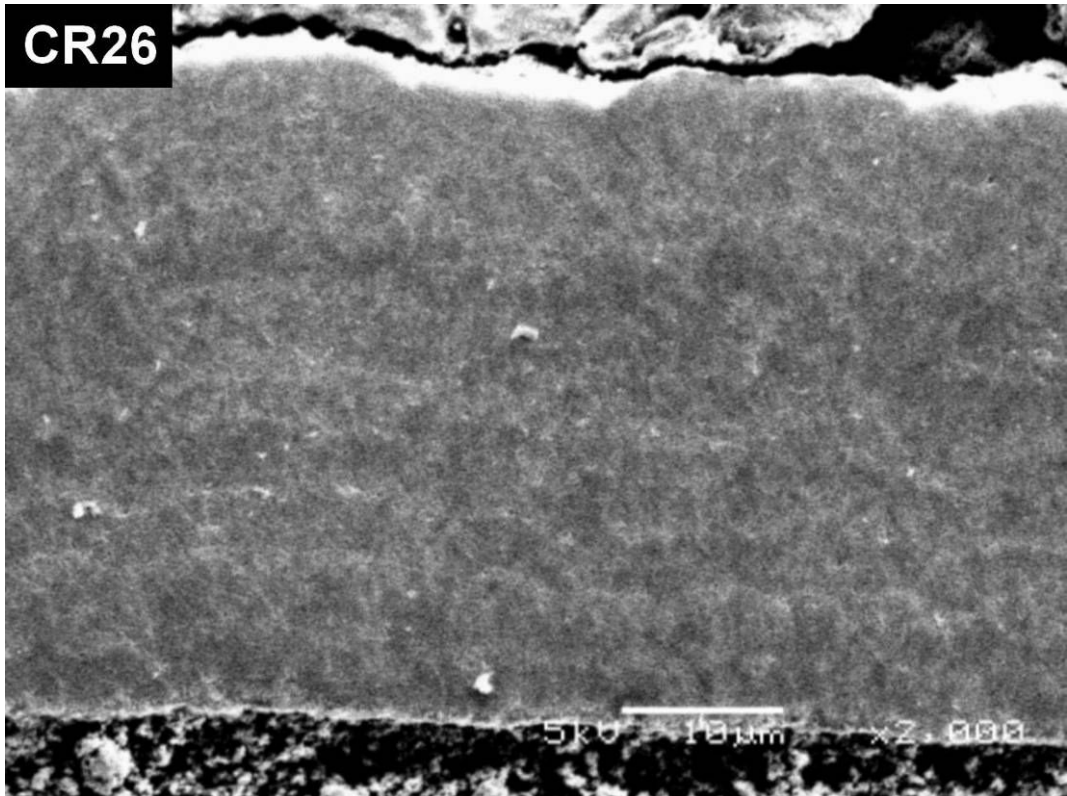
CR18

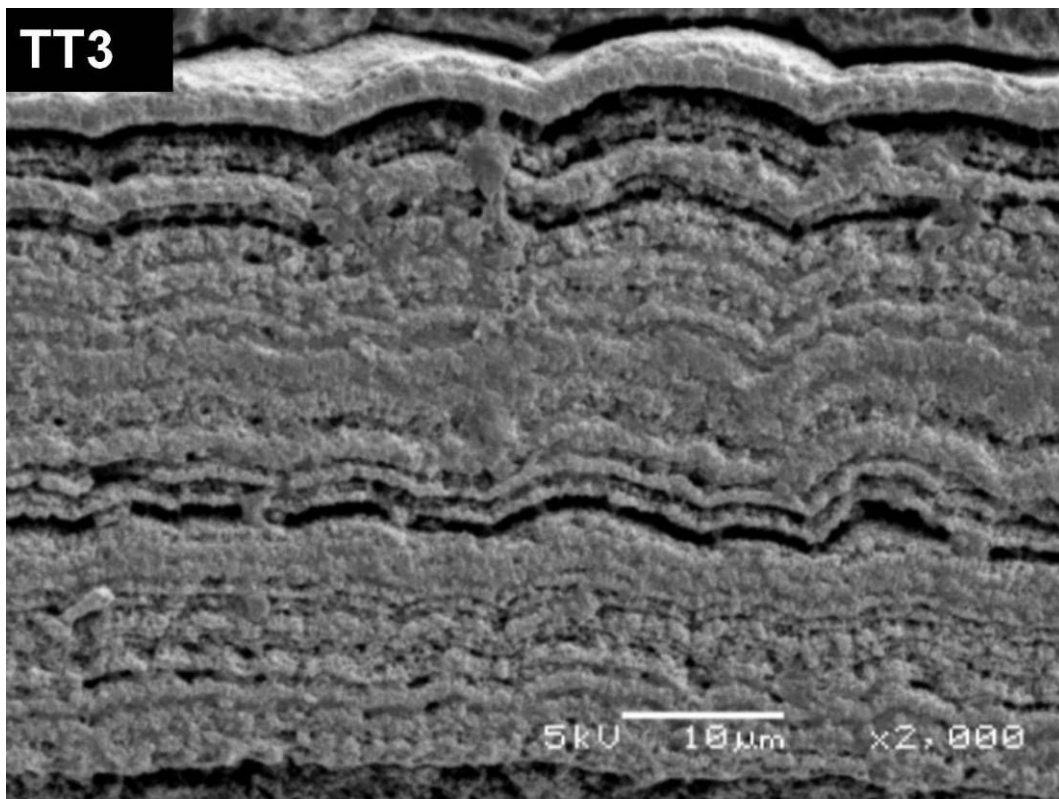
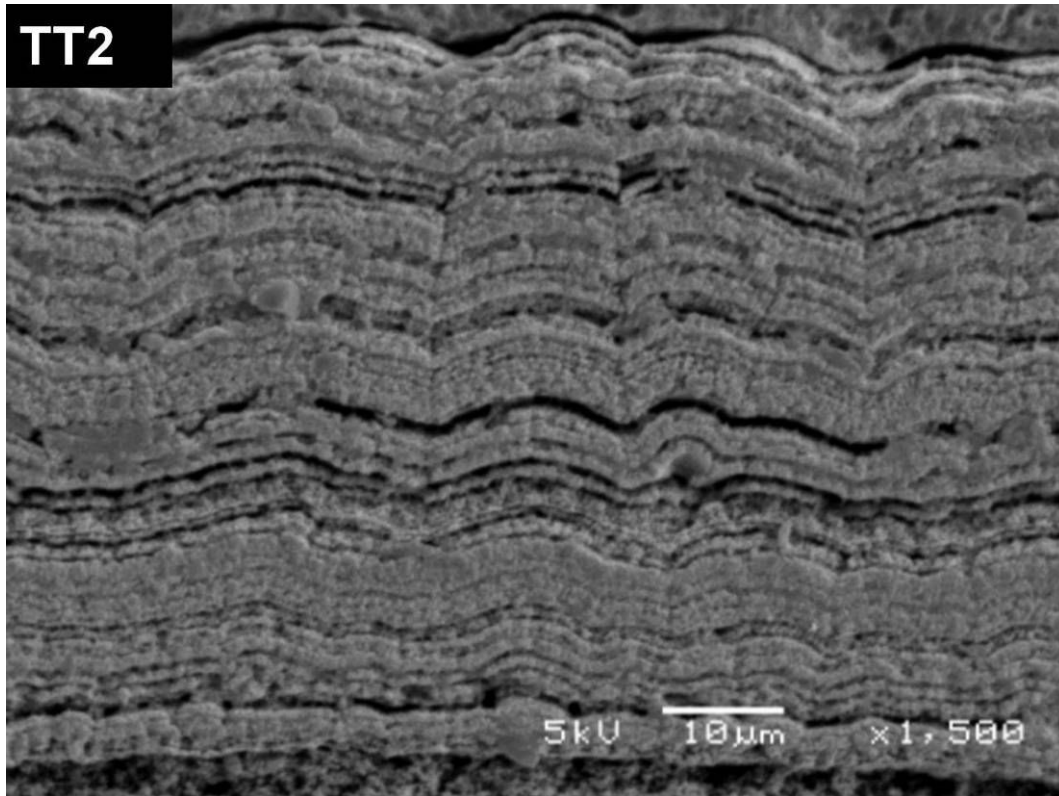


CR19

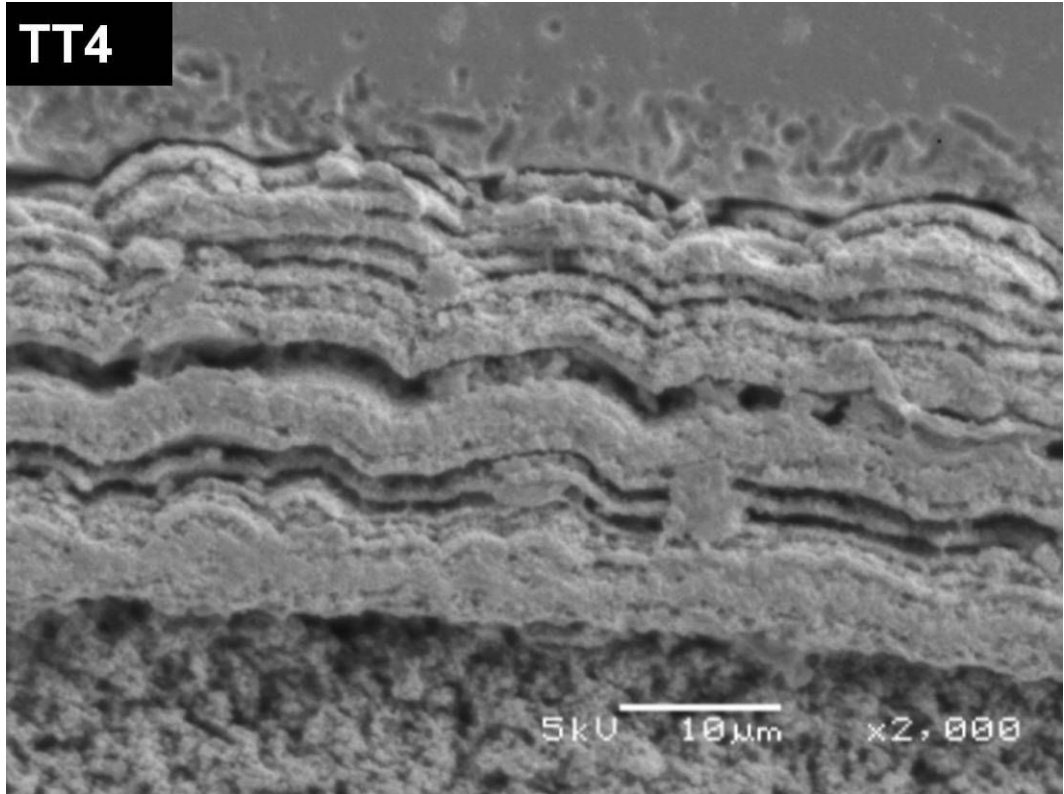




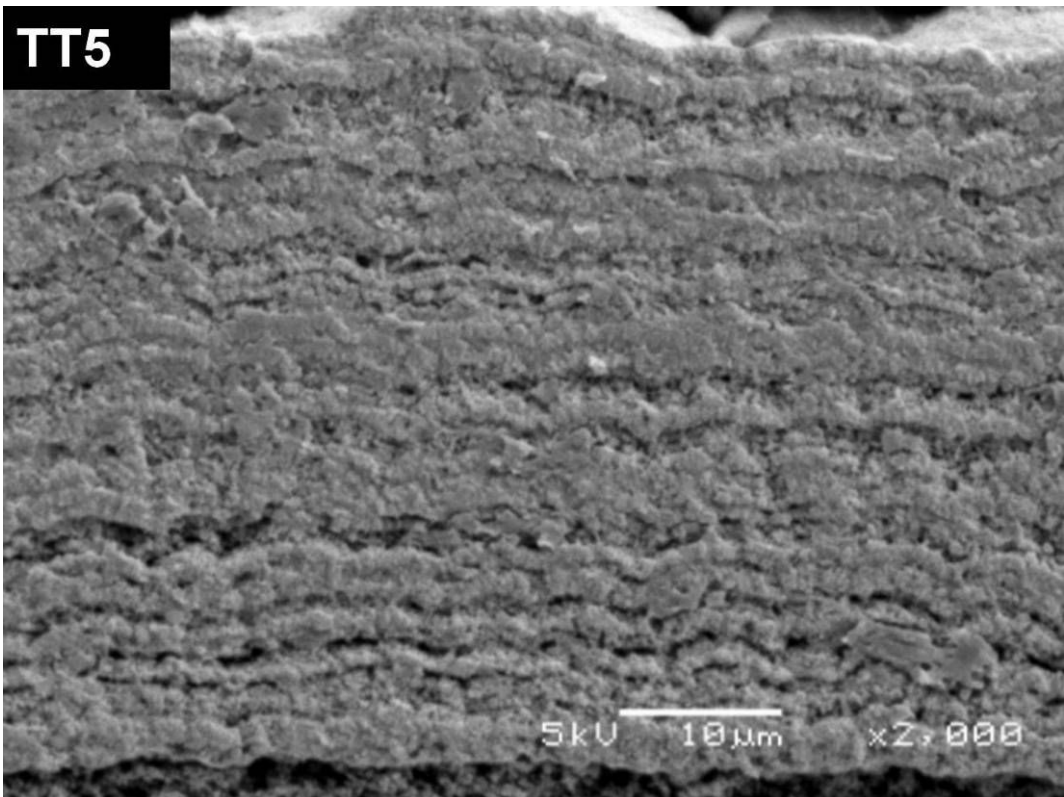




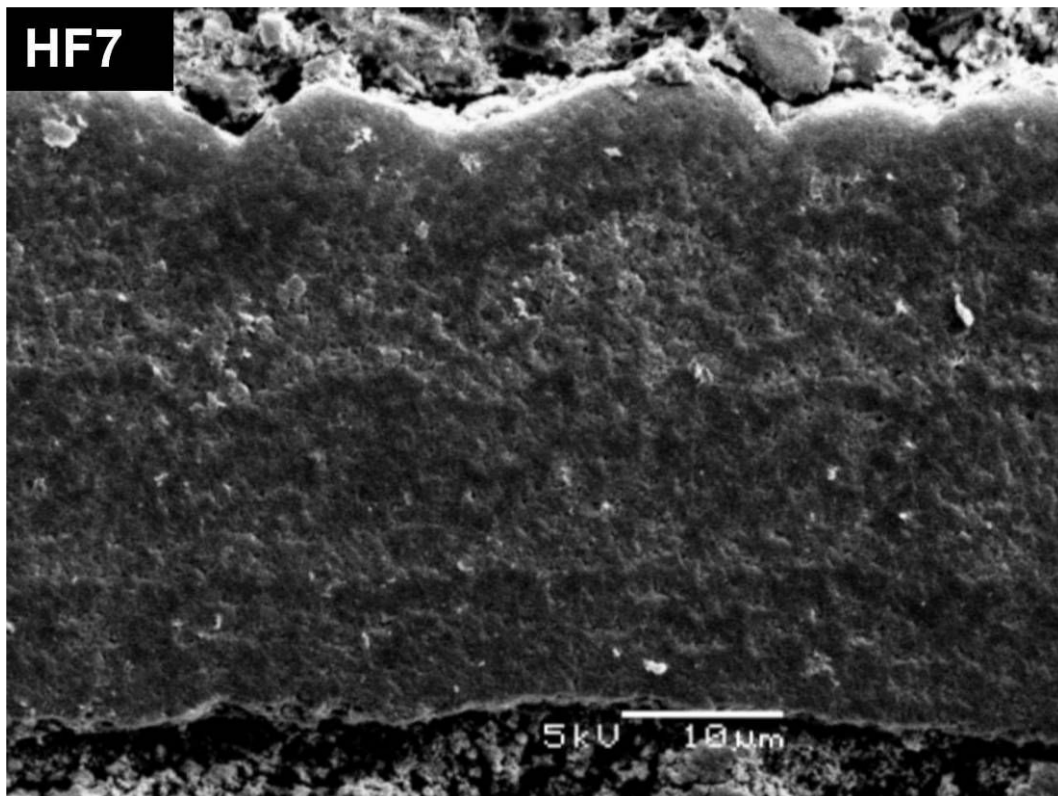
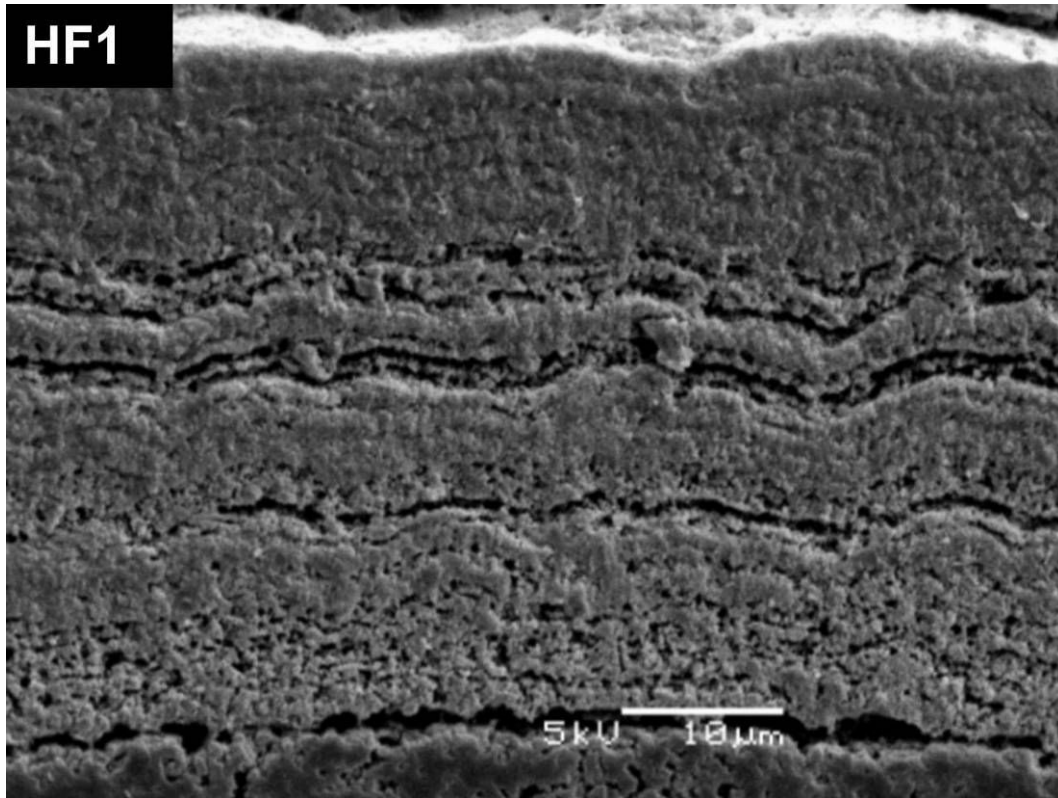
TT4

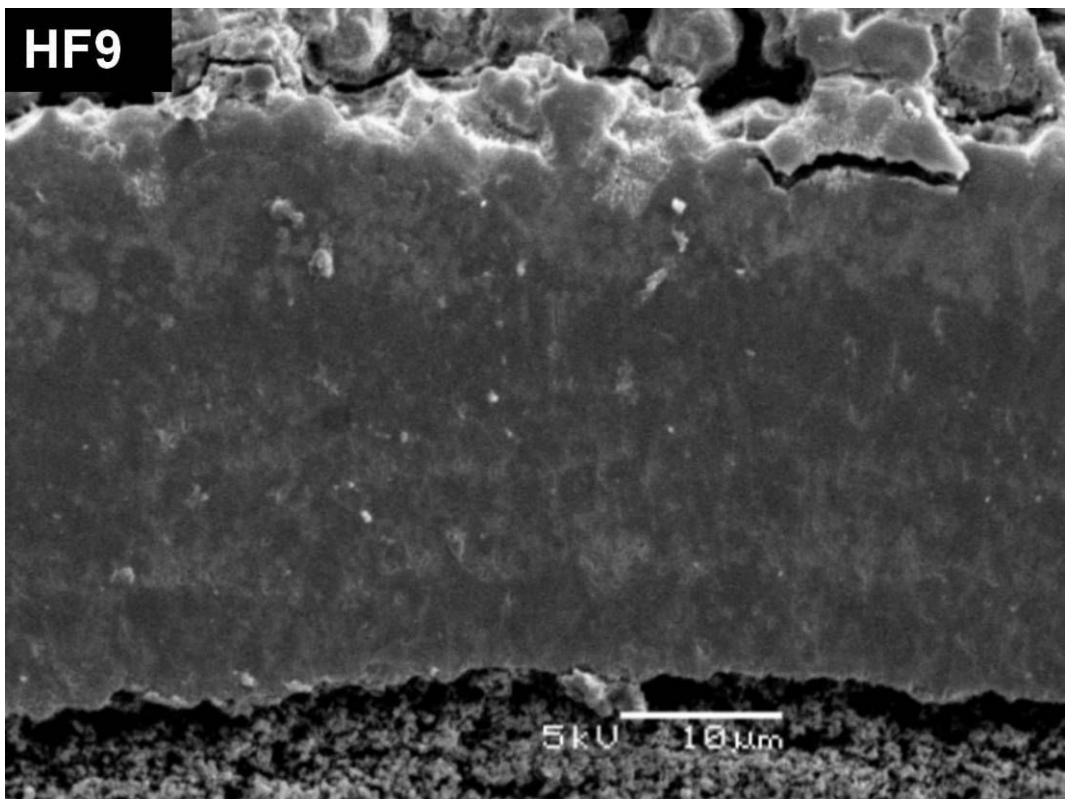
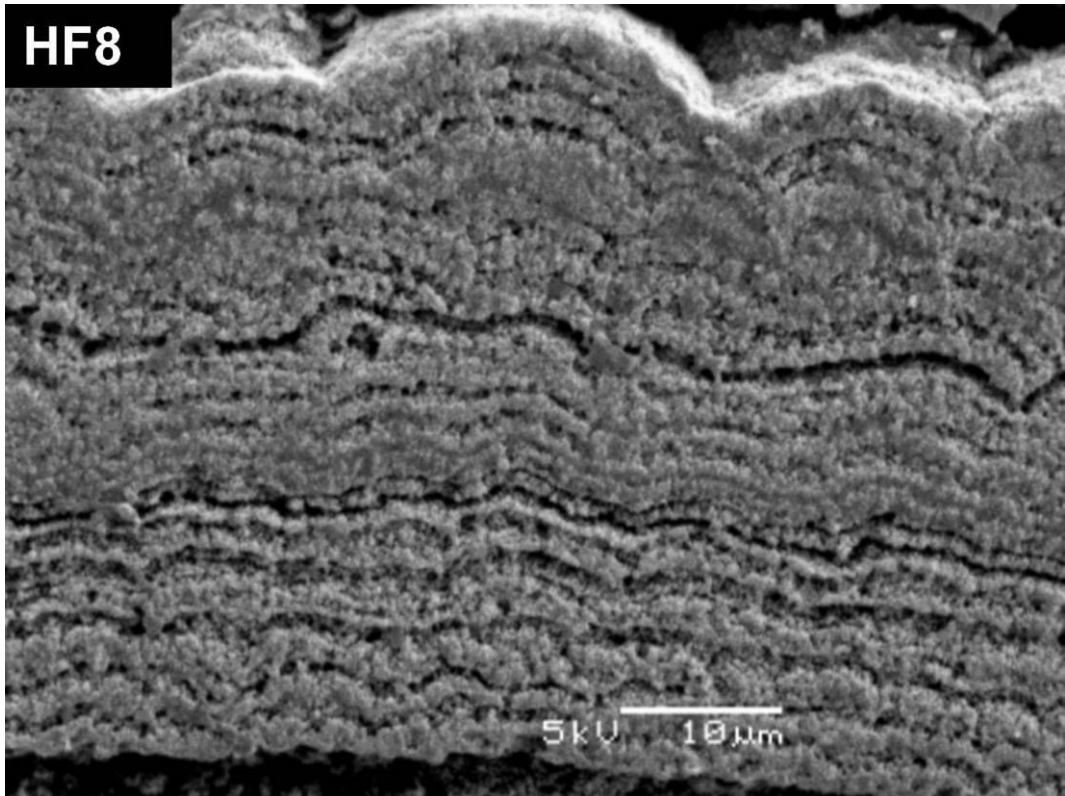


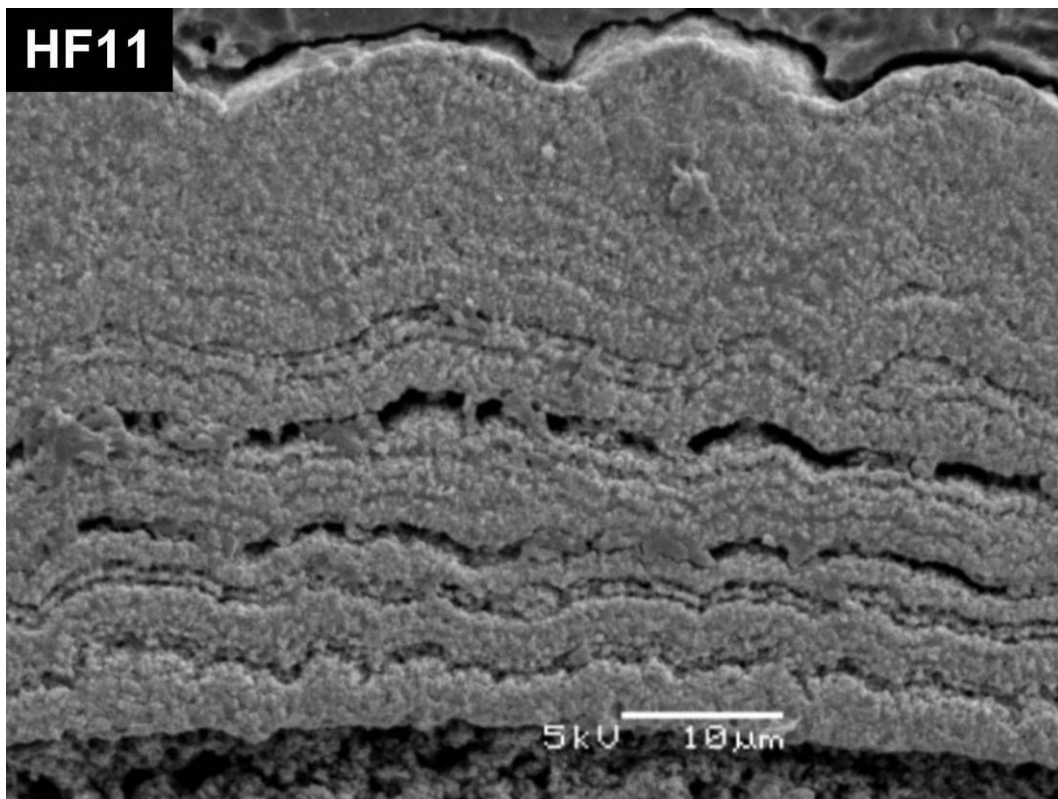
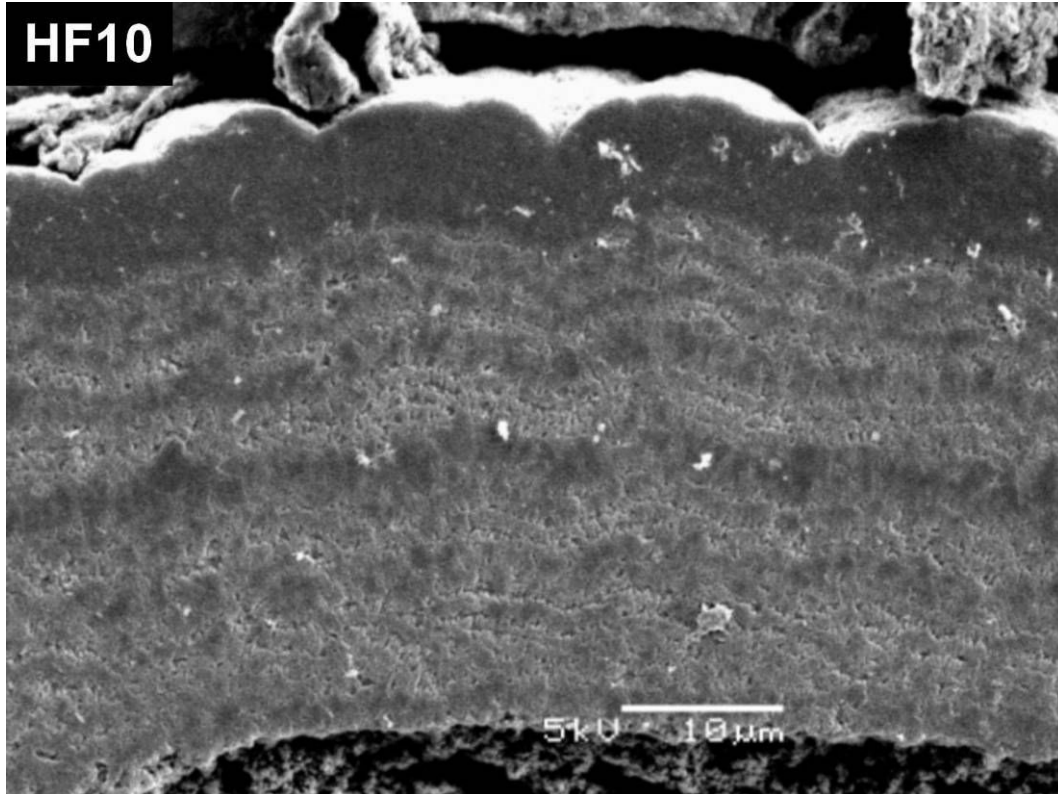
TT5

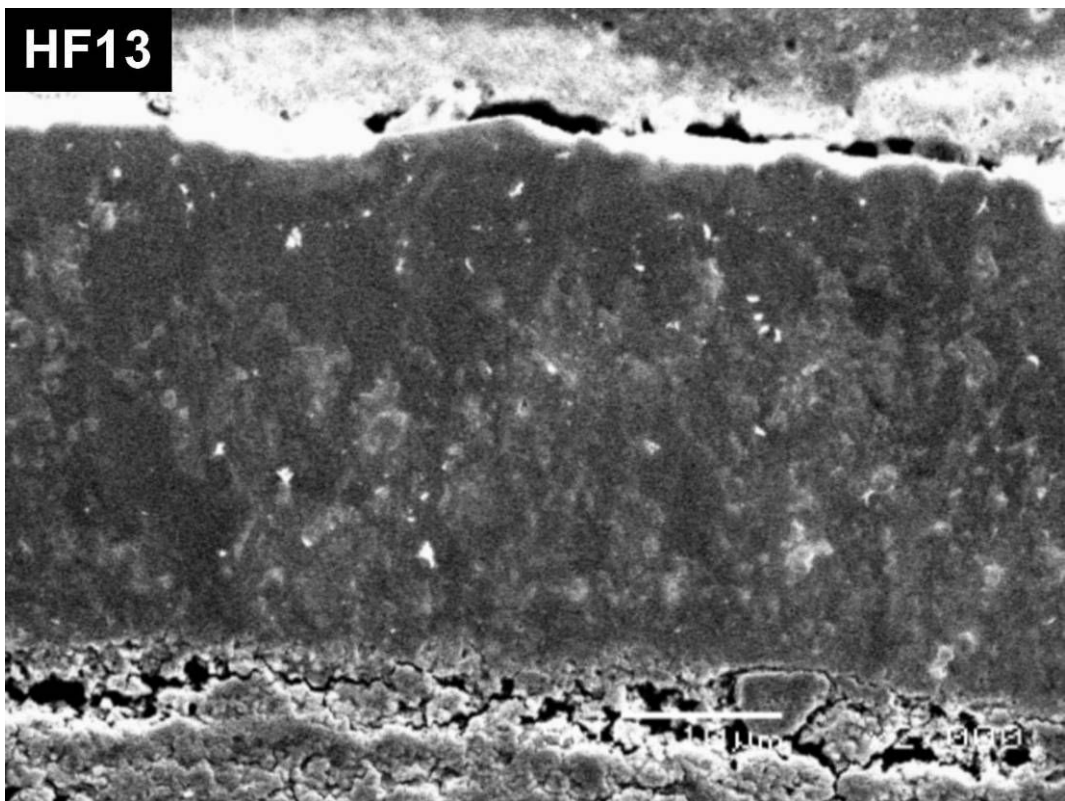
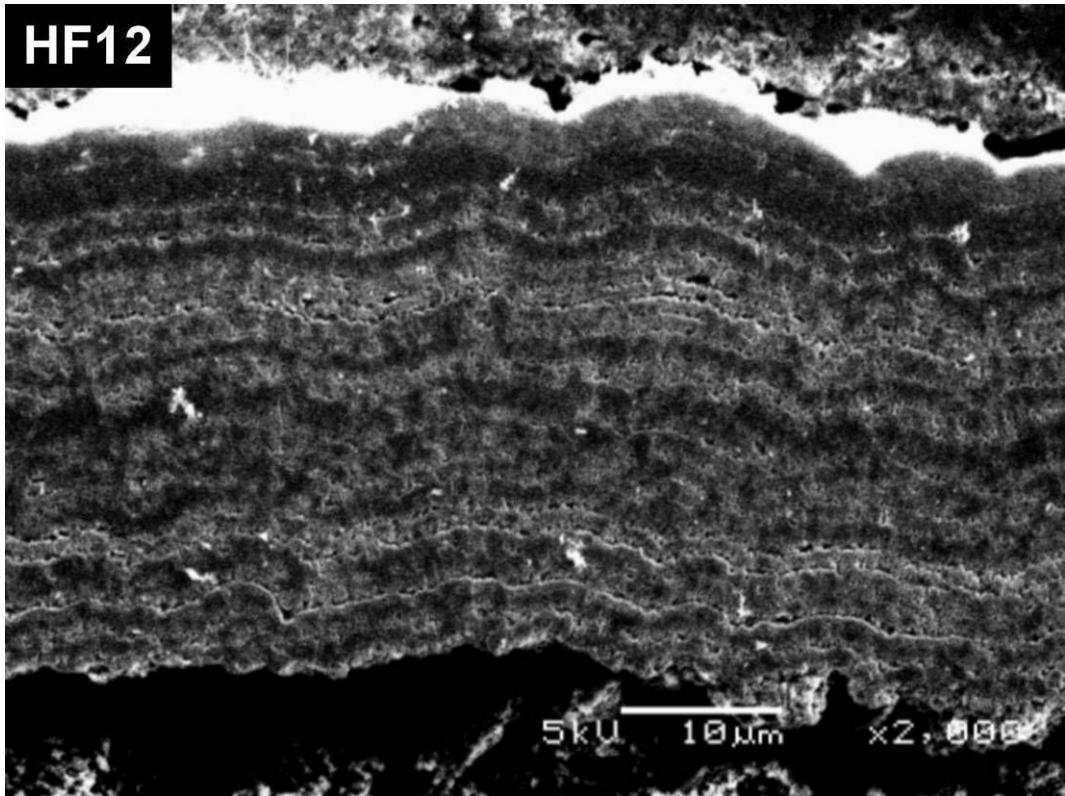


2.2 HOT INLET

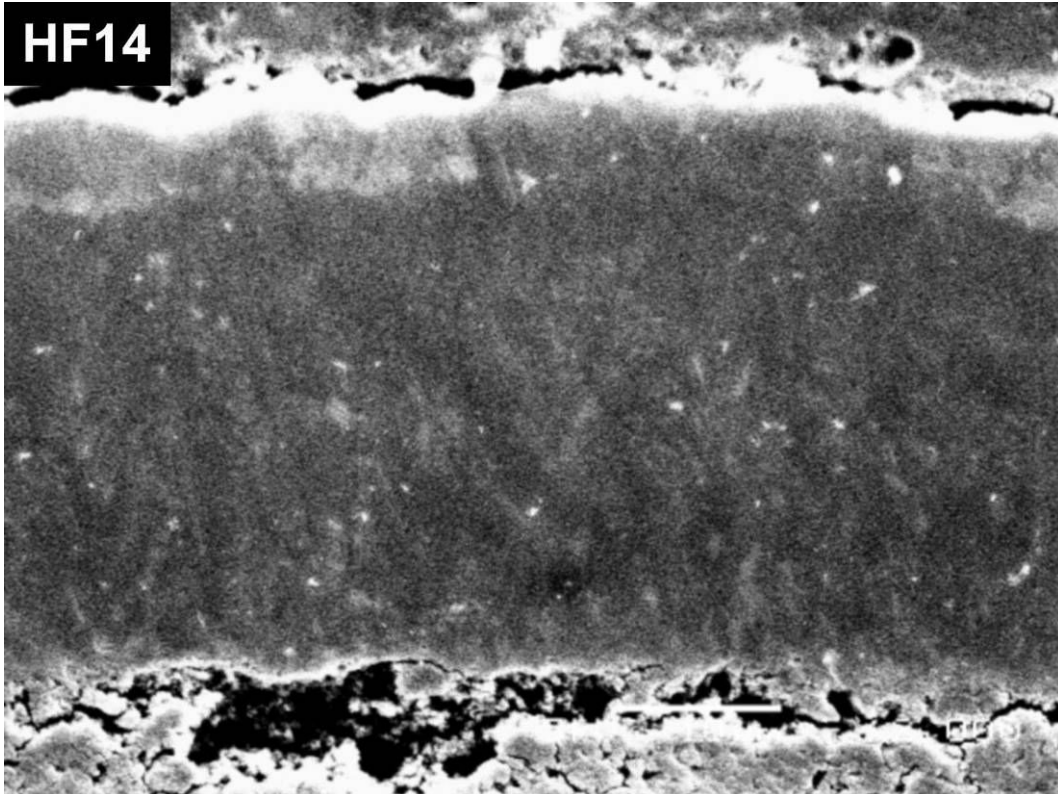




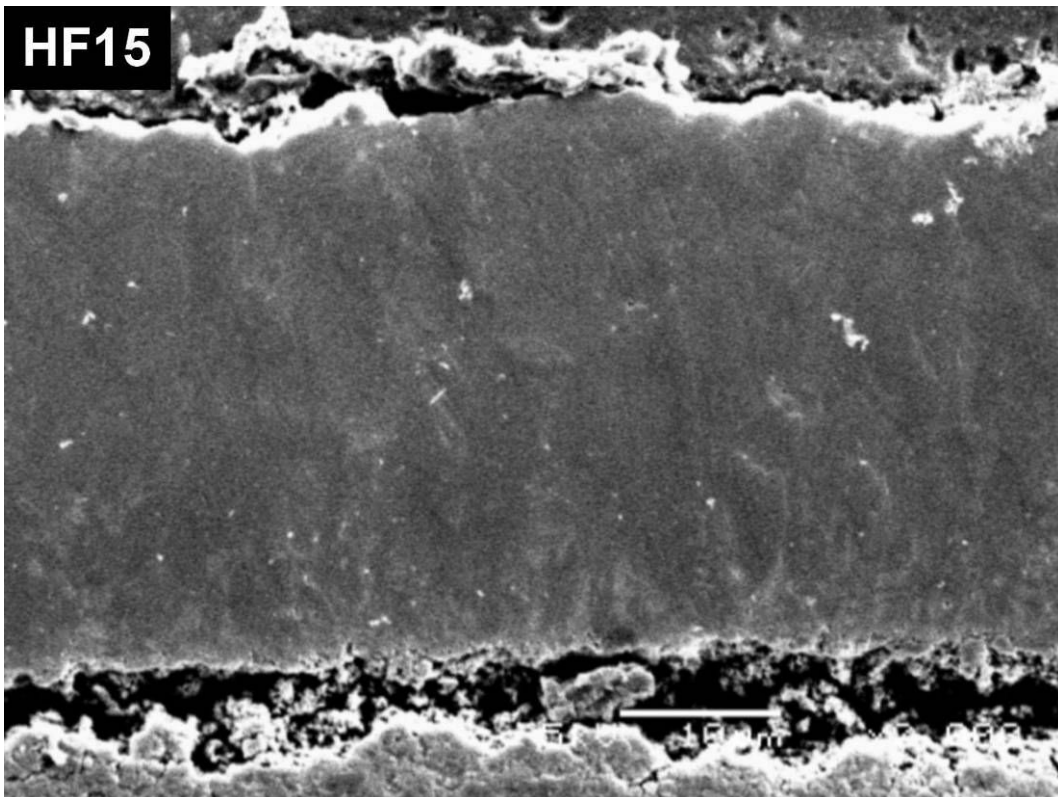


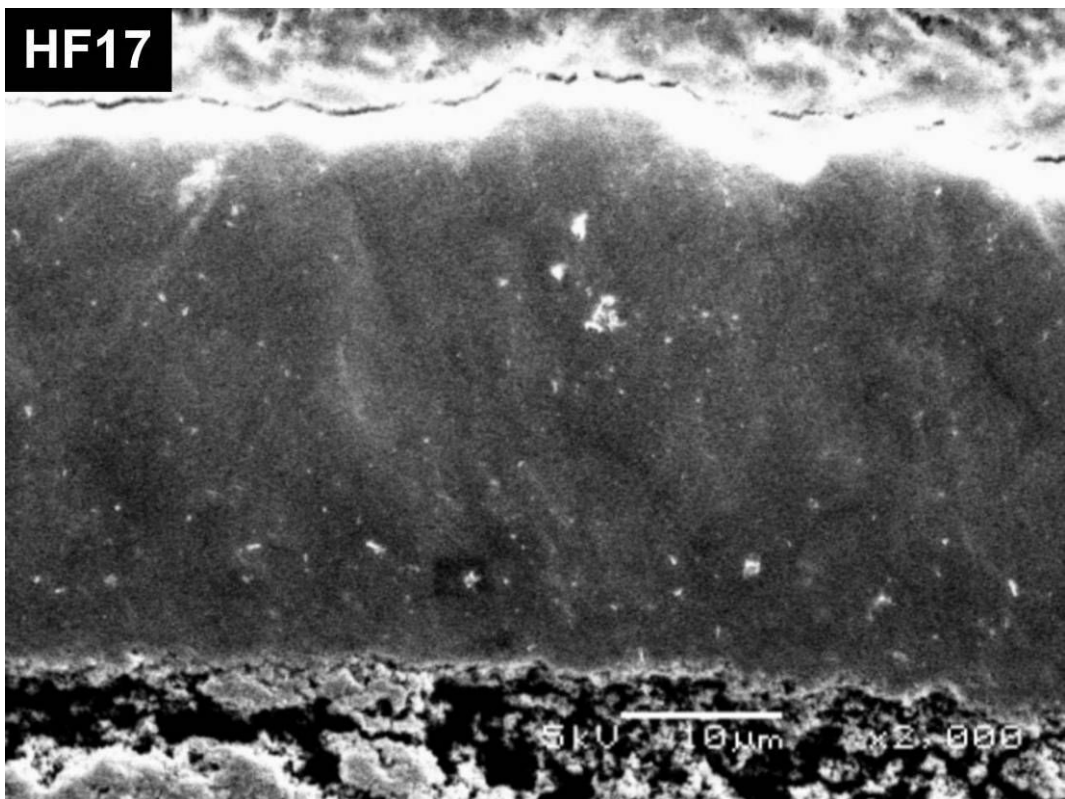
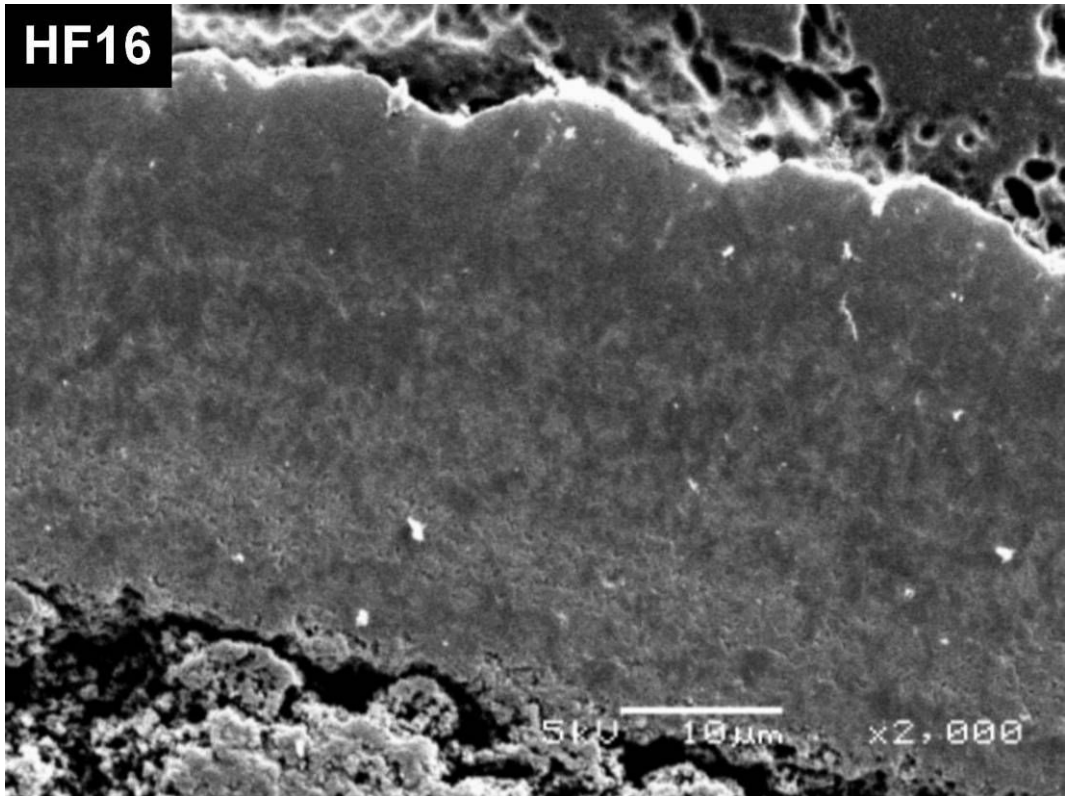


HF14

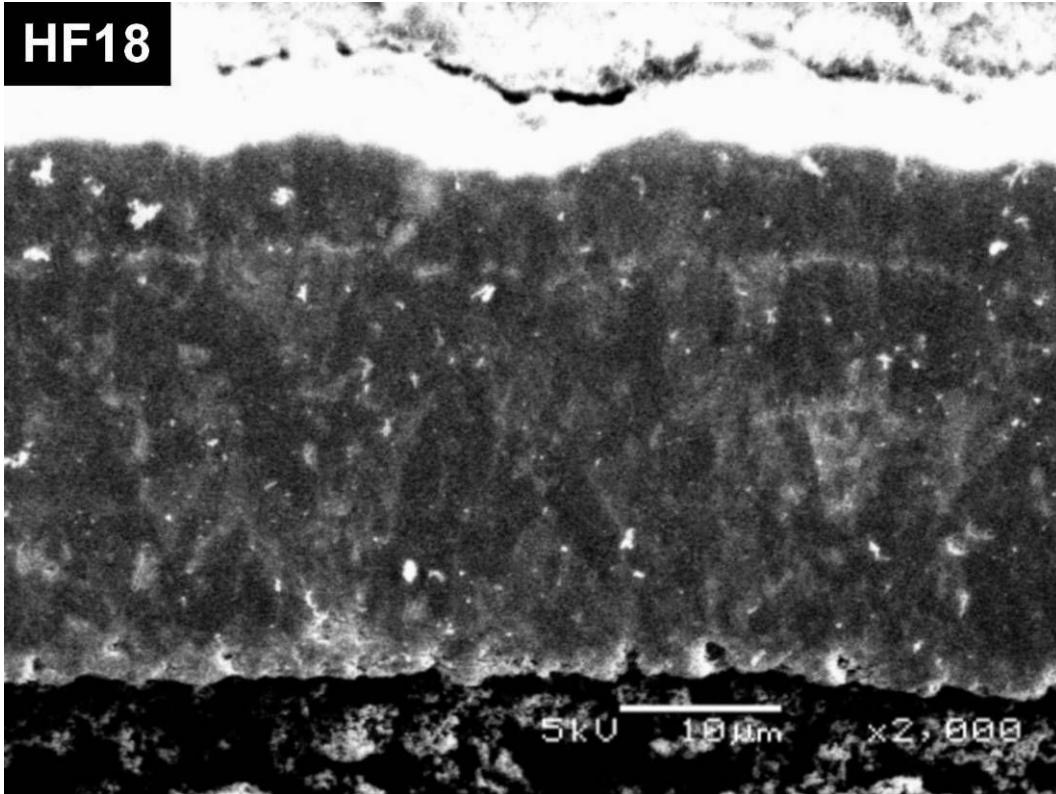


HF15

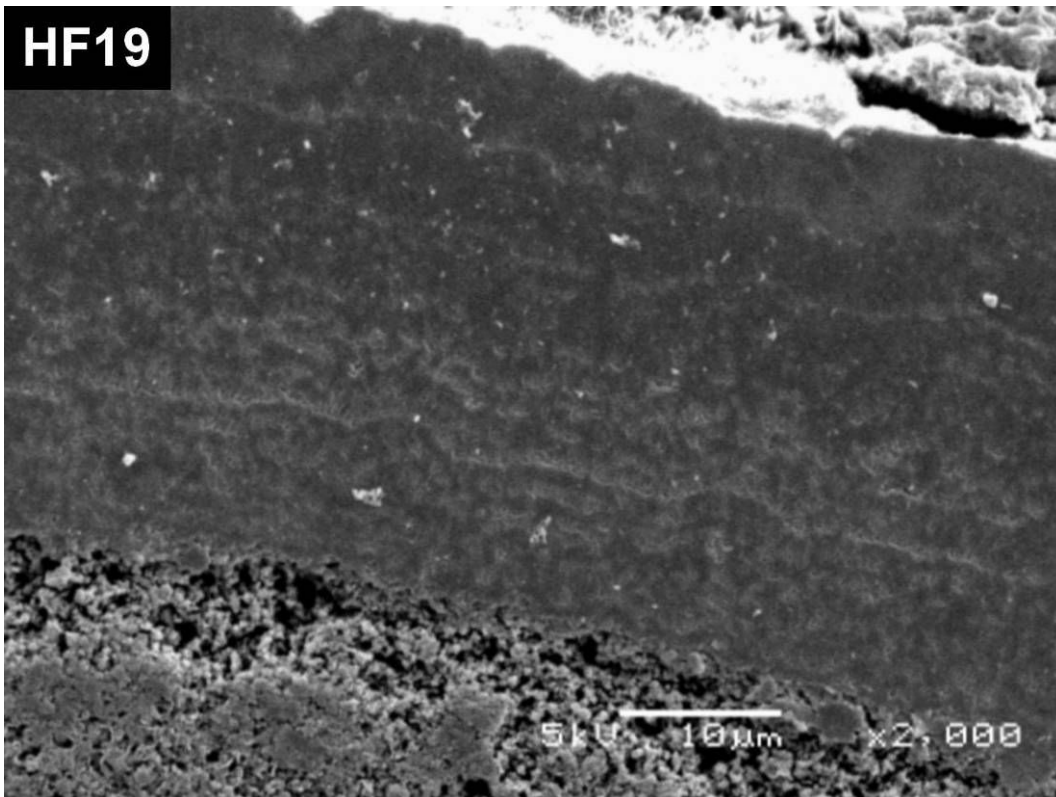


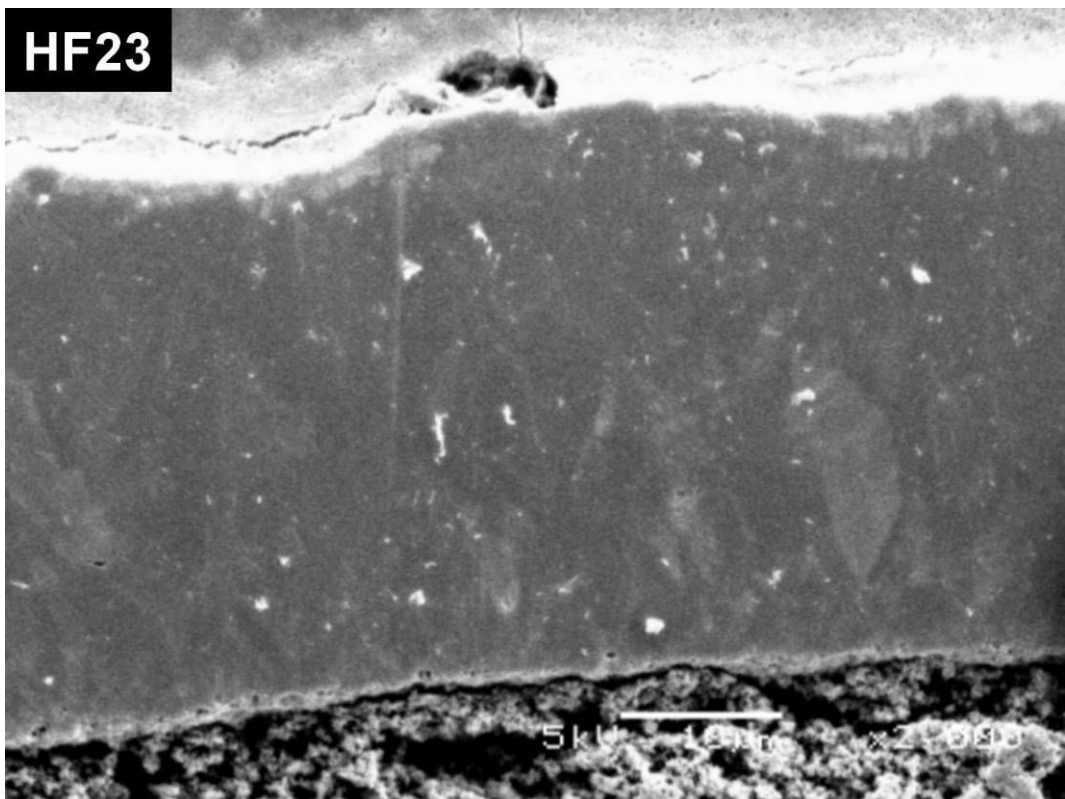
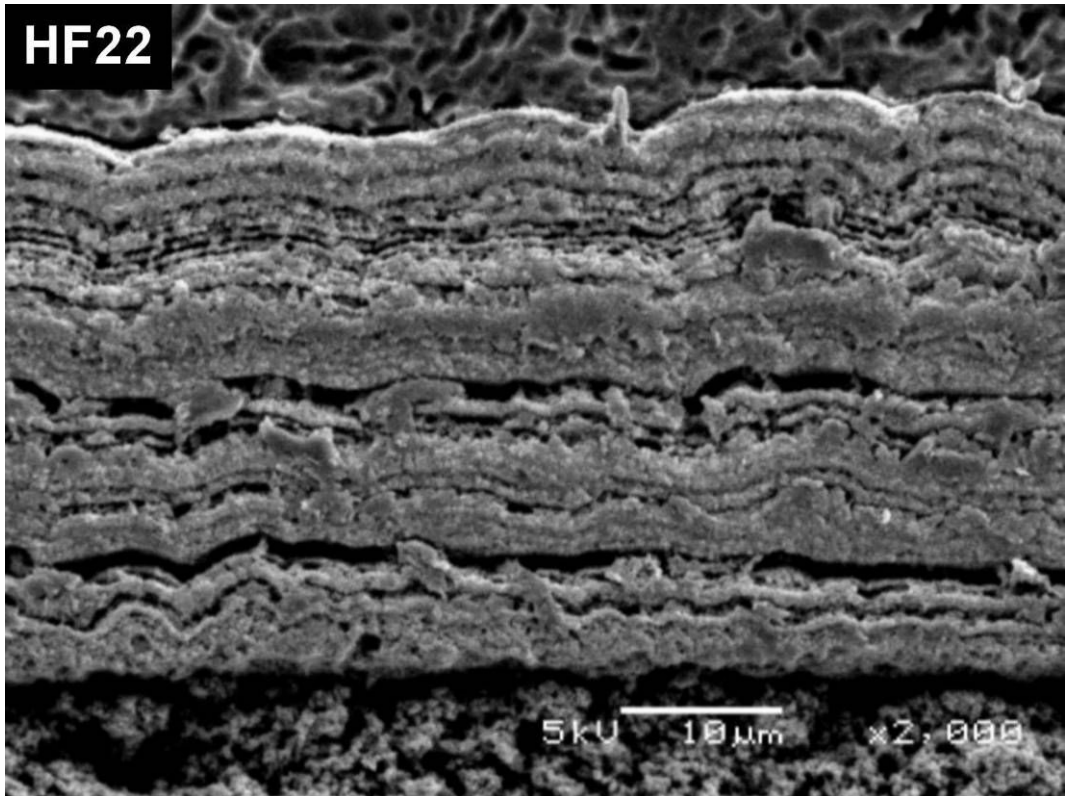


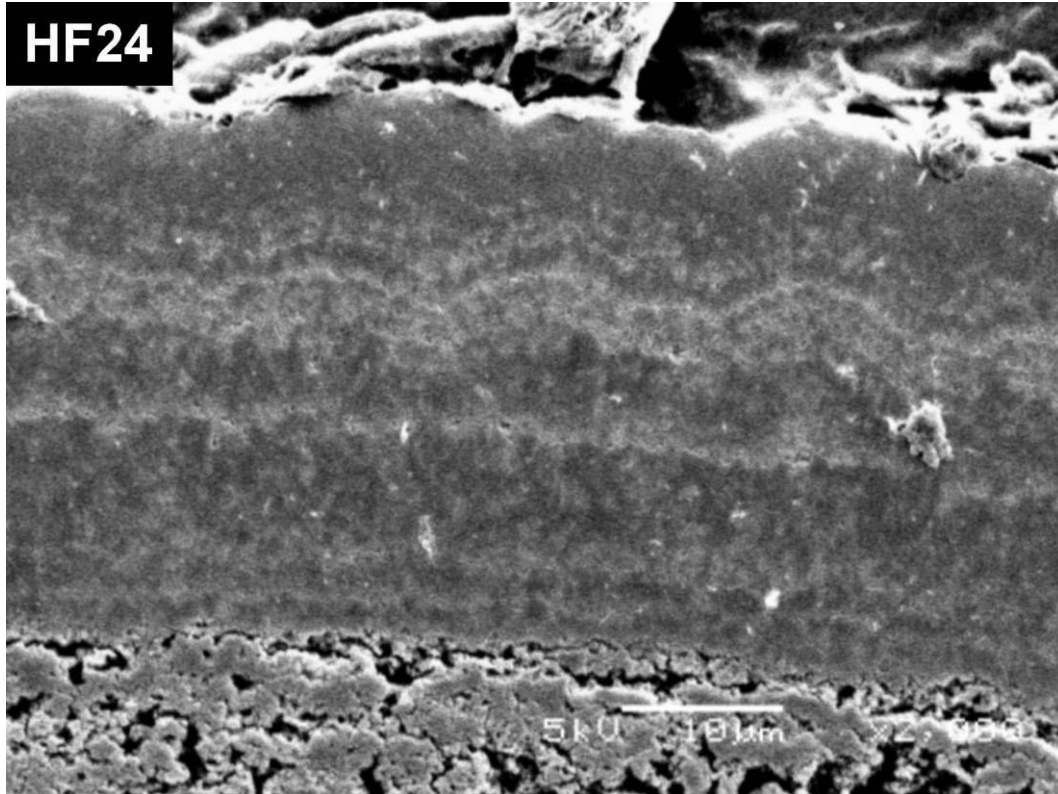
HF18



HF19

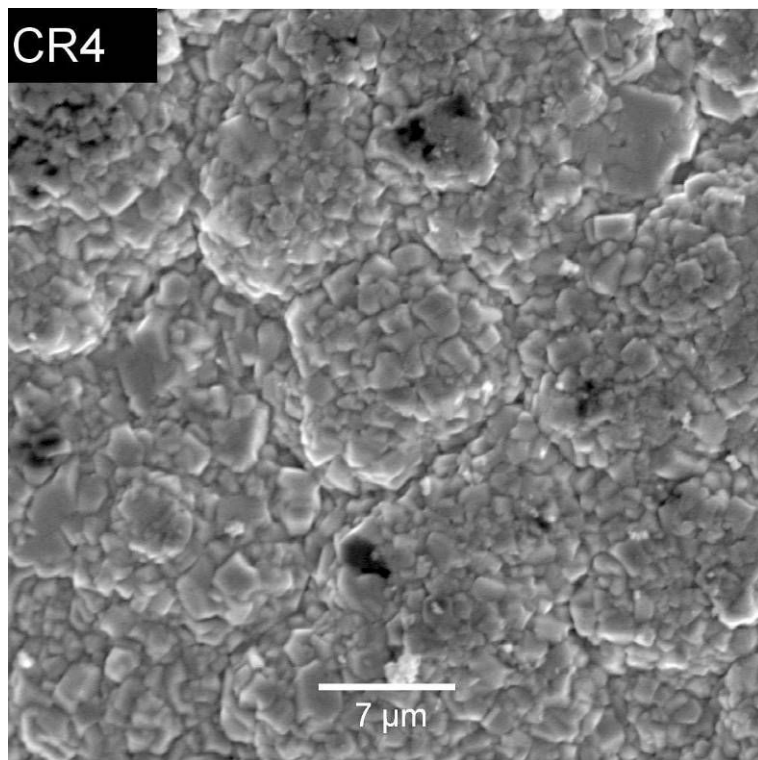
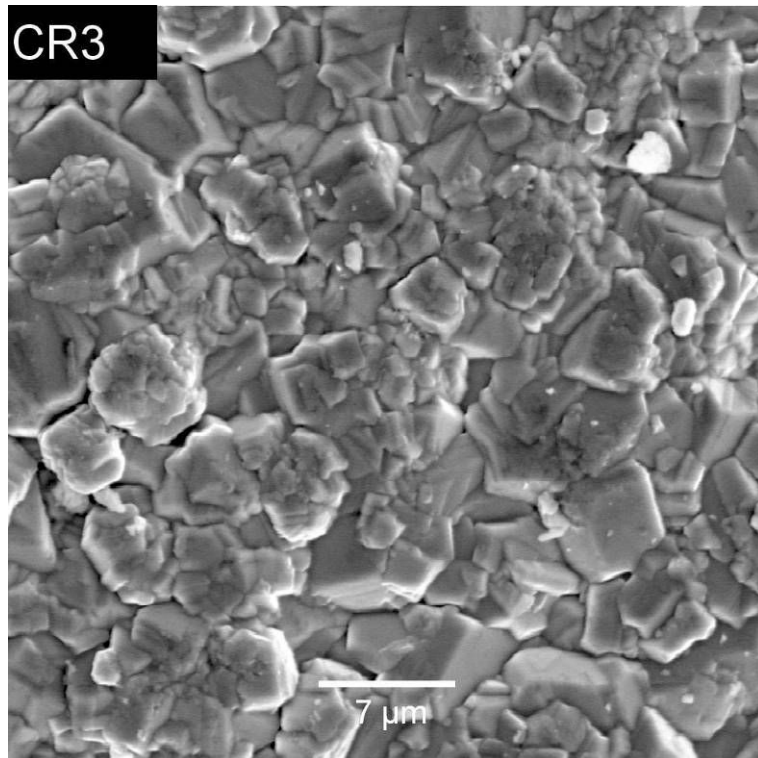


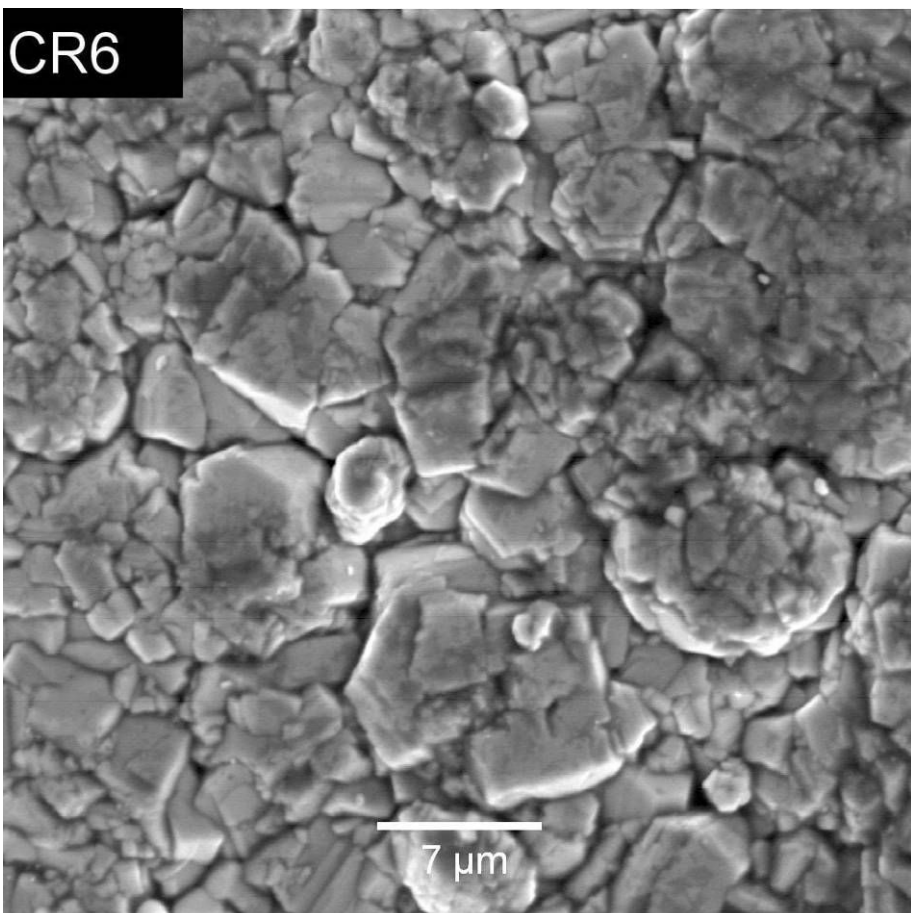
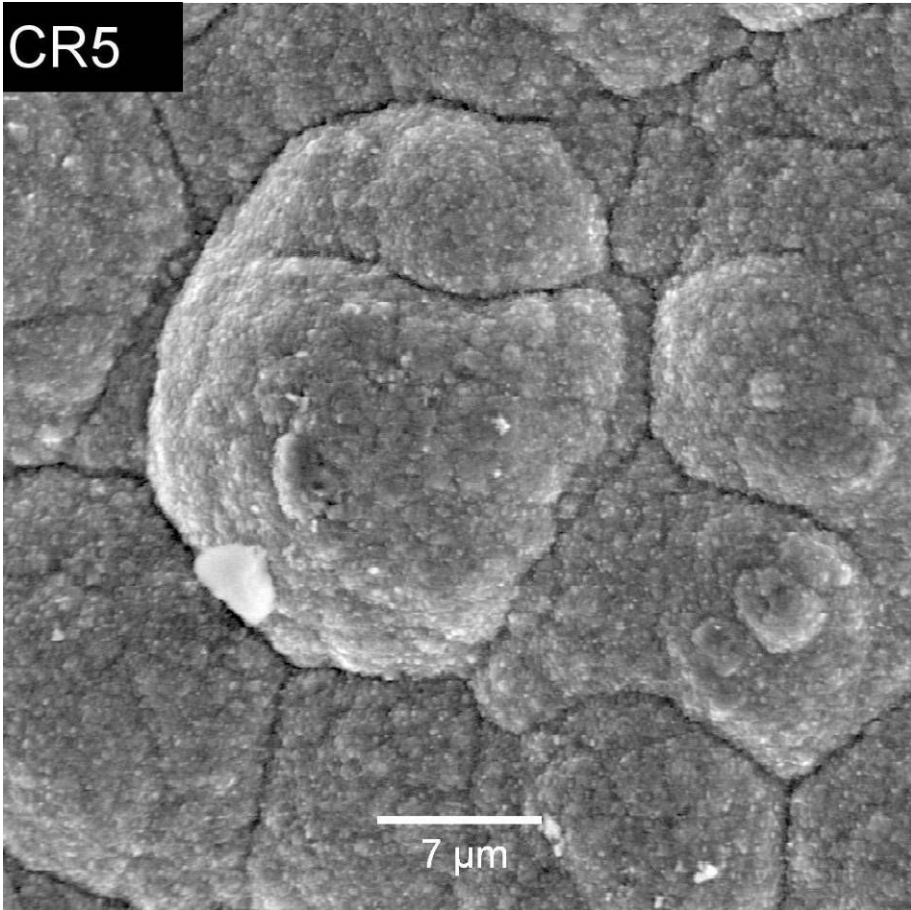


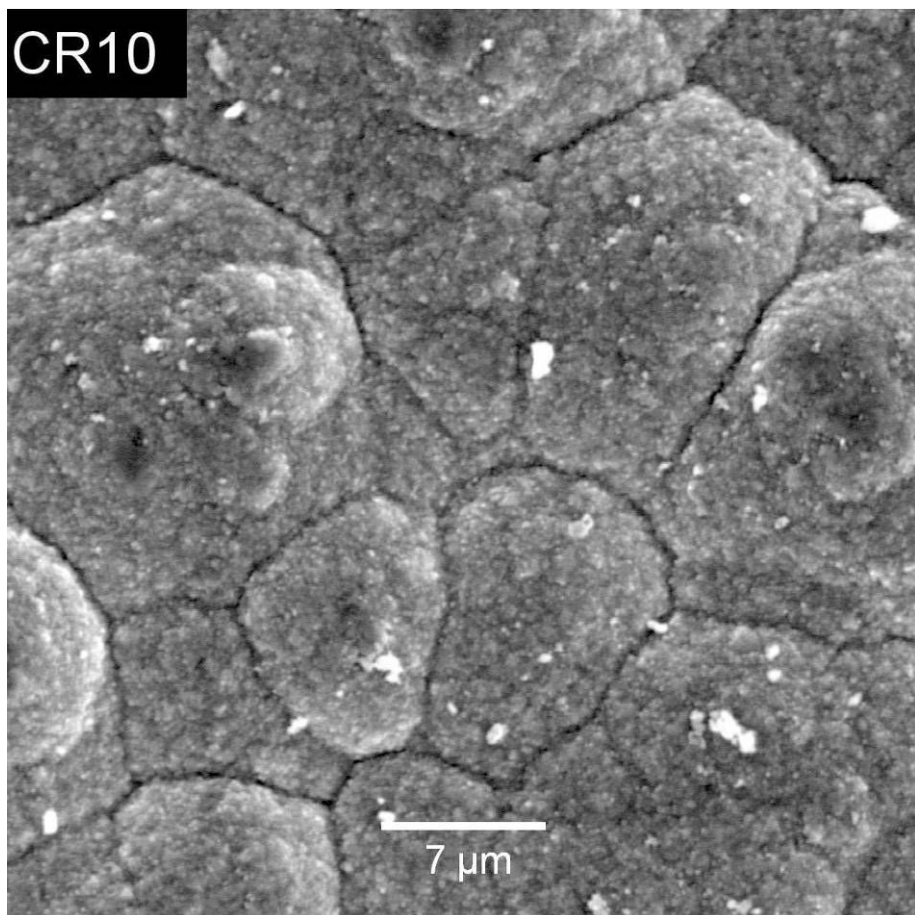
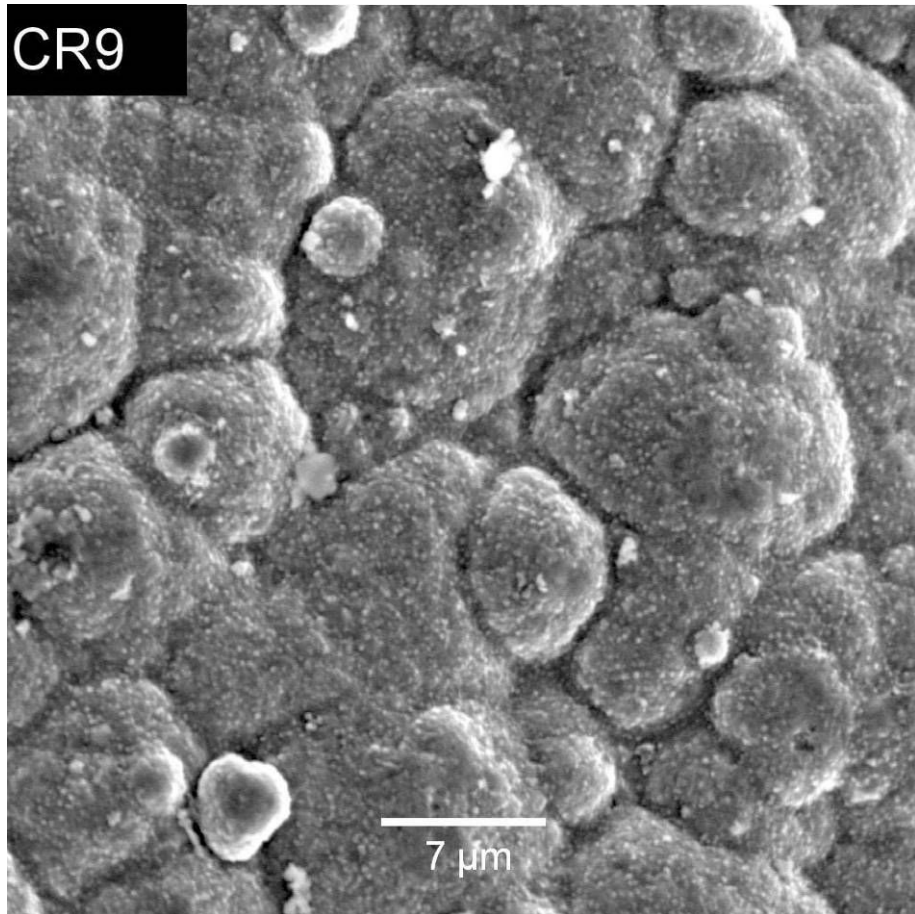


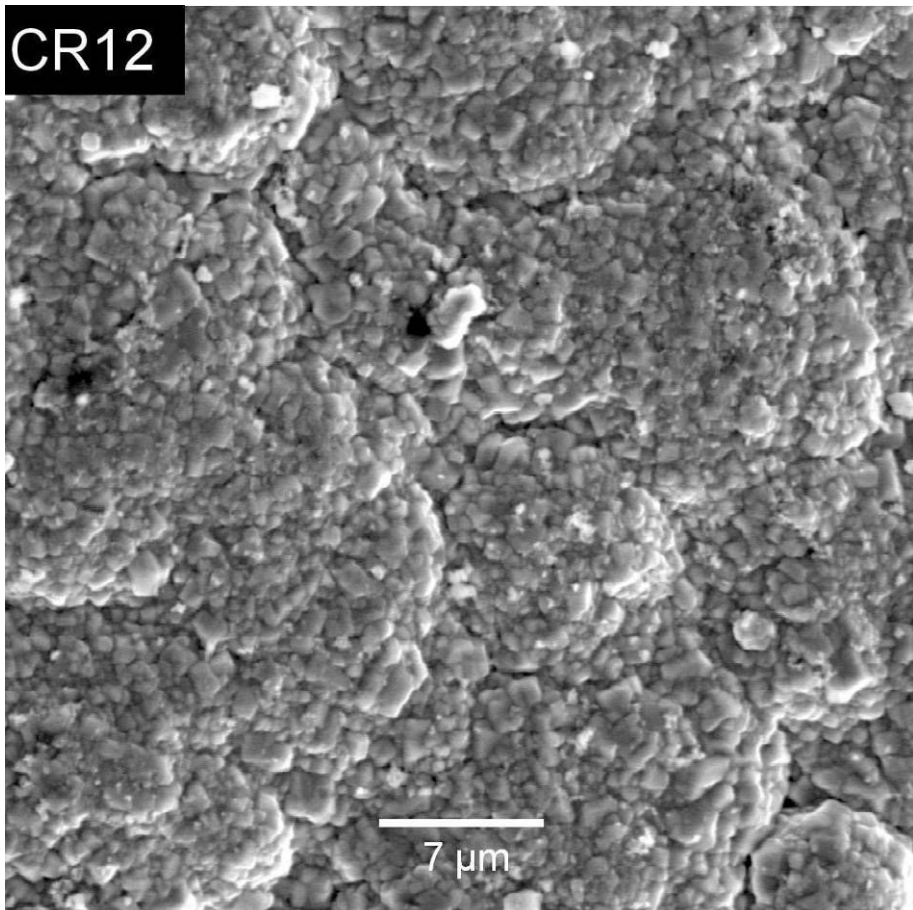
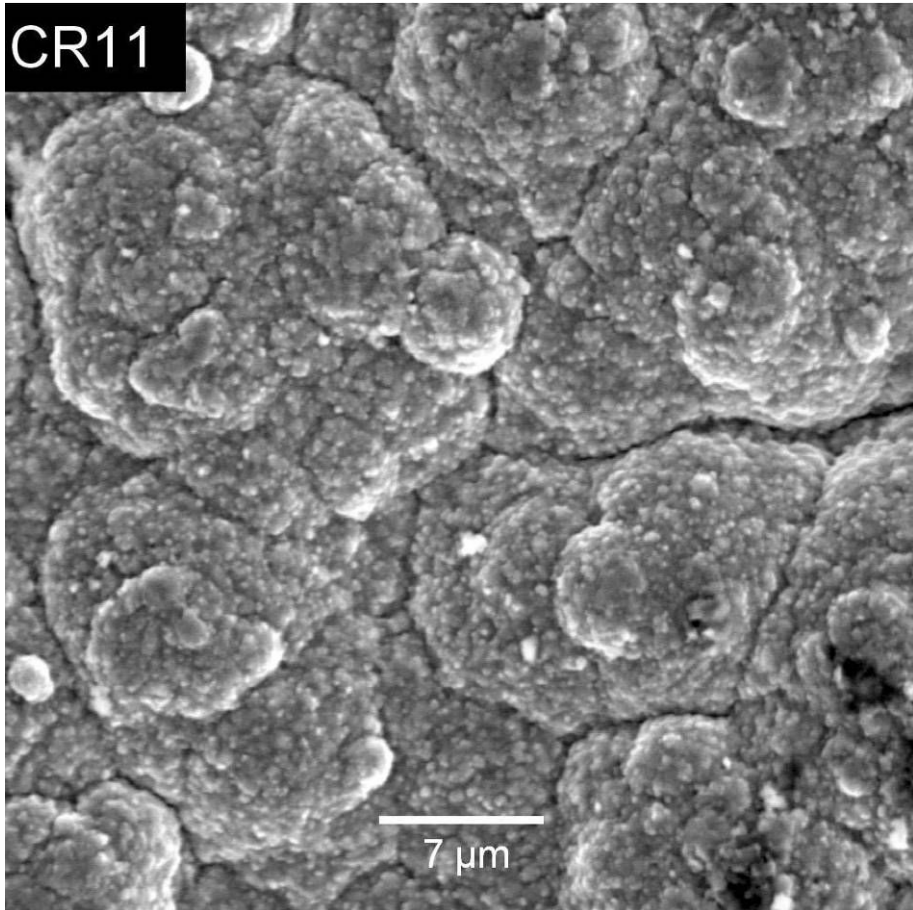
3 SURFACE STRUCTURE SECONDARY ELECTRON IMAGE

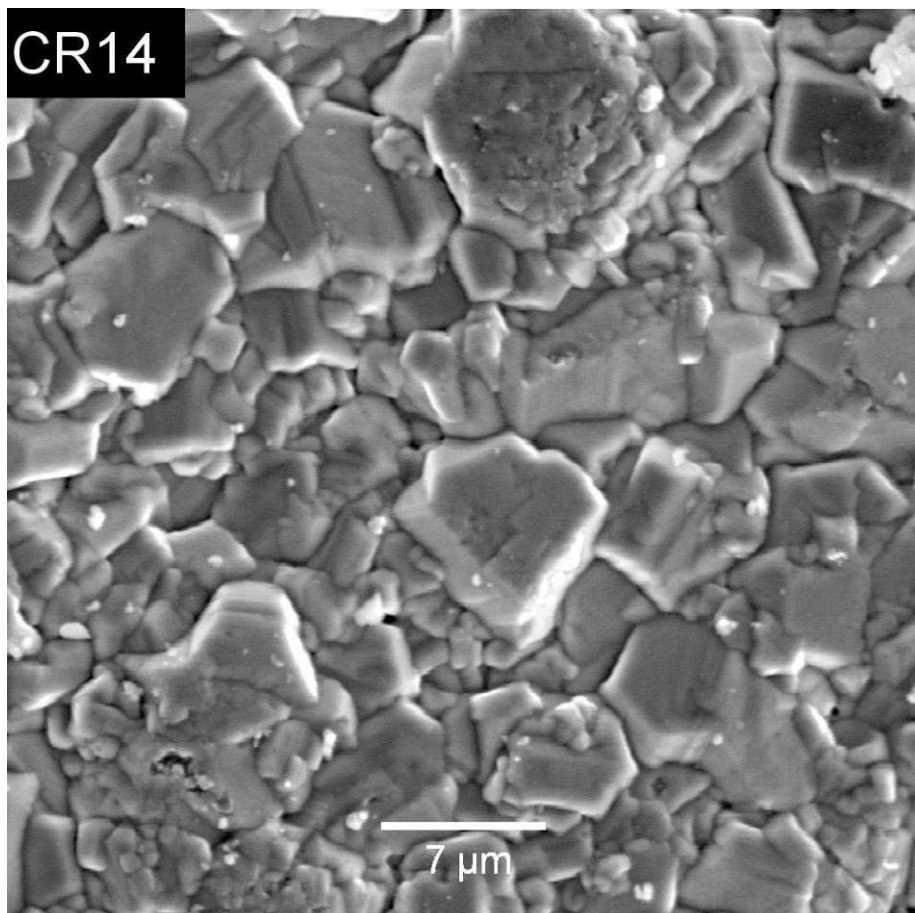
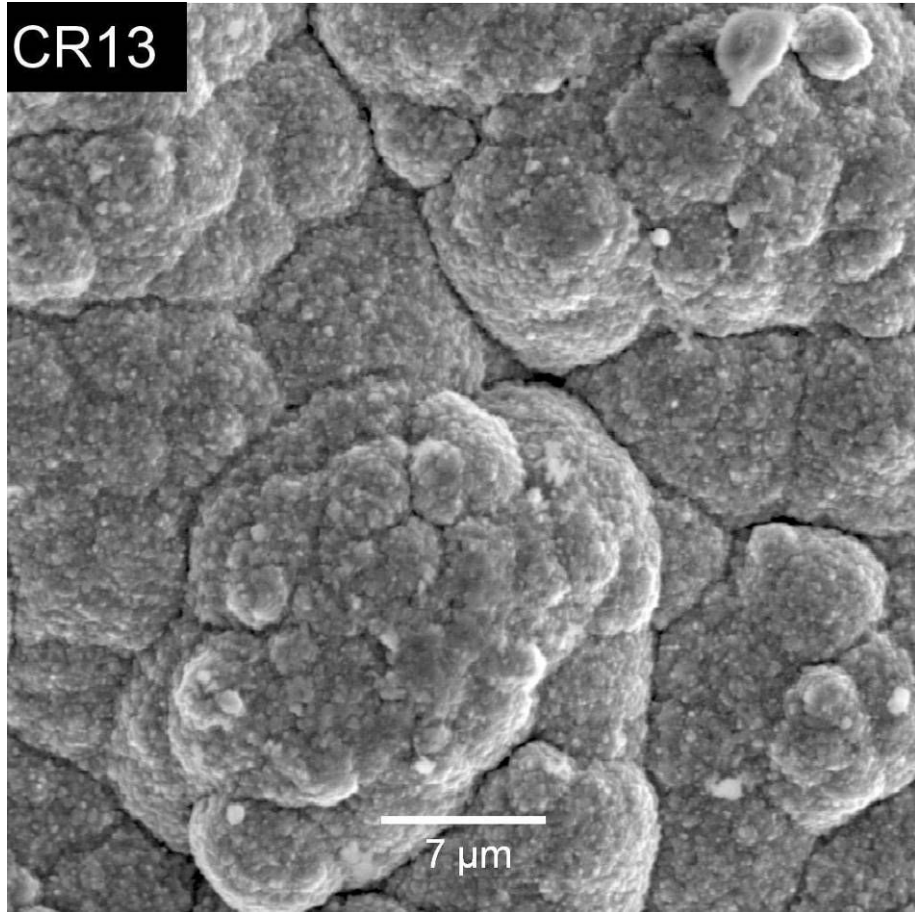
3.1 COLD INLET.

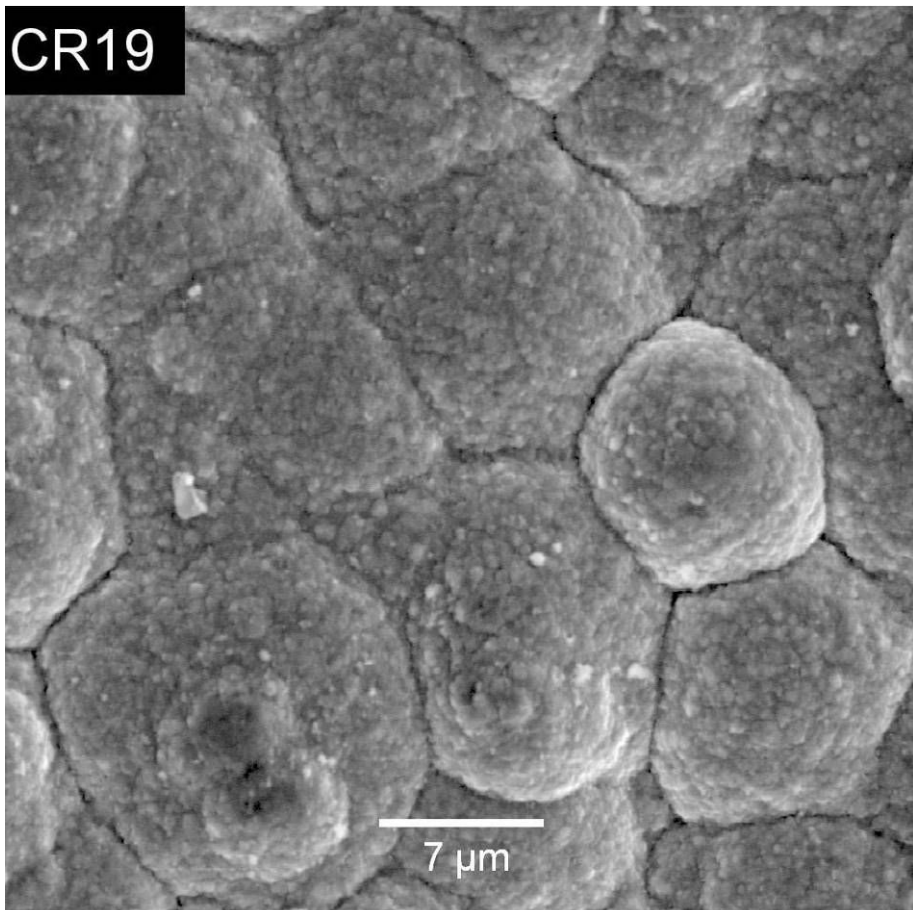
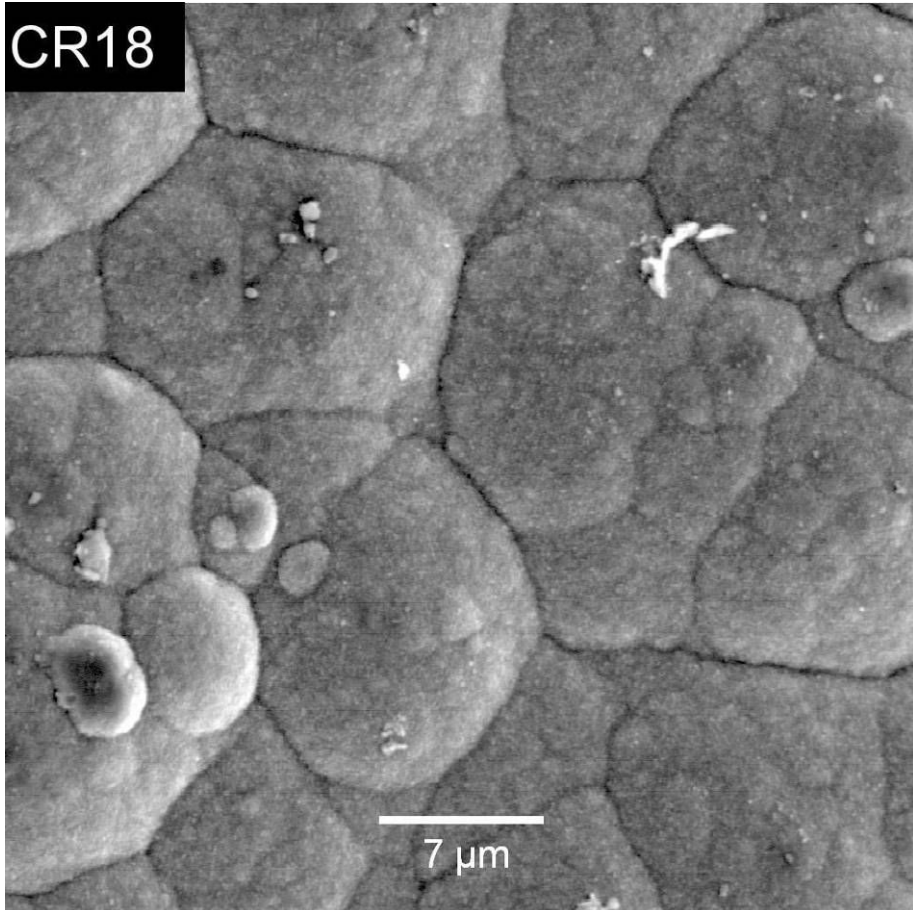




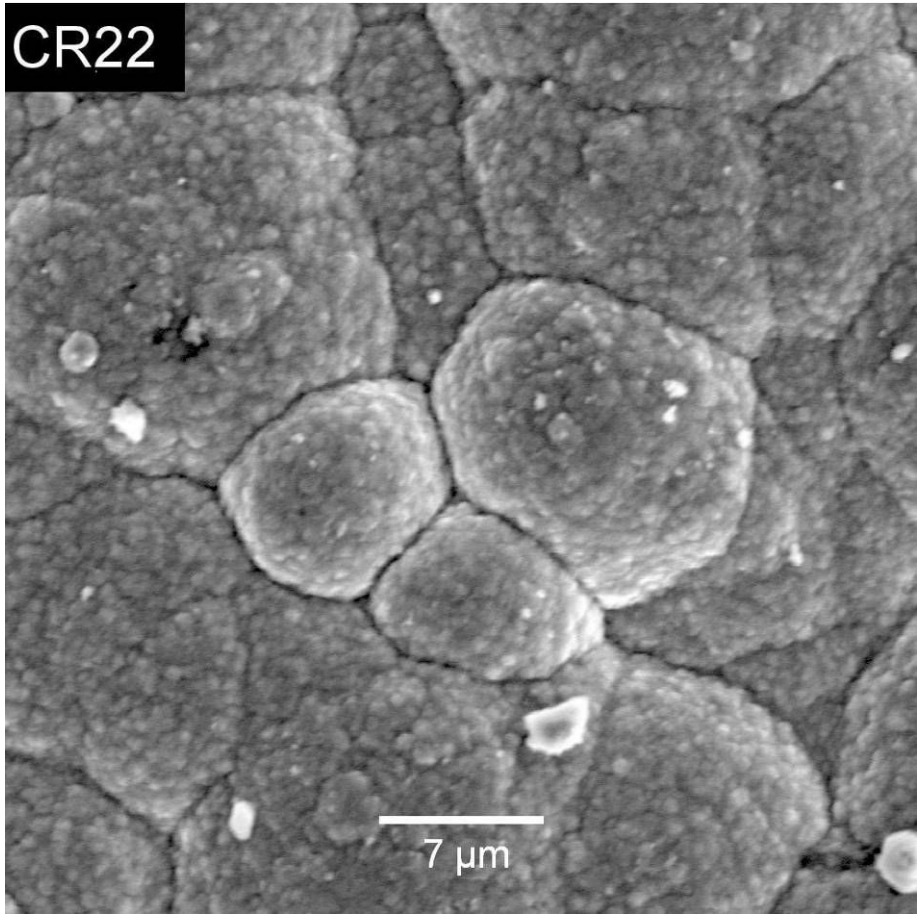




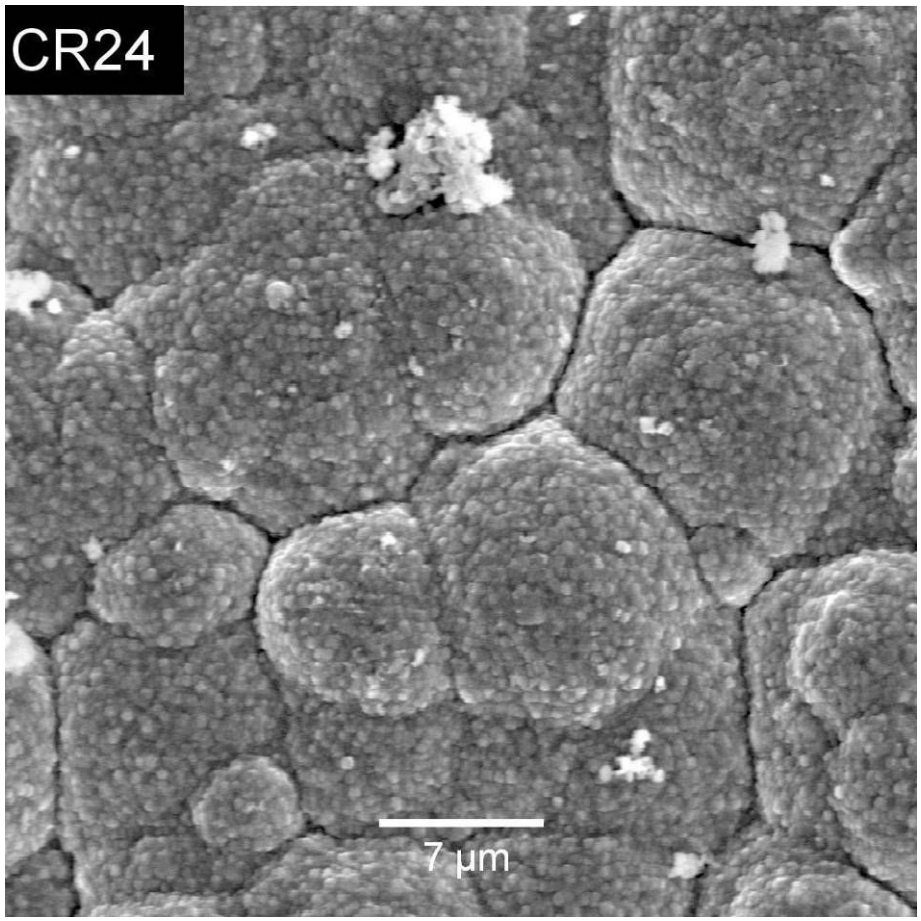


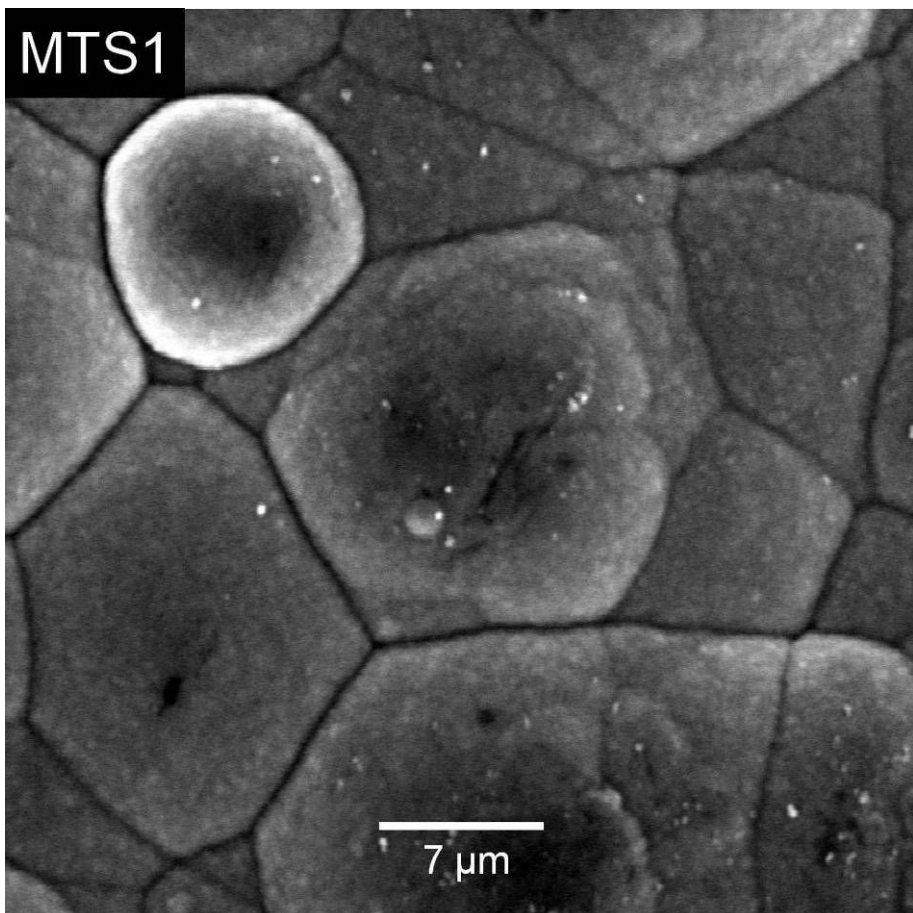
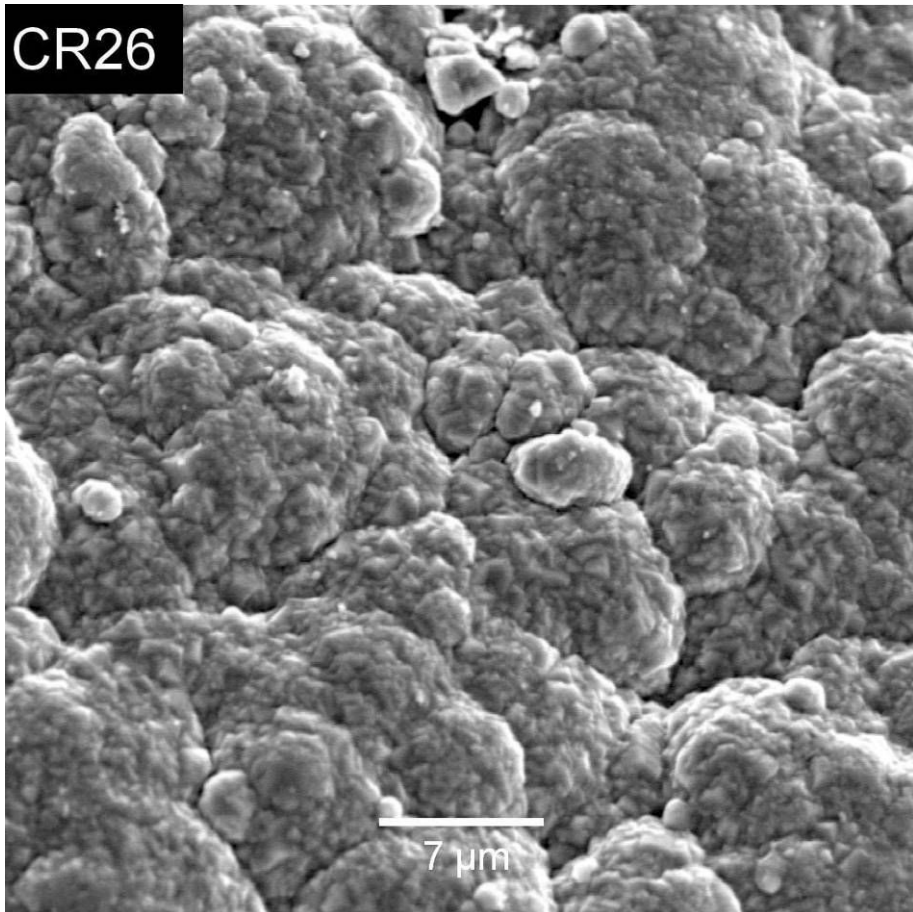


CR22



CR24





3.2 HOT INLET

